University of Nottingham
UK | CHINA | MALAYSIA

# Assessment of nanomaterials in enhancing the thermophysical properties of phase change materials for thermal management

**Adeel Arshad**

Thesis submitted to the University of Nottingham
for the degree of Doctor of Philosophy in
Mechanical Engineering

**August 2021**

*First and foremost, I dedicate to my mother, Shahnaz Arshad, the most hard–working, patienceful and intellectually–curious woman I know, who made me fall in love with books, and who dreamt the dream that I am living today.*
*To my father, Muhammad Arshad Shad, who never lost faith in me, even when I hit rock bottom.*

# *Abstract*

The rapidly growing and innovation of electronics devices with advanced *smart* and *faster* features raises a "thermal challenge" for an effective and clean cooling technology to ensure the reliable and safe operating temperature range of integrated circuits. A novel *zero–noise*, *zero–power* and *zero–emission* passive thermal management technology based on phase–change thermal energy storage systems has turned out a revolutionary advancement in smart cooling technologies. Such a cleaner, sustainable and reliable thermal management technology is integrated with such materials that have an intrinsic potential of absorbing/releasing the thermal energy during phase–transformation, called phase change materials (PCMs). The PCM can absorb/release the high energy storage density while melting/solidification process with stable phase–transition temperature range. Meanwhile, it has some issues mainly lower thermal conductivity, subcooling, less thermal stability, etc.

The present research explores the development and evaluation of new smart and novel *energy storage materials* in form of *nanocomposite phase change materials* (NCPCMs) with higher thermal conductivity, optimum enthalpy of fusion and higher heat transfer improvement with higher stability and lower subcooling for constant and transient thermal solutions. The comprehensive research literature provides the background of existing literature of nanomaterials, PCMs its classifications, NCPCMs and its classifications, stability of NCPCMs, issues and challenges of NCPCMs. To this extent, the novel mono and hybrid NCPCMs of different metallic–oxide and carbon–additives nanomaterials are prepared using two-step method and characterized to evaluate the thermophysical properties, stability and to study the heat transfer and phase–transition phenomenon during the melting/cooling process. The two different commercially available PCMs, RT–28HC and RT–35HC with phase–transition temperatures of 28 °C and 34–36 °C, respectively, are chosen, which are the most suitable for passive thermal management of smart electronic devices, photovoltaic modules and Li–ion batteries, working under the safe and reliable operating temperature range of 30–40 °C. Nanomaterials such as metallic–oxide ($TiO_2$, $Al_2O_3$, CuO) and carbon–additives (MWCNTs, GNPs, GO, rGO) are dispersed as thermal conductive materials (TCMs) to enhance the physical, chemical and thermal properties and heat transfer enhancement under natural convective conditions. Initially, the mass concentration of $TiO_2$ nanomaterials is varied from 0.0 wt.% to 2.0 wt.% in the case of mono NCPCMs. After considering the optimum mass concentration of 1.0 wt.% of nanomaterials, the comparisons are carried out of mono and hybrid nanomaterials by keeping the mass concentration ratio of 75%/25% of the total mass concentration. Secondly, the comparison of mono and hybrid NCPCMs are carried using $TiO_2$, $Al_2O_3$ and CuO based metallic–oxide nanomaterials and the thermal performance is examined by filling in a mini heat sink. Thirdly, the carbon–additives such as MWCNTs, GNPs, GO, rGO are dispersed in RT–35HC and mono and hybrid NCPCMs are synthesized and evaluated the thermophysical properties. Fourthly, the comparison of carbon–additives (GNPs and MWCNTs) and metallic–oxide ($Al_2O_3$ and CuO) based nano and hybrid NCPCMs is carried out to explore the best type and combination of mono and hybrid nanomateri-

als between the metallic–oxide and carbon–additives. The detailed experimentation is carried out using various characterization techniques such as Environmental Scanning Electron Microscopy (ESEM) and Energy–dispersive X–ray Spectroscopy (EDX), Fourier–Transform Infrared Spectroscopy (FT–IR), X–ray Diffraction (XRD), Thermogravimetric analysis (TGA) and derivative thermogravimetry (DTG), Differential Scanning Calorimeter (DSC), and Thermal Conductivity Analyser. In addition, the melting/cooling phenomenon and heat transfer performance were studied using Infrared Thermography (IRT) tests. Finally, a CuO coated metal–foam mini heat sink is designed to pour the pure PCMs and NCPCMs to evaluate the phase–change thermal cooling performance at different power levels, to mimic the heat generation inside the electronic devices.

The summarized results revealed that the carbon–additives based NCPCMs had better stability, more enhanced thermophysical and uniform melting/cooling phenomenon with low subcooling issues. A better and enhanced physical, chemical and thermal stability was achieved comparing all mono and hybrid NCPCMs of all cases with the help of surfactant. Moreover, the best stability was obtained with GNPs and MWCNTs based hybrid NCPCMs compared to all other mono and hybrid NCPCMs. The surface morphological, structural investigation and transmission spectrum disclosed the presence of GNPs, MWCNTs, GO, rGO, $TiO_2$, $\gamma-Al_2O_3$ and CuO nanomaterials in NCPCMs. The enhanced thermal conductivity results were obtained of hybrid NCPCMs and the maximum thermal conductivity of 0.443 W/m.K and thermal conductivity enhancement of 107.6% was obtained for GNPs+MWCNTs dispersed hybrid nanomaterials compared to the RT–35HC. The optimum values of latent–heats of melting/solidification of 230.82/234.19 J/g, the 13.75% enhancement in specific heat capacity, the less degree of subcooling of 3.47 °C and 0.22% deviation in peak melting temperature were observed for GNPs+MWCNTs dispersed hybrid NCPCMs. The enhancement in specific heat capacity is based on three modes: (i) higher specific heat of nanomaterials, (ii) interfacial interactional layers between solid–liquid and (iii) semi–solid liquid layers of molecules adhering to the surface of nanomaterials. The highest thermal conductivity enhancement was due to the 3D structural matrix consisted of 1D (MWCNTs) and 2D (GO/rGO/GNPs) nanomaterials structural arrangement. This 3D matrix of hybrid NCPCMs forms the 3D path for which the phonon transmission and lattice vibration transport the heat effectively in all directions of the PCM. The reduction in heat sink base temperature was achieved 8.23% with $Al_2O_3$+CuO based hybrid NCPCMs and 9.7% and 8.72% for 1.0 and 0.5 filling thickness ratio of metal–foam without PCM and with PCM, respectively, which proposed the most preferable, efficient and reliable best thermal performance for passive cooling of electronics devices.

# *Acknowledgements*

All attributes and knowledge that
you see were taught to me by other
people,
My own reality is merely that of an
empty vessel

–Saadi

Foremost, I would like to express my sincere gratitude to my supervisors, Dr. Mark Jabbal and Prof. Yuying Yan for their valuable advice, continuous support, patience during my PhD study. Their immense knowledge and plentiful experience have encouraged me in all the time of my academic research and daily life. I would like to extend my sincere gratitude to Dr. Mark, who read my numerous revisions and helped make some sense of the confusion. Also thanks to my internal accessor, Prof. Alasdair Cairns, who offered guidance and support during my internal annual examinations.

I would like to offer my special thanks and appreciation to Prof. Jo Darkwa, who has a big name in area of Energy Storage Technologies, for his insightful comments and suggestions at the start of my research. Without his support, guidance and overall insights in this field have made this an inspiring experience for me.

I would also like to thank Dr. Nicola Weston for the help with ESEM imaging, Dr. Nigel Neate, Dr. Hannah Constantin for learning and assisting with FT–IR and XRD analysis, and Dr. Jason Greaves for their technical support, guidance and assistance to learn IRT, TGA and DSC experimental techniques and instruments to accomplish my research at the Wolfson Building and Nanoscale and Microscale Research Centre at the University of Nottingham, UK. I would like to thank all the administrative and technical staff members in the L2 and L4 buildings who have been kind enough to advise and help in their respective roles. It is their kind help and support that have made my research and experimental work to make it possible on time without any trouble and stress. Also, I extend my thanks to all my colleagues at University of Nottingham for

their continuous encouragement and support, as well as to all of my friends and colleagues from Nottingham and outside for their time, advice and moral support.

I would like to extend my sincere thanks to the University of Nottingham, especially the Faculty of Engineering for awarding me the *Faculty of Engineering Research Excellence Ph.D Scholarship* to pursue my Ph.D research program. I would like to offer my special thanks to Prof. Buddhika Hewakandamby, the Chair of Fluids and Thermal Engineering (FLUTE) Research Group, providing me with the financial means to complete this project.

Last, but not least, my warm and heartfelt gratitude go to my parents, especially my mother, for their tremendous support and hope they had given to me. My accomplishments and success are because their prayers. Deepest thanks to my siblings, who keep me grounded, remind me of what is important in life, and are always supportive of my adventures. Without that hope, this thesis would not have been possible. Thank you all for the strength you gave me. I love you all...!

# *List of Publications*

### Journal articles

1. **Arshad, A.**, Jabbal, M., Yan, Y., & Darkwa, J. (2019). The micro–/nano–PCMs for thermal energy storage systems: a state of art review. *International Journal of Energy Research*, 43(11), 5572-5620. https://doi.org/10.1002/er.4550 [Chapter 2]

2. **Arshad, A.**, Jabbal, M., Yan, Y., & Reay, D. (2019). A review on graphene based nanofluids: Preparation, characterization and applications. *Journal of Molecular Liquids*, 279, 444-484. https://doi.org/10.1016/j.molliq.2019.01.153 [Chapter 2]

3. **Arshad, A.**, Jabbal, M., & Yan, Y. (2020). Synthetic jet actuators for heat transfer enhancementa critical review. *International Journal of Heat and Mass Transfer*, 146, 118815. https://doi.org/10.1016/j.ijheatmasstransfer.2019.118815 [Chapter 1 & 2]

4. **Arshad, A.**, Jabbal, M., Shi, L., Darkwa, J., Weston, N. J., & Yan, Y. (2021). Development of $TiO_2$/RT–35HC based nanocomposite phase change materials (NCPCMs) for thermal management applications. *Sustainable Energy Technologies and Assessments*, 43, 100865. https://doi.org/10.1016/j.seta.2020.100865 [Chapter 3]

5. **Arshad, A.**, Jabbal, M., & Yan, Y. (2020). Thermophysical characteristics and application of metallic–oxide based mono and hybrid nanocomposite phase change materials for thermal management systems. *Applied Thermal Engineering*, 181, 115999. https://doi.org/10.1016/j.applthermaleng.2020.115999 [Chapter 4]

6. **Arshad, A.**, Jabbal, M., Shi, L., & Yan, Y. (2021). Thermophysical characteristics and enhancement analysis of carbon-additives phase change mono and hybrid materials for thermal management of electronic devices. *Journal of Energy Storage*, 34, 102231. https://doi.org/10.1016/j.est.2020.102231 [Chapter 5]

7. **Arshad, A.**, Jabbal, M., & Yan, Y. (2020). Preparation and characteristics evaluation of mono and hybrid nano-enhanced phase change materials (NePCMs) for thermal management of microelectronics. *Energy Conversion and Management*, 205, 112444. https://doi.org/10.1016/j.enconman.2019.112444 [Chapter 6]

8. **Arshad, A.**, Jabbal, M., Sardari, P. T., Bashir, M. A., Faraji, H., & Yan, Y. (2020). Transient simulation of finned heat sinks embedded with PCM for electronics cooling. *Thermal Science and Engineering Progress*, 18, 100520. https://doi.org/10.1016/j.tsep.2020.100520

9. **Arshad, A.**, Jabbal, M., Faraji, H., Talebizadehsardari, P., Bashir, M. A., & Yan, Y. (2021). Numerical study of nanocomposite phase change material-based heat sink for the passive cooling of electronic components. *Heat and Mass Transfer*, 1-15. https://doi.org/10.1007/s00231-021-03065-2

10. **Arshad, A.**, Jabbal, M., Faraji, H., Bashir, M. A., Talebizadehsardari, P., & Yan, Y. (2021). Thermal process enhancement of HNCPCM filled heat sink: Effect of hybrid nanoparticles ratio and shape. *International Communications in Heat and Mass Transfer*, 125: 105323. https://doi.org/10.1016/j.icheatmasstransfer.2021.105323

11. **Adeel Arshad**, Mark Jabbal, Yuying Yan. Thermal performance of a PCM based heat sink in presence of nanoparticles and metal–foam to enhance cooling performance of electronics. Submitted and peer reviewed *International Journal of Heat and Mass Transfer*

12. **Adeel Arshad**, Mohammed Ibrahim Alabdullatif, Mark Jabbal, Yuying Yan. Toward the thermal management of electronic devices: A parametric investigation of finned heat sink filled with phase change materials. Submitted and peer reviewed *International Communications in Heat and Mass Transfer*.

### Conference articles

1. **Arshad, A.**, Jabbal, M., & Yan, Y. (2020, July). Thermal performance of PCM-based heat sink with partially filled copper oxide coated metal-foam for thermal management of microelectronics. In 2020 *19th IEEE Intersociety Conference on Thermal and Thermomechanical Phenomena in Electronic Systems (iTherm)* pp. 697-702. IEEE. doi: 10.1109/ITherm45881.2020.9190574 [Chapter 7]

2. **Arshad, A.**, Jackman, L., Jabbal, M., & Yan, Y. (2021). Experimental Investigation of Mini Pin-Fin Heat Sink Filled with PCM for Thermal Management. In *Advances in Heat Transfer and Thermal Engineering* (pp. 533-536). Springer, Singapore. https://doi.org/10.1007/978-981-33-4765-6_92

3. **Arshad, A.**, Talebizadehsardari, P., Bashir, M. A., Ikhlaq, M., Jabbal, M., Huang, K., & Yan, Y. (2021). Transient Simulation of Finned Heat Sinks Embedded with PCM for Electronics Cooling. In *Advances in Heat Transfer and Thermal Engineering* (pp. 527-531). Springer, Singapore. https://doi.org/10.1007/978-981-33-4765-6_91

4. **Arshad, A.**, Faraji, H., Jabbal, M., & Yan, Y. (2021, June). A numerical study of HNCPCM filled metal-foam strips based heat sink for passive cooling. In 2021 *20th IEEE Intersociety Conference on Thermal and Thermomechanical Phenomena in Electronic Systems (iTherm)* (pp. 524-530). IEEE. doi:10.1109/ITherm51669.2021.9503194

5. **Arshad, A.**, Alabdullatif, M. I., Jabbal, M., & Yan, Y. (2021, June). Thermal cooling of electronics using hybrid nanoparticles dispersed PCM based finned heat sink. In 2021 *20th IEEE Intersociety Conference on Thermal and Thermomechanical Phenomena in Electronic Systems (iTherm)* (pp. 531-537). IEEE. doi:10.1109/ITherm51669.2021.9503159

6. **Adeel Arshad**, Mark Jabbal, Hamza Faraji, Yuying Yan. Solidification improvement of a hybrid nanoparticles dispersed pcm based finned heat sink. Proceedings of the *17th UK Heat Transfer Conference (UKHTC2021)*, 8-10 September 2021, Nottingham, UK.

# Contents

**Abstract** i

**Acknowledgements** iii

**List of Publications** v

**1 Introduction** 1

1.1 Background . . . 1

1.2 Cooling techniques and challenges . . . 5

1.3 Research Motivation . . . 9

1.4 Mechanisms . . . 12

1.4.1 Thermal energy storage mechanism . . . 12

1.4.2 Thermal conduction mechanism . . . 13

1.4.2.1 Solid . . . 13

1.4.2.2 Liquid . . . 15

1.5 Research Questions . . . 16

1.6 Aims and Objectives . . . 17

1.7 Research methodology . . . 18

1.8 The structure of the Thesis . . . 21

**2 Literature Review** 23

2.1 Introduction . . . 23

2.2 Nanomaterials (NMs) . . . 26

2.2.1 Classification of Nanomaterials and their characteristics . 29

2.2.1.1 According to origin of nanomaterials . . . 29

2.2.1.1.1 Natural . . . 30

2.2.1.1.2 Artificial . . . 30

2.2.1.2 According to dimensionality of nanomaterials . 30
2.2.1.2.1 Zero-dimensional (0D) . . . . . 30
2.2.1.2.2 One-dimensional (1D) . . . . . 31
2.2.1.2.3 Two-dimensional (2D) . . . . . 31
2.2.1.2.4 Three-dimensional (3D) . . . . . 31
2.2.1.3 According to morphology of nanomaterials . . . 31
2.2.1.3.1 High aspect–ratio . . . . . 32
2.2.1.3.2 Low aspect–ratio . . . . . 32
2.2.1.4 According to composition of nanomaterials . . . 32
2.2.1.4.1 Single material . . . . . 32
2.2.1.4.2 Composites . . . . . 32
2.2.1.5 According to uniformity and agglomeration of nanomaterials . . . . . 33
2.2.1.5.1 Isometric: . . . . . 33
2.2.1.5.2 Inhomogeneous: . . . . . 34
2.2.1.6 According to structure of nanomaterials . . . . 34
2.2.1.6.1 Organic nanomaterials . . . . . 34
2.2.1.6.2 Inorganic nanomaterials . . . . . 34
2.2.1.6.3 Polymeric nanomaterials . . . . . 34
2.2.1.6.4 Composites nanomaterials . . . . . 35
2.3 Thermal energy storage (TES) . . . . . 35
2.3.1 Sensible heat storage (SHS) . . . . . 35
2.3.2 Latent heat storage (LHS) . . . . . 35
2.3.3 Chemical energy storage (CES) . . . . . 37
2.3.3.1 Chemical reaction heat storage (CRHS) . . . . 37
2.3.3.2 Chemical sorption heat storage (CSHS) . . . . 39
2.4 PCMs and their classifications . . . . . 39
2.4.1 Organic PCMs (OPCMs) . . . . . 44
2.4.1.1 Paraffin compounds . . . . . 44
2.4.1.2 Non–paraffin compounds . . . . . 45

2.4.1.2.1 Fatty acids . . . 45
2.4.1.2.2 Alcohols . . . 46
2.4.1.2.3 Esters . . . 46
2.4.1.2.4 Poly(ethylene glycol)s . . . 46
2.4.2 Inorganic PCMs (IPCMs) . . . 47
2.4.2.1 Salt . . . 47
2.4.2.2 Salt hydrates . . . 48
2.4.2.3 Metallics . . . 49
2.4.3 Eutectics . . . 50
2.5 Nanocomposite PCMs . . . 51
2.6 Ideal characteristics of NCPCM . . . 51
2.7 Preparation of NCPCMs . . . 54
2.7.1 One–step method . . . 57
2.7.2 Two–step method . . . 58
2.8 Classifications of NCPCMs . . . 63
2.8.1 Metallic–additives NCPCMs . . . 64
2.8.2 Metallic–oxide additives NCPCMs . . . 65
2.8.3 Carbon–additives NCPCMs . . . 68
2.9 Characteristics evaluation techniques of NCPCMs . . . 74
2.9.1 Chemical Analysis . . . 75
2.9.1.1 X–Ray diffraction (XRD) . . . 75
2.9.1.2 Fourier transformed infrared spectroscopy (FT–IR) . . . 76
2.9.1.3 Energy-dispersive X-ray spectroscopy (EDX) . . . 77
2.9.2 Thermal Analysis . . . 77
2.9.2.1 Thermal conductivity analysers . . . 77
2.9.2.2 Differential scanning calorimeter (DSC) . . . 78
2.9.2.3 Thermogravimetrical analysis (TGA) . . . 78
2.9.2.4 Infrared thermography (IRT) test . . . 78

2.9.3 Physical Analysis . . . . . 79
2.9.3.1 Dynamic Light Scattering (DLS) . . . . . 79
2.9.3.2 Scanning electron microscopy (SEM) . . . . . 79
2.10 Stability of NCPCMs . . . . . 80
2.10.1 Physical stability . . . . . 80
2.10.2 Chemical stability . . . . . 82
2.10.3 Thermal stability . . . . . 82
2.10.4 Thermal reliability . . . . . 83
2.10.5 Methods to enhance the stability of NCPCMs . . . . . 86
2.10.6 Stability mechanism of NCPCMs . . . . . 88
2.11 Issue and challenges of NCPCMs . . . . . 89
2.12 Summary of the literature review . . . . . 90

**3 Development of metallic–oxide mono nanocomposite phase change materials 94**

3.1 Introduction . . . . . 95
3.2 Experimental description . . . . . 99
3.2.1 Materials . . . . . 99
3.2.2 Preparation of nanocomposite PCMs . . . . . 99
3.3 Characterization methods . . . . . 100
3.3.1 Morphology and chemical interaction analysis . . . . . 101
3.3.2 Thermophysical properties analysis . . . . . 102
3.4 Results and discussions . . . . . 103
3.4.1 Morphological and elemental analysis . . . . . 103
3.4.2 Chemical composition analysis . . . . . 105
3.4.3 Crystallography analysis . . . . . 106
3.4.4 Thermal stability analysis . . . . . 108
3.4.5 Phase-change thermal properties analysis . . . . . 110
3.4.6 Thermal conductivity analysis . . . . . 115
3.4.7 Specific heat capacity analysis . . . . . 118
3.4.8 Infrared thermography analysis . . . . . 123

3.5 Concluding Remarks . . . . . 124

**4 Development of metallic–oxide mono and hybrid nanocomposite phase change materials 127**

4.1 Introduction . . . . . 128

4.2 Experimental procedure and characterizations . . . . . 132

4.2.1 Materials . . . . . 132

4.2.2 Preparation of nanocomposite PCMs . . . . . 132

4.3 Characterizations techniques . . . . . 133

4.3.1 Microstructural and chemical interaction analysis . . . . 133

4.3.2 Thermophysical properties analysis . . . . . 134

4.3.3 Thermal cooling performance analysis . . . . . 135

4.4 Results and discussions . . . . . 137

4.4.1 ESEM and EDX analysis . . . . . 137

4.4.2 FT-IR analysis . . . . . 138

4.4.3 XRD analysis . . . . . 142

4.4.4 TGA and DTG analysis . . . . . 143

4.4.5 DSC analysis . . . . . 144

4.4.6 Thermal conductivity measurements . . . . . 150

4.4.7 Specific heat capacity analysis . . . . . 152

4.4.8 IRT analysis . . . . . 156

4.4.9 Transient thermal analysis . . . . . 157

4.4.9.1 Melting process . . . . . 159

4.4.9.2 Cooling process . . . . . 159

4.5 Concluding Remarks . . . . . 161

**5 Development of carbon–additives phase change mono and hybrid materials 164**

5.1 Introduction . . . . . 165

5.2 Research Methodology . . . . . 169

5.2.1 Materials selection . . . . . 169

5.2.2 Preparation of NCPCMs composites . . . . . 169

5.2.3 NCPCMs characterizations . . . . . 171
5.2.3.1 Physical and chemical analysis . . . . . 171
5.2.3.2 Thermal analysis . . . . . 173
5.3 Results and discussions . . . . . 174
5.3.1 Surface morphology analysis . . . . . 174
5.3.2 Chemical composition analysis . . . . . 175
5.3.3 Crystallography analysis . . . . . 178
5.3.4 Thermal stability analysis . . . . . 179
5.3.5 Phase–change thermal properties analysis . . . . . 181
5.3.6 Thermal conductivity analysis . . . . . 187
5.3.7 Specific heat capacity analysis . . . . . 191
5.4 Concluding remarks . . . . . 198

**6 Development of metallic–oxide and carbon–additives phase change mono and hybrid materials 201**

6.1 Introduction . . . . . 202
6.2 Experimental procedure . . . . . 207
6.2.1 Materials . . . . . 207
6.2.2 Preparation of NCPCMs . . . . . 208
6.2.3 Characterizations methods . . . . . 208
6.2.3.1 Environmental Scanning electron microscopy (ESEM) and Energy–dispersive X–ray spectroscopy (EDX) . . . . . 209
6.2.3.2 Fourier–transform infrared spectroscopy (FTIR) 209
6.2.3.3 X–ray diffraction (XRD) . . . . . 210
6.2.3.4 Thermogravimetric analysis (TGA) and derivative thermogravimetry (DTG) . . . . . 210
6.2.3.5 Differential scanning calorimeter (DSC) . . . . 210
6.2.3.6 Thermal conductivity measurement . . . . . 211
6.2.3.7 Infrared thermography (IRT) test . . . . . 211
6.3 Results and discussions . . . . . 211

6.3.1 Morphological and elemental analysis . . . . . 211
6.3.2 FT–IR analysis . . . . . 215
6.3.3 XRD analysis . . . . . 217
6.3.4 TGA and DTG analysis . . . . . 219
6.3.5 DSC analysis . . . . . 222
6.3.6 Thermal conductivity analysis . . . . . 231
6.3.7 Infrared thermography (IRT) analysis . . . . . 235
6.4 Concluding remarks . . . . . 237
**7 Experimental analysis of metal–foam/PCM based heat sink 240**
7.1 Introduction . . . . . 241
7.2 Experimental Setup and Measurement . . . . . 243
7.3 Results and discussion . . . . . 247
7.3.1 Heat transfer performance of filling thickness ratio without PCM . . . . . 247
7.3.2 Heat transfer performance of filling thickness of metal foam ratio with PCM . . . . . 248
7.3.3 Heat transfer performance at different power levels for charging and discharging cycles . . . . . 250
7.4 Conclusions . . . . . 251
**8 Conclusions and Future Recommendations 253**
8.1 Conclusions . . . . . 253
8.2 Recommendations for the future research . . . . . 259
**Bibliography 262**
**Appendices 299**
**A List of Abbreviations 299**
**B List of Paraffins 301**
**C List of Fatty acids 303**
**D List of Poly(ethylene glycol)s 304**
**E List of Salt and Salt hydrates 305**

**F List of Metallics** **311**

**G List of Eutectics** **313**

**H List of Metallic–additives NCPCMs** **317**

**I List of Metallic–oxide additives NCPCMs** **321**

**J List of Carbon–additives NCPCMs** **326**

# List of Tables


1.1 *Heat transfer research needs for the definition of thermal design criteria* (Nakayama, 1986) . . . . . 9

2.1 Advantages and disadvantages of PCMs (Smith et al., 2014; Liu et al., 2015b; Hyun et al., 2014) . . . . . 42

2.2 Methods of preparation of NCPCM. . . . . 55

2.3 Summary of NCPCM synthesized by Stirring and Sonication technique . . . . . 61

2.3 Summary of NCPCM synthesized by Stirring and Sonication technique . . . . . 62

2.4 Thermal conductivity values of metallic NMs at 300 K (Babar and Ali, 2019; Bergman et al., 2011). . . . . 65

2.5 Thermal conductivity values of metallic-oxide NMs at 300 K (Bergman et al., 2011; Khan et al., 2019). . . . . 66

3.1 *Thermophysical properties of RT–35HC.* . . . . . 99

3.2 *Decomposition temperatures and residue of $TiO_2$ and RT–35HC based NCPCMs.* . . . . . 110

3.3 *Thermal properties of $TiO_2$ and RT–35HC based NCPCMs*.* . . 114

3.4 *Coefficients of the third–order polynomials in solid–state, $C_p$ (J/g.°C).* . . . . . 121

4.1 *Thermophysical properties of RT–35HC.* . . . . . 132

4.2 *The temperature changes and residue of $TiO_2$, $Al_2O_3$, $CuO$ and RT–35HC based mono and hybrid NCPCMs.* . . . . . 144

4.3 *Phase–change thermal properties of $TiO_2$, $Al_2O_3$, CuO and RT–35HC based mono and hybrid NCPCMs**. . . . . 149
4.4 *Coefficients of the third-order polynomials in solid-state, $C_p$ (J/g.°C).* 156

5.1 Thermophysical properties of PCM (RT–35HC). . . . . 169
5.2 *The decomposition temperatures and residual amount of carbon–additives mono and hybrid NCPCMs.* . . . . . 181
5.3 *Phase–change thermal properties of carbon–additives mono and hybrid NCPCMs**. . . . . 186
5.4 *Coefficients of the third–order polynomials in solid–state, $C_p$ (J/g.°C).* . . . . . 195

6.1 Thermal properties of RT–28HC. . . . . 207
6.2 Decomposition temperatures and residue of mono and hybrid NCPCMs. . . . . 221
6.3 Phase-change properties of mono and hybrid NCPCMs*. . . . . 230

7.1 Thermophysical properties of PCM and heat sink. . . . . 246
7.2 Properties of copper metal–foam . . . . . 246

B.1 *Thermophysical properties of paraffins.* . . . . . 301

C.1 *Thermo-physical properties of fatty acids.* . . . . . 303

D.1 *Thermo-physical properties of PEGs.* . . . . . 304

E.1 *Thermo-physical properties of salt hydrates.* . . . . . 305

F.1 *Thermo-physical properties of metallics PCMs.* . . . . . 311

G.1 *Thermophysical properties of organic–organic (fatty acids compounds) eutectic PCMs.* . . . . . 313
G.2 *Thermophysical properties of organic–organic (PEO/fatty acids compounds) eutectic PCMs.* . . . . . 314
G.3 *Thermophysical properties of inorganic–inorganic eutectic PCMs.* 314

H.1 Summary of the developed metallic NMs additives NCPCM. . . 318
H.1 Summary of the developed metallic NMs additives NCPCM. . . 319
H.1 Summary of the developed metallic NMs additives NCPCM. . . 320

I.1 Summary of the developed metallic-oxide NMs additives NCPCM. 322
I.1 Summary of the developed metallic-oxide NMs additives NCPCM. 323
I.1 Summary of the developed metallic-oxide NMs additives NCPCM. 324
I.1 Summary of the developed metallic-oxide NMs additives NCPCM. 325

J.1 Summary of the developed carbon-additives NMs additives NCPCM. 327
J.1 Summary of the developed carbon-additives NMs additives NCPCM. 328
J.1 Summary of the developed carbon-additives NMs additives NCPCM. 329
J.1 Summary of the developed carbon-additives NMs additives NCPCM. 330
J.1 Summary of the developed carbon-additives NMs additives NCPCM. 331
J.1 Summary of the developed carbon-additives NMs additives NCPCM. 332
J.1 Summary of the developed carbon-additives NMs additives NCPCM. 333
J.1 Summary of the developed carbon-additives NMs additives NCPCM. 334
J.1 Summary of the developed carbon-additives NMs additives NCPCM. 335
J.1 Summary of the developed carbon-additives NMs additives NCPCM. 336
J.1 Summary of the developed carbon-additives NMs additives NCPCM. 337

# List of Figures


1.1 *Projection of maximum heat flux and power dissipation for microprocessor chips*(Murshed and de Castro, 2017). . . . . 2

1.2 *The ITRS (2006) projections of chip size, transistor density and physical gate length of high performance microprocessor chips*(Murshed and de Castro, 2017). . . . . 3

1.3 *Temperature dependence of failure rate of electronics devices*(Murshed and de Castro, 2017). . . . . 5

1.4 *Innovative cooling technologies for TM of electronics*(Anandan and Ramalingam, 2008; Lasance and Simons, 2005). . . . . 7

1.5 *Comparison of heat removal rate (heat flux) by conventional methods* (Murshed and de Castro, 2017). . . . . 8

1.6 *Major causes of electronics failures* (Yeh, 1995). . . . . 9

1.7 *Temperature variation of PCM during heating and cooling processes* (Leong et al., 2019). . . . . 11

1.8 *Spring vibration heat transfer system composed of crystal atoms and abstract phonons (Wu et al., 2019).* . . . . . 15

1.9 *(a) Schematic symbol of phonon (b) Temperature gradient from heat source to cold sink and phonon energy (Mehra et al., 2018).* 16

1.10 *Phonon scattering modes of (a) phonon-phonon scattering, (b) phonon-impurity scattering and (c) phonon-boundary scattering. (Mehra et al., 2018).* . . . . . 16

1.11 *Methodology of research adopted in current thesis.* . . . . . 20

2.1 *Logarithmical length scale showing size of nanomaterials compared to biological components and definition of nano and micro sizes (Buzea et al., 2007).* . . . . . 28
2.2 *Classification of NMs from the point of view of nanostructure dimensions, morphology, composition, uniformity and agglomeration state (Buzea et al., 2007).* . . . . . 29
2.3 *Classification of NMs according to composition.* . . . . . 33
2.4 *Classification of thermal energy storage*(Sharma et al., 2009). . . 36
2.5 *Phase transition diagram of PCMs involving interchangeable thermal regimes under thermal excitation and de–excitation states. Lower excitation state signifies the transition point where PCMs undergo solid-solid phase change which is based on structural changes such as $\beta$-phase taking place first, while $\alpha$-phase occurs just after $\beta$-phase but below the melting point. Mush state is expected to consist of marginal fraction of $\alpha$-phase and major fraction of liquid state (Gulfam et al., 2019).* . . . . . 37
2.6 *Classes of materials that can be used as PCMs with respect to their melting temperature and melting enthalpy (graph: ZAE Bayern)* (Mehling and Cabeza, 2007). . . . . 40
2.7 *Melting temperature and latent heat of fusion relationship of various PCMs* (Su et al., 2015). . . . . 40
2.8 *Classification of PCMs* (Pielichowska and Pielichowski, 2014; Sharma et al., 2015). . . . . 41
2.9 *Ideal characteristics of NCPCM.* . . . . . 53
2.10 Customised synthesised methods of NCPCM. . . . . 55
2.11 Schematic representation of one–step method. . . . . 58
2.12 Schematic representation of two–step method. . . . . 60
2.13 Classifications of nanocomposite PCMs. . . . . 63
2.14 Thermal conductivity values of metallic NMs at 300 K. . . . . 65
2.15 Thermal conductivity values of metallic-oxide NMs at 300 K. . . 67

2.16 Thermal properties of carbon allotropes and their derivatives (Balandin, 2011). . . . . 70

2.17 Structures of graphene-based materials show (a) the pristine graphene (pure-arranged carbon atoms) with $sp^2$-hybridized carbon atoms, and the chemically modified graphene, including (b) GO; (c) rGO and (d) GQD (Suvarnaphaet and Pechprasarn, 2017). . . . . 71

2.18 Classification grid for the categorization of different graphene types according to three fundamental graphene–based material properties: number of graphene layers, average lateral dimension, and atomic carbon/oxygen ratio. The different materials drawn at the six corners of the box represent the ideal cases according to the lateral dimensions and the number of layers (Wick et al., 2014). . . . . 71

2.19 Different allotropes of carbon (Atta et al., 2015). . . . . 72

2.20 *characteristics evaluation techniques of NCPCMs.* . . . . . 75

2.21 *Sedimentation images of $Al_2O_3$/paraffin NCPCMs in the absence (A) and in the presence (BE) of SSL after 1 day* (Nourani et al., 2016a). . . . . 81

2.22 *Images of 3 wt% of $TiO_2$/paraffin NCPCMs (a) with SSL (b) without SSL* (Sami and Etesami, 2017). . . . . 81

2.23 *FT-IR spectra for NPG, NPG+0.5, 1 and 3wt% CuO before and after 100 thermal cycles* (Praveen and Suresh, 2018). . . . . 82

2.24 *FT-IR spectra before and after cycling for: a) 3wt% GNPs/MA NCPCM; b) 3wt% MWCNTs/MA NCPCM; and c) 3wt% NG/MA NCPCM* (He et al., 2019b). . . . . 83

2.25 *(a) TGA and (b) DTG thermograms of TGA curves of PA and NEOPCM4 (Sharma et al., 2016).* . . . . . 84

2.26 *TGA curve of NPG, NPG+0.5, 1 and 3wt% CuO before and after 100 thermal cycles* (Praveen and Suresh, 2018). . . . . 84

2.27 *Effect of thermal cycles on phase change temperature during (a) melting and (b) solidification. Effect of thermal cycles on latent heat during (c) melting and (d) solidification (Harikrishnan et al., 2014).* . . . . . 85

2.28 Schematic of the stabilizing mechanisms, (a) electrostatic stabilization, (b) steric stabilization, (c) and (e) stabilizing mechanism of triethanolamine (TEA) as dispersant for the $TiO_2$erythritol system, (d) the structure of SDBS. (Zhichao et al., 2015). . . . . 89

3.1 *Schematic diagram of sample preparation of $TiO_2$ and RT–35HC based NCPCMs.* . . . . . 101

3.2 *$TiO_2$ NCPCMs after sonication : (a) NCPCM1, (b) NCPCM2, (c) NCPCM3, (d) NCPCM4.* . . . . . 101

3.3 *ESEM images of (a)$TiO_2$ NPs, NCPCM4 (b) LFD and (c) BSED at 500 magnification, (d) LFD and (e) BSED at 1000 magnification. The grey zones show the RT–35HC and white dots are the $TiO_2$ nanoparticles which are agglomerated on the nanoscale but dispersed on the microscale.* . . . . . 104

3.4 *EDX mapping of NCPCM4 (a) carbon-(red), (b) oxygen-(cyan), (c) Titanium-(green).* . . . . . 105

3.5 *EDX map of Qxygen, Titanium, and carbon elements present in NCPCM4.* . . . . . 106

3.6 *FT-IR spectrum of $TiO_2$ and RT–35HC based NCPCMs.* . . . . 107

3.7 *XRD spectrum of $TiO_2$ and RT–35HC based NCPCMs.* . . . . . 107

3.8 *(a) TGA and (b) DTG thermograms of $TiO_2$ and RT–35 based NCPCMs.* . . . . . 109

3.9 *The results of (a) Melting, (b) Solidification curves, (c) Phase–change enthalpies, (d) Degree of super–cooling and (e) Comparison of latent–heats of fusions of $TiO_2$ and RT–35HC based NCPCMs.* . . . . . 111

3.10 *Effective thermal conductivity of $TiO_2$ and RT–35HC based NCPCMs as a function of temperature.* . . . . . 116

3.11 *Effective thermal conductivity enhancement of $TiO_2$ and RT–35HC based NCPCMs as a function of temperature.* . . . . . 117

3.12 *Effective thermal conductivity ratios of $TiO_2$ and RT–35HC based NCPCMs as a function of temperature: (a) solid–phase, (b) liquid–phase.* . . . . . 118

3.13 *Schematic representation of thermal conductive networks in $TiO_2$/RT–35HC NCPCMs with increasing loading of $TiO_2$: (a) 0.5 wt.%, (b) 1.0 wt.%, (c) 1.5 wt.%, (d) 2.0 wt.%.* . . . . . 119

3.14 *The $C_p$ curves of pure RT–35HC and NCPCMs: (a)-solid–phase (b) liquid–phase.* . . . . . 120

3.15 *(a) Comparison of $C_p$ curves and (b) specific heat capacity enhancement of pure RT–35HC and NCPCMs.* . . . . . 121

3.16 *Infrared thermography images of the melting process of NCPCM1-(A), NCPCM2-(B), NCPCM3-(C) and NCPCM4-(D): at different time steps with temperature variation in °C.* . . . . . 124

4.1 *Schematic diagram of synthesizing of $TiO_2$, $Al_2O_3$, $CuO$ and RT–35HC based mono and hybrid NCPCMs.* . . . . . 134

4.2 *NCPCMs after sonication : (a) $NCPCM_{TiO_2}$, (b) $NCPCM_{Al_2O_3}$, (c) $NCPCM_{CuO}$, (d) $NCPCM_{Al_2O_3+CuO}$.* . . . . . 134

4.3 *Schematic diagram of experimental setup.* . . . . . 137

4.4 *ESEM images of $NCPCM_{TiO_2}$ (a) LFD and (b) BSED, $NCPCM_{Al_2O_3}$ (c) LFD and (d) BSED, $NCPCM_{CuO}$ (e) LFD and (f) BSED, and $NCPCM_{Al_2O_3+CuO}$ (g) LFD and (h) BSED.* . . . . . 139

4.5 *EDX mapping of $NCPCM_{TiO_2}$ (a) carbon-(red), (b)-oxygen-(purple), (c) Titanium-(green), (d)-EDX map of oxygen, carbon, and titanium elements present in $NCPCM_{TiO_2}$.* . . . . . 140

4.6 *EDX mapping of $NCPCM_{Al_2O_3+CuO}$ (a) carbon-(red), (b)-oxygen-(cyan), (c) aluminum-(green), (d) Copper-(Brown) and (e) EDX map of carbon, oxygen, aluminum and copper elements present in $NCPCM_{Al_2O_3+CuO}$.* . . . . . 141

4.7 *FT–IR spectrum of $TiO_2$, $Al_2O_3$, $CuO$ and RT–35HC based mono and hybrid NCPCMs.* . . . . . 142

4.8 *XRD pattern of $TiO_2$, $Al_2O_3$, $CuO$ and RT–35HC based mono and hybrid NCPCMs.* . . . . . 143

4.9 *(a)-TGA and (b)- DTG thermograms of $TiO_2$, $Al_2O_3$, $CuO$ and RT–35HC based mono and hybrid NCPCMs.* . . . . . 145

4.10 *The results of (a) Melting, (b) Solidification curves, (c) Phase–change enthalpies, (d) Degree of super–cooling and (e) Comparison of latent–heats of fusions of $TiO_2$, $Al_2O_3$, $CuO$ and RT–35HC based mono and hybrid NCPCMs.* . . . . . 147

4.11 *The results of (a) effective thermal conductivity and (b) effective thermal conductivity enhancement factor of $TiO_2$, $Al_2O_3$, $CuO$ and RT–35HC based mono and hybrid NCPCMs as a function of temperature.* . . . . . 151

4.12 *Specific heat capacity curves of $TiO_2$, $Al_2O_3$, $CuO$ and RT–35HC based mono and hybrid NCPCMs: (a) solid–phase (b) liquid–phase.* . . . . . 153

4.13 *(a) Comparison of specific heat capacity, (b) specific heat capacity enhancement of $TiO_2$, $Al_2O_3$, $CuO$ and RT–35HC based mono and hybrid NCPCMs.* . . . . . 155

4.14 *IRT images of the melting process of $NCPCM_{Al_2O_3}$-(X), $NCPCM_{CuO}$-(Y) and $NCPCM_{Al_2O_3+CuO}$-(Z) at different time steps with temperature variation in °C.* . . . . . 158

4.15 *(a) Melting process and (b) solidifying process of $TiO_2$, $Al_2O_3$, $CuO$ and RT–35HC based mono and hybrid NCPCMs.* . . . . . 160

5.1 Schematic diagram of samples preparation of carbon–additives mono and hybrid NCPCMs. . . . . 170

5.2 NCPCMs after 5 mins: (a) NCPCM$_{MWCNT}$, (b) NCPCM$_{GO}$, (c) NCPCM$_{rGO}$, (d) NCPCM$_{GNP}$, (e) NCPCM$_{GO+MWCNT}$, (f) NCPCM$_{rGO+MWCNT}$, (g) NCPCM$_{GNP+MWCNT}$. . . . . 172

5.3 NCPCMs after 50 mins: (a) NCPCM$_{MWCNT}$, (b) NCPCM$_{GO}$, (c) NCPCM$_{rGO}$, (d) NCPCM$_{GNP}$, (e) NCPCM$_{GO+MWCNT}$, (f) NCPCM$_{rGO+MWCNT}$, (g) NCPCM$_{GNP+MWCNT}$. . . . . 173

5.4 ESEM images of mono and hybrid NCPCMs (a) RT–35HC (b) NCPCM$_{MWCNT}$, (c) NCPCM$_{GO}$ (d) NCPCM$_{GO+MWCNT}$ (e) NCPCM$_{rGO}$ (f) NCPCM$_{rGO+MWCNT}$ (g) NCPCM$_{GNP}$ and (h) NCPCM$_{GNP+MWCNT}$. . . . . 176

5.5 *FT–IR spectrum of carbon–additives mono and hybrid NCPCMs.* 177

5.6 *XRD pattern of carbon–additives mono and hybrid NCPCMs.* . . 178

5.7 *(a)-TGA and (b)- DTGA thermograms of carbon–additives mono and hybrid NCPCMs.* . . . . . 180

5.8 *The results of (a) heating (b) cooling (c) phase–change enthalpies (d) degree of subcooling and (e) comparison of experimental and calculated latent–heats of carbon–additives mono and hybrid NCPCMs.* . . . . . 184

5.9 *The results of (a) effective thermal conductivity and (b) effective thermal conductivity enhancement factor of carbon–additives mono and hybrid NCPCMs as a function of temperature.* . . . . . 188

5.10 *Schematic representation of 3D thermal conductive arrangement of carbon–additives hybrid NCPCMs.* . . . . . 191

5.11 *Specific heat capacity curves of carbon–additives mono and hybrid NCPCMs: (a) solid-phase (b) liquid-phase.* . . . . . 192

5.12 *(a) Comparison of specific heat capacity and (b) specific heat capacity enhancement of carbon–additives mono and hybrid NCPCMs.* 194

5.13 *Schematic representation of inter-molecular interaction modes in NCPCMs causes the enhancement in specific heat capacity (a) MODE–I: High surface energy of the surface atoms in the lattice, (b) MODE–II: Interfacial interactions between the lattice atoms and liquid molecules, (c) MODE–III: A layer of semi–solid molecules adhering to the surface of lattice–atoms.* . . . . . 198

6.1 *Preparation process of NCPCMs with GNPs, MWCNTs, CuO and $Al_2O_3$.* . . . . . 209

6.2 *ESEM images of (a) RT–28HC, (b) RT–28HC/GNPs, (c) RT–28HC/MWCNTs, and (d) RT–28HC/GNPs+MWCNTs.* . . . . 212

6.3 *ESEM images of RT–28HC/$Al_2O_3$+CuO (a) LFD and (b) BSED. (The grey zones show the RT–28HC and white dots are the $Al_2O_3$+CuO nanoparticles which are agglomerated on the nanoscale but dispersed on the microscale.)* . . . . . 213

6.4 *EDX mapping of RT–28HC/$Al_2O_3$+CuO hybrid NCPCM: (a)-Carbon (red), (b)-Oxygen (purple), (c)-Aluminium (green), (d)-Copper (Brown), and (e)-EDX map of oxygen, copper, aluminium, and carbon elements present in RT–28HC/$Al_2O_3$+CuO.* 214

6.5 *Elemental spectrum and compositional analysis of RT–28HC/$Al_2O_3$+CuO.* 215

6.6 *FT–IR spectrum of GNPs, MWCNT, RT–28HC based mono and hybrid NCPCMs.* . . . . . 216

6.7 *FT–IR spectrum of CuO, $Al_2O_3$, RT–28HC based mono and hybrid NCPCMs.* . . . . . 217

6.8 *XRD pattern of GNPs, MWCNT, RT–28HC based mono and hybrid NCPCMs.* . . . . . 219

6.9 *XRD pattern of CuO, $Al_2O_3$, RT–28HC based mono and hybrid NCPCMs.* . . . . . 219

6.10 *(a)-TGA and (b)-DTG thermograms of carbon–based mono and hybrid NCPCMs.* . . . . . 221

6.11 *(a)-TGA and (b)-DTG thermograms of carbon–based metallic oxide–based mono and hybrid NCPCMs.* . . . . . 222

6.12 *DSC curves of carbon–based mono and hybrid NCPCMs.* . . . . 223

6.13 *DSC curves of metallic oxide–based mono and hybrid NCPCMs.* 224

6.14 *Phase change enthalpies of carbon–based mono and hybrid NCPCMs.* 225

6.15 *Phase change enthalpies of metallic oxide–based mono and hybrid NCPCMs.* . . . . . 226

6.16 *Degree of super–cooling of carbon–based mono and hybrid NCPCMs.* 227

6.17 *Degree of super–cooling of metallic oxide–based mono and hybrid NCPCMs.* . . . . . 227

6.18 *Comparison of latent–heats of carbon–based mono and hybrid NCPCMs.* . . . . . 228

6.19 *Comparison of latent–heats of metallic–oxide based mono and hybrid NCPCMs.* . . . . . 228

6.20 *Effective thermal conductivity of carbon–based mono and hybrid NCPCMs as a function of temperature.* . . . . . 232

6.21 *Effective thermal conductivity of metallic oxide–based mono and hybrid NCPCMs as a function of temperature.* . . . . . 232

6.22 *Effective thermal conductivity enhancement factor of carbon–based mono and hybrid NCPCMs as a function of temperature.* . 234

6.23 *Effective thermal conductivity enhancement factor of metallic oxide–based mono and hybrid NCPCMs as a function of temperature.* . . . . . 234

6.24 *Infrared thermography images of the melting process of RT–28HC-(X), RT–28HC/$Al_2O_3$+CuO-(Y) and RT–28HC/GNPs+MWCNTs-(Z) at different time steps with temperature variation in °C.* . . 236

7.1 Schematic diagram of experimental setup. . . . . 244

7.2 Transient distribution of base temperature for different filling thickness ratios without PCM: (a) Charging, (b) Discharging. . 247

7.3 Transient distribution of base temperature for different filling thickness ratios with PCM: (a) Charging, (b) Discharging. . . . 249
7.4 Temperature distribution of $\gamma_{mf} = 1.0$ at different power levels: (a) Charging, (b) Discharging. . . . . 251

# Chapter 1

# Introduction

Thermal management of electronics devices consisting of compact three dimensional (3D) integrated circuits (ICs) was the real challenge from the past and rising in the current era. With the invention of transistors in Bell Telephone laboratories in 1947 (Bardeen and Brattain, 1948) by John Bardeen and Walter Brattain, electronic devices have been taken towards miniaturization. The real question, as well as the challenge in the electronics industry is how to make possible the development of efficient and reliable cooling technologies. The rise in compactness and advance features in applications of smart electronic devices leads towards the generation of internal high heat flux as a by-product. From the definition of American Heritage Dictionary, the *heat* is defined as *the form of energy related to kinetic energy of atoms or molecules with the capability of being transmitted through solid and fluid media by conduction, through fluid media by convection, and through empty space by radiation.*

## 1.1 Background

Government and private multi–national organizations have involved with data processing, storage, and telecommunications using higher performance mini– and micro–scale electronics technologies of higher power densities particularly for high performance chips. In a typical data centre, roughly 33% of the elec-

tricity consumption is allocated to the thermal management of sever electronics (Garimella et al., 2012). Simultaneously, the total global electricity usage in data centres has increased from approximately 152 billion kWh/year in 2005 to 238 billion kWh/year in 2010 which is roughly 1.3% of global electricity (Garimella et al., 2013). In the USA alone, the total data centre energy usage amounted to 91 billion kWh/year in 2013 and is projected to reach 140 billion kWh/year in 2020 (Whitney and Delforge, 2014). As a consequences of these, there are major issues such as energy consumption, operational costs and the overall carbon footprints of server housing facilities. In 2004, according to the International Electronics Manufacturing Initiative (iNEMI) technology roadmap (Pfahl and McElroy, 2005) the high heat flux from high performance microprocessors ICs and the maximum power dissipation were projected to reach about 190 W/cm$^2$ and 360 W by 2020, presented in Fig. 1.1. However, the generation of internal heat flux from many mini–and micro–scale electronics are much higher than the projection reported in iNEMI roadmap. In 2007 (Agostini et al., 2007), a study was reported on next generation computer chips which are facing the problem of removal of high heat flux around 300 W/cm$^2$ while maintaining their chip temperature below 85 °C.

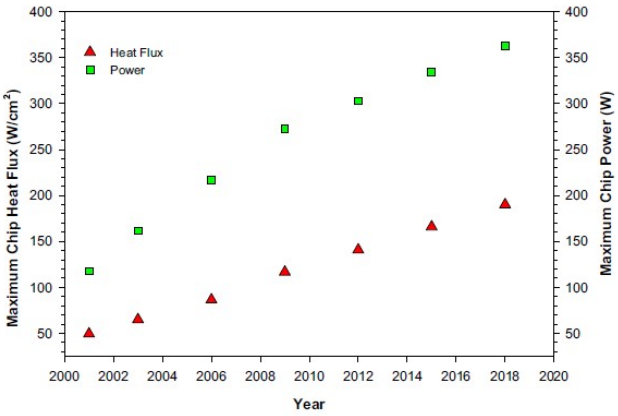


**Figure 1.1:** *Projection of maximum heat flux and power dissipation for microprocessor chips(Murshed and de Castro, 2017).*

According to the International Technology Roadmap for Semiconductors (ITRS) (Gargini), in 2006, the projections of key feature of semiconductor components were presented, shown in Fig. 1.2. From Fig. 1.2, it is analysed that transistor

chip size is continuously decreasing to 6 nm while the transistor density is rising up to 20 billion transistors/cm$^2$ by 2020. Further, the chip size production was estimated to remain around 100 mm$^2$. The miniaturization of electronics components are categorized into three level of scales as follows:

- Medium–scale integration (MSI): with $50-1000$ components/chip in the 1960.
- Large–scale integration (LSI): with $1000-100,000$ components/chip in the 1970.
- Very large–scale integration (VLSI): with $100,000-10,000,000$ components/chip in the 1980.

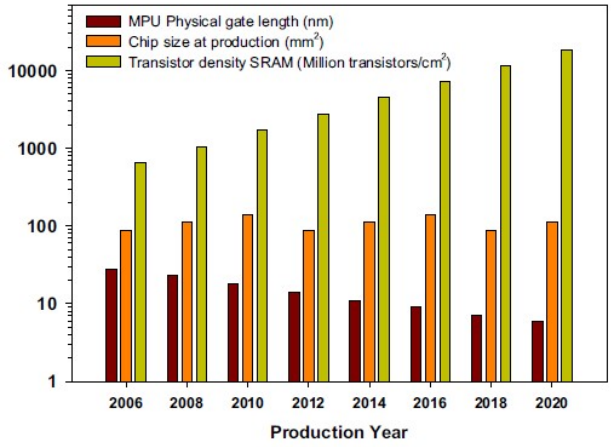


**Figure 1.2:** *The ITRS (2006) projections of chip size, transistor density and physical gate length of high performance microprocessor chips(Murshed and de Castro, 2017).*

After 1980, with the development of high–heat–flux generating electronics devices gained attention of the development of higher heat removal cooling technologies for better thermal management of both commercial and defence electronics which are dissipating heat around 1000 W/cm$^2$ and even more (Mudawar, 2001). According to the famous prediction of by Moore (1965), known as Moore's Law (Schaller, 1997), the number of transistors that can be placed on an IC extensively increasing exponentially. This progression is leading towards the shrinkage of feature size, increased transistor density, increasing the

circuit speed and higher chip performance. Generally the high–heat–flux generated inside the ICs is evaluated as the heat dissipation rate from various range of electronics devices. The heat heat fluxes are generally classified as following (Ohring, 1998b):

- High–heat–flux (HHF): $10^2 - 10^3$ W/cm$^2$
- Ultra–high–heat–flux (UHF): $10^3 - 10^4$ W/cm$^2$
- Extreme–heat–flux (EHF): $> 10^4$ W/cm$^2$

Modern electronics devices are designed on the objectives of *smaller* and *faster*. However, this compactness in size leads towards high power densities and high operating temperatures causing a reduction in performance of electronics devices. If the rate of internal heat generated not removed is equal or greater than the heat dissipation rate then ultimately the device temperature will keep increasing. As a consequences of this, electronics devices will lose their reliability and performance leading towards the failure of the device. The U.S. Department of Defense (Cluley, 1974) presented a report on the reliability prediction of electronics devices by defining the *failure factor*. The failure factor, which is the ratio of the failure rate at any temperature to the failure rate at 75 °C, increases exponentially with the increase of the base temperature of the electronics device, shown in Fig. 1.3.

Pedram and Nazarian(Pedram and Nazarian, 2006) reported a comprehensive study on the thermal modelling of very large-scale integration (VLSI) and concluded that more than 50% of all ICs failures are related to thermal issues. The operating temperature of a ICs chip is calculated by the following liner equation:

$$T_{chip} = T_a + R.\frac{P_{Tot}}{A} \tag{1.1}$$

where $T_{chip}$ is the average chip temperature, $T_a$ is the ambient temperature, $P_{Tot}$ is the total power consumption, $A$ is the chip area and $R$ is the equivalent

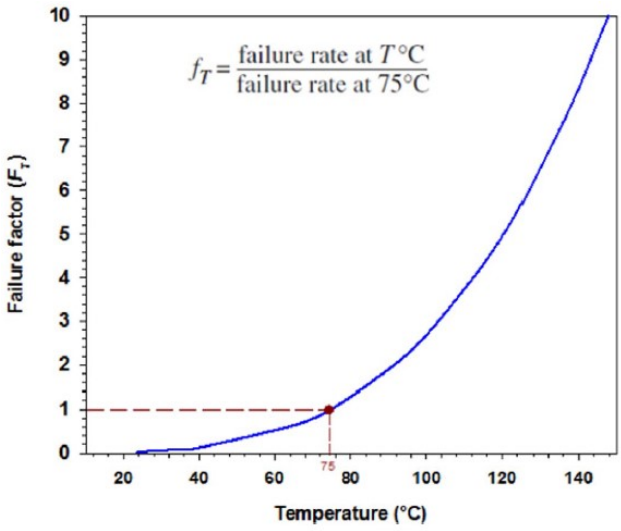


**Figure 1.3:** *Temperature dependence of failure rate of electronics devices(Murshed and de Castro, 2017).*

thermal resistance of the IC chip and heat sink. Furthermore, the reliability of the ICs for many semiconductors is exponentially dependent on the operating temperature and median–time–to–failure (MTF) in hours and can be calculated by the well–known Black's correlation (Black, 1969):

$$MTF = AJ^{-2}\exp^{Q/kT} \tag{1.2}$$

where $A$ is a process and geometry dependent constant, $J$ is the average DC current density ($/cm^2$), $Q$ is the activation energy which is equal to ∼0.7 eV, $k$ is Boltzmann's constant and $T$ is the absolute operating temperature (K).

## 1.2 Cooling techniques and challenges

The cooling technologies are categorized into two major classifications:

**1-Active cooling:** The active cooling technologies require external power source such as fan, pump and compressor for higher cooling capacity and removal of high rate of heat flux.

**2-Passive cooling:** The passive cooling technologies utilize the capillary or gravitational buoyancy forces to circulate the cooling fluid. Additionally,

the heat generated inside the electronics is absorbed by latent heat fusion of heat the cooling material and further heat transfer occurs through conduction, convection and radiation without any additional energy source. The poor heat transfer augmentation rate in some cases eclipses the merits of not using any other input energy.

A detail classification of cooling technologies for thermal solutions of electronics is shown in Fig. 1.4. The emerging technologies such as thermosyphons (Pal et al., 2002), heat pipes (Maydanik et al., 2005), free cooling Zhang et al. (2014a), micro minichannel (Liang and Mudawar, 2019), spray cooling (Kim, 2007), impinging jet (Bintoro et al., 2005), thermoelectric coolers (Simons and Chu), phase change materials based cooling (Baby and Balaji, 2012; Arshad et al., 2018b) and synthetic jet cooling (Li et al., 2015; Pavlova and Amitay, 2006) showed a great potential on cooling performance of high heat generating electronics devices.

Here, the brief summery of conventional cooling technologies and their effectiveness for cooling of electronics are presented. Based on the heat transfer effectiveness thermal management solution can be classified into four general categories as follows (Murshed and de Castro, 2017; Anandan and Ramalingam, 2008):

1. Radiation and free convection
2. Forced air–cooling
3. Forced liquid–cooling
4. Liquid evaporation

The rate of heat flux removal from electronics devices adopting the above methods is presented in Fig. 1.5 for a temperature difference of 80 °C between the heated surfaces and ambient. It is revealed that liquid evaporation cooling technique has maximum potential to remove the heat flux at better rate

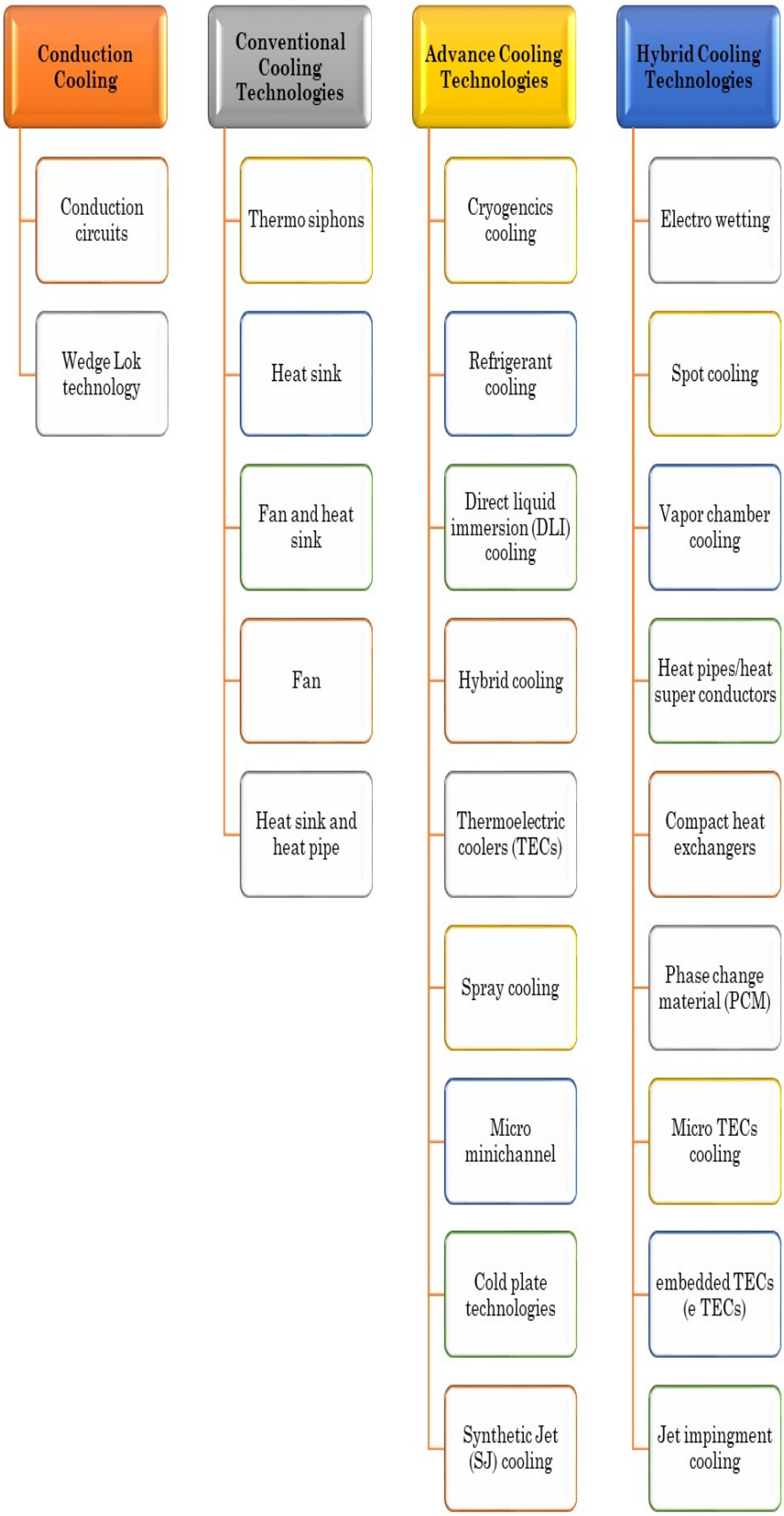


**Figure 1.4:** *Innovative cooling technologies for TM of electronics(Anandan and Ramalingam, 2008; Lasance and Simons, 2005).*

followed by the forced convection cooling using liquid as a coolant. Similarly, the using air as a coolant, the forced convection air cooling has less capability of heat removal rate but this method is widely used to cool electronics such as CPU processors, laptops etc. The lowest rate of heat flux removal is by free or natural convection which is suitable to low heat generated electronics because of simple design, reliability and low cost of cooling device.

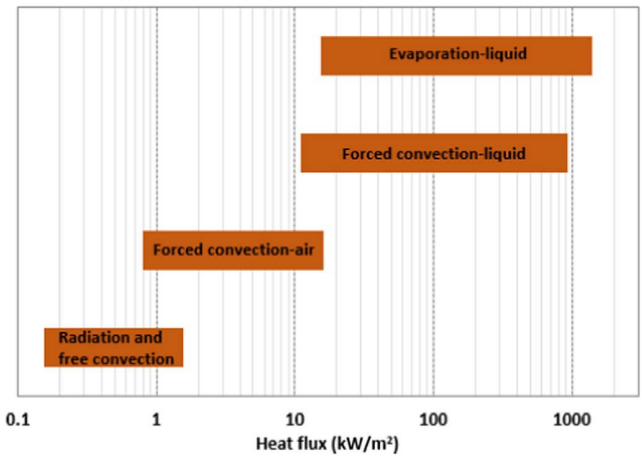


**Figure 1.5:** *Comparison of heat removal rate (heat flux) by conventional methods (Murshed and de Castro, 2017).*

Thermal design is the major and limiting factor for achieving the higher packaging densities. Fundamentally, there are two major cooling challenges: (i) removal of increasing heat flux, (ii) highly non–uniform power dissipation which faced during the cooling using any type of cooling technology for electronics packages. A study on thermal management of electronic equipment by Nakayama (Nakayama, 1986) reported the need the effective heat flow for the advancement of thermal packaging engineering in two major directions: (i) definition of appropriate design criteria and (ii) the establishment of the data base. The Fig. 1.6 (Yeh, 1995) represents the major causes of electronics failures and it can be seen that the major contribution of failure is due temperature since the power thermal design of cooling media.

The Table 1.1 represents the need of heat transfer for the effective and reliable thermal design of cooling package. From above aforementioned discussion, the continued miniaturization in technology and high demand in performance

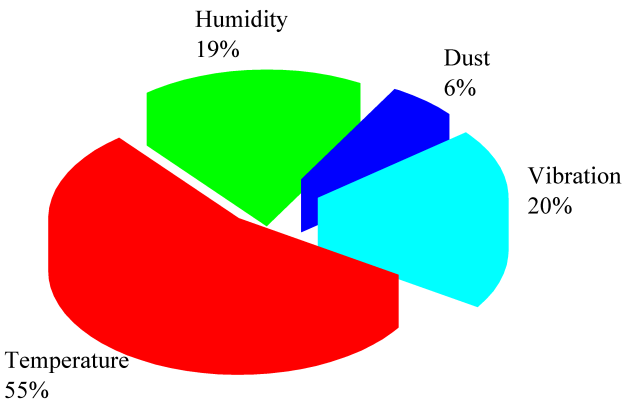


**Figure 1.6:** *Major causes of electronics failures (Yeh, 1995).*

with reliableness in electronics packages resulting the gradually increase in generation high–heat–flux hence the operating temperature. As a consequence of this the conventional cooling technologies are falling down to make possible for efficient cooling to meat demand for thermal management of modern *smart* and *faster* electronics devices. As s result of this, the new innovative cooling technologies are needed to introduce in market which can produce the required heat transfer coefficient removing.

Table 1.1: *Heat transfer research needs for the definition of thermal design criteria* (Nakayama, 1986)

| Level | Trends of Technology | Modes of Failure | Research Needs |
|---|---|---|---|
| **Chip** | Miniaturization of circuit patterns enlargement of chip area | Thermal activation energy by electrical-conductor/contact degradation Mechanical-fatigue of interconnections chemical-corrosion | Analytical and experimental tools to investigate thermal fields |
| **Package** | Flip-chip mounting Multi-chip packing | Thermal fatigue of solder joints Fracture of bonded interface in the package | Thermochemical properties of packing materials |
| **Board** | Surface mounting | Thermal fatigue of solder joint | Thermochemical properties of composite materials |

## 1.3 Research Motivation

From the aforesaid discussion on challenges and their potential features of cooling techniques for electronic devices, it has been seen there is not even a single technology which can cope reliably with the fast growing heat flux removal

demands. From the past two decades, the passive thermal management technologies have revealed promising and significant results in terms of thermal cooling performance using phase change materials (PCMs) as a *energy storage materials*. Since, the turn of the $21^{st}$ century, the era of high performing future generation smart electronic devices, next generation ground vehicles with complicated and high power electronics systems, super–charging and higher–power density modern electric batteries have been developing with improved efficiency and performance. PCMs are extremely effective and have the advantages of latent-heat storage capability, at constant temperature during the phase–transition process, because of the high latent–heat enthalpy of fusion. During the peak hours of energy loads or operating modes of electronic components, the PCM can absorb excessive internally generated heat and reject it during the off peak hours. Thereby, they prevent the electronic components from failure or breakdown due to overheating. PCMs based passive thermal management systems propose an indirect cooling solution with lower thermal resistance and safe operation surety. Since, PCMs, especially paraffins, inherently possess high latent–heat of fusion and higher energy storage density with lower volume change. It requires the small amount of PCM to fulfil the demand of the thermal management system by absorbing the large amount of heat energy when it undergoes the phase–change (melting/freezing) process without temperature rise and volume change, as shown in Fig. 1.7. The poor thermal conductivity and sub–cooling phenomenon during phase transition of paraffins cause to reduce the heat transfer ability and increase the temperature gradient and initiate the local overheating at the interface of PCM melting layer and across the system boundaries. These issues of paraffin PCMs make it challenging for the use of passive TM systems for constant and transient applications. The melting interface of PCM and system boundaries causes to increase the thermal resistance which acts as a barrier results in reduces the usage PCM in transient thermal cooling solution. Successful efforts have been carried out to improve the heating/cooling rate by implementing different thermal conduc-

tivity enhancement methods of PCMs. The different enhancement methods include the incorporation of fins, foams and combination of fin–foams of different higher thermal conductive materials i.e. metals and alloys have been integrated with PCMs. These metallic inserts in the form of fins and foams however reduce the effective volume of the PCM and create the barrier of melt currents of molten PCM in natural heat transfer convection. In addition, these also increases the overall weight of the PCM based TM system which undermines its applicability for compact electronic devices. Thus, to avoid the volume reduction of the PCM, lower the natural heat transfer convection performance and reduce the cooling device weight, higher thermal conductive nanomaterials can be dispersed into the PCMs. The introduction and dispersion of nanomaterials in PCMs, also called "nanocomposite phase change materials (NCPCMs)", not only enhance the thermal conductivity of PCMs and specific heat capacity but also reduce the interfacial thermal resistance and self nucleation. The dispersion of nanomaterials can be either of single type of nanomaterials in PCMs, called the "mono NCPCMs", or the combination of two different nanomaterials in PCMs, called the "hybrid NCPCMs". In addition, nanomaterials of various morphology dispersed in PCMs form a thermal conduction path, reduce the phonon scattering and enhance the heat transfer rate, the chemical and thermal stability.

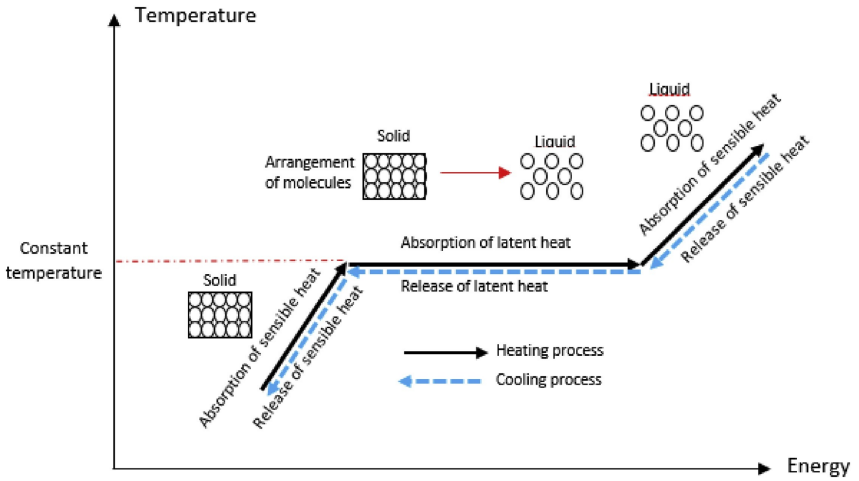


**Figure 1.7:** *Temperature variation of PCM during heating and cooling processes (Leong et al., 2019).*

## 1.4 Mechanisms

As the core of thermal management technology using PCMs is not only absorb or release the excessive heat generated from electronics while phase–transition process, but also maintain approximately constant temperature, providing the excellent possibilities of energy storage, conversion and transmission. However, some inherent shortcomings limit the practical usage of PCMs. To overcome their drawbacks and further enhance the thermal performance, it is important to further discuss the thermal energy storage and thermal conduction mechanisms of PCMs.

### 1.4.1 Thermal energy storage mechanism

The physics of phase transition is defined as the mutual transformation between the different phases under certain thermodynamic condition such as pressure or temperature reaches a certain value (Poplavko, 2019a). The conversion can be expressed as (a) *first–order* phase transition during which the phase transition occurs from one phase to another e.g., melting or crystallization and vaporization or condensation; (b) *second–order* phase transition during which some physical properties transform e.g., the transition from paramagnetic to ferromagnetic (Comes et al., 1976). The phase–change energy storage can be expressed by the first–order phase transformation processes. The total heat storage capacity of a PCM within the storage temperature range of storage which is calculated using Eq. 1.3 as follows:

$$Q = \int_{T_i}^{T_m} mC_p.dt + m\alpha_m \Delta H_m + \int_{T_m}^{T_f} mC_p.dt \tag{1.3}$$

where, $Q$ (J) is the quantity of total heat stored, $T_i$ (°C), $T_m$ (°C) and $T_f$ (°C) are the initial, melting and final temperatures, respectively, $m$ (kg) mass of the heat storage medium, $C_p$ (J/kg.K) is the specific heat capacity,$\alpha_m$ is the faction of melted mass and $\Delta H_m$ (J/kg) is the heat of fusion per unit mass.

### 1.4.2 Thermal conduction mechanism

#### 1.4.2.1 Solid

**(1) Insulator:** Since, the PCMs especially paraffin wax and poly(ethylene glycol)s are considered as insulators. When the solid PCM is in charging or heating mode, it has the two surfaces at different temperatures. Then the thermal energy is transferred from the hot surface towards the cold surface through phonon transmission. Phonons behave like the heat packets which responsible for the transport of heat from one surface to end of the other surface. The thermal conductivity ($k$) of the insulator is defined as follows:

$$k = \frac{1}{3} C_v \lambda \bar{v} \tag{1.4}$$

where $C_v$ is the heat capacity per unit volume, $\lambda$ is the free path, and $\bar{v}$ is the wave velocity of the lattice wave.

**(2) Conductor:** Some metallic PCMs belong to the conductor, such as Ga and Bi-In alloy. The heat transport of metals is affected by the two independent mechanisms: thermal energy is transmitted by (i) free electrons and (ii) lattice vibration and phonons. At room temperature and above, there is a certain connection between electrical conductivity and thermal conductivity of pure metals, called Wiedcmann–Franz law:

$$k = L_0 \sigma T \tag{1.5}$$

where $L_0$ is the Lorentz constant, $\sigma$ is the electrical conductivity coefficient, and $T$ is the absolute temperature.

The heat transport can be achieved through the lattice vibration and free electrons in solids. In metallic PCMs, the heat transport is mainly contributed by the free electrons. Whereas, nonmetallic inorganic PCMs have few free electron and cannot be good thermal conduction carri-

ers because the electrons bound in their ionic crystal lattice (Minnich, 2015). For nonmetallic or organic PCMs, the conduction of heat mainly depends on the vibration of the crystal lattice (Capinski et al., 1999). The lattice vibration is the main thermal conduction mechanism of thermal or heat conduction in PCMs. As a consequence of this, the phonons are the main contributor as a heat carriers in PCMs. In crystal lattice, the particles vibrate near the equilibrium position even at lower temperature. Thus, the lattice of the PCM structure can be attributed as a coupled spring and mass system, as shown in Fig. 1.8. While the crystal lattice is subjected to heat, the vibration starts deviation from the equilibrium position. After that, high energy phonons are generated and diffuse form heat source to sink which gradually lose the heat energy while motion to the cold sink. As a result of high energy phonons form a temperature gradient which is responsible of the heat flow due to thermal phonon. Fig. 1.9a illustrates the concept of phonon in which two features of phonon are captured, one is its wave like nature which is represented through tail and second is its particle nature represented by a circle with $P$. Whereas, Fig. 1.9b presents the temperature gradient between the hot source towards the cold sink due to the diffusion of the phonons. Therefore, thermal conduction is a nonequilibrium phenomenon (Mehra et al., 2018; Poplavko, 2019b). Since the phonons play a key significant role in heat transfer of non–metallic PCMs. Generally, the stronger the phonon diffusion in PCM, the better will be the thermal conduction capability and thus the higher thermal conductivity. Contrarily, if phonon transport is blocked non–metallic PCMs, it will lead to the lower thermal conductivity. Indeed, the there are different modes of poor phonon transport, called phonon scattering, inside the non–metallic PCMs which deteriorate the phonon diffusion, shown in Fig. 1.10. These three modes of phonon scattering can be classified as: (i) phonon–phonon scattering, (ii) phonon-impurity scattering and

(iii) phonon-boundary scattering. Phonon scattering can be expressed as phenomena which can lead to change the direction, momentum or energy of the phonon. Thus, phonon scattering is the dominating the reason of poor heat conduction in non–metallic PCMs. In composite materials such as composite PCM, the phonon scattering is mainly attributed to the interfacial thermal resistances which appear from acoustic mismatch at the filler–matrix interface (Xu et al., 2001).

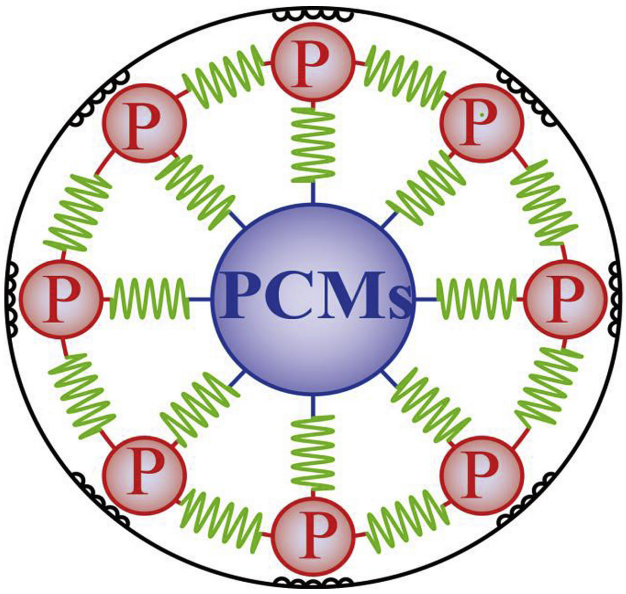


**Figure 1.8:** *Spring vibration heat transfer system composed of crystal atoms and abstract phonons (Wu et al., 2019).*

#### 1.4.2.2 Liquid

In liquid PCMs, the thermal conduction is because of the speed of sound (Ross et al., 1984). Bridgman correlates the speed of sound in liquid with the thermal conductivity of the the liquid given as follows (Bridgman, 1923):

$$k = \frac{2Rv_{lq}}{\left(\frac{M}{\rho}\right)^{2/3}} \tag{1.6}$$

where $R$ si the gas constant, $v_{lq}$ is the speed of the sound in liquid, $\rho$ is the density of the liquid, and $M$ is the molecular weight weight of the liquid.

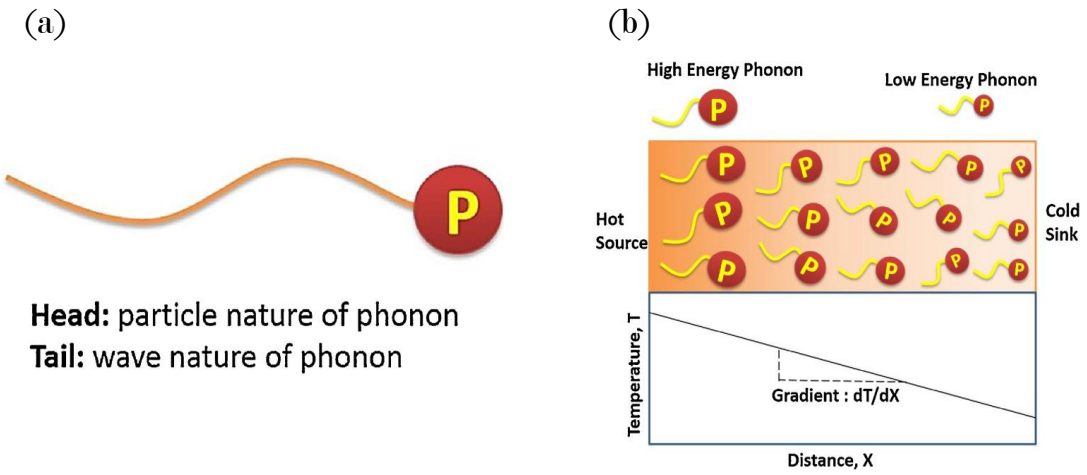


**Figure 1.9:** *(a) Schematic symbol of phonon (b) Temperature gradient from heat source to cold sink and phonon energy (Mehra et al., 2018).*

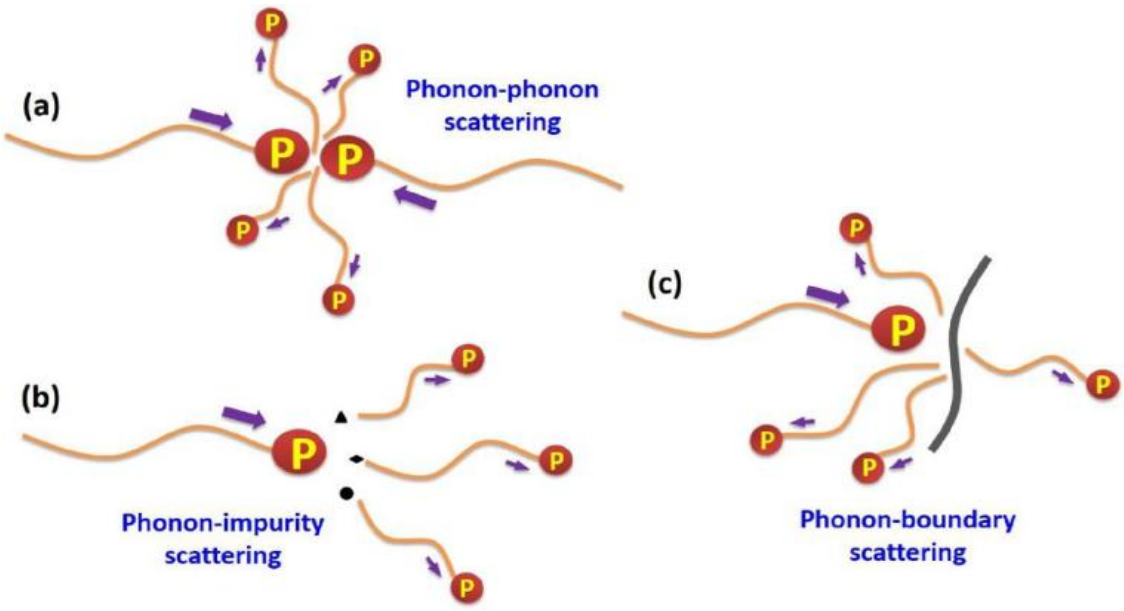


**Figure 1.10:** *Phonon scattering modes of (a) phonon-phonon scattering, (b) phonon-impurity scattering and (c) phonon-boundary scattering. (Mehra et al., 2018).*

## 1.5 Research Questions

The current research focuses on the passive thermal management of electronics devices operating at lower-to-higher power densities using NCPCMs. There are several important parameters of NCPCMS, in terms of its thermophysi-

cal properties, that affect or define the phase–transition phenomenon during melting/cooling process, heat storage and heat transfer capability integrated with passive cooling device.

- Is it possible to enhance the heat transfer and maintain the heat storage capacity of PCMs with the addition of nanomaterials?
- What will be the best combination of hybrid nanomaterials of metallic and non–metallic additives and effect on thermophysical properties of PCMs to obtain the higher thermal conductivity, optimum enthalpy of fusion and uniform heat transfer cooling?
- How to achieve the best physical, chemical and thermal stability of NCPCMs by dispersing the metallic and non–metallic additives?
- What will be the effect of NCPCMs and coated metal–foam/PCM composite embedded heat sink of various thickness ratios and volumetric fractions of PCM under constant heating levels?

## 1.6 Aims and Objectives

As mentioned in Section 1.3 paraffins based PCMs have some inherent limitations that resist its direct application with PCMs based passive thermal management technology. Furthermore, to make it possible for commercialization, there are still some challenges needed to overcome for the development of NCPCMs. To accomplish this, the core aim of this research is to develop novel mono and hybrid NCPCMs based on different nanomaterials with better thermophysical properties. Moreover, to design a novel compact coated metal–foam embedded heat sink assembly filled with and without PCMs and NCPCMs for better thermal cooling performance. To achieve these goals, the following objectives are defined:

I – To review the latest research on nanomaterials, PCMs, NCPCMs, stability and issues and challenges of NCPCMs.

II – To synthesise and study the thermophysical properties and achieve the uniform dispersion, physical, chemical and thermal stability of metallic–oxides nanomaterials based mono NCPCMs.

III – To synthesise and study the thermophysical properties and achieve the uniform dispersion, physical, chemical and thermal stability of metallic–oxides nanomaterials based mono and hybrid NCPCMs.

IV – To synthesise and study the thermophysical properties and achieve the uniform dispersion, physical, chemical and thermal stability of carbon–additives nanomaterials based mono and hybrid NCPCMs.

V – To synthesise and study the thermophysical properties and achieve the uniform dispersion, physical, chemical and thermal stability of metallic–oxide and carbon–additives nanomaterials based mono and hybrid NCPCMs.

VI – To study the enhancement mechanism of thermal conductivity and specific heat capacity of mono and hybrid NCPCMs.

VII – To investigate the thermal performance of a mini heat sink filled with and without PCM and coated metal–foam at varying input heat power levels to explore the optimum thickness ratio and higher latent–heating phase.

## 1.7 Research methodology

This thesis discusses the research of NCPCMs as a new passive coolant developed on a laboratory scale for passive cooling of compact integrated electronic circuits. The overview of the current thesis is presented in shown Fig. 1.11. To achieve the above mentioned research objectives in Section 1.6, a series of

experimental studies were carried out at the Wolfson Building and Nanoscale and Microscale Research Centre at the University of Nottingham, to synthesise and characterize the NCPCMs and to evaluate the thermophysical properties and to study the heat transfer and phase–transition phenomenon during melting/cooling process. For effective heat storage and transfer using PCMs, the latent–heat and thermal conductivity are the key thermal properties of PCMs which improve the passive thermal management efficiency. Therefore, a PCM with higher latent-heat and thermal conductivity with stable chemical structure is the most suitable. In the present research, two different commercially available PCMs RT–28HC and RT–35HC with melting temperatures of 28 °C and 34–36 °C, respectively, and almost similar latent–heat of capacities of ∼240–250 kJ/kg.K are chosen, which are the most suitable for thermal management of electronic devices, photovoltaic modules and Li–ion batteries, working under the safe and reliable operating temperature range of 30–40 °C. Different metallic–oxide ($TiO_2$, $Al_2O_3$ and CuO) and carbon–additives (MWCNTs, GNPs, GO, rGO) have been dispersed by varying mass concentration from 0.0 wt.% to 2.0 wt.% in case of mono NCPCMs. Whereas, the optimum mass concentration ratio of hybrid mono NCPCMs is kept of 75%/25% of the total mass concentration or loading content of 1.0 wt% of nanomaterials. Detailed experimentation was conducted to explore the physical, chemical and thermal properties using different characterization techniques of Environmental Scanning Electron Microscopy (ESEM) and Energy-dispersive X-ray spectroscopy (EDX), Fourier-transform infrared spectroscopy (FT–IR), X–ray diffraction (XRD), Thermogravimetric analysis (TGA) and derivative thermogravimetry (DTG), Differential scanning calorimeter (DSC), and Thermal Conductivity Analyser (TCA). In addition, melting/cooling phenomenon and heat transfer performance was studied using Infrared Thermography (IRT) tests. The surface microstructure, chemical and physical interaction, thermal properties including phase–change melting/solidification temperatures, melting/solidifying latent–heat enthalpies, specific heat capacity, thermal conduc-

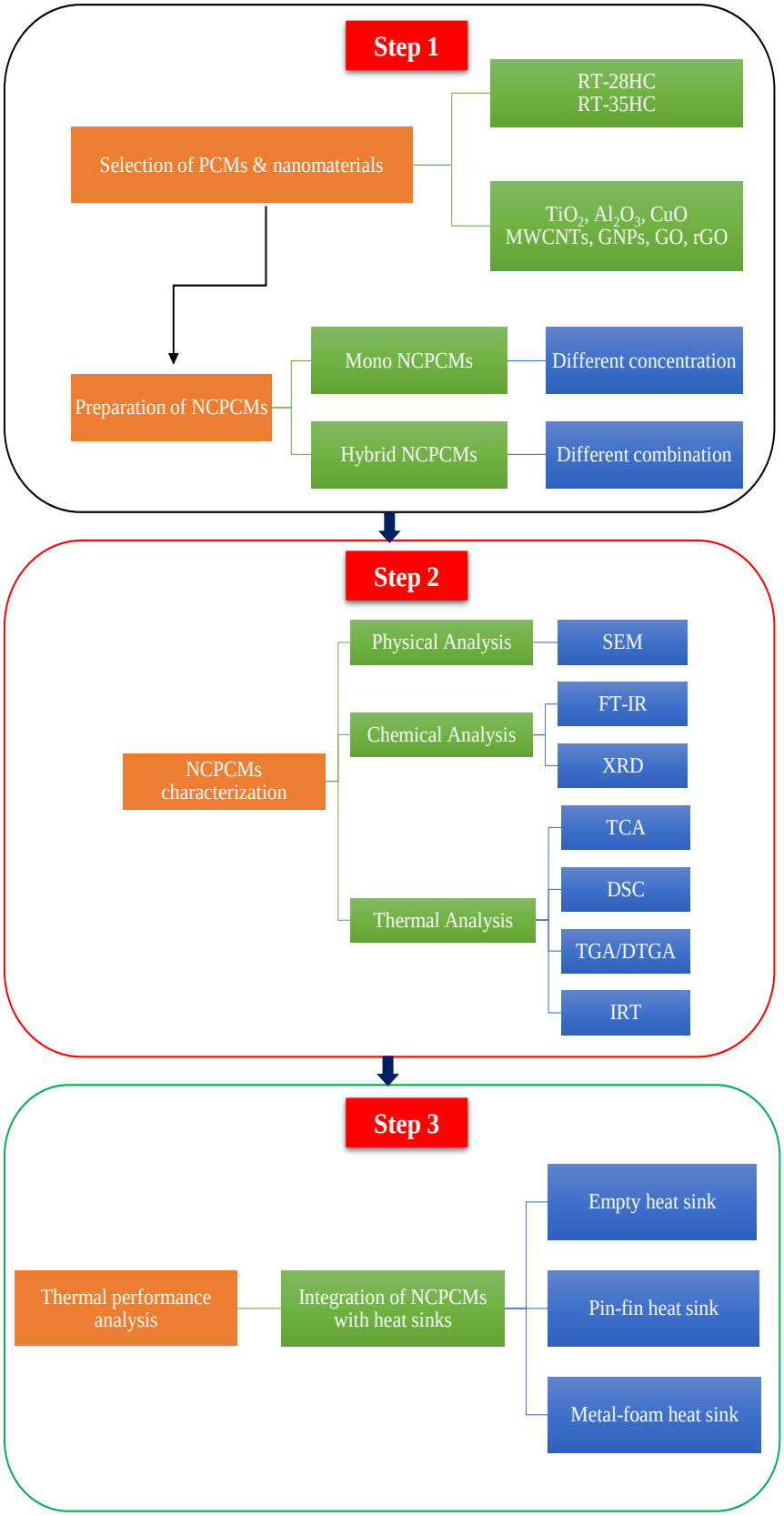


**Figure 1.11:** *Methodology of research adopted in current thesis.*

tivity, thermal stability and reliability are analysed using above mentioned characterization techniques. In addition, the thermal conductivity enhancement mechanism and modes of specific heat capacity enhancement were explained schematically. An experimental rig was designed to conduct the experiments of a heat sink based on pure PCM and NCPCMs assembly and different power levels, to mimic heat generation, are applied to perform the thermal cooling performance analysis as a passive cooling thermal management system.

## 1.8 The structure of the Thesis

This present thesis is presented in an alternative format as published research paper of each chapter.

Chapter 2 provides the background of existing literature of nanomaterials, PCMs and its classifications, NCPCMs and its classifications, stability of NCPCMs, issues and challenges of NCPCMs.

Chapter 3 presents the development of mono NCPCMs based on RT–35HC and $TiO_2$ nanomaterials under different loading contents and the results of various thermophysical properties.

Chapter 4 reports the study on the development of metallic–oxide ($TiO_2$, $Al_2O_3$ and CuO) nanomaterials with RT–35HC based mono and hybrid NCPCMs. The results of various thermophysical properties and thermal performance NCPCMs filled heat sinks is explored for transient thermal cooling solutions.

Chapter 5 consists on the development of mono and hybrid NCPCMs of MWCNTs, GNPs GO and rGO based carbon–additives with RT–35HC. The results of physical, chemical and phase–change thermal properties are presented in detailed.

Chapter 6 examines the comparison of carbon–additives (GNPs and MWCNTs) and metallic–oxide ($Al_2O_3$ and CuO) based nano and hybrid NCPCMs. The comparison of various thermophysical is presented. The detailed physical,

chemical, thermal and melting phenomenon of mono and hybrid NCPCMs are discussed.

Chapter 7 reports the experimental analysis of PCM and CuO coated metal–foam embedded heat sink assembly. The thermal performance of different thickness ratios of metal–foams and volumetric fractions of PCM based heat sink is explored.

In the final Chapter 8 summarizes the conclusion of thesis drawn from the results and future recommendations are mentioned which will lead towards the better NCPCMs based thermal management system

# Chapter 2

# Literature Review[1][2]

## 2.1 Introduction

After energy crisis of the 1970s, the world is facing worse shortage of energy resources and facing economic decline cumulatively. Researchers are looking forward towards different energy storage technologies based on renewable and sustainable resources to meet the future energy requirements (Salunkhe and Shembekar, 2012). The phase change thermal energy storage (TES) technology using phase change materials (PCMs) ensures the storage, transportation and wider domestic and industrial applications of thermal energy. The TES technology has the high heat capacity and enthalpy of fusion with capability of absorbing and releasing extensive amount of thermal energy while phase transition. The thermal performance of phase change TES technology employing PCMs which are also known as *latent heat storage materials* (LHSMs), solely depends on the properties of PCMs. On the bases of chemical composition, PCMs are classified in to major categories, *organic phase change materials* (OPCMs) and *inorganic phase change materials* (IPCMs). The positive ad-

[1]This Chapter is published as:
**Arshad, A.**, Jabbal, M., Yan, Y., & Darkwa, J. (2019). The micro/nanoPCMs for thermal energy storage systems: a state of art review. *International Journal of Energy Research*, 43(11), 5572-5620. https://doi.org/10.1002/er.4550

[2]**Arshad, A.**, Jabbal, M., Yan, Y., & Reay, D. (2019). A review on graphene based nanofluids: Preparation, characterization and applications. *Journal of Molecular Liquids*, 279, 444-484. https://doi.org/10.1016/j.molliq.2019.01.153

vantage of PCMs especially, OPCMs which includes paraffins (*n-alkanes*) and non–paraffins (*n-alkenes*) materials, are more stable and high energy storage density and no segregation, non–toxic, self–nucleation (super–cooling), non–corrosiveness and non–reactive (Jegadheeswaran and Pohekar, 2009). Contrarily, IPCMs have the high volumetric energy storage density, relatively high thermal conductivity and flame retardancy. In spite of this, IPCMs possess the sub–cooling and phase separation which reduce their instant release and utilization of thermal energy for large–scale TES applications.

The OPCMs have the lower thermal conductivity (Wang et al., 2013) also they suffer the leakage problem and sub–cooling phenomenon during phase transition (Qiu et al., 2013). The lower thermal conductivity of OPCMs materials reduces the rate of heat transfer which causes increase in temperature gradient and insensitivity to temperature changes across the system boundaries. The OPCMs with potential advantage as TES materials are being under applications of air conditioning i.e. natural air cooling (Waqas and Din, 2013), cold thermal storage and absorption refrigeration (Li et al., 2013a), waste heat recovery (Shon et al., 2014), solar energy storage (Khan et al., 2018), thermal regulating fabric (Nejman et al., 2014), passive heating of building (Kong et al., 2013), heat pipes (Riffat et al., 2001), desalination (Sarwar and Mansoor, 2016), thermal management of electronic devices and electric vehicle batteries (Arshad et al., 2018a; Hussain et al., 2018), space craft (Mulligan et al., 1996), and other integrated thermal control systems such as trombe wall, PCM filled wallboards, shutter, concrete, under floor heating systems, ceiling boards and hot water supply (Sharma et al., 2009; Zhou et al., 2012). However, the leakage issue and lower thermal conductivity of OPCMs causes harm with interacting medium and losses the energy efficiency of the thermal system.

In the past, to solve the aforementioned challenges related with both types of PCMs, efforts have been made. Various conventional approaches such as the adding up of more water, nucleating agents, thickeners and stirring of the salt solution have been employed to control the predicaments of IPCMs in their

constant dissolution and crystallization procedure (Cabeza et al., 2003). In contrary, the addition of conductive fillers and flame-retardants has reduced the disadvantages of OPCMs. On the other hand, these efforts would certainly lessen the energy storage density of PCMs due to the presence of inactive mass (Milián et al., 2017). At present, nanoconfinement technologies have attracted a lot of interest and present a new opportunity for considerable refinement in the thermophysical properties of PCMs while sustaining their energy storage capacity (Graham et al., 2017; Huang et al., 2014a). There are several advantages associated with nanoconfinement like small domain size, large surface area, diverse surface functionalities, controlled volume expansion, reduced reactivity with the external environment and high heat transfer rate.

Several techniques have been under investigation by researchers employing extended surfaces such as plate–fins, pin–fins, metal–foam, metal–metrix, honeycomb, composites, encapsulation and multiple PCMs, used as *thermal conductivity materials* (TCMs). However, the PCM filled in extended surfaces, metal–matrix, metal–foam increases the weight of the thermal management system which reduces its applicability with smart and compact systems. Additionally, the interaction of fixed configuration TCMs while in conduction or convection heat transfer modes also possess the heat significant challenges during phase transformation. Hence, it is a great importance and challenge for thermal management system to maintain or achieve a critical limit between the thermal conductivity and latent heat fusion of PCMs.

The current era, the modern research has now diverted towards the *nanoscale* technology, referred to as *nanotechnology*, for developing the nanoscale materials to used in thermal management systems. *Nanoscale* is usually defined at $0.1 - 100$ nm or smaller than $1/10^{th}$ of a micrometer in at least one dimension; also nanoscale is used for the materials smaller than 1 $\mu$m (Visakh, 2016). Nanomaterials, the materials at nanoscale, are being introduced with the PCMs to enhance the heat transfer characteristics of the PCMs. The nanomaterials of highly thermal conductivity of ultra-fine nano sized if added to a

fluid called advanced heat transfer fluid, *nanofluid* which has the significantly higher thermal conductivity enhancement as compared to the base fluid; contrarily, the addition of nanomaterials in solid referred to as *nanocomposite*. In current era, the nanomaterials enhanced fluids and materials are extensively used to enhance the heat transfer mechanism and thermophysical properties for various applications (Yu and Xie, 2012; Das et al., 2006; Wang and Mujumdar, 2007, 2008). Introducing of nanomaterials (NMs) as TCMs in PCMs, called the nanocomposite phase change materials (NCPCMs) and have been investigated globally using various class of NMs and PCMs of thermal management systems. Additionally, literature have studied the various thermophysical properties such as thermal conductivity, viscosity, latent-heat, specific heat capacity, sub-cooling etc. dispersing the NMs into PCMs. In this context, a comprehensive literature review is presented covering the classification of PCMs, NMs and their classification, NCPCMs and their classification based on structure of the NMs. The detailed discussion of characteristics evaluation techniques are mentioned to study the thermophysical properties and stability of the NCPCMs. The stability which is a real challenge of the NCPCMs is discussed with respect to physical, chemical and thermal properties point of view to explore the functionality and thermodynamic nature as an energy storage materials for thermal management applications. Finally, the key issues and challenges of NCPCMs are highlighted for the availability of NCPCMs are commercial level.

## 2.2 Nanomaterials (NMs)

Today, nanoscience, nanotechnology and nanomaterials (NMs) have become the common terminologies not only for scientist but only for industrialist. The history of NMs began after the big bang theory forming the nanoparticles and nanostructures. The term *NMs* is defined fundamentally in two definitions. Firstly and the most broadest definition of NMs, is that the materials which

have external dimension or an internal structure or surface structure in the nanoscale. This definition is mostly suited for research proposals where NMs often have high priority. Secondly, which is based the morphology of NMs, states that NMs have properties that depend inherently on the smaller grain size. The European Union commission suggests that the following definition for a NM (Buzea and Pacheco, 2016):

*NM means a natural, incidental or manufactured material containing particles, in an unbound state or as an aggregate or as an agglomerate and where, for* 50% *or more of the particles in the number size distribution, one or more external dimensions is in the size range of* $1-100$ *nm. In some specific cases and where warranted by concerns for the environment, health, safety or competitiveness the number size distribution threshold of* 50% *may be replaced by a threshold between* 1 *and* 50%.

A **nanoparticle** is defined as the particle with at least one dimension smaller than 1 $\mu$m, and potentially as small as atomic and molecular length scale ($\sim$ 0.2 nm) (Buzea and Pacheco, 2016). Nanoparticles can have the amorphous or crystalline form, and their surfaces act as carriers for liquid droplets or gases. Many researchers limit the size of NMs to 50 nm or 100 nm (Sudha et al., 2018; Borm et al., 2006), the choice of this upper limit is being justified by the fact that some physical properties of nanoparticles approach to those bulk materials when size reaches values.

According to these definition most of the material in nature are categorized as NMs, as their internal structure is restrained at nanoscale. The enormous development in nanotechnology helps to design, characterize, produce and apply nanostructure, nanodevices and nanosystems by restricting the shape and size at nanometer scale. The nanometer is metric unit of length which is equal to one-billionth of meter or $10^{-9}$ m (Sudha et al., 2018).

From the above discussion, it is potentially important, and timely, to unify the terminology for addressing the size of particle in nanotechnology, engineering, environmental and medical sciences. The materials can be classified

as per particles, regardless of their source. The size of particles can be varied between 1 nm and several microns. Thus, they can classified as either nanoparticles (any dimension less than 1 $\mu$m) or microparticles (all dimension larger than 1 $\mu$m). This illustrates the differences between the sizes of microparticles and nanoparticles, the Figure 2.1 shoes the sizes of several micro and nanostructures (Buzea et al., 2007).

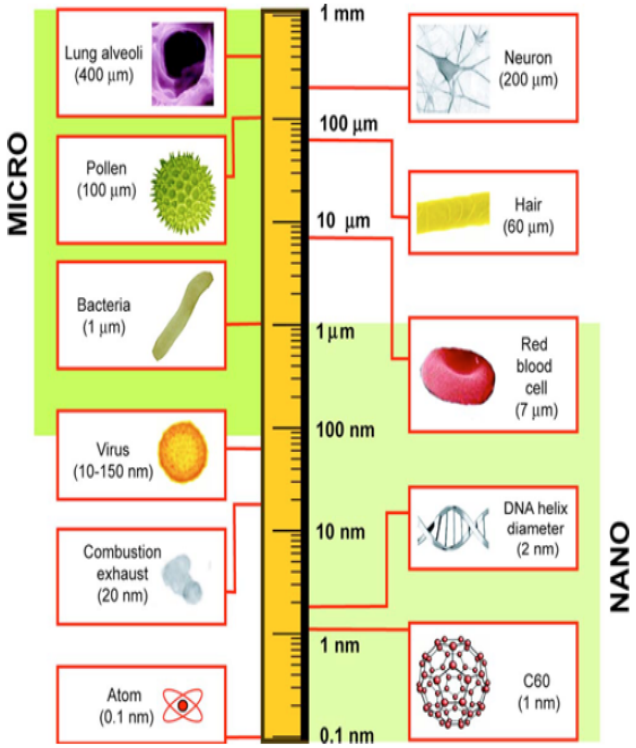


**Figure 2.1:** *Logarithmical length scale showing size of nanomaterials compared to biological components and definition of nano and micro sizes (Buzea et al., 2007).*

The NMs possess the unique physical (optical, magnetic), mechanical, thermal and chemical properties than the same material but in bulk form. There are two main factors which contribute to this: (i) surface effects and (ii) quantum effects which exhibit with decrease in size. Surface effects contribute to a smooth scaling of physical properties i.e. increases the surface area of the particle and high particle number per unit mass, because of an increased fraction of the atoms at the surface of the particle compared to its interior (Prasad et al., 2018). Thus, surface effects enhance the chemical reactivity of NMs result in reduced the melting point of NMs compared to the larger size particles

or bulk materials. Quantum effects require the confinement of electrons within a very small nanoparticle, or quantum dot which manifest in a quantized energy spectrum. resulting in the appearance of magnetic moments, especially in that nanoparticles made of nonmagnetic materials in bulk form e.g. gold, platinum, and palladium (Sudha et al., 2018).

### 2.2.1 Classification of Nanomaterials and their characteristics

The classification of nanomaterials are categorized based on their origin, dimensionality, morphology, composition, structure, uniformity and agglomeration, as shown in Fig. 2.2 (Buzea et al., 2007).

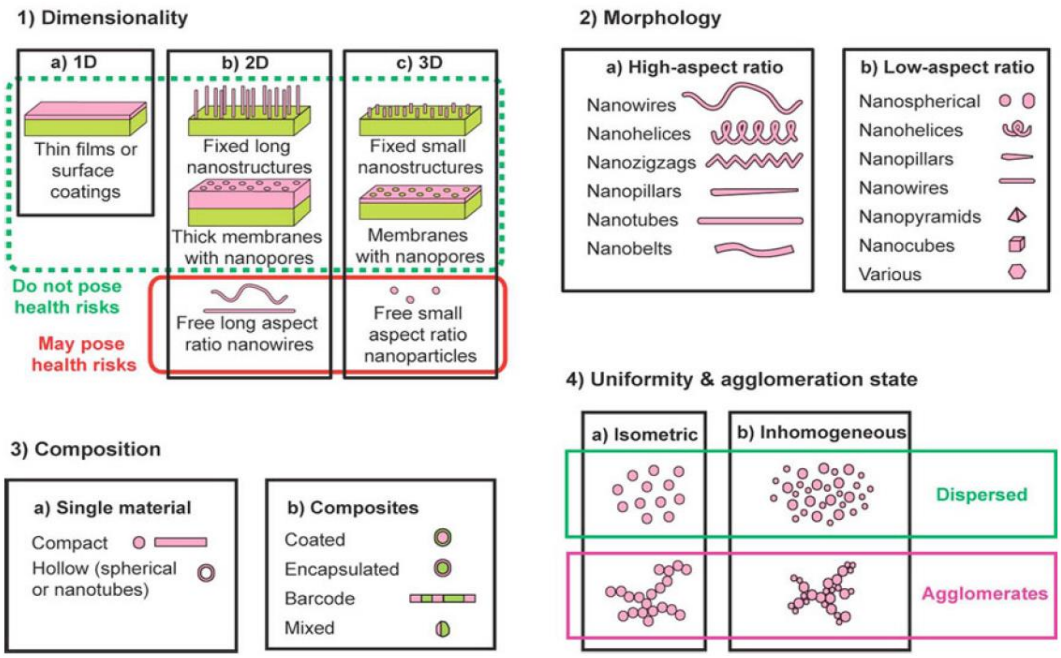


**Figure 2.2:** *Classification of NMs from the point of view of nanostructure dimensions, morphology, composition, uniformity and agglomeration state (Buzea et al., 2007).*

#### 2.2.1.1 According to origin of nanomaterials

According to origin the NMs are classified as follows:

**2.2.1.1.1 Natural** The natural NMs are present inherently by the creator in the natural nanoworld and originate from the animals, plants, insects, and minerals without any alternation or transformation. Natural NMs are further categorized in inorganic natural NMs (e.g. minerals, clay, carbon etc.), NMs from space, NMs from the animal and plant kingdoms (building block of biomaterials, shell, exoskeletons, endoskeletons, skin, cotton bacterial fibers, diatoms, and diatoms), NMs in insects (chitin, chitin structures in inset and butterfly wings) (Hornyak et al., 2008; Chirayil et al., 2017).

**2.2.1.1.2 Artificial** The artificial NMs are developed experimentally by various mechanical and chemical processes. The typical examples are quantum dots, metal-oxides, carbon fibers and nanotubes, graphene etc.

### 2.2.1.2 According to dimensionality of nanomaterials

On the basis of dimensions, Pokropivyn and Skorokhod (Pokropivny and Skorokhod, 2007) classified the nanostructures as (i) zero-dimensional ($0D$), (ii) one–dimensional ($1D$), (iii) two–dimensional ($2D$), (iv) three–dimensional ($3D$) which is generalization on the basis of the concept of aspect-ratio (P.M. and Morlanes, 2016), as shown in Fig. 2.2.

**2.2.1.2.1 Zero-dimensional (0D)** The $0D$ NMs include all the measured dimensions are within the nanoscale range. The most common NMs under $0D$ are atomic clusters, filaments, and nanoparticles.These NMs have all features or dimensions is less than 100 nm (Capsal et al., 2011). Commonly, $0D$ NMs are: (i) amorphous or crystalline, (ii) single crystalline or polycrystalline, (iii) composed of single or multiple chemical elements, (iv) exist various shapes and forms, and (v) exhibit individually or incorporated in a matrix as metallic, ceramic and polymeric (An et al., 2006). Additionally, the $3D$ nanostructures can be developed in the form of uniform and heterogeneous arrays of $0D$ NMs.

**2.2.1.2.2 One-dimensional (1D)** The $1D$ NMs exhibit one dimension larger than the other dimension (i.e. length is larger than the width) outside the nanoscale, which leads to needle-like-shaped NMs. Typically, nanotube (SHE et al., 2007), nanorods, nanowires (Wang, 2006), and nanofibers are included as $1D$ NMs. In $1D$ NMs, electrons are confined within the two dimensions which prevent their free movement. Thin films, developed from $1D$ NMs based nanostructures, can be deposited by various techniques in a controlled environment to be only one atom thick, thus a so–called monolayer.

**2.2.1.2.3 Two-dimensional (2D)** The $2D$ NMs possess the two of the dimensions outside the nanoscale and exhibit the plate–like or layer type geometry. These include nanosheets, nanofilms, nanolayers, and nanocoatings. The thickness of $2D$ NMs is in the nanometer range. Free particles with larger aspect ratio, with dimensions in the nanoscale range, are also considered as $2D$ NMs. In $2D$ NMs. the electron are confined within the one dimension which do not allow them to move freely within the associated dimensions.

**2.2.1.2.4 Three-dimensional (3D)** The $3D$ NMs do not possess any of the dimension in the nanoscale range and all three arbitrary dimensions are beyond 100 nm. These include nanophase materials consisting of equiaxed nanometer sized grains. The $3D$ nanostructures are not confined to the nanoscale in all dimensions, so the usually known as bulk NMs. Owing to the bulk nanostructures, $3D$ NMs can contain dispersions of nanoparticles, bundle of nanowires, nanotubes and nanofibers as well as multiple nanolayers. In $3D$ NMs, the electrons are fully delocalized which allowing the free movement of electrons within all dimensions (Bashir and Liu, 2015; Zhang et al., 2014b).

### 2.2.1.3 According to morphology of nanomaterials

The classification of NMs on the basis of morphology are carried out by keeping in account the morphological characteristics such as flatness, sphericity and

aspect-ratio. Generally, on the basis of aspect-ratio, the NMs exhibit high and low aspect-ratio (Buzea and Pacheco, 2016; Buzea et al., 2007), as shown in Fig. 2.2.

**2.2.1.3.1 High aspect–ratio** The high aspect-ratio NMs include nanowires and nanotubes existing various shapes such as zigzag, helices, belts or conical shapes with diameters varies with length.

**2.2.1.3.2 Low aspect–ratio** The NMs with low aspect-ratio include spherical, oval, cubic, pyramid, helical, and pillar shapes.

#### 2.2.1.4 According to composition of nanomaterials

On the basis of composition, the NMs are classified as a single and composite of several materials (Buzea and Pacheco, 2016; Buzea et al., 2007), as shown in Fig. 2.2.

**2.2.1.4.1 Single material** The single NMs based on a pure single composition are generally synthesized of varying morphological characteristics by various methods such as gas phase processes, vapor deposition synthesis, colloidal or liquid phase method, and mechanical processes.

**2.2.1.4.2 Composites** The composite NMs consist the composition of various NMs with different shapes and forms, and exist both naturally and naturally. The NMs found in nature are often possess the agglomerations of materials of different composition. Composites are further categorized in three form, namely, ceramic–matrix nanocomposite, metal–matrix nanocomposite, and polymer–matrix nanocomposite, as shown in Fig. 2.3 (Babar and Ali, 2019).

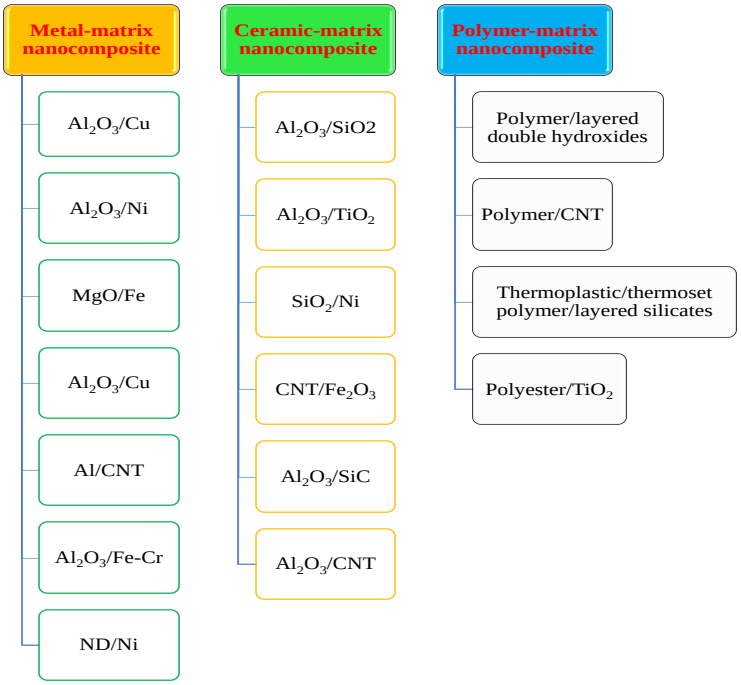


**Figure 2.3:** *Classification of NMs according to composition.*

#### 2.2.1.5 According to uniformity and agglomeration of nanomaterials

On the basis of chemistry and electromagnetic properties (i.e. surface charge and magnetism), NMs can exist dispersed aerosols, as suspension/colloids, or in an agglomerate/aggregate states. According to the uniformity of NMs, they may be classified as isometric and inhomogeneous, additionally, the agglomeration of the NMs can be dispersed or agglomerate (Buzea and Pacheco, 2016; Buzea et al., 2007), as shown in Fig. 2.2.

**2.2.1.5.1 Isometric:** The isometric of NMs may exhibit the uniformly dispersed or agglomerates depends on the mixing phenomenon and adhesion (weak physical interaction) force. In both cases the primary particles hold their shape and size uniformly either in single phase or dual phase or suspension. When the NMs are suspended in the liquid, the dispersion and agglomeration depend on the surface morphology and functionalization which present it either hydrophobicity or hydrophilicity.

**2.2.1.5.2 Inhomogeneous:** Similar to the isometric existence of NMs, they can be inhomogeneous either in uniformly dispersed or agglomeration/aggregation states. The inhomogeneous of NMs can be defined as the non-uniform nanoparticles both in size and form. The agglomerates generate because of adhesion forces between the primary nanoparticles (e.g. joined together at corners or edges) forming as larger particles, depending upon the size of primary nanoparticles.

#### 2.2.1.6 According to structure of nanomaterials

**2.2.1.6.1 Organic nanomaterials** Organic NMs are generally called carbon–based NMs and have broader interest in researcher community from decades ago because of the extremely lower weight of carbon and versatility. The typical examples are carbon nanotubes, carbon nanofiber, fullerenes, expanded graphite, graphite powder, graphene, graphene oxide, reduced graphene oxide, graphene nanoplatelets, etc (Visakh, 2016).

**2.2.1.6.2 Inorganic nanomaterials** Inorganic NMs are generally called metal–based NMs. The typical examples are metallic (Au, Ag, Fe, Cu, etc.) and metal–oxide (ZnO, CuO, $TiO_2$, $Al_2O_3$, etc.) nanoparticles, quantum dots (CdSe, ZnSe, ZnS, etc.) (P.M. and Morlanes, 2016).

**2.2.1.6.3 Polymeric nanomaterials** Polymeric NMs are composed of different kind of polymers which can be loaded with an active compounds entrapped or surface-absorbed onto the polymeric core and produced as nanocapsules or nanospheres (Zielińska et al., 2020; Han et al., 2018). Polymeric NMs are biodegradable and biocompatible and potentially used for drug delivery of various deceases. Dendrimers are in the category of polymer NMs which are radially symmetrical molecules with homogeneous and nanosized structure with a symmetric core, inner shell and outer shell (Carvalho et al., 2020).

**2.2.1.6.4 Composites nanomaterials** The composite NMs consist of one or two multiphase solid materials in which at least one is nanosized. The composite NMs are generally categorized as ceramic–matrix nanocomposite, metal–matrix nanocomposite, and polymer–matrix nanocomposite, as shown in Fig. 2.3 (Babar and Ali, 2019).

## 2.3 Thermal energy storage (TES)

The Thermal energy storage (TES) are classified into two categories; thermal and chemical energy storage, as shown in Fig. 2.4. TES stores the energy in the form of sensible heat storage (SHS) and latent heat storage (LHS) while chemical energy storage (CES) generates energy via chemical reaction.

### 2.3.1 Sensible heat storage (SHS)

In SHS phenomenon, thermal energy is stored inside the materials (i.e. solid or liquid) in sensible mode by raising its temperature. The heat is transferred into the system depending upon the specific heat capacity, amount of material and change in temperature while charging and discharging phases.

$$Q = \int_{T_i}^{T_f} mc_p dT = mc_p(T_f - T_i) \tag{2.1}$$

### 2.3.2 Latent heat storage (LHS)

In LHS phenomenon, heat is transferred during absorption (fusion latent heat) and rejection (solidification latent heat) at constant temperature into the material, see Fig. 2.5. The PCMs undergo the phases from “solid–to–liquid” or “liquid–to–solid”. The LHS of the system with PCMs can be determined by

$$Q = \int_{T_i}^{T_m} mc_p dT + ma_m \Delta h_m + \int_{T_m}^{T_f} mc_p dT \tag{2.2}$$

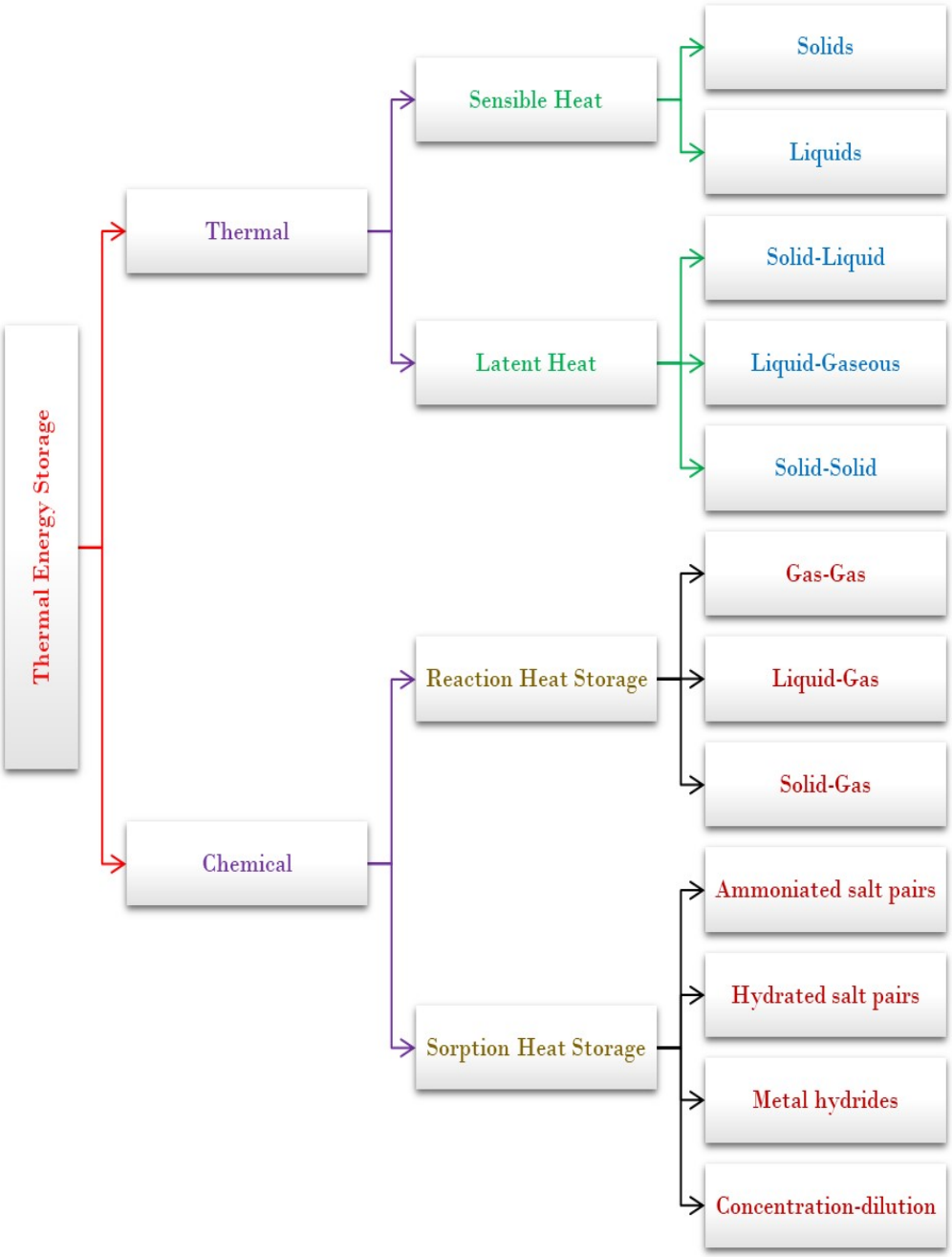


**Figure 2.4:** *Classification of thermal energy storage(Sharma et al., 2009).*

$$Q = m[c_{sp}(T_m - T_i) + a_m \Delta h_m + c_{lp}(T_f - T_m)] \tag{2.3}$$

where, $a_m$ is the melt fraction of PCM and $\Delta h_m$ is the melting heat per unit pass $J/kg$.

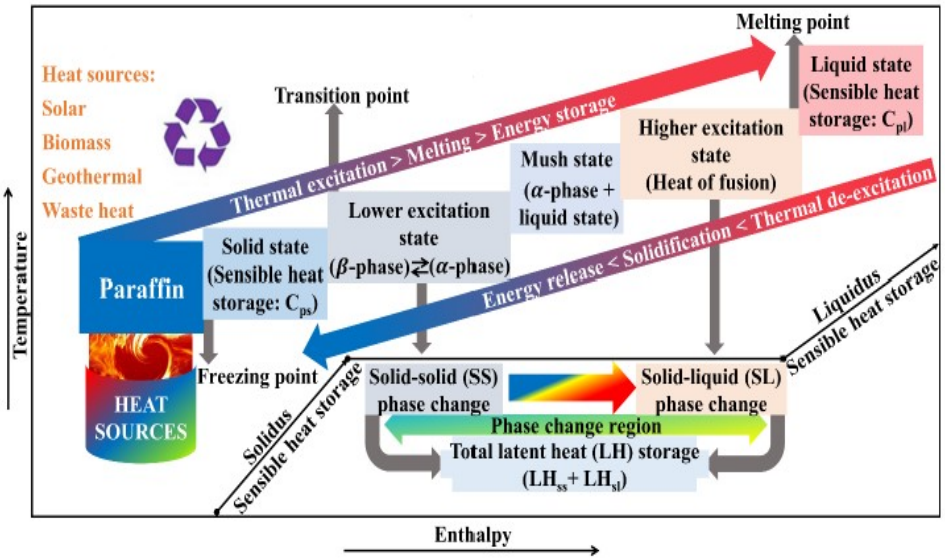


**Figure 2.5:** *Phase transition diagram of PCMs involving interchangeable thermal regimes under thermal excitation and de–excitation states. Lower excitation state signifies the transition point where PCMs undergo solid-solid phase change which is based on structural changes such as $\beta$-phase taking place first, while $\alpha$-phase occurs just after $\beta$-phase but below the melting point. Mush state is expected to consist of marginal fraction of $\alpha$-phase and major fraction of liquid state (Gulfam et al., 2019).*

### 2.3.3 Chemical energy storage (CES)

The chemical energy storage (CES) is further classified into two main categories based on the reaction mechanism: (i) chemical reaction heat storage (CRHS) and (ii) chemical sorption heat storage (CSHS). The reversible and sorption processes have greater potential to store the thermal energy. The brief details of both CRHS and SCHS are describe as follows:

#### 2.3.3.1 Chemical reaction heat storage (CRHS)

Energy stored by CRHS may be occurred by forward and reverse direction. Heat storage and heat dissipation during chemical reaction are referred by endothermic and exothermic reactions. Endothermic reaction forms the products using endothermic energy. In reverse direction, exothermic energy gained by the products can be used under specific conditions through exothermic reaction. The general chemical reaction representation of CRHS is described as (Yan et al., 2015; Ahmed et al., 2017):

1. During charging

$$U + V + thermal\ energy \longrightarrow X + Y \tag{2.4}$$

2. Reactants store the thermal energy for longer duration

3. During discharging

$$X + Y \longrightarrow U + V + thermal\ energy \tag{2.5}$$

During charging, the reactants $U$ and $V$ form the products $X$ and $Y$ through an endothermic dissociation reaction. The chemical energy which is stored in form of chemical potential energy by products $X$ and $Y$, which is further utilised for long period storing products $X$ and $Y$ separately. While during discharging, the reactants $U$ and $V$ are regenerated in reversible reaction resulting from the synthesis reaction of products $X$ and $Y$. The thermal energy stored in thermo-chemical materials is defined as (Pardo et al., 2014):

$$Q = n_{U,V} \Delta H_r \tag{2.6}$$

Where $n_{U,V}$ is the mole number of the reactants $U$ and $V$ $(mol)$ and $\Delta H_r$ is the enthalpy of reaction $(KWh.mol^{-1})$. Schaube et al. (Schaube et al., 2012) proposed the storage of thermal energy by reversible thermo-chemical reaction of $Ca(OH)_2 + thermal\ energy \Longleftrightarrow CaO + H_2O$. Another simple example of thermo-chemical energy storage was presented by Steinfeld et al. (Steinfeld et al., 1999) with dissociation of $Fe_3O_4$. The authors reported that solar energy was sufficient to break the $Fe_3O_4$ into $3FeO$ and $1/2O_2$. Further, when the $FeO$ came in reaction with $H_2O$ while storing it reformed again $Fe_3O_4$ at low temperature.

#### 2.3.3.2 Chemical sorption heat storage (CSHS)

The chemical sorption heat storage (CSHS) principally also relies on the reversible chemical reaction. During endothermic reaction (adsorption), heat is stored while during the exothermic reaction (desorption) it is released. In sorption phenomenon during CSHS a specific gas or vapour (sorbate) is captured or dissolved onto the surface of any solid or inner of liquid (sorbent). The typical thermodynamic reaction of CSHS is as follows (Yan et al., 2015):

$$AZ \times (n+p)G(s) + p\Delta H_r \Longleftrightarrow AZ \times nG(s) + pG(g) \tag{2.7}$$

Here, $AZ$ is solid chemical reactant or liquid absorbent. The reacting salts are usually metallic halides (e.g. $CaCl_2$, $MnCl_2$, $COCl_2$, $BaCl_2$, $NiCl_2$, $NaBr$, etc.). The $G$ is the gas reactant, (e.g. $NH_3$, $H_2O$, $H_2$, etc.), $\Delta H_r$ the reaction enthalpy, $p$ is the equilibrium pressure of solid–gas pair.

## 2.4 PCMs and their classifications

Phase change materials (PCMs) also called the latent–heat storage materials (LHSMs) have potential application in TES systems because of having high thermal storage densities and high latent heat of fusion as compared with sensible heat storage materials. The thermal energy in PCMs, transfers in two modes of (i) SHS and (ii) LHS comprising a state or phase change from "solid–to–liquid" or "liquid–to–solid". Ideal phase transition diagram is presented in Fig. 2.5 (Casini, 2016). It can be seen from Fig. 2.5 that unlike the conventional SHS materials, PCMs absorb and dissipate the heat at constant temperature and pressure, further store $4-15$ times more heat energy per unit volume as compared to SHS materials. The Fig. 2.6 represents the wide range of materials that are categorized as a PCMs with respect to their melting temperature and melting enthalpy (Mehling and Cabeza, 2007).

From the last four decades, various classes of the materials such as paraffin

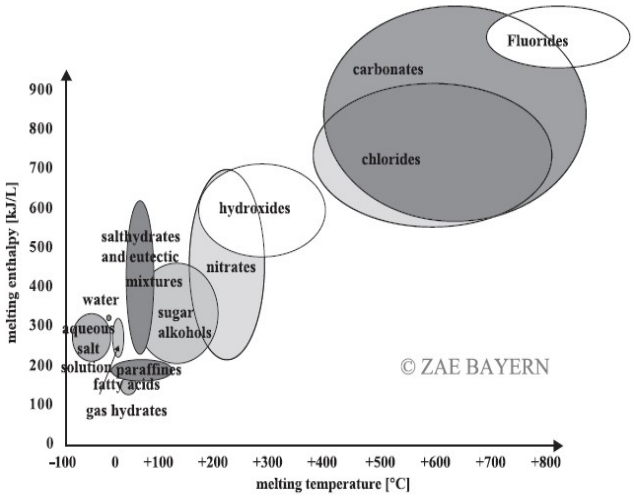


**Figure 2.6:** *Classes of materials that can be used as PCMs with respect to their melting temperature and melting enthalpy (graph: ZAE Bayern) (Mehling and Cabeza, 2007).*

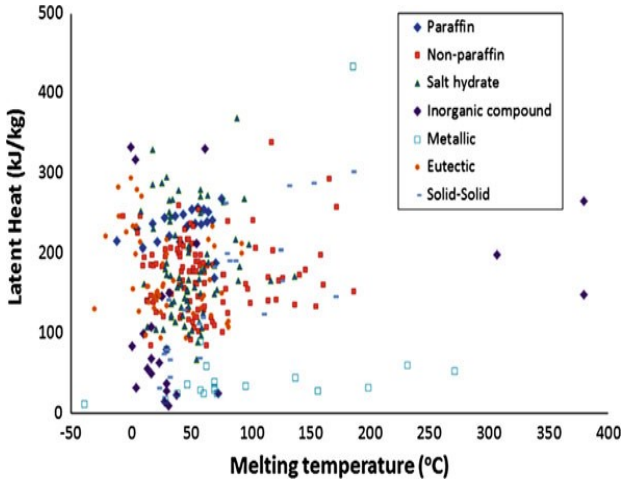


**Figure 2.7:** *Melting temperature and latent heat of fusion relationship of various PCMs (Su et al., 2015).*

waxs, fatty acids, salt hydrates, metal alloys, polymers and organic and inorganic compounds of eutectics are considered as the potential PCMs for TES sytems. Generally, PCMs are classified in three major groups based upon the phase transformation temperature range (Pielichowska and Pielichowski, 2014; Du et al., 2018).

- Low temperature PCMs ($T_m < 15°C$): Used in food industry and refrigeration and air-conditioning.

- Medium temperature PCMs ($15°C < T_m < 90°C$): used in electronic,

textile, medical, solar, batteries, heating and cooling of buildings.

- High temperature PCMs ($T_m > 90°C$): used in industrial, power generation and aerospace applications.

Fig. 2.7 represents the relationship between the melting temperature range and latent heat of fusion of various PCMs (Su et al., 2015). Generally the PCMs are classified as organic, inorganic and eutectic, and detailed classification are further categorized as shown in Fig. 2.8. The advantages and disadvantage of main classes of PCMs are presented in Table 2.1 (Smith et al., 2014; Liu et al., 2015b).

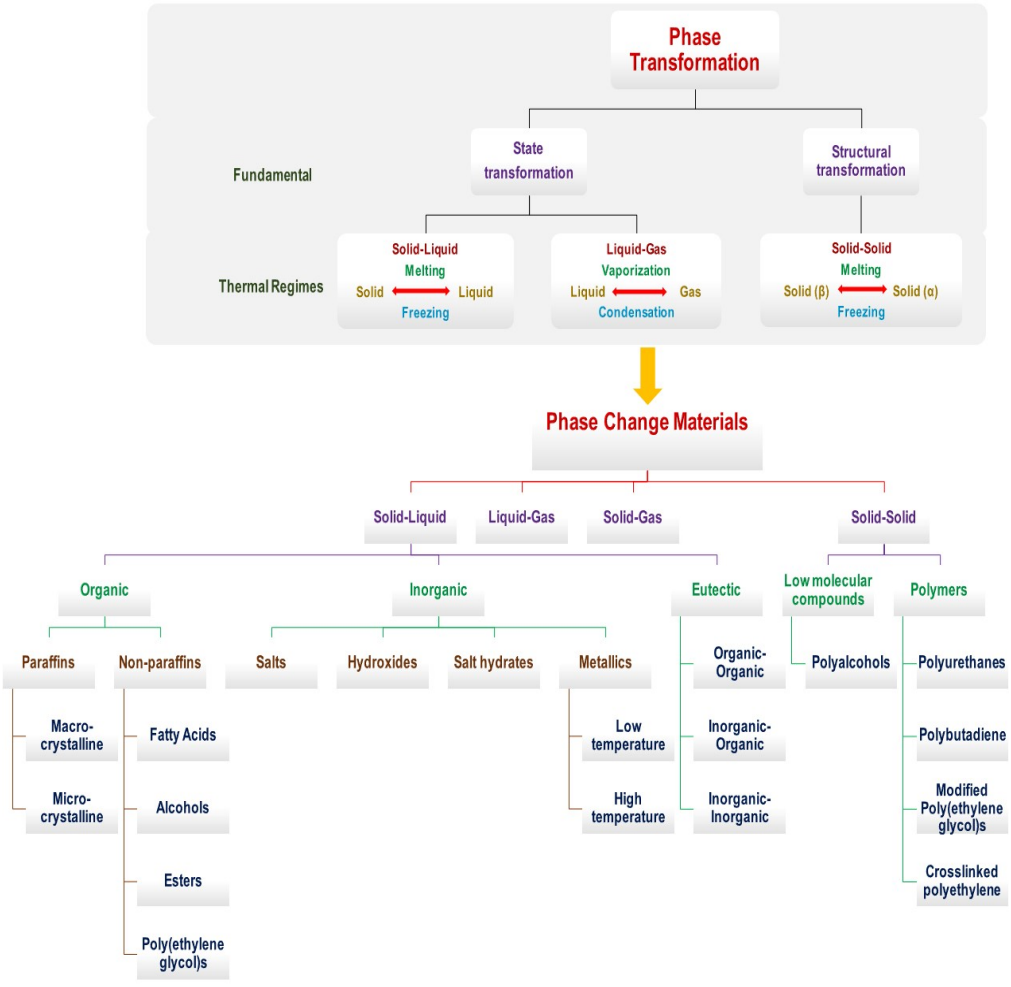


**Figure 2.8:** *Classification of PCMs (Pielichowska and Pielichowski, 2014; Sharma et al., 2015).*

Table 2.1: Advantages and disadvantages of PCMs (Smith et al., 2014; Liu et al., 2015b; Hyun et al., 2014)

| | | **Advantages** | **Disadvantages** |
|---|---|---|---|
| Organic PCMs | Paraffins | High latent heat of fusion | Low thermal conductivity |
| | | Chemically stable and inert | Moderately flammable |
| | | Favourable phase equilibrium | High cost of pure paraffins |
| | | Non-corrosive | Non-compatible with plastics |
| | | Little sub-cooling | Moderately flammable |
| | | Non-toxic | Lower phase change enthalpy |
| | | Non-explosive | |
| | | Available in wider temperature range | |
| | | Small volume change | |
| | | No segregation | |
| | | Recyclable | |
| | | Compatible with other materials | |
| | | Congruently melting | |
| | Non-Paraffins | High latent heat of fusion | Low thermal conductivity |
| | | Little sub-cooling (depends on the application) | Flammable |
| | | Low flash point | Instability at high temperatures |
| Inorganic PCMs | Salt hydrates | Sharp melting point | Phase separation |
| | | High thermal conductivity | Sub-cooling |
| | | High latent heat fusion per unit volume | Cycling stability |
| | | Small volume change | Corrosive |
| | | Low cost | Slight toxic |
| | | Higher phase change enthalpy | Phase segregation |
| | | Compatible with plastics | High density |
| | | Non-flammable | Poor nucleation |
| | | Easily available | |
| | Metals | Sharp melting point | Corrosive |
| | | High thermal conductivity | Toxic |
| | | Small volume change | High density |
| | | Good electrical conductivity | Expensive |
| | | Small volume change | |
| | | High latent heat fusion per unit volume | |

| | | Sharp melting point | Less chemically inert |
|---|---|---|---|
| Eutectics | Organic-Organic | Slightly high volumetric storage density | Lack of test and limited data on thermophysical properties |
| | | Desire melting temperature | |
| | | Easy to prepare | |
| | Inorganic-Organic | Small vapour pressure | |
| | | Biorenewability | |
| | Inorganic-Inorganic | Biodegradability | |
| | | Low toxicity | |
| | | Non-flammability | |

### 2.4.1 Organic PCMs (OPCMs)

The organic PCMs have a wide range of application in TES systems and they include the *paraffin* and *non–paraffin* compounds (fatty acids, alcohols, esters, and Poly(ethylene glycol)s).

#### 2.4.1.1 Paraffin compounds

The paraffins are the straight chain *n-alkanes* belongs to a family of saturated hydrocarbons representing with chemical formula of $C_nH_{2n+2}$, where $n$ is the number of carbons (C). The materials having $n$ between 1 and 4 are gaseous, between 5 and 17 are liquids and more than 17 are solids. The materials when the C atoms are in range of $20 \leq n \leq 40$ are considered paraffin wax, (See Appendix B). Generally, the longer length of hydrocarbon chain has the higher melting temperature. Paraffin materials are generally most commonly used in TES application because of their high latent heat during fusion/crystallization. Paraffin compounds are safer, reliable, predictable and less expensive as compared to the IPCMs. From previous investigations (Parks et al., 1946, 1949; Finke et al., 1954; Messerly et al., 1967; Atkinson et al., 1969) the paraffins are found to store, absorb and release large amount of heat during large numbers of melt–freeze cycles and show no phase segregation. During long phase transition cycles, the paraffins show the favourable characteristics such non-corrosive, chemically inert, colourless, ecologically harmless, non–toxic and low–vapour pressure. Contrarily, the paraffins possess the low oxidation when exposed to oxygen, thus required the leak–proof containers. Additionally, the paraffins have low thermal conductivity especially in liquid phase, however, a lot of techniques or thermal conductivity enhancers such as extruded fins (e.g. plate–fin, pin–fin, perforated–fins etc.), metallic–foams, metal–matrices and nanoparticles are used to enhance this property (Zhang et al., 2018; Qureshi et al., 2018).

#### 2.4.1.2 Non–paraffin compounds

The non-paraffins (*n-alkenes*) compounds are generally sub-categorized into fatty acids, alcohols, esters and poly(ethylene glycol)s. The non-paraffins have high latent heat of fusion, lower thermal conductivity, inflammability, low flash point, varying level of toxicity and unstable at higher temperatures.

**2.4.1.2.1 Fatty acids** The fatty acids represented with chemical formula $CH_3(CH_2)_{2n}COOH$ are found in the form of acids derived from vegetable and animals sources. The fatty acids are long hydrocarbon chain of carbon from 10–30, hydrogen atoms and carboxyl group (COOH) which makes the fatty acids as PCMs non-toxic, biodegradable, low corrosion, chemically and thermally stable. The fatty acids categories into six groups: caprylic acid (CA), capric acid, myristic acid (MA), palmatic acid (PA) and stearic acid (SA) (Abhat, 1983; Bailey, 1945). Commonly, fatty acids are saturated or unsaturated having one or more double bonds. Due the molecular structure of the unsaturated fatty acids have lower melting temperatures which allows the closer molecular interaction. Moreover, the fatty acids are highly flammable which limits their application at higher temperature, flames and oxidizing agents (Sharma et al., 2015; Hyun et al., 2014). The phase transition temperature and latent heat fusion of fatty acids are varied from $-5$ to 70 °C and 45 to 210 kJ/kg, respectively. The additional features of the fatty acids are that they have suitable range of melting temperature which favor them in LHS applications. Also they are capable thermal cycles (heating and freezing) without any degradation in thermal properties (Feldman et al., 1995, 1989, 1991) with little or no sub-cooling (Pielichowski and Flejtuch, 2003a). Moreover, fatty acids are more expensive than paraffins and possess a obnoxious odour (Sharma et al., 2009). The thermophysical properties of some common fatty acids are listed in Appendix C.

**2.4.1.2.2 Alcohols** The alcohols also known as *polyalcohols* are under investigation by researchers (Gunasekara et al., 2016; Diarce et al., 2015; Barrio et al., 2016) as a potential PCMs because of the association with nanomaterials or special composites resulting increasing the applicability for energy storage. The alcohols have the temperature range between 90 to 200 °C and some alcohols like xylitol, erythitol and mannitol have higher amount of heat of fusion (Shen et al., 2018).

**2.4.1.2.3 Esters** Esters are derived from acids through which the one hydroxyl (−OH) group is replaced by the one alkyl (−O) group. The esters possess the solid-liquid phase transition over a narrow temperature range forming the mixture of eutectic having no or small sub–cooling. Most of the esters are widely commercial available for polymer, cosmetic and textile applications (Scalat et al., 1996; Feldman and Banu, 1996; Nikolić et al., 2003; Aydın, 2013).

**2.4.1.2.4 Poly(ethylene glycol)s** The polyethylene glycols (PEGs) which are also known as polyethylene oxide (PEO) or polyoxyethylene (POE), are important semi–crystalline polymer composed of dimethyl ether chains, HO–$CH_2$–($CH_2$–O–$CH_2$–)$_n$–$CH_2$–OH. With the hydroxyl group at the end of chain makes it favourable to mix with water as well as in organic materials. Generally, the PEGs are employed as a component of packing materials with water paints, textile fibres, coating of papers and as a solubilizing agent in drugs. The PEG in various grades (400, 600, 1000, 3400, 10000, 20000, 35000, 100000, 1000000) (Pielichowska and Pielichowski, 2014; Sharma et al., 2015) are extensively used as new PCMs in TES application both experimentally and numerically because they possess high enthalpy of fusion. The high enthalpy of fusion of PEGs attributes to a high degree of crystallinity (Pielichowski et al., 2004). Relative molecular mass or molecular weight of PEGs plays a greater influence in the applications of PEGs as melting temperature of PEGs depends on the relative molecular mass. Increasing molecular mass of PEGs increases the

melting temperature hence increases the latent heat of phase change. Further, the molecular mass has the influence on the degree of crystallinity ranging from 83.8% to 96.4% (Pielichowski and Flejtuch, 2002). Generally the melting temperature of PEG vary from 4 to 70 °C with corresponding heat of fusion range from 117 to 174 J/g. Additional features of PEGs are that they are non–flammable, non–toxic, non–corrosive, inexpensive, chemically and thermally stable, however, like other OPCMs the PEG also has lower thermal conductivity. Also the mixture of fatty acids and PEGs have been investigated to obtain the desired range of melting temperature and latent heat of fusion. The details of PEGs with thermal properties are give in Appendix D.

### 2.4.2 Inorganic PCMs (IPCMs)

The second major class of PCMs is inorganic PCMs (IPCMs) which are further sub-divided into salts, salt hydrates, metals and alloys. The IPCMs usually have similar enthalpies per mass as the OPCMs but they have higher enthalpies per unit volume because of existing high densities. The positive features of IPCMs are that they posses high thermal conductivity, sharp melting temperature, higher phase change enthalpy and wide range of melting ranges but the negative features are corrosiveness, phase segregation, sub-cooling, lack of thermal stability and phase separation.

#### 2.4.2.1 Salt

These the inorganic salts with a formula of $A_xB_y$ where $A_x$ and $B_y$ are the cation and anion, respectively. The salts have the higher temperature range but they have less heat of fusion. The common example of using salts as a high temperature energy storage materials in concentrated solar power. A few examples of salts are $BaCl_2$, $CaSO_3$, $LaCl_3$, LiBr and so on (Donkers et al., 2017).

#### 2.4.2.2 Salt hydrates

The salt hydrates are the alloys of inorganic salts and water forming a crystalline solid of general formula of $A_xB_y.nH_2O$, here $A_xB_y$ is representing the salt component, $n$ is the numbers of water molecules and $H_2O$ is the water. The salts hydrates generally make the ion-dipole or hydrogen bonds where the water molecules are located in well–defined structure. The phase transformation from solid–to–liquid in salt hydrates is the dehydration/hydration of the salts which is similar process of melting/freezing in thermodynamics. At phase transformation temperature, the hydrated crystal breaks into a lower hydrate with $m$ moles of water as:

$$AB.nH_2O \longrightarrow AB.mH_2O + (n-m)H_2O \tag{2.8}$$

or the anhydrous salt and water

$$AB.nH_2O \longrightarrow AB + nH_2O \tag{2.9}$$

On the basis of melting behaviour, the salt hydrates are classified as:

- Congruent melting: when the anhydrous salt is completely soluble in its hydration water at the melting temperature.
- Incongruent melting: when the salt is not entirely soluble in its hydration water at the melting temperature.
- Semi-congruent melting: when the solid and liquid phases are in equilibrium during phase transition having different melting composition because of the conversion of the salt hydrate to a lower salt hydrate having less amount of hydration water (Sharma et al., 2009).

The promising properties of the salt hydrates are (i) high latent heat of fusion per unit volume, (ii) small volume change on melting, (iii) relatively high thermal conductivity (almost double of paraffin wax) (da Cunha and Eames,

2016). Furthermore, salt hydrates are not very corrosive, compatible with plastics and only slightly toxic. The major issue in most important salt hydrates which have high heat of fusion and suitable melting temperature is that they melt incongruently. During the dehydration process, the $n$ or $n-m$ moles of hydration water are less sufficient to dissolve anhydrous or lower hydrate salts resulting in the solution become supersaturated. As a consequences of this the anhydrous or lower hydrate salts, due to their relative higher densities, settle at the bottom of container. This supersaturation leads to density differences, phase separation and sedimentation. Another problem in salt hydrates is the poor nucleation rate resulting in super or sub-cooling. This leads to freezing of liquid at lower temperature and a loss of energy. To overcome these problems of incongruent melting can be reduced by (i) mechanical stirring, (Pielichowska and Pielichowski, 2014) (ii) encapsulating the PCM, (iii) use of excess water to prevent supersaturation (iv) modifying the chemical composition and (v) adding nucleation agents to provide nucleation sites for the salts (Sharma et al., 2009; Biswas, 1977; Jovanović et al., 2016; Niyas and Muthukumar, 2018). The detail thermophysical properties of salt hydrates are given in Appendix E.

#### 2.4.2.3 Metallics

The other subcategory of IPCMs is low melting metals which can be used as LHS materials as PCMs. The potential features of these metals are that they possess (i) higher thermal conductivity, (ii) good electrical conductivity, (iii) small specific heat, (iv) small volume change in phase transformation, (v) low latent of heat of fusion per unit weight, however high latent–heat of fusion per unit volume (due to large density). A few decades before the metallics were not considered as energy storage materials because of their high density and melting temperature. However, with the remarkable advancement in nanotechnology, nanomaterials with metallic nanoparticles have made the metallic alloys more potential in TES applications. The lower melting temperature such as (Bi, Pb, In, Sn, Cd and their alloys) have been under investigation

for laser system, USB flash memory (Ge and Liu, 2012) and absorptive heart sink for smart electronics application (Ge and Liu, 2013; Kumar et al., 2011). Appendix F shows the thermophysical properties of low–melting point metals and their alloys used as LHS materials.

### 2.4.3 Eutectics

The third major class of PCMs is eutectics which is further sub–divided into organic–organic, inorganic–organic and inorganic–inorganic (Sharma et al., 2015). A eutectic is a low melting composition PCM which comprises on two or more low melting temperature components, each of which melts and freezes congruently forming a mixture of the components crystals while crystallization (Sharma et al., 2009; Telkes, 1952). The chemical composition or elements of eutectics make them to melt and freeze at lower temperature. The potential advantage of eutectics over the other PCMs are their phase transition temperature which can be adjusted by mixing the different weight ratios of the components. Such as compositions of tetradecane with octadecane, docosane and hexadecane have the temperature range of 1.5–5.6 °C. The other positive features of eutectics are that they melt and solidify without segregation and sub-cooling. During melting and freezing in an insinuate blend of crystals leaving little possibility of separation. Pielichowski and Flejtuch (Nikolić et al., 2003) studied the blends of PEG, polypropylene oxide (PPO) and polytetrahydrofuran (PTHF) of different molecular weights with fatty acids (CA, LA, MA, PA and SA) as TES materials. Recently, Atinafu et al. (Atinafu et al., 2018) synthesized the MA–SA into porous carbon matrixes and found the 117.65% enhancement in thermal conductivity and 45.69% in latent heat of melting. According to organic–organic, inorganic–inorganic and organic–inorganic eutectic PCMs, the detailed thermophysical properties are given in Appendix G.

## 2.5 Nanocomposite PCMs

The *nanocomposite* are usually defined the dispersion of nanoscale nanoparticles, nanospheres or embedding the nanostructures into the bulk materials (i.e. PCMs). To incorporate the NMs into PCM is called the nanocomposite PCMs (NCPCMs). The purpose to disperse the NMs in bulk materials to enhance the certain vital properties related to the specific operational needs. In case of PCMs, which are also known LHSMs, are classified as organic, inorganic and eutectic compounds, as shown in Fig. 2.8, have several drawbacks related to their thermophysical properties which cause to reduce the operational performance. Thus, to enhance the thermophysical properties of PCMs specially OPCMs which possess the lower thermal conductivity various NMs of different structures are dispersed as TCMs. Therefore, dispersion of NMs as TCMs into the PCMs will enhance the TM and TES performance of the latent–heat TES systems.

## 2.6 Ideal characteristics of NCPCM

An ideal characteristics of NCPCM significantly influence the thermal management systems while performing at varying operating conditions. Thus, for an ideal NCPCM, it is necessary to meet the specific criteria and environment conditions for a longer duration. The Fig. 2.9 presents the ideal characteristics of NCPCM which are necessary for utilization of thermal management applications. Since, these ideal characteristics of NCPCM depend on their fundamental chemical, physical, thermal and economics properties which are as follows (Wei et al., 2018):

- **Sufficient phase–transition temperature:** The suitable phase change temperature of NCPCM is very essential and must match the operating conditions of specific application at melting and solidification temperature points.

- **High latent–heat of fusion:** The latent–heat of fusion, also called enthalpy of fusion, of the NCPCM is the most desirable thermal property to absorb large amount of heat with less amount of volume especially to reduce the size of the TM system which makes it light weight. The NCPCMs based on the organic PCMs have the tendency to absorb higher latent–heat of fusion.

- **High thermal conductivity:** The higher thermal conductivity provides the additional capability to store thermal energy while sensible–heating phase resulting lower the charging and discharging phases. The inorganic materials dispersed NCPCMs have the more potential to increase the thermal conductivity resulting in transmit the heat at higher rate. However, the increase in thermal conductivity of NCPCMs causes the less absorption of latent–heat fusion.

- **Durability:** The NCPCM must has to withstand from damage, friction, and leakage. The strength of NCPCM has to sustain its mechanical properties while flowing through system.

- **High density and small volume change at phase–transition:** The high density of the NCPCM helps to reduce size of encapsulated container at smaller level. The small volume change while phase transformation help to minimize the complexity of the NCPCM storage container.

- **Congruent melting:** The congruent melting of the NCPCM helps to prevent the irreversible segregation resulting reduces the loss of storage capacity while recycling.

- **Favourable phase–equilibrium:** The favourable or suitable phase–equilibrium temperature ensure the heat storage and extraction at constant temperature in thermal management system.

- **Long–term chemical stability:** The continuous charging and discharging of NCPCMs, water loss, decomposition or chemical interaction

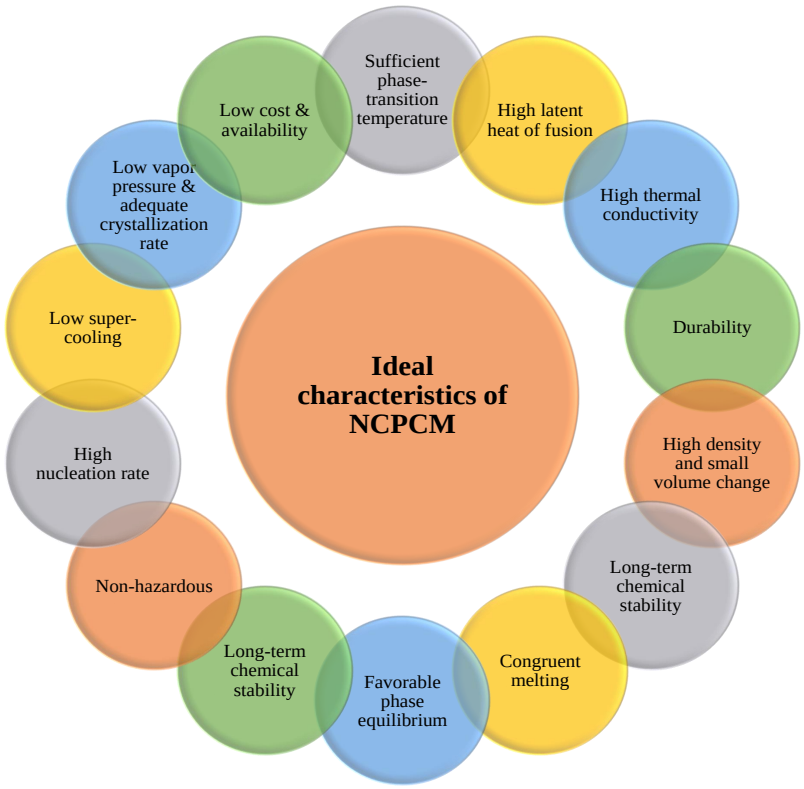


**Figure 2.9:** *Ideal characteristics of NCPCM.*

with storage container can undergo the degradation in NCPCMs. So, it is highly preferred that NCPCMs should maintained its long–term chemical stability and corrosion resistance interacting with other materials.

- **Non–hazardous:** For safety measures, the NCPCM should be non–toxic, non–flammable and non–explosive.

- **High nucleation rate:** An ideal NCPCM should have high nucleation rate and good crystallization rate.

- **Low super–cooling or sub–cooling:** The low sub–cooling, also called super–cooling, ensures the melting and cooling at the same temperature which is due to metastable condition of the NCPCM while solidification which means that during cooling the NCPCM is not in thermodynamics equilibrium state. The super–cooling particularity occurs in salt–hydrates which prevents the extraction of thermal energy.

- **Low vapour pressure and adequate crystallization rate:** The low pressure and rapid crystallization of NCPCM help to reduce the design complexity of NCPCM thermal management system.

- **Low cost and availability:** The cost and availability of NCPCM have the major significance on the overall cost of the TM system. As the development of NCPCM requires high precision and clean environment so it may increase the cost of NCPCM.

## 2.7 Preparation of NCPCMs

The preparation of NCPCMs requires the well–established and highly precise methods for the dispersion of NMs into the base PCM to achieve the homogeneous and stable mixture. A few customised methods to synthesis the NCPCM are described in Table 2.2 and shown in Fig. 2.10. Generally, the two most common methods of NCPCM preparation are $(I)$ *one–step method* and $(II)$ *two–step method* for proper mixing and stabilization. The key challenge of uniform dispersion of NMs is to utilize the proper mixing and a well–stabilize technique. A non–uniform or not well distributed mixture of NMs into the base PCM, tend to form the agglomerate and sediment, particularly while the solidification or cooling process of NCPCM because of strong Van der Waal forces and high surface areas among the nanosized powder (Mahian et al., 2019).

**Figure 2.10:** *Customised synthesised methods of NCPCM.*

Table 2.2: Methods of preparation of NCPCM.

| Synthesis process | PCM | NMs | Description | Reference |
|---|---|---|---|---|
| Vacuum impregnation method | CA | EG | The 10g porous EG was placed inside the flask which was connected to a water tromp apparatus to evacuate the air from the porous EG. The evacuation process was continued for about 30 min under vacuum conditions. Then liquid PCM was allowed to flow into the flask to cover all the porous EG through the valve of the PCM container. Further, the air was allowed to enter the flask again to force the liquid fatty acid to penetrate into the pore space of EG. Meanwhile, the constant temperature above the melting temperature of the fatty acid was maintained through the heater to heat the composite PCM to test the fatty acid exudation from the porous spaces. The amount of fatty acid absorption by EG was evaluated by observing the fatty acid exudation from composite. | (Sari et al., 2008) |

| | | | | |
|---|---|---|---|---|
| Varnish layer | n–Octadecane | xGNPs | The PCM (n-octadecane) was first melted and then was mixed directly with the exfoliated graphene nanoplatelets (xGNPs). The liquid homogeneous mixture of n-octadecane/xGNPs was poured into the cylindrical shaped hollow mould to form the cylindrical shape specimens. The cylindrical hollow moulds were covered with varnish before and after the mixture of n–octadecane/xGNPs into the mould to form the layer to prevent the leakage during phase change. Then, all the specimens of n–octadecane/xGNPs were dried at 25 °C and 50% relative humidity for 48 hrs. | (Xu et al., 2017) |
| Kneader mixing technique | Octadecane | EG | The EG powders were dried before mixing with octadecane at 105 °C for 24 hrs in a vacuum oven to evacuate the air and water. The octadecane was heated above its melting temperature and then it was directly impregnated on the EG stirring at 30 rpm and 80 °C for 1 hr for thoroughly mixing and penetration. Then, the mixture of octadecane and EG was allowed to cool at room temperature. | (Kim et al., 2016) |
| Autoclave method | Tetradecanol (TD) | EG | The organic PCM (TD), EG and anhydrous ethanol were mixed in an autoclave. The ethanol was used to improve the absorptivity of PCM molecules and to improve the uniform dispersion of EG into the TD. Then, the autoclave was sealed and heated at 120 °C for 24 hrs and allowed to cool at room temperature. Finally, the mixture of TD/EG/ethanol was taken out from autoclave and heated at 50 °C to evaporate the ethanol and then it was dried under vacuum for 24 hrs to obtain the TD/EG composite. | (Zeng et al., 2014) |

| | | | | |
|---|---|---|---|---|
| Sonication & Ultrasonication | RT–22HC | Graphene | The organic paraffin PCM, RT-22HC, was melted above its melting temperature and nano graphene was mixed into the melted RT–22HC. Then, the mixture of RT–22HC/graphene was stirred and placed into ultrasonicator bath at a frequency of 40 Hz. The sonication process was continued for 3 hrs at 45 °C until the graphene was dispersed into the RT-22HC. | (Putra et al., 2017) |
| Stirring & Sonication | Hexadecane, Octadecane, Paraffin wax | xGNPs | The PCM was melted at a constant temperature above their melting temperature by using hot–plate. The, the xGNPs powder was mixed into the liquid PCM and stirring was contined for 20 min at 1000 rpm. Finally, the mixture of liquid PCM/xGNPs was ultrasonicated for 20 min and allowed to cool at room temperature. | (Jeon et al., 2012) |

### 2.7.1 One–step method

In one–step or single–step method, the synthesising and dispersing of nanoparticle are carried out simultaneously in the base PCM in liquid state in preparation of NCPCM, as show in Fig. 2.11. All other processes such as drying, storage, stirring, transportation, and dispersion of nanoparticles are avoided to enhance the stability and to minimize the agglomeration of nanoparticles, that is the reason this process is named as one–step method (Arshad et al., 2019b). Uniformly dispersed nanoparticles can be prepared resulting in improved stable suspension in the based PCMs and reduced production cost. This method provides the most effective NCPCM because it provides the better stability and avoids the formation of clusters and oxides. The synthetization of NCPCM via one–step method is difficult on a large scale because of higher production cost. Mohamed et al. (Mohamed et al., 2017) mixed the nano $Al(NO_3)_3.9H_2O$, Urea and petroleum wax and the mixture was microwaved for 3–5 min. Teng et al. (Teng and Yu, 2012a) synthesised the NCPCM using direct–synthesis method

with $Al_2O_3$, $TiO_2$, $SiO_2$ and ZnO nanoparticles and mixed with paraffin wax. Three different mass concentration of 1.0, 2.0, and 3.0 wt% were selected and mixture was homogenized for 40 min at 120 °C to obtain further homogeneous solution.

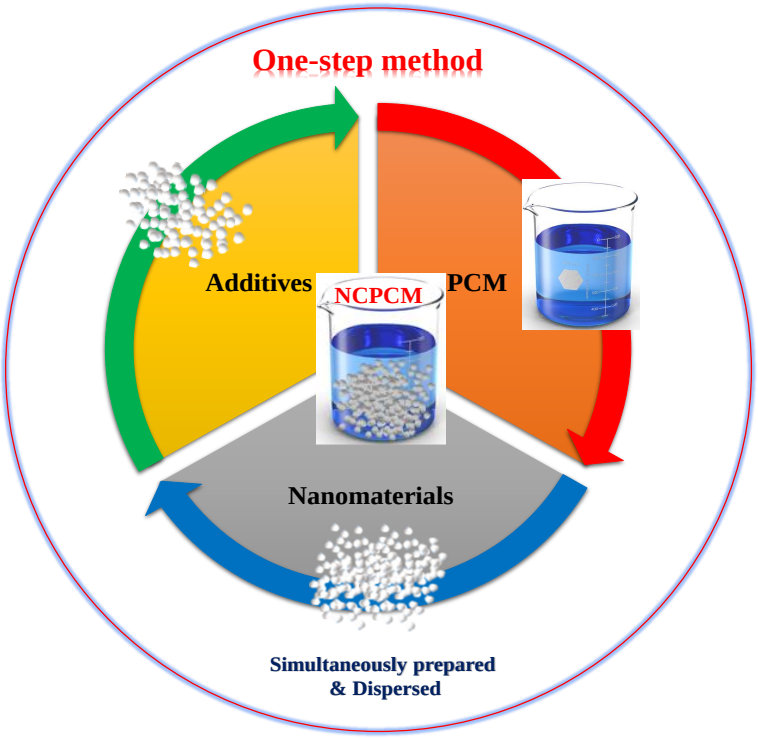


**Figure 2.11:** *Schematic representation of one–step method.*

### 2.7.2 Two–step method

The most widely used method to synthesize NCPCMs is the two–step method, which utilizes the nanoparticles, nanofibers, nanorods, nanowires, nanosheets, nanotubes, droplets, and other nanomaterials. Initially, the dry powder is prepared through mechanical and chemical methods such as milling, grinding, sol–gel, and vapour phase. This nanosized powder is then mixed with the host PCMs and different methods such as magnetic stirring, ultrasonic vibrators, magnetic force agitation, high–shear mixing, homogenizing and ball milling are used. Constant stirring reduces the agglomeration of NCPCMs, which is a major issue of synthesizing of NCPCMs (Tariq et al., 2020b). From

previous investigations, it has been explored that due to high surface area and surface activity, nanoparticles have the tendency to aggregate. Also, to prepare the NCPCMs via two–step method using oxide nanoparticles than metallic nanoparticles are more stable because the oxide nanoparticles have the lower density and higher surface area compared to the nonoxide nanoparticles. The most effective solution to enhance the stability of NCPCMs is the use of surfactants. Fig. 2.12 represents the two–step method to prepare the NCPCMs. Although this method is economical to produce the NCPCMs, there are some issues of drying, storage and transportation. The thermal conductivity of NCPCMs is decreased due to agglomeration and clogging. However, the microstructure of nanoparticles can be varied and enhanced by altering the synthesis parameters such as temperature, ultrasonic and microwave irradiation, reactant and additive types, concentrations and order. Moreover, various surfactants have been used during synthesising to avoid nanoparticles aggregation and clogging by creating a barrier and reducing the surface tension at the interface of nanoparticles and PCM. Various surfactants such as Sodium Dodecyl Sulphate (SDS) (Latibari et al., 2013), Sodium Dodecyl Benzene Sulfonate (SDBS) (Arshad et al., 2020a), Poly Vinyl Pyrrolidine (PVP) (Bahiraei et al., 2017), Ethanol (Parameshwaran et al., 2014) while sythesing of NCPCMs. The two–step method is quite an economic way to produce NCPCMs at commercial scale. The preparation of NCPCM adopting two–step method requires a certain time for stirring and sonication which is based on the selected base PCM and type of the NMs. Many notable researchers adopted the two–step method synthesized the NCPCM under the stirring and sonication range of approximately 60–120 min and 60–180 min, respectively. The detail of selecting various PCM, NMs, stirring and sonication durations of one–step and two–step methods are summarised in Table 2.3.

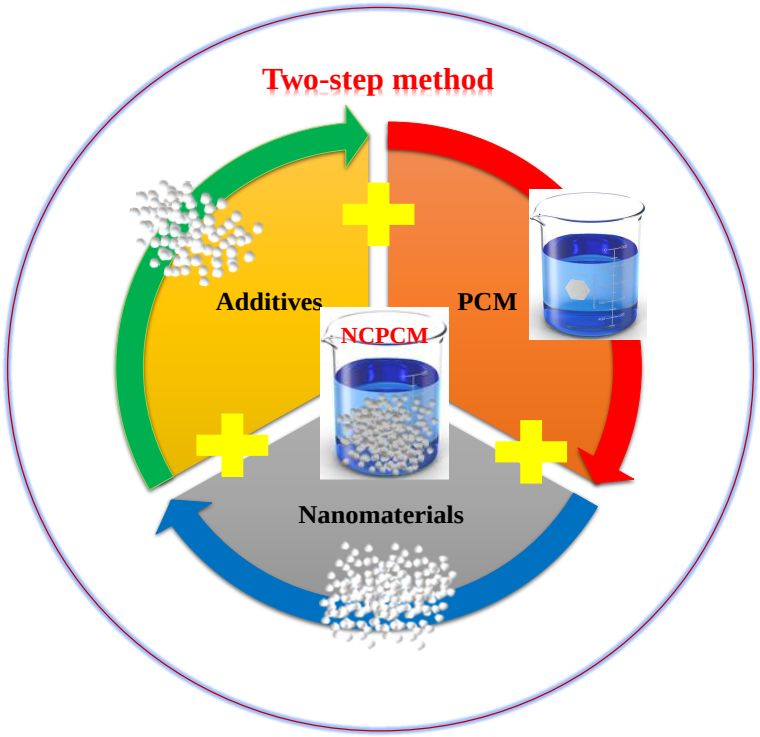


**Figure 2.12:** *Schematic representation of two–step method.*

Table 2.3: Summary of NCPCM synthesized by Stirring and Sonication technique

| Preparation method | Base PCM | Nanoparticles | Stirring time | Sonication time | Surfactant | Reference |
|---|---|---|---|---|---|---|
| Two–step | Different organic solvents | $TiO_2$ | - | 60 min | - | (Bae et al., 2003) |
| Two–step | Poly carboxylic acid | $TiO_2$ | - | 30 min | - | (Bozzi et al., 2005) |
| Two–step | Paraffin wax | SWCNTs, MWCNTs, CNFs | - | 240 min | - | (Shaikh et al., 2008) |
| Two–step | PA | CNTs | | - | - | (Wang and Meng, 2010) |
| Two–step | Ethanol | Ag nanowires | - | 60 min | 1-tetradecanol | (Zeng et al., 2010) |
| One-step | Paraffin wax | $Al_2O_3$, $TiO_2$, $SiO_2$ and ZnO | 40 min | 60 min | - | (Teng and Yu, 2012a) |
| Two-step | PAO | Indium Powder | 10 min | 90 min | - | (Wu et al., 2013) |
| Two–step | Liquid paraffin | MWCNTs | - | - | - | (Zabalegui et al., 2014) |
| Two–step | CA/PA | Graphite nanosheets | - | 60 min | - | (Sayyar et al., 2014) |
| Two–step | LA/SA | $TiO_2$, CuO, ZnO | - | 60 min | SDBS | (Harikrishnan et al., 2014) |
| Two–step | Paraffin wax | $TiO_2$, $Al_2O_3$ | 15 min | 50 min | - | (Chaichan et al., 2015) |
| Two–step | Ethyl trans-cinnamate | Ag-$TiO_2$ | 60 min | 30 min | Ethanol | (Parameshwaran and Kalaiselvam, 2016) |
| Two-step | RT45, RT55 | $Al_2O_3$ | 20 min | 150 min | - | (Colla et al., 2015, 2017b) |
| Two–step | Paraffin wax | SiC, $Al_2O_3$, CuO | - | 60 min | - | (Al-Waeli et al., 2017b,a) |
| One–step | Petroleum wax | $Al_2O_3$ | - | 30 min | - | (Mohamed et al., 2017) |
| Two–step | Paraffin wax | $TiO_2$ | - | - | SSL | (Sami and Etesami, 2017) |
| Two–step | RT20, RT25 | $Al_2O_3$, Carbon black | 30 min | 150 min | - | Colla et al. (2017a) |
| Two–step | Tricosane | $Al_2O_3$ | - | 30 min | - | (Krishna et al., 2017) |
| Two–step | CA and OA | Activated carbon nanosheets | - | 180-240 min | - | (Hussain et al., 2017) |
| Two–step | Paraffin wax | CNF, GNP, Graphite | 30 min | 120 min | Poly Vinyl Pyrrolidone-40 | (Bahiraei et al., 2017) |
| Two–step | RT42 | CuO | - | 1440 min | - | (Sharma et al., 2017) |
| Two–step | CA | CuO | - | 30 min | - | (Kumar et al., 2017) |
| Two–step | Paraffin | GNP | - | 30 min | - | (Ramakrishnan et al., 2017) |
| Two–step | OA, Paraffin wax | Gr Powder | 15 min | 2 min | - | (Narayanan et al., 2017) |
| Two–step | $CaCl_26H_2O$ | $Al_2O_3$, $TiO_2$, Cu, $SiO_2$ | 30 min | 30 min | SDBS, SDS, Span-80, CTAB | (Li et al., 2017) |
| Two–step | Paraffin wax | AlC | 60 min | 30 min | - | (Chen et al., 2017) |
| Two–step | RT50 | CuO | - | 30-45 min | - | (Pahamli et al., 2017) |
| Two–step | $Mn(NO_3)_2$ | $Fe_3O_4$ | - | 240 min | - | (Alimohammadi et al., 2017) |
| Two–step | NPG | CuO | 180 min | - | - | (Venkitaraj et al., 2018) |
| Two–step | NPG | CuO | 120 min | 10 min | - | (Praveen and Suresh, 2018) |

Table 2.3: Summary of NCPCM synthesized by Stirring and Sonication technique

| **Preparation method** | **Base PCM** | **Nanoparticles** | **Stirring time** | **Sonication time** | **Surfactant** | **Reference** |
|---|---|---|---|---|---|---|
| Two–step | Paraffin wax | Ag, CuO, $Al_2O_3$, MWCNTs | 4320 min | - | Tween 60 | (Bashar and Siddiqui, 2018) |
| Two–step | $NaLiCO_3$ | MgO, Ggraphite flake | 30 min | - | - | (Li et al., 2019a) |
| Two–step | RT35HC | $Al_2O_3$ | - | 180 min | - | (Abdelrahman et al., 2019) |
| Two–step | RT-44HC, RT-64HC | GNPs | 180 min | 180 min | - | (Tariq et al., 2020a) |
| Two–step | Paraffin wax | CuO | | 40 min | Span-80 | (Wang et al., 2020) |
| Two–step | LA/SA | Diatomite, EG | 30 min | 8 min | - | (Liu et al., 2010) |
| Two–step | RT-28HC | GNP, MWCNTs, $Al_2O_3$, CuO | 180 min | 60 min | SDBS | (Arshad et al., 2020b) |
| Two–step | RT-35HC | $TiO_2$, $Al_2O_3$, CuO | 180 min | 60 min | SDBS | (Arshad et al., 2020d) |
| Two–step | RT35HC | $TiO_2$ | 181 min | 60 min | SDBS | (Arshad et al., 2020a) |
| Two–step | Paraffin wax | CuO | 120 min | 240 min | - | (Kumar et al., 2021) |
| Two–step | Paraffin wax | $Al_2O_3$ | 120 min | 120 min | - | (Kothari et al., 2021) |

## 2.8 Classifications of NCPCMs

The major classification of NCPCMs are categorised as (I) organic NCPCMs, (II) inorganic NCPCMs and (III) hybrid NCPCMs, as shown in Fig. 2.13. The inorganic NCPCMs are further categorized as metallic, metallic–oxide and quantum dots–additives NCPCMs based on the structure of NMs. Moreover, the organic NCPCMs are referred as carbon–additives NCPCMs which are based on the different allotropes of carbon based NMs such as carbon nanotubes, carbon nanofiber, fullerenes, expanded graphite, graphite powder, graphene, graphene oxide, reduced graphene oxide, graphene nanoplatelets, etc. The hybrid NCPCMs are newly developed NCPCMs which are the mixture of two, three or more NMs of carbon/carbon, metallic/metallic–oxide, metallic–oxide/metallic–oxide, carbon/metallic, carbon/metallic–oxide with PCMs.

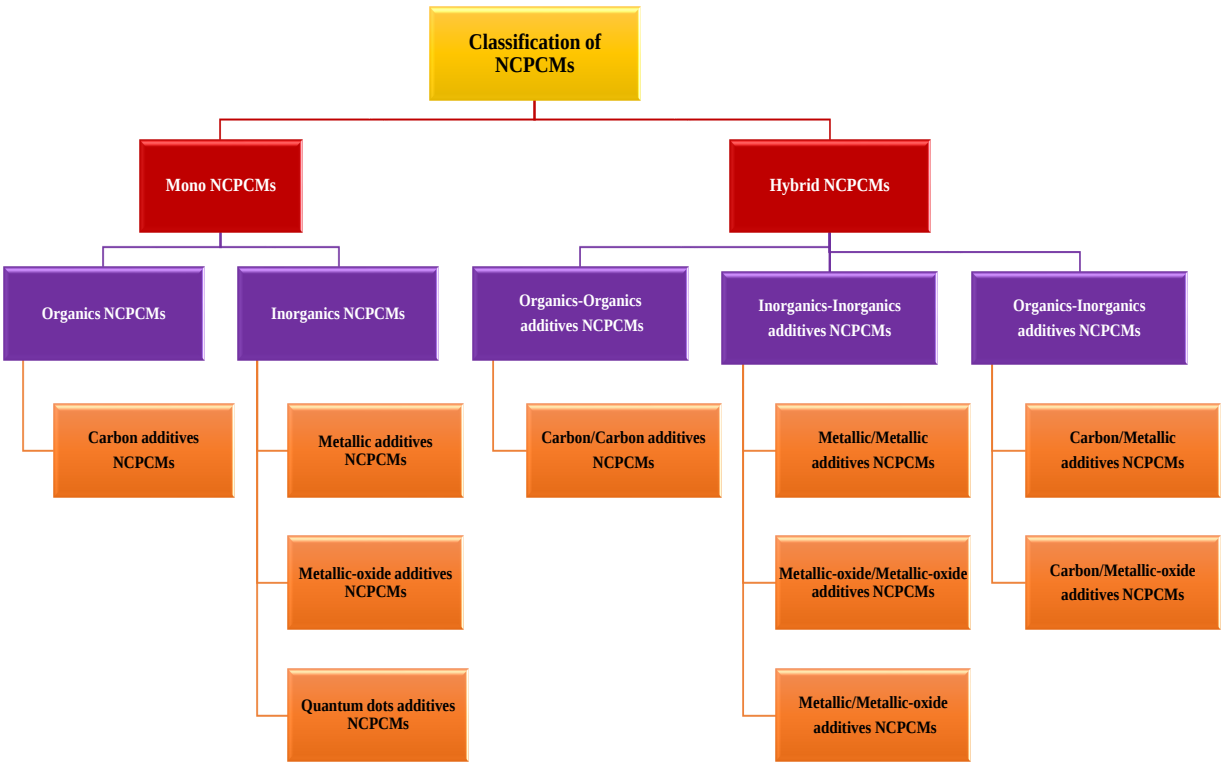


**Figure 2.13:** *Classifications of nanocomposite PCMs.*

### 2.8.1 Metallic–additives NCPCMs

Metallic NMs are the excellent thermal conductors of thermal or heat energy as inorganic NMs. Among the metallic NMs, the silver (Ag) NM has the best thermal as well as electrical conductivity having the thermal conductivity of 430 W/m.K. The thermal conductivities of common NMs used for the development of NCPCMs and NFs are listed in Table 2.4 and Fig. 2.14. The copper (Cu) has the higher thermal conductivity than the gold (Au) however, the Cu has the thermal conductivity near to Ag. The Ag and Au are exorbitant and suffer to oxidation and have higher cost. The Cu NM are the most commonly used in many applications due to significantly less cost than the Ag and Au. In spite of that, most of the metallic NMs have been utilized for the development of metallic NCPCMs to enhance thermophysical properties of PCMs. Few studies have been reported till yet using metallic NMs with different PCMs. Until now, the scientists have explored the thermophysical properties of Ag, Cu, SiC, AlN and $Si_3N_4$ NMs with different PCMs. The most common PCMs which have been used as a base PCMs are paraffin wax, tetradecanol (TD), polyethylene glycol (PEG), n–eicosane. Wu et al. (Wu et al., 2012) investigated the thermophysical properties of paraffin and Cu based NCPCMs by varying the loading content of 0.2 wt%, 0.5 wt%, 1.2 wt%, and 2.0 wt%. The enhancement in thermal conductivity was obtained of 14.2% for solid and 18.1% for liquid phases at 2.0 wt% of Cu nanoparticles. Deng et al. (Deng et al., 2016) used the PEG and Ag nanowires with loading contents of 7.1 wt%, 13.7% and 19.3%. The higher thermal conductivity enhancement of 6.0, 8.5, and 11.3 times at 7.1 wt%, 13.7% and 19.3%, respectively. A decreasing trend in latent-heat fusion was observed having 110.0, 102.0 and 99.1 J/g at 7.1 wt%, 13.7% and 19.3%, respectively. Chen et al. (Chen et al., 2017) synthesised the NCPCMs by dispersing the Al nanoparticles in paraffin wax of varying loading content from 0.2 to 10.0 wt%. The authors obtained the enhancement in thermal conductivity from ∼27% to ∼106% from 0.2 to 10.0

wt%, respectively. The detailed summary of the few developed metallic NMs additives NCPCMs are presented in Appendix H.

Table 2.4: Thermal conductivity values of metallic NMs at 300 K (Babar and Ali, 2019; Bergman et al., 2011).

| **Metallic NMs** | **k (W/m.k)** |
|---|---|
| Silver (Ag) | 430 |
| Copper (Cu) | 401 |
| Gold (Au) | 317 |
| Aluminum (Al) | 237 |
| Tungsten (W) | 174 |
| Magnesium (Mg) | 156 |
| Silicon (Si) | 148 |
| Zinc (Zn) | 116 |
| Iron (Fe) | 80.2 |
| Platinum (Pt) | 71.6 |
| Lead (Pb) | 35.3 |
| Boron (B) | 27 |
| Zirconium (Zr) | 22.7 |
| Titanium (Ti) | 21.9 |

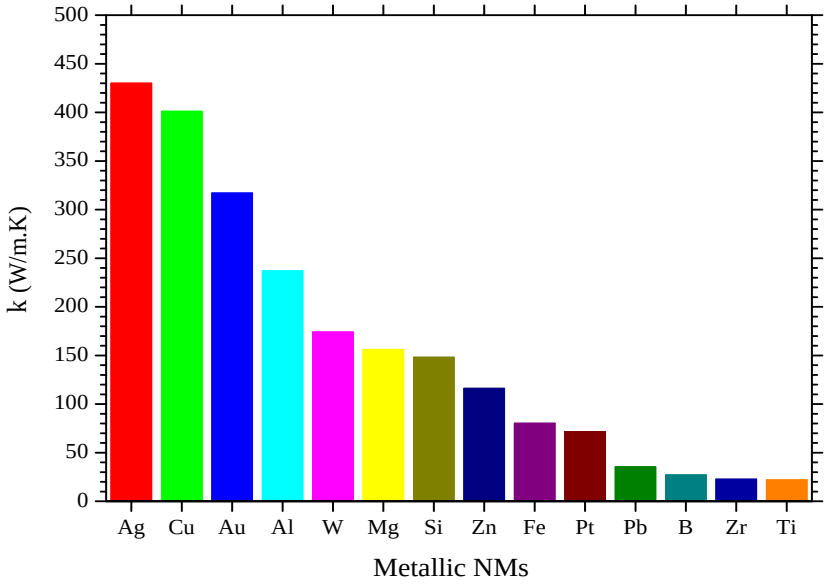


**Figure 2.14:** *Thermal conductivity values of metallic NMs at 300 K.*

### 2.8.2 Metallic–oxide additives NCPCMs

The metal-oxide NMs have been extensively explored with fluids and PCMs from last few decades to develop the NFs and NCPCMs. In comparison to the

metallic NMs, the metallic–oxide NMs have less thermal conductivity. Thus, they are not the good conductor of heat as compared to the metallic NMs. The highest value of thermal conductivity has been reported of of 272 W/m.K for BeO followed by the MgO and CuO which have the thermal conductivity values of 61.92 and 60 W/m.K, respectively, as listed in Table 2.5 and Fig. 2.15. The $Al_2O_3$, CuO and $TiO_2$ are the most widely used with PCM to synthesis the NCPCMs which can be identified from Table 2.5. Despite of the less thermal conductivity of metallic–oxide NMs compared to the metallic NMs, the metallic–oxide NMs are more chemically stable, less weight density, less synthesis cost and more reliable performance. Many researchers are working on different mechanisms for the thermal controllability of structures. The metallic–oxide NMs as a supportive materials into the PCMs have taken keen attention in current era due their higher thermal properties and enhance the chemical and thermal stability.

Table 2.5: Thermal conductivity values of metallic-oxide NMs at 300 K (Bergman et al., 2011; Khan et al., 2019).

| **Metallic-oxide NMs** | **k (W/m.k)** |
|---|---|
| Beryllium oxide (BeO) | 272.00 |
| Magnesium Oxide (MgO), | 61.92 |
| Copper oxide (CuO) | 60.00 |
| Aluminum oxide ($Al_2O_3$), sapphire | 46.00 |
| Aluminum oxide ($Al_2O_3$), polycrystalline | 36.00 |
| Tin Oxide ($SnO_2$) | 31.38 |
| Zinc oxide (ZnO) | 21.00 |
| Yttrium Oxide ($Y_2O_3$), | 14.23 |
| Nickel Oxide (NiO), | 12.97 |
| Ferric oxide ($Fe_2O_3$) | 12.55 |
| Cerium (IV) Oxide ($CeO_2$) | 11.72 |
| Cobalt Oxide (CoO), | 10.04 |
| Gadolinium Oxide ($Gd_2O_3$), | 10.04 |
| Titanium dioxide ($TiO_2$) | 8.90 |
| Strontium Titanate ($SrO.TiO_3$), | 5.86 |
| Silicon dioxide ($SiO_2$), polycrystalline | 1.3-1.4 |

For instance, Babapoor et al. (Babapoor and Karimi, 2015; Babapoor et al., 2016) synthesised the composite PCMs using $SiO_2$, $Al_2O_3$, $Fe_2O_3$, ZnO nanoparticles and measured the thermophysical properties. They achieved the highest thermal conductivity with 8 wt.% of $Fe_2O_3$ nanoparticles. However, the authors suggested that $Al_2O_3$ nanoparticles were preferable for TM applications.

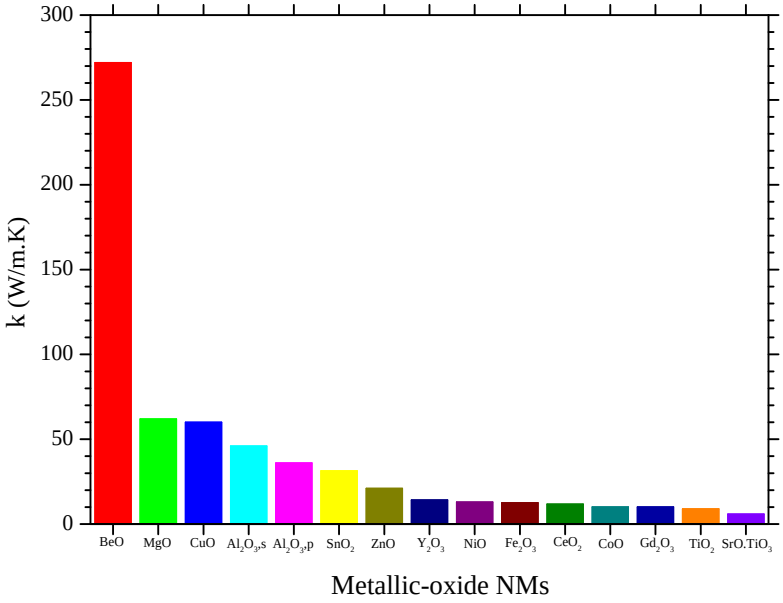


**Figure 2.15:** *Thermal conductivity values of metallic-oxide NMs at 300 K.*

Nourani and his co–authors (Nourani et al., 2016b,a) prepared NCPCMs using $Al_2O_3$ nanoparticles of weight concentrations of 0.5, 5, 7.5, and 10 wt.% and (sodium stearoyl lactylate) SSL used as a surfactant to enhance the stability of $Al_2O_3$ nanoparticles in paraffin wax. The effective thermal conductivity enhancement ratios were found of 31% and 13% in solid and liquid phases, respectively, at 10.0 wt.%. Sharma et al. (Sharma et al., 2016) used the $TiO_2$ nanoparticles of weight concentrations of 0.5, 1.0, 3.0, and 5.0 wt.% and palmitic acid as a PCM to prepare the NCPCMs. The highest thermal conductivity and lowest heat of fusion were obtained of 0.35 W/m.K and 180.03 kJ/kg, respectively, at 5.0 wt.% of $TiO_2$. Li et al. (Li et al., 2017) synthesised the NCPCMs using calcium chloride hexahydrate ($CaCl_26H_2O$) as a PCM with $\gamma-Al_2O_3$ and measured the phase–change thermal properties. The maximum thermal conductivity was obtained of 1.373 W/m.K at 2.0 wt.% of $\gamma-Al_2O_3$ nanoparticles. Sami and Etesami (Sami and Etesami, 2017) prepared the NCPCMs of using $TiO_2$ and paraffin with mass fractions of 0.5, 0.7, 1, 2, 3 and 4 wt.% with and without SSL used as a surfactant. Results explored the optimum concentration of 3 wt.% of $TiO_2$ nanoparticles with the 47.8% increase in thermal conductivity with SSL compared to the pure

paraffin. Further, authors suggested that addition of SSL in NCPCMs showed the better dispersion and thermal stability compared with pure paraffin and $TiO_2$/paraffin composite. Bashar and Siddiqui (Bashar and Siddiqui, 2018) prepared the NCPCMs using various types of nanoparticles, Ag, CuO, $Al_2O_3$ and MWCNTs and added in paraffin wax. A higher heat transfer coefficient of 18% and 14% was obtained for CuO and Ag nanoparticles, respectively, compared with pure paraffin wax. Praveen and Suresh (Praveen and Suresh, 2018) prepared the composite PCMs using solid–solid neopentyl glycol (NPG) and CuO nanoparticles for thermal management application. It was found that maximum thermal conductivity and phase change enthalpy of 0.61 W/m.K and 112.4 kJ/kg, respectively, were obtained at 3.0 wt.% of CuO. Recently, Li et al. (Li et al., 2019a) synthesized MgO dispersed in eutectic carbonate salt of $NaLiCO_3$ and studied the thermal properties of light and heavy weight MgO nanoparticles. The results found that light weight MgO nanoparticles of particle size $3-5$ nm had the maximum thermal conductivity of $\sim 5.5$ W/m.K compared to heavy weight MgO nanoparticles of similar size.

The detailed summary of metallic-oxide additives NCPCMs listed in Appendix I reveals that the mostly researchers used the paraffin wax as base PCM and $Al_2O_3$, CuO, $TiO_2$, ZnO, $SiO_2$, $CeO_2$, $Fe_2O_3$, $Fe_3O_4$ and $ZrO_2$ NMs have been added in different types of PCMs till yet. From most of the previous studies, the authors reported that increasing the loading content of NMs increased the thermal conductivity and decreased the latent-heat capacity of the PCM.

### 2.8.3 Carbon–additives NCPCMs

Carbon which is an abundant element, playing an emerging role in the development carbon based NCPCMs. Carbon is found in forms the variety of allotropes which occupy a unique place in terms of their thermal properties, as shown in Fig. 2.16a. The thermal conductivity of different alltropes of carbon various over a large range from ∼0.01 W/m.K in amorphous carbon to more

than 2000 W/m.K in diamond or graphene at room temperature (Balandin, 2011). The thermal conductivity of CNTs varies from ∼3000 to ∼3500 W/m.K at room temperature (Pop et al., 2006; Kim et al., 2001) – exceeds from the diamond, which is the best bulk heat conductor. The thermal conductivity of bulk carbon allotropes (graphite, diamond and amorphous carbon) has been under confusion for the discussion of graphene and nanostructured carbons. Among the modern researcher and scientist there is confusion of thermal conductivity of graphite having basal planes of high–quality. The thermal conductivity values of high-purity graphite ($sp^2$ bonding), diamond ($sp^3$) and amorphous carbon (disordered mixture of $sp^2$ and $sp^3$) can be seen from Fig. 2.16b based on the previous recommended values of experimental data reported in Ref. (Ho et al., 1972). From Fig. 2.16b, it can be predicted that pyrolytic graphite, which is similar to the highly oriented pyrolytic graphite (HOPG) has in–plane thermal conductivity of ∼2000 W/m.K at room temperature whereas the cross–plane pyrolytic graphite has very smaller thermal conductivity of ∼20 W/m.K. Another type of chemically pure graphite, called pitch–bonded or polycrystalline graphite has smaller order of magnitude in–plane thermal conductivity of ∼200 W/m.K. In polycrystalline graphite, the crystal axes are not highly oriented and grain boundaries or gain size are more pronounced, which reduces the thermal conductivity compared to the HOPG. In all bulk carbon allotropes, the heat is mainly carried out by acoustic phonons. It can be seen that thermal conductivity decreases as $\sim 1/T$ which is characteristic of crystalline solids, whereas thermal conductivity is limited by phonon Umklapp scattering (Balandin, 2011). In diamond and HOPG, the maximum thermal conductivity is obtained ∼70 K and ∼100 K, respectively. In amorphous carbon, the thermal conductivity varies from ∼0.01 W/m.K at $T = 4$ K to ∼2 W/m.K at $T = 500$ K. The thermal conductivity increases monotonically with temperature which is expected for disordered NMs where the heat conduction mechanism hops by the localized excitations (Cahill and Pohl, 1989).

Graphene (GE), “the mother of all graphitic forms of carbon”, is a single layer

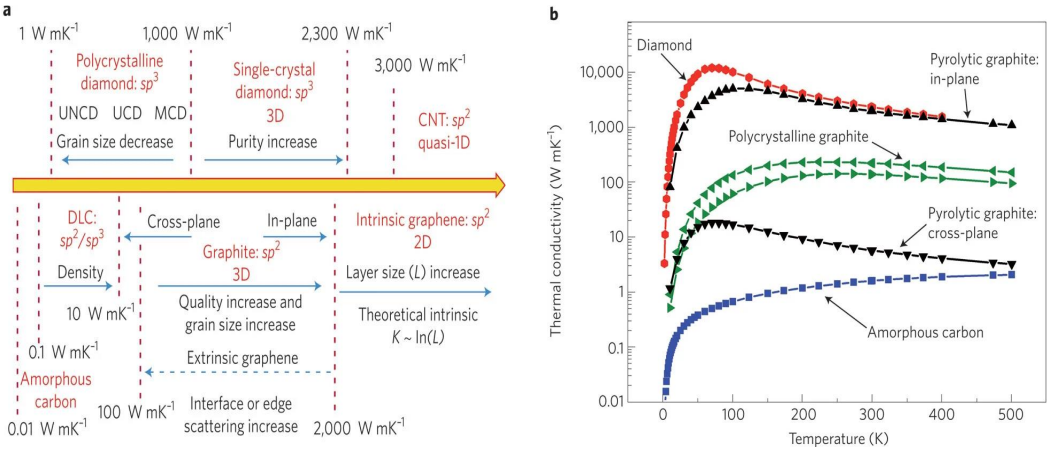


**Figure 2.16:** *Thermal properties of carbon allotropes and their derivatives (Balandin, 2011).*

of carbon atoms that are held together by a backbone of overlapping $sp^2$–bonded, in hexagonal (honey–comb) pattern, carbon atoms (Duplock et al., 2004). The extraordinary and significant characteristics of graphene initiate from the $2p$ orbitals which form the $\pi-$ bonds. These $\pi-$bonds are further hybridized together to form the $\pi-\pi$ bands that are delocalized over the sheet of carbon that form the GE. As a consequence of this, GE presents highly stiffness with exhibiting higher thermal conductivity, high mobility of charge carriers, zero effective mass, impermeable to gases and optically transparent (Balandin, 2011). Fig. 2.17 illustrates the major type of GE–based materials which are being used to prepare NCPCMs for various engineering applications. The structure of pristine GE is characterized as a $2D$ array and $sp^2$–hybridization of pure carbon atoms are arranged in a hexagonal lattice with covalent bonds. Moreover, the functionalized graphenes are produced by synthesis and preparation such as the carbon core structure can be oxidized forming graphene oxide (GO), the reduced structure with vacancy defects is reduced graphene oxide (rGO), and structures a few nanometres in size with quantum phenomena are graphene quantum dots (GQDs) (Li et al., 2016a). The graphene nanoplatelets (GNPs) are consisted of nanoscale stacks of platelet–shaped graphene sheets. The carbon–carbon length is GNPs is $\approx 0.142$ nm of light weight and high as-

pect ratio with planer shape and have tremendous ability to disperse into the other materials e.g. PCMs or fluids etc. (Arjmandi et al., 2018). Thus, developing a higher-value nanocomposite materials of excellent thermal, mechanical and electrical properties of GE. The classification of graphene–based materials on the basis of three fundamental attributes (number of graphene layers, the atomic carbon/oxygen ratio, and average lateral dimensions) is shown in Fig. 2.18.

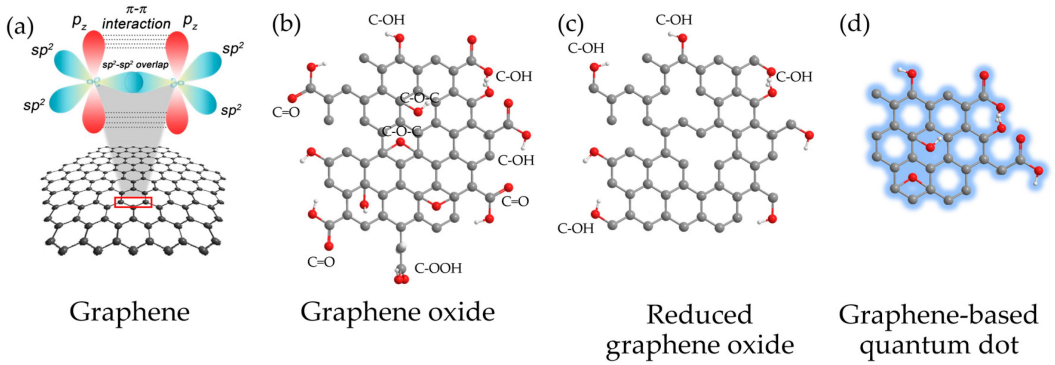


**Figure 2.17:** *Structures of graphene-based materials show (a) the pristine graphene (pure-arranged carbon atoms) with $sp^2$-hybridized carbon atoms, and the chemically modified graphene, including (b) GO; (c) rGO and (d) GQD (Suvarnaphaet and Pechprasarn, 2017).*

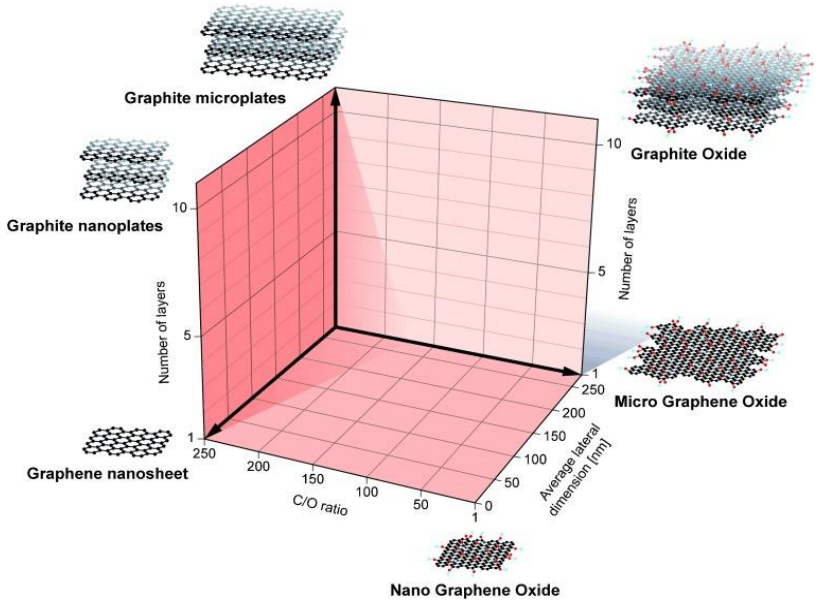


**Figure 2.18:** *Classification grid for the categorization of different graphene types according to three fundamental graphene–based material properties: number of graphene layers, average lateral dimension, and atomic carbon/oxygen ratio. The different materials drawn at the six corners of the box represent the ideal cases according to the lateral dimensions and the number of layers (Wick et al., 2014).*

The carbon–additives of various allotropes have excellent physical, chemical, electrical, thermal and barrier properties and these allotropes can be classified in to for different categories according to the dimensionality–(I) $0D$, (II) $1D$, (III) $2D$, and (IV) $3D$. In $0D$, the carbon atoms are bonded together in tabular, spherical, or ellipsoidal formations formations, i.e. carbon dots (CDs) and fullerenes. In $1D$, the carbon atoms formed the tubular shape with diameter typically in nanometers, i.e. carbon nanotubes (CNTs) including single–wall carbon nanotubes (SWCNTs) and multi–wall carbon nanotubes (MWCNTs) and carbon nanofibres (CNFs). In $2D$, the carbon atoms compacted in a nanoscale single layer–type sheet formed the honeycomb or hexagonal lattice, i.e. graphene (GE), graphene oxide (GO), reduced graphene oxide (rGO). In $3D$, the carbon atoms are bonded together in a tetrahedral lattice arrangement like in diamond or the carbon atoms are bonded together in sheets of a hexagonal lattice like graphite (GT), expanded graphite (EG) and carbon foam (CF). Fig. 2.19 presents the dimensions and structures of these carbon allotropes.

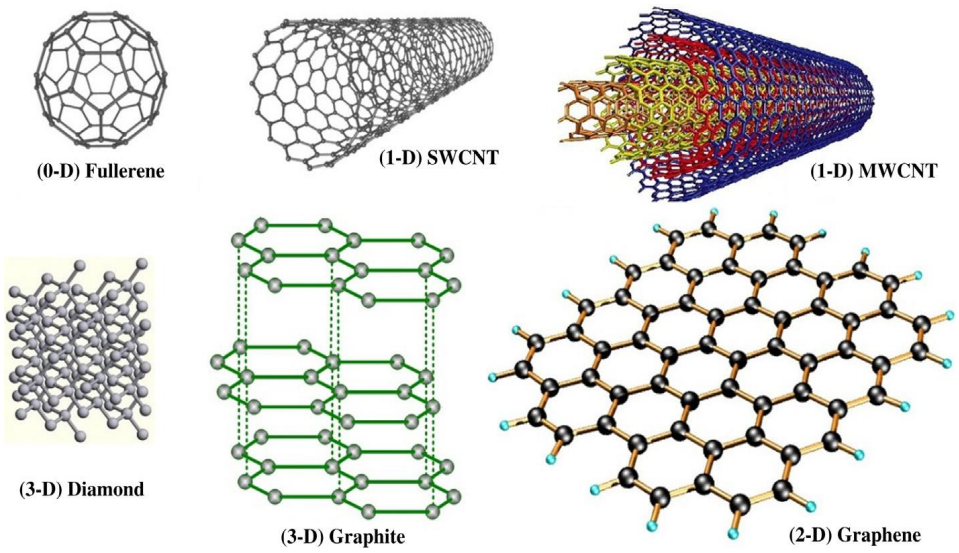


**Figure 2.19:** *Different allotropes of carbon (Atta et al., 2015).*

The addition of NMs have been evaluated to improve the thermal conductivity and specific heat and to reduce the interfacial thermal resistance. The addition of NMs in PCMs form a thermal conduction path, reduce the phonon

scattering and enhance the heat transfer rate. The carbon–based nanomaterials family, which possess all the dimensionality and morphology, have proven the remarkable thermophysical properties for the applications of LHTES and TM systems when added into the PCMs (Jebasingh and Arasu, 2020a; Wu et al., 2020). Various carbon–based additives, including CNTs (Choi et al., 2014; Li et al., 2014a,b; Fan et al., 2015; Zou et al., 2018), CNF (Nomura et al., 2015, 2016; Bahiraei et al., 2017), GE (Choi et al., 2014; Li et al., 2014b), GO (Wu et al., 2019; Yang et al., 2017), GT (Choi et al., 2014; Wu et al., 2019), EG (Ling et al., 2015; Li et al., 2020c), GNPs (Bahiraei et al., 2017; Zou et al., 2018; Wu et al., 2019) and graphite nanoplatelets (Warzoha and Fleischer, 2014; Bahiraei et al., 2017) have been used as thermal conductive materials (TCMs), to prepare and characterize the NCPCMs for thermal management and TES. The thermal conductivity of NCPCMs depends not merely on the innate thermal conductivity of the nanoparticles but it also strongly depends on the interactional compatibility of the PCM and nanoparticles. In earlier studies, Choi et al. (Choi et al., 2014) used MWCNTs, GT and GE as TCMs and determined the thermal conductivity of the NCPCMs for TES applications. The authors used the poly vinyl pyrrolidone (PVP) as a surfactant and stearic acid as a PCM. The maximum thermal conductivity was found to be 21.5% using GE of 0.1 vol.% with PVP. Pristine CNTs and grafted CNTs with paraffin–based NCPCMs was prepared by Li et al. (Li et al., 2014a). The results showed that grafted CNTs were shorter in size than pristine CNTs and the better dispersibility with PCM was found with grafted CNTs. In addition, grafted CNTs had the higher thermal conductivity than pristine CNTs/paraffin NCPCMs. Li et al. (Li et al., 2014b) used MWCNTs, GE and GT mixed into stearic acid with two mass percentages of 1.0% and 5.0%. The heat transfer performance and thermal conductivity analysis were carried out and the results revealed that the thermal conductivity of GT-based NCPCMs at 5.0% mass percentage was 12 times higher than the pure stearic acid. Warzoha and Fleischer (Warzoha and Fleischer, 2014) examined single

and multilayer GE into paraffin PCMs from GE layers from 3 to 44. It was observed that thermal conductivity enhancement of GE-mixed paraffin PCMs was due to the presence of GE nanoparticles, which was a stronger function of bending stiffness of GE than its intrinsic thermal conductivity. Bahiraei et al. (Bahiraei et al., 2017) synthesized three types of carbon-based nanoparticles namely CNFs, GNPs and GT nanoplatelets with paraffin wax as a PCM. The results showed the graphite–based NCPCMs with 7.5% and 10% mass fractions had the best thermal performance for thermal management applications. Zou et al. (Zou et al., 2018) prepared and studied the thermal conductivity and charging/discharging behaviour of MWCNTs, GE and MWCNTs/GE based NCPCMs using paraffin wax as PCM. The results showed that hybrid MWCNTs/GE based NCPCMs had the higher thermal conductivity. Recently, Li et al. (Li et al., 2020c) prepared the composite PCM using sodium sulfate decahydrate ($Na_2SO_4.10H_2O$) and expanded graphite (EG) for TES application. The results revealed that by dispersing 7 wt.% of EG, the latent–heat of melting and cooling were obtained of 114.0 and 105.5 J/g, respectively. In addition, the thermal conductivity was obtained of 1.96 W/m.k. The detailed summary of carbon-additives NCPCMs listed in Appendix J.

## 2.9 Characteristics evaluation techniques of NCPCMs

The characterisation of NCPCMs depends on the desired thermal, physical, and chemical properties. The development of NCPCMs are only valuable and successful when they fulfil the industrial and end-users requirements to meet the TM requirements. The characteristics of NCPCMs are performed using various quantitative and qualitative techniques as per the evaluation of the property, as shown in Fig. 2.20, The following major techniques are used to characterise the NCPCMs for analysis of chemical, physical and thermal

properties.

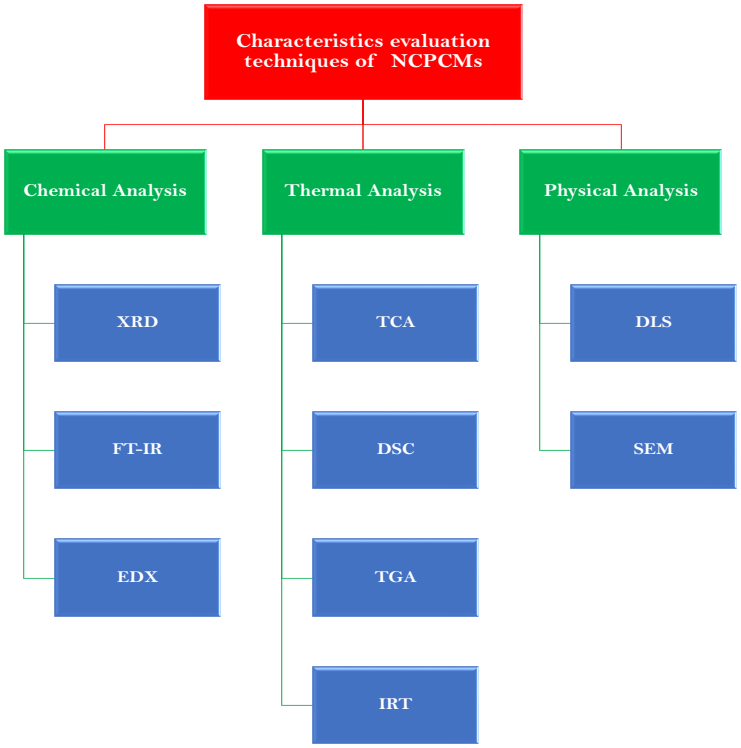


**Figure 2.20:** *characteristics evaluation techniques of NCPCMs.*

## 2.9.1 Chemical Analysis

### 2.9.1.1 X–Ray diffraction (XRD)

The X–ray diffraction (XRD) or X–ray power diffraction (XPRD) technique is adopted to measure the crystalloid phase, material structure, crystallite atomic arrangement and size, crystal orientation or texture and parameters such as crystallinity, strain and distinguishes the amorphous and crystalline material. The physics of the diffraction of the X–ray is similar to the diffraction of the electrons or neutrons except the only difference of the scattering mechanism. This technique ensures the crystalline structure of micro/nano capsules preferably suitable for inorganic shell materials. For instance, Kashi et al. (Kashi et al., 2018) determined the diffraction pattern of GNPs, PLA and PBAT from nanocomposites of PLA/GNPs and PBAT/GNPs. The diffraction peaks of GNPs was observed at 26.5° of corresponding plane of (002) without any

change. Li et al. (Li et al., 2020a) determined the diffraction peaks of diatomite and EG from the composite PCM of LA–SA/diatomite/EG. The stable crystal structure of diatomite was observed even after microwave treatment.

#### 2.9.1.2 Fourier transformed infrared spectroscopy (FT–IR)

The Fourier transformed infrared spectroscopy (FT–IR) technique evaluates the chemical composition or the functional groups of organic and inorganic NMs and NCPCMs. The FT–IR is an effective analytical technique to identify the "chemical family" of the NMs and PCMs. Further, FT–IR also confirms identifying the specific impurities in a pure compound in collection of the unique absorption bands. The FT–IR is preferred method of infrared spectroscopy passing the IR radiation through the sample. Some IR radiation is absorbed by the sample and some transmit through the sample. At the detector a spectrum arises due the singles which represents a molecular *fingerprint* of the sample. In IR spectroscopy the different spectral fingerprints arise due to the chemical structure (atoms and molecules) of different materials. In FT–IR method, the infrared spectra is obtained firstly collecting an interferogram of a sample using an interferometer. Further, Fourier Transform (FT) is applied on the interferogram resulting spectrum is obtained. The FT–IR spectrometer collects and digitizes the interferogram performing the FT function and then displays the spectrum. For example, various researchers presented the FT–IR peaks to represent the chemical composition of NCPCMs. Venkitaraj et al. (Venkitaraj et al., 2018) carried out the FT–IR tests of pure NPG and nanocomposite of NPG/CuO. The authors observed the no change in IR spectrum of NPG with the addition of CuO nanoparticles which reveals that there is no new bond valence between CuO and NPG, and only physical interaction is present.

#### 2.9.1.3 Energy-dispersive X-ray spectroscopy (EDX)

The energy-dispersive X-ray spectroscopy (EDS or EDX) is an analytical technique which is used to investigate the surface elemental analysis or chemical characterization or elemental composition of a sample. The EDX technique detects the X-rays emitted from the sample during the bombardment of a high-energy beam of charged particles such as electrons or a beam of X-rays focused into the sample. Normally, EDX technique is carried out in conjunction with scanning electron microscopy (SEM). Chieruzzi et al. (Chieruzzi et al., 2015) presented the EDX images to visualize the elemental maps of Si, Al and Si-Al in $SiO_2$ and $Al_2O_3$ nanoparticles dispersed in $KNO_3$ based nanocomposite.

### 2.9.2 Thermal Analysis

#### 2.9.2.1 Thermal conductivity analysers

Thermal conductivity (TC) is the major and fundamental property for the evaluation of NCPCMs for efficient thermal management systems. The key purpose of dispersing the NMs such as nanoparticles, nanotubes, nanofibers and nanosheets to enhance the thermal conductivity of base PCM significantly. The thermal conductivity of NCPCMs can be measured either by steady-state or transient-state methods (Speyer, 1993; Palacios et al., 2019). The radial heat flow (Huang et al., 2007) and guarded hot-plate (Xamán et al., 2009) methods are typical examples of steady-state methods. Whereas, transient hot-wire (Assael et al., 2008; Harish et al., 2013), laser flash method (Parker et al., 1961; Yang et al., 2016b), transient plane source (Li et al., 2013b; Kim et al., 2014), modulated DSC (Marcus and Blaine, 1994), $3\omega$ (Cahill, 1990; Oh et al., 2008), and thermocouple (Zeng et al., 2006) methods (Zhao et al., 2016) are transient–state methods.

#### 2.9.2.2 Differential scanning calorimeter (DSC)

The differential scanning calorimeter (DSC) is one of the most widely adopted technique to measure the thermo–analytical properties such as melting onset and peak temperatures, cooling onset and peak temperatures, heat capacity, latent-heat of melting and cooling, and degree of supercooling (defined as the difference of peak melting and cooling temperatures) (Geng et al., 2018). During DSC analysis the amount of energy absorbed or released upon heating or cooling is measured providing qualitative and quantitative data while endothermic (heat absorption) and exothermic (heat rejection) phase transitions. In DSC analysis, the change of heat flux is recorded with respect to time, however, the heating rate and sample mass is the most important because the changing heat rate and sample mass will give temperature–heat flow responses (Dğşc et al., 2018; Jiang et al., 2018).

#### 2.9.2.3 Thermogravimetrical analysis (TGA)

The thermogravimetry or thermogravimetrical analysis (TA) technique measures the amount and rate change of the material weight as a function of temperature or at isothermal condition as a function of time in a controlled atmospheric conditions upon melting and solidification (Lian et al., 2018). The change in the mass of sample material of NCPCMs are examined under the various thermal modes such as desorption, absorption, sublimation, vaporization, oxidation, reduction and decomposition (Lu et al., 2018).

#### 2.9.2.4 Infrared thermography (IRT) test

Infrared thermography (IRT) is a non-destructive technique which detects the thermal variations over a sample in which the thermal camera captures and creates the images by using infrared radiation emitted from the object, at the infrared band of the electromagnetic spectrum. Zou et al. (Zou et al., 2018) presented the IR images of NCPCMs, taken at different time steps of 5 min

from 5 min to 45 min, to evaluate the thermal performance of during melting process. Li et al. (Li et al., 2020a) presented the heating and cooling processes of with and without EG based NCPCMs. The rise/fall of temperature could be see clearly through IR images by changing the colour during heating/cooling processes. A uniform and better heat transfer was observed with the addition of EG into the LA–SA, used as a PCM.

### 2.9.3 Physical Analysis

#### 2.9.3.1 Dynamic Light Scattering (DLS)

Dynamic Light Scattering (DLS) which is also called as Photon Correlation Spectroscopy or Quasi–Elastic Light Scattering can measures the particle size at nano-meter level. In DLS, the sample is illuminated with intensity of scattered light and motion of particle is measured with the fluctuations of the scattered light at a known scattering angle (Foerter-Barth and Teipel, 2000).The DLS theoretically relies on the brownian motion of the suspended particles to determine the size of the particles. The brownian motion, which is the random disordered motion of particles resulting the random collision of molecules. Generally, the larger particles follow the lower velocity and smaller particles with higher velocities recoil more strongly. The observed velocities of particle resulting of molecules Brownian motion are related to determine the particle size and distribution with the help of diffusion coefficient. Zhang et al. (Zhang et al., 2012b) measured the MWCNTs nanoparticles size distribution dispersed in hexadecane and average hydrodynamic diameter of MWCNT-1-decanol was measured of 2761.3 nm or 2.76 $\mu$m.

#### 2.9.3.2 Scanning electron microscopy (SEM)

The scanning electron microscopy (SEM) technique, based on the scattered electrons, is used to examine the surface morphology, microstructural features, elemental composition andto visualize the surface elemental distribu-

tion of nanoparticles in NCPCMs. The SEM uses a higher–energy beam of electron on the surface of the sample which generates the various signals showing the image of sample surface. These variety of signals reveal the various characteristics information of the sample including topography (the surface features or texture), morphology (the shape and size), composition (elements and compounds) and crystallography (atoms arrangement) (Chieruzzi et al., 2015; Jebasingh and Arasu, 2020b,a) .

## 2.10 Stability of NCPCMs

The stability of NCPCMs is the real challenge for the current industrial revolution. Stability of NCPCMs mainly concerns with the thermal and chemical stability to ensure the long-term usage of NCPCMs. Generally a number of repeated thermal cyclic tests are performed to validate the thermal reliability by measuring the thermophysical properties. The quality of the NCPCMs is evaluated by assuring that there is no geometrical variation, sedimentation, aggregation and crystallization of inter layer materials and so far. A thermodynamically and chemically NCPCMs ensures the long-term performance as TES materials for industrial and research applications. Further, thermal and chemical stability of the NCPCMs enhance the economic feasibility maintaining their latent–heat of fusion and melting for employing under repeated melting/freezing cycles with time.

### 2.10.1 Physical stability

The physical stability of NCPCMs can be analysed, with moderate or good transparency, by physical visualization of the settlement of dispersed NMs into the base PCM by keeping the syntheszed NCPCMs for several hours with any disturbance. Nourani et al. (Nourani et al., 2016a) studied the physical stability of $Al_2O_3$/paraffin NCPCMs through visualization of sample placing in an incubator at a temperature of 60 °C for a week. Sodium stearoyl lacty-

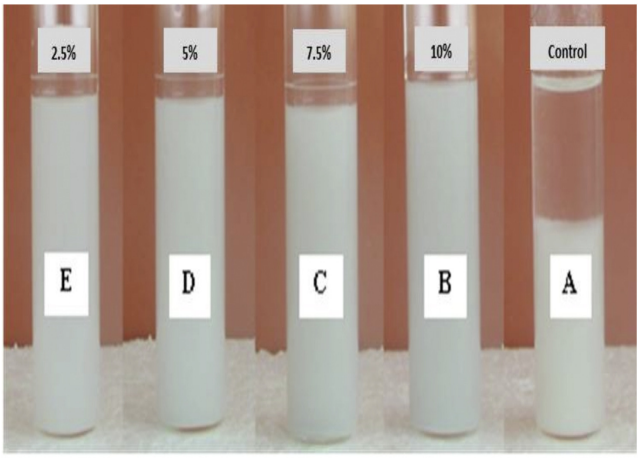


**Figure 2.21:** *Sedimentation images of $Al_2O_3$/paraffin NCPCMs in the absence (A) and in the presence (BE) of SSL after 1 day (Nourani et al., 2016a).*

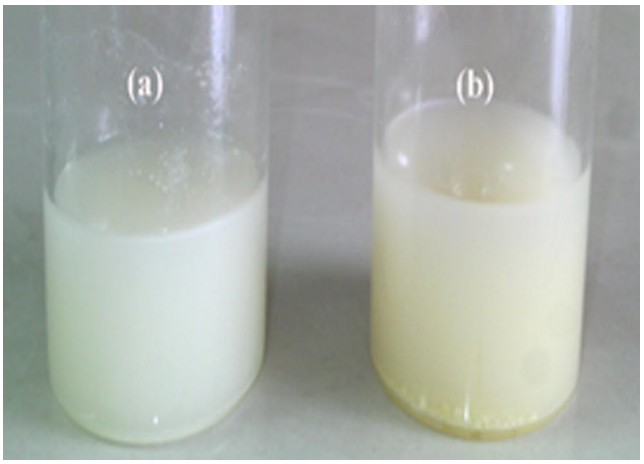


**Figure 2.22:** *Images of 3 wt% of $TiO_2$/paraffin NCPCMs (a) with SSL (b) without SSL (Sami and Etesami, 2017).*

late (SSL) was added with with a mass ratio of 1:3:5 as the surfactant to improve the stability of $Al_2O_3$ nanoparticles. The NCPCMs samples without SSL showed the precipitation after one-day however, NCPCMs samples containing SSL showed the good stability, as shown in Fig. 2.22. Sami and Etesami (Sami and Etesami, 2017) studied the physical stability of $TiO_2$/paraffin NCPCMs with and without adding SSL surfactant with mass ratio of 1:4 for SSL/$TiO_2$. The physical images of at 1 wt% and 3 wt% of $TiO_2$/paraffin without SSL tended to aggregate together and less dispersion of $TiO_2$ was observed. While with SSL, a better dispersion of $TiO_2$ nanoparticles occurred due to the reduction in surface energy of the nanoparticles, as shown in Fig. 2.22.

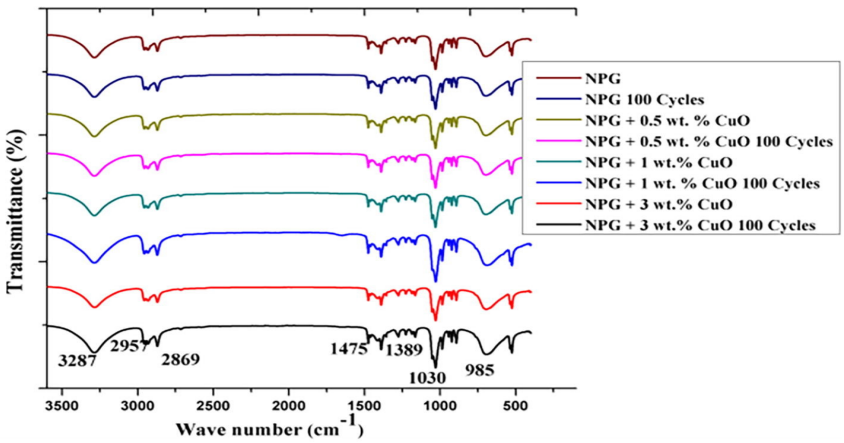


**Figure 2.23:** *FT-IR spectra for NPG, NPG+0.5, 1 and 3wt% CuO before and after 100 thermal cycles (Praveen and Suresh, 2018).*

### 2.10.2 Chemical stability

For the long term chemical stability of the NCPCMs means to keep the chemical structure or sustain the functional groups of the NMs and PCMs even after the long term usage of NPPCMs during melting and solidification processes. After thermal cyclic tests of NCPCMs are tested using FT–IR and results are compared with the FT–IR spectrum before the cyclic tests. Praveen and Suresh (Praveen and Suresh, 2018) carried out the cyclic test up to 100 cycles of CuO/NGP based NCPCMs and then samples were tested using FT–IR. The results showed that there were not significant difference between pure NGP and CuO/NGP samples and similar FT-IR spectra was observed of uncycled and thermally cycled samples of CuO/NGP based NCPCMs, as shown in Fig. 2.23. He et al. (He et al., 2019b) analysed the FT–IR spectra of GNPs, MWCNTs, NG and MA based NCPCMs after 300 thermal cycles, as shown in Fig. 2.24. The stable chemical structures of NCPCMs were observed even after thermal cycles.

### 2.10.3 Thermal stability

Thermal stability of NCPCMs after several heating/cooling thermal cycles is determined through the TGA and DTG tests. The thermal stability is determined based on the onset temperature and percentage amount of residual of

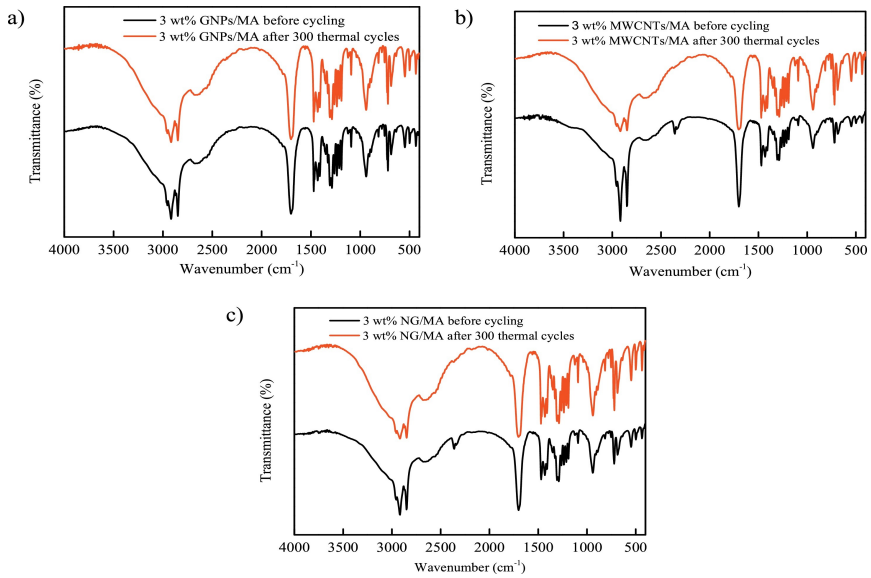


**Figure 2.24:** *FT-IR spectra before and after cycling for: a) 3wt% GNPs/MA NCPCM; b) 3wt% MWCNTs/MA NCPCM; and c) 3wt% NG/MA NCPCM (He et al., 2019b).*

the pure PCM and NCPCMs. Sharma et al. (Sharma et al., 2016) carried out the TGA and DTG test of $TiO_2$/PA based NCPCM. The onset and maximum degradation temperatures of NEOPCM4, which is 5 wt% of $TiO_2$, at around 202 °C and 286 °C, respectively, and the charred amount of residue was 4.5%. The results, as shown in Fig. 2.25, of TGA and DTG proved that the dispersion of $TiO_2$ nanoparticles improved the stability of PA. Praveen and Suresh (Praveen and Suresh, 2018) carried out the TGA tests of CuO/NGP based NCPCMs before and after 100 thermal cycles, as shown in Fig. 2.26. The thermal degradation of cycled and uncycled of NGP and CuO/NGP samples were at slower rate initially while heating and confirmed that NGP and CuO/NGP samples are thermally stable in temperature range of 30-100 °C.

### 2.10.4 Thermal reliability

Unlike the physical and chemical stability, the thermal reliability is the most important factor for longer term application of NCPCMs for thermal management applications without any degradation and losing the thermal performance. The thermal reliability of PCMs and NCPCMs can be determined by measuring the phase–change thermal properties of PCMs and NCPCMs after

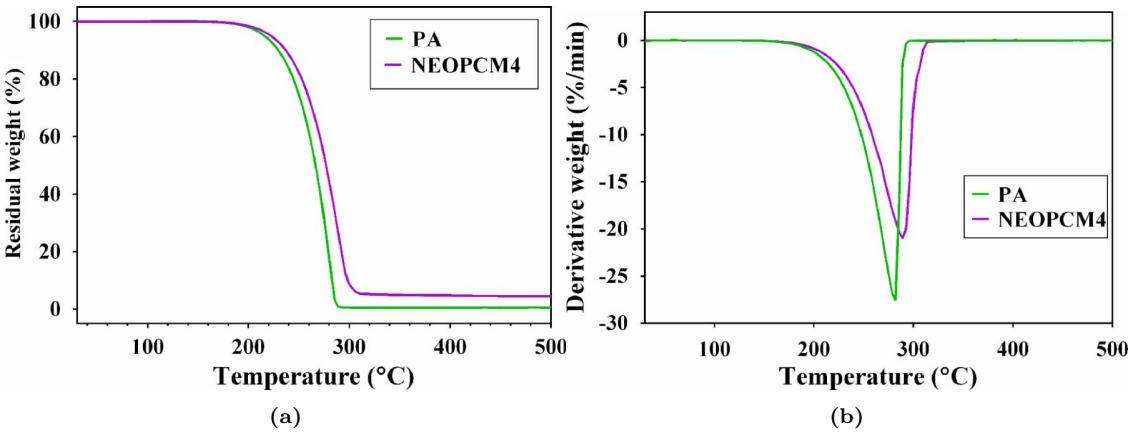


**Figure 2.25:** *(a) TGA and (b) DTG thermograms of TGA curves of PA and NEOPCM4 (Sharma et al., 2016).*

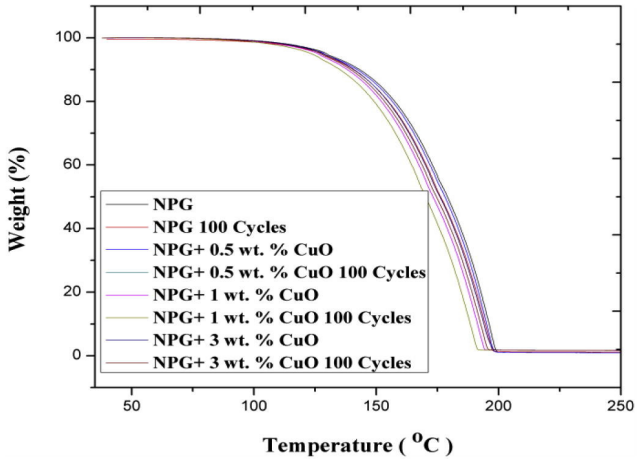


**Figure 2.26:** *TGA curve of NPG, NPG+0.5, 1 and 3wt% CuO before and after 100 thermal cycles (Praveen and Suresh, 2018).*

several repeated thermal heating/cooling cycles. The reliability of NCPCMs is affected due to phase–change process while melting/solidification process. Thermal cycles or thermal cycling tests can be conducted using thermal cyclic tester conducting sever repeated thermal cycles. Harikrishnan et al. (Harikrishnan et al., 2014) carried out the melting and solidification cycles up to 5000 thermal cycles of $TiO_2$, CuO and ZNO dispersed NCPCMs with LA–SA to evaluate the long term thermal reliability. The thermal properties such as melting and solidification temperatures, latent–heat of melting and solidification. The maximum changes in melting temperatures were found of -2.34%, -1.78%, -2.12% and -1.90% for base PCM, $TiO_2$, CuO and ZNO dispersed NCPCMs, respectively, as shown in Fig. 2.27a. Similarly, the maximum changes in melt-

ing temperatures were obtained of -2.08%, -1.55%, -1.39% and -1.24% for base PCM, $TiO_2$, CuO and ZNO dispersed NCPCMs, respectively, as shown in Fig. 2.27b. The variations of latent-heat of melting and solidification of NCPCMs, are shown in Fig. 2.27c and 2.27d, respectively. The maximum reductions of latent-heat of melting of $TiO_2$, CuO and ZNO dispersed NCPCMs were obtained of 2.37%, 1.67%, 1.72% and 1.61%, respectively, compared to the base PCM. Likewise, the maximum reductions of solidification latent-heats were 2.56%, 1.54%, 1.63% and 1.48% of $TiO_2$, CuO and ZNO dispersed NCPCMs, respectively, compared to the base PCM. A little reductions in thermal properties of NCPCMs are obtained which are permissible. Such deviations are due the thermophysical changes in NCPCMs because of the addition of nanoparticles.

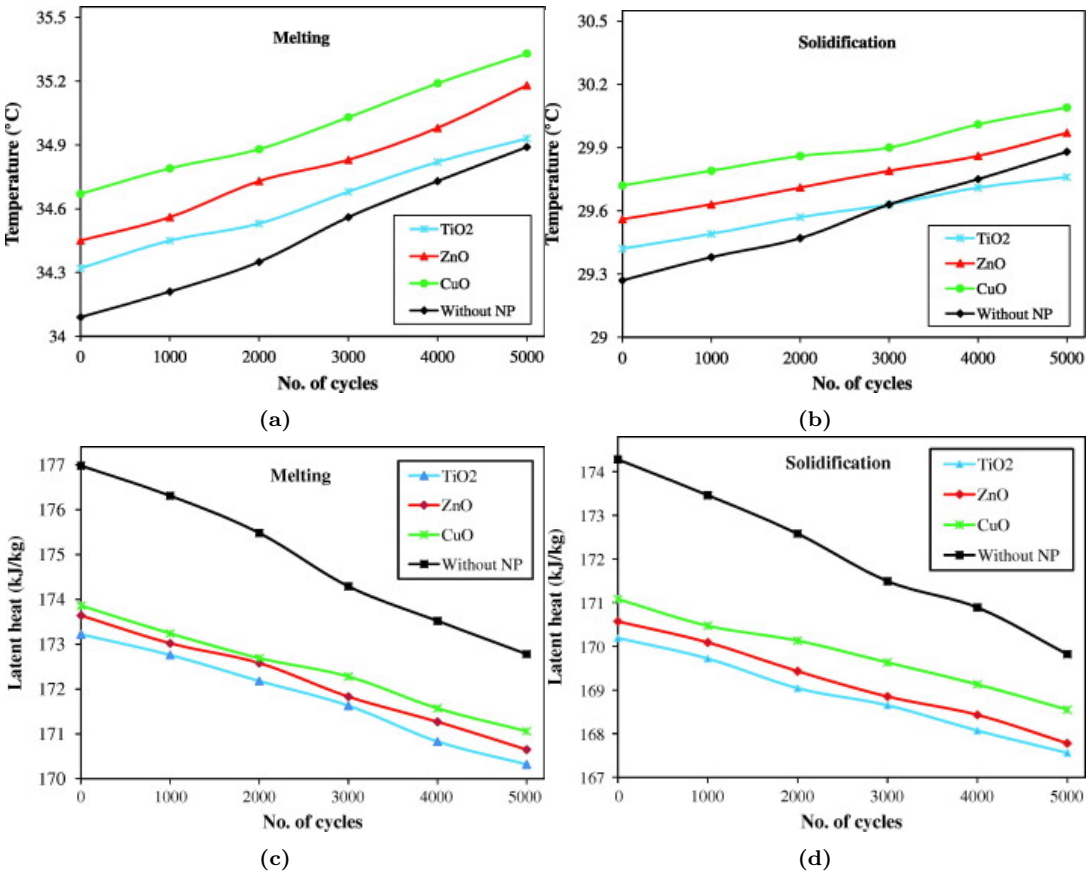


**Figure 2.27:** *Effect of thermal cycles on phase change temperature during (a) melting and (b) solidification. Effect of thermal cycles on latent heat during (c) melting and (d) solidification (Harikrishnan et al., 2014).*

### 2.10.5 Methods to enhance the stability of NCPCMs

The following solutions are carried out to enhance the stability of NCPCMs:

**Use of surfactant in NCPCMs:** The surfactants (also called dispersant) that are used in NCPCMs, is an easy, popular and economic method to enhance the stability of two–phase NCPCMs by affecting the surface characteristics of the mixture. The dispersant normally consists of two portions; one is the hydrophobic tail portion, usually long chain hydrocarbon, and second is hydrophilic polar head portion. The use of surfactant in two–phase mixture increases the interface conjunction of two materials, which introduces a degree of continuity between the two–phase systems, also known as wettability. The dispersant reduces the surface tension at the interface of NMs and base PCMs thus increasing the suspension time of NMs. Surfactants are selected as per requirement, which convert the hydrophobic surfaces of NMs to hydrophilic and vice versa to increase the solubility of aqueous and non–aqueous solutions. According to composition of the head, surfactants are categorized into four classes as follows:

- Nonionic surfactants–without charge head groups (include polyethylene oxide, alcohols, and other polar groups). Typical examples are Triton X–100, Polyvinyl Pyrrolidone (PVP), 1–tetradecanol, Span–80, Tween–60 and Tannic Acid (TA) (Zeng et al., 2010; Parameshwaran and Kalaiselvam, 2016; Bahiraei et al., 2017; Li et al., 2017; Bashar and Siddiqui, 2018).
- Anionic surfactants: With negatively charged head groups (include long–chain fatty acids, sulfosuccinates, alkyl sulfates, phosphates, and sulfonates). Typical examples are Sodium Dodecyl Sulfate (SDS), Sodium Dodecylbenzene Sulfonate (SDBS), Sodium Stearoyl Lactylate (SSL), Sodium Octanoate (SOCT), Sodium Cholate (SC),

Sodium Taurodeoxy Cholate (STC), Gum Arabic (GA), and Oleic acid (Harikrishnan et al., 2014; Nourani et al., 2016a; Sami and Etesami, 2017; Li et al., 2017).

- Cationic surfactants: With positively charged head groups (include protonated long–chain amines and long–chain quaternary ammonium compounds). Typical examples are Cetyl Trimethyl Ammonium Bromide (CTAB), Hexadecyl Trimethyl Ammonium Bromide (HCTAB), and Dodecyl Trimethyl Ammonium Bromide (DTAB) (Li et al., 2017).
- Amphoteric surfactants: With zwitterionic head groups (depend on pH and include betaines and amine oxides).

The selection of a suitable surfactant has significant importance based polarity of the solvent such as for non–polar solvent like hydrocarbons. Choosing an unsuitable surfactant can cause sedimentation, clogging, and aggregation which affects the thermal properties of nanofluids such as viscosity, thermal conductivity, specific heat.

**Surface modification technique:** The surface modification technique is a *surfactant–free technique* which can provide a long–term stability of NCPCMs. Nanoparticle surface modification refers to the modification and processing of the surface of nanoparticles by physical and chemical deep processing methods, thereby controlling the internal stress, increasing the repulsive force between the nanoparticles, reducing the gravitation between the particles, and purposefully changing the surface of the nanoparticles with physical and chemical properties (morphology, crystal structure, defect state, stress state, functional group surface energy, surface hydrophobicity, surface wettability, surface potential, surface adsorption and reaction characteristics, etc.), which give the nanoparticle a new function and meet the needs of nanoparticles processing and applications. The use of surfactants, although quite an effective and promising

technique to increase the dispersibility of nanoparticles with base PCMs, may cause several problems (B and A, 2020; Sharaf et al., 2020). For instance, heat transfer contamination medium, formation of foam while heating, creating thermal resistance between the nanoparticles and host fluid, because of the interaction of the surfactant molecules with surfaces of nanoparticles. The proper selection of functionalized nanoparticles has the tendency to improve the long–term stability of NCPCMs which represents the surfactant–free technique.

### 2.10.6 Stability mechanism of NCPCMs

The stability mechanism of NCPCMs is defined as the rate of aggregation of NMs dispersed in base PCM, which is generally explained by the frequency of collisions and probability of cohesion during collision. NMs start to adhere together to form aggregates at larger scale or size, when in dispersion, resulting in sedimentation or phase transition between the base PCM and NMs. According to the theory of Derjaguin, Verway, Landau, and Overbeek (DVLO) (Missana and Adell, 2000; Popa et al., 2010), which is based on colloidal stability, the stability of a particle in any solution is determined by the sum of Van der Waals attractive forces and the electrical double layer repulsive forces that exist between the NMs as they approach each other due to the Brownian motion they are undergoing. If the attractive Van der Waals forces are larger than the repulsive forces between the particles then the particles will collide or aggregate and will settle at the base of the PCM resulting in a non-stable suspension. Contrarily, if the net electrical repulsive forces are high between the particles, then the suspension will remain stable and NMs will not aggregate (Sharaf et al., 2020).

There are two basic chemical stability mechanism of NMs in suspensions: (i) electrostatic stabilization and (ii) steric stabilization, as shown in Fig. 2.28a and 2.28b, respectively (Zhichao et al., 2015; Chakraborty and Panigrahi,

2020). The electrostatic stabilization involves the absorbed ionic polymers in a suspension system which builds up a charged layer around the NMs. This formed charged layer enhances the repulsion force between NMs. The steric stabilization depends on the two factors: (a) volume restriction component, (b) mixing or osmotic component, involving compression of the absorbed layer. Some surfactants provide the both electrostatic and steric stabilization mechanisms such as SDBS, as shown in Fig. 2.28d.

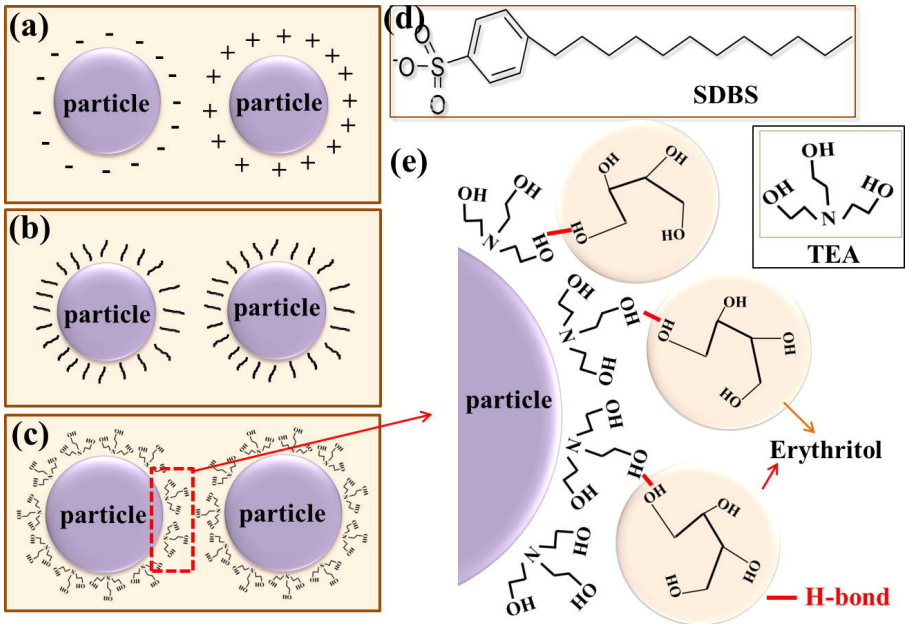


**Figure 2.28:** *Schematic of the stabilizing mechanisms, (a) electrostatic stabilization, (b) steric stabilization, (c) and (e) stabilizing mechanism of triethanolamine (TEA) as dispersant for the $TiO_2$erythritol system, (d) the structure of SDBS. (Zhichao et al., 2015).*

## 2.11 Issue and challenges of NCPCMs

Since the purpose of dispersion of NMs into the PCMs to improve the thermophysical properties mainly the thermal conductivity of the base PCM. The literature proved that the thermal conductivity of pure PCMs was improved and also reduction in latent-heat was reduced. However, the overall the thermal performance is not so significant because of the higher enhancement in thermal conductivity. However, the following are the some major issues and challenges needed to resolve for commercial availability of the NCPCMs for

practical thermal management applications.

- The preparation of NCPCMs is still a key challenge. There is need of uniform and stable dispersion of NMs with PCM to reduce the formation of NMs aggregates and sedimentations.

- The addition of surfactants along with the NMs may improve homogeneous dispersion of NMs in PCMs. However, this technique change the thermophysical properties of base PCM or NCPCM and thus, effects the overall thermal performance of NCPCMs.

- The addition of expensive NMs such carbon-additives causes the higher production cost of NCPCMs. Hence, hindering the commercial availability and application of NCPCMs as the production of NMs and NCPCMs demands the advanced and sophisticated equipment.

- The experimental and theoretical mechanism of thermophysical properties is still debatable by the addition of NMs in PCMs.

- There is need to find the optimum amount of percentage dispersion of NMs for each PCM is still critical and important.

- Thermal stability and reliability is very important factor and critical issue for the long–term application of NCPCMs for various applications.

- There is emergence need of the empirical correlations of thermophysical properties such thermal conductivity, viscosity and density of the NCPCMs of certain type of NMs and PCMs combination.

## 2.12 Summary of the literature review

This review chapter comprehensively covers research progress on the development of NCPCMs conducted from the last few decades. Initially, the ideal

characteristics of NCPCMs are elaborated for the selection of a specific criteria and application. The detailed classification of NMs and PCMs are mentioned according to different categories. Further, the main discussion of on the preparation and classification of NCPCMs based on the type of the NMs are categorized. In a similar way, detailed characteristics evaluation techniques of chemical, thermal and physical properties have been discussed. Stability and reliability of NCPCMs based on physical, chemical and thermal properties are also discussed. The following conclusions are summarized from this review:

- The researchers, engineers, and scientist should consider the ideal characteristics or factors such as phase–transition temperatures and latent-heat of melting and solidification while heating and cooling, thermal conductivity, viscosity, volume expansion, specific heat capacity, density, vapour pressure, effect of subcooling, cost and safety while selection of PCMs and NMs for the development of NCPCMs.

- The selection of NMs critically determines the enhancement in thermal properties and hence higher heat transfer performance which solely depends on the type, size, shape and structure of the NMs.

- The latent–heat thermal energy storage of PCM or NCPCMs has the significant impact for passive thermal management applications.

- The organic PCMs specially paraffin compounds are widely of lower melting temperature and also they possess preferable heat storage capacity during phase–change process.

- The detailed thermophysical properties of organic, inorganic and eutectic PCMs are listed in tabular form for the ease of reader which will help to select the base PCM for synthesizing the NCPCMs.

- The different methods of the preparation of NCPCMs are explained and it is concluded that two–step method has been widely adopted by the

researchers and scientist. The two–step method allows the easily and low cost development of NCPCMs.

- The detailed information regarding the development and thermophysical properties of metallic, metal–oxide and carbon additives NCPCMs are listed in Appendices H, I, and J, respectively.

- The Cu NMs are the most commonly used in development of NCPCMs due to significantly less cost than the Ag and Au with paraffin based PCMs.

- The data presents that carbon-additives such GE, xGnP, CNTs and EG are the commonly preferred NMs because of less density, higher thermal conductivity and show the higher enhancement in thermophysical properties and stability of NCPCMs.

- The comparison of metallic, metal–oxide and carbon–additives based NCPCMs show the carbon–additives show the better physical and thermal stability than the metallic, metal–oxide NMs up to 1000 cycles because of lower density.

- The metallic, metal–oxide and carbon–additives reduce the melting and solidification time. However, carbon–additives like modified GA enhances the melting and solidification time.

- The NMs of smaller size show the better dispersion in PCM and increase the thermophysical properties and hence, the improve the thermal performance. However, the optimum performance of NCPCMs is based on the size and shape of the NMs and crystal structure of the PCM.

- The better physical and thermal stability of NCPCMs were found of carbon–additives such SWCNTs, MWCNTs, EG, GE before and after several repeated thermal cycles. Thus, dispersion of carbon-additives

in PCM enhances the stability of NCPCMs because of the increasing attractive force between PCM and NMs molecules.

- The higher concentration of NMs increases the dispersion rate, thus affects thermophysical properties and rate of melting/solidification of NCPCMs. However, increasing the loading content of NMs from certain level causes to deviate the thermophysical properties and thermal performance in negative trend of the base PCM. Thus, identifying an optimum amount of NMs content to disperse in PCM is very important for long–term thermal performance of thermal management system.

- The NCPCMs are the most suitable for thermal management and TES applications in conjunction with various subsystems such as heat sinks, micro–mini–channels, heat pipes, heat exchangers, wall–boards, panels and slabs and so on.

# Chapter 3

# Development of metallic–oxide mono nanocomposite phase change materials[1]

## Abstract

This experimental study covers the development of novel nanocomposite phase change materials (NCPCMs) based on RT–35HC as a phase change material (PCM) and titanium oxide ($TiO_2$) as thermal conductivity enhancement material, for thermal management applications. The $TiO_2$ loadings were varied from 0.0 to 2.0 wt.% in pure RT–35HC samples and characterized for their chemical, physical and thermal properties by different characterization methods. The microstructures, chemical structures, lattice structures showed the presence of $TiO_2$ nanoparticles inside RT–35HC. The results revealed that thermal properties including phase–change temperature, melting/solidifying latent–heat enthalpies, specific heat capacity and thermal conductivity were decreased by the introduction of $TiO_2$ nanoparticles. This study confirmed

[1]This Chapter is published as:
**Arshad, A.**, Jabbal, M., Shi, L., Darkwa, J., Weston, N. J., & Yan, Y. (2021). Development of $TiO_2$/RT–35HC based nanocomposite phase change materials (NCPCMs) for thermal management applications. *Sustainable Energy Technologies and Assessments*, 43, 100865. https://doi.org/10.1016/j.seta.2020.100865.

that NCPCMs based on $TiO_2$/RT–35HC revealed the phase–change enthalpies and thermal conductivities of $238.33 - 227.74$ J/g and $0.238 - 0.341$ W/m.K, respectively. In addition, significant chemical and thermal stability and no phase segregation were observed with the increase in loading of $TiO_2$ nanoparticles. The newly developed $TiO_2$/RT–35HC base NCPCMs revealed acceptable chemical stability, thermal reliability, and efficient conjugate heat transfer performance. Thereby, NCPCMs exhibit the potential application for thermal energy storage and thermal management of electronic devices, Li–ion batteries and photovoltaic (PV) modules.

**Keywords:** Phase change material, $TiO_2$, RT–35HC, Nanocomposite phase change materials, Thermal management

## 3.1 Introduction

The recent global energy demand and supply has raised the attention of research in order to introduce efficient alternatives of thermal management (TM) and thermal energy storage (TES) systems. Specifically, the nature's blessed resources of fuels, formed by the natural processes called fossil fuels, are still being considered as key energy supply resources. However, the greenhouse emissions related to their use are still a challenge to mitigate the global climate change. The integrated systems with dual capability of TM and TES have been widely used for improving the energy efficiency and heat storage capability because of using phase change materials (PCMs) (Bashir et al., 2020). Thus, PCMs, as TES materials, have the tendency to absorb heat energy in two phase transformations (i.e. solid–to–liquid and liquid–to–solid) and have been used air conditioning systems, desalination, refrigeration, cooling of electronic devices and electric vehicle batteries (Ali and Arshad, 2017; Gulfam et al., 2019; Faraji et al., 2020). The organic PCMs specially paraffins have been under utilization of TM and lower temperature TES systems due to their intrinsic properties of (i) higher latent–heat of fusion, (ii) durable chemical sta-

bility, (iii) desirable phase–transition temperature, (iv) lower subcooling and (v) less expenses (Hyun et al., 2014). In spite of these, paraffins also exhibit the lower thermal conductivity causing to reduce the overall heat flow rate during phase transformation (Carrillo et al., 2019). Scientists and researchers have adopted a few techniques including: (i) extruded metal fins (Arshad et al., 2018b; Ali et al., 2018a; Mahdi et al., 2019), (ii) metal foams and porous materials (Yang et al., 2019; Huang et al., 2019; Umair et al., 2019), (iii) dispersing nanoparticles and nanofiber (Keshteli and Sheikholeslami, 2019; Leong et al., 2019; Shah, 2018; Aftab et al., 2018) (iv) encapsulated micro/nano–capsules (Liu et al., 2015a; Arshad et al., 2019a; Shchukina et al., 2018) to improve the thermal conductivity of PCMs.

In recent years, nanoparticles (NPs) have attracted the attention of scientists and industrialists due to their outstanding properties promoting innovation in the field of engineering and industrial processes. NPs specially the metallic–oxides have two major advantages which include: (i) structural changes which alter the lattice symmetry and cell parameters and (ii) surface properties changes which influence the thermal conductivity and chemical properties because of increase in band gap (Qiu et al., 2019). Various studies have been reported using different PCMs and NPs based on the operating conditions and melting temperature of PCMs. It is however important to consider thermal and rheological properties while endothermic/exothermic process for the determination of thermal characteristics of PCMs integrated with metallic–oxide NPs (Akin and Sonmezoglu, 2018).

For instance Bashar and Siddiqui (Bashar and Siddiqui, 2018) prepared NCPCMs by dispersing MWCNT, Ag, CuO and $Al_2O_3$ NPs into the paraffin wax. In comparison with pure paraffin wax, the enhancement in heat transfer coefficient was achieved of 18% and 14% with CuO and Ag NPs, respectively. Li et al. (Li et al., 2017) used the $\gamma-Al_2O_3$ NPs and calcium chloride hexahydrate ($CaCl_2.6H_2O$) as a PCM and studied the various thermal properties such as thermal conductivity, degree of subcooling and latent–heat of melt-

ing/solidifying of composite PCMs. Results reported the highest thermal conductivity of 1.373 W/m.K at 2.0 wt.% of $\gamma-Al_2O_3$ NPs. Sharma et al. (Sharma et al., 2016) synthesized the NCPCMs using $TiO_2$ NPs by changing the mass loading of 0.5, 1.0, 3.0, and 5.0 wt.% into the palmitic acid, used as a PCM. Authors reported the highest thermal conductivity and lowest latent–heat of 0.35 W/m.K and 180.03 kJ/kg 5.0 wt.% of $TiO_2$. Sami and Etesami (Sami and Etesami, 2017) prepared $TiO_2$/paraffin NCPCMs with weight concentration of 0.5, 0.7, 1, 2, 3 and 4 wt.% with and without sodium stearoyl lactylate (SSL) as a surfactant. Authors found the optimum concentration of $TiO_2$ of 3 wt.% resulted in 47.8% enhancement in thermal conductivity as compared to the pure paraffin. In addition, they suggested that by adding the SSL as a surfactant in NCPCMs showed the better dispersion and thermal stability for compared to NCPCMs without SSL. More further, they suggested that NCPCMs using SLL had the better dispersion and stability of $TiO_2$ NPs compared with the with SSL NCPCMs.

Teng and Yu (Teng and Yu, 2012a) prepared samples of NCPCMs with paraffin wax and by considering 1, 2 and 3 wt.% weight concentrations of different NPs (ZnO, $SiO_2$, $TiO_2$ and $Al_2O_3$). The authors found that NCPCMs containing $TiO_2$ NPs showed better results of thermal storage properties and reduced the onset decomposition temperature to make PCMs applicable to heat storage and thermal management systems compared to $Al_2O_3$, $SiO_2$, and ZnO nanoparticles. Wang et al. (Wang et al., 2014) prepared $TiO_2$/paraffin wax NCPCMs with weight concentration ranging from $0-7.0$ wt.% without any surfactant. They reported that the thermal conductivity of NCPCMs was improve till 3.0 wt.% of $TiO_2$ and then it was decreased. Motahar et al. (Motahar et al., 2014) investigated the rheological and thermal properties composite PCMs of consisted of n-Octadecane and $TiO_2$ NPs with weight concentration range of $0-5.0$ wt.%. It was reported that the heat transfer occurred through conduction in solid phase and later on by convection mode. However, the natural convection mode lowered the melting rate as the weight concentration of $TiO_2$

was increased because of the increase in viscosity. Chen et al. (Chen et al., 2017) reported the NCPCMs synthesized by carbon–coated aluminium NPs (Al–C) with paraffin wax. Authors found the thermal conductivity of 0.189 W/m.K with 4 wt.% of Al–C which was 206.5% higher in comparison with paraffin wax at 25°C. Nourani et al. (Nourani et al., 2016b,a) prepared the paraffin wax and $Al_2O_3$ based NCPCMs with loading content of 0.5, 5, 7.5, and 10 wt.% of $Al_2O_3$ and SSL as a surfactant for better stability dispersion. For solid and liquid phases, the effective thermal conductivity enhancement was found of 31% and 13%, respectively, at 10.0 wt.%. Babapoor and his co–authors (Babapoor et al., 2016; Babapoor and Karimi, 2015) prepared mono and hybrid NCPCMs using $SiO_2$, $Al_2O_3$, $Fe_2O_3$, ZnO NPs and investigated the thermal and phase–change properties in solid and liquid phases. Authors obtained the higher thermal diffusivity with $Fe_2O_3$ at 8 wt.%. Moreover, it was recommended that $Al_2O_3$ NPs were the most suitable for TM applications. Pahamli et al. (Pahamli et al., 2017) synthesized the NCPCMs using CuO and RT–50 by using 2 and 4 wt.%. The higher thermal conductivity enhancement was obtained of 3.9% and 7.2% with 2 wt.% and 4 wt.%, respectively. Recently, Praveen and Suresh (Praveen and Suresh, 2018) investigated the thermophysical and heat transfer characteristics using CuO and neopentyl glycol (NPG) composite PCMs. Authors found the thermal conductivity and latent–heat of 0.61 W/m.K and 112.4 kJ/kg, respectively, with 3.0 wt.% of CuO.

For effective heat storage and transfer using PCMs, the latent–heat and thermal conductivity are the key thermal properties of PCMs which improve the TM efficiency. Therefore, a PCM with higher latent–heat and thermal conductivity with stable chemical structure is the most suitable. The literature reveals that most of the studies focused on the development of NCPCMs used for the high temperature TES applications. The current study focuses on synthesising of new NCPCMs which will be the most suitable for thermal management of electronic devices, photovoltaic modules and Li–ion batteries, working under

the safe and reliable operating temperature range of 30–40 °C (Siddique et al., 2018; Sahoo et al., 2016a). In order to keep in mind the safe operating temperature, a commercially available PCM (RT–35HC) is selected having melting temperature of 34-36 °C. To enhance the thermal properties and heat storage capacity at an optimum level, various loading from 0.0 to 2.0 wt.% of $TiO_2$ nanoparticles are dispersed. In this work, various properties of NCPCMs are investigated including morphology, chemical structure, crystal phase, specific heat, thermal conductivity, phase–change thermal properties, thermal stability and reliability

## 3.2 Experimental description

### 3.2.1 Materials

In this work, the RT–35HC (34–36 °C) was selected as a PCM which is commercially available product by Rubitherm GmbH, Germany, categorized under the paraffin PCMs. Nano Titanium (IV) dioxide ($TiO_2$), anatase powder (particle size $< 25$ nm, 99.7% trace metals basis, surface area: $45 - 55$ $m^2/g$, density: 3.9 g/mL at 25 °C) and sodium dodecylbenzene sulfonate (SDBS) were purchased from Sigma-Aldrich, Inc. UK. The thermal properties of RT–35HC are listed in Table 3.1. All the materials were used without any further chemical processing because they are analytical reagent grade.

Table 3.1: *Thermophysical properties of RT–35HC.*

| Melting temperature (°C) | Thermal conductivity (W/m.K) | Latent heat (J/kg.K) | Specific heat (J/kg.K) | Density ($kg/m^3$) |
|---|---|---|---|---|
| 34–36 | 0.2 | 240,000 | 2000 | 880 (solid)<br>770 (liquid) |

### 3.2.2 Preparation of nanocomposite PCMs

For the preparation of NCPCMs, a highly precise two–step method was opted which have been used extensively to prepare the nanofluids (Arshad et al.,

2019b), as shown in Fig. 3.1. RT–35HC was used as a base PCM and $TiO_2$ NPs were added with weight concentration of 0.5, 1.0, 1.5 and 2.0wt.% which acted as thermal conductivity enhancers (TCEs). In addition sodium dodecylbenzene sulfonate (SDBS) was added with the ratio 4 : 1 for each loading of the $TiO_2$. In first step, the RT–35HC was melted completely at its liquid state by providing the heat through a hot–water bath operating at constant temperature of 70 °C. To achieve the uniform dispersion of $TiO_2$ in RT–35HC, a constant fraction of the surfactant (SDBS) was added into the liquid RT–35HC which improves the stability of $TiO_2$ NPs because of its hydrophobic and hydrophilic structure. The mixture was stirred through a magnetic stirrer homogeneously at 70 °C and 450 rpm for 30 mins. Thenceforth, the $TiO_2$ nanoparticles were added and stirred for further 3 hrs for stable and uniform dispersions of $TiO_2$ in RT–35HC. The prepared NCPCMs were labelled NCPCM1, NCPCM2, NCPCM3 and NCPCM4 for weight concentration of 0.5, 1.0, 1.5 and 2.0 wt.%, respectively. Secondly, the ultrasonication was performed of each sample of NCPCMs for 60 mins maintaining the constant temperature of 70 °C using an ultrasonic vibrator at a frequency of 40kHz (Asadi et al., 2019). The ultrasonication process improves homogeneous and stable dispersion of $TiO_2$ and minimizes the agglomeration and sedimentation, as shown in Fig. 3.2.

## 3.3 Characterization methods

The characterization of NCPCMs was carried out by various methods to study the surface morphology, chemical and physical interaction, thermal properties including phase–change temperature, melting/solidifying latent–heat enthalpies, specific heat capacity, thermal conductivity, thermal stability and thermographic images of temperature distribution.

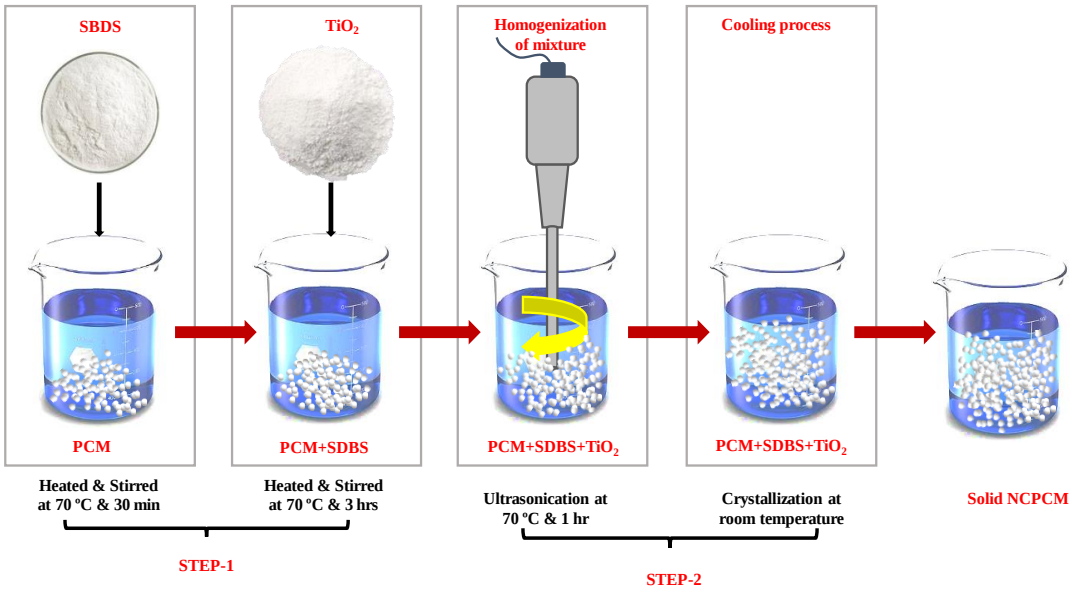


**Figure 3.1:** *Schematic diagram of sample preparation of $TiO_2$ and RT–35HC based NCPCMs.*

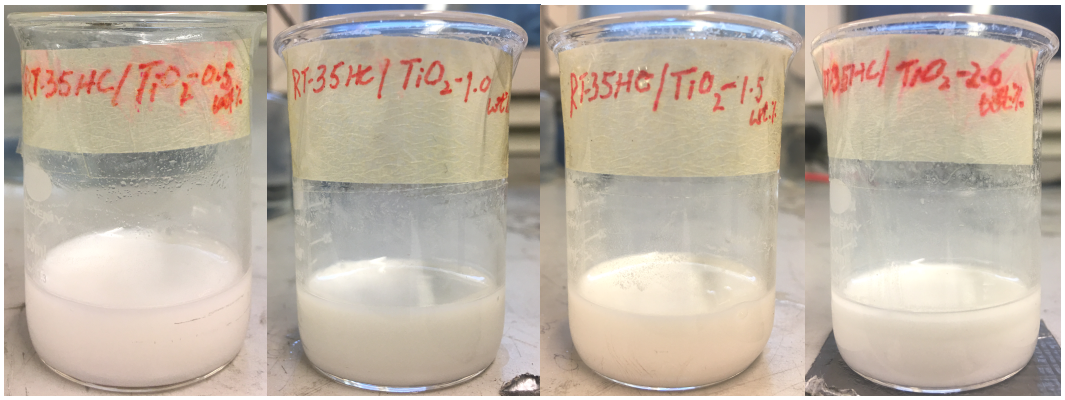

(a) (b) (c) (d)

**Figure 3.2:** *$TiO_2$ NCPCMs after sonication : (a) NCPCM1, (b) NCPCM2, (c) NCPCM3, (d) NCPCM4.*

### 3.3.1 Morphology and chemical interaction analysis

To visualize the surface morphology and elemental distribution of $TiO_2$ NPs in the NCPCMs, an environmental scanning electron microscopy (ESEM, FEI Quanta-650) was used along with energy-dispersive X–ray spectroscopy (EDS). To investigate the chemical composition of $TiO_2$ NPs and all samples, the fourier transfer infrared spectroscope (FI–TR, Bruker Tensor-27) at room temperature from $400 - 4000$ cm$^{-1}$ range 4 cm$^{-1}$ spectral resolution and accuracy

of 0.01 $cm^{-1}$. The crystallographic analysis was analysed from X-ray powder diffraction (XRD) patterns $TiO_2$ NPs and all samples, obtained with Bruker (D8–Advance, Bruker UK Limited) X–ray diffractometer with a monochromatic Cu–K$\alpha$ radiation ($\lambda = 1.5406\mathring{A}$) within $2\theta$ range of 5–60 °.

### 3.3.2 Thermophysical properties analysis

To check the thermal stability and degradation temperature of NCPCMs, thermogravimetric analysis (TGA) and derivative thermogravimetry (DTG) were performed through SDT–Q600 simultaneous TGA/DSC having 0.1$\mu$g precision. A sample mass range of $5 - 8$ mg was placed in an aluminium pan and test was performed in range of 20–400 °C with step rate of 10 °C$min^{-1}$ under the $N_2$ purging flow rate of 100 mL/min.

The phase–transition temperatures and enthalpies of RT–35HC and NCPCMs were measured using differential scanning calorimeter (DSC-2500, TA instrument Inc., UK) between temperature range of 10–50 °C at a temperature rate of 1 °C$min^{-1}$ in a pure $N_2$ environment with ±0.04% accuracy and ±0.005°C precision. The specific heat capacity was measured from temperature range of 20-60 °C at 3 °C$min^{-1}$ constant heating rate by adopting Sapphire method. An aluminium Tzero Hermetic pan and lid was used filled with the sample mass around $3 - 5$ mg precisely with no leakage.

The thermal conductivity of pure RT–35HC and NCPCMs was measured using TCi$^{TM}$ thermal conductivity analyser (TCA) by C–Therm Technologies Ltd, Canada following the modified transient plane source (MTPS) method (ASTM–D7984) with the precision and accuracy better than 1% and 5%, respectively. The thermal conductivity was measured as a function of temperature ranging from 20 to 55 °C. Five readings were measured at constant temperature and an average value was considered with ±1.0% uncertainty.

To take the thermographs to NCPCMs, infrared thermography (IRT) tests were performed over a IR thermographic camera (FLIR–SC2600–EA2). To

provide a uniform heating, the samples were heated in a water pot on a hot plate.

## 3.4 Results and discussions

### 3.4.1 Morphological and elemental analysis

The ESEM scanning images, representing the micro–structural features and surface morphologies of $TiO_2$ NPs and NCPCM4 shown in Fig. 3.3. The spherical shape of $TiO_2$ NPs can be seen from Fig. 3.3a. Figs. 3.3b and 3.3c represent the low vacuum secondary electron detector (LFD) and backscatter electron detector (BSED) images at 500 magnification for low vacuum mode. Whereas, Figs. 3.3d and 3.3e show the LFD and BSED images at 1000 magnification. It can be seen that $TiO_2$ NPs are uniformly dispersed (white regions) over the surface of solid RT–35HC (dark regions) which is due the repulsive bonding of the SDBS acting as a surfactant. In addition, the homogeneous and heterogeneous percolation of $TiO_2$ in RT–35HC can be observed in both of lower and higher magnifications. The presence of zones characterized by the heterogeneous aggregates of $TiO_2$ NPs and zones of pure RT–35HC can be observed clearly. Similar observations of aggregation with $SiO_2/Al_2O_3$ nanoparticles had been reported by Chieruzzi et al. (Chieruzzi et al., 2015). In the liquid phase of NCPCMs, solvation, "Brownian motion" and "electrostatic repulsion" cause the NPs to separate individually. However, this collision increases between the NPs by increasing the NPs concentration and Van der Waals force becomes stronger at a short range which results in the formation of aggregates and sedimentation of NPs at high concentration. Moreover, as the concentration increases, the density of NPs per unit area also increases which yields the more pathways for thermal transport in PCM (Warzoha et al., 2015). The uniform dispersion and percolation of NPs depend on the size of the NPs. A better dispersion of NPs into PCMs can be achieved

with smaller size of NPs.

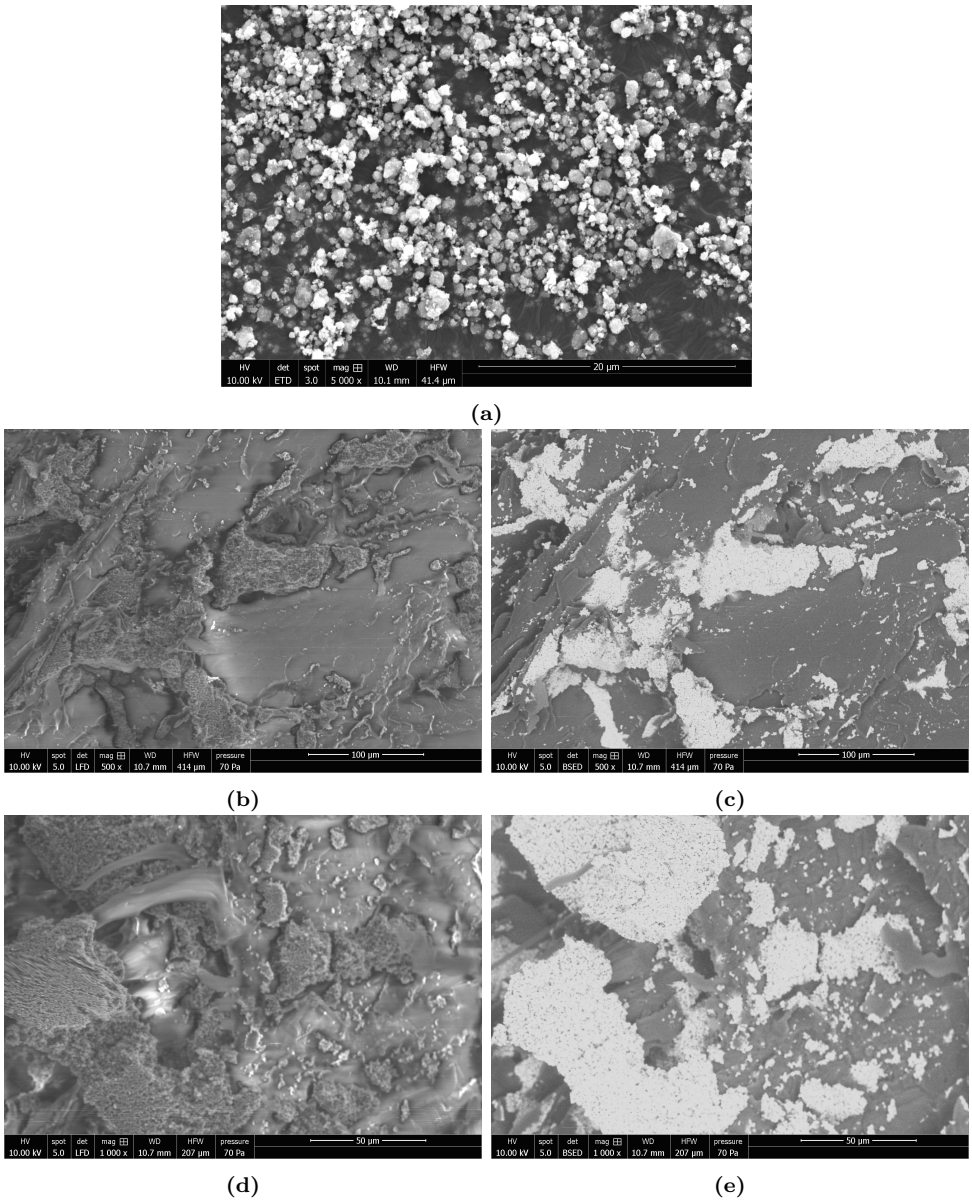


**Figure 3.3:** *ESEM images of (a)$TiO_2$ NPs, NCPCM4 (b) LFD and (c) BSED at 500 magnification, (d) LFD and (e) BSED at 1000 magnification. The grey zones show the RT–35HC and white dots are the $TiO_2$ nanoparticles which are agglomerated on the nanoscale but dispersed on the microscale.*

The better understanding and visualization of NCPSMs, EDX maps of NCPCMs are shown in Fig. 3.4. The Figs. 3.4a, 3.4b, and 3.4c present the elemental distribution of carbon (C), oxygen (O) and titanium (Ti), respectively, of 2.0 wt.% of $TiO_2$ NPs dispersed in RT–35HC. The red colour presents in various zones of Fig. 3.4a, shows the presence of C elements in RT–35HC, synthesized as a paraffin based PCM. Similarly, the cyan and green colours represent the

aggregates of O and Ti elements present compound of $TiO_2$ nanoparticles and RT–35HC PCM. The distribution of C, Ti and O in different colours can be illustrate in single image present in $TiO_2$ dispersed NCPCM in Fig. 3.5. It can be revealed that ESEM and EDX images show the agglomerated $TiO_2$ NPs in difference zones of the NCPCM which correlate with the Ref. (Chieruzzi et al., 2015). Thus, the NPs with smaller size reveal the better dispersion into the PCM (Saterlie et al., 2011; Evans et al., 2008).

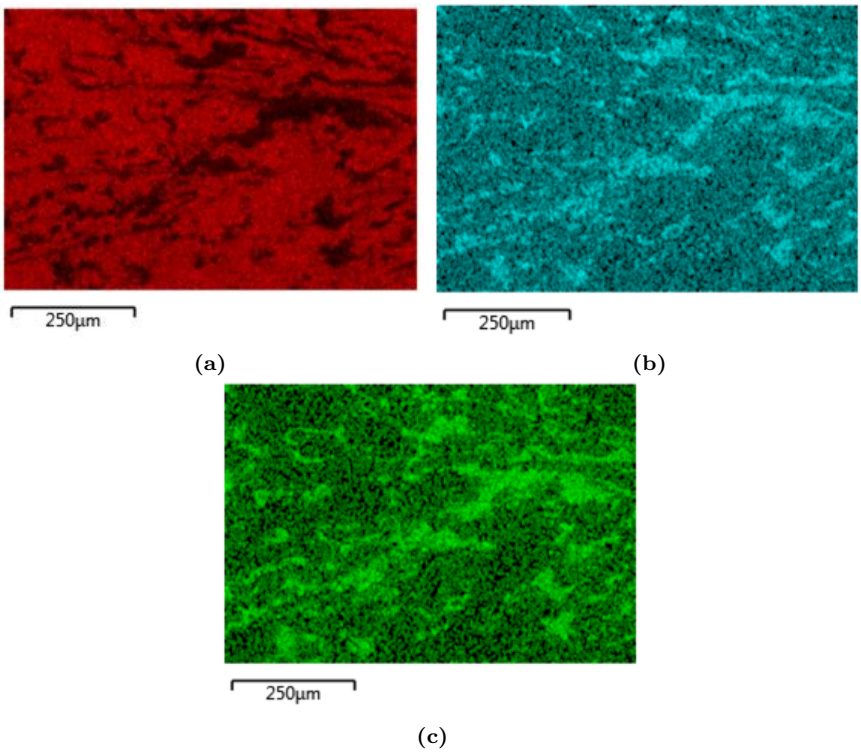


**Figure 3.4:** *EDX mapping of NCPCM4 (a) carbon-(red), (b) oxygen-(cyan), (c) Titanium-(green).*

### 3.4.2 Chemical composition analysis

The chemical composition and structural interaction of $TiO_2$ NPs dispersed NCPCMs were verified by FT–IR analysis. Fig. 3.6 shows the transmittance band of FT–IR spectra of $TiO_2$, RT–35HC and NCPCM1-4 between wave numbers of 500 and 4000 $cm^{-1}$. The peaks around 510 and 526 $cm^{-1}$ are attributed to the Ti–O stretching vibrations in $TiO_2$. For the spectrum of RT–35HC, it is observed that the three absorption bands at 2955, 2913, 2849

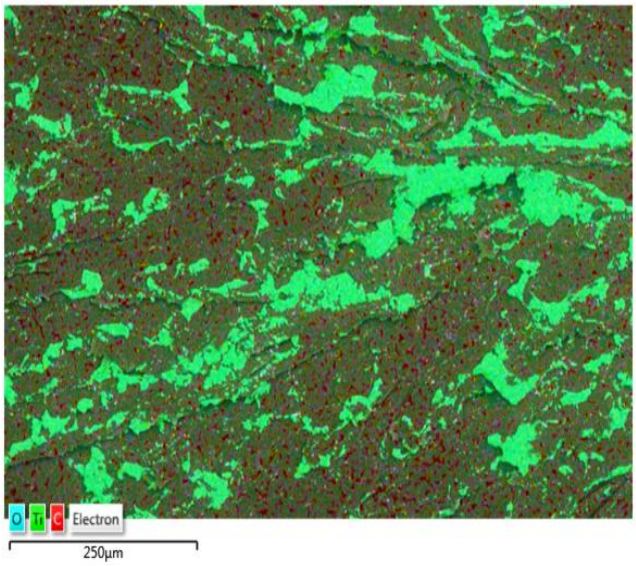


**Figure 3.5:** *EDX map of Qxygen, Titanium, and carbon elements present in NCPCM4.*

$cm^{-1}$ assigned to medium C–H symmetrical and anti–symmetrical stretching vibration of methyl ($–CH_3$) and methylene ($–CH_2–$) groups. The scissoring of $–CH_2–$ appears at 1472 $cm^{-1}$ and deformation of antisymmetric stretching vibration $–CH_3$ group in RT–35HC. The series of absorption bands at 1371, 1125, and 891 $cm^{-1}$ are attributed to the C–H bending and scissoring vibrations. A weak rocking vibration of C–H appears at 715 $cm^{-1}$ in long-chain methyl group. No new peak is observed in NCPCM1–4 as revealed from FT–IR results. More further, it can be seen that there is also no peak shift. Thus, there occurs no chemical reaction between the SDBS, $TiO_2$ and RT–35HC and only physical interaction is present.

### 3.4.3 Crystallography analysis

The crystal structure and crystalline phase of $TiO_2$ NPs, RT–35HC and NCPCM1–4 were identified through XRD pattern and results were matched with the international centre for diffraction data (ICDD) database, as shown in Fig. 3.7. The XRD diffraction of peaks of $TiO_2$ NPs at $2\theta = 25.3°$, 37.79°, 48.03°, 53.88° and 55.06° represent the lattice planes of (101), (004), (200), (105) and (211), respectively, which confirm the anatase form of the $TiO_2$ NPs with PDF No.

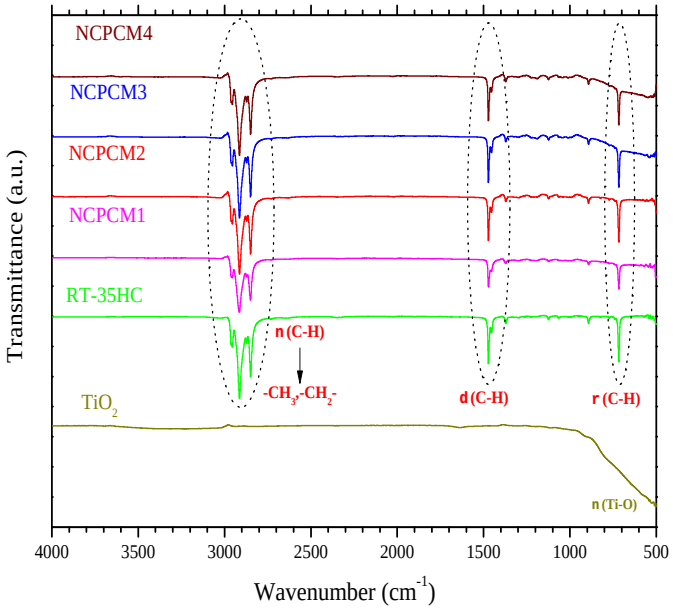


**Figure 3.6:** *FT-IR spectrum of $TiO_2$ and RT–35HC based NCPCMs.*

03-065-5714. The diffraction peaks of pure RT–35HC was observed at 6.85° (002), 10.48° (003), 13.91° (004), 17.44° (005), 19.32° (010), 19.80° (011), 20.83° (012), 22.43° (013), 23.32° (105), 24.78° (-101), 25.65° (110), 28.12° (008), 31.75° (009), 34.75° (-110), 35.27° (0010), 39.83° (0-22), 42.73° (0012), 44.60° (207), 52.68° (220), 53.41° (-2-14) and 57.55° (-205) which attributed to the crystal planes of *n-eicosane* ($C_{20}H_{42}$) with PDF No. 00-045-1543. The

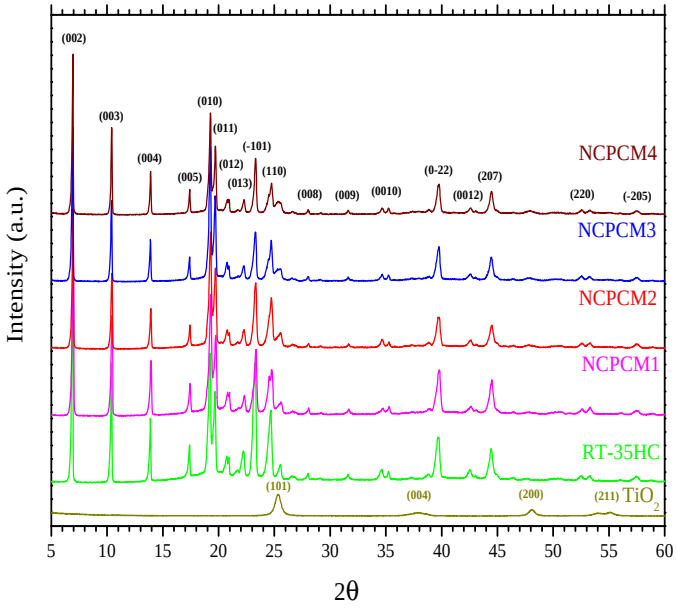


**Figure 3.7:** *XRD spectrum of $TiO_2$ and RT–35HC based NCPCMs.*

physical presence of $TiO_2$ NPs can be found in NCPCMs such as at higher con-

centration of 2.0 wt.% of $TiO_2$ NPs are found at 25.34°, 39.62°, 47.74°, 54.81° and 56.00° which are well indexed as (101), (004), (200), (211) and (105), respectively, in NCPCM4. Therefore, the XRD results of NCPCMs illustrate that dimensions of unit cell of RT–35HC crystal structure has not changed in NCPCMs and all the samples contain the peaks of $TiO_2$ NPs.

### 3.4.4 Thermal stability analysis

Thermal stability analysis of pure RT–35HC and NCPCM1–4 are shown in Fig. 3.8, conducted by TGA and DTG. The thermal stability was analysed depending upon the onset decomposition temperature ($T_{onset}$) of PCM degradation and rate of weight loss ($R_{wl}$). From Figs. 3.8a and 3.8b, it represent that a one–step and two–step thermal degradation processes are attributed to the TGA and DTG curves, respectively. The TGA curves show that there exists no weight loss distinguishably up to 120 °C in any sample. The weight loss starts appearing with the rise of temperature and $R_{wl}$ increases with further increase of temperature. For RT–35HC, the initial $T_{onset}$ starts at 217.70 °C and maximum degradation temperature ($T_{max.degradation}$) is 255.01 °C with 1.85% residue ($\gamma$). The complete decomposition of RT–35HC is because of the evaporation which breakdown the hydrocarbon chain of RT–35HC into monomers ($CH_3CH$:$CH$+$CH_4$). From the results presented in Table 3.2 it has been observed that by increasing weight concentration of $TiO_2$, the initial $T_{onset}$ also increases with a rise in $\gamma$ content of the material. The $\gamma$ concentration rises up to 3.79% in case of NCPCM4, which is maximum value among the given samples in Table 3.2. It can be seen from Fig. 3.8 that NCPCM4 showed maximum thermal stability. It can be seen from that the thermal stability increase with the increase of weight concentration of $TiO_2$ in RT–35HC. This improved trend in thermal stability can be explained by the following reasons: (i) *the $T_{onset}$ is related to the entire specific heat capacity ($C_p$) of $TiO_2$/RT–35HC nanocomposites which can be raised by the $C_p$ of $TiO_2$ NPs, and* (ii)

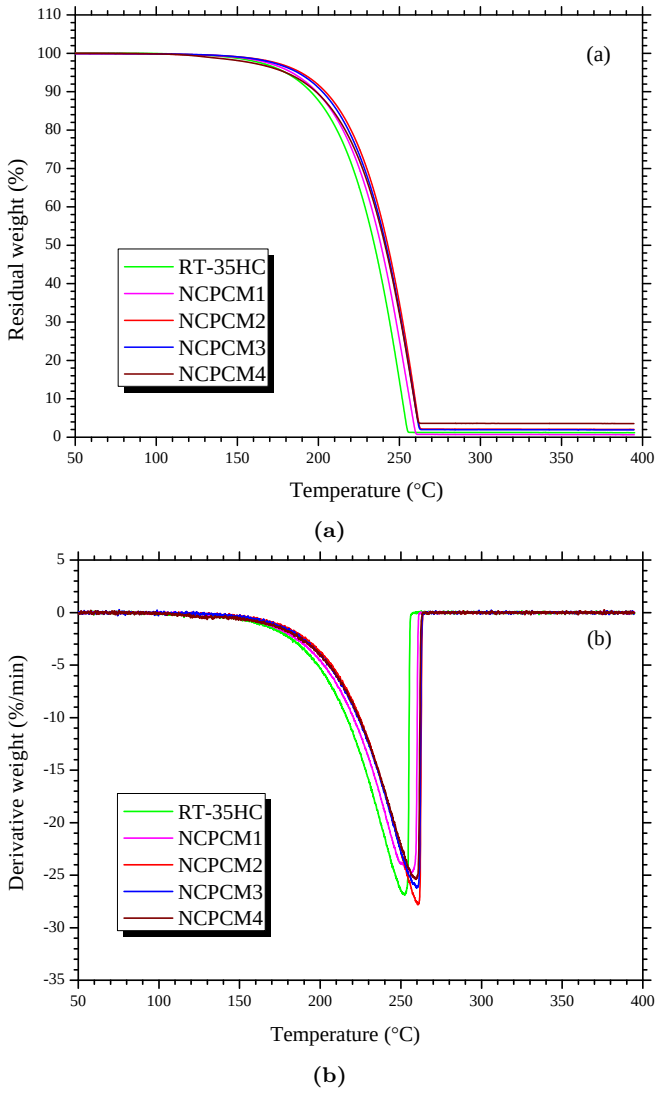


**Figure 3.8:** *(a) TGA and (b) DTG thermograms of $TiO_2$ and RT–35 based NCPCMs.*

*enhanced thermal conductivity of NCPCMs which can transfer heat faster and uniformly within the PCM* (Chen et al., 2017). In NCPCMs, the $TiO_2$ NPs create the protective layer on the surface of pure RT–35HC which delay vaporization of RT–35HC during the thermal degradation. As NPs are likely to sediment which effect the thermal properties. Therefore, the DTG curves of NCPCM1–4 shown in Fig. 3.8b confirm that the dispersion NPs enhance the thermal stability of RT–35HC. Since, no decompositions in materials have been observed until ∼150 °C. So, hybrid can effectively be used for TM of electronic devices, Li–ion batteries and PV modules and TES applications.

Table 3.2: *Decomposition temperatures and residue of $TiO_2$ and RT–35HC based NCPCMs.*

| Sample | $T_{onset}$ (°C) | $T_{max.degradation}$ (°C) | $\gamma$ (%) |
|---|---|---|---|
| RT–35HC | 217.70 | 255.01 | 1.85 |
| NCPCM1 | 219.97 | 260.26 | 1.51 |
| NCPCM2 | 226.77 | 263.55 | 1.96 |
| NCPCM3 | 224.70 | 262.54 | 2.17 |
| NCPCM4 | 223.50 | 262.29 | 3.79 |

### 3.4.5 Phase-change thermal properties analysis

The phase–change thermal properties of pure RT–35HC and NCPCMs are determined using DSC for melting/cooling cycles, as shown in Fig. 3.9. Figs. 3.9a and 3.9b present the DSC thermographs of endothermic and exothermic curves, respectively, and corresponding measured values of phase–transition temperatures and latent–heat of melting/cooling are summarized in Table 3.3. With the addition of $TiO_2$ NPs, phase–changes thermal properties have slightly changed during the synthesizing process. Latent–heat of melting/solidifying of NCPCMs decreases by increasing the $TiO_2$ NPs loadings. The pure RT–35HC and NCPCMs show the single endothermic peaks during melting which reflect an isomorphous crystalline form of RT–35HC either in pristine state or in composite state. On the other hand, it can be noticeably observed that pure RT–35HC and NCPCMs show the bimodal crystallization behaviour by showing a main exothermic peak temperature along with an additional peak of higher temperature during solidification process. This two–phase transitions phenomenon can be explained due to the appearance of a metastable rotator phase prior to completing the complete crystallization as a results of the heterogeneous nucleation during the cooling process, which has been mostly reported for the paraffin waxes (Yavari et al., 2011; Liu et al., 2017).

From the DSC results, the comparison of the melting ($\Delta H_m$) and solidification ($\Delta H_s$) enthalpies of pure RT–35HC and NCPCMs are presented in Fig. 3.9c. The $\Delta H_m$ and $\Delta H_s$ of pure RT-35HC are determined of 255.88 and 260.06 J/g, respectively. The reduction in $\Delta H_m$ of NCPCM1–4 has been obtained

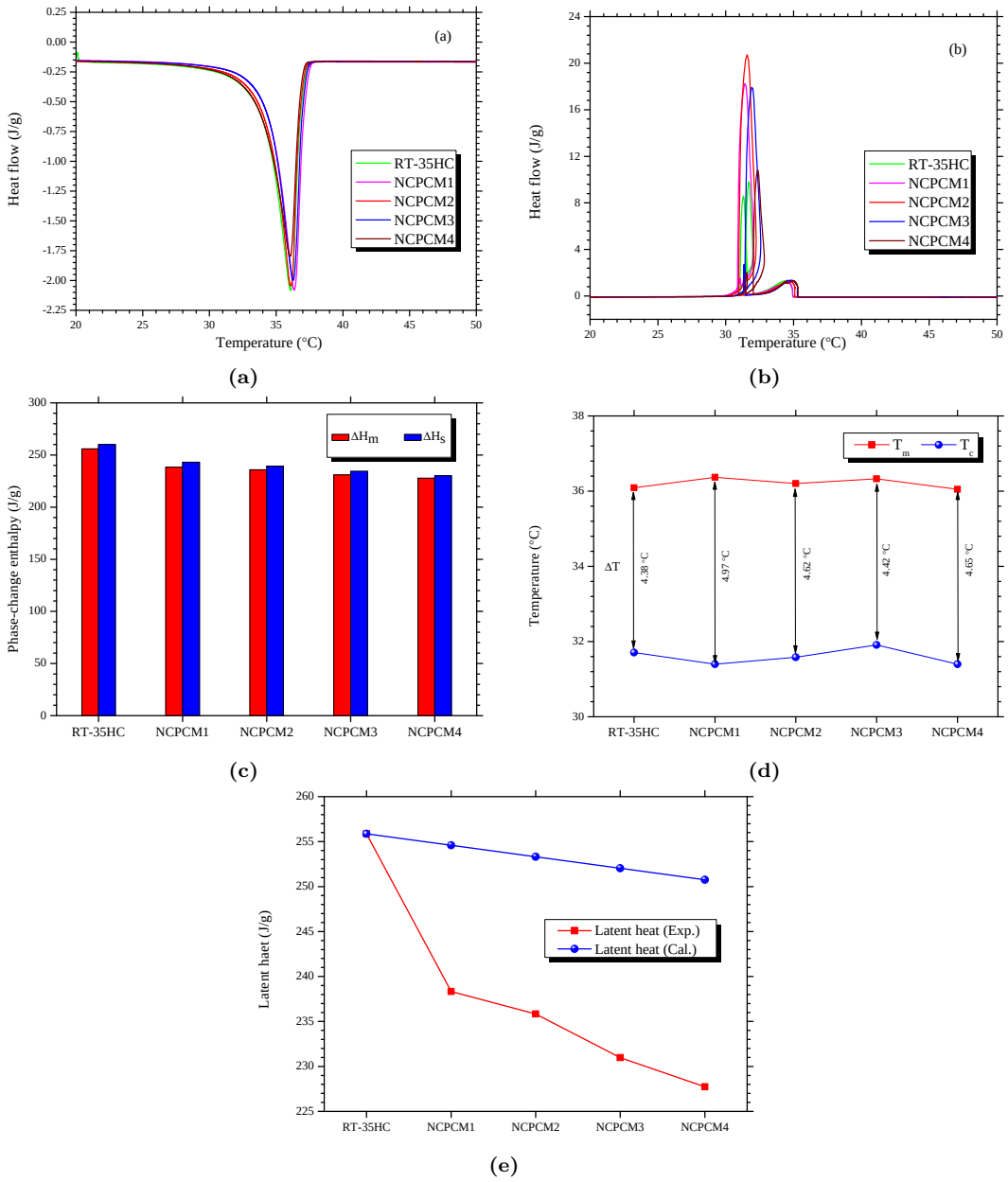


**Figure 3.9:** *The results of (a) Melting, (b) Solidification curves, (c) Phase–change enthalpies, (d) Degree of super–cooling and (e) Comparison of latent–heats of fusions of $TiO_2$ and RT–35HC based NCPCMs.*

of 6.86%, 7.83%, 9.74% and 11.0% compared with RT–35HC. In similar way, the reduction in $\Delta H_s$ are obtained of 6.54%, 7.98%, 9.90% and 11.54% for NCPCM1–4, respectively. In comparison with RT–35HC, the maximum reduction $\Delta H_m$ and $\Delta H_s$ are obtained for NCPCM4 at 2.0 wt.% of $TiO_2$ which are 11.0% and 11.54%, respectively, which is due to the addition of $TiO_2$ NPs. The Eq. 3.1 is used to calculate the mass fraction ($\omega$) of RT–35HC in crystal-

lized form in NCPCMs, as follows:

$$\omega = \frac{\Delta H_{NCPCM}}{\Delta H_{PCM}} \times 100 \tag{3.1}$$

where, $\Delta H_{NCPCM}$ and $\Delta H_{PCM}$ are the endothermic latent–heat of NCPCM and pure PCM, respectively. During melting and solidification processes, the $TiO_2$ NPs replace the RT35–HC molecules resulting in reduce the latent–heat capacity of the NCPCM which lead to the absorption or release of more energy. The stronger the interaction between $TiO_2$ and RT35–HC, higher will be the latent–heat capacity of the NCPCM. Fig. 3.9d illustrates the results of degree of super–cooling ($\Delta$T) of pure RT–35HC and NCPCMs. The peak melting temperature ($T_m$) and crystallization temperature ($T_c$) of RT–35HC are determined as 36.09 °C and 31.71 °C, respectively. However, the slight variations are observed in $T_c$ which are due the crystallization confinement of $TiO_2$ NPs surface layers within the NCPCMs. Furthermore, this interfacial surface layers cause to form the imperfect RT–35HC resulting in a slight variation in $T_m$. Thus, these factors cause to increase the $\Delta$T. Maximum deviations in $T_m$ are determined as $-0.78\%$, $-0.30\%$, $-0.67\%$ and $0.11\%$ for NCPCM1–4, respectively, compared with the RT–35HC. Similar to this, by comparing with RT–3HC, the maximum deviations in $T_c$ are found of $0.98\%$, $0.41\%$, $-0.63\%$ and $0.98\%$ for NCPCM1–4, respectively. Furthermore, to achieve the crystallization point depression, heterogeneous nucleation can be acceptable by adding the $TiO_2$ NPs in RT–35HC (Yavari et al., 2011). However, it has been proved that higher difference in $\Delta$T is an evidently disadvantageous to use the PCM for TM and TES applications. Since it can exhibit the hysteresis response during conjugate heat transfer.

The experimental and theoretical results of latent–heat of enthalpies of RT–35HC and NCPCMs are presented in Fig. 3.9e, calculated by the Eq. 3.2

(Tian et al., 2015):

$$\Delta L_{NCPCM} = \Delta L_{PCM} \cdot \omega = \Delta L_{PCM}(1 - \varphi) \tag{3.2}$$

where, $\varphi$ and $\omega$ are the mass fraction of pure PCM and NPs, respectively. $\Delta L_{PCM}$ and $\Delta L_{NCPCM}$ are the experimental and theoretical latent–heat of enthalpies of pure PCM and NCPCM, respectively. The results reveal that experimental measurements of latent–heat of fusion are less than compared with the theoretical results, as shown in Fig. 3.9e. The relative error (RE) in experimental and theoretical values has been obtained $6 \sim 9\%$ for NCPCM1–4, given in Table 3.3. The similar trend of deviations in experimental and theoretical values latent–heat of fusion have reported in Refs. (Liu et al., 2017; Sharma et al., 2016; Tian et al., 2015). The discrepancies in latent–heat values are because of the morphology, NPs size, shape, lattice structure and thermophysical properties (i.e. density, surface area, specific heat capacity and thermal conductivity etc.) of $TiO_2$ NPs in RT–35HC.

Table 3.3: *Thermal properties of $TiO_2$ and RT–35HC based NCPCMs*.*

| Sample | Melting | | | | | Solidification | | | | | $\omega$ (%) | $\Delta$ T |
|---|---|---|---|---|---|---|---|---|---|---|---|---|
| | $T_{oset,m}$ | $T_{peak,m}$ | $\Delta H_{m,exp}$ | $\Delta H_{m,cal}$ | RE (%) | $T_{oset,c}$ | $T_{peak,c}$ | $\Delta H_{c,exp}$ | $\Delta H_{c,cal}$ | RE (%) | | |
| RT–35 | 34.06 | 36.09 | 255.88 | - | - | 31.47 | 31.71 | 260.79 | - | - | 100 | 4.38 |
| NCPCM1 | 34.46 | 36.37 | 238.33 | 254.60 | 6.39 | 31.99 | 32.05 | 243.04 | 258.76 | 6.08 | 93.14 | 4.32 |
| NCPCM2 | 34.26 | 36.20 | 235.84 | 253.32 | 6.90 | 31.48 | 31.99 | 239.30 | 257.46 | 7.05 | 92.17 | 4.21 |
| NCPCM3 | 34.44 | 36.33 | 230.97 | 252.04 | 8.36 | 30.95 | 31.58 | 234.32 | 256.16 | 8.53 | 90.26 | 4.75 |
| NCPCM4 | 33.88 | 36.05 | 227.74 | 250.76 | 9.18 | 30.86 | 31.40 | 230.06 | 254.86 | 9.73 | 89.00 | 4.65 |

$T_{oset,m}$: onset melting temperature, $T_{peak,m}$: peak melting temperature, $\Delta H_{m,exp}$: experimental latent–heat of melting, $\Delta H_{m,cal}$: calculated latent–heat of melting, $T_{oset,c}$: onset solidifying temperature, $T_{peak,c}$: peak solidifying temperature, $\Delta H_{c,exp}$: experimental latent–heat of solidifying, $\Delta H_{c,cal}$: calculated latent–heat of solidifying, RE: relative error, $\omega$: mass percentage of RT–35HC, $\Delta$T: degree of super–cooling

### 3.4.6 Thermal conductivity analysis

The results of effective thermal conductivity variations and percentage enhancement of RT–35HC and NCPCMs are illustrated in Figs. 3.10 and 3.11, respectively, as function of temperature. As expected, the increasing trend in effective thermal conductivity was achieved with the increase of $TiO_2$ NPs loading in NCPCMs for solid and liquid phases. For efficient and effective TM, the effective thermal conductivity of the PCM contributed significantly in heat storage/release rate while melting/cooling cycle. A PCM with lower effective thermal conductivity causes to minimize the rate of total heat storage/release both in conduction and convection modes while phase transformation. With the addition of $TiO_2$ NPs, the maximum thermal conductivity of 0.480 W/m.K was achieved at 2.0 wt.% of $TiO_2$ and 35 °C. The temperature range between 34–36 °C is the phase–transition temperature range of pure RT–35HC at which the NCPCMs are in metastable condition. The crystalline structure of the RT–35HC becomes unstable and the increase in temperature accelerates the molecular vibration of in the lattice, thus effective thermal conductivity of pure RT–35HC and NCPCMs increases dramatically at the melting point ($\sim$ 35°C) (Motahar et al., 2014). Fig. 3.11 presents the effective thermal conductivity of solid–phase (20–30 °C), phase–change ($\sim$35 °C) and liquid–phase (40–55 °C) regions of pure RT–35HC and NCPCM1–4. The constant trend in enhancement of effective thermal conductivity was observed in solid and liquid phases. However a sharp increase and decrease trend was observed when the temperature increased from 30 °C to 35 °C and then 35 °C to 40 °C, respectively. Such deviations in results evidences that effective thermal conductivity of NCPCMs closely depends on the operating temperature. This phenomenon was due to the random motion of molecules within a disordered microstructure of lattice in liquid–phase. This random molecular motion collapses the percolation network established by NPs under the solid–phase (He et al., 2019c). The effective thermal conductivities values of 0.333, 0.338 and 0.341 W/m.K are measured

for NCPCM4 at temperature of 30 °C, 25 °C and 20 °C, respectively, as shown in Fig. 3.10. The relative enhancement in effective thermal conductivities are obtained of 59.4%, 59.6% and 59.5% at temperature of 30 °C, 25 °C and 20 °C, respectively, for NCPCM4, as shown in Fig. 3.11.

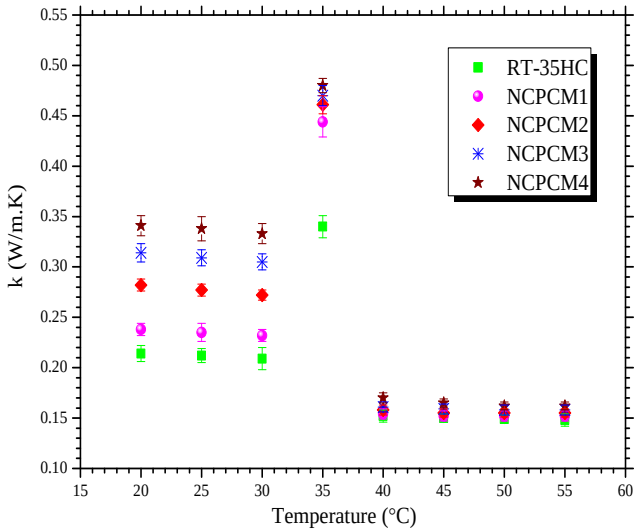


**Figure 3.10:** *Effective thermal conductivity of $TiO_2$ and RT–35HC based NCPCMs as a function of temperature.*

The following Eq. 3.3 was used to calculate the effective thermal conductivity enhancement factor after dispersing the $TiO_2$ NPs into the RT–35HC:

$$\eta = \frac{k_{NCPCM} - k_{PCM}}{k_{PCM}} \times 100 \tag{3.3}$$

where, $k_{PCM}$ and $k_{NCPCM}$ are the thermal conductivity of pure PCM and the NCPCM, respectively. It can be seen from Fig. 3.11 that effective thermal conductivity enhancement percentage increases linearly with increasing of $TiO_2$ loading both in solid and liquid phase. The maximum enhancement percentage of 11.4%, 31.9%, 46.9% and 59.5% for NCPCM1, NCPCM2, NCPCM3 and NCPCM4, respectively, at 20 °C. In addition, Figs. 3.12a and 3.12b present the results of effective thermal conductivity ratio, a given by Eq. 3.4:

$$\xi = \frac{k_{NCPCM}}{k_{PCM}} \tag{3.4}$$

It can be revealed from that the value of $\xi$ is greater than 1 which means

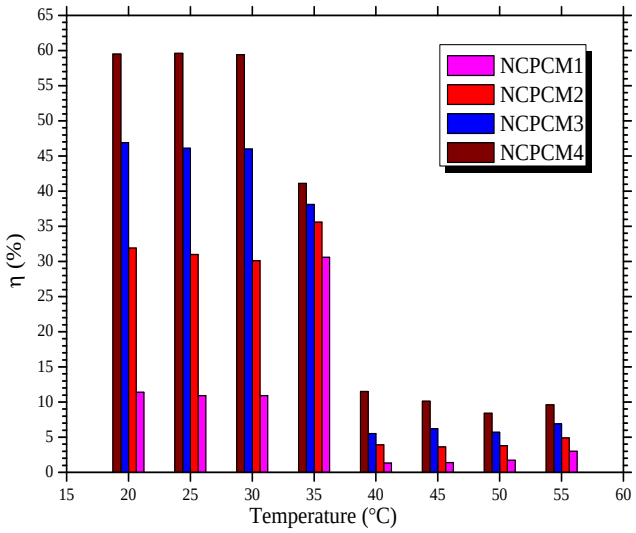


**Figure 3.11:** *Effective thermal conductivity enhancement of $TiO_2$ and RT–35HC based NCPCMs as a function of temperature.*

that NCPCMs have the higher effective thermal conductivity than the pure PCM. In addition, higher values of $\xi$ are obtained for NCPCMs having solid–phase compare to the liquid–phase. The correlations have been developed to predict the effective thermal conductivity of NCPCMs as a function of loading of nanoparticles for solid and liquid phases at temperature of 25 °C and 55 °C, respectively, as given below:

At 25 °C:

$$k_{NCPCM} = k_{PCM}(0.31\varphi + 0.986) \tag{3.5}$$

At 55 °C:

$$k_{NCPCM} = k_{PCM}(0.046\varphi + 1.003) \tag{3.6}$$

The enhancement mechanism of effective thermal conductivity of $TiO_2$ nanoparticles in RT–35HC is shown Fig. 3.13. At lower concentration of 0.5 wt.%, the $TiO_2$ NPs well dispersed independently in the RT–35HC, which reduces the thermal Interfacial resistance and enhance the heat flow, resulting in a slightly improvement of the effective thermal conductivity, as shown in Fig. 3.13a. When the loading increases about 0.5 $\sim$ 1.0 wt.%, a small part of $TiO_2$ NPs are formed as clusters due to the intermolecular interaction between the small particles. These clusters are in favour of forming segmental thermal

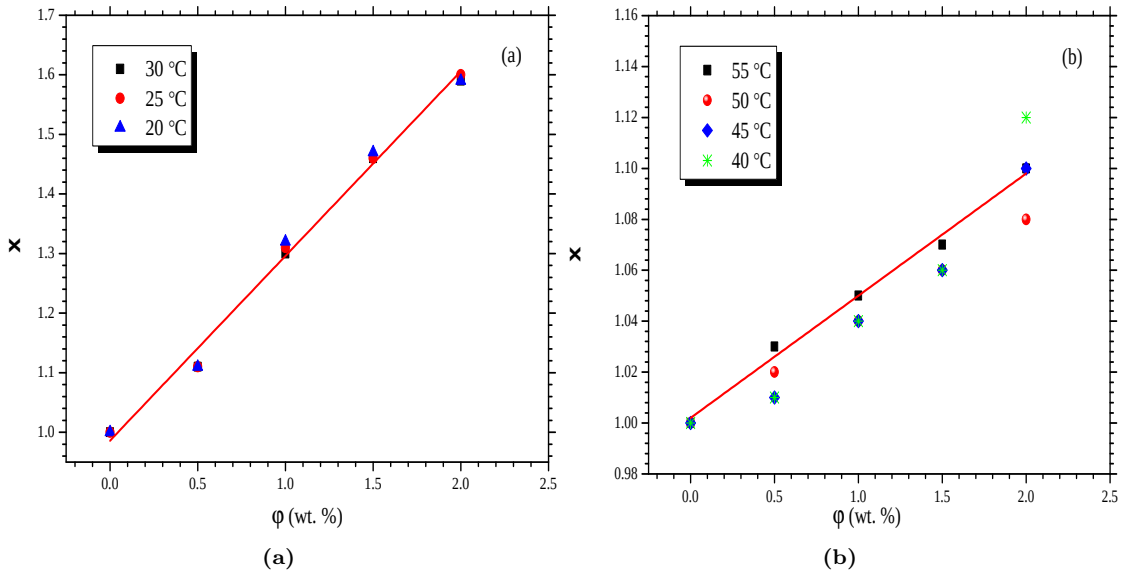


(a) (b)

**Figure 3.12:** *Effective thermal conductivity ratios of $TiO_2$ and RT–35HC based NCPCMs as a function of temperature: (a) solid–phase, (b) liquid–phase.*

conductive networks which improve the heat transferring path, as shown in Fig. 3.13b, and thus improve the thermal conductivity of NCPCMs. Further increasing the concentration of $TiO_2$ from 1.0 $\sim$ 2.0 wt.%, the NPs can easily be connected to build up the complete thermal conductive networks, as shown in Figs. 3.13c and 3.13d, which lead to significant improvement in effective thermal conductivity (Chen et al., 2017).

### 3.4.7 Specific heat capacity analysis

Specific heat capacity ($C_p$) results of pure RT–35HC and NCPCMs are presented in Fig. 3.14 from temperature range of 10–60 °C to explore the results for solid and liquid phases. Since the $C_p$ contributes less effect in total TES because of the lower TES density in sensible heating storage. However, the additional effects are observed when PCM is applied in any TM and TES system along with the latent–heating storage. Thus, the comparison of $C_p$ for solid and liquid phases of pure RT–35HC and NCPCMs are presented in Figs. 3.14a and 3.14b, respectively. From Fig. 3.14a, it can be illustrated that $C_p$ of NCPCMs increases gradually with temperature from 14 °C to 30 °C in solid–phase, however, the constant trend is observed in liquid–phase. The present

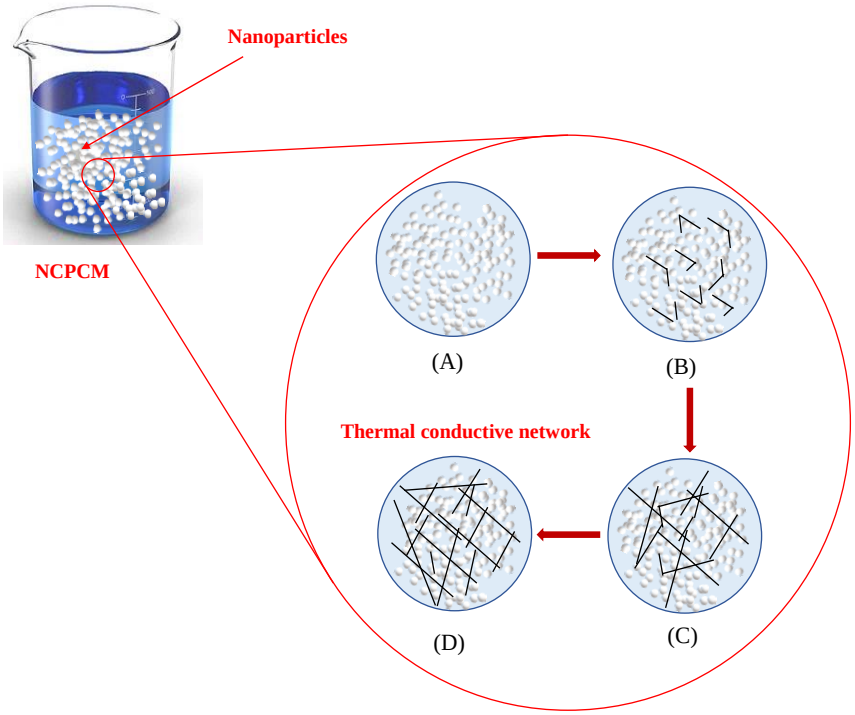


**Figure 3.13:** *Schematic representation of thermal conductive networks in $TiO_2$/RT–35HC NCPCMs with increasing loading of $TiO_2$: (a)* 0.5 *wt.%, (b)* 1.0 *wt.%, (c)* 1.5 *wt.%, (d)* 2.0 *wt.%.*

results of $C_p$ of both phases showed the good agreement in variation of $C_p$ with the previous studies (Mehrali et al., 2014a; Chieruzzi et al., 2015). It can been revealed from Fig. 3.14a that the addition of $TiO_2$ NPs increase the $C_p$ of pure PCM for both solid and liquid–phases as the weight percentage increases. For solid and liquid phases, the $C_p$ values of pure RT–35HC are measured of 1.88 and 1.77 J/g.°C, respectively. The higher values of $C_p$ are obtained of 2.84 and 2.56 J/g.°C at 25 °C and 50 °C, respectively, for NCPCM4. The polynomial equations are generated for solid phase from 14 °C to 30 °C for each NCPCM1–4 after fitting the experimental data, mentioned in Eq. 3.7 and coefficients are given in Table 3.4.

$$C_P = AT^3 + BT^2 + CT + D \tag{3.7}$$

Fig. 3.15 illustrates the comparison of $C_p$ for pure RT–35HC and NCPCM1–4 for 25 °C and 50 °C to report the data for solid and liquid phases. It can be

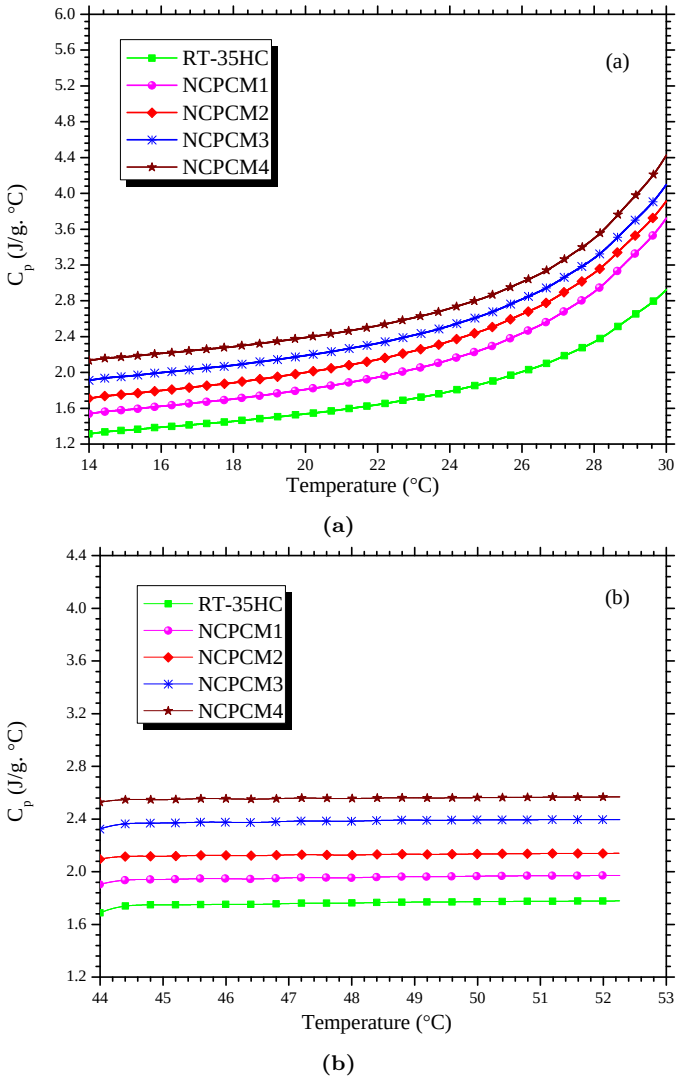


**Figure 3.14:** *The $C_p$ curves of pure RT–35HC and NCPCMs: (a)-solid–phase (b) liquid–phase.*

seen that with the increase of the $TiO_2$ loading, $C_p$ increases for both solid and liquid phases and the maximum enhancements are obtained of 50.90% and 44.55%, respectively, for solid and liquid phases NCPCM4 compared with the pure RT–35HC. The $C_p$ enhancement factor ($\zeta$) is calculated by using Eq. 3.8 to evaluate the NPs effect in heat transfer rate, as follows:

$$\zeta = \frac{C_{P_{NCPCM}} - C_{P_{PCM}}}{C_{P_{PCM}}} \times 100 \tag{3.8}$$

where, $C_{P_{NCPCM}}$ and $C_{P_{PCM}}$ are the $C_p$ of the NCPCM and PCM, respectively.

The enhancement in $C_p$ is associated with the following reasons: (i) an enhanced anharmonicity (In molecular vibrations the anharmonicity is very small

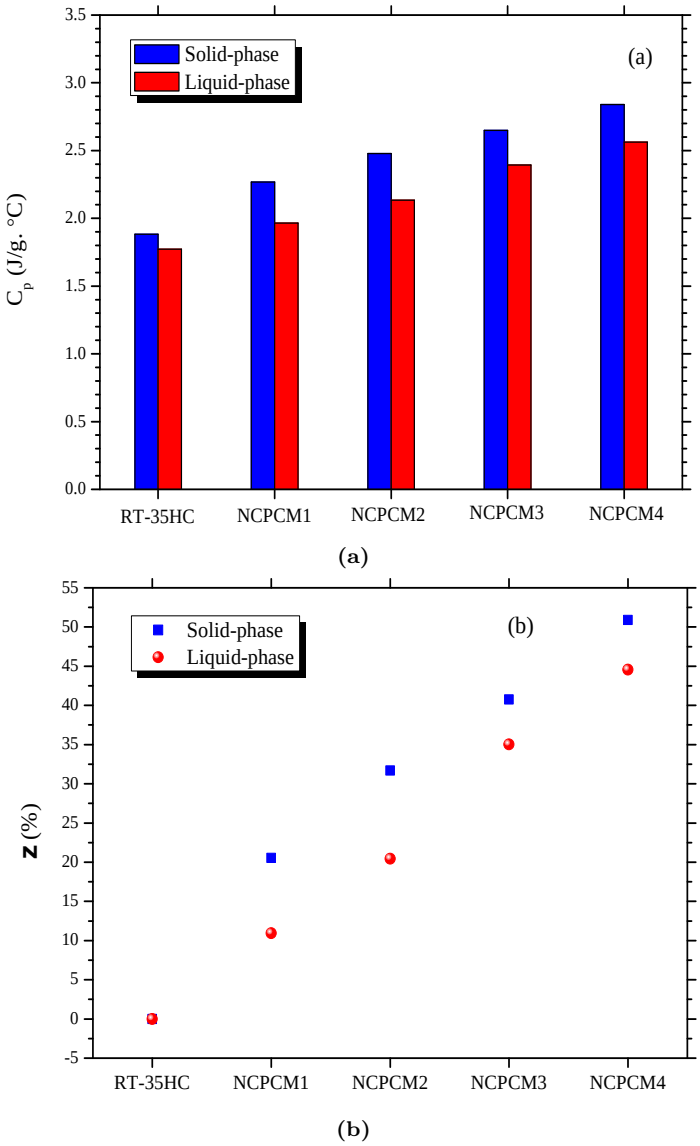


**Figure 3.15:** *(a) Comparison of $C_p$ curves and (b) specific heat capacity enhancement of pure RT–35HC and NCPCMs.*

Table 3.4: *Coefficients of the third–order polynomials in solid–state, $C_p$ (J/g.°C).*

| | A | B | C | D | $R^2$ |
|---|---|---|---|---|---|
| RT–35HC | 0.0006 | -0.0349 | 0.6687 | -2.9832 | 0.9988 |
| NCPCM1 | 0.0009 | -0.0493 | 0.9384 | -4.4479 | 0.9984 |
| NCPCM2 | 0.0008 | -0.0457 | 0.8701 | -3.8549 | 0.9987 |
| NCPCM3 | 0.0009 | -0.0489 | 0.9319 | -4.0415 | 0.9985 |
| NCPCM4 | 0.0011 | -0.0583 | 1.1128 | -4.9497 | 0.9974 |

near the equilibrium position, becomes large as the vibration moves away from the equilibrium position, and is very large as dissociation is approached.) of the atomic interaction due to their volume expansion, (ii) impurities (Hellstern et al., 1989), (iii) the grain boundaries of nanosized materials which possess an excess volume with respect to the perfect crystal lattice and (iv) the high specific surface energies related to the high surface area of the NPs per unit volume (Wang et al., 2006, 2001). Theoretically, the $C_p$ of materials is directly related to crystal structure, or its vibrational and configurational entropy which significantly affected by the nearest–neighbour configurations. Nanosized materials are structurally characterized by the metastable grain boundaries in which the nearest–neighbour configurations are much different from the coarse–grained state (Wang et al., 2001).

In addition, the morphology of NPs also influences significantly, since the smaller size NPs provide the larger interfacial surface area per unit mass between solid NPs and surrounding material, thus increases the contribution of interfacial effects in the suspension (Timofeeva et al., 2009; Xie et al., 2002; Koca et al., 2018). The interfacial interaction of solid–solid or solid–liquid may alter phonon spectrum or phonon vibration mode of NPs near the surface area and therefore, change the $C_p$ of NCPCM (Le-Ping et al., 2010). The high specific superficial interface area of NPs can adsorb liquid molecules to its surface which form the liquid layers. These liquid layers constrain the NPs and alter their free–boundary surface atoms into the non–free interior atoms (Wang et al., 2006; Le-Ping et al., 2010). Therefore, the variation in $C_p$ of NCPCMs is because of the varied Gibbs free energy of the NPs and liquid layers. For a two phase mixture (index $m$), the Gibbs free energy change is given by $\Delta G_m = \Delta H_m - T\Delta S_m$. The Gibbs free energy difference between the solid–liquid phases is determined from the average force that the applied field exerts on the system. The chemical potential of nanoparticles dispersions is straightforwardly based the material properties for fluid diffusion in between nanoparticles which is defined by the diffusion coefficient of nanoparticle dif-

fusion in a fluid as a function of the mass fraction. This diffusion coefficient also depends on particle size, surface chemistry, fluid composition, electrostatic effects and active particles. Moreover, the density–dependence of the chemical potential of dispersion implied as well. If the base fluid is polymeric of nature in a way that nanoparticles can alter their configuration either physically or chemically. Finally, the interchange energy associated with particle–matrix interaction, can be linked to a nano–layer of dense structured fluid around the nanoparticles (Pedersen, 2013; Machrafi, 2020).

### 3.4.8 Infrared thermography analysis

The thermographics images of NCPCM1–4 are presented in Fig. 3.16 to visualize the surface temperature distribution at different time interval from 5 to 30 min at a constant base temperature of hot–plate. The melting phenomenon of NCPCMs with different loadings of $TiO_2$ can be seen clearly for each time step. There is a clear difference in temperature between the samples and background due to the latent–heat absorption of NCPCMs during phase–transition. The change in colours from blue to red are showing the range of temperature from lower to higher because of constant heating. The thermographic images reflect the real time uniform surface temperature distribution of NCPCMs and uniform melting of each sample can be observed during heating. The quick flow away and melting of NCPCMs were observed as the loading of $TiO_2$ increase from 0.5 to 2.0 wt.%, as shown in Fig. 3.16c. While solid–liquid phase transformation, the NCPCMs experienced the uniform natural convection heat transfer enhancement. Fig. 3.16d shows the complete melting NCPCM3 and NCPCM4 occurs at 20 min whereas the temperature variations, reflected from colours, show that NCPCM4 has the higher temperature compared to NCPCM3. The reason behind is that NCPCM4 has the higher concentration of $TiO_2$ which increases the heat transfer rate results in reduces the melting time of NCPCM4. In addition, thermographic images

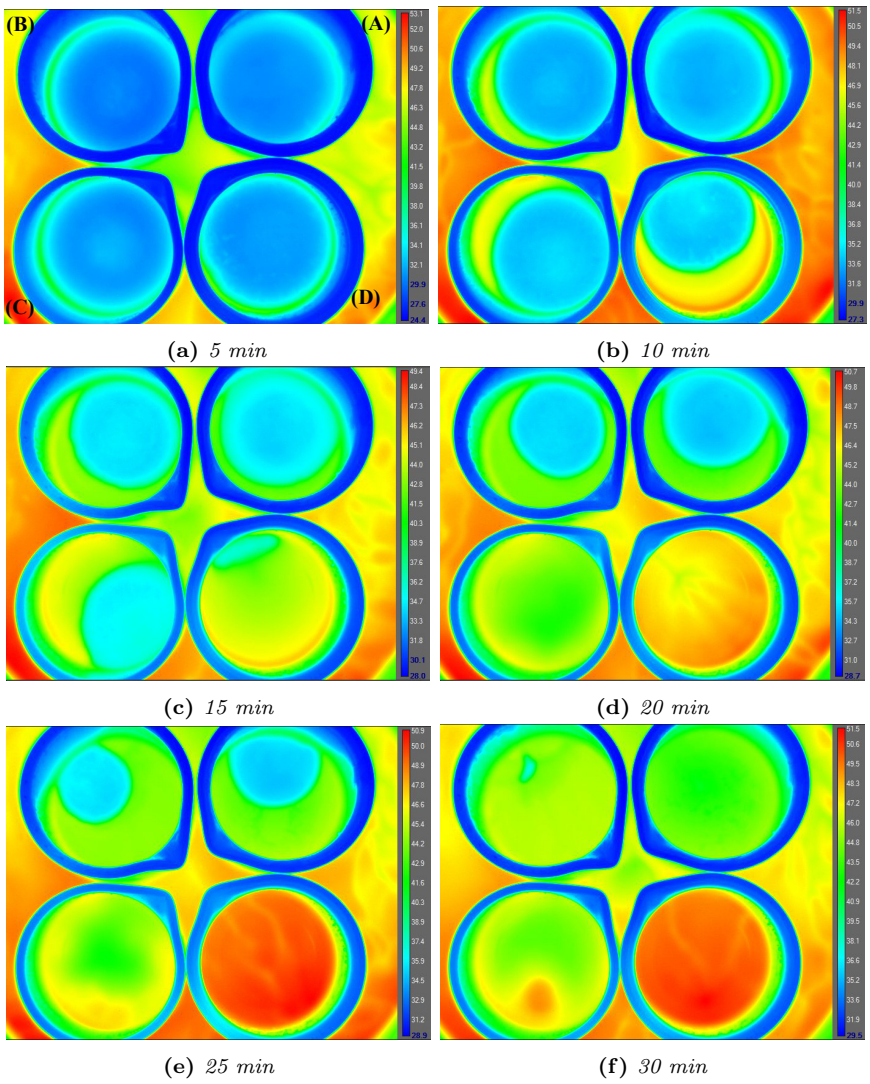


**(a)** *5 min* **(b)** *10 min*

**(c)** *15 min* **(d)** *20 min*

**(e)** *25 min* **(f)** *30 min*

**Figure 3.16:** *Infrared thermography images of the melting process of NCPCM1-(A), NCPCM2-(B), NCPCM3-(C) and NCPCM4-(D): at different time steps with temperature variation in °C.*

show the uniform melting process which is due the homogeneous dispersion of $TiO_2$ NPs in RT–35HC, resulting in improve the heat absorption/dissipation rate for TM and TES applications.

## 3.5 Concluding Remarks

The current experimental study investigated the chemical, physical and thermal properties of $TiO_2$ dispersed nanocomposite phase change materials (NCPCMs) of varying loading into the RT–35HC. The chemical, physical and thermal properties of NCPCMs were determined by various material characteristic

techniques such as ESEM, FT–IR, TGA, DSC and TCA to explore the best NCPCM for efficient TM and TES applications. The key findings are summarized as follows:

- The ESEM and XRD results revealed that uniform dispersion of $TiO_2$ nanoparticles into RT–35HC. The presence of $TiO_2$ nanoparticles in pure RT–35HC was observed through surface morphological and crystallography analysis.

- The FT–IR spectrum revealed that there is no chemical interaction of $TiO_2$ nanoparticles with RT–35HC and there is only physical interaction of $TiO_2$ with RT–35HC.

- The TGA and DTG results show that all NCPCMs have good thermal and chemical stability. With the addition of $TiO_2$ improved the thermal and chemical stability of pure RT–35HC.

- The latent–heat of fusion was decreased with increasing the loading of $TiO_2$. The optimum values of latent–heat of 235.84 J/g at 1.0 wt.% of corresponding thermal conductivity of 0.284 W/m.K. In addition maximum deviation in latent heat and peak melting temperature were observed of 11.0% and 0.11%, respectively, at 2.0 wt.% of $TiO_2$.

- The maximum thermal conductivities were obtained at phase–transition temperature of 0.444, 0.461, 0.471 and 0.480 W/m.K for NCPCM1–4, respectively. However, higher thermal conductivity of 0.341 W/m.K was obtained in solid–phase of corresponding thermal conductivity enhancement percentage of 59.5% at 2.0 wt.% of $TiO_2$ compared to the pure RT–35HC.

- The addition of the $TiO_2$ nanoparticles increases the specific heat capacity of the pure PCM for both solid and liquid phases. Furthermore, specific heat capacity of NCPCMs increases with the increase of the $TiO_2$ mass concentrations. The higher values of specific heat capacities were

obtained as 2.84 and 2.56 J/g.°C at 25 °C and 50 °C, respectively, at 2.0 wt.% of $TiO_2$ compared to the pure RT–35HC.

- The uniform melting and temperature distribution were observed from IR thermographic images which revealed that with the increase of $TiO_2$ mass concentrations heat transfer rate increases.

It can be concluded from the presented results that newly developed $TiO_2$/RT–35HC base nanocomposite PCMs presented acceptable improvement in TES properties and efficient phase–change heat transfer characteristics. Thus, these nanocomposite PCMs have significant potential in passive TM systems for electronic devices, Li–ion batteries, photovoltaic modules and direct utilization in solar thermal energy storage.

# Chapter 4

# Development of metallic–oxide mono and hybrid nanocomposite phase change materials[1]

## Abstract

This experimental study covers the chemical, physical, thermal characterization and application of novel nanocomposite phase change materials (NCPCMs) dispersed by $TiO_2$, $Al_2O_3$, and CuO nanoparticles for thermal management systems. A commercial–grade of paraffin, namely RT–35HC, was considered as a phase change material (PCM). The mono and hybrid NCPCMs were synthesized at a constant weight concentration of 1.0 wt.%. In the first phase, various characterization techniques were used to explore the thermophysical properties and chemical interaction of mono and hybrid NCPCMs. In the second phase, the thermal cooling performance was investigated by filling the prepared NCPCMs in a heat sink at various input power levels. The results showed the uniform dispersion of $TiO_2$, $Al_2O_3$, and CuO nanoparticles onto

[1]This Chapter is published as:
**Arshad, A.**, Jabbal, M., & Yan, Y. (2020). Thermophysical characteristics and application of metallic-oxide based mono and hybrid nanocomposite phase change materials for thermal management systems. *Applied Thermal Engineering*, 181, 115999.https://doi.org/10.1016/j.applthermaleng.2020.115999

the surface of both mono and hybrid NCPCMs without altering the chemical structure of RT–35HC. The optimum latent–heat of fusion and highest thermal conductivity of 228.46 J/g and 0.328 W/m.K were obtained, respectively, of $Al_2O_3$+CuO dispersed hybrid NCPCM compared to pure RT–35HC. In comparison of RT–35HC, the increasing trend in specific heat capacity was observed of NCPCMs and 36.47% enhancement was obtained for hybrid NCPCM in solid–phase. The reduction in heat sink base temperature was achieved of 3.67%, 6.13%, 13.95% and 8.23% for NCPCM$_{TiO_2}$, NCPCM$_{Al_2O_3}$, NCPCM$_{CuO}$ and NCPCM$_{Al_2O_3+CuO}$, respectively, compared to RT–35HC. Further, no phase segregation, less subcooling, smaller phase transition temperature, higher chemical and thermal stability were observed with hybrid NCPCMs which can be used potentially for thermal management of electronic devices, Li–ion batteries and photovoltaic (PV) modules systems.

**Keywords:** Phase change material, $TiO_2$, $Al_2O_3$, CuO, Nanocomposite phase change materials, Thermal management

## 4.1 Introduction

Energy, Economy and Environment (3E) have the most powerful and urgency importance in current global issues and challenges (Bosselman et al., 2006). Carbon dioxide ($CO_2$) emissions, both natural and human sources, has been significantly increasing and contributing a major role in greenhouse and global climate change (Quadrelli and Peterson, 2007). Around 87% of $CO_2$ emissions are due to the human sources come from the utilization of fossil fuels coal, natural gas and oil (Jotzo et al., 2012). Nonetheless, the fossil fuels are still the dominant energy sources for power generation with their share increasing 66% in 2005 to 77% in 2050. Therefore, $CO_2$ emissions would increase by 61% over 2011 levels by 2050 (Akashi et al., 2013). To minimize the $CO_2$ emissions, there is the critical need of alternative and sustainable energy resources to reduce the emerging demand of fossil fuels. With the development

of nanotechnology, the heat and mass transfer in nanoconned systems such as nanofluid (Shi et al., 2020a) and nano-composites brings novel insight for energy conversion and storage (Shi et al., 2020b) which make a contribution in thermal management applications. The thermal energy storage (TES) systems based on heat storage materials have been used extensively for energy conversion, storage and transportation in thermal management applications of electronic devices, photovoltaic (PV) modules, Li–ion batteries systems etc. (Arshad et al., 2017; Gulfam et al., 2019). Phase change materials (PCMs) as heat storage materials meet the series of requirements with higher energy storage density with suitable phase transition temperature range, good stability and low supercooling. For effective heat storage and heat transfer using PCMs, the latent-heat and thermal conductivity are the key thermal properties which improve the thermal management efficiency. Organic PCMs exhibit the best heat storage properties but they have low thermal conductivity which reduces the overall thermal response factor, heat transfer rate and efficiency. Thus, a PCM with higher latent–heat and thermal conductivity with stable chemical structure is the most suitable. To overcome this issue, researchers have introduced several heat transfer enhancement techniques including extruded metal–fins (Ali et al., 2018c), metal–foam and porous materials (Al-Jethelah et al., 2019), nanomaterials (Tarelho et al., 2018) encapsulated micro/nano–capsules (Shchukina et al., 2018).

Nanomaterials as a supportive materials into the PCMs have taken keen attention in current era due their higher thermal properties and enhance the chemical and thermal stability. For instance, Babapoor et al. (Babapoor and Karimi, 2015; Babapoor et al., 2016) synthesised the composite PCMs using $SiO_2$, $Al_2O_3$, $Fe_2O_3$, ZnO nanoparticles and measured the thermophysical properties. They achieved the highest thermal conductivity with 8 wt.% of $Fe_2O_3$ nanoparticles. However, the authors suggested that $Al_2O_3$ nanoparticles were preferable for thermal management applications. Nourani and his co-authors (Nourani et al., 2016a,b) prepared NCPCMs using $Al_2O_3$ nanopar-

ticles of weight concentrations of 0.5, 5, 7.5, and 10 wt.% and SSL used as a surfactant to enhance the stability of $Al_2O_3$ nanoparticles in paraffin wax. The effective thermal conductivity enhancement ratios were found of 31% and 13% in solid and liquid phases, respectively, at 10.0 wt.%. Chieruzzi et al. (Chieruzzi et al., 2015) synthesised the mono and hybrid composite PCMs of potassium nitrate ($KNO_3$), used as a PCM, by adding $SiO_2$, $Al_2O_3$ and hybrid of $SiO_2/Al_2O_3$ having 1.0 wt.%. The best results were obtained with $SiO_2$ nanoparticles with a decrease of $2-3°C$ in onset temperatures and 9.5% increase in specific heat. Sharma et al. (Sharma et al., 2016) used the $TiO_2$ nanoparticles of weight concentrations of 0.5, 1.0, 3.0, and 5.0 wt.% and palmitic acid as a PCM to prepare the NCPCMs. The highest thermal conductivity and lowest heat of fusion were obtained of 0.35 W/m.K and 180.03 kJ/kg, respectively, at 5.0 wt.% of $TiO_2$. Yang et al. (Yang et al., 2016a) prepared the paraffin and palygorskite mixed composite PCM and revealed the melting temperature and latent heat of 54–56°C and 132.18 J/g, respectively. Li et al. (Liu et al., 2017) synthesised the NCPCMs using calcium chloride hexahydrate ($CaCl_26H_2O$) as a PCM with $\gamma-Al_2O_3$ and measured the phase–change thermal properties. The maximum thermal conductivity was obtained of 1.373 W/m.K at 2.0 wt.% of $\gamma-Al_2O_3$ nanoparticles. Sami and Etesami (Sami and Etesami, 2017) prepared the NCPCMs of using $TiO_2$ and paraffin with mass fractions of 0.5, 0.7, 1, 2, 3 and 4 wt.% with and without SSL used as a surfactant. Results explored the optimum concentration of 3 wt.% of $TiO_2$ nanoparticles with the 47.8% increase in thermal conductivity with SSL compared to the pure paraffin. Further, authors suggested that addition of SSL in NCPCMs showed the better dispersion and thermal stability compared with pure paraffin and $TiO_2$/paraffin composite. Bashar and Siddiqui (Bashar and Siddiqui, 2018) prepared the NCPCMs using various types of nanoparticles, Ag, CuO, $Al_2O_3$ and MWCNTs and added in paraffin wax. A higher heat transfer coefficient of 18% and 14% was obtained for CuO and Ag nanoparticles, respectively, compared with pure paraffin wax. Praveen and Suresh

(Praveen and Suresh, 2018) prepared the composite PCMs using solid–solid neopentyl glycol (NPG) and CuO nanoparticles for thermal management application. It was found that maximum thermal conductivity and phase change enthalpy of 0.61 W/m.K and 112.4 kJ/kg, respectively, were obtained at 3.0 wt.% of CuO. Recently, Li et al. (Li et al., 2019a) synthesized MgO dispersed in eutectic carbonate salt of $NaLiCO_3$ and studied the thermal properties of light and heavy weight MgO nanoparticles. The results found that light weight MgO nanoparticles of particle size 3–5 $\mu$m had the maximum thermal conductivity of $\sim$ 5.5 W/m.K compared to heavy weight MgO nanoparticles of similar size.

The literature reveals that most of the studies focused on the development of NCPCMs used for the high temperature TES applications. The current study focuses on synthesising of new NCPCMs which will be the most suitable for thermal management of electronic devices, PV modules and Li–ion batteries, working under the safe and reliable operating temperature range of 30–40 °C (Sahoo et al., 2016a). In addition, the literature indicates that a very little work has been performed on mono and hybrid NCPCMs. Therefore, the present study aims to improve on the thermophysical properties of a commercially available PCM to enhance the thermal performance. The microstructure, chemical and thermal properties are investigated of $TiO_2$, $Al_2O_3$, and CuO nanoparticles dispersed mono and hybrid NCPCMs. Further, various characterization techniques were adopted to analysis the surface morphology, chemical and physical interaction, thermal properties including phase–change temperature, melting/solidifying latent–heat enthalpies, specific heat capacity, thermal conductivity, thermal stability and reliability. The newly developed NCPCMs were then poured in a heat sink to investigated the transient temperature thermal response to explore the thermal cooling performance.

## 4.2 Experimental procedure and characterizations

### 4.2.1 Materials

In present study, the RT–35HC (a commercial grade of paraffin) was used as a PCM with phase–transition temperature of $34 - 36°C$, purchased from Rubitherm GmbH, Germany. Three different metallic–oxide nanoparticles such as copper oxide (CuO) (particle size $< 50$ nm, surface area: 29 $m^2/g$), aluminium oxide ($Al_2O_3$) (particle size 13 nm, surface area: 85–115 $m^2/g$), nano Titanium (IV) dioxide ($TiO_2$), anatase powder (particle size $< 25$ nm, surface area: 45–55 $m^2/g$, density: 3.9 g/mL at 25 °C) were purchased from Sigma–Aldrich, UK. In all samples Sodium dodecylbenzene sulfonate (SDBS) was used, obtained from Sigma–Aldrich, UK. Table 4.1 is summarized the thermophysical properties of RT–35HC. All materials were used as they received without further chemical treatment.

Table 4.1: *Thermophysical properties of RT–35HC.*

| Melting temperature (°C) | Thermal conductivity (W/m.K) | Latent–heat of fusion (J/kg.K) | Specific heat (J/kg.K) | Density ($kg/m^3$) |
|---|---|---|---|---|
| 34–36 | 0.2 | 240,000 | 2000 | 880 (solid)<br>770 (liquid) |

### 4.2.2 Preparation of nanocomposite PCMs

The schematic diagram of preparation of NCPCMs is shown in Figure 4.1. A well–precise two–step preparation method was carried out to synthesize the mono and hybrid NCPCMs, which has been used extensively in preparation of nanofluids (Arshad et al., 2019b). The RT–35HC was used a base PCM and $TiO_2$, $Al_2O_3$ and CuO nanoparticles were used as an additives. The purpose of adding the nanoparticles is to enhance the thermal properties. In first part of NCPCMs preparation, the RT–35HC was melted at a temper-

ature of 70 °C constantly through a hot–water bath. The SDBS was then added, as a surfactant, into the RT–35HC at fully melted stage with a ratio of 1:4 wt.% of nanoparticles to enhance the dispersion stability. The nucleating agent mixture of RT–35HC and SDBS was stirred vigorously at 450 rpm and kept for 30 min at 70 °C. Thereafter, constant amount of 1.0 wt.% of $TiO_2$, $Al_2O_3$, CuO and $Al_2O_3$+CuO were added separately into RT–35HC and stirring was continued for further 3 hrs to achieve a uniform and stable dispersion of nanoparticles. The mass ratio for hybrid NCPCMs was kept 75%/25% of $CuO/Al_2O_3$ to keep the total mass percentage constant. In second part of the NCPCMs preparation, the ultrasonication process was carried out for 60 min at ultrasonic frequency of 40 kHz (Asadi et al., 2019). The ultrasonication process improved the stable dispersion of nanoparticles more homogeneously and minimized the sedimentation and aggregation, as shown in Fig. 4.2. The four different samples of the mono and hybrid NCPCMs were prepared and labelled as $NCPCM_{TiO_2}$, $NCPCM_{Al_2O_3}$, $NCPCM_{CuO}$ and $NCPCM_{Al_2O_3+CuO}$. Lastly, samples of NCPCMs were cooled to the ambient temperature.

## 4.3 Characterizations techniques

### 4.3.1 Microstructural and chemical interaction analysis

An environmental scanning electron microscopy (ESEM, FEI Quanta–650) attached with the energy–dispersive X–ray spectroscopy (EDX) system was employed to examine the surface morphology, microstructure and to visualize the surface elemental distribution of nanoparticles in NCPCMs. Fourier–transform infrared spectroscope (FT–IR, Bruker Tensor–27) was used to record the absorption spectra between the wave range of $400 - 4000$ $cm^{-1}$ at room temperature with the spectral resolution of 4 $cm^{-1}$ and wavenumber accuracy of 0.01 $cm^{-1}$ to study the chemical composition and functional groups of NCPCMs. X–ray diffractometer (XRD, Bruker D8 Advance with Da Vinci) was used to

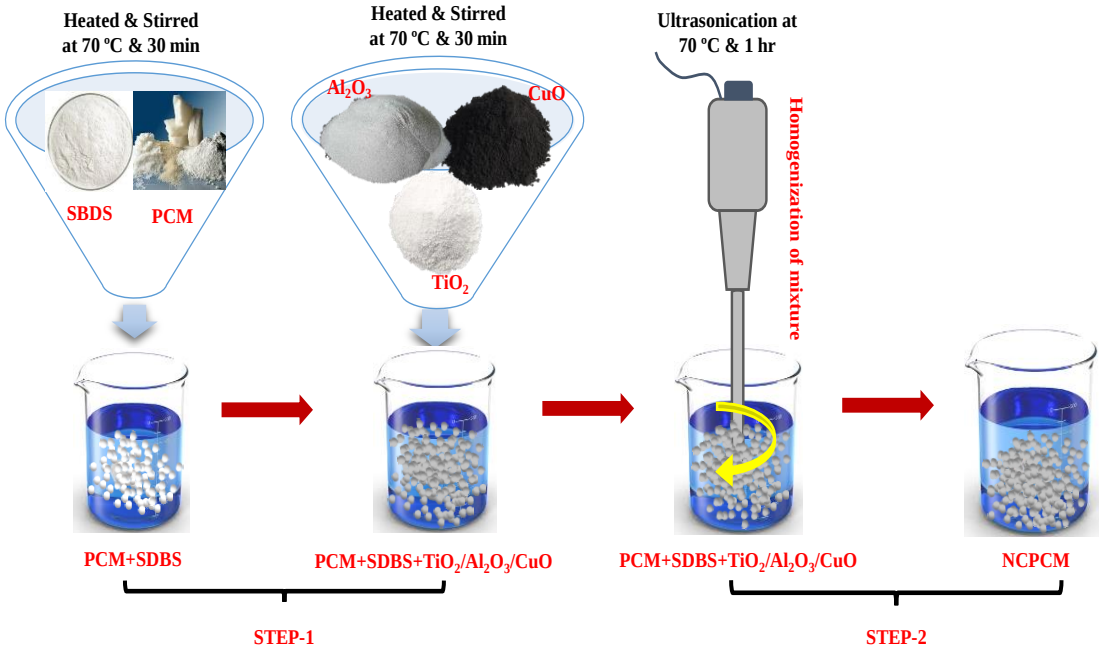


**Figure 4.1:** *Schematic diagram of synthesizing of $TiO_2$, $Al_2O_3$, CuO and RT–35HC based mono and hybrid NCPCMs.*

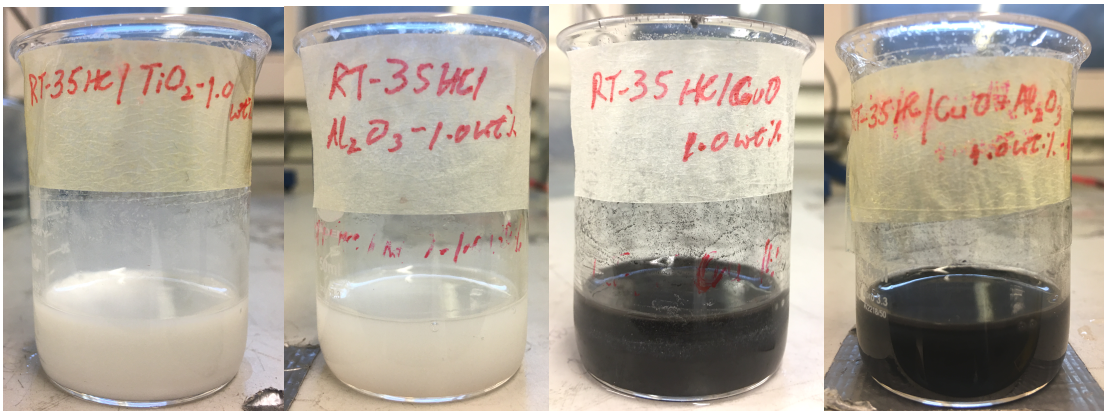


**Figure 4.2:** *NCPCMs after sonication : (a) $NCPCM_{TiO_2}$, (b) $NCPCM_{Al_2O_3}$, (c) $NCPCM_{CuO}$, (d) $NCPCM_{Al_2O_3+CuO}$.*

measure the XRD pattern of NCPCMs with the $2\theta$ angle range of 5–60° with a monochromatic Cu–K$\alpha$ radiation ($\lambda = 1.5406$ Å).

### 4.3.2 Thermophysical properties analysis

The TGA/DSC (SDT–Q600 TA instrument Inc., UK) (error ±0.1 $\mu$g) was used to perform the thermogravimetric analysis (TGA) and derivative ther-

mogravimetry (DTG) analysis of NCPCMs to measure the rate of weight loss and decomposition to address the thermal stability of NCPCMs. The aluminium pan was used filled with sample mass of 4–7 mg and heating rate was kept at 10°C/min for a range of 20–400 °C under purified nitrogen purging of 100 mL/min flow rate. Differential scanning calorimeter (DSC–2500, TA instrument Inc., UK) was used to measure the phase transition thermal properties of NCPCMs. The heating and cooling rate was kept of 1 °C/min for a range of 10–50 °C. The specific heat capacity was measured of all samples using sapphire method (ASTM–E1269) at a heating rate of 3 °C/min between temperature 10 °C and 50 °C. The calorimeter has the accuracy of ±0.04% with temperature precision of ±0.005 °C. The TCi$^{TM}$ thermal conductivity analyser (TCA) (C–THERM Technologies Ltd. Canada) was used to measure the thermal conductivity of RT–35HC and NCPCMs adopting a modified transient plane source (MTPS) method (ASTM–D7984). The thermal conductivity was measured as function of temperature from 20 °C and 55 °C. For each sample, at a constant temperature, five measurements were taken and averaged was reported and maximum uncertainty in measurement was obtained of ±1.0%. An IR thermographic camera (FLIR–SC2600–EA2) was used to perform the infrared thermography (IRT) tests to obtain the thermal images of samples. The samples were filled immersed in a water pot and constant temperature was provided through the hot–plate.

### 4.3.3 Thermal cooling performance analysis

The experimental setup to perform the thermal cooling performance analysis was carried out using a passive cooling thermal management system, as shown in Fig. 4.3. The schematic diagram shows that thermal management system consists mainly the heat sink, data acquisition system, DC power supply and the laptop. The heat sink assembly consists of plate type silicon rubber heater (OMEGALUX), K–type thermocouples (OMEGA), rubber mat for in-

sulation, perspex sheet to visualize the physical melt fractions of RT–35HC and NCPCMs. In the experimental set up, the heat sink assembly was assumed perfectly insulated using a rubber pad, having very low thermal conductivity. The rubber pad was placed at the bottom and around the heat sink with a 50 mm extended width/thickness of the actual dimensions of heat sink. A constant temperature was measured at the outside of the insulation during the experiment which was the same with environment room temperature. The top surface of the heat sink was covered with acrylic sheet having a thickness of 5 mm by keeping silicon gasket which prevent the PCM leakage, to visualize the physical melt front of molten PCM. A copper made heat sink was manufactured using computer numerical control (CNC) machine. Pure RT–35HC and NCPCMs were poured inside the heat sink. To ensure the proper stability, reduce the aggregation and uniform distribution of nanoparticles, each sample of NCPCMs was sonicated before pouring into the heat sink. A DC power supply made of Keysight Technologies (N6700C, 0.5 A/100 V) was used to provide different power levels of 3–5 W at ambient temperature, to mimic heat generation. A PC based digital data acquisition system (Agilent 34972A, USA) was used to record the temperature variation through thermocouples inserted at different points on the heat sink. The data acquisition system was connected to the laptop and Agilent Technologies, Inc. (Taft Ave. Loveland, USA) software is used to record the temperature at interval of 5 s during the experimentation. The uncertainty of the measured quantities is associated with the least count of the corresponding measurement devices. The uncertainty in temperature measurement according to according to ASTM standard (Burns et al., 1993) in a temperature range of 0–100 °C with maximum variation of ±0.1 °C. The uncertainty in data logger is ±0.1 °C. The uncertainties in voltage and current are measured of ±0.01 V and ±0.001 A, respectively. The uncertainty in heat input are calculated using Kline and McClintock (Kline, 1953) technique and minimum and maximum uncertainties are obtained of 1.68% and 1.91%, respectively.

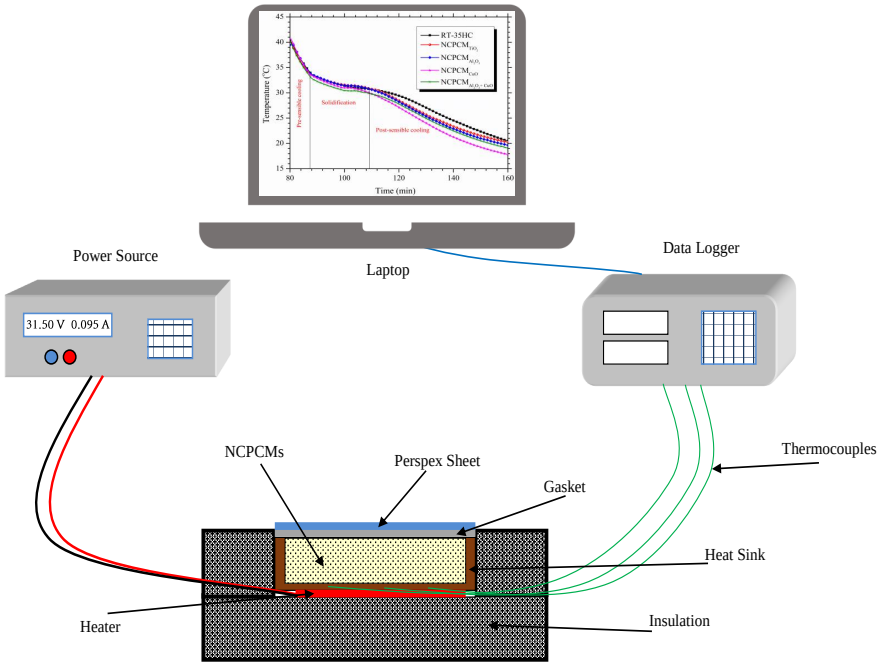


**Figure 4.3:** *Schematic diagram of experimental setup.*

## 4.4 Results and discussions

### 4.4.1 ESEM and EDX analysis

The microstructure and surface morphology of mono and hybrid NCPCMs analysed by the ESEM are presented in Fig. 4.4. The surface microstructural features of NCPCM$_{TiO_2}$, NCPCM$_{Al_2O_3}$, NCPCM$_{CuO}$ and NCPCM$_{Al_2O_3+CuO}$ are presented in Figs. 4.4a, 4.4b, 4.4c, 4.4d, 4.4e, 4.4f, 4.4g and 4.4h of LFD and BSED images, respectively. It can be seen from Fig. 4.4 that the dispersion of nanoparticles in RT–35HC is uniform representing in white regions which is due to the repulsive bonding of the dispersing agent. Since the loading of nanoparticles is constant and very less despite the fact, all nanoparticles are well dispersed and embedded enough to show their presence in NCPCMs. Besides, the homogeneous and heterogeneous percolation of nanoparticles in RT–35HC can be observed from LFD and BSED images. The grey and white dots represent the RT–35HC and nanoparticles ($TiO_2$, $Al_2O_3$ and CuO) which are agglomerated on the nanoscale but dispersed on the microscale. From Fig.

4.4, the presence of zones characterized by the heterogeneous aggregates of nanoparticles and RT–35HC can be observed clearly. Similar observations of nanoparticles percolation in NCPCMs have been reported in Refs. (Babapoor et al., 2016; Chieruzzi et al., 2015). While solid–liquid phase transition of NCPCMs, the solvation, "Brownian motion" and "electrostatic repulsion" cause the nanoparticles to separate individually. However, this collision becomes more prominent between the nanoparticles by increasing the loading of the nanoparticles and Van der Waals force becomes stronger at a short range resulting in the formation of aggregates and sedimentation of nanoparticles at high concentration. Therefore, the uniform dispersion and percolation of nanoparticles depend on the size of the nanoparticles. The EDX maps of NCPCM$_{TiO_2}$ and NCPCM$_{Al_2O_3+CuO}$ are shown in Figs. 4.5 and 4.6, respectively. Figs. 4.5a, 4.5b and 4.5c show the distribution of carbon (C), oxygen (O) and titanium (Ti) elements, respectively, present in NCPCM$_{TiO_2}$. The presence of all elements C, Ti and O in different colours can be seen in single image of $TiO_2$ dispersed NCPCM$_{TiO_2}$ in Fig. 4.5d. The EDX mapping of carbon (C), oxygen (O), aluminium (Al), and copper (Cu) elements of hybrid NCPCM$_{Al_2O_3+CuO}$ can be seen in Figs. 4.6a, 4.6b, 4.6c and 4.6d, respectively. Fig. 4.6e shows the presence of all C, Al, Cu and O elements in various colours in NCPCM$_{Al_2O_3+CuO}$. The ESEM and EDX images show the smaller zones of agglomeration of nanoparticles. The similar observations have been reported in previous studies (Chieruzzi et al., 2015; Sharma et al., 2016). Consequently, it is recommended that for more better and uniform dispersion of the nanoparticles in PCM, the smaller size, low density and higher surface area nanoparticles are preferable (Saterlie et al., 2011; Evans et al., 2008).

### 4.4.2 FT-IR analysis

The chemical composition and structural interaction of $TiO_2$, $Al_2O_3$ and CuO dispersed NCPCMs were characterized by FT–IR spectroscopy. Fig. 4.7

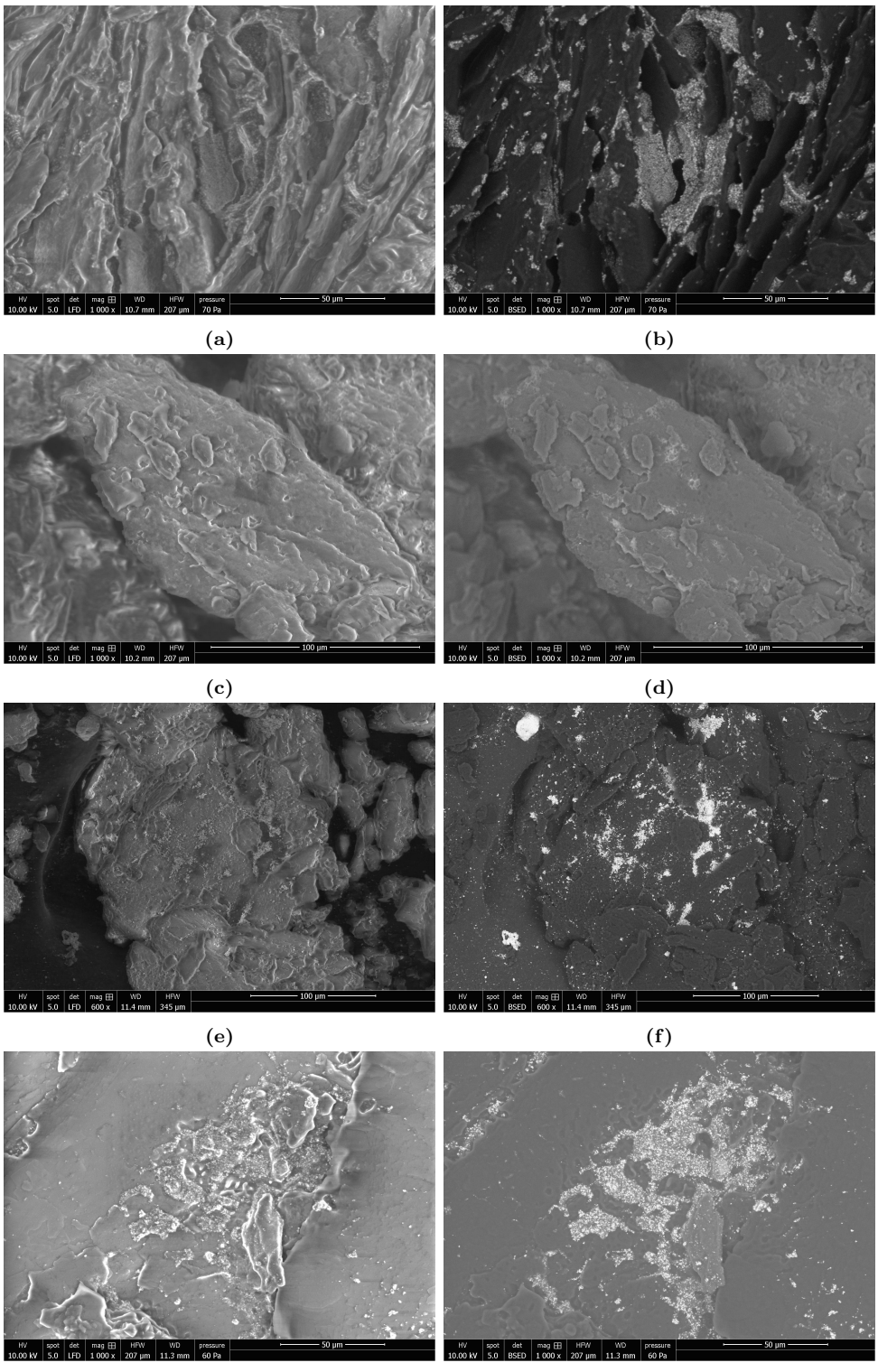


**Figure 4.4:** *ESEM images of $NCPCM_{TiO_2}$ (a) LFD and (b) BSED, $NCPCM_{Al_2O_3}$ (c) LFD and (d) BSED, $NCPCM_{CuO}$ (e) LFD and (f) BSED, and $NCPCM_{Al_2O_3+CuO}$ (g) LFD and (h) BSED.*

presents the FT–IR spectrum of nanoparticles, RT–35HC and NCPCMs and absorption peaks were observed. For instance, the three absorption peaks at 2955 $cm^{-1}$, 2913 $cm^{-1}$, 2849 $cm^{-1}$ represent the medium C–H symmetrical

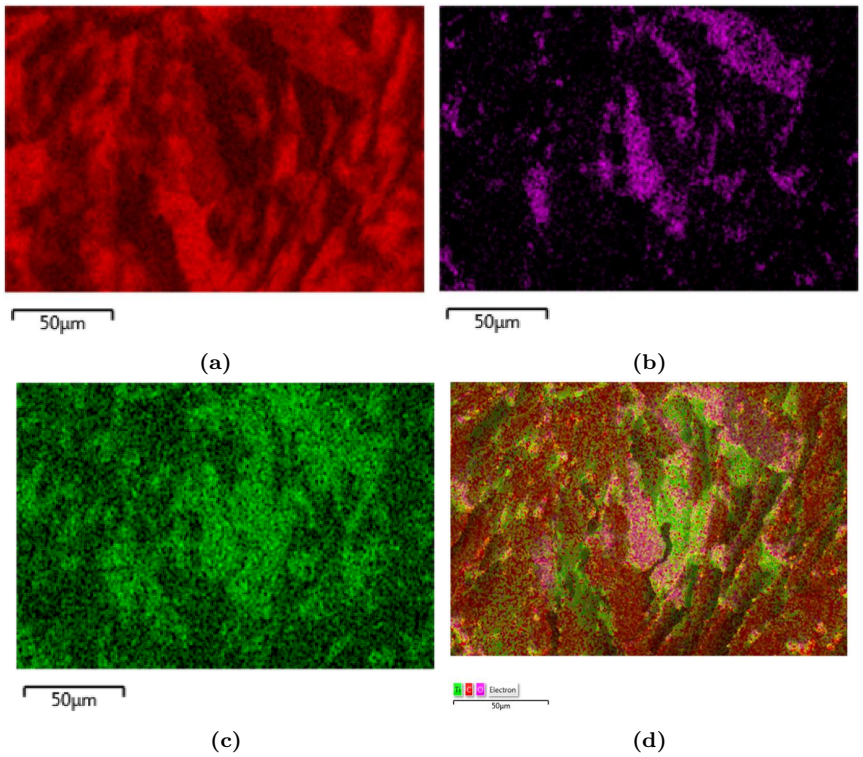


**Figure 4.5:** *EDX mapping of $NCPCM_{TiO_2}$ (a) carbon-(red), (b)-oxygen-(purple), (c) Titanium-(green), (d)-EDX map of oxygen, carbon, and titanium elements present in $NCPCM_{TiO_2}$.*

and anti–symmetrical stretching vibration of methyl (–$CH_3$) and methylene (–$CH_2$–) group. The peak at 1472 $cm^{-1}$ identifies the medium C–H scissoring of –$CH_2$– and deformation of antisymmetric stretching vibration –$CH_3$ group in RT–35HC. The FT–IR spectrum also shows a series of absorption peaks at 1371, 1125, and 891 $cm^{-1}$ which are due to the C–H bending and scissoring vibrations. The peak at 715 $cm^{-1}$ represents to the weak rocking vibration of C–H in long–chain methyl group. The FT–IR spectrum of $TiO_2$ shows the two peaks around 510 and 526 $cm^{-1}$ which are attributed to the Ti–O stretching vibrations in $TiO_2$. In case of CuO, there are two stretching bands at 880 $cm^{-1}$ and 1432 $cm^{-1}$ which represent the characteristics bands of Cu–OH functional group (Bakhtiari and Darezereshki, 2011; Faisal et al., 2011). Furthermore, there is a small peak can be observed at 729 $cm^{-1}$ which indicates the standard adsorption spectra pattern of the amorphous structure or disordered defects of $\gamma-Al_2O_3$. It can be revealed that both mono and hybrid NCPCMs presented the consistent peaks with that of the pure RT–

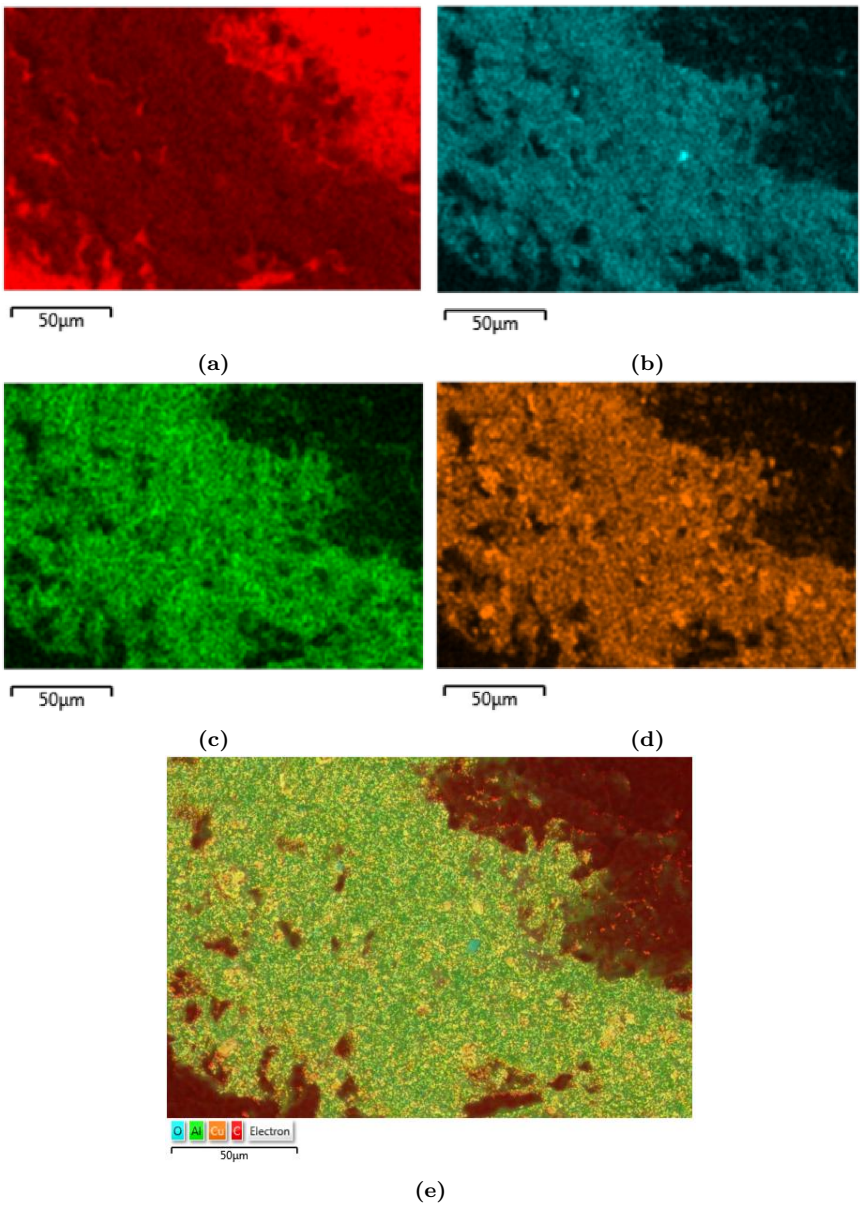


**Figure 4.6:** *EDX mapping of $NCPCM_{Al_2O_3+CuO}$ (a) carbon-(red), (b)-oxygen-(cyan), (c) aluminum-(green), (d) Copper-(Brown) and (e) EDX map of carbon, oxygen, aluminum and copper elements present in $NCPCM_{Al_2O_3+CuO}$.*

35HC which means that NCPCMs contained similar characteristics of pure RT–35HC without emergence of new peak or any peak shift. This means that there no considerable chemical interaction occurred between the $TiO_2$, $Al_2O_3$ and CuO and RT–35HC and there is only physical interaction which indicate that prepared mono and hybrid NCPCMs are chemical stable.

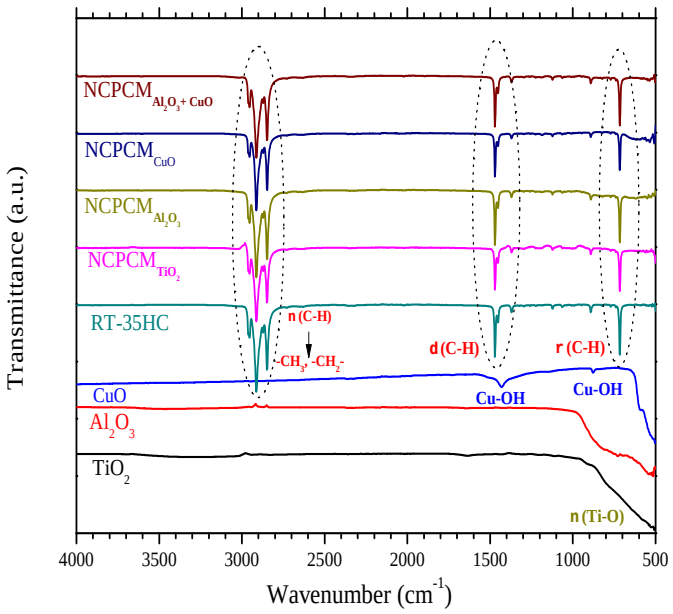


**Figure 4.7:** *FT–IR spectrum of $TiO_2$, $Al_2O_3$, CuO and RT–35HC based mono and hybrid NCPCMs.*

### 4.4.3 XRD analysis

The crystallography analysis of $TiO_2$, $Al_2O_3$, CuO, RT–35HC and NCPCMs were identified through XRD patterns to study the crystalline phase and dimensions of unit cell, as shown in Fig. 4.8. The diffraction peaks of $2\theta$ at 25.3° (101), 37.79° (004), 48.03° (200), 53.88° (105) and 55.06° (211) confirm the anatase form of the $TiO_2$ (PDF No. 03-065-5714). The peaks of $Al_2O_3$ confirmed the presence of $\gamma-$phase of $Al_2O_3$ nanoparticles at $2\theta$ = 19.50° (013), 32.80° (022), 34.60° (117), 36.76° (122), 39.50° (026) and 45.64° (220) with PDF No. 00-046-1131. The diffraction peaks at $2\theta$ = 32.50° (110), 35.54° (111), 38.70° (111), 46.26° (112), 48.71° (202), 53.48° (020), and 58.26° (202) confirmed the CuO (PDF No. 01-073-6023). The sharp diffraction peaks of pure RT–35HC was observed at 6.85° (002), 10.48° (003), 13.91° (004), 17.44° (005), 19.32° (010), 19.80° (011), 20.83° (012), 22.43° (013), 23.32° (105), 24.78° (-101), 25.65° (110), 28.12° (008), 31.75° (009), 34.75° (-110), 35.27° (0010), 39.83° (0-22), 42.73° (0012), 44.60° (207), 52.68° (220), 53.41° (-2-14) and 57.55° (-205) which attributed to the crystal planes of *n-eicosane* ($C_{20}H_{42}$) with PDF No. 00-045-1543. As the loading of $TiO_2$, $Al_2O_3$ and CuO was kept

constant of 1.0 wt.%, a less amount of nanoparticles dispersed in pure RT–35HC. Consequently, less significant physical changes were observed in mono and hybrid NCPCMs. The XRD results revealed that the crystalline phase of RT–35HC did not alter, further both mono and hybrid NCPCMs samples contain the peaks of $TiO_2$, $Al_2O_3$ and CuO.

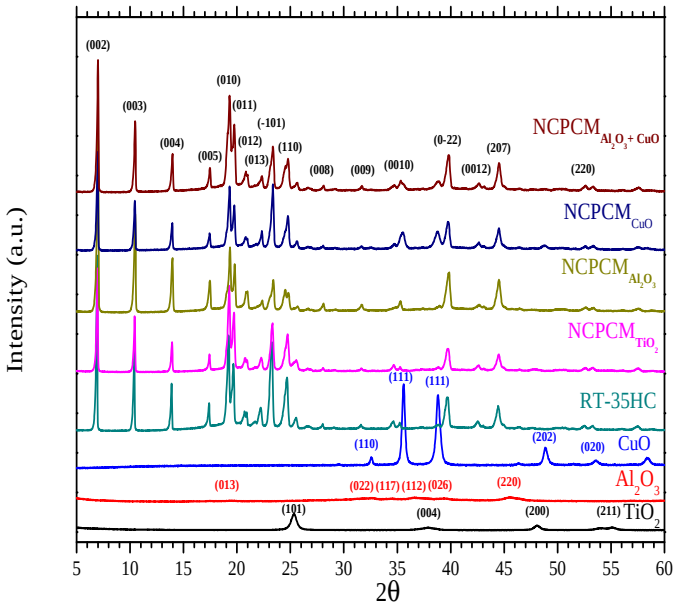


**Figure 4.8:** *XRD pattern of $TiO_2$, $Al_2O_3$, CuO and RT–35HC based mono and hybrid NCPCMs.*

### 4.4.4 TGA and DTG analysis

Fig. 4.9 presents the thermal gravimetric analysis of RT–35HC and hybrid NCPCMs to investigate their thermal stability. The thermal stability of NCPCMs is estimated on the onset temperature of PCM degradation and rate of weight loss at which is occurs. The TGA and DTG curves show the one-step and two-step thermal degradation process, respectively. The TGA curves of RT–35HC and NCPCMs, shown in Fig. 4.9a, represent that there is no distinguishable weight loss in any sample up to ∼120 °C. The rate of weight loss increases with the increase of temperature and reaches at the maximum degradation temperature with constant residual. For RT–35HC, the initial disintegration starts at 217.70 °C and maximum degradation temperature is 255.01 °C with

1.85% charred residue. While decomposition process, caused by the evaporation of pure RT–35HC, the hydrocarbon chains breakdown into monomers ($CH_3CH$:$CH+CH_4$). The onset decomposition and maximum degradation temperatures of all samples are summarized in Table 4.2 and in case of hybrid NCPCM$_{Al_2O_3+CuO}$, the charred reside was 3.62% at 262.78 °C and remained constant subsequently. In NCPCMs, the nanoparticles create the protective layer on the surface of RT–35HC which delays the vaporization of RT–35HC during the thermal degradation. The DTG curves of RT–35HC and NCPCMs are shown in Fig. 4.9b and revealed that addition of nanoparticles have improved the thermal stability, because no decompositions was observed in samples until ∼150 °C. Thus, hybrid NCPCM$_{Al_2O_3+CuO}$ can effectively be used for thermal management systems. The improvement in thermal stability can be explained by the following reasons: (i) *the onset decomposition temperature is related to the specific heat capacity of NCPCMs which can be raised by the specific heat capacity of nanoparticles* and (ii) *enhanced thermal conductivity of NCPCMs which can transfer heat faster and uniformly within the PCM* (Chen et al., 2017).

Table 4.2: *The temperature changes and residue of $TiO_2$, $Al_2O_3$, CuO and RT–35HC based mono and hybrid NCPCMs.*

| Sample | Onset decomposition temperature (°C) | Maximum-rate degradation temperature (°C) | Residue (%) |
|---|---|---|---|
| RT–35HC | 217.70 | 255.01 | 1.85 |
| NCPCM$_{TiO_2}$ | 226.77 | 263.55 | 1.96 |
| NCPCM$_{Al_2O_3}$ | 225.24 | 264.07 | 4.01 |
| NCPCM$_{CuO}$ | 228.37 | 264.57 | 6.04 |
| NCPCM$_{Al_2O_3+CuO}$ | 224.87 | 262.78 | 3.62 |

### 4.4.5 DSC analysis

DSC analysis presents the phase–transition temperatures and latent–heat of melting/solidification of NCPCMs, as shown in Fig. 4.10. Figs. 4.10a and 4.10b present the endothermic and exothermic curves, respectively, of RT–35HC and NCPCMs and measured values of phase–transition thermal properties are summarized in Table 4.3. It can be seen that the addition of nanoparticles have slightly changed the thermal properties of RT–35HC af-

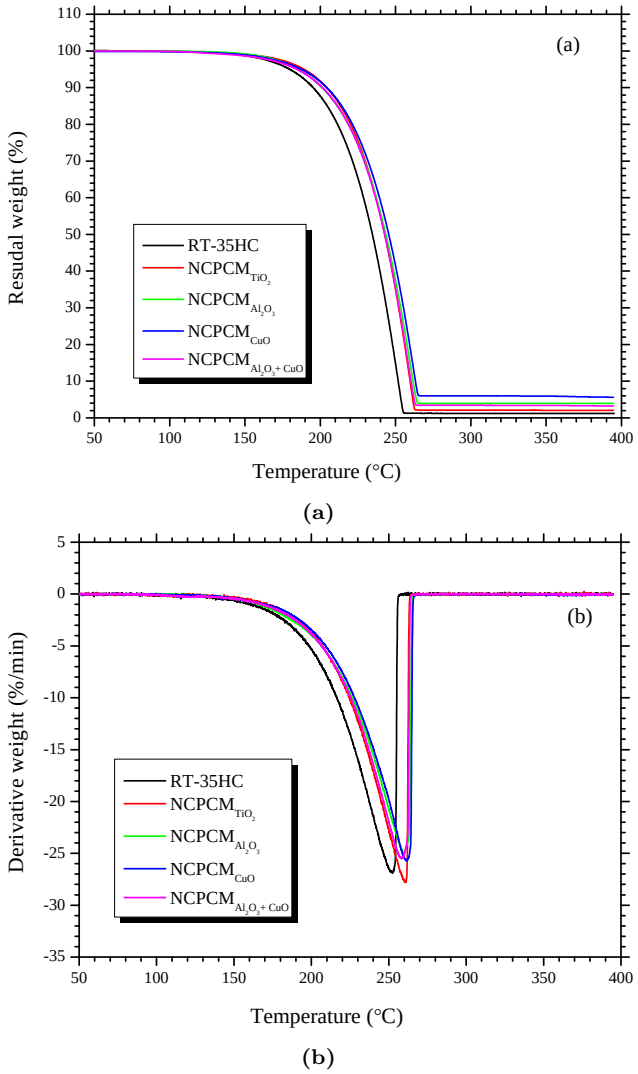


**Figure 4.9:** *(a)-TGA and (b)- DTG thermograms of $TiO_2$, $Al_2O_3$, CuO and RT–35HC based mono and hybrid NCPCMs.*

ter synthesizing. The latent-heat of melting/solidification of NCPMCs were decreased with the addition of nanoparticles, as expected. A single endothermic peak is observed of RT–35HC and NCPCMs during melting, indicating an isomorphous crystalline form of RT–35HC either in a pristine state or in the NCPCMs one. Contrary, a bimodal crystallization behaviour is predicted of RT–35HC and NCPCMs by presenting a main exothermic peak temperature along with an additional peak of higher temperature during solidification process. This two–phase transitions phenomenon is ascribed by the appearance of a metastable rotator phase prior to completing the complete crystallization as a results of the heterogeneous nucleation during the cooling process

(Yavari et al., 2011; Arshad et al., 2020b). The comparison of the melting ($\Delta H_m$) and solidification ($\Delta H_s$) enthalpies of RT–35HC and NCPCMs are presented in Fig. 4.10c. The $\Delta H_m$ and $\Delta H_s$ of RT–35HC are determined of 255.88 and 260.06 J/g, respectively. The reduction in $\Delta H_m$ of NCPCM$_{TiO_2}$, NCPCM$_{Al_2O_3}$, NCPCM$_{CuO}$ and NCPCM$_{Al_2O_3+CuO}$ has been obtained of 7.83%, 8.24%, 8.59% and 10.72% as compared to the pure RT–35HC. Similarly, the maximum reduction in $\Delta H_s$ latent–heats are 7.98%, 7.08%, 9.47%, and 11.81% for NCPCM$_{TiO_2}$, NCPCM$_{Al_2O_3}$, NCPCM$_{CuO}$ and NCPCM$_{Al_2O_3+CuO}$, respectively. The reduction in latent-heats are due to the addition of nanoparticles and mass fraction ($\omega$) of crystallized RT–35HC in NCPCMs is determined by the Eq. 4.1:

$$\omega = \frac{\Delta H_{NCPCM}}{\Delta H_{PCM}} \times 100 \tag{4.1}$$

where, $\Delta H_{NCPCM}$ and $\Delta H_{PCM}$ are the endothermic latent–heat of NCPCM and pure PCM, respectively. While synthesising of NCPCMs, the nanoparticles replace the RT–35HC molecules resulting in reduce the latent–heat capacity of the NCPCMs which lead to the absorption/release of more energy. The degree of super–cooling ($\Delta T$) of NCPCMs is presented in Fig. 4.10d. The peak melting temperature ($T_m$) and crystallization temperature ($T_c$) of RT–35HC are determined as 36.09 °C and 31.71 °C, respectively. The maximum deviations in $T_m$ are determined as −0.30%, −1.14%, −0.97% and −0.08% for NCPCM$_{TiO_2}$, NCPCM$_{Al_2O_3}$, NCPCM$_{CuO}$ and NCPCM$_{Al_2O_3+CuO}$, respectively, compared to the RT–35HC. The slight variations are observed in $T_c$ which are due the crystallization confinement of the nanoparticles surface layers within the NCPCMs. This interfacial surface layers cause to form the imperfect RT–35HC resulting in a slight variation in $T_m$. These two factors result in an increase in $\Delta T$. The reduction in $\Delta T$ for NCPCM$_{Al_2O_3+CuO}$ is obtained of 4.32 °C, which shows the better significance hybrid nanoparticles as nucleating agents compared to the mono nanoparticles in terms of its surface adsorption and effective homogeneous nucleation. Fig. 4.10e illustrates

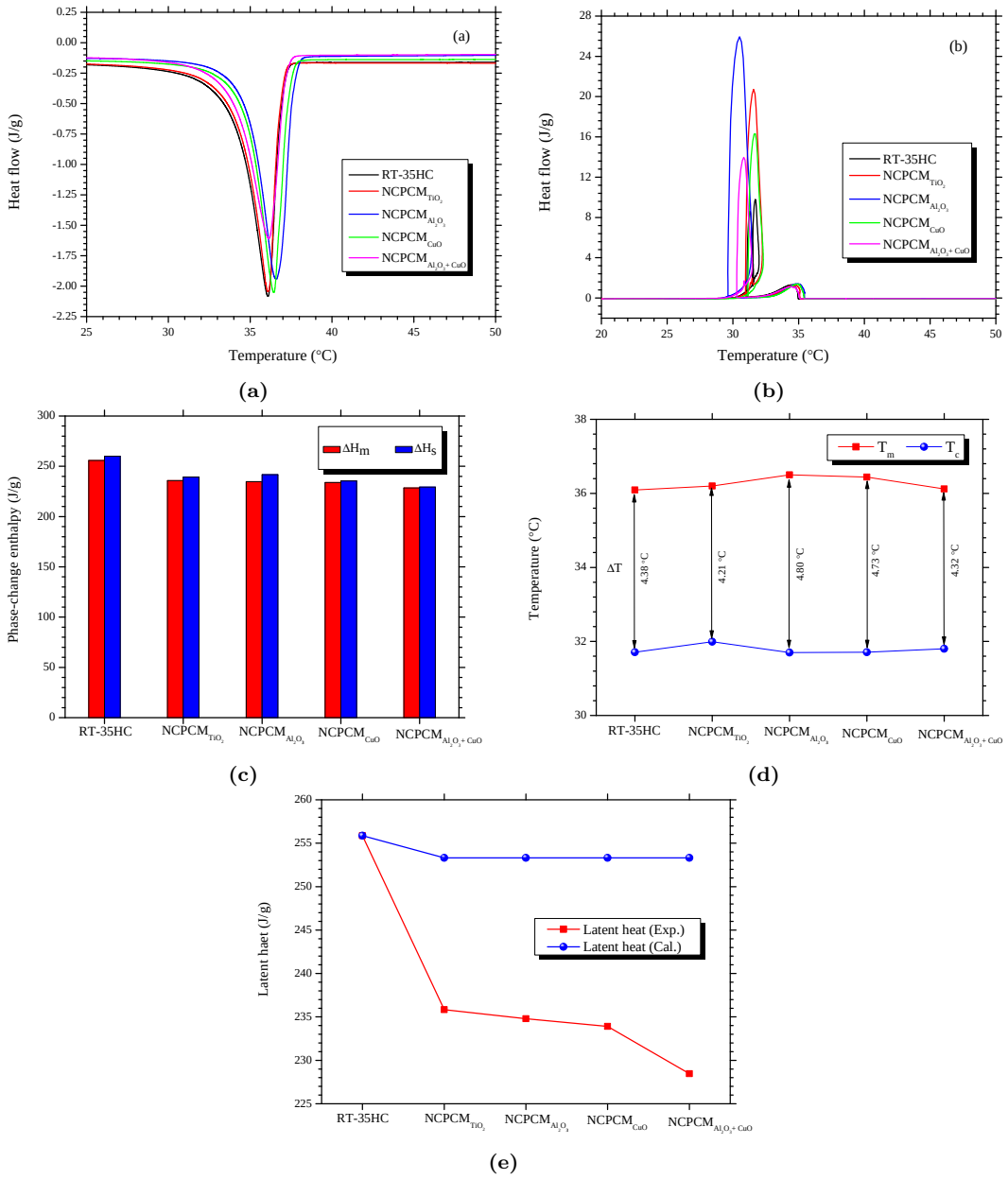


**Figure 4.10:** *The results of (a) Melting, (b) Solidification curves, (c) Phase–change enthalpies, (d) Degree of super–cooling and (e) Comparison of latent–heats of fusions of $TiO_2$, $Al_2O_3$, CuO and RT–35HC based mono and hybrid NCPCMs.*

the experimental and calculated latent–heat of fusion for NCPCMs, calculated using Eq. 4.2 (Tian et al., 2015):

$$\Delta L_{NCPCM} = \Delta L_{PCM} \cdot \omega = \Delta L_{PCM}(1 - \varphi) \tag{4.2}$$

where $\Delta L_{NCPCM}$ and $\Delta L_{PCM}$ calculated and experimental latent–heat of fusion of NCPCM and PCM, respectively, $\omega$ and $\varphi$ are the mass fraction of PCM and nanoparticles, respectively. It can be revealed that experimental

values of latent–heat of fusion of mono and hybrid NCPCMs are lower than the calculated values. The deviation in results is due to the thermophysical properties and type of the nanoparticles, since the loading of all nanoparticles in NCPCMs is constant. The relative error (RE) of experimental and calculated values has been obtained 6 $\sim$ 9% for all NCPCMs, given in Table 4.3. The similar trend of deviations in experimental and calculated values latent–heat of fusion have reported in Refs. (Tian et al., 2015; Arshad et al., 2020b). The results reveal that NCPCM$_{Al_2O_3+CuO}$ has the optimum value of latent–heat which is preferable for thermal management systems. The discrepancies in latent–heat values are because of the surface morphology, structure, size and rate of dispersion of the nanoparticles while synthesising the NCPCMs.

Table 4.3: *Phase–change thermal properties of $TiO_2$, $Al_2O_3$, CuO and RT–35HC based mono and hybrid NCPCMs*.*

| Sample | Heating | | | | | Cooling | | | | | $\omega$ (%) | $\Delta$ T |
|---|---|---|---|---|---|---|---|---|---|---|---|---|
| | $T_{oset,m}$ | $T_{peak,m}$ | $\Delta H_{m,exp}$ | $\Delta H_{m,cal}$ | RE (%) | $T_{oset,c}$ | $T_{peak,c}$ | $\Delta H_{c,exp}$ | $\Delta H_{c,cal}$ | RE (%) | | |
| RT–35HC | 34.06 | 36.09 | 255.88 | - | - | 31.47 | 31.71 | 260.79 | - | - | 100 | 4.38 |
| $NCPCM_{TiO_2}$ | 34.26 | 36.20 | 235.84 | 253.32 | 6.90 | 31.48 | 31.99 | 239.30 | 257.46 | 7.05 | 92.17 | 4.21 |
| $NCPCM_{Al_2O_3}$ | 34.76 | 36.50 | 234.79 | 253.32 | 7.32 | 29.61 | 31.70 | 241.65 | 257.46 | 6.14 | 91.76 | 4.80 |
| $NCPCM_{CuO}$ | 34.70 | 36.44 | 233.91 | 253.32 | 7.66 | 31.13 | 31.71 | 235.42 | 257.46 | 8.56 | 91.41 | 4.73 |
| $NCPCM_{Al_2O_3+CuO}$ | 33.87 | 36.12 | 228.46 | 253.32 | 9.81 | 30.28 | 30.82 | 229.34 | 257.46 | 9.81 | 89.28 | 4.32 |

$T_{oset,m}$: Onset melting temperature, $T_{peak,m}$: Peak melting temperature, $\Delta H_{m,exp}$: Experimental latent–heat of melting, $\Delta H_{m,cal}$: Calculated latent–heat of melting, $T_{oset,c}$: Onset cooling temperature, $T_{peak,c}$: Peak cooling temperature, $\Delta H_{c,exp}$: experimental latent–heat of cooling, $\Delta H_{c,cal}$: Calculated latent–heat of cooling, RE: Relative error, $\omega$: Mass percentage of RT–35HC, $\Delta$T: Degree of supercooling

### 4.4.6 Thermal conductivity measurements

Fig. 4.11 presents the results of effective thermal conductivity ($k$) and effective thermal conductivity enhancement factor ($\eta$) of RT–35HC and NCPCMs. It can be seen that by dispersing the nanoparticles thermal conductivity generally increases because of the higher effective thermal conductivity of nanoparticles. The effective thermal conductivity of RT–35HC and NCPCMs is measured for solid–phase (20–30 °C), phase–change (∼35 °C) and liquid–phase (40–55 °C) regions with an increment of 5 °C. It can be evidenced that the constant trend is predicted in enhancement in effective thermal conductivity in solid and liquid phases. However, a sharp increasing and decreasing behaviour was predicted when the temperature increased from 30 °C to 35 °C and 35 °C to 40 °C, respectively. This behaviour reveals that effective thermal conductivity is strongly depended on the temperature. The phenomenon of sudden increase and decrease in effective thermal conductivity was due to the random motion of molecules within a disordered microstructure of lattice in liquid–phase. The maximum effective thermal conductivities of 0.340, 0.464, 0.461, 0.469 and 0.472 W/m.K were obtained at phase–change temperature (∼35 °C) for RT–35HC, NCPCM$_{TiO_2}$, NCPCM$_{Al_2O_3}$, NCPCM$_{CuO}$ and NCPCM$_{Al_2O_3+CuO}$, respectively, shown in Fig. 4.11a. However, the maximum effective thermal conductivities for solid phase at 20 °C were obtained of 0.214, 0.320, 0.282, 0.331 and 0.328 W/m.K for RT–35HC, NCPCM$_{TiO_2}$, NCPCM$_{Al_2O_3}$, NCPCM$_{CuO}$ and NCPCM$_{Al_2O_3+CuO}$, respectively. The higher effective thermal conductivities at phase–change temperature (∼35 °C) is because of the phase–change temperature range 34–36 °C at which the NCPCM is in metastable condition. At phase–change temperature, the crystalline structure of RT–35HC becomes unstable and the increase in temperature accelerates the molecular vibration of the lattice, thus effective thermal conductivity of RT–35HC and NCPCMs increases dramatically at the melting point (∼ 35°C) (Wang and Meng, 2010). It can be clearly observed that NCPCM$_{Al_2O_3+CuO}$ has the highest effective

thermal conductivity in all three phases. Furthermore, the percentage of $\eta$ of RT–35HC and NCPCMs is shown in Fig. 4.11b, as given by Eq. 4.3:

$$\eta = \frac{k_{NCPCM} - k_{PCM}}{k_{PCM}} \times 100 \tag{4.3}$$

where, $k_{NCPCM}$ and $k_{PCM}$ are the thermal a conductivity of NCPCM and pure PCM, respectively. Figure 4.11b presents an increasing trend in en-

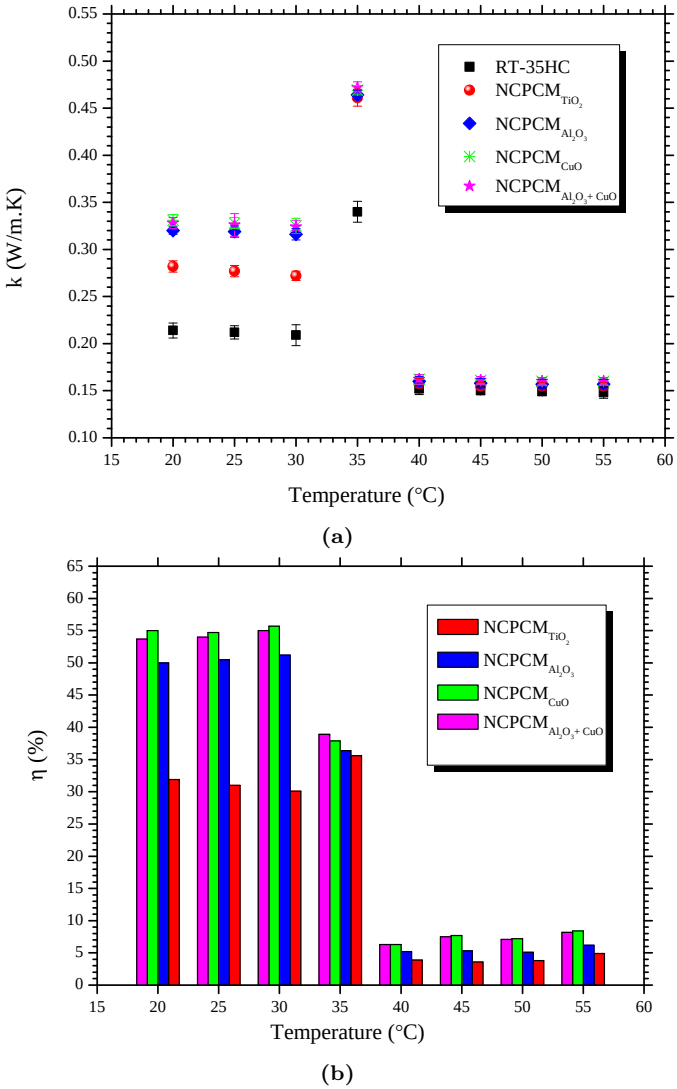


**Figure 4.11:** *The results of (a) effective thermal conductivity and (b) effective thermal conductivity enhancement factor of $TiO_2$, $Al_2O_3$, $CuO$ and RT–35HC based mono and hybrid NCPCMs as a function of temperature.*

hancement effective thermal conductivity are observed with change of temperature. A relative enhancements of 55.0%, 54.0% and 53.7% are obtained for NCPCM$_{Al_2O_3+CuO}$ at 30 °C, 25 °C and 20 °C, respectively, compared to

the RT–35HC. However, higher percentage enhancement in effective thermal conductivity is observed for $NCPCM_{CuO}$ of 55.7%, 54.7% and 55.0% at 30 °C, 25 °C and 20 °C, respectively, compared to the RT–35HC. The higher enhancement in effective thermal conductivity in case of CuO nanoparticles is because of higher thermal conductivity and other thermophysical properties of CuO nanoparticles compared to the hybrid $Al_2O_3$+CuO nanoparticles. The variations in effective thermal conductivity results in case of mono and hybrid NCPCMs are due to the nanoparticles size, morphology, density, thermal conductivity and dispersion stability into the NCPCMs. The $Al_2O_3$ and $TiO_2$ nanoparticles have the smaller size, density and higher surface area compared to CuO nanoparticles. Therefore, they have more stronger degree of homogenization and dispersion rate into the RT–35HC. Thenceforth, the combination of $Al_2O_3$+CuO hybrid nanoparticles having different thermophysical properties reveal the finer dispersion stability. Further more, the boundary layer of thermal resistance of nanoparticles and lattice molecules of PCM contribute a major factor in variation of effective thermal conductivity results (Mahian et al., 2019). Generally, there exists two major factors that cause the enhanced phenomenon of thermal conductance within the NCPCMs. Firstly, higher effective thermal conductivity of the nanoparticles and secondly the motion of the nanoparticles in NCPCMs in liquid–phase which causes a quasi–convection phenomenon (Babapoor and Karimi, 2015; Arshad et al., 2020b).

### 4.4.7 Specific heat capacity analysis

The specific heat capacity results of RT–35HC and NCPCMs are shown in Figure 4.12 for solid and liquid phases as a function of temperature from 10 °C to 60 °C. Since the specific heat capacity has the less effect in total thermal energy storage due to low thermal energy storage density in sensible heat storage phase. Regardless, specific heat capacity influences additional effects in the total heat stored by a PCM within the storage temperature range of

storage which is calculated using Eq. 4.4 as follows:

$$Q = \int_{T_i}^{T_m} mC_p.dt + m\alpha_m \Delta H_m + \int_{T_m}^{T_f} mC_p.dt \tag{4.4}$$

where, $Q$ (J) is the quantity of total heat stored, $T_i$ (°C), $T_m$ (°C) and $T_f$ (°C) are the initial, melting and final temperatures, respectively, $m$ (kg) mass of the heat storage medium, $C_p$ (J/kg.K) is the specific heat capacity,$\alpha_m$ is the faction of melted mass and $\Delta H_m$ (J/kg) is the heat of fusion per unit mass. From Eq. 4.4, it is important to investigate the specific heat capacity variations with temperature to analysis heat transfer and heat storage performance. The specific heat capacity of NCPCMs increases gradually with temperature

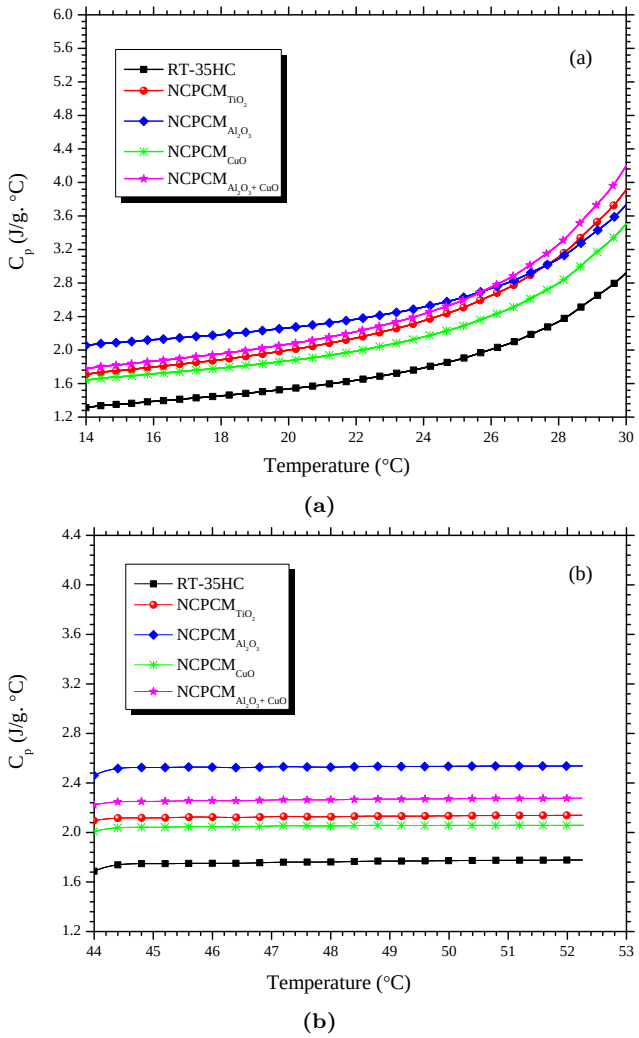


**Figure 4.12:** *Specific heat capacity curves of $TiO_2$, $Al_2O_3$, $CuO$ and RT–35HC based mono and hybrid NCPCMs: (a) solid–phase (b) liquid–phase.*

between 14 °C to 30 °C in solid–phase (Fig. 4.12a) while it remains constant in liquid–phase (Fig. 4.12b). The presented results of specific heat capacity of both phases showed the good agreement with the previous studies (Mehrali et al., 2014a; Chieruzzi et al., 2015). The specific heat capacities of RT–35HC for solid and liquid phases are obtained of 1.88 and 1.77 J/g.°C, respectively. It can be revealed that with addition of the nanoparticles, the specific heat capacity of NCPCMs increases both in solid and liquid phases. The higher values of specific heat capacities are obtained of 2.61 and 2.53 J/g.°C at 25 °C and 50°C, respectively, for NCPCM$_{Al_2O_3}$. The polynomial equations are generated for RT–35HC and NCPCMs for solid–phase after fitting the experimental data mentioned in Eq.4.5 and coefficients are given in Table 4.4.

$$C_P = AT^3 + BT^2 + CT + D \tag{4.5}$$

Fig. 4.13 represents the comparison of the comparison of specific heat capacities for RT–35HC and NCPCMs for 25 °C and 50 °C for solid and liquid phases, respectively. Fig. 4.13 shows that variations in specific heat capacity are significantly depends on the size, type and specific heat capacity of the nanoparticles. The specific heat capacity enhancement factor ($\zeta$) is calculated using Eq. 4.6 to evaluate the effect of nanoparticles in enhancement of specific heat capacity:

$$\zeta = \frac{C_{P_{NCPCM}} - C_{P_{PCM}}}{C_{P_{PCM}}} \times 100 \tag{4.6}$$

where, $C_{P_{NCPCM}}$ and $C_{P_{PCM}}$ are the specific heat capacity of the NCPCM and PCM, respectively. The maximum enhancements are obtained of 38.62% is achieved for NCPCM$_{Al_2O_3}$, whereas it is 36.47% for NCPCM$_{Al_2O_3+CuO}$ in solid phase compared to the RT–35HC.

The enhancement in specific heat capacity is associated with the following reasons: (i) an enhanced anharmonicity of the atomic interaction due to their volume expansion, (ii) impurities (Hellstern et al., 1989), (iii) the grain boundaries of nanosized materials which possess an excess volume with respect to

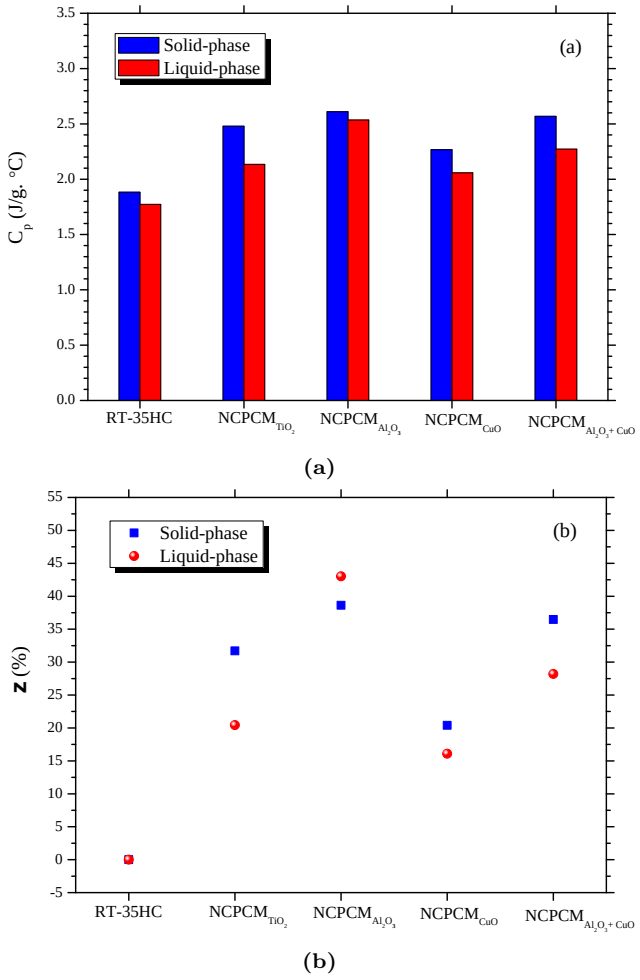


**Figure 4.13:** *(a) Comparison of specific heat capacity, (b) specific heat capacity enhancement of $TiO_2$, $Al_2O_3$, CuO and RT–35HC based mono and hybrid NCPCMs.*

the perfect crystal lattice and (iv) the high specific surface energies related to the high surface area of the nanoparticles per unit volume (Wang et al., 2006, 2001). In addition, the morphology of the nanoparticles also influences significantly, since the smaller size nanoparticles provide the larger interfacial surface area per unit mass between solid nanoparticles and surrounding material, thus increase the contribution of interfacial effects in the suspension (Timofeeva et al., 2009; Xie et al., 2002; Koca et al., 2018). The high specific surficial interface area of nanoparticles can adsorb liquid molecules to its surface which form the liquid layers. These liquid layers constrain the nanoparticles and alter their free–boundary surface atoms into the non–free interior atoms (Wang et al., 2006; Le-Ping et al., 2010). Therefore, the variation in specific heat capacity of NCPCMs is because of the varied Gibbs free energy

Table 4.4: *Coefficients of the third-order polynomials in solid-state, $C_p$ (J/g.°C).*

| | A | B | C | D | $R^2$ |
|---|---|---|---|---|---|
| RT–35HC | 0.0006 | -0.0349 | 0.6687 | -2.9832 | 0.9988 |
| NCPCM$_{TiO_2}$ | 0.0008 | -0.0457 | 0.8701 | -3.8549 | 0.9987 |
| NCPCM$_{Al_2O_3}$ | 0.0007 | -0.0397 | 0.7606 | -2.8072 | 0.9981 |
| NCPCM$_{CuO}$ | 0.0008 | -0.0425 | 0.8092 | -3.5154 | 0.9985 |
| NCPCM$_{Al_2O_3+CuO}$ | 0.0010 | -0.0567 | 1.0825 | -5.1234 | 0.9981 |

of the nanoparticles and liquid layers. Since, for a two phase mixture (index $m$), the Gibbs free energy change is given by $\Delta G_m = \Delta H_m - T\Delta S_m$. The Gibbs free energy difference between the solid–liquid phases is determined from the average force that the applied field exerts on the system. The chemical potential of nanoparticles dispersions is straightforwardly based the material properties for fluid diffusion in between nanoparticles which is defined by the diffusion coefficient of nanoparticle diffusion in a fluid as a function of the mass fraction. This diffusion coefficient also depends on particle size, surface chemistry, fluid composition, electrostatic effects and active particles. Moreover, the density–dependence of the chemical potential of dispersion implied as well. If the base fluid is polymeric of nature in a way that nanoparticles can alter their configuration either physically or chemically. Finally, the interchange energy associated with particle–matrix interaction, can be linked to a nano–layer of dense structured fluid around the nanoparticles (Pedersen, 2013; Machrafi, 2020).

### 4.4.8 IRT analysis

The IR thermographic images of mono and hybrid NCPCMs are shown in Fig. 4.14 which presents the surface temperature distribution during the melting process at different time steps. The melting stages of NCPCM$_{Al_2O_3}$, NCPCM$_{CuO}$ and NCPCM$_{Al_2O_3+CuO}$ can be seen clearly at each time step, labelled as (X), (Y) and (Z), respectively, as shown in Fig. 4.14a. The change in temperature of mono and hybrid NCPCMs can be observed from the temperature scale which indicates the lower to higher temperature variations from

blue to red colours, respectively. The uniform melting of each sample is observed while heating at constant temperature. The quick flow away and shrinkage is observed in NCPCM$_{CuO}$, shown in Fig. 4.14f. This phenomenon during phase change from solid–to–liquid causes to lose its shape–stability completely. In case of hybrid NCPCM$_{Al_2O_3+CuO}$, uniform phase transition is observed with slight shrinkage and flow away due to the heating-impact effect. Since, the NCPCMs only contain the 1 wt.% of $Al_2O_3$+CuO, therefore only slight shrinkage is observed. It has been reported that the flow away and shrinkage level decrease with the increase of the loading of nanoparticles. The melting process of NCPCM$_{Al_2O_3+CuO}$ shows that it does not melt completely till at 35 min and surface temperature of hybrid NCPCM is lower than the mono NCPCM. This reveals that the best heat transfer performance due to thermal properties and thermal stability. The heat transfer enhancement in hybrid NCPCM$_{Al_2O_3+CuO}$ is due to the uniform and homogeneous dispersion of $Al_2O_3$ and CuO nanoparticles in RT-35HC along with the higher effective thermal conductivity. Moreover, the thermographic images of NCPCM$_{Al_2O_3+CuO}$ show the enhanced latent–heat phase duration and uniform natural convection heat transfer which can be used in thermal management systems for electronics.

### 4.4.9 Transient thermal analysis

The transient thermal analysis was carried out by investigating the melting and cooling processes of pure RT-35HC and NCPCMs, as shown in Fig. 4.15 at a power level of 4 W. All samples were poured into a copper made heat sink after sonication to ensure the homogeneous dispersion of nanoparticles. The purpose of using the heat sink in current study, was to investigate the real time thermal response of NCPCMs compared to pure PCM. Since the heat sink has been widely used as heat exchanger that transfers the heat generated inside the electronics towards the ambient through a fluid medium. The RT–

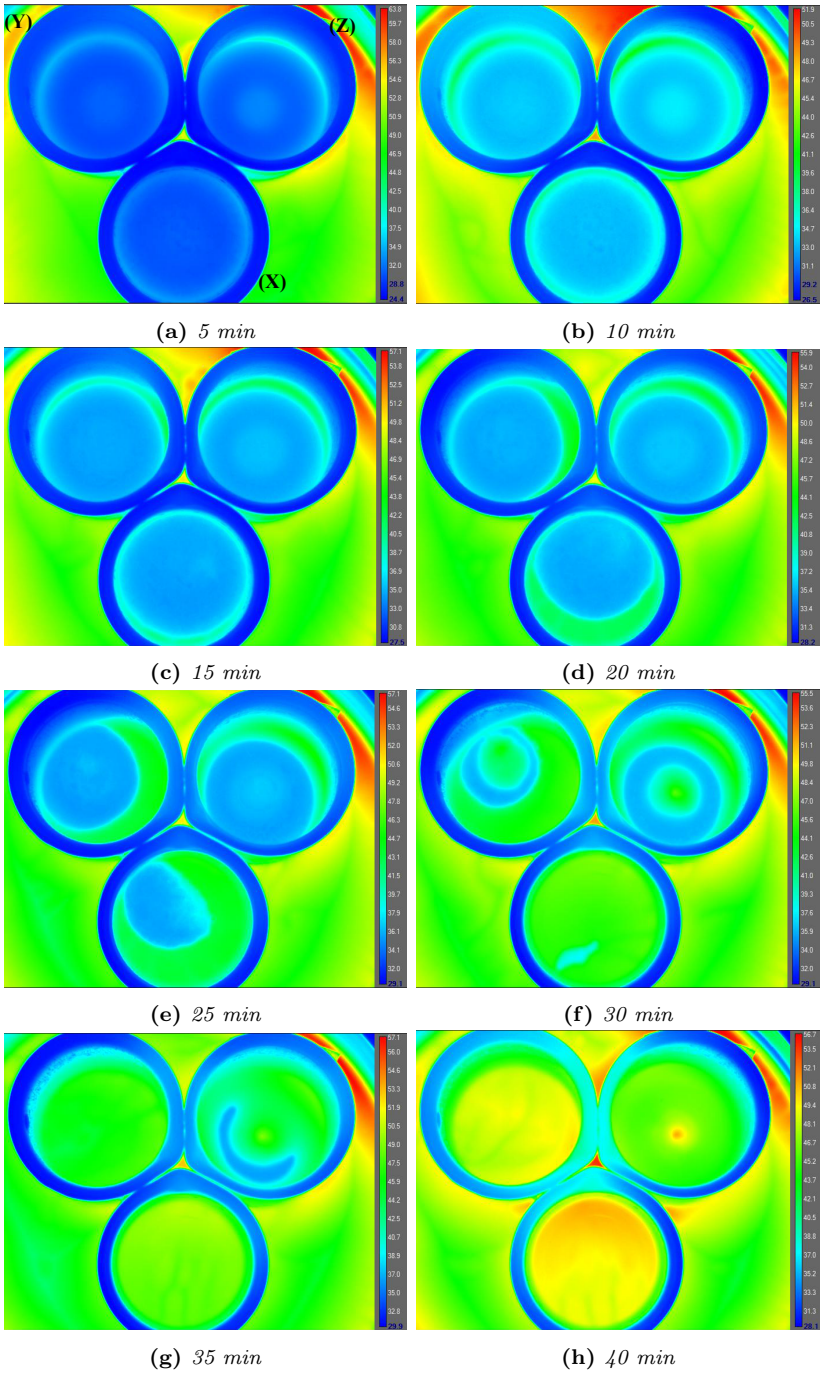


**(a)** *5 min* **(b)** *10 min*

**(c)** *15 min* **(d)** *20 min*

**(e)** *25 min* **(f)** *30 min*

**(g)** *35 min* **(h)** *40 min*

**Figure 4.14:** *IRT images of the melting process of* $NCPCM_{Al_2O_3}$*-(X),* $NCPCM_{CuO}$*-(Y) and* $NCPCM_{Al_2O_3+CuO}$*-(Z) at different time steps with temperature variation in* $^\circ C$*.*

35HC and NCPCMs were used as fluid medium inside the heat sink as passive cooling medium.

#### 4.4.9.1 Melting process

The melting curves of RT–35HC, NCPCM$_{TiO_2}$, NCPCM$_{Al_2O_3}$, NCPCM$_{CuO}$ and NCPCM$_{Al_2O_3+CuO}$ are shown in Fig. 4.15a. It can be seen from melting process that there is rapid increase of temperature linearly in all samples up to the first 20 min without showing any phase change. Heat transfer occurs in sensible heat transfer mode because of temperature gradient and specific heat capacity of the samples before melting starts. In addition, the heat transfer depends on the thermal conductivity of the samples. The quicker heating rate was observed for NCPCMs because of higher thermal conductivity. Since the loading content is constant in each sample, thus the variation in average heat sink base temperature is very small. Specific heat capacity and effective thermal conductivity of each sample also contribute a major role in total heat transfer rate. In second stage, NCPCMs started melting and a large amount of heat was absorbed because of latent–heat of fusion. Thus, the heat sink base temperature increased slowly which eventually enhanced the thermal performance of NCPCMs based heat sink, used for passive cooling of electronic devices. The viscosity of composite PCM increases directly by adding the nanoparticles along with thermal conductivity. The optimum heat transfer and storage of composite PCM also depends on the viscosity of NCPCMs at loading content of 1.0wt.%. The lower temperature rise of heat sink base is beneficial for the thermal management of electronic devices, Li–ion battery and PV modules.

#### 4.4.9.2 Cooling process

The cooling curves of RT–35HC, NCPCM$_{TiO_2}$, NCPCM$_{Al_2O_3}$, NCPCM$_{CuO}$ and NCPCM$_{Al_2O_3+CuO}$ are shown in Fig. 4.15b. The transient temperature variation of heat sink base temperature can be divided into three different stages:

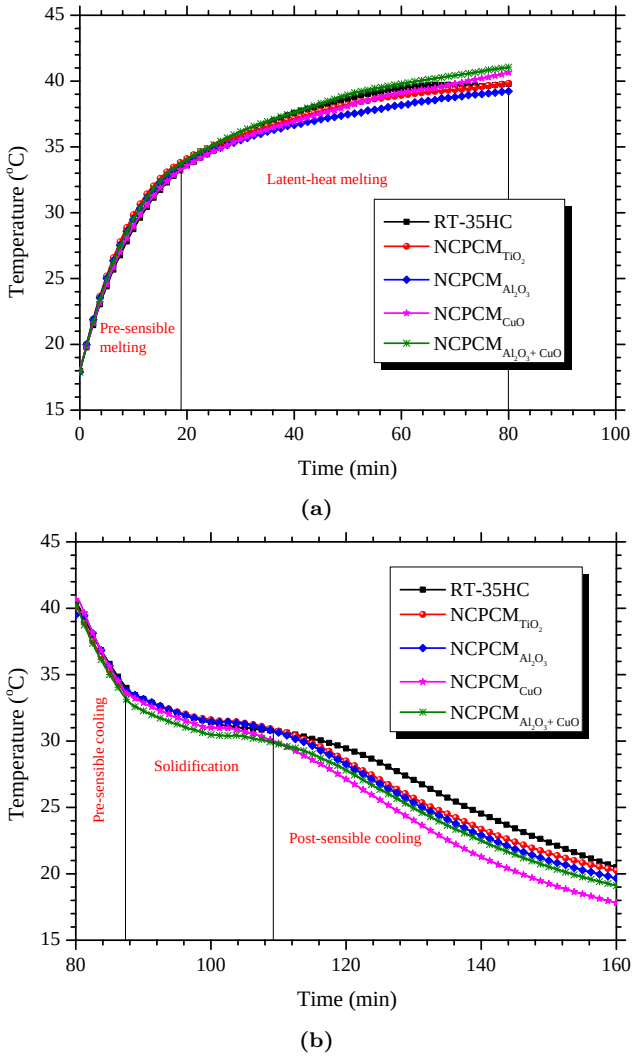


**Figure 4.15:** *(a) Melting process and (b) solidifying process of $TiO_2$, $Al_2O_3$, $CuO$ and RT–35HC based mono and hybrid NCPCMs.*

pre-sensible cooling, latent-heat of solidification and post-sensible cooling. It can be observed closely that NCPCMs have the faster decrement in temperature compared to the pure PCM. The higher rate of temperature decrease reflects the higher thermal conductivity enhancement of NCPCMs due the addition of $TiO_2$, $Al_2O_3$, CuO nanoparticles. During the cooling process, the base temperature decreased sharply and NCPCMs released their sensible heat to cool down up to their congealing temperature. Further, the NCPCMs started solidifying process due to their latent–heat of solidification at ambient temperature through natural convection phenomenon. The minimum temperatures of 22.36 °C, 21.54 °C, 20.99 °C, 19.24 °C and 20.52 °C were recorded for RT–35HC, NCPCM$_{TiO_2}$, NCPCM$_{Al_2O_3}$, NCPCM$_{CuO}$ and NCPCM$_{Al_2O_3+CuO}$,

respectively, after 150 min of cooling process. The reduction in heat sink base temperature was achieved of 3.67%, 6.13%, 13.95% and 8.23% for NCPCM$_{TiO_2}$, NCPCM$_{Al_2O_3}$, NCPCM$_{CuO}$ and NCPCM$_{Al_2O_3+CuO}$, respectively, compared to RT–35HC. It can be observed that cooling process was longer than the melting process. Also, phase change process of PCM and NCPCMs was more prolonged while cooling process than the melting process. The reason behind such irregular melting and cooling phenomenon depends on the heating/cooling rate. While cooling process, the melting rate was higher than the cooling process which took the less time to change the solid–liquid phase than the cooling process during phase transition from liquid to solid phase. The results revealed that the addition of nanoparticles improve the cooling rate of PCM result in decreases the average temperature heat sink base. Thus, NCPCMs filled heat sink improves the cooling efficiency and enhance the reliability of electronic devices.

## 4.5 Concluding Remarks

The current experimental study explores the physical, chemical and thermal properties of metallic oxide nanoparticles ($TiO_2$, $Al_2O_3$ and CuO) based nanocomposite phase change materials. Material characteristic techniques such as ESEM, FT–IR, TGA, DSC and TCA were used to investigate optimum thermal properties for efficient thermal management systems. The critical findings are summarized as follows:

- The surface morphological analysis of ESEM revealed the uniform dispersion and presence of $TiO_2$, $Al_2O_3$ and CuO nanoparticles in RT–35HC. Furthermore, XRD patterns confirmed the presence of all the nanoparticles in both mono and hybrid NCPCMs.

- The FT-IR spectrum presents that there is no chemical interaction between the nanoparticles and RT–35HC, and no peak shifting was ob-

served. Hence, there is only physical interaction of $TiO_2$, $Al_2O_3$ and CuO nanoparticles with RT–35HC.

- The TGA and DTG analysis explored that all mono and hybrid NCPCMs did not loss the chemical and thermal stability. In fact, the addition of $TiO_2$, $Al_2O_3$ and CuO nanoparticles improved the thermal and chemical stability of RT–35HC. Moreover, the hybrid NCPCM$_{Al_2O_3+CuO}$ showed the better stability than mono NCPCMs (NCPCM$_{TiO_2}$, NCPCM$_{Al_2O_3}$ and NCPCM$_{CuO}$).

- Overall, the phase–change enthalpy of melting/solidification was decreased with the addition of $TiO_2$, $Al_2O_3$ and CuO nanoparticles in both mono and hybrid NCPCMs. The latent–heat of melting of 235.84, 234.79, 233.9 and 228.46 J/g were obtained for of NCPCM$_{TiO_2}$, NCPCM$_{Al_2O_3}$, NCPCM$_{CuO}$ and NCPCM$_{Al_2O_3+CuO}$, respectively. Similarly, the latent–heat of solidification of 239.30, 241.65, 235.4 and 229.34 were obtained for of NCPCM$_{TiO_2}$, NCPCM$_{Al_2O_3}$, NCPCM$_{CuO}$ and NCPCM$_{Al_2O_3+CuO}$, respectively. The maximum deviation in peak melting temperatures were observed of $-1.14\%$ for NCPCM$_{Al_2O_3}$ and hybrid NCPCM$_{Al_2O_3+CuO}$ showed the deviation of $-0.08\%$.

- The thermal conductivity result predicted that hybrid NCPCM$_{Al_2O_3+CuO}$ mass percentage ratio of 75%/25% showed the maximum thermal conductivity of 0.328 W/m.K with thermal conductivity enhancement of 53.7% compared to RT–35HC.

- The increasing trend in the specific heat capacity of NCPCMs were observed. The maximum enhancements were obtained of 38.62% for NCPCM$_{Al_2O_3}$, whereas it was 36.47% for hybrid NCPCM$_{Al_2O_3+CuO}$ in solid phase compared to the pure RT–35HC. However, the enhancement in specific heat capacity depends on the nanoparticles size, type, density, surface area and morphology of the nanoparticles.

- The uniform melting and temperature distribution were observed from IR thermographic images of mono and hybrid NCPCMs. The enhancement in melting time was obtained with hybrid NCPCM$_{Al_2O_3+CuO}$ because of uniform dispersion of $Al_2O_3$ and CuO nanoparticles having varying densities and particle sizes. The reduction in heat sink base temperature was achieved of 3.67%, 6.13%, 13.95% and 8.23% for NCPCM$_{TiO_2}$, NCPCM$_{Al_2O_3}$, NCPCM$_{CuO}$ and NCPCM$_{Al_2O_3+CuO}$, respectively, compared to RT–35HC.

The current study finally concludes that newly synthesized metallic oxide nanoparticles based hybrid nanocomposite phase change materials have the better improvement in the thermal energy storage properties compared to the mono NCPCMs, which ultimately enhance the rate of heat transfer. Thereby, hybrid nanocomposite phase change materials can be successfully used in passive thermal management systems for electronic devices, Li–ion batteries, PV modules and direct utilization in solar thermal energy storage.

# Chapter 5

# Development of carbon–additives phase change mono and hybrid materials[1]

## Abstract

A novel zero–noise and clean thermal management technology (TMT), based on phase–change thermal energy storage (TES) technology, has turned out the new vision for researchers and industrialist involved in electronics industry. Therefore, this paper highlights a new direction by developing the nanocomposite phase change materials (NCPCMs) by combing the carbon–additives with phase change material. Four different types of carbon–additives of multi–wall carbon nanotube (MWCNT), graphene oxide (GO), reduced graphene oxide (rGO) and graphene nanoplatelet (GNP) were dispersed in RT–35HC, used as a PCM, with the combinations of mono (MWCNT, GO, rGO and GNP) and hybrid (GO+MWCNT, rGO+MWCNT and GNP+MWCNT) nanoparticles. A constant mass percentage of 1.0 wt.% was selected for both mono and hybrid

[1]This Chapter is published as:
**Arshad, A.**, Jabbal, M., Shi, L., & Yan, Y. (2021). Thermophysical characteristics and enhancement analysis of carbon-additives phase change mono and hybrid materials for thermal management of electronic devices. *Journal of Energy Storage*, 34, 102231.https://doi.org/10.1016/j.est.2020.102231

combinations of nanoparticles to explore the best type and dispersion scheme for productive and effective thermal management applications. All the synthesised NCPCMs were characterized using various characterization methods to study microstructural features, surface chemistry, lattice dimensions, stability, thermal and phase–change TES characteristics. The key findings reveal the best chemical and thermal stability, uniform dispersion of carbon–based nanoparticles in RT–35HC without modifying the molecular structure. The highest thermal conductivity enhancements of 182.7%, 183.8% and 185.3%, and optimum value of enthalpy of fusions of 237.42, 235.35 and 230.82 J/g were achieved for hybrid NCPCM$_{GO+MWCNT}$, NCPCM$_{rGO+MWCNT}$, and NCPCM$_{GNP+MWCNT}$, respectively. in comparison of mono NCPCMs. The phenomenon of thermal conductivity and specific heat capacity were explained systematically. Conclusively, the minimum subcooling, specific heat capacity enhancement and smaller phase–transition temperature reveal that GNP+MWCNT dispersed hybrid NCPCM can be potentially used for thermal management applications.
**Keywords:** Thermal management technology, Nanocomposite phase change materials, MWCNT, GO, rGO, GNP, Phase change material

## 5.1 Introduction

In current century, the revolutionary advancement in microelectronics including the miniaturization and parallel multi–functions performance demands a novel thermal management cooing solution. This progressing trend has led towards the development of micro level electronic components with higher power level. Thence, a serious challenge has been rising of overheating within the internal circuits of electronic devices which is deteriorating the operating features and lifetime performance. To overcome this challenge, there exists an emerging need of a novel thermal cooling technology which can sustain the cooling performance and operating life of electronic devices. A *quiet* and *clean* cooling technology with *zero* power consumption has a remarkable introduction in

advanced smart cooling technologies, based on the latent–heat thermal energy storage (LHTES) system (Ali et al., 2018b). Such a cleaner sustainable energy technology LHTES system is integrated with materials that have an intrinsic potential of absorbing and releasing the thermal energy. These materials are called phase change materials (PCMs) which can store the large amount of heat because of high energy storage density during charging and discharging cycles. The melting and solidification enthalpies of the PCMs are effectively utilized when integrated with a cooling system and thermal loads can be controlled through operating parameters (Arshad et al., 2019a). In spite of that, PCMs exhibit some issues mainly lower thermal conductivity, super–cooling, less thermal stability, etc. which reduce the heat transfer performance while cooling. Recently, the different design and material aspects of PCM based cooling systems have been explored such as the leakage phenomenon (Xiao et al., 2020), structure design (Lv et al., 2020a), enhancing the mechanical properties (He et al., 2019a) and evaluating the long-term durability (Lv et al., 2020b). The energy technologists and researchers have been contributing the great efforts to improve the thermophysical properties by adopting various performance enhancement techniques such as by dispersing the nanomaterials, encapsulation, shape–stabilization and embedding metal–foams (Arshad et al., 2020c), metallic fins (Ali and Arshad, 2017) or heat pipes (Putra et al., 2020; Zhang et al., 2020). These days addition of highly thermal conductive matrix and chemically treated surfaces of nanomaterials have taken over the key attention for researchers and scientist. Surface modification and grafting functional groups are the main methods along with the addition of three–dimensional (3D), two–dimensional (2D), one–dimensional (1D) and zero–dimensional (0D) structural additives (Buzea and Pacheco, 2016). Nanomaterials additives including nanoparticles, nanosheets, nanotubes, nanofibers, nanorods, nanowires and quantum dots exhibit a specific structural configuration (Buzea and Pacheco, 2016).The addition of nanomaterials have been evaluated to improve the thermal conductivity and specific heat and to reduce

the interfacial thermal resistance. The addition of nanomaterials in PCMs form a thermal conduction path, reduce the phonon scattering and enhance the heat transfer rate. The carbon–based nanomaterials family, which possess all the dimensionality and morphology, have proven the remarkable thermophysical properties for the applications of LHTES and thermal management systems when added into the PCMs (Jebasingh and Arasu, 2020b; Wu et al., 2020). For instance, Choi et al. (Choi et al., 2014) synthesized the NCPCMs using three different carbon additives such as MWCNTs, graphite, and graphene to determine the thermal conductivity for TES applications. The authors used the hot–wire method and found that graphene showed the highest thermal conductivity enhancement of 21.5% at 0.1 vol.% loading. Moreover, they obtained the enhancement in heat transfer up to 3.35 times higher with 5.0 vol.% of graphite. Li et al. (Li et al., 2014a) used the grafted CNT by grafting polyhydric alcohol and mixed into the paraffin as a PCM to prepare the NCPCMs. Results showed the 38% graft ratio of stearyl alcohol grafted CNT and found the highest thermal conductivities of 0.7903 W/m.K at 4 wt.%. Li et al. (Li et al., 2014b) selected the MWCNT, graphene and graphite as a carbon additives and stearic acid as a PCM to prepare the phase change NCPCMs for TES applications. Results revealed that by adding the carbon additives the heat conduction mode improved whereas heat convection mode was weakened. The best charging and discharging rates were obtained around 37% and 320%, respectively, with 5.0% of graphite added NCPCM. Moreover, a 12 times enhancement was obtained in thermal conductivity with 5.0% of graphite added NCPCM. Fan et al. (Fan et al., 2015) tested the CNT and GNP based composite PCM in heat sink for TES application at various concentrations. The authors determined the various thermophysical properties and found the 5.3% and 7.3% reduction in latent–heat fusion for CNT and GNP based composite PCM, respectively, at 3 wt.%. The thermal conductivity was enhanced of 31.1% and 170% for CNT and GNP based composite PCM, respectively, at 3 wt.%. Bahiraei et al. (Bahiraei et al., 2017) conducted the experimental and

numerical study based on composite PCM by using CNF, GNP and graphite nanoparticles. Maximum thermal conductivity enhancements were obtained using graphite nanoparticles at 7.5 wt.% and 10 wt.% about 620% and 1100%, respectively, in solid–phase. Zou et al. (Zou et al., 2018) synthesised the carbon additives (MWCNT and graphene) and paraffin based composite PCM for Li–ion battery cooling application. Authors found the higher thermal conductivity enhancement with 3/7 mass ratio of MWCNT/graphene of 31.8%, 55.4% and 124% compared with GNP, MWCNT and pure PCM, respectively. Recently, Li et al. (Li et al., 2020b) prepared the composite PCM using sodium sulfate decahydrate ($Na_2SO_4.10H_2O$) and expanded graphite (EG) for TES application. The results revealed that by dispersing 7 wt.% of EG, the latent–heat of melting and cooling were obtained of 114.0 and 105.5 J/g, respectively. In addition, the thermal conductivity was obtained of 1.96 W/m.k.

The literature reveals that most of the studies focused on TES applications of composite PCMs. In this study, four different carbon additives (MWCNT, GO, rGO and GNP) were dispersed in the RT–35HC in two different schemes: mono and hybrid. A constant loading content of 1.0 wt.% was considered for both mono (MWCNT, GO, rGO and GNP) and hybrid (GO+MWCNT, rGO+MWCNT and GNP+MWCNT) NCPCMs. The ratio between hybrid nanoparticles of GO+MWCNT, rGO+MWCNT and GNP+MWCNT was kept constant of 3:1. A detailed experimentation was carried out to investigate the surface structure, chemical and physical interaction, thermal conductivity, specific heat capacity, phase–change enthalpies of solid–liquid and liquid–solid stages, degree of supercooling, chemical and thermal stability of NCPCMs as a function of temperature. In addition, the thermal conductivity enhancement mechanism and modes of specific heat capacity enhancement were explained schematically. Finally, this work contributes significantly to the area of thermal management of electronic systems.

## 5.2 Research Methodology

### 5.2.1 Materials selection

A commercially available an organic PCM, namely RT-35HC was chosen having phase transition temperature of 34-36 °C which was purchased from Rubitherm GmbH, Germany. Table 5.1 is summarized the thermophysical properties of RT–35HC. Four different carbon–based nanomaterials such as graphene nanoplatelet (GNP), graphene oxide (GO), reduced graphene oxide (rGO) and multiwall carbon nanotube (MWCNT) were selected as a thermal conductive materials (TCMs). The GNP (thickness <3-5 nm, lateral diameter $< 10\mu$m and carbon purity $98 \pm 1.0$ wt.%), GO (flake thickness: $\leq$2 nm, lateral diameter: $< 4\mu$m and carbon purity: $60 \pm 5.0$ wt.%) and rGO (flake thickness: <100 nm, lateral diameter: $< 20\mu$m and carbon purity: $85 \pm 7.5$ wt.%) were obtained from 2–Dtech Ltd/Versarien PLC, UK. The MWCNT (outer diameter $5 - 15$nm and length of $10 - 30\mu$m, and purity $> 95$ wt.%) was procured from Carbon Nanotubes Plus, USA. The sodium dodecylbenzene sulfonate (SDBS) was purchased from Sigma-Aldrich, UK. All materials are utilized without carrying out any further chemical processing.

Table 5.1: Thermophysical properties of PCM (RT–35HC).

| Physical properties | RT–35HC |
|---|---|
| Melting temperature (°C) | 34–36 |
| Heat storage capacity (kJ/kg) | 240 |
| Thermal conductivity (W/m.K) | 0.2 |
| Specific heat capacity (J/kg.K) | 2000 |
| Density (kg/m$^3$) | 880 (solid)<br>770 (liquid) |

### 5.2.2 Preparation of NCPCMs composites

In present study, a two–step method was adopted to synthesize the composite of NCPCMs which has been reported extensively (Arshad et al., 2019b). Fig. 5.1 illustrates complete schematic representation of all mono and hybrid sam-

ples of NCPCMs. RT–35HC was used as a base PCM and GNP, GO, rGO and MWCNT were added as additives to enhance the thermophysical properties of RT–35HC. The mass loading of the additives was kept constant of 1.0 wt.% for both mono and hybrid NCPCMs. Additionally, sodium dodecylbenzene sulfonate (SDBS) was added with the ratio 4 : 1 for each loading of the GNP, GO, rGO and MWCNT nanoparticles. While synthesising the hybrid NCPCMs, the MWCNT was mixed simultaneously with GNP, GO and rGO keeping the total mass concentration of 1.0 wt.%. The ratio of mass concentration of hybrid NCPCMs (GNP/MWCNT, GO/MWCNT and rGO/MWCNT) was kept 75%/25% of 1.0 wt.%. In first step of NCPCMs preparation, the PCM, RT–

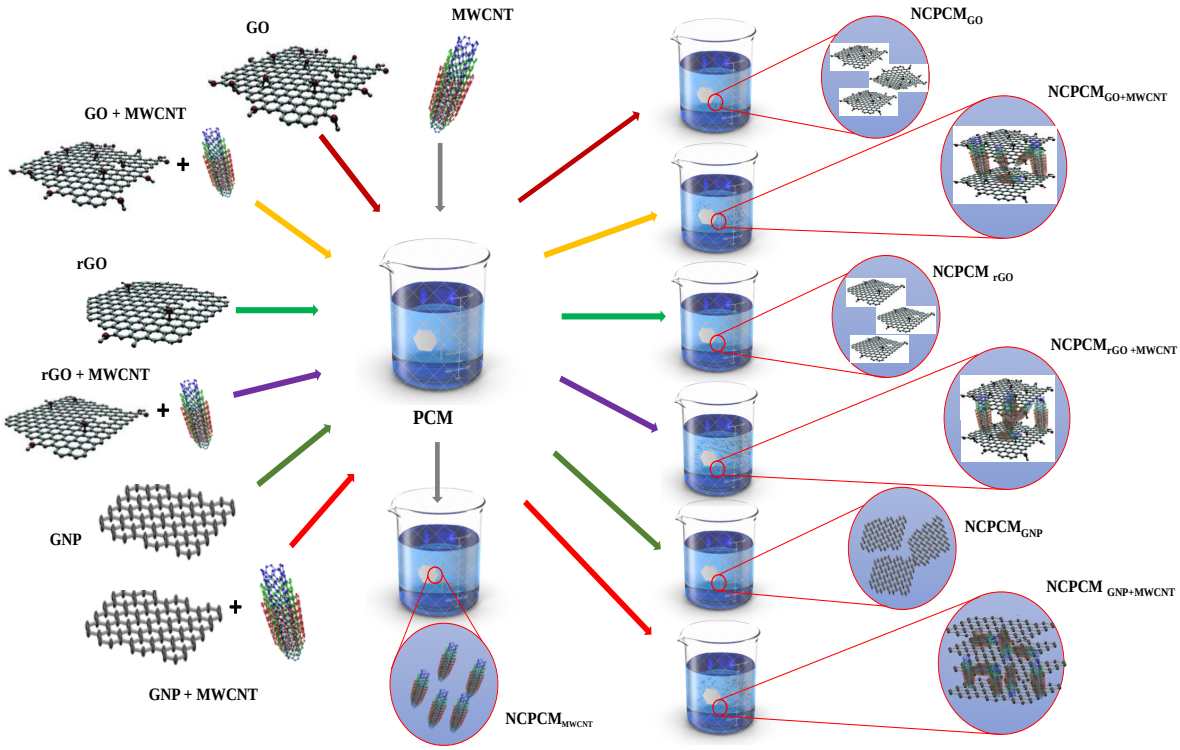


**Figure 5.1:** *Schematic diagram of samples preparation of carbon–additives mono and hybrid NCPCMs.*

35HC, was melted until it did not shift into the liquid-phase by using a hot–water bath maintaining at 70 °C temperature constantly. A constant ratio of SDBS was mixed into the liquid RT–35HC as surfactant to improve dispersion of GNP, GO, rGO and MWCNT nanoparticles in RT–35HC more uniformly. As a kind of anionic surfactant, SDBS has good surface activity and strong

hydrophilicity thus it effectively reduces the tension of PCM surface during synthesizing the NCPCMs. Then the mixture of RT–35HC/SDBS was stirred for 30 min using a magnetic stirrer at rate of 450 rpm and temperature of 70 °C. After that, GNP, GO, rGO, MWCNT, GNP/MWCNT, GO/MWCNT and rGO/MWCNT were added separately to prepare the desired mono and hybrid NCPCMs. To achieve the homogeneous and stable dispersion of additives, the stirring of mixture was further continued for 3 hrs to improve the thermophysical properties and uniform melting/cooling of NCPCMs. The sample were labelled as NCPCM$_{MWCNT}$, NCPCM$_{GO}$, NCPCM$_{rGO}$, NCPCM$_{GNP}$, NCPCM$_{GNP+MWCNT}$, NCPCM$_{GO+MWCNT}$ and NCPCM$_{rGO+MWCNT}$, based on the mono and hybrid carbon–additives scheme.

In second step of NCPCMs preparation, all the samples were sonicated using probe at 40 kHz frequency for 60 min to enhance the homogeneity and dispersion of carbon–additives and to minimize the sedimentation and aggregation. A uniform dispersion of all mono and hybrid carbon-additives used in current can be seen from photographs of prepared samples both in liquid and solid states shown in Figs. 5.2 and 5.3, respectively. Later on, all the samples of NCPCMs were cooled at the ambient temperature.

### 5.2.3 NCPCMs characterizations

To study the physical, chemical and thermal properties of synthesised NCPCMs, different characterization techniques were carried out including ESEM, FTIR, XRD, DSC, TGA and thermal conductivity analyser (TCA).

#### 5.2.3.1 Physical and chemical analysis

To visualize the microstructural features, surface topography and dispersion of carbon–additives in NCPCMs, an environmental scanning electron microscopy (ESEM, FEI Quanta–650) was used. To study the chemical composition and record the absorption spectra of powdered GNP, GO, rGO, MWCNT, RT–

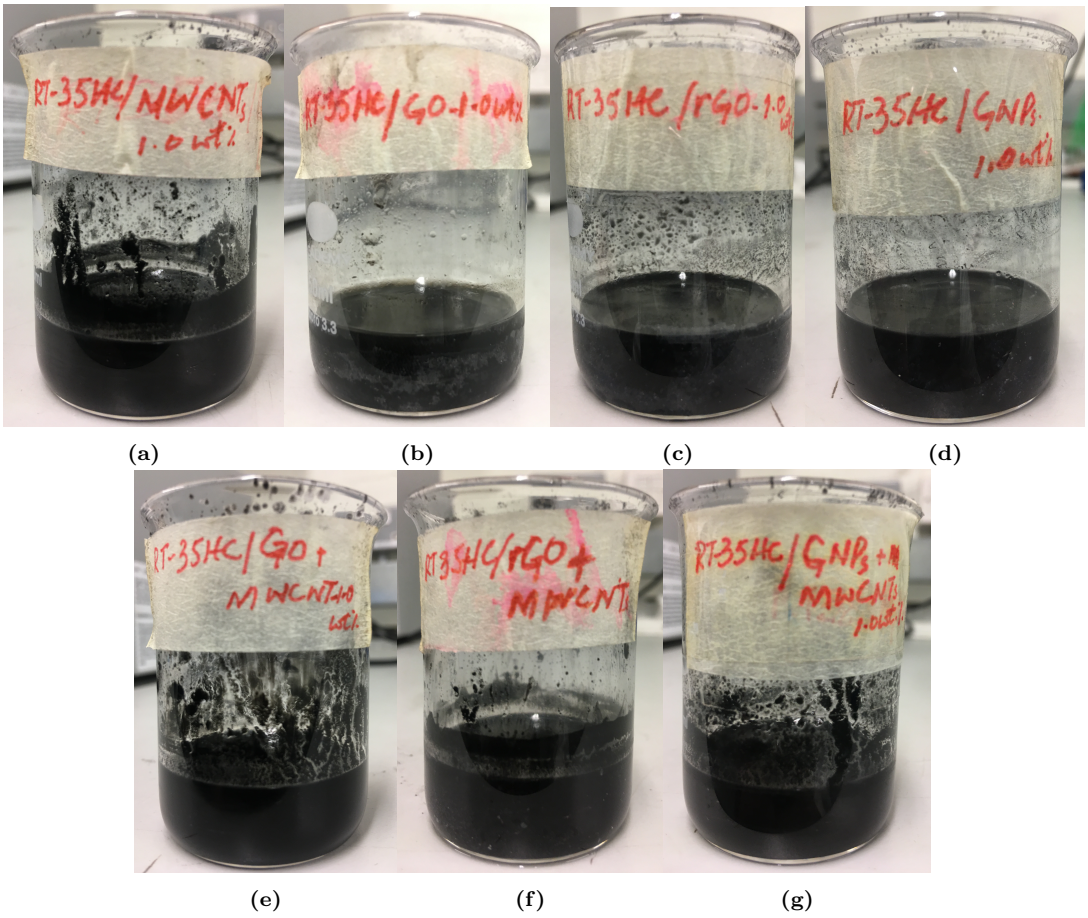


**Figure 5.2:** *NCPCMs after 5 mins: (a) $NCPCM_{MWCNT}$, (b) $NCPCM_{GO}$, (c) $NCPCM_{rGO}$, (d) $NCPCM_{GNP}$, (e) $NCPCM_{GO+MWCNT}$, (f) $NCPCM_{rGO+MWCNT}$, (g) $NCPCM_{GNP+MWCNT}$.*

35HC and synthesized NCPCMs at room temperature, fourier transform infrared spectroscope (FTIR, Bruker Tensor–27) was employed. The tests were conducted between wavelength range of 500–4000 $cm^{-1}$ with spectral resolution and accuracy of 4 $cm^{-1}$ and 0.01 $cm^{-1}$, respectively. The study lattice planes and crystallographic structure of powdered GNP, GO, rGO, MWCNT, RT–35HC and synthesized NCPCMs, the X–ray diffraction (XRD) patterns were obtained by using Bruker D8–Advance with Da Vinci (Bruker (UK) Ltd) with a monochromatic Cu–K$\alpha$ radiation ($\lambda = 1.5406\mathring{A}$) from angle $2\theta$ range between 5° to 60°.

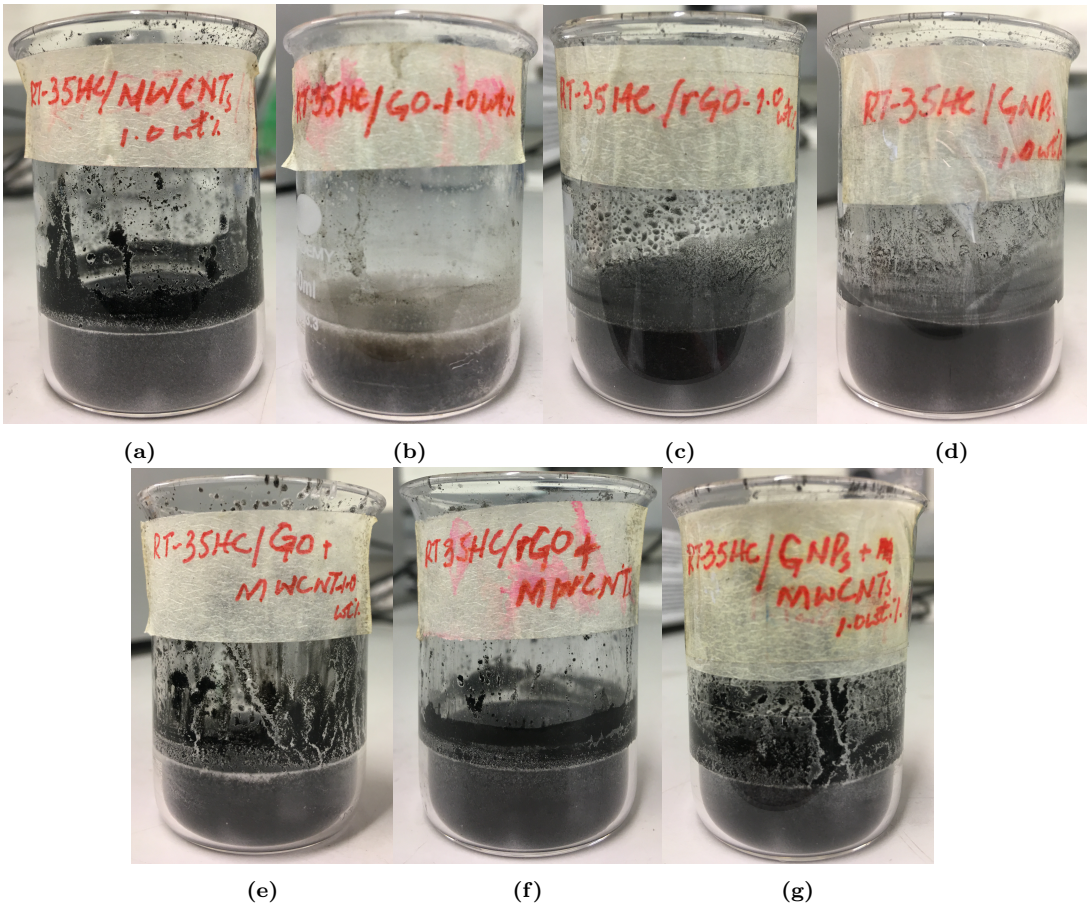


**Figure 5.3:** *NCPCMs after 50 mins: (a) $NCPCM_{MWCNT}$, (b) $NCPCM_{GO}$, (c) $NCPCM_{rGO}$, (d) $NCPCM_{GNP}$, (e) $NCPCM_{GO+MWCNT}$, (f) $NCPCM_{rGO+MWCNT}$, (g) $NCPCM_{GNP+MWCNT}$.*

#### 5.2.3.2 Thermal analysis

The thermal conductivity was measured of all samples using thermal conductivity analyser (TCA) TCi$^{TM}$ by C–Therm Technologies Ltd. Canada, as a function of temperature (20-55°) by adopting the modified transient plane source (MTPS) method (ASTM–D7984). The TCA instrument has the capability to measure thermal conductivity range from 0-500 W/m.K with 5% accuracy and 1% precision. Five readings are recorded for each sample at a specific temperature and average value is reported. A maximum relative error and uncertainty were obtained of ±2.0% and ±1.0%, respectively. The thermal stability of all samples were analysed using thermogravimetric analysis (TGA) and derivative thermogravimetry analysis (DTGA), obtained from SDT–Q600 TA instrument Inc., UK having the precision of 0.1 $\mu$g. A sample mass of about

5–7 mg was filled in a pan, made of aluminium, and three different tests were heated at a rate of 10 °Cmin$^{-1}$ from temperature 20 °C to 400 °C under pure $N_2$ environment of purging flow rate of 100 mLmin$^{-1}$. The phase–transition temperatures and latent–heat enthalpies of all samples were determined by employing differential scanning calorimeter (DSC-2500, TA instrument Inc., UK) while endothermic and exothermic processes. Three tests were performed for each sample from temperature range 10 °C to 50 °C at constant temperature rate of 1 °Cmin$^{-1}$ under $N_2$ flow conditions with accuracy and precision of ±0.04% and ±0.005 °C, respectively. The specific heat capacity of all samples was measured at constant heating rate of 3 °Cmin$^{-1}$ from temperature 10 °C to 50 °C by following Sapphire–method. A sample mass of about 3-5 mg was sealed inside a Tzero Hermetic pan, made of aluminium, with the lid to avoid any leakage.

## 5.3 Results and discussions

### 5.3.1 Surface morphology analysis

The surface morphology and microstructural features of GNP, GO, rGO and MWCNT based mono and hybrid NCPCMs are shown in Fig. 5.4. The surficial microstructure of pure RT–35HC, NCPCM$_{MWCNT}$, NCPCM$_{GO}$, NCPCM$_{GO+MWCNT}$, NCPCM$_{rGO}$, NCPCM$_{rGO+MWCNT}$, NCPCM$_{GNP}$ and NCPCM$_{GNP+MWCNT}$ are presented in Figs. 5.4a, 5.4b, 5.4c, 5.4d, 5.4e, 5.4f, 5.4g and 5.4h, respectively. The uniform dispersion of GNP, GO, rGO and MWCNT can be visualized from Fig. 5.4 in all mono and hybrid NCPCMs because of the repulsive bonding of the SDBS, acting as a dispersing agent. Although the mass faction of GNP, GO, rGO and MWCNT is constant and very less, even though a uniform dispersion and enough embeddedness of nanoparticles can be observed in RT–35HC. Along with this, small homogeneous and heterogeneous percolation zones of GNP, GO, rGO and MWCNT mono and hybrid nanoparticles can be

observed in NCPCMs. The presence of similar homogeneous and heterogeneous zones of various nanoparticles used as mono and hybrid combinations have been reported in previous studies (Chieruzzi et al., 2015; Arshad et al., 2020b). The morphological features of hybrid NCPCMs (NCPCM$_{GO+MWCNT}$, NCPCM$_{rGO+MWCNT}$ and NCPCM$_{GNP+MWCNT}$) reflect the three-dimensional arrangement of hybrid combinations of GNP, GO, rGO and MWCNT nanoparticles. This three–dimensional path of hybrid nanoparticles is because of two different molecular arrangement of carbon-based additives. Since MWCNT are consisted of nested single–wall carbon nanotubes (SWCNT) of different diameters which are rolled up of multiple layers of graphite sheets to form the tubular or cylindrical shape (Aqel et al., 2012). The GO and rGO have the structure of two–dimensional layer or sheet forming the thin films (Wypych, 2019). The GNP consists of short stacks of graphene sheets forming a two–dimensional nano platelet shapes which are identical to those found in the walls of carbon nanotubes, but in a planar form (Cataldi et al., 2018). Therefore, this three–dimensional path of hybrid nanoparticles has a significant effect to transfer the heat in all regions of RT–35HC. In addition, two different mass ratios of GNP+MWCNT, GO+MWCNT and rGO+MWCNT hybrid nanoparticles form the different morphologies because of different molecular shapes and physical properties (i.e. density, particle size, surface area etc.) results in the good harmonious effects of heat transfer enhancement.

### 5.3.2 Chemical composition analysis

Fig. 5.5 shows the functional groups and chemical composition of GNP, GO, rGO and MWCNT nanoparticles dispersed mono and hybrid NCPCMs. The structural interaction is illustrated through FT–IR spectrum characterized by FTIR spectroscopy. Because of the absence of functional groups, there were no significant stretching and bending peaks observed of infrared spectra GNP, GO, rGO and MWCNT. Despite of this, a series of absorption peaks of RT–35HC,

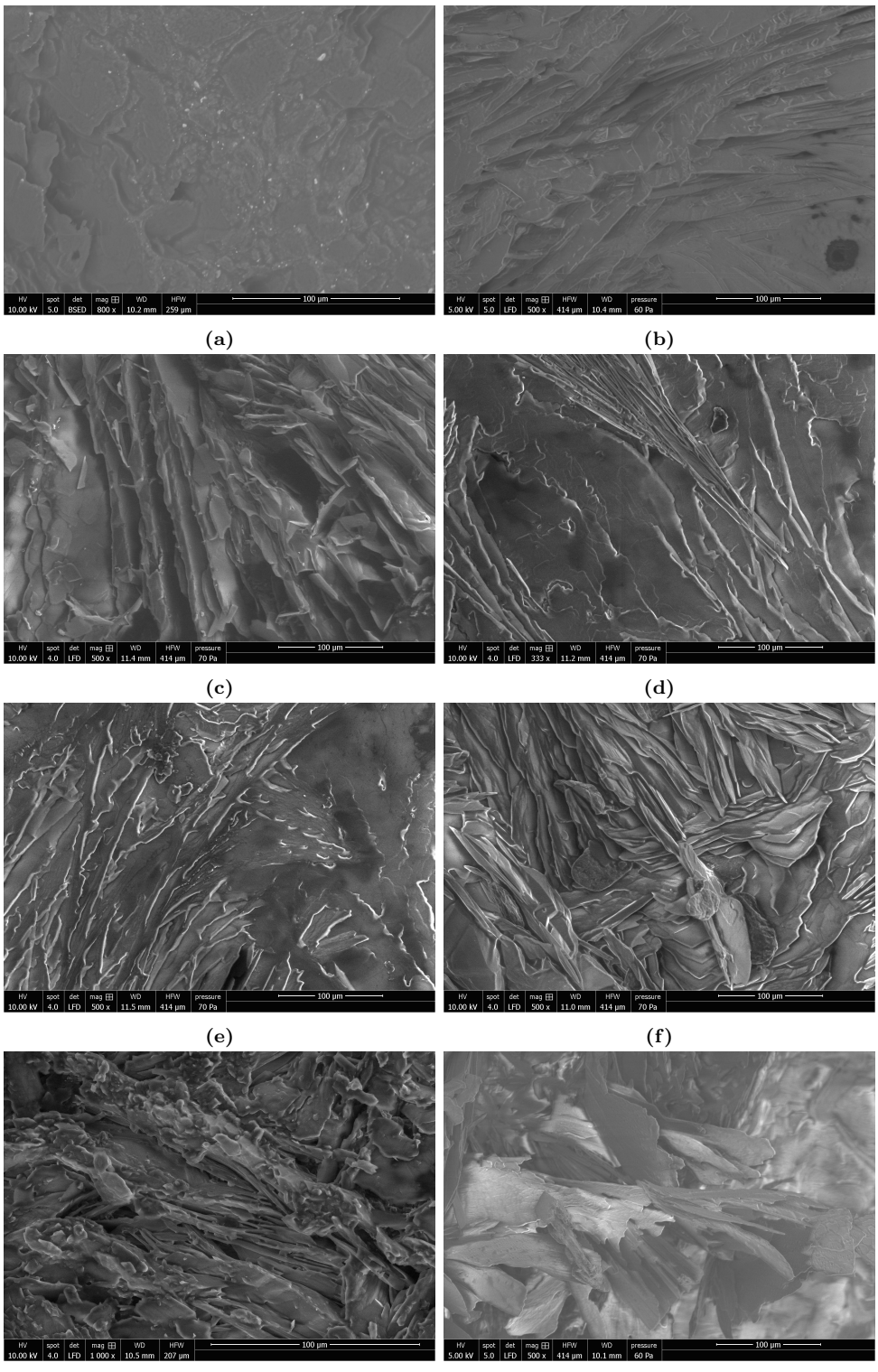


**Figure 5.4:** *ESEM images of mono and hybrid NCPCMs (a) RT–35HC (b) $NCPCM_{MWCNT}$, (c) $NCPCM_{GO}$ (d) $NCPCM_{GO+MWCNT}$ (e) $NCPCM_{rGO}$ (f) $NCPCM_{rGO+MWCNT}$ (g) $NCPCM_{GNP}$ and (h) $NCPCM_{GNP+MWCNT}$.*

mono and hybrid NCPCMs were obtained. A series of absorption peaks were observed of pure RT–35HC and NCPCMs. The spectrum of RT–35HC shows the three absorption peaks at 2955, 2913 and 2849 $cm^{-1}$ which represent the

medium C–H symmetrical and anti–symmetrical stretching vibration of methyl ($–CH_3$) and methylene ($–CH_2–$) group. The peak at 1472 $cm^{-1}$ identifies the medium C–H scissoring of $–CH_2–$ and deformation of antisymmetric stretching vibration $–CH_3$ group in RT–35HC. A series of absorption peaks at 1371, 1125,

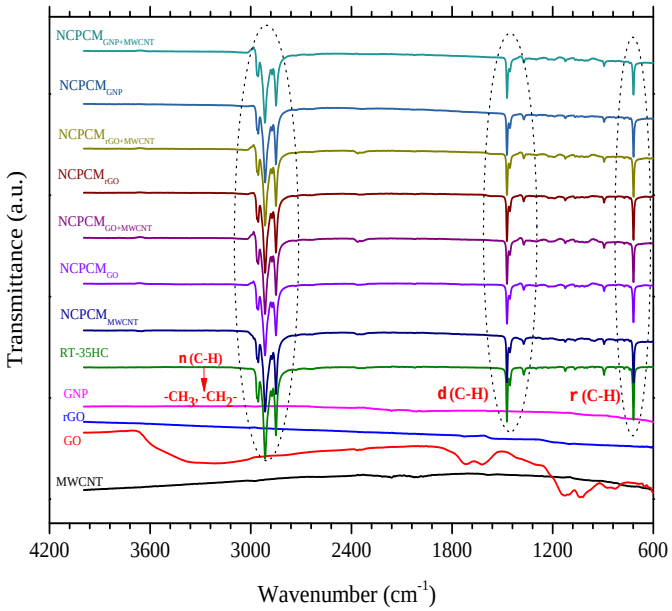


**Figure 5.5:** *FT–IR spectrum of carbon–additives mono and hybrid NCPCMs.*

and 891 $cm^{-1}$ which are due to the C–H bending and scissoring vibrations. In addition, the peak at 715 $cm^{-1}$ represents to the weak rocking vibration of C–H in long–chain methyl group. From Fig. 5.5, it can be observed that carbon–additives mono and hybrid NCPCMs reflected the consistent peaks similar that of the RT–35HC. This shows that mono and hybrid NCPCMs possess the similar characteristics which RT–35HC exists without emergence of any new peak or peak shift. Therefore, the FTIR results reveal that no considerable chemical interaction occurred between the GNP, GO, rGO, MWCNT and RT–35HC. Further, there is only physical interaction between the nanoparticles and RT–35HC which illustrate that prepared mono and hybrid NCPCMs are chemical stable.

### 5.3.3 Crystallography analysis

The crystalline phase and dimensions of unit cell of GNP, GO, rGO, MWCNT and RT–35HC and their mono and hybrid NCPCMs were analysed through crystallography analysis by using XRD. Figure 5.6 illustrates the crystal structure XRD patterns of GNP, GO, rGO, MWCNT, RT–35HC and prepared NCPCMs to confirm the presence of GNP, GO, rGO and MWCNT in RT–35HC. The XRD spectrum of MWCNTs confirmed the presence of carbon nanotubes peaks at 25.91° (002) and 42.95° (100) with the PDF No. 00-058-1638 (Keller et al., 2004). The diffraction peak at $2\theta$ = 9.7° at reflection plane (001) confirm the presence of GO (Yasin et al., 2018). Since the rGO is the further obtained after thermochemical treatment, the diffraction peak appeared at $2\theta \approx 30°$, at reflection plane (002) (Yasin et al., 2018). The XRD pattern at 26.54°, 42.36°, 44.56° and 54.66° of corresponding reflection planes of (002), (100), (101) and (004), respectively, confirm the graphene layers of GNP with PDF No. 00-056-0159. The sharp diffraction peaks of RT-35HC

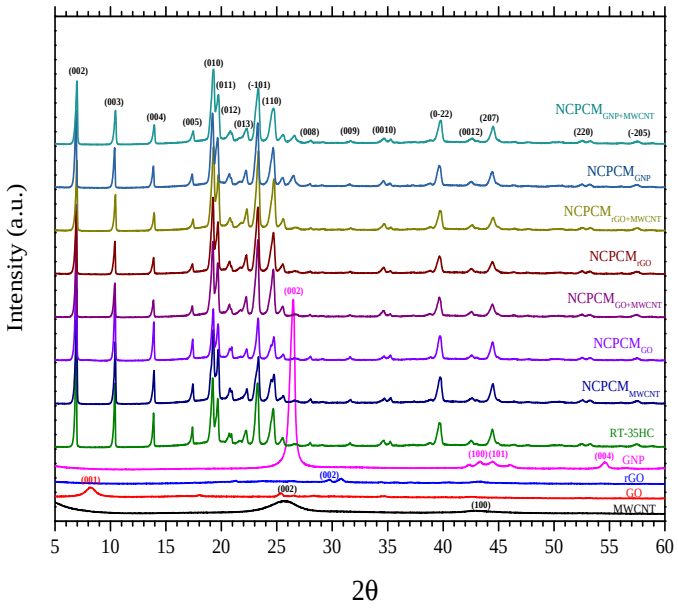


**Figure 5.6:** *XRD pattern of carbon–additives mono and hybrid NCPCMs.*

was observed at 6.85° (002), 10.48° (003), 13.91° (004), 17.44° (005), 19.32° (010), 19.80° (011), 20.83° (012), 22.43° (013), 23.32° (105), 24.78° (-101), 25.65° (110), 28.12° (008), 31.75° (009), 34.75° (-110), 35.27° (0010), 39.83°

(0-22), 42.73° (0012), 44.60° (207), 52.68° (220), 53.41° (-2-14) and 57.55° (-205) which attributed to the crystal planes of *n-eicosane* ($C_{20}H_{42}$) with PDF No. 00-045-1543. Although a constant and less amount of GNP,GO, rGO and MWCNT was dispersed in RT–35HC. As a consequence of this, less significant physical changes were observed in mono and hybrid NCPCMs. In addition, the XRD peaks revealed that the crystal structure of RT–35HC did not change. More further NCPCM$_{MWCNT}$, NCPCM$_{GO}$, NCPCM$_{GO+MWCNT}$, NCPCM$_{rGO}$, NCPCM$_{rGO+MWCNT}$, NCPCM$_{GNP}$ and NCPCM$_{GNP+MWCNT}$ samples contain the peaks of GNP,GO, rGO and MWCNT.

### 5.3.4 Thermal stability analysis

Thermal stability analysis of RT–35HC, mono and hybrid NCPCMs was carried out through thermal gravimetric analysis, as shown in Fig. 5.7. The TGA and DTGA curves of RT–35HC, mono and hybrid NCPCMs are presented in Figs. 5.7a and 5.7b, respectively. The thermal stability of the RT–35HC and NCPCMs was estimated two parameters; (i) onset temperature degradation ($T_{onset}$) and (ii) rate of weight loss ($R_{wl}$) during kinetic process. There are four mechanisms of weight loss which include decomposition, evaporation, reduction and desorption. It can be seen from Figs.5.7a and 5.7b that TGA and DTGA curves possess the one–step and two–step thermal degradation process, respectively. The TGA curves of RT–35HC, mono and hybrid NCPCMs represent that there is no distinguishable weight loss in any sample up to ∼120 °C. More further, it can be observed that by increasing temperature the rate of weight loss increases directly and reaches at the maximum degradation temperature ($T_{max.degradation}$) with constant residual ($\gamma$). In case of RT–35HC, the $T_{onset}$ and $T_{max.degradation}$ were recorded of 208.18 °C and 249.29 °C with 0.31% $\gamma$. During the decomposition process, the hydrocarbon chains of pure RT–35HC breakdown into monomers ($CH_3CH$:$CH$+$CH_4$) because of evaporation. The detailed summary of $T_{onset}$ and $T_{max.degradation}$ of RT–35HC, mono and hy-

brid NCPCMs are provided in Table 5.2. The maximum $\gamma$ of 4.60% and 3.26%

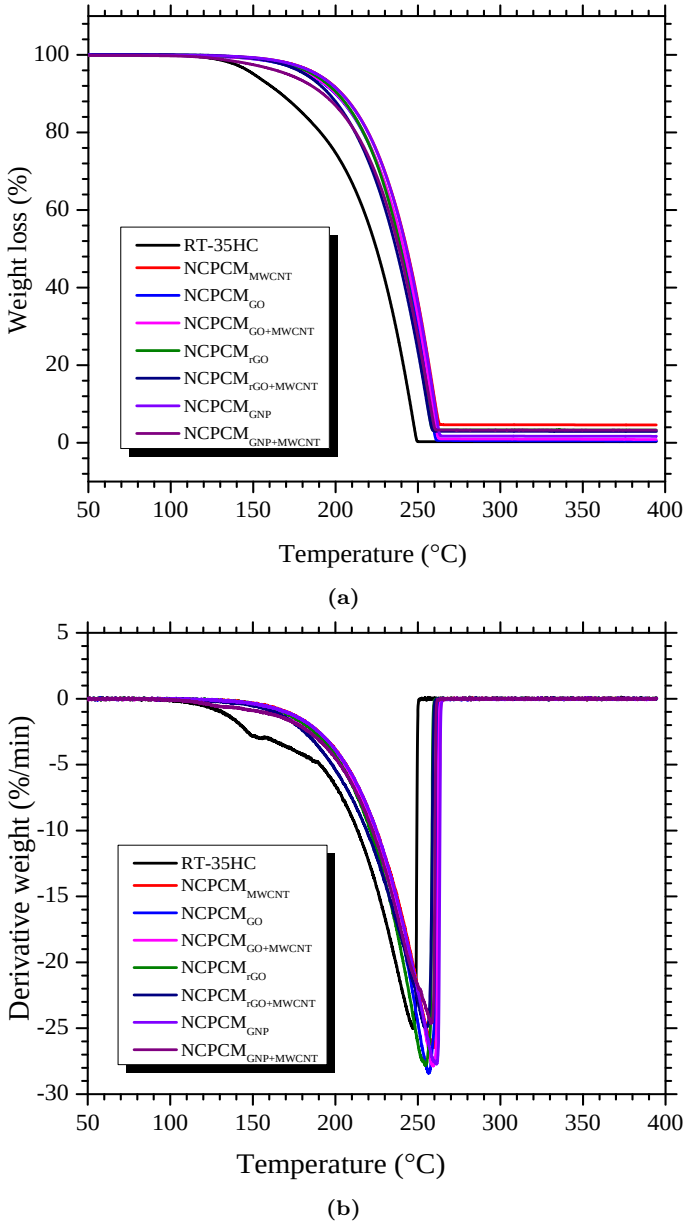


**Figure 5.7:** *(a)-TGA and (b)- DTGA thermograms of carbon–additives mono and hybrid NCPCMs.*

were obtained for NCPCM$_{MWCNT}$ and NCPCM$_{GNP+MWCNT}$, respectively, and remained constant subsequently. For mono and hybrid NCPCMs, the GNP, GO, rGO, MWCNT, GNP+MWCNT, GO+MWCNT and rGO+MWCNT create a protective layer on RT–35HC surface. This protective layer delays the vaporization of RT–35HC during the thermal degradation. The DTGA curves of RT–35HC, mono and hybrid NCPCMs are shown in Fig. 5.7b and revealed that addition of GNP, GO, rGO, MWCNT, GNP+MWCNT, GO+MWCNT

and rGO+MWCNT nanoparticles have improved the thermal stability. There is no decompositions was observed in samples until ∼140°C. The TGA and DTGA results revealed that hybrid NCPCMs have the best thermal and chemical stability which can be potentially used for thermal management of applications. This improved capability of thermal stability can be explained by the following reasons: (i) *the $T_{onset}$ is related to the entire specific heat capacity of NCPCMs which can be raised by the specific heat capacity of GNP, GO, rGO, MWCNT, GNP+MWCNT, GO+MWCNT and rGO+MWCNT nanoparticles*, and (ii) *enhanced thermal conductivity of NCPCMs which can transfer heat faster and uniformly within the PCM* (Chen et al., 2017).

Table 5.2: *The decomposition temperatures and residual amount of carbon–additives mono and hybrid NCPCMs.*

| Sample | $T_{onset}$ (°C) | $T_{max.degradation}$ (°C) | $\gamma$ (%) |
|---|---|---|---|
| RT–35HC | 208.18 | 249.29 | 0.31 |
| $NCPCM_{MWCNT}$ | 226.15 | 262.60 | 4.60 |
| $NCPCM_{GO}$ | 225.21 | 260.60 | 0.60 |
| $NCPCM_{GO+MWCNT}$ | 225.93 | 262.12 | 1.02 |
| $NCPCM_{rGO}$ | 223.38 | 258.25 | 3.34 |
| $NCPCM_{rGO+MWCNT}$ | 218.53 | 258.45 | 2.98 |
| $NCPCM_{GNP}$ | 227.27 | 263.14 | 1.65 |
| $NCPCM_{GNP+MWCNT}$ | 219.88 | 260.26 | 3.26 |

### 5.3.5 Phase–change thermal properties analysis

The endothermic and exothermic peaks of RT–35HC, mono and hybrid NCPCMs were analysed to determine the phase–change thermal properties, as shown in Fig. 5.8. Figs. 5.8a and 5.8b present the heating and cooling curves, respectively, of RT–35HC, mono and hybrid NCPCMs and measured values of latent–heat of melting/solidification and phase–transition temperatures are summarized in Table 5.3. There is slight variation in peak melting and solidification temperatures observed of RT–35HC because of addition of GNP, GO, rGO and MWCNT nanoparticles. Moreover, due to the addition of nanoparticles latent–heat of melting and solidification of $NCPCM_{MWCNT}$, $NCPCM_{GO}$, $NCPCM_{GO+MWCNT}$, $NCPCM_{rGO}$, $NCPCM_{rGO+MWCNT}$, $NCPCM_{GNP}$ and $NCPCM_{GNP+MW}$

were decreased expectedly. It can be revealed from Fig. 5.8a that single endothermic peaks are obtained of RT–35HC, mono and hybrid NCPCMs which is indicating an isomorphous crystalline form of RT–35HC either in a pristine state or in nanocomposite form. Contradictory, during the solidification process a bimodal crystallization behaviour is obtained of all samples. The first smaller peak represent to the crystallization temperature while second peak corresponds to the modification or transition of lattice structure from triclinc structure to the hexagonal structure (Kolesnikov and Syunyaev, 1985; Ghossein et al., 2017). This two phase transformation phenomenon is attributed due to the appearance of a metastable rotator phase prior to completing the complete crystallization as a results of the heterogeneous nucleation during the cooling process (Yavari et al., 2011; Arshad et al., 2020b). Below the melting temperature of paraffins always exist in crystalline form either they exist in pure single chemical compound or in composite form (Nabil and Khodadadi, 2013). According to the magnitude and parity of $n$ in n–alkanes, $C_{2n}H_{2n}+2$ are crystallized in four isostructural sets for $n \geq 6$ (Nyburg and Potworowski, 1973):

- Triclinic, for $n$ $(even) \leq 26$ (Mller and Lonsdale, 1948)
- Monoclinic, if the paraffin is pure, for $26 \leq n$ $(even) \leq 36$ (Broadhurst, 1962)
- Orthorhombic, if the paraffin is not pure, for $26 \leq n$ $(even) \leq 36$ (Broadhurst, 1962)
- Orthorhombic, for $11 \leq n$ $(odd) \leq 39$ (Piper and Malkin, 1930)

Fig. 5.8c presents the comparison of phase–change enthalpies while melting ($\Delta H_m$) and solidification ($\Delta H_s$) of RT–35HC, mono and hybrid NCPCMs. For RT–35HC, the $\Delta H_m$ and $\Delta H_s$ are obtained of 255.88 and 260.06 J/g, respectively. It can be seen that latent–heat enthalpies of hybrid NCPCM were decreased higher than the mono NCPCMs. The reduction in $\Delta H_m$ was obtained

of 7.21%, 8.02% and 9.79% for NCPCM$_{GO+MWCNT}$, NCPCM$_{rGO+MWCNT}$ and NCPCM$_{GNP+MWCNT}$, respectively, compared with RT–35HC. Similarly, the reduction in $\Delta H_s$ was 7.30%, 8.33% and 9.95% for NCPCM$_{GO+MWCNT}$, NCPCM$_{rGO+MWCNT}$ and NCPCM$_{GNP+MWCNT}$, respectively, compared with RT–35HC. This reduction in $\Delta H_m$ and $\Delta H_s$ are because of the dispersion of mono (GNP, GO, rGO and MWCNT) and hybrid (GO+MWCNT, rGO+MWCNT and GNP+MWCNT) nanoparticles. The mass fraction ($\omega$) of RT–35HC in NCPCMs is determined by the Eq. 5.1:

$$\omega = \frac{\Delta H_{NCPCM}}{\Delta H_{PCM}} \times 100 \tag{5.1}$$

Where, $\Delta H_{NCPCM}$ and $\Delta H_{PCM}$ are the endothermic latent–heat of NCPCM and pure PCM, respectively. While synthesising of NCPCMs, mono (GNP, GO, rGO and MWCNT) and hybrid (GO+MWCNT, rGO+MWCNT and GNP+MWCNT) nanoparticles replace the RT–35HC molecules. As a consequence, the latent–heat capacity of NCPCM is reduced which lead to the less absorption or release of more energy. Fig. 5.8d presents results of degree of subcooling ($\Delta T$) of RT–35HC, mono and hybrid NCPCMs. In case of RT–35HC, the peak melting (T$_m$) and crystallization (T$_c$) temperatures are obtained of 36.09 °C and 31.71 °C, respectively. The results of $\Delta T$ of mono and hyrid NCPCMs revealed a fluctuating trend which is because of the type of nanoparticles. Since, the loading content of mono (GNP, GO, rGO and MWCNT) and hybrid (GO+MWCNT, rGO+MWCNT and GNP+MWCNT) nanoparticles is constant. The deviations in T$_m$ in case of hybrid for NCPCM$_{GO+MWCNT}$, NCPCM$_{rGO+MWCNT}$ and NCPCM$_{GNP+MWCNT}$ are found of 0.06%, 1.33% and 0.22%, respectively, compared to the RT–35HC. The variation in T$_m$ and T$_c$ are due to the crystallization confinement of mono (GNP, GO, rGO and MWCNT) and hybrid (GO+MWCNT, rGO+MWCNT and GNP+MWCNT) nanoparticles surface layers within the NCPCMs. In addition, the interfacial surface layers causes to form the imperfect RT–35HC and results in a slight variation in T$_m$ and T$_c$. These factors cause an increase in $\Delta T$. The heterogeneous nu-

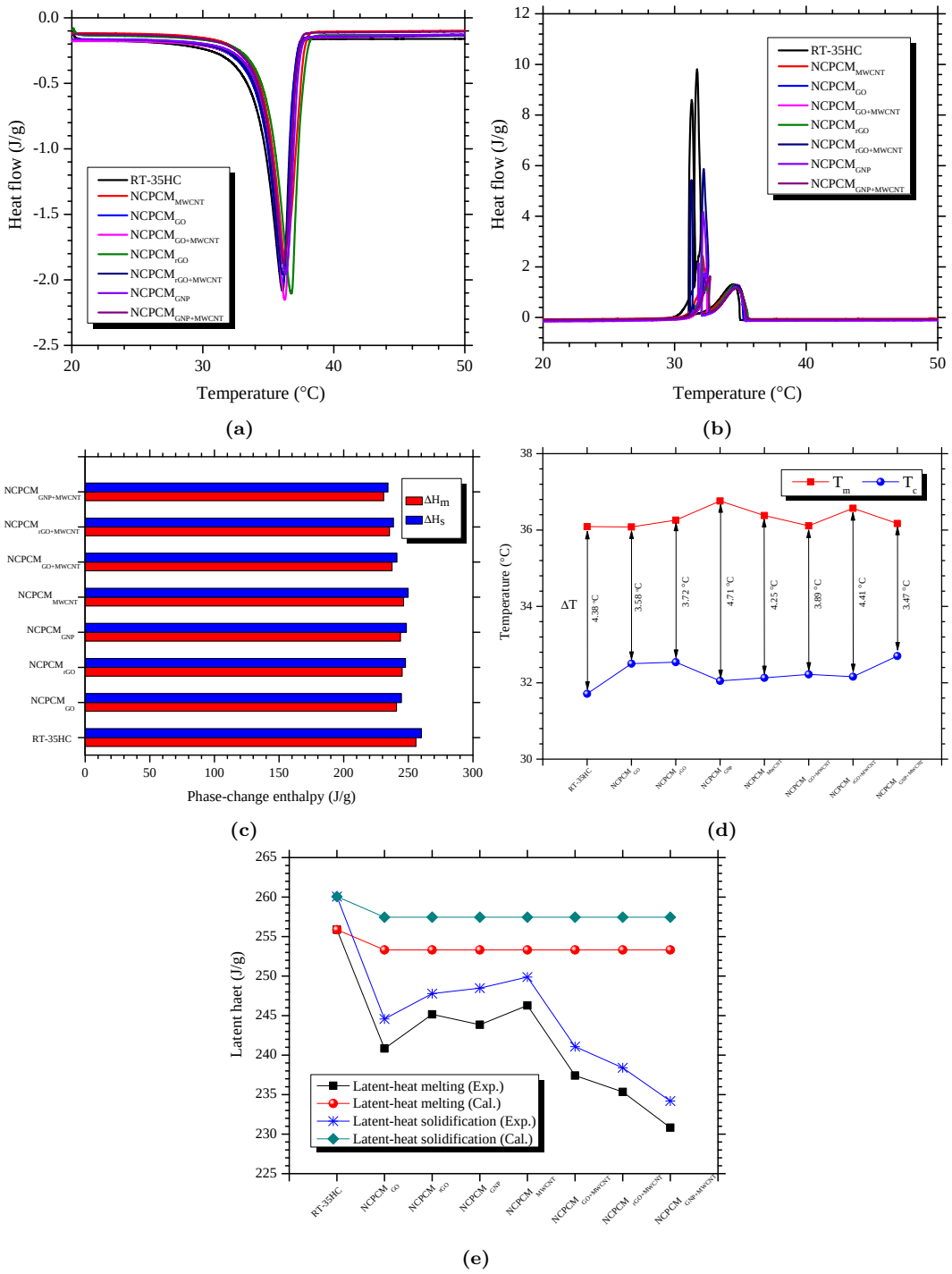


**Figure 5.8:** *The results of (a) heating (b) cooling (c) phase–change enthalpies (d) degree of subcooling and (e) comparison of experimental and calculated latent–heats of carbon–additives mono and hybrid NCPCMs.*

cleation may be favoured because of the addition of nanoparticles at the cost of crystallization point depression (Yavari et al., 2011). It has been extensively reported that the high $\Delta T$ is evidently disadvantageous for utilization of PCM in thermal management because it can result in a hysteresis response to heat transfer.

The effect of experimental and calculated latent–heats of melting and solidification of RT–35HC and NCPCMs are illustrated in Fig. 5.8e. The Eq. 5.2 was used to calculate the theoretical values of latent–heats (Tian et al., 2015; Arshad et al., 2020b):

$$\Delta L_{NCPCM} = \Delta L_{PCM} \cdot \omega = \Delta L_{PCM}(1 - \varphi) \tag{5.2}$$

where, $\Delta L_{NCPCM}$ is the calculated latent–heat of melting and solidification of NCPCM, $\Delta L_{PCM}$ represents the latent–heat of pure PCM, $\omega$ and $\varphi$ are the mass fraction of pure PCM and nanoparticles, respectively. The results reveal that measured values of latent–heats of melting and solidification are lower than the calculated values. The deviations in values are because of the surface morphology, particle size, shape, crystal structure and thermophysical properties (i.e. density, surface area, thermal conductivity, specific heat etc.) of mono (GNP, GO, rGO and MWCNT) and hybrid (GO+MWCNT, rGO+MWCNT and GNP+MWCNT) nanoparticles. Since the mass fraction of all nanoparticles in constant in mono and hybrid NCPCMs. The relative error (RE) in experimental and calculated values of latent–heat of melting and solidification was obtained of $3 \sim 9\%$ for all NCPCMs, given in Table 5.3. Similar deviations in experimental and calculated latent–heats of melting and solidification have been reported in previous studies (Sarı et al., 2009; Wang et al., 2009b; Tian et al., 2015; Sharma et al., 2016).

Table 5.3: *Phase–change thermal properties of carbon–additives mono and hybrid NCPCMs*.*

| Sample | Heating | | | | | Cooling | | | | | $\omega$ (%) | $\Delta$ T (°C) |
|---|---|---|---|---|---|---|---|---|---|---|---|---|
| | $T_{oset,m}$ (°C) | $T_{peak,m}$ (°C) | $\Delta H_{m,exp}$ (J/g) | $\Delta H_{m,cal}$ (J/g) | RE (%) | $T_{oset,c}$ (°C) | $T_{peak,c}$ (°C) | $\Delta H_{c,exp}$ (J/g) | $\Delta H_{c,cal}$ (J/g) | RE (%) | | |
| RT–35HC | 34.06 | 36.09 | 255.88 | - | - | 31.47 | 31.71 | 260.79 | - | - | 100.00 | 4.38 |
| $NCPCM_{GO}$ | 34.31 | 36.08 | 240.83 | 253.32 | 4.93 | 32.44 | 32.50 | 244.57 | 257.46 | 5.01 | 94.12 | 3.58 |
| $NCPCM_{rGO}$ | 34.47 | 36.26 | 245.16 | 253.32 | 3.22 | 32.47 | 32.54 | 247.79 | 257.46 | 3.76 | 95.81 | 3.72 |
| $NCPCM_{GNP}$ | 34.81 | 36.76 | 243.85 | 253.32 | 3.74 | 31.99 | 32.05 | 248.48 | 257.46 | 3.49 | 95.30 | 4.71 |
| $NCPCM_{MWCNT}$ | 34.54 | 36.38 | 246.28 | 253.32 | 2.78 | 32.03 | 32.13 | 249.88 | 257.46 | 2.94 | 96.25 | 4.25 |
| $NCPCM_{GO+MWCNT}$ | 34.32 | 36.11 | 237.42 | 253.32 | 6.28 | 32.04 | 32.22 | 241.08 | 257.46 | 6.36 | 92.79 | 3.89 |
| $NCPCM_{rGO+MWCNT}$ | 35.09 | 36.57 | 235.35 | 253.32 | 7.09 | 32.06 | 32.16 | 238.39 | 257.46 | 7.41 | 91.98 | 4.41 |
| $NCPCM_{GNP+MWCNT}$ | 34.46 | 36.17 | 230.82 | 253.32 | 8.88 | 32.57 | 32.70 | 234.19 | 257.46 | 9.04 | 90.21 | 3.47 |

*$T_{oset,m}$: onset melting temperature, $T_{peak,m}$: peak melting temperature, $\Delta H_{m,exp}$: experimental latent-heat of melting,
$\Delta H_{m,cal}$: calculated latent-heat of melting, $T_{oset,c}$: onset solidifying temperature, $T_{peak,c}$: peak solidifying temperature,
$\Delta H_{c,exp}$: experimental latent–heat of solidifying, $\Delta H_{c,cal}$: calculated latent–heat of solidifying, RE: relative error,
$\omega$: Mass percentage of RT–35HC, $\Delta$T: Degree of subcooling

### 5.3.6 Thermal conductivity analysis

Effective thermal conductivity and effective thermal conductivity enhancement of RT–35HC, mono (NCPCM$_{MWCNT}$, NCPCM$_{GO}$, NCPCM$_{rGO}$ and NCPCM$_{GNP}$) and hybrid (NCPCM$_{GO+MWCNT}$, NCPCM$_{rGO+MWCNT}$, and NCPCM$_{GNP+MWCNT}$) NCPCMs were measured as a function of temperature from 20 °C to 55 °C, as shown in Fig. 5.9. The result showed a monotonic behaviour of effective thermal conductivity by dispersing the MWCNT, GO, rGO and GNP nanoparticles. The effective thermal conductivity of NCPCMs was increased because of higher effective thermal conductivity of MWCNT, GO, rGO and GNP nanoparticles, as shown in Fig. 5.9a. Effective thermal conductivity of RT–35HC, mono and hybrid NCPCMs was measured for three different phases of solid–phase, phase–change and liquid–phase at different temperature ranges of 20–30 °C, ∼35 °C and liquid phase (40–55 °C, respectively. A constant trend was achieved in enhancement in effective thermal conductivity of all samples both in solid and liquid phases and higher effective thermal conductivity was obtained in solid phase. This shows that effective thermal conductivity is strongly depended on temperature change. The higher effective thermal conductivity in solid–phase is because of the orderly microstructure of RT–35HC, mono and hybrid NCPCM compared to the disorderly microstructure exists in liquid–phase. Since, the heat flow, in solid and liquid, is associated with the lattice vibration and motion of the free electron as the molecules vibrate within their lattice structures. This lattice vibration and free electron motion is stronger in solids than the liquids. Thus, RT–35HC and NCPCMs exhibit the higher effective thermal conductivity in solid–phase than liquid–phase. A sudden increase in effective thermal conductivity was observed at ∼35 °C for all samples. The phenomenon of sharp increase of effective thermal conductivity is associated with phase transition process of RT–35HC. At phase–transition temperature, the random motion of molecules occur within disordered microstructure of matrix in solid–

liquid phase transformation. This molecular motion collapse the percolation network established by nanoparticles under the solid phase (Prasher et al., 2005; Wu et al., 2020). In solid–phase at 20 °C, the maximum effective ther-

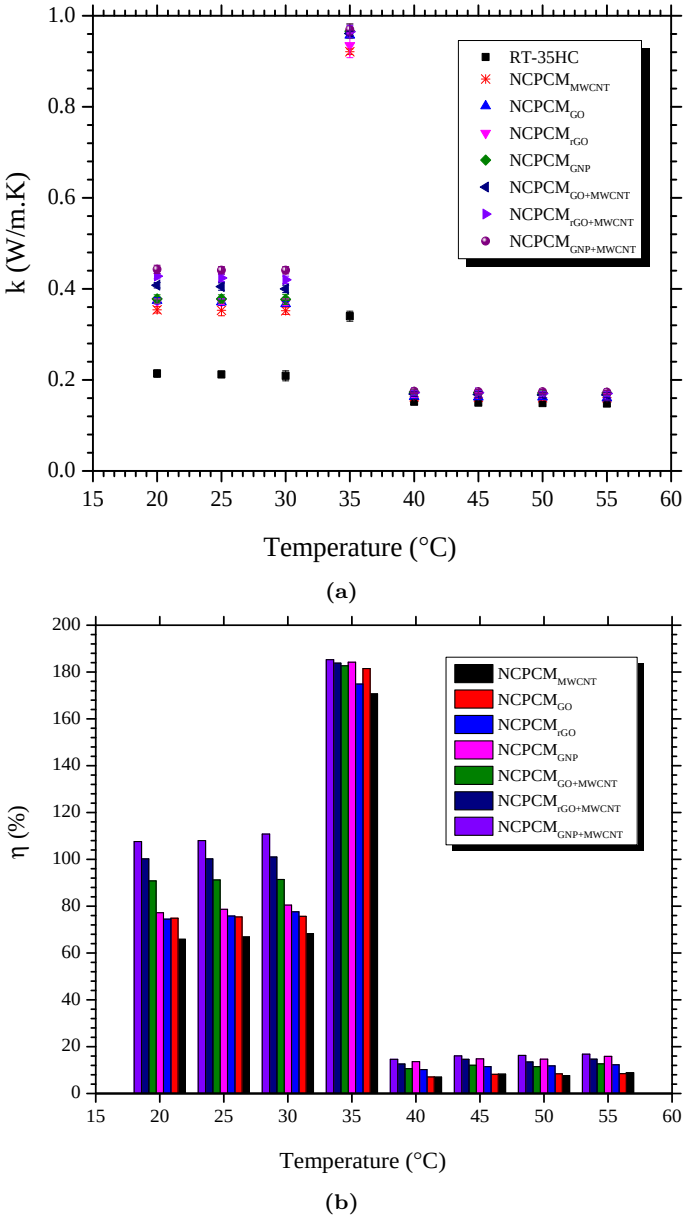


**Figure 5.9:** *The results of (a) effective thermal conductivity and (b) effective thermal conductivity enhancement factor of carbon–additives mono and hybrid NCPCMs as a function of temperature.*

mal conductivities of 0.214, 0.374, 0.373, 0.378, 0.354, 0.408, 0.428 and 0.443 W/m.K were obtained for RT–35HC, NCPCM$_{GO}$, NCPCM$_{rGO}$, NCPCM$_{GNP}$, NCPCM$_{MWCNT}$, NCPCM$_{GO+MWCNT}$, NCPCM$_{rGO+MWCNT}$, and NCPCM$_{GNP+MWCNT}$, respectively. At phase–change temperature (∼35 °C), the maximum effective thermal conductivities were found of 0.340, 0.957, 0.935, 0.966, 0.921, 0.961,

0.965 and 0.970 W/m.K were obtained for RT–35HC, NCPCM$_{GO}$, NCPCM$_{rGO}$, NCPCM$_{GNP}$, NCPCM$_{MWCNT}$, NCPCM$_{GO+MWCNT}$, NCPCM$_{rGO+MWCNT}$, and NCPCM$_{GNP+MWCNT}$, respectively. Since the temperature between 34–36 °C is the phase transition temperature range of RT–35HC at this point all the samples are metastable condition. At phase transformation temperature range, the crystal structure of RT–35HC becomes unstable. With the increase of temperature, the molecular vibrational motion accelerate with lattice results in increases the effective thermal conductivity sharply at melting temperature (∼35 °C) (Wang and Meng, 2010; Wu et al., 2020). It be seen that hybrid NCPCMs have the thermal conductivity compared to the mono NCPCMs. More further, the higher effective thermal conductivity was achieved for NCPCM$_{GNP+MWCNT}$ compared with NCPCM$_{GO+MWCNT}$ and NCPCM$_{rGO+MWCNT}$ in case of hybrid NCPCMs. The results of percentage enhancement in effective thermal conductivity of mono and hybrid NCPCMs is shown in Fig. 5.9b. The Eq. 5.3 was used to calculate the effective thermal conductivity enhancement factor ($\eta$) of mono and hybrid NCPCMs.

$$\eta = \frac{k_{NCPCM} - k_{PCM}}{k_{PCM}} \times 100 \tag{5.3}$$

where, $k_{NCPCM}$ and $k_{PCM}$ are the thermal conductivity of the NCPCM and pure PCM, respectively. Fig. 5.9b illustrates that the percentage enhancement of effective thermal conductivity increases for the case of mono and hybrid NCPCMs. The higher enhancement was achieved at phase transition temperature followed by solid–phase and then liquid–phase. The relative percentage enhancement in effective thermal conductivity was obtained of 74.9%, 77.7%, 77.%, 66.0%, 90.8%, 100.2%, and 107.6% for NCPCM$_{GO}$, NCPCM$_{rGO}$, NCPCM$_{GNP}$, NCPCM$_{MWCNT}$, NCPCM$_{GO+MWCNT}$, NCPCM$_{rGO+MWCNT}$, and NCPCM$_{GNP+MWCNT}$, respectively, at 20°C compared with RT–35HC. However, the maximum enhancement in effective thermal conductivity was achieved at phase–change temperature of ∼ 35°C. The maximum enhancement was ob-

tained of 181.5%, 174.9%, 184.2%, 170.7%, 182.7%, 183.8%, and 185.3% for NCPCM$_{GO}$, NCPCM$_{rGO}$, NCPCM$_{GNP}$, NCPCM$_{MWCNT}$, NCPCM$_{GO+MWCNT}$, NCPCM$_{rGO+MWCNT}$, and NCPCM$_{GNP+MWCNT}$, respectively, compared with RT–35HC. Moreover, it can be seen from Fig. 5.9b that hybrid NCPCMs have the highest effective thermal conductivity enhancement compared with mono NCPCMs. The variation in effective thermal conductivity results of mono and hybrid NCPCMs is because of the surface morphology, particle size, shape, crystal structure, thermophysical properties (i.e. density, surface area, thermal conductivity, specific heat etc.) as well as the inherent thermal conductivity of mono (GNP, GO, rGO and MWCNT) and hybrid (GO+MWCNT, rGO+MWCNT and GNP+MWCNT) nanoparticles. Furthermore, the thermal boundary layer resistance between the nanoparticles and matrix molecules have significant factor of discrepancies (Mahian et al., 2019).

The effective thermal conductivity enhancement of NCPCMs is based on several factors due to the diffusion of nanoparticles such as concentrations, Brownian motion, clustering, interfacial thermal resistance, purity, high aspect ratio and intermolecular interaction (Jebasingh and Arasu, 2020a). At phase transmission of NCPCMs, the effective thermal conductivity enhancement is higher because of the constant kinetic energy despite of phase change occurrence (Jebasingh and Arasu, 2020b). In addition of this, the mechanism of effective thermal conductivity of hybrid (GO+MWCNT, rGO+MWCNT and GNP+MWCNT) nanoparticles in RT–35HC is shown Fig. 5.10. An ideal schematic representation of 1D (MWCNT) and 2D (GO/rGO/GNP) nanoparticles structural arrangement is presented that illustrating a three–dimensional (3D) structural matrix. This 3D matrix of hybrid NCPCMs form the 3D path for which the *phonon transmission* and *lattice vibration* transport the heat effectively in all directions of the RT–35HC (Zou et al., 2018; Arshad et al., 2020b). In non–metallic PCMs, the vibration of crystal lattice is the main mechanism of heat conduction. Consequently, the phonons are the main carriers of heat flow in the PCM (Wu et al., 2020). More further, the thermal

boundary resistance is reduced in hybrid NCPCMs between nanoparticles and PCM which enhances the heat flow, resulting in improves of the thermal conductivity.

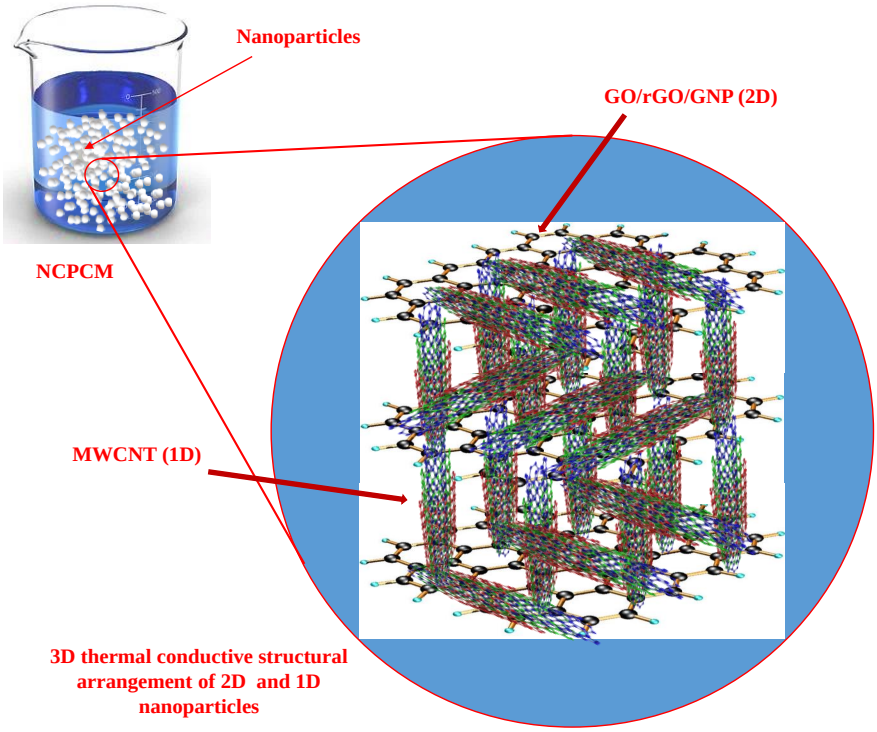


**Figure 5.10:** *Schematic representation of 3D thermal conductive arrangement of carbon–additives hybrid NCPCMs.*

### 5.3.7 Specific heat capacity analysis

Fig. 5.11 illustrates the specific heat capacity ($C_p$) of RT–35HC, mono and hybrid NCPCMs for both solid and liquid phases. The results are presented as a function of temperature from temperature range 10–60 °C. Although the $C_p$ has less effect in total thermal energy storage density because of less thermal energy storage in sensible heating phase. However, the $C_p$ contributes the additional effects during heat transfer rate within a PCM based system, calculated by Eq. 5.4 as follows:

$$Q = \int_{T_i}^{T_m} mC_p.dt + m\alpha_m \Delta H_m + \int_{T_m}^{T_f} mC_p.dt \tag{5.4}$$

where, $Q$ (J) is the quantity of total heat stored, $T_i$ (°C), $T_m$ (°C) and $T_f$ (°C) are the initial, melting and final temperatures, respectively, $m$ (kg) mass of the heat storage medium, $C_p$ (J/kg.K) is the specific heat capacity, $\alpha_m$ is the faction of melted mass and $\Delta H_m$ (J/kg) is the heat of fusion per unit mass. It can be evaluate from Eq. 5.4 that specific heat capacity is important thermal property to investigate the heat transfer and heat storage analysis.

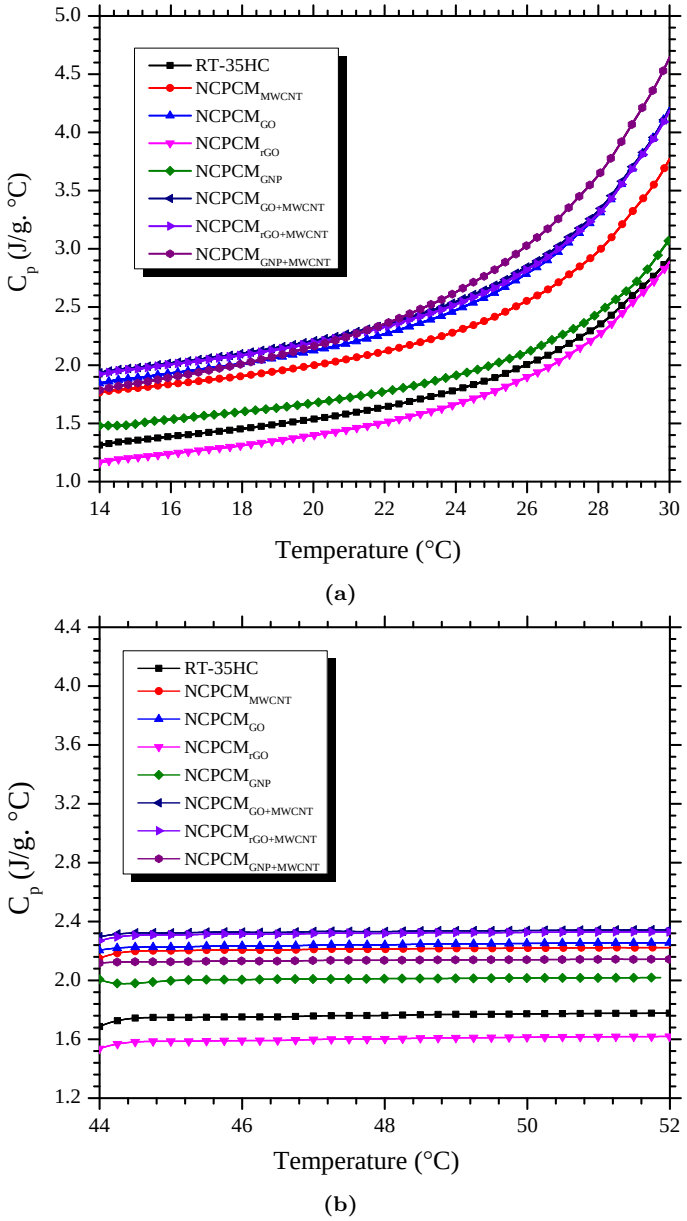


**Figure 5.11:** *Specific heat capacity curves of carbon–additives mono and hybrid NCPCMs: (a) solid-phase (b) liquid-phase.*

The comparison of $C_p$ of RT–35HC, mono and hybrid NCPCMs shows that $C_p$ increases gradually with temperature between 14 °C to 30 °C in solid–

phase while it remains constant in liquid–phase, as shown in Figs. 5.12a and 5.12b, respectively. Similar trend in enhancement in $C_p$ has been reported in previous studied (Mehrali et al., 2014a; Aydın and Aydın, 2012). The $C_p$ of RT–35HC is obtained of 1.88 and 1.77 J/g.°C for solid and liquid phases, respectively. The $C_p$ results of mono and hybrid NCPCMs reveal that $C_p$ increases both in solid and liquid phases. The $C_p$ values of 2.40, 2.61, 1.77, 2.0, 2.34, 2.33 and 2.14 J/g.°C were determined for NCPCM$_{MWCNT}$, NCPCM$_{GO}$, NCPCM$_{rGO}$, NCPCM$_{GNP}$, NCPCM$_{GO+MWCNT}$, NCPCM$_{rGO+MWCNT}$, and NCPCM$_{GNP+MWCNT}$, respectively, in solid–phase at 25 °C. Whereas, for liquid–phase at 50 °C, the $C_p$ values of 2.22, 2.25, 1.61, 2.02, 2.67, 2.65 and 2.80 J/g.°C were obtained for NCPCM$_{MWCNT}$, NCPCM$_{GO}$, NCPCM$_{rGO}$, NCPCM$_{GNP}$, NCPCM$_{GO+MWCNT}$, NCPCM$_{rGO+MWCNT}$, and NCPCM$_{GNP+MWCNT}$, respectively. The polynomial equations are generated for solid phase from 14 °C to 30 °C for RT–35HC, mono and hybrid NCPCMs after curve fitting the experimental data mentioned in Eq. 5.5 and coefficients are given in Table 5.4.

$$C_P = AT^3 + BT^2 + CT + D \tag{5.5}$$

The comparison result of $C_p$ and $C_p$ enhancement factor ($\zeta$) of RT–35HC, mono and hybrid NCPCMs are presented in Figs. 5.12a and 5.12b, respectively. The specific heat capacity enhancement factor ($\zeta$) is calculated to evaluate the effect of nanoparticles in enhancement of heat transfer rate in the PCM, as given by Eq. 5.6:

$$\zeta = \frac{C_{P_{NCPCM}} - C_{P_{PCM}}}{C_{P_{PCM}}} \times 100 \tag{5.6}$$

where, $C_{P_{NCPCM}}$ and $C_{P_{PCM}}$ are the $C_p$ of the NCPCM and PCM, respectively. The enhancements in $C_p$ are obtained of 27.65%, 38.54%, −6.22%, 6.37%, 24.27%, 23.58% and 13.75% for NCPCM$_{MWCNT}$, NCPCM$_{GO}$, NCPCM$_{rGO}$, NCPCM$_{GNP}$, NCPCM$_{GO+MWCNT}$, NCPCM$_{rGO+MWCNT}$, and NCPCM$_{GNP+MWCNT}$, respectively, in solid–phase at 25 °C compared to the RT–35HC. Similarly, the enhancements in $C_p$ for NCPCM$_{MWCNT}$, NCPCM$_{GO}$, NCPCM$_{rGO}$, NCPCM$_{GNP}$,

NCPCM$_{GO+MWCNT}$, NCPCM$_{rGO+MWCNT}$, and NCPCM$_{GNP+MWCNT}$ are determined of 25.21%, 27.02%, −8.95%, 13.76%, 50.81%, 49.61% and 58.09%, respectively, in liquid–phase at 50 °C compared to the RT–35HC. From Fig.5.12, it is revealed that variations in $C_p$ are significantly depends on the type of nanoparticles and its inherent $C_p$ in pure form. In addition, the nanoparticles size, density, surface area and morphology contribute the most prominent effects in enhancement in $C_p$.

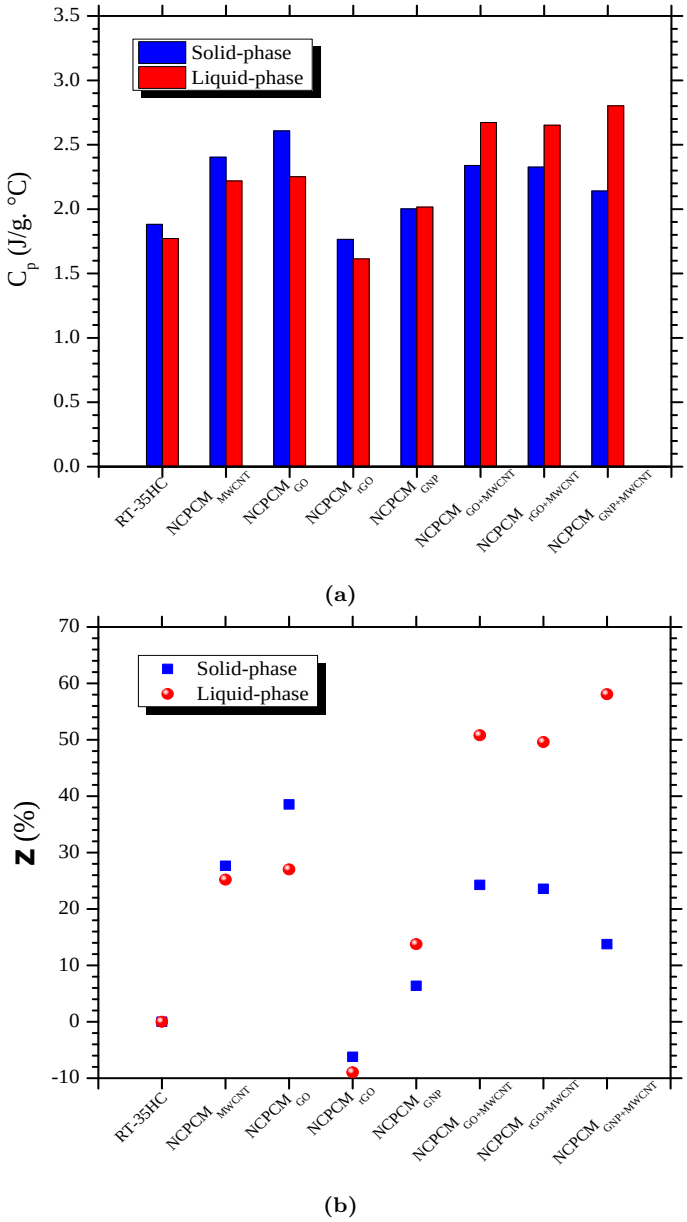


**Figure 5.12:** *(a) Comparison of specific heat capacity and (b) specific heat capacity enhancement of carbon–additives mono and hybrid NCPCMs.*

The enhancement in $C_p$ is associated with the following reasons: (i) an en-

Table 5.4: *Coefficients of the third–order polynomials in solid–state, $C_p$ (J/g.°C).*

| | A | B | C | D | $R^2$ |
|---|---|---|---|---|---|
| RT–35HC | 0.0006 | -0.0349 | 0.6687 | -2.9832 | 0.9988 |
| NCPCM$_{MWCNT}$ | 0.0009 | -0.0489 | 0.9319 | -4.1725 | 0.9979 |
| NCPCM$_{GO}$ | 0.0010 | -0.0566 | 1.0788 | -5.0226 | 0.9981 |
| NCPCM$_{rGO}$ | 0.0007 | -0.0380 | 0.7278 | -3.5055 | 0.9986 |
| NCPCM$_{GNP}$ | 0.0007 | -0.0385 | 0.7426 | -3.3195 | 0.9976 |
| NCPCM$_{GO+MWCNT}$ | 0.0010 | -0.0534 | 1.0192 | -4.5702 | 0.9981 |
| NCPCM$_{rGO+MWCNT}$ | 0.0010 | -0.0548 | 1.0453 | -4.7404 | 0.9979 |
| NCPCM$_{GNP+MWCNT}$ | 0.0010 | -0.0556 | 1.0507 | -4.9125 | 0.9990 |

hanced anharmonicity of the atomic interaction due to their volume expansion, (ii) impurities (Hellstern et al., 1989), (iii) the grain boundaries of nanosized materials which possess an excess volume with respect to the perfect crystal lattice and (iv) the high specific surface energies related to the high surface area of the nanoparticles per unit volume (Wang et al., 2001, 2006). Theoretically, the $C_p$ of materials is directly related to crystal structure, or its vibrational and configurational entropy which significantly affected by the nearest–neighbour configurations. Nanosized materials are structurally characterized by the metastable grain boundaries in which the nearest–neighbour configurations are much different from the coarse–grained state (Wang et al., 2001). The anomalous enhancement in $C_p$ can be elaborated by three independent inter–molecular interaction mechanisms (or modes), as shown in Fig. 5.13.

- ***Higher $C_p$ of nanoparticles compared to the bulk material due to higher specific surface energy*:** Since, the size of nanoparticles lies in nanometer scale and $C_p$ predicted from theoretical thermal equilibrium model for mixture, given in Eq. 5.7, should be the function of the nominal nanoparticle diameter. In a crystalline lattice of the nanoparticles, the surface atoms are less constrained because of the less number of bonds. As the bonding between the atoms can be visualized acting like spring, the surface atoms vibrate at a higher amplitudes and lower natural frequency resulting in the higher surface energy. Therefore, phonon

spectrum of nanoparticles can be analysed and have discrete numbers which depends on the size of the nanoparticles. When the size of the nanoparticles is decreased the specific heat capacity of the nanoparticles is enhanced (Wang et al., 2001, 2006).

$$C_{p,t} = \frac{\phi_p \rho_p C_{p,p} + \phi_f \rho_f C_{p,f}}{\phi_p \rho_p + \phi_f \rho_f} \tag{5.7}$$

where, $C_{p,t}$ is the effective $C_p$ of NCPCM, $C_{p,p}$ and $C_{p,f}$ are specific heat capacities nanoparticle and fluid (PCM), respectively, $\rho_p$ and $\rho_f$ are densities of nanoparticle and fluid (PCM), respectively and $\phi_p$ and $\phi_f$ are volume fractions of nanoparticle and fluid (PCM), respectively.

- ***Interfacial interaction energy of solid–fluid*:** Since, the nanoparticles have the highly surface area per unit mass which cause to increase the interfacial interaction between the nanoparticles and surrounding liquid molecules resulting in increases the interfacial thermal resistance and capacitance. The interfacial interaction resistance causes a barrier to heat flow between the nanoparticles and surrounding liquid molecules that decreases the benefit of dispersing the highly conductive nanoparticles. In NCPCM, interfacial region obstructs phonon transport due to phonon scattering which is found in organic/inorganic interface results in thermal transport is also affected by the chemistry of such interfaces (Losego and Cahill, 2013; Ong et al., 2013; Mehra et al., 2018). Due to lattice mismatch at interfacial interaction boundary layer, various phonon scattering like elastic, inelastic, specular, or diffusive can adversely impact heat conduction (Imamura et al., 2003; Chen et al., 1997; Hopkins and Norris, 2007; Mehra et al., 2018). The highly interfacial thermal resistance and capacitance enhance the additional thermal energy storage mechanism due to the vibrational energies between the nanoparticles atoms and adhering liquid molecules (Prasher et al., 2005; Xue et al., 2004).

- ***Adhesive semi–solid layering of liquid molecules adhering to the nanoparticles*:** The liquid molecules of molten PCM adhering on the surface of the nanoparticles create a semi–solid liquid layer. The liquid molecule on surface of the nanoparticles act like a semi–solid layer with higher thermal characteristics than the bulk liquid PCM. The thickness of this adhesion layer can be approximately 2–5 nm, depend on the surface energy of the nanoparticles, evaluated by molecular dynamics simulations which is directly proportional to size of the nanoparticles. The thickness of that adhesive semi–solid liquid layers depend on the surface energy of the nanoparticles and possess smaller inter-molecular spacing on the surface compared to the higher inter-molecular spacing in the bulk liquid. Hence, this layering have higher thermal transport than the bulk PCM and increases the effective $C_p$ of NCPCMs. In addition to this, the number of adhered layers of the liquid molecules are the function of surface energy of the crystalline interface. The nanoparticles of smaller size with constant weight concentration, the mass fraction of adhered semi–solid liquid layer molecules is increased proportionally on the nanoparticles surface (Oh, 2005; Shin and Banerjee, 2011). The vibrational properties and interactions between the atoms of nanoparticles and liquid molecules at the interface are also altered because of the effect of interface pressure. Effect of pressure has two primary consequences. First, decrease separation in adjacent polymeric chains by decreasing their atomic distance. Secondly, increase the frequency of vibration of molecules. Because of the effect of pressure at the interface, this semi–solid layering adhering to the surface lattice-atoms. a compression layer of more ions is generated which absorbs more specific heat capacity.

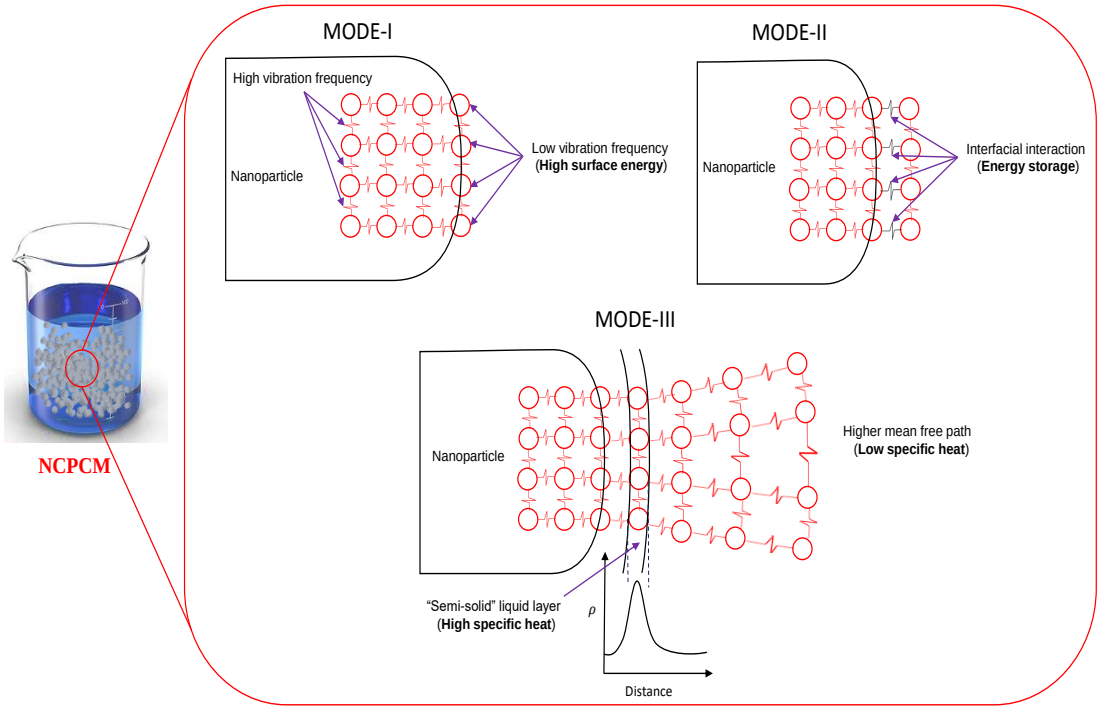


**Figure 5.13:** *Schematic representation of inter-molecular interaction modes in NCPCMs causes the enhancement in specific heat capacity (a) MODE–I: High surface energy of the surface atoms in the lattice, (b) MODE–II: Interfacial interactions between the lattice atoms and liquid molecules, (c) MODE–III: A layer of semi–solid molecules adhering to the surface of lattice–atoms.*

## 5.4 Concluding remarks

This experimental study presents the development of carbon–additives nano–enhanced phase change materials (NCPCM) for the application of efficient thermal management systems (electronics, PV modules, Li–ion batteries etc.) and solar–thermal energy storage. The two major schemes of mono (MWCNT, GO, rGO and GNP) and hybrid (GO+MWCNT, rGO+MWCNT and GNP+MWCNT) nanoparticles were dispersed in PCM (RT–35HC) having constant mass concentration of 1.0 wt.%. The chemical, physical and thermal properties were determined using ESEM, FTIR, XRD, TGA, DSC and TCA and critical findings are summarized as follows:

- The ESEM and XRD results of microstructure and crystalline phase reveal the presence of MWCNTs, GO, rGO and GNP nanoparticles in

both mono and hybrid NCPCMs. More further, the uniform dispersion of both mono (MWCNT, GO, rGO and GNP) and hybrid (GO+MWCNT, rGO+MWCNT and GNP+MWCNT) nanoparticles was observed in all NCPCMs.

- No chemical interaction and peak shifting were observed neither in mono (NCPCM$_{MWCNT}$, NCPCM$_{GO}$, NCPCM$_{rGO}$ and NCPCM$_{GNP}$) nor in hybrid (NCPCM$_{GO+MWCNT}$, NCPCM$_{rGO+MWCNT}$ and NCPCM$_{GNP+MWCNT}$) NCPCMs. Thus, it can be proved that there is only physical interaction of all mono and hybrid nanoparticles with RT–35HC.

- The best chemical and thermal stability were achieved through TGA and DTGA analysis of all mono and hybrid NCPCMs. Further, it was observed that hybrid NCPCMs were more stable than mono NCPCMs because of $3D$ morphological nature of hybrid (GO+MWCNT, rGO+MWCNT and GNP+MWCNT) nanoparticles.

- The enhanced thermal conductivity results were obtained of hybrid NCPCM with thermal conductivities of 0.408, 0.428 and 0.443 W/m.K for NCPCM$_{GO+MWCNT}$, NCPCM$_{rGO+MWCNT}$, and NCPCM$_{GNP+MWCNT}$, respectively, compared with mono NCPCMs. The enhancement was achieved of 90.8%, 100.2% and 107.6% for for NCPCM$_{GO+MWCNT}$, NCPCM$_{rGO+MWCNT}$, and NCPCM$_{GNP+MWCNT}$ respectively, compared to the RT–35HC. It can concluded that hybrid NCPCM$_{GNP+MWCNT}$ with mass percentage ratio of 75%/25% has the highest thermal conductivity enhancement because of the optimum mass ratios, type and morphology of GNP+MWCNT nanoparticles.

- The DSC results reveal that latent–heat of fusion and solidification were decreased with the addition of both mono (MWCNT, GO, rGO and GNP) and hybrid (GO+MWCNT, rGO+MWCNT and GNP+MWCNT) nanoparticles in all NCPCMs. The latent–heat of fusion for NCPCM$_{GO}$, NCPCM$_{rGO}$, NCPCM$_{GNP}$, NCPCM$_{MWCNT}$, NCPCM$_{GO+MWCNT}$, NCPCM$_{rGO+MWCNT}$

and NCPCM$_{GNP+MWCNT}$ were obtained of 240.83, 245.16, 243.85, 246.28, 237.42, 235.35 and 230.82 J/g, respectively. The latent–heat of solidification of 244.57, 247.79, 248.48, 249.88, 241.08, 238.39 and 234.19 J/g were predicted for NCPCM$_{GO}$, NCPCM$_{rGO}$, NCPCM$_{GNP}$, NCPCM$_{MWCNT}$, NCPCM$_{GO+MWCNT}$, NCPCM$_{rGO+MWCNT}$, and NCPCM$_{GNP+MWCNT}$, respectively. Since, the hybrid NCPCM$_{GNP+MWCNT}$ has the thermal conductivity and optimum capacity of latent–heat of fusion/solidification, the less degree of subcooling of 3.47°C was achieved which showed the best NCPCM melting and cooling heat transfer process. The deviation in peak melting temperature was observed of 0.22% for hybrid NCPCM$_{GNP+MWCNT}$.

- The specific heat capacity results of mono and hybrid NCPCMs reveal the increasing trends of compared with RT–35HC. The enhancement of 13.75% was achieved with hybrid NCPCM$_{GNP+MWCNT}$ compared to RT–35HC in solid–phase. The enhancement in specific heat capacity is based on three modes: (i) higher specific heat of nanoparticles, (ii) interfacial interactional layers between solid–liquid and (iii) semi–solid liquid layers of molecules adhering to the surface of nanoparticles.

From the above mention key findings conclude and suggest that carbon–additives hybrid nanoparticles (GO+MWCNT, rGO+MWCNT and GNP+MWCNT) dispersed NCPCMs have the best thermal performance in terms of thermal management and thermal energy storage. More specially, the GNP+MWCNT dispersed hybrid NCPCM has the optimum capacity of latent–heat storage and higher thermal conductivity which improve the heat transfer rate in conduction and convection modes and heat absorption capacity. Hence, hybrid NCPCMs can be potentially used for thermal management and thermal storage applications.

# Chapter 6

# Development of metallic–oxide and carbon–additives phase change mono and hybrid materials[1]

## Abstract

Efficient, clean and quiet thermal management has become a vital challenge in for cooling of electronic devices. To enhance the capability and efficiency of passive thermal management, novel composite materials have been designed by the combination of graphene nanoplatelets (GNPs), multiwall carbon nanotubes (MWCNTs), aluminium oxide ($Al_2O_3$) and copper oxide (CuO) dispersed in the RT–28HC used as a phase change material (PCM). The series of mono and hybrid nanocomposite phase change materials (NCPCMs) were synthesized using constant mass fraction of 1.0 wt.% of each type of nanoparticles to establish the optimum NCPCM in terms of thermal properties for effi-

[1]This Chapter is published as:
**Arshad, A.**, Jabbal, M., & Yan, Y. (2020). Preparation and characteristics evaluation of mono and hybrid nano-enhanced phase change materials (NePCMs) for thermal management of microelectronics. *Energy Conversion and Management*, 205, 112444. https://doi.org/10.1016/j.enconman.2019.112444

cient thermal management of microelectronics. Various material characteristic techniques such as ESEM, FT–IR, XRD, TGA, DTG, DCS, IRT and thermal conductivity apparatus were used and microstructure, chemical composition, crystallinity, thermal and phase–change heat transfer characteristics were investigated extensively for each sample of NCPCM. The results showed good chemical and thermal stability of all NCPCMs without changing the chemical structure of RT–28HC. The surface morphology and crystal formation analysis revealed the uniform dispersion of nanoparticles onto the surface of RT–28HC. In comparison of mono and hybrid NCPCMs, the results showed the hybrid NCPCM at GNPs/MWCTs mass percentage ratio of 75%/25% had the highest thermal conductivity enhancement of 96% compared to the pure PCM having optimum value of phase–change enthalpy of 245.18 J/g. Finally, enhancement in phase transition while melting and thermal properties evidenced that hybrid NCPCMs can be used as potential candidate for the thermal management of microelectronics.

**Keywords:** Thermal management, Graphene nanoplatelets (GNPs), Multi-wall carbon nanotubes (MWCNTs), Aluminium oxide ($Al_2O_3$), copper oxide (CuO), Nanocomposite phase change materials

## 6.1 Introduction

Dramatic changes in global climate and greenhouse emissions are two major concerns of the world, resulting from the use of fossil fuels. Therefore, there is a need for an energy demand which can fulfil a broad range of renewable and sustainable energy resources such as solar, wind, biomass, geothermal, and wave to overcome the growing demand for fossil fuels. In addition, thermal energy storage (TES) is widely used for various energy conversion and transportation systems in solar energy conversion and thermal management. The three major TES technologies include sensible–heat–storage (SHS), latent–heat–storage (LHS), and thermo–chemical–storage (TCS). LHS has great potential to store

the heat due to small variation in temperature and high energy storage density, which is promising for thermal management of electronic devices. Using phase change materials (PCMs) for LHS offers high energy storage density compared with SHS materials. PCMs, especially organic PCMs including paraffins and non–paraffins, exhibit high latent of fusion which make them highly suitable for latent heat storage energy technologies (LHSET). Meanwhile, organic PCMs possess low thermal conductivity which reduces the heat transfer enhancement. To enhance the heat transfer enhancement and TES performance of organic PCMs, some strategies such as encapsulation (Arshad et al., 2019a) and shape–stabilization (Feng et al., 2019) have been carried out. There are several thermal conductive materials (TCMs) which have been embedded with PCMs to overcome their low thermal conductivity such as metal–fins (Ashraf et al., 2017), metal–foam (Rehman et al., 2019), carbon–additives (Keshteli and Sheikholeslami, 2019), metallic and metal–oxides nanoparticles (Leong et al., 2019).

Various carbon–based additives, including carbon nanotubes (CNTs) (Choi et al., 2014; Li et al., 2014a,b; Fan et al., 2015; Zou et al., 2018), carbon nanofiber (CF) (Nomura et al., 2016, 2015; Bahiraei et al., 2017), graphene (GE) (Choi et al., 2014; Li et al., 2014b), graphene oxide (GO) (Wu et al., 2019; Yang et al., 2017), graphite (Wu et al., 2019; Choi et al., 2014; Li et al., 2014b), expanded graphite (EG) (Ling et al., 2015), graphene nanoplatelets (GNPs) (Wu et al., 2019; Zou et al., 2018; Bahiraei et al., 2017) and graphite nanoplatelets (Warzoha and Fleischer, 2014; Bahiraei et al., 2017) have been used as TCMs, to prepare and characterize the NCPCMs for thermal management and TES. The thermal conductivity of NCPCMs depends not merely on the innate thermal conductivity of the nanoparticles but it also strongly depends on the interactional compatibility of the PCM and nanoparticles. In earlier studies, Choi et al. (Choi et al., 2014) used MWCNTs, graphite and graphene as TCMs and determined the thermal conductivity of the NCPCM for TES applications. The authors used the PVP as a surfactant and stearic

acid as a PCM. The maximum thermal conductivity enhancement was found to be 21.5% using graphene of 0.1 vol.% with PVP. Pristine CNTs and grafted CNTs with paraffin–based NCPCM was prepared by Li et al. (Li et al., 2014a). The results showed that grafted CNTs were shorter in size than pristine CNTs and the better dispersibility with PCM was found with grafted CNTs. In addition, grafted CNTs had the higher thermal conductivity than pristine CNTs/paraffin NCPCMs. Li et al. (Li et al., 2014b) used MWCNTs graphene and graphite mixed into stearic acid with two mass percentages of 1.0% and 5.0%. The heat transfer performance and thermal conductivity analysis were carried out and the results revealed that the thermal conductivity of graphite–based NCPCMs at 5.0% mass percentage was 12 times higher than the pure stearic acid. Bahiraei et al. (Bahiraei et al., 2017) synthesized three types of carbon-based nanoparticles namely carbon nanofibers, graphene nanoplatelets and graphite nanoplatelets with paraffin wax as a PCM. The results showed the graphite–based NCPCM with 7.5% and 10% mass fractions had the best thermal performance for thermal management applications. Warzoha and Fleischer (Warzoha and Fleischer, 2014) examined single and multilayer graphene into paraffin PCMs from graphene layers from 3 to 44. It was observed that thermal conductivity enhancement of graphene-mixed paraffin PCMs was due to the presence of graphene nanoparticles, which was a stronger function of bending stiffness of graphene than its intrinsic thermal conductivity. Recently, Zou et al. (Zou et al., 2018) prepared and studied the thermal conductivity and charging/discharging behaviour of MWCNTs, graphene and MWCNTs/graphene based NCPCMs using paraffin wax as PCM. The results showed that hybrid MWCNTs/graphene based NCPCMs had the higher thermal conductivity.

Similarly, several researchers have used various types of metallic and metal oxides nanoparticles such as Ag (Bashar and Siddiqui, 2018), Cu (Li et al., 2017), $Al_2O_3$ (Bashar and Siddiqui, 2018; Li et al., 2017; Nourani et al., 2016b,a; Colla et al., 2017a; Chieruzzi et al., 2015; Babapoor and Karimi, 2015; Babapoor et al., 2016), CuO (Bashar and Siddiqui, 2018; Pahamli et al., 2017; Praveen

and Suresh, 2018), MgO, $TiO_2$ (Li et al., 2017; Sharma et al., 2016; Zhichao et al., 2015), $SiO_2$ (Li et al., 2017; Chieruzzi et al., 2015; Babapoor and Karimi, 2015; Babapoor et al., 2016), $Fe_2O_3$ (Babapoor and Karimi, 2015; Babapoor et al., 2016), and ZnO (Babapoor and Karimi, 2015; Babapoor et al., 2016). Bashar and Siddiqui (Bashar and Siddiqui, 2018) used four different types of nanoparticles, Ag, CuO, $Al_2O_3$ and MWCNTs and mixed with paraffin wax. It was found that the heat transfer coefficient was 18% and 14% higher with CuO and Ag, respectively, than the pure paraffin wax. Nourani et al. (Nourani et al., 2016b,a) synthesised paraffin wax and $Al_2O_3$ based NCPCMs with 0.5, 5, 7.5, and 10 wt.% of $Al_2O_3$ and used SSL as a surfactant to improve the dispersion stability of $Al_2O_3$ nanoparticles. Results showed effective thermal conductivity enhancement ratios of 31% and 13% at 10.0 wt.% in solid and liquid states, respectively. Colla et al. (Colla et al., 2017a) prepared NCPCM using $Al_2O_3$ and carbon black (CB) of 1.0 wt.% with RT20 and RT25 as PCMs. Thermal conductivity of 0.234 and 0.242 W/m.K was achieved with RT20/$Al_2O_3$ and RT25/$Al_2O_3$, respectively, and for RT20/CB and RT25/CB it was 0.344 and 0.323 W/m.K, respectively. Li et al. (Li et al., 2017) used calcium chloride hexahydrate ($CaCl_26H_2O$) as a PCM with $\gamma-Al_2O_3$ and studied the phase change behaviour, super cooling, thermal conductivity and latent heat of NCPCMs. A maximum thermal conductivity of 1.373 W/m.K was achieved at 2.0 wt.% of $\gamma-Al_2O_3$. Babapoor and his co–authors (Babapoor and Karimi, 2015; Babapoor et al., 2016) measured the thermal properties and heat storage characteristics of $SiO_2$, $Al_2O_3$, $Fe_2O_3$, ZnO and hybrid of all nanoparticles mixed into paraffin wax in solid and liquid states. The highest enhancement was obtained with $Fe_2O_3$ at 8 wt.%, however, the authors proposed that $Al_2O_3$ was most suitable for thermal management application. Chieruzzi et al. (Chieruzzi et al., 2015) synthesised NCPCMs using $SiO_2$, $Al_2O_3$ and a hybrid of $SiO_2$/$Al_2O_3$ of 1.0 wt.% and potassium nitrate ($KNO_3$) as PCM. The results found that $SiO_2$ nanoparticles had the best results of decreasing onset temperatures by 2–3 °C and increasing specific heat by 9.5%.

Pahamli et al. (Pahamli et al., 2017) dispersed 2 wt.% and 4 wt.% of CuO into PCM, paraffin RT50 and found a maximum thermal conductivity enhancement of 3.9% and 7.2%, respectively, during the phase change state. Praveen and Suresh (Praveen and Suresh, 2018) studied the thermal, chemical and heat transfer performance of solid–solid neopentyl glycol (NPG) and CuO NCPCMs for thermal management application. A maximum thermal conductivity of 0.61 W/m.K was obtained at 3.0 wt.% of CuO. The lowest value of phase change enthalpy obtained was 112.4 kJ/kg at 3.0 wt.% of CuO. Sharma et al. (Sharma et al., 2016) prepared a NCPCM using $TiO_2$ with mass fractions of 0.5, 1.0, 3.0, and 5.0% and palmitic acid. A maximum thermal conductivity of 0.35 W/m.K and minimum latent heat of 180.03 kJ/kg was obtained at 5.0 wt.% of $TiO_2$. Zhichao et al. (Zhichao et al., 2015) used erythritol as PCM and $TiO_2$ of 0.1 vol.%, 0.2 vol.%, 0.5 vol.%, 1.0 vol.% and 2.0 vol.% volume fractions. It was found that the heat capacity of NCPCMs was significantly enhanced by 45% and 14% in solid and liquid states, respectively, compared to pure erythritol at 0.2 vol.% of $TiO_2$. Recently, Putra et al. (Putra et al., 2019) prepared the shape-stable PCMs using the Beewax as a PCM and MWCNTs as TCM with ratios of 5 and 20 wt.%. The authors found the thermal conductivities of 0.46 and 0.58 W/m.K with weight ratios of 5 and 20 wt.%, respectively of MWCNTs. Further, they found the melting temperatures of 60.2°Cand 59.8°C, and latent heat values of 115.5 and 91.6 J/g with 5 and 20 wt.% weight ratios of MWCNTs, respectively. He et al. (He et al., 2019c) synthesised the NCPCMs using myristic acid as a PCM and dispersed the GNPs, MWCNTs and nano–graphite with weight concentrations of 1, 2 and 3 wt.%. The authors found the best thermal performance with GNPs followed by MWCNTs and nano–graphite. The enhancement in thermal conductivity was achieved by 76.26%, 47.30% and 44.01% for GNPs, MWCNTs and nano–graphite, respectively, under the weight concentration of 3 wt.%. Zhang et al. (Zhang et al., 2020) prepared the NCPCMs using n–eicosane as PCM, $SiO_2$ as supporting matrix and EG as TCM with weight concentrations

of 3, 5 and 7 wt.%. It was found that melting and solidifying latent heats were 135.80 J/g and 125.93 J/g, respectively, at 7 wt.% of EG and thermal conductivity enhancement was enhanced by 2.37 times in $SiO_2$/n–eicosane NCPCM without EG.

In order to increase the thermal enhancement of PCMs, the present study aims to improve the thermal conductivity of PCM and to maintain its heat storage capacity at an optimum level. The mono and hybrid NCPCMs were synthesized by dispersing carbon–based (GNPs and MWCNTs) and metal–oxides based (CuO and $Al_2O_3$) nanoparticles at constant mass fraction of 1.0 wt.%. Further, morphology, chemical and thermal properties are characterized using various characterization techniques.

## 6.2 Experimental procedure

### 6.2.1 Materials

Commercial grade of paraffin, namely RT–28HC, is used as a PCM with melting temperature of 27–29 °C in the current study. The thermophysical properties of PCM are listed in Table 6.1. Graphene nanoplatelets (GNPs) of thickness <3-5 nm, lateral diameter $< 10$ $\mu$m and $98 \pm 1.0\%$ purity of carbon were purchased from 2–Dtech Ltd/Versarien PLC, UK. Multi–wall carbon nanotubes (MWCNTs) of outer diameter $5 - 15$ nm and length of $10 - 30$ $\mu$m, and purity $> 95$ wt.% were purchased from Carbon Nanotubes Plus, USA. Nanoparticles of copper oxide (CuO) of $< 50$ nm, aluminium oxide ($Al_2O_3$) of 13 nm, and Sodium dodecylbenzene sulfonate (SDBS), were purchased from Sigma–Aldrich, UK. All materials were used without performing any further chemical processing.

Table 6.1: Thermal properties of RT–28HC.

| Melting temperature (°C) | Thermal conductivity (W/m.K) | Latent heat (J/kg.K) | Specific heat (J/kg.K) | Density (kg/m$^3$) |
|---|---|---|---|---|
| 27–29 | 0.2 | 250,000 | 2000 | 880 (solid)<br>770 (liquid) |

### 6.2.2 Preparation of NCPCMs

A well–precise, two–step method was adopted to synthesize the mono and hybrid NCPCMs by using PCM (RT–28HC) and nanoparticles (GNPs, MWCNTs, CuO and $Al_2O_3$), as shown in Fig. 6.1. RT–28HC was used as base PCM and a constant mass fraction of 1.0$wt.$% of GNPs, MWCMTs, CuO, $Al_2O_3$ GNPs/MWCNT and CuO/$Al_2O_3$ was dispersed as a thermal conductivity enhancer (TCE) medium. Firstly, RT–28HC was melted by heating it at constant temperature of 50 °C in a hot–water bath. After complete melting of RT–28HC, SDBS in the ratio of 4 : 1 of nanoparticles was added as a surfactant (capping agent) for uniform dispersions of nanoparticles into the RT–28HC. The solution of RT–28HC and SDBS was mixed homogenously at a stirring rate of 450 rpm for 30 mins. Thenceforth, constant amount of GNPs, MWCMTs, CuO, $Al_2O_3$ GNPs/MWCNT and CuO/$Al_2O_3$ were added at a constant mass of 1.0 wt.% separately to prepare the six different samples of the mono and hybrid–NCPCM. Further, the mixtures were stirred at a stirring rate of 450 rpm for 2.5 hrs for stable and uniform dispersions of nanoparticles. While adding the GNPs, MWCNTs, CuO and $Al_2O_3$ simultaneously, the total mass percentage was 1.0 wt.% and the mass ratio of GNPs/MWCNTs and CuO/$Al_2O_3$ was 75%/25%. Secondly, to minimize agglomeration and sedimentation and to improve more homogeneous and stable dispersion of nanoparticles, ultrasonication was performed on the mixture for 60 mins while maintaining a constant temperature of 50°C using an ultrasonic vibrator at a frequency of 40 kHz (Sharma et al., 2016; Asadi et al., 2019).

### 6.2.3 Characterizations methods

The morphology, chemical and thermal properties of NCPCM were characterized using various facilities as described herein.

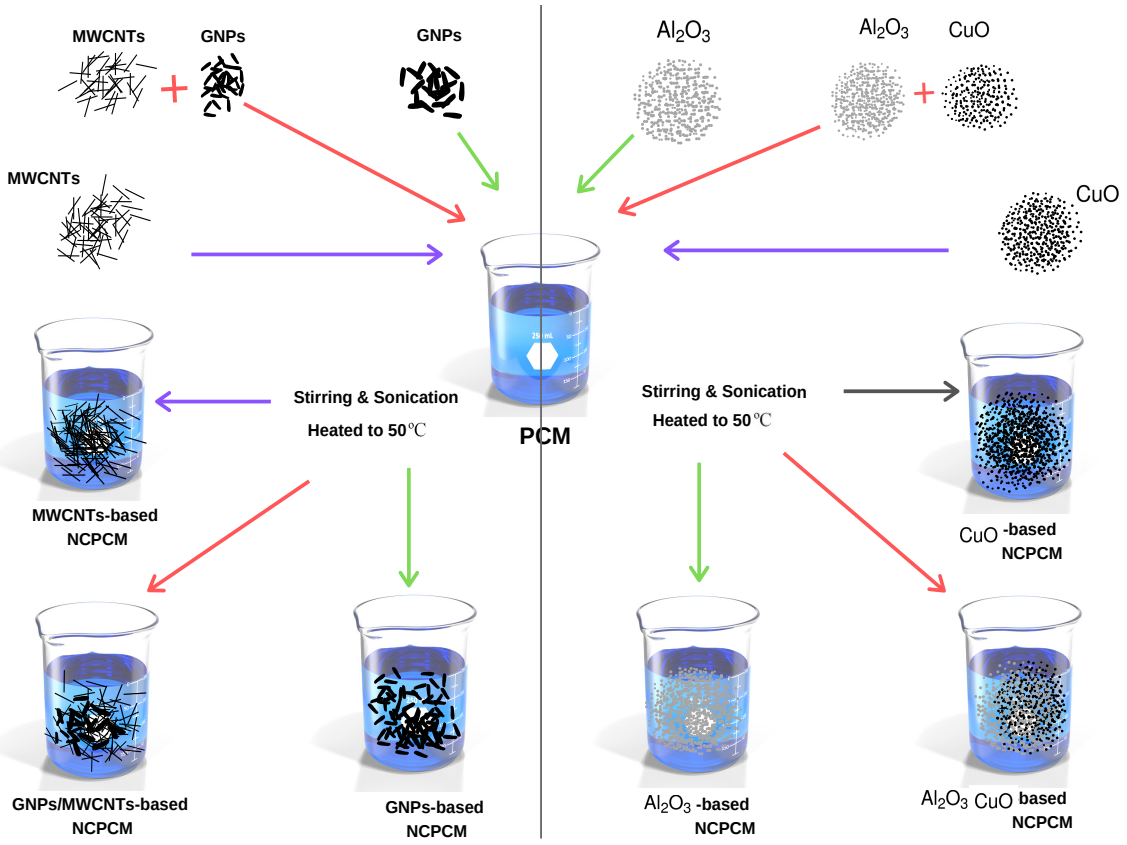


**Figure 6.1:** *Preparation process of NCPCMs with GNPs, MWCNTs, CuO and $Al_2O_3$.*

#### 6.2.3.1 Environmental Scanning electron microscopy (ESEM) and Energy–dispersive X–ray spectroscopy (EDX)

The surface morphology, microstructure and uniform dispersion of NCPCM was examined using an environmental scanning electron microscopy (ESEM, FEI Quanta–650). To determine the elemental composition and surface elemental distribution of NCPCM, energy–dispersive X-ray spectroscopy (EDX) analysis was used.

#### 6.2.3.2 Fourier–transform infrared spectroscopy (FTIR)

The chemical composition and functional groups were determined using Fourier–Transform Infrared Spectroscope (FTIR, Bruker Tensor–27 FT–IR Spectrometer) between the wave range of $400 - 4000$ cm$^{-1}$, with a spectral resolution of 4 cm$^{-1}$ and wavenumber accuracy of 0.01 cm$^{-1}$.

#### 6.2.3.3 X–ray diffraction (XRD)

X–ray diffraction (XRD) pattern was measured by an X–ray diffractometer (XRD, Bruker D8 Advance with Da Vinci) between the angle range of 5° to 60° to visualize the crystalloid phase and crystallographic structure of NCPCM. The x–ray tube generates copper k–alpha x–rays, which is often abbreviated to Cu–K$\alpha$ ($\lambda = 1.5406\mathring{A}$). The x–ray tube runs at 40 kV and 40 mA.

#### 6.2.3.4 Thermogravimetric analysis (TGA) and derivative thermogravimetry (DTG)

The weight loss and thermal stability of NCPCM were predicted using thermogravimetrical analysis (TGA) and rate of decomposition of NCPCM was predicted using derivative thermogravimetry (DTG) curves simultaneously using TGA/DSC (SDT–Q600 TA instrument Inc., UK) with a balance precision of 0.1 $\mu$g (Error $\pm$0.1 $\mu$g). The samples ($4 - 7$ mg) were placed in an aluminium pan and heated from 20°C to 400°C at a rate of 10°C/min under a purified nitrogen atmosphere flow rate of 100 mL/min.

#### 6.2.3.5 Differential scanning calorimeter (DSC)

The phase change properties such as phase change melting/solidification temperatures and latent heat of fusion were measured for pure PCM and NCPCMs using a TA instrument differential scanning calorimeter (DSC–2500, TA instrument Inc., UK) equipped with the cooling attachment, under a purified nitrogen atmosphere. The accuracy of the calorimeter was within $\pm$0.04% and temperature precision was $\pm$0.005°C. All measurements of DSC were taken at constant heating/cooling of 1 °C/min between 10°C and 50°C. A precise amount of sample mass in the range of $3 - 5$ mg was placed inside a T–zero Hermetic aluminium pan at room temperature and sealed with a lid to ensure full contact between the sample and pan.

#### 6.2.3.6 Thermal conductivity measurement

To measure the thermal conductivity of pure PCM and NCPCMs, TCi$^{TM}$ Thermal Conductivity Analyser (C–THERM Technologies Ltd. Canada) was used at a constant temperature of 25°C, which is based on a modified transient plane source (MTPS) method and confirms the ASTM D7984. The instrument measures thermal conductivity within the range from 0 to 500 W/mK with an accuracy and precision of 5% and 1%, respectively. The sample of 20 mm diameter and thickness from 3−5 mm was prepared. At a specific temperature, fifteen readings were recorded for each NCPCM and the average value taken. Three measurements were recorded for each sample at constant temperature and averaged value was reported. A maximum relative error of ±2.0% was found. The uncertainty of measurement was estimated within ±1.0%.

#### 6.2.3.7 Infrared thermography (IRT) test

Infrared thermography (IRT) tests were performed to evaluate the temperature-regulating property of pure RT–28HC, mono and hybrid NCPCM by using an IR thermographic camera (FLIR–SC2600–EA2). Each sample was filled in a beaker and then immersed in a pot of water on a hot–plate at constant temperature.

## 6.3 Results and discussions

### 6.3.1 Morphological and elemental analysis

The surface morphological characteristics and microstructures of prepared mono and hybrid NCPCMs based on GNPs, MWCNTs, CuO and $Al_2O_3$ were examined by ESEM. Fig. 6.2 presents the surface microstructural features of pure RT–28HC, RT–28HC/GNPs, RT–28HC/MWCNTs, and RT–28HC/GNPs+MWCNTs. The uniform dispersion of GNPs and MWCNTs can been seen in the RT–28HC from the ESEM images, as shown in Figs. 6.2b–

6.2d. The uniform distribution of carbon-based additives within the PCM is because of the repulsive bonding of the SDBS which was used as a dispersant. The mass fraction of GNPs and MWCNTs was very low (1.0 wt.%), however, these are well dispersed and embedded enough to show their presence. In addition, the presence of these highly thermally conductive carbon–based additives plays a significant role in enhancement of thermal conductivity and thus enhance the heat transfer ability of RT–28HC. Fig. 6.2d shows the morphological structure of hybrid NCPCM, RT–28HC/GNPs+MWCNTs which shows effective three-dimensional paths of carbon–based additives. These 3D paths of hybrid NCPCM would be an effective mode to transfer the heat in all regions of the RT–28HC. Thus, two different mass percentage of GNPs and MWCNTs having different morphology may obtained good harmonious effects of heat transfer enhancement. The microstructure of CuO and $Al_2O_3$

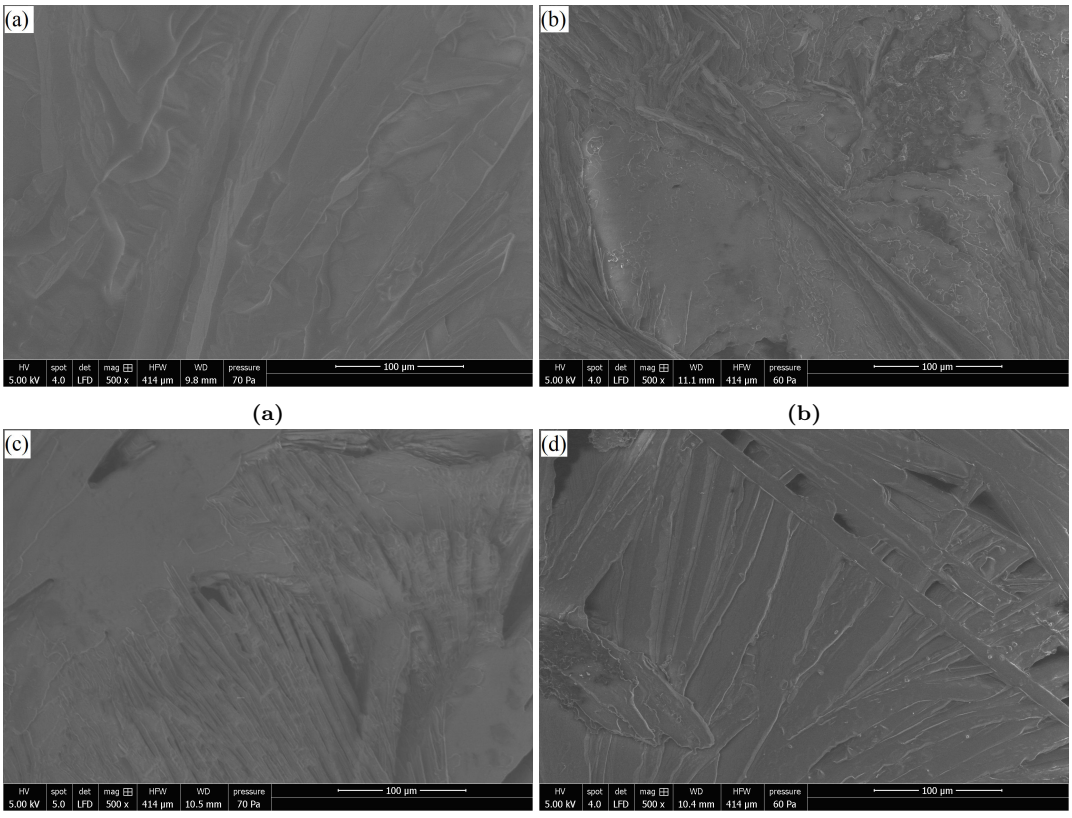


**Figure 6.2:** *ESEM images of (a) RT–28HC, (b) RT–28HC/GNPs, (c) RT–28HC/MWCNTs, and (d) RT–28HC/GNPs+MWCNTs.*

based metallic oxide nanoparticles in hybrid NCPCM, RT–28HC/CuO+$Al_2O_3$

of 1.0 wt.%, is presented in Fig. 6.3. Fig. 6.3a shows the ESEM image using low vacuum secondary electron (LFD) detector, whereas Fig. 6.3b shows the ESEM image using backscatter electron (BSE) detector for low vacuum mode. From Fig. 6.3a and 6.3b, it can be observed by the zones with the presence of non–homogeneous aggregates of $CuO+Al_2O_3$ nanoparticles on the surface of pure RT–28HC. Similar observations have been reported by Chieruzzi et al. (Chieruzzi et al., 2015) with $SiO_2/Al_2O_3$ of 1.0 wt.%. Although the mass fraction of both nanoparticles ($CuO+Al_2O_3$) is very low, 1.0 wt.%, the percentage of CuO is 75% of 1.0 wt.% which may cause the small patches of aggregates due to its higher density compared to the $Al_2O_3$ and RT–28HC.

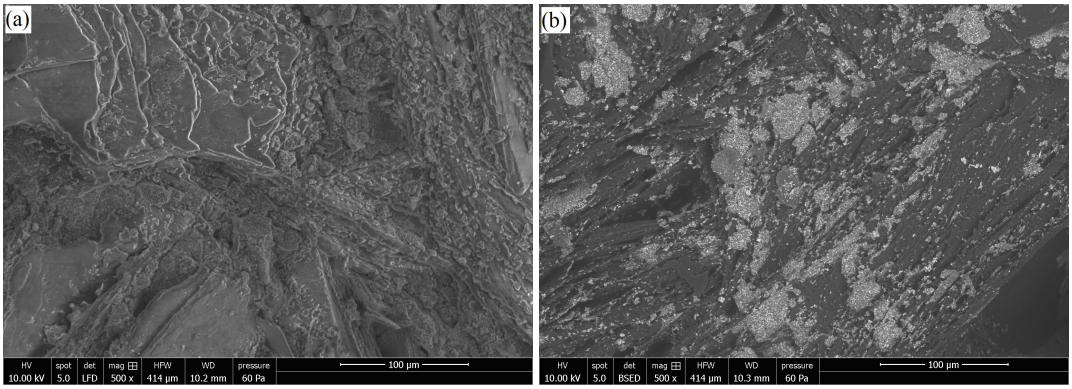


**(a)** **(b)**

**Figure 6.3:** *ESEM images of RT–28HC/$Al_2O_3$+CuO (a) LFD and (b) BSED. (The grey zones show the RT–28HC and white dots are the $Al_2O_3$+CuO nanoparticles which are agglomerated on the nanoscale but dispersed on the microscale.)*

For better visualization and understanding, EDX maps and elemental composition of RT–28HC/$CuO+Al_2O_3$ are shown in Figs. 6.4 and 6.5, respectively. Figs. 6.4a–6.4d show the distribution of carbon (C), aluminium (Al), oxygen (O) and copper (Cu), respectively; elements present in the hybrid NCPCM of RT–28HC/$CuO+Al_2O_3$. In Fig. 6.4a, the red colour shows the presence of C element in different regions of the material of RT–28HC PCM, while the dark colour represents the aggregates of Cu, Al and O elements. Similarly, green, purple, and brown colours represent the aggregates of Al, O and Cu elements present in compounds of CuO, $Al_2O_3$ and RT–28HC. The presence of all elements C, Al, Cu and O in different colours can be seen in Fig. 6.4e. A clear

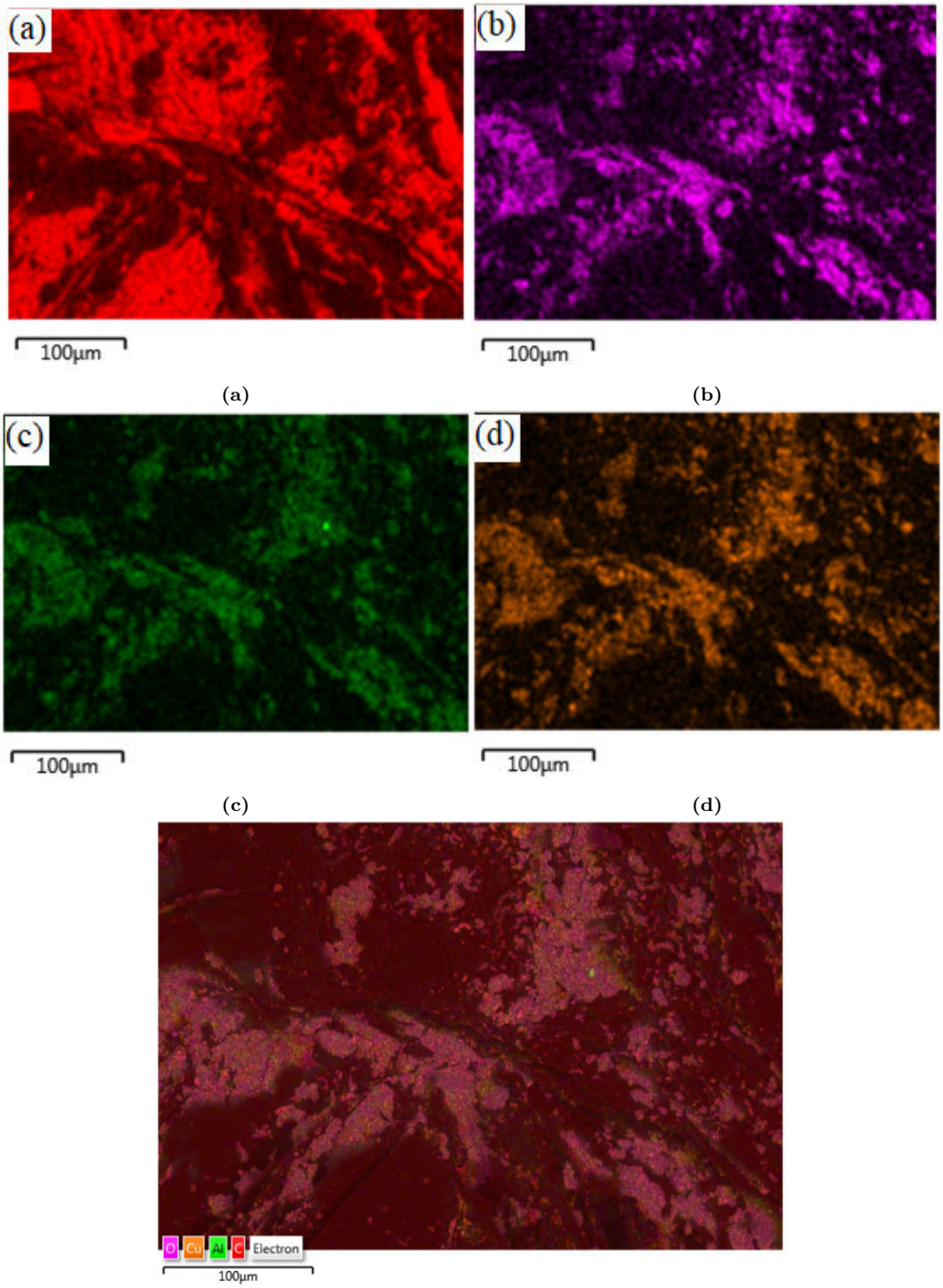


**Figure 6.4:** *EDX mapping of RT–28HC/$Al_2O_3$+CuO hybrid NCPCM: (a)-Carbon (red), (b)-Oxygen (purple), (c)-Aluminium (green), (d)-Copper (Brown), and (e)-EDX map of oxygen, copper, aluminium, and carbon elements present in RT–28HC/$Al_2O_3$+CuO.*

observation of aggregates of nanoparticles can be seen in different regions of the NCPCM. The elemental composition of all four elements present in CuO, $Al_2O_3$ and RT–28HC can been identified from Fig. 6.5. It is revealed from Fig. 6.5 that the weight percentage of all elements in hybrid NCPCM consisting of CuO, $Al_2O_3$ and RT–28HC is equal according to their compositions used in the mixture. From the elemental mapping and composition analysis, it can been seen that CuO nanoparticles are more dispersed than the $Al_2O_3$ within RT–28HC, as per the used percentage of $CuO/Al_2O_3$. In addition, ESEM and EDX show agglomeration of nanoparticles. Similar observations have been reported by Chieruzzi et al. (Chieruzzi et al., 2015). Therefore, better and more uniform dispersion of the nanoparticles can be achieved by using smaller sized nanoparticles (Saterlie et al., 2011; Evans et al., 2008).

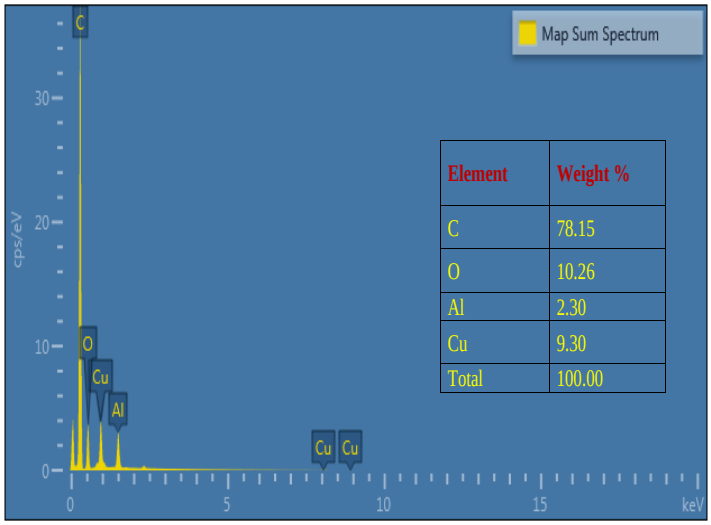


**Figure 6.5:** *Elemental spectrum and compositional analysis of RT–28HC/$Al_2O_3$+CuO.*

### 6.3.2 FT–IR analysis

The chemical interaction of carbon–based (GNPs and MWCNTs) and metallic oxide–based (CuO and $Al_2O_3$) nanoparticles in mono and hybrid NCPCMs were characterized by FT–IR spectroscopy. Fig. 6.6 shows the transmittance band of FT–IR spectra of GNPs, MWCNTs, RT–28HC, RT–28HC/GNPs, RT–28HC/MWCNTs and RT–28HC/GNPs+MWCNTs between wave num-

bers of 500 and 3500 $cm^{-1}$. There are not significant stretching and bending peaks observed of infrared spectra of MWCNTs and GNPs because of the absence of functional groups. For the spectrum of RT–28HC, three transmittance peaks at 2955 $cm^{-1}$, 2913 $cm^{-1}$, 2847 $cm^{-1}$ represent the medium symmetrical stretching vibration of C–H alkane group. The peak at 1470 $cm^{-1}$ identifies the medium C–H scissoring of $–CH_2–$ and $–CH_3$ group in RT–28HC. The peak at 718 $cm^{-1}$ represents the weak rocking vibration of C–H in long-chain methyl group. The bands observed at 633 $cm^{-1}$ and 541 $cm^{-1}$ correspond to the deformation vibration of C–H. The FT–IR spectrum of RT–28HC/GNPs, RT–28HC/MWCNTs and RT–28HC/GNPs+MWCNTs shows neither any significant new peak nor any major peak shifts in the NCPCMs, which indicates that there is an only physical interaction of RT–28HC, GNPs, MWCNTs and SDBS. Therefore, infrared spectrum results indicate that there is no rearrangement of the functional group, which reveals that no chemical reaction takes place between RT–28HC, GNPs and MWCNTs. Fig. 6.7 presents the FT–IR

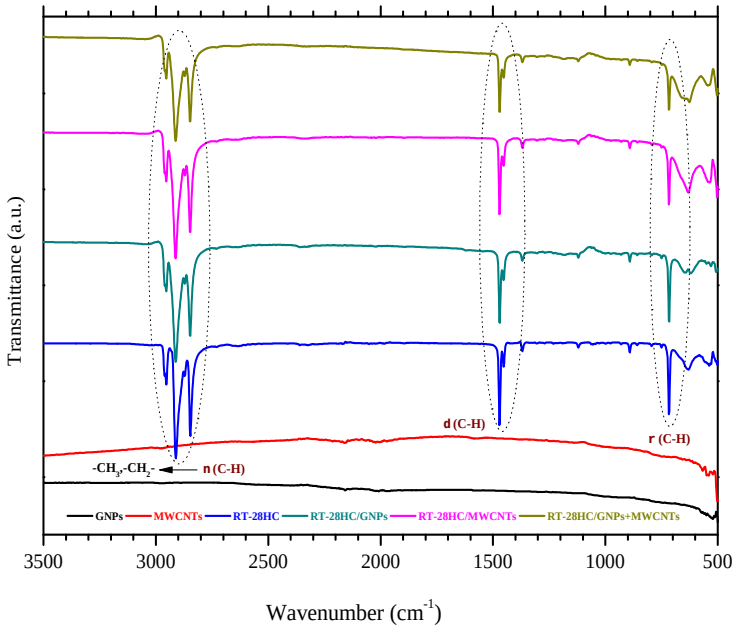


**Figure 6.6:** *FT–IR spectrum of GNPs, MWCNT, RT–28HC based mono and hybrid NCPCMs.*

spectrum results of CuO, $Al_2O_3$, RT–28HC, RT–28HC/$Al_2O_3$, RT–28HC/CuO and RT–28HC/$Al_2O_3$+CuO. In the case of CuO nanoparticles, there are two

stretching bands at 880 $cm^{-1}$ and 1432 $cm^{-1}$ which represent the characteristics bands of Cu–OH functional group (Bakhtiari and Darezereshki, 2011; Faisal et al., 2011). Moreover, a small peak can be observed at 729 $cm^{-1}$ which indicates the standard adsorption spectra pattern of the amorphous structure or disordered defects of $\gamma-Al_2O_3$ (Lestari et al., 2018). The FT–IR spectrums of RT–28HC/$Al_2O_3$, RT–28HC/CuO and RT–28HC/$Al_2O_3$+CuO exhibit similar trends as GNPs and MWCNTs based mono and hybrid NCPCMs, as shown in Fig. 6.6. It can be seen that $Al_2O_3$ and CuO based mono and hybrid NCPCMs do not exhibit any major new peak or peak shifts which represent only the physical interaction of $Al_2O_3$ and CuO nanoparticles in NCPCMs. Similar trends of infrared spectra of NCPCMs have previously been observed (Mei et al., 2011; Mehrali et al., 2013b; Sharma et al., 2016).

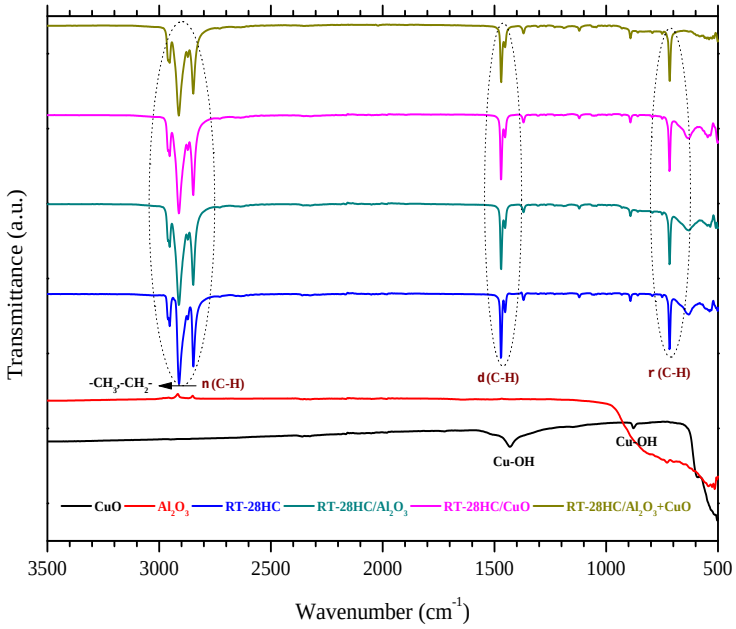


**Figure 6.7:** *FT–IR spectrum of CuO, $Al_2O_3$, RT–28HC based mono and hybrid NCPCMs.*

### 6.3.3 XRD analysis

To analyse the crystal structure of the carbon-based and metallic oxide-based NCPCMs, especially in the crystalline phase, XRD spectrum were identified and compared with the data retrieved from the International Centre for Diffrac-

tion Data (ICDD), as shown in Figs. 6.8 and 6.9, respectively. The XRD peaks confirmed the presence of MWCNTs, GNP, $Al_2O_3$ and CuO nanoparticles in RT–28HC. Fig. 6.8 shows the crystal structure XRD spectrum of MWCNTs, GNPs, mono (RT–28HC/GNPs and RT–28HC/MWCNTs) and hybrid NCPCM (RT–28HC/GNPs+MWCNTs). The diffraction peaks of $2\theta$ at 25.91° (002) and 42.95° (100) confirmed the carbon nanotubes with the PDF No. 00–058–1638 (Keller et al., 2004). The XRD sharp peaks of GNPs at 26.54°, 42.36°, 44.56° and 54.66° correspond to the planes of (002), (100), (101) and (004), respectively, of graphene layers with PDF No. 00–056–0159. The XRD patterns of both MWCNTs and GNPs can be seen in Fig. 6.8. The comparisons of XRD peaks of $Al_2O_3$ confirmed the presence of $\gamma-$phase of $Al_2O_3$ nanoparticles of $2\theta$ at 19.50° (013), 32.80° (022), 34.60° (117), 36.76° (122), 39.50° (026) and 45.64° (220) with PDF No. 00–046–1131. The diffraction peaks of CuO at 32.50° (110), 35.54° (111), 38.70° (111), 46.26° (112), 48.71° (202), 53.48° (020), and 58.26° (202) with PDF No. 01–073–6023 (Åsbrink and Norrby, 1970). The XRD peaks of $Al_2O_3$ and CuO are shown in Fig. 6.9. The sharp diffraction peaks of pure RT–28HC at $2\theta$ = 7.67°, 11.49°, 15.37°, 19.25°, 19.75°, 22.20°, 23.35°, 24.75°, 27.09°, 31.02°, 35.00°, 39.64° and 44.64° are attributed to the crystal planes of *n–Octadecane* ($C_{18}H_{38}$) at (002), (003), (004), (010), (011), (401), (102), (111), (007), (008), (009), (122) and (0110), respectively, with PDF No. 00–053–1532. Since the mass fraction, 1.0 wt.%, is a very small amount of nanoparticles (MWCNTs, GNPs, $Al_2O_3$ and CuO) dispersed in RT–28HC, less significant physical changes in the mono and hybrid NCPCMs are observed. Thus, XRD patterns reveals that crystal formation of RT–28HC did not alter and both mono and hybrid NCPCMs contains the peaks of GNPs, MWCNTs, $Al_2O_3$ and CuO.

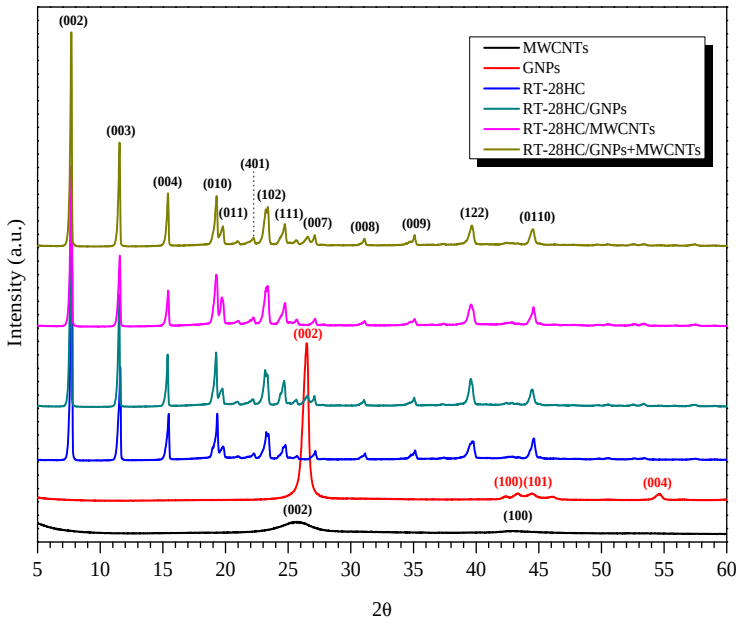


**Figure 6.8:** *XRD pattern of GNPs, MWCNT, RT–28HC based mono and hybrid NCPCMs.*

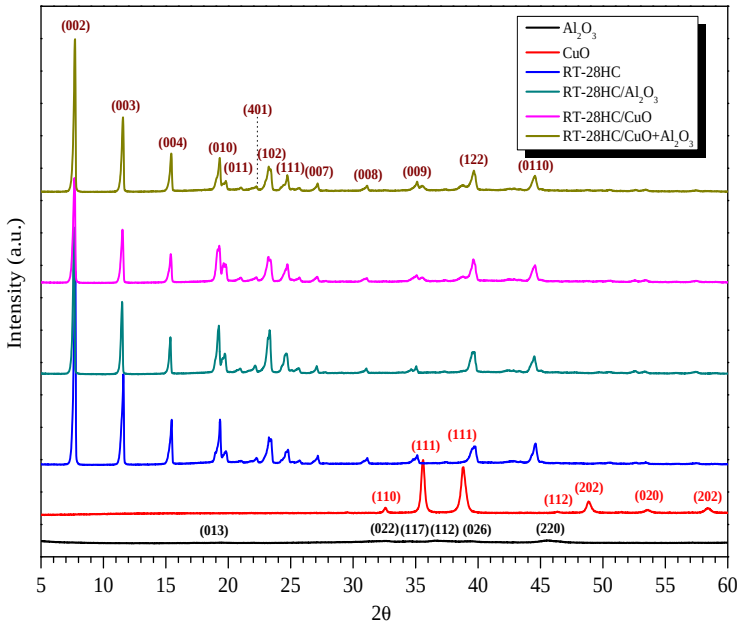


**Figure 6.9:** *XRD pattern of CuO, $Al_2O_3$, RT–28HC based mono and hybrid NCPCMs.*

### 6.3.4 TGA and DTG analysis

Thermal stability of pure and hybrid NCPCMs were performed by conducting TGA and DTG analysis. The thermal stability is estimated based on the onset temperature of PCM degradation and the weight loss rate at which it occurs. A one–step thermal degradation process can be seen for NCPCMs

from TGA curves as it happens continuously. However, a two–step can be observed in DTA curves. The TGA and DTG curves of carbon–based (GNPs and MWCNTs) and metallic oxide–based (CuO and $Al_2O_3$) NCPCMs are presented in Figs. 6.10 and 6.11, respectively. From TGA curves it can be seen that there is no perceptible weight loss up to ∼120 °C for all mono and hybrid NCPCMs samples. However, the weight loss appeared onward when the temperature increased and rate of the weight loss increased with the increase of the temperature. The TGA curve shows from Fig. 6.10a that RT–28HC starts decomposing from a temperature of 193.73 °C until maximum–rate degradation temperature at 230.95 °C, with a remaining charred residue of 0.65%. This complete decomposition is caused by the evaporation of RT–28HC, in which hydrocarbon chains breakdown into monomers. In the case of hybrid NCPCM (RT–28HC/GNPs+MWCNTs), there no change in weight loss was observed at 120 °C, with the onset decomposition temperature and maximum–rate degradation temperature at 203.91°C and 241.70 °C, respectively, with a charred residue of 1.68%. Similarly, the onset decomposition and maximum–rate degradation temperature were 205.14°C and 242.53 °C, respectively, for RT–28HC/$Al_2O_3$+CuO, as shown in Fig. 6.11a.

Since the mass concentration of GNPs, MWCMTs, $Al_2O_3$, CuO, GNPs+MWCNTs and $Al_2O_3$+CuO is much less in RT–28HC, so these carbon–based and metallic oxide–based additives had only a small effect on thermal stability. In NCPCMs, the GNPs, MWCNTs, $Al_2O_3$ and CuO layers create a protective layer on the surface of RT–28HC, which delays vaporization of RT–28HC during the thermal degradation. As nanoparticles are likely to sediment which effect the thermal properties, the constant amount of 1.0 wt.% of nanoparticles has a small variation in temperature change during the weight loss. The DTG curves of mono and hybrid NCPCMs shown in Figs. 6.10b and 6.11b confirm that the dispersion of nanoparticles enhance the thermal stability of RT–28HC. The onset decomposition and maximum degradation temperatures of all samples are summarized in Table 6.2. Since no decompositions in materials have been

observed until 120 °C, hybrid NCPCMs can effectively be used for thermal management of electronic devices.

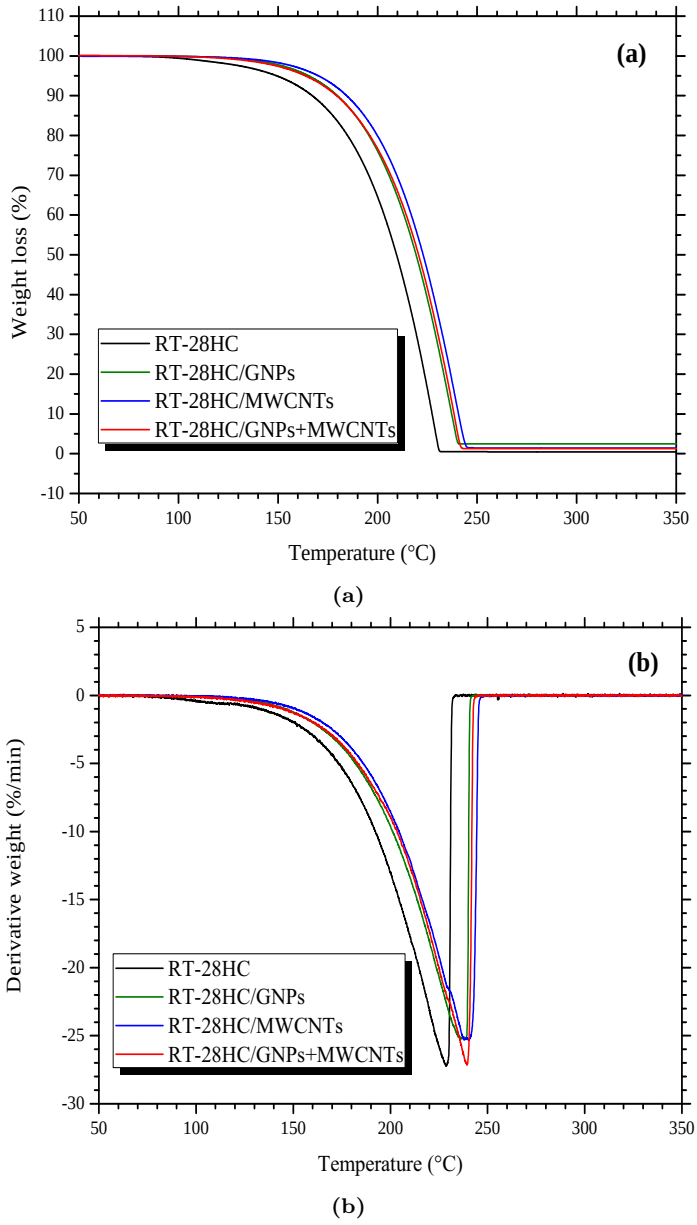


**Figure 6.10:** *(a)-TGA and (b)-DTG thermograms of carbon–based mono and hybrid NCPCMs.*

Table 6.2: Decomposition temperatures and residue of mono and hybrid NCPCMs.

| Sample | Onset decomposition temperature (°C) | Maximum–rate degradation temperature (°C) | Residue (%) |
|---|---|---|---|
| RT–28HC | 193.73 | 230.95 | 0.65 |
| RT–28HC/GNPs | 201.45 | 240.22 | 2.71 |
| RT–28HC/MWCNTs | 205.11 | 244.06 | 2.17 |
| RT–28HC/GNPs+MWCNTs | 203.91 | 241.70 | 1.68 |
| RT–28HC/$Al_2O_3$ | 207.48 | 245.80 | 2.32 |
| RT–28HC/CuO | 205.19 | 244.98 | 2.73 |
| RT–28HC/$Al_2O_3$+CuO | 205.14 | 242.53 | 3.61 |

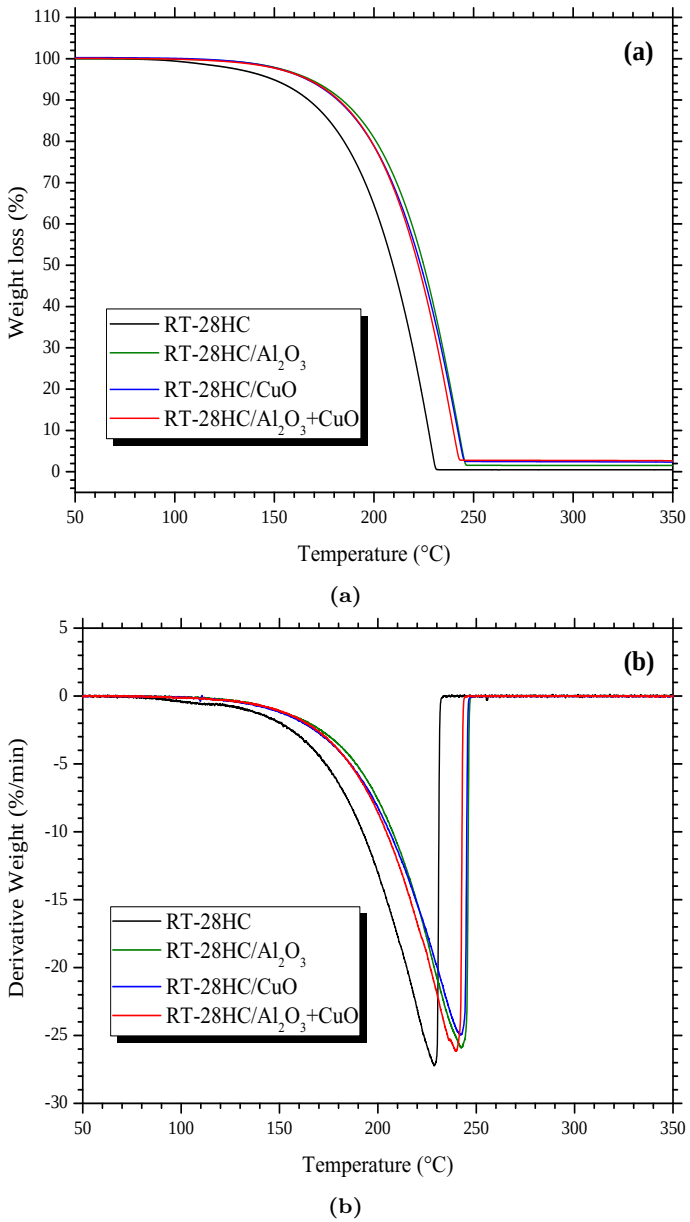


**Figure 6.11:** *(a)-TGA and (b)-DTG thermograms of carbon–based metallic oxide–based mono and hybrid NCPCMs.*

### 6.3.5 DSC analysis

Phase–change properties, such as phase change temperatures and latent-heats during melting and solidification of pure RT–28HC and NCPCMs, have been investigated using DSC. Figs. 6.12 and 6.13 illustrate DSC measurements of carbon–based and metallic oxide–based nanoparticles NCPCMs, respectively, during the melting process. The measured values of corresponding thermal properties are summarized in Table 6.3. It can be seen that the

addition of nanoparticles (GNPs, MWCNTs, $Al_2O_3$ and CuO) have slightly affected the thermal properties. In addition, the latent heat of melting and solidification of all mono and hybrid NCPCMs were decreased with the addition of GNPs, MWCNTs, $Al_2O_3$ and CuO as expected. The maximum reduction in melting latent–heats of RT–28HC/GNPs, RT–28HC/MWCNTs and RT–28HC/GNPs+MWCNTs have been found to be 2.37%, 2.56% and 3.75%, respectively, as compared to the pure RT–28HC. Similarly, the maximum reduction in solidification latent–heats are 2.83%, 2.85%, 3.54% for RT–28HC/GNPs, RT–28HC/MWCNTs and RT–28HC/GNPs+MWCNTs, respectively. The maximum reduction in latent–heats of melting are 2.14%, 3.02% and 2.44% for RT–28HC/$Al_2O_3$, RT–28HC/CuO and RT–28HC/$Al_2O_3$+CuO, respectively. In addition, the maximum reduction in solidification latent–heats are 2.26%, 2.92% and 2.61% for RT–28HC/$Al_2O_3$, RT–28HC/CuO and RT–28HC/$Al_2O_3$+CuO, respectively. Single endothermic peaks are observed during the melting of RT–28HC and NCPCMs samples, indicating an isomorphous crystalline form of RT–28HC either in a pristine state or in the NCPCMs one. Whereas, a bimodal crystallization exothermic peaks are observed by RT–28HC and NCPCMs samples. Normally, the cooling curve of the n–Alkanes

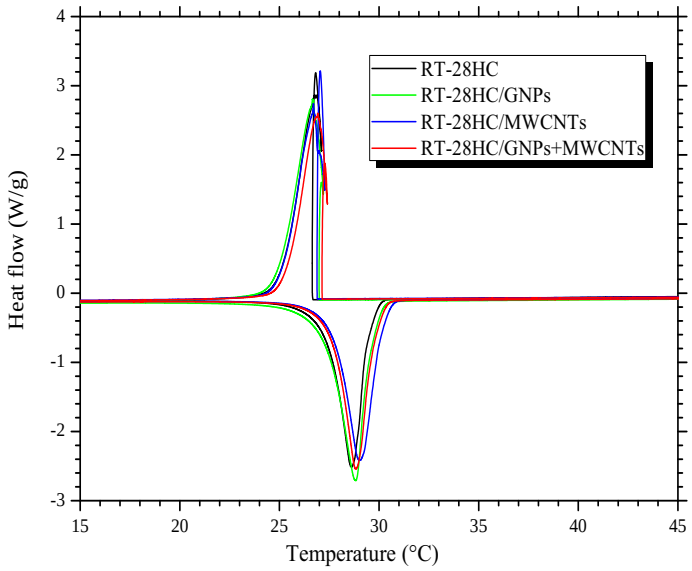


**Figure 6.12:** *DSC curves of carbon–based mono and hybrid NCPCMs.*

is divided into three sections of crystallization peaks, alpha ($\alpha$), beta ($\beta$) and

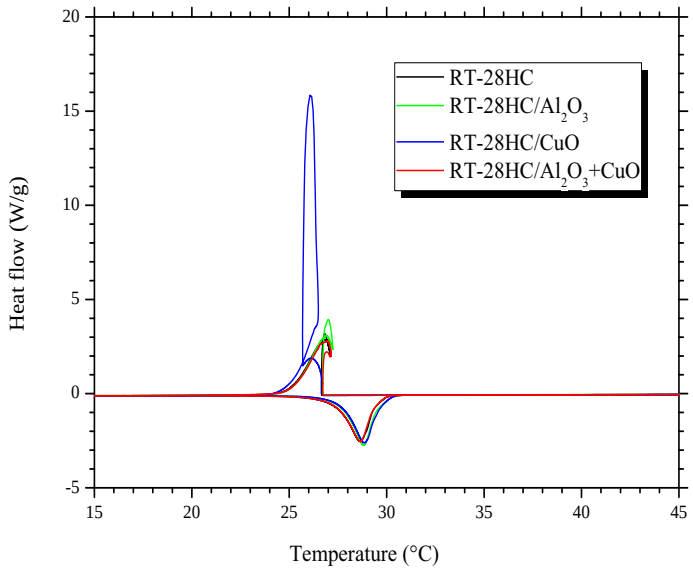


**Figure 6.13:** *DSC curves of metallic oxide–based mono and hybrid NCPCMs.*

gamma ($\gamma$). On the DSC cooling curve, the exothermic $\alpha-$peak corresponds to the heterogeneously nucleated liquid–rotator transition, the $\beta-$peak is attributed to the homogeneously nucleated rotator-crystal transition, and the $\gamma-$peak corresponds to the heterogeneously nucleated liquid–crystal transition. Further, $\alpha-$peak appears a high shoulder at higher temperature than the $\beta$-peak which appears at low temperature shoulder. Whereas, $\gamma-$peak forms the highest peak than the $\alpha$ and $\beta$ peaks but at lower temperature compared to $\alpha$ and $\beta$ peaks while cooling process. This means that more than 80% of the latent heat is released at the lower temperature due the formation of $\gamma-$peak in n–Alkanes (Zhang et al., 2005). In addition, the shoulder height of each peak further depends on the cooling rate of n–Alkanes. The literature has reported that with the increase of heating and cooling rate, the only one peak is observed while heating. Whereas, the two or three peaks were observed for all cooling rates (Yu et al., 2014). Therefore, the multiple peaks in exothermic process are caused by the difference of cooling rates. While crystallization process at different cooling rates, the crystallization peaks are found to be shifted at higher temperatures and more prominent appearance of $\alpha$, $\beta$ and $\gamma-$peaks are observed with the decrease of cooling rate. Whereas, both onset and peak melting temperatures increase with the increase of heating rate (Yu et al., 2014;

Anwar et al., 2013). The bimodal crystallization behaviour with pure PCM and NCPCMs is because the formation of crystallization peaks which correspond to different temperatures. During cooling, the PCM and NCPCM start solidification from liquid phase and formed a first small $\alpha-$peak at higher temperature at which solidification commences and concludes by forming a metastable rotator phase (liquid–to–rotator transition) as a result of heterogeneous nucleation. A sharp $\gamma-$peak is representing the main exothermic peak, where the rotator phase transformed into a stable triclinic crystalline phase as a result of homogeneous nucleation (Oliver and Calvert, 1975; Taggart et al., 1996; Kraack et al., 2000). From the DSC results, the comparison of the

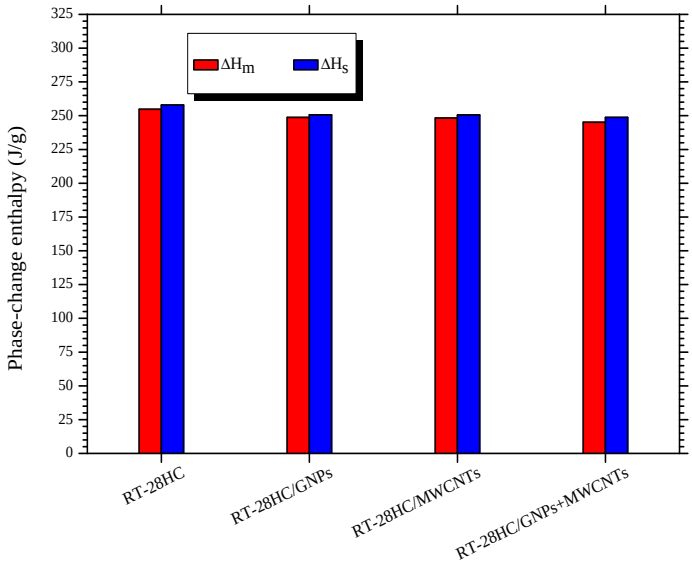


**Figure 6.14:** *Phase change enthalpies of carbon–based mono and hybrid NCPCMs.*

melting ($\Delta H_m$) and solidification ($\Delta H_s$) enthalpies are presented in Figs. 6.14 and 6.15 for carbon–based and metallic oxide–based nanoparticles NCPCMs, respectively. The $\Delta H_m$ and $\Delta H_s$ of pure RT–28HC was found to be 254.93 and 257.90 J/g, respectively. However, a slight reduction in both can be observed for NCPCMs which is due to the introduction of GNPs, MWCNTs, $Al_2O_3$ and CuO nanoparticles. The mass fraction ($\omega$) of crystallized RT–28HC in NCPCMs is determined by Eq. 6.1:

$$\omega = \frac{\Delta H_{NCPCM}}{\Delta H_{PCM}} \times 100 \tag{6.1}$$

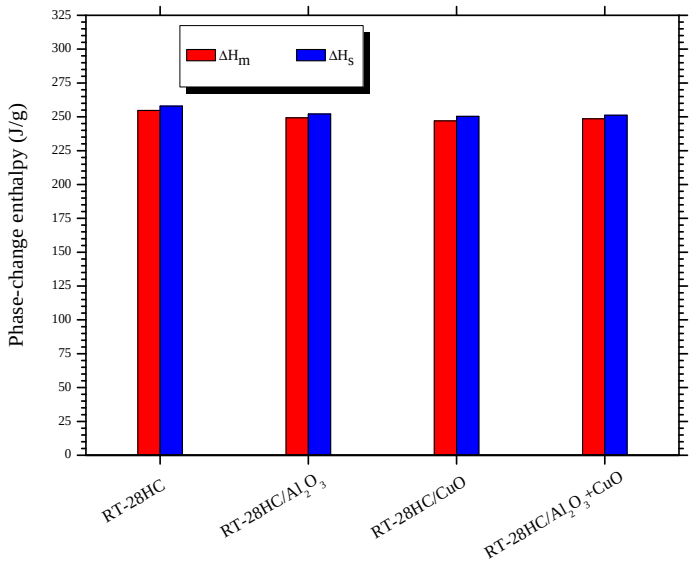


**Figure 6.15:** *Phase change enthalpies of metallic oxide–based mono and hybrid NCPCMs.*

where, $\Delta H_{NCPCM}$ and $\Delta H_{PCM}$ are the endothermic latent–heat of NCPCMs and pure PCM, respectively.

The degree of super–cooling ($\Delta T$) of NCPCMs are shown in Figs. 6.16 and 6.17 for carbon–based and metallic oxide–based nanoparticles NCPCMs, respectively. The peak melting temperature ($T_m$) and crystallization temperature ($T_c$) of RT–28HC were found to be 28.89 °C and 26.80 °C, respectively. The maximum deviations in $T_m$ and $T_c$ are determined as −0.28% and −0.60% for RT–28HC/GNPs, −0.24% and −0.93% for RT–28HC/MWCNTs, and −0.17% and −0.78% for RT–28HC/GNPs+MWCNTs, respectively, compared to RT–28HC. Similarly, the maximum deviations in $T_m$ and $T_c$ are −0.03% and −0.78% for RT–28HC/$Al_2O_3$, −0.17% and −0.56% for RT–28HC/CuO, and −0.14% and −0.60% for RT–28HC/$Al_2O_3$+CuO, respectively. The reduction in $\Delta T$ for hybrid NCPCMs are found to be 1.93°C and 1.97°C for RT–28HC/GNPs+MWCNTs and RT–28HC/$Al_2O_3$+CuO, respectively, which demonstrates the more signified role of GNPs+MWCNTs as nucleating agents compared with $Al_2O_3$+CuO in terms of its surface adsorption and effective homogeneous nucleation. Factually, the addition of nanoparticles in RT–28HC, the heterogeneous nucleation may be favoured at the cost crystallization point

depression (Yavari et al., 2011). It has been extensively reported that a high $\Delta T$ is evidently disadvantageous for utilization of PCM in thermal management because it can result in a hysteresis response to heat transfer. Figs.

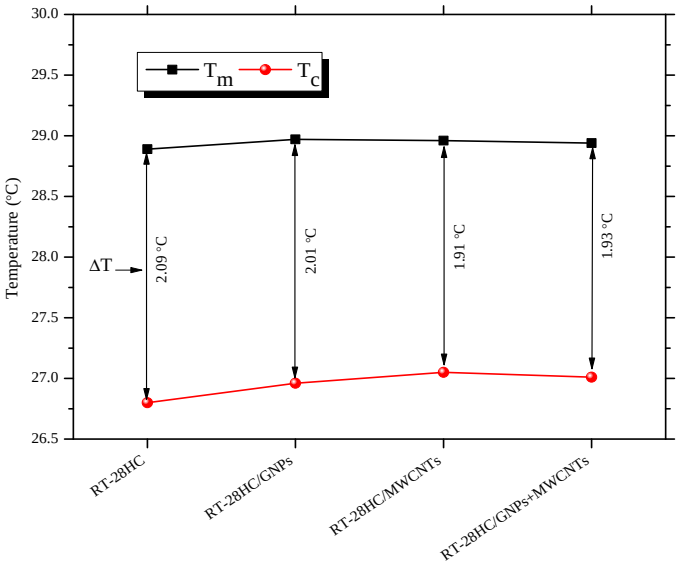


**Figure 6.16:** *Degree of super–cooling of carbon–based mono and hybrid NCPCMs.*

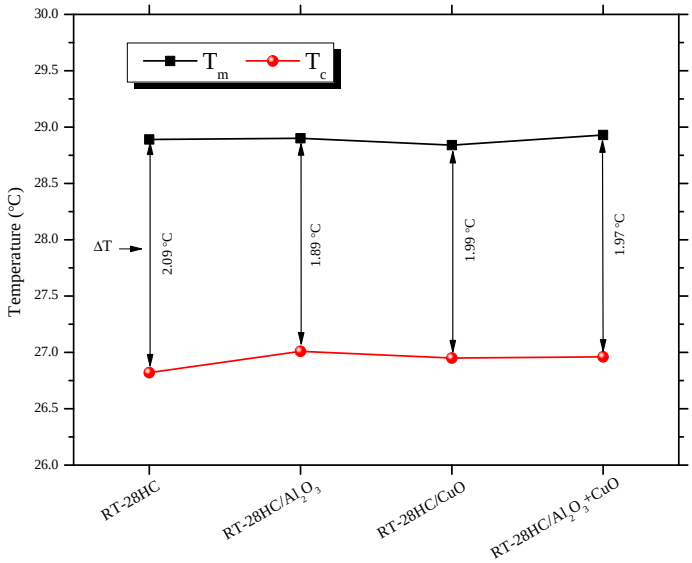


**Figure 6.17:** *Degree of super–cooling of metallic oxide–based mono and hybrid NCPCMs.*

6.18 and 6.19 illustrate the experimental and calculated latent-heat of fusion for NCPCMs, which can be calculated from Eq. 6.2 (Tian et al., 2015):

$$\Delta L_{NCPCM} = \Delta L_{PCM} \cdot \omega = \Delta L_{PCM}(1 - \varphi) \tag{6.2}$$

where, $\Delta L_{NCPCM}$ represents the calculated latent–heat of fusion of NCPCM, $\Delta L_{PCM}$ represents the latent heat of pure PCM, and $\omega$ and $\varphi$ are the mass fraction of pure PCM and nanoparticles, respectively.

It can be observed from Figs. 6.18 and 6.19 that the experimentally mea-

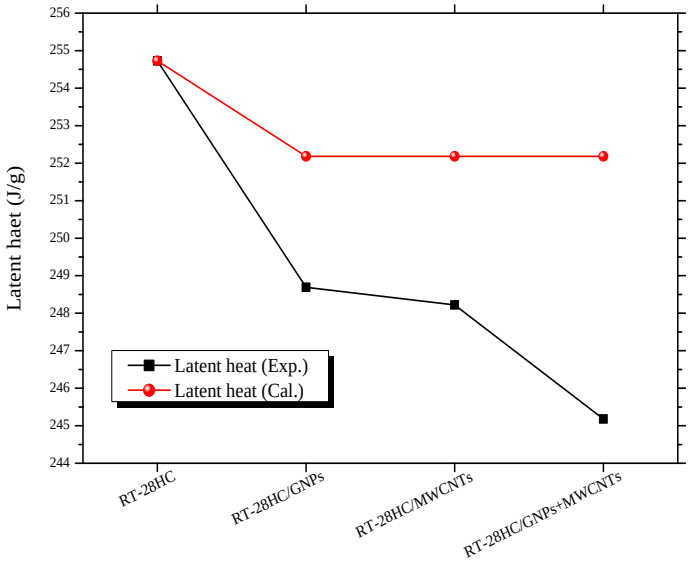


**Figure 6.18:** *Comparison of latent–heats of carbon–based mono and hybrid NCPCMs.*

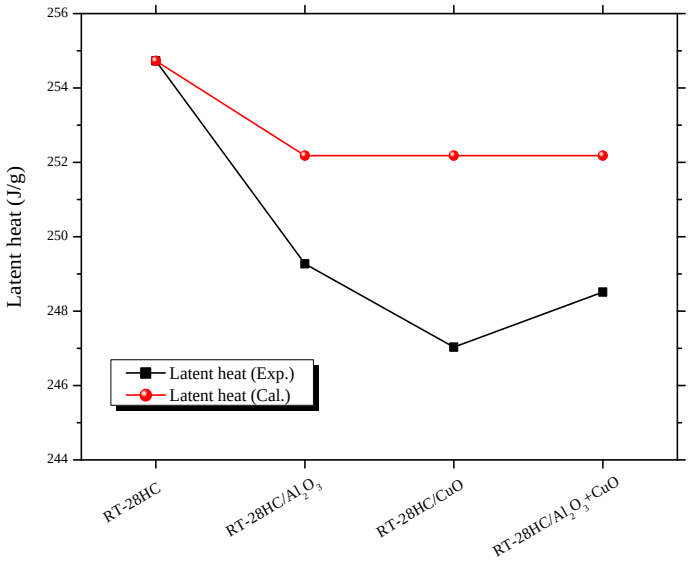


**Figure 6.19:** *Comparison of latent–heats of metallic–oxide based mono and hybrid NCPCMs.*

sured latent–heat of fusion for each NCPCM is lower than that of the calculated value. The deviation in values is based on the type of nanoparticles, as the mass fraction of all the nanoparticles is constant 1.0 wt.%. Similar deviations

in experimental and calculated values have been reported in the investigations of Li et al. (Li et al., 2017), Sharma et al. (Sharma et al., 2016), Tian et al. (Tian et al., 2015) and Wang et al. (Wang et al., 2009b). In addition, a relative error of 2.78% and 1.46% are obtained between the calculated and experimental values of RT–28HC/GNPs+MWCNTs and RT–28HC/$Al_2O_3$+CuO, respectively, with the hybrid NCPCMs having latent–heat fusion of 245.18 J/g and 248.51 J/g, respectively. The results show that the hybrid NCPCM of RT–28HC/GNPs+MWCNTs at 1.0 wt.% has the optimum value of latent heats, which is favourable for thermal management applications. The decrease in latent–heats results in the increase of thermal conductivity. Furthermore, the discrepancies in the calculated values may be due the surface morphology, structure, size and rate of dispersion of nanoparticles in RT–28HC.

Table 6.3: Phase-change properties of mono and hybrid NCPCMs*.

| Sample | Melting | | | | | Solidification | | | | | $\omega$ (%) | $\Delta$ T |
|---|---|---|---|---|---|---|---|---|---|---|---|---|
| | $T_{oset,m}$ | $T_{peak,m}$ | $\Delta H_{m,exp}$ | $\Delta H_{m,cal}$ | RE (%) | $T_{oset,c}$ | $T_{peak,c}$ | $\Delta H_{c,exp}$ | $\Delta H_{c,cal}$ | RE (%) | | |
| RT–28HC | 27.38 | 28.89 | 254.73 | – | – | 26.64 | 26.80 | 257.90 | – | – | 100 | 2.09 |
| RT–28HC/GNPs | 27.40 | 28.97 | 248.69 | 252.18 | 1.38 | 26.98 | 26.66 | 250.61 | 255.32 | 1.85 | 97.63 | 2.01 |
| RT–28HC/MWCNTs | 27.70 | 28.96 | 248.22 | 252.18 | 1.57 | 26.89 | 27.05 | 250.55 | 255.32 | 1.87 | 97.44 | 1.91 |
| RT–28HC/GNPs+MWCNTs | 27.60 | 28.94 | 245.18 | 252.18 | 2.78 | 27.13 | 27.01 | 248.77 | 255.32 | 2.57 | 97.44 | 1.93 |
| RT–28HC/$Al_2O_3$ | 27.63 | 28.90 | 249.27 | 252.18 | 1.15 | 26.72 | 27.01 | 252.08 | 255.32 | 1.27 | 97.86 | 1.89 |
| RT–28HC/CuO | 27.64 | 28.94 | 247.03 | 252.18 | 2.04 | 25.65 | 26.95 | 250.36 | 255.32 | 1.94 | 96.98 | 1.99 |
| RT–28HC/$Al_2O_3$+CuO | 27.37 | 28.93 | 248.51 | 252.18 | 1.46 | 26.71 | 26.96 | 251.18 | 255.32 | 1.62 | 97.56 | 1.97 |

* $T_{oset,m}$ : onset melting temperature, $T_{peak,m}$ : peak melting temperature, $\Delta H_{m,exp}$: experimental latent-heat of melting,

$\Delta H_{m,cal}$ : calculated latent-heat of melting, $T_{oset,c}$ : onset solidifying temperature, $T_{peak,c}$ : peak solidifying temperature,

$\Delta H_{c,exp}$ : experimental latent-heat of solidifying, $\Delta H_{c,cal}$ : calculated latent-heat of solidifying, RE: relative error,

$\omega$: Mass percentage of RT–35HC, $\Delta$T: Degree of supercooling

### 6.3.6 Thermal conductivity analysis

The primary function of PCM in thermal management application is to absorb and release the thermal energy while melting and solidifying effectively. The rate of thermal energy storage and release during fusion and crystallization is highly dependent on the thermal conductivity of the PCM. The low thermal conductivity of the pure PCMs reduces both the rate of heat storage and release and restrict its applications. A PCM with higher thermal conductivity increases the heat transfer rate during melting and solidification processes, which in turn reduces the melting and solidification time (Arshad et al., 2019a). Fig. 6.20 presents the thermal conductivities of pure RT–28HC, RT–28HC/GNPs, RT–28HC/MWCNTs and RT–28HC/GNPs+MWCNTs. Similarly, Fig. 6.21 presents the effective thermal conductivities of pure RT–28HC, RT–28HC/$Al_2O_3$, RT–28HC/CuO and RT–28HC/$Al_2O_3$+CuO. The effective thermal conductivities of RT–28HC dispersed with carbon–based and metallic oxides–based nanoparticles are measured at temperature of 20 °C and 25 °C for solid–phase and 30–45 °C for liquid–phase with an increment of 5°C. It can observed from Figs. 6.20 and 6.21 that effective thermal conductivity generally increases with the addition of nanoparticles, which is due to the higher effective thermal conductivity of nanoparticles compared to the pure PCM. The higher effective thermal conductivities were obtained for pure RT–28HC and NCPCMs at temperature of 20 °C and 25 °C in solid–phase. Contrarily, the lower effective thermal conductivity values were observed in liquid–phase at temperature range from 30 °C to 45 °C. This reveals that the effective thermal conductivity is strongly dependent on temperature. This decreasing trend in effective thermal conductivity of pure RT–28HC and NCPCMs with temperature is because of the turning of the orderly microstructure of pure RT–28HC in solid–phase into disorderly microstructure in liquid-phase. In solids, the heat is conducted by lattice vibrations as the molecules vibrate within their lattice structure. This lattice vibration and motion of free electron

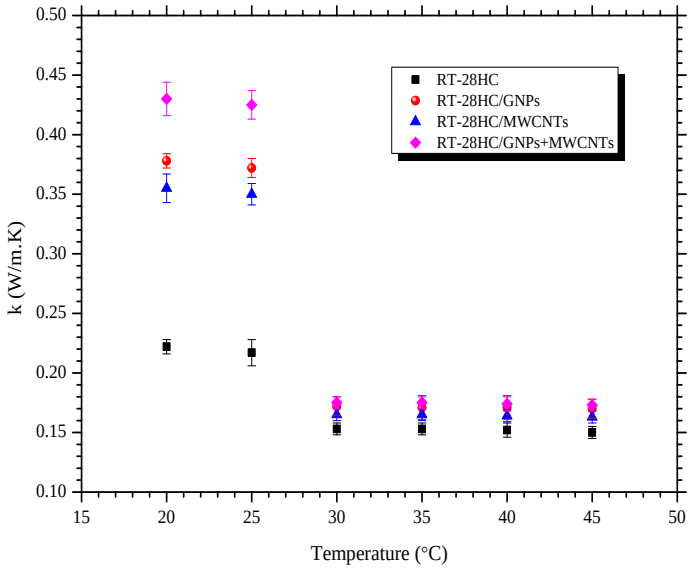


**Figure 6.20:** *Effective thermal conductivity of carbon–based mono and hybrid NCPCMs as a function of temperature.*

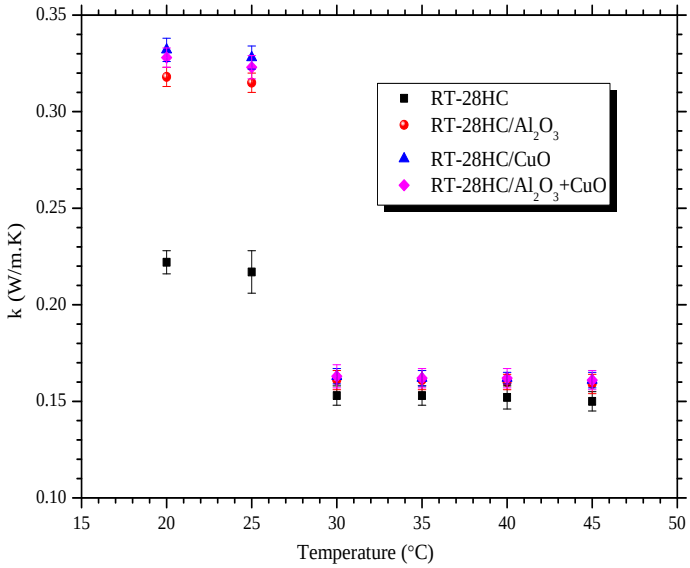


**Figure 6.21:** *Effective thermal conductivity of metallic oxide–based mono and hybrid NCPCMs as a function of temperature.*

are the most efficient in solids than liquids. Therefore solids generally possess the higher thermal conductivity than liquids. Effective thermal conductivities of 0.378, 0.355 and 0.430 W/m.K were obtained for RT–28HC/GNPs, RT–28HC/MWCNTs and RT–28HC/GNPs+MWCNTs, respectively at 20°C, as shown in Fig. 6.20. Effective thermal conductivities of RT–28HC/$Al_2O_3$, RT–28HC/CuO and RT–28HC/$Al_2O_3$+CuO were 0.318, 0.332 and 0.328 W/m.K, respectively, at 20°C, as shown in Fig. 6.21. It can be clearly observed that

the hybrid NCPCM with GNPs+MWCNTs weight percentage of 75%/25% has the highest effective thermal conductivity among all other mono and hybrid NCPCMs. Figs. 6.22 and 6.23 illustrate the effective thermal conductivity enhancement factor of NCPCMs to evaluate the effect of nanoparticles in enhancement of heat transfer rate, as given by Eq. 6.3:

$$\eta = \frac{k_{NCPCM} - k_{PCM}}{k_{PCM}} \times 100 \tag{6.3}$$

where, $k_{NCPCM}$ and $k_{PCM}$ are the thermal conductivity of the NCPCM and pure PCM, respectively.

It can be seen from Figs. 6.22 and 6.23 that the effective thermal conductivity enhancement increases non–linearly with respect to temperature for a specific NCPCM, either of carbon–based or metallic oxide–based. The relative enhancement in effective thermal conductivity shows that RT–28HC/GNPs+MWCNTs has the higher enhancement of 96% and 94% at 25 °C and 20 °C, respectively, in solid–phase compared to the RT–28HC/GNPs and RT–28HC/MWCNTs, as shown in Fig. 6.22. The higher effective thermal conductivity enhancement of RT–28HC/GNPs+MWCNTs is because of the hybrid NCPCMs form three–dimensional heat transfer path, which permits transfer of the thermal energy in all regions of the RT–28HC while heating/cooling (Zou et al., 2018). A slight decreasing trend can be observed for the case of RT–28HC/$Al_2O_3$+CuO hybrid NCPCM, which has a maximum effective thermal conductivity enhancement of 49% and 48% at 25 °C and 20 °C, respectively, compared to RT–28HC/CuO which has 51% and 50% enhancement in thermal conductivity at 25 °C and 20 °C, respectively, as shown in Fig. 6.23. The variation in results of RT–28HC/CuO and RT–28HC/$Al_2O_3$+CuO is because of the size, morphology, density and dispersion stability of the nanoparticles as well as their inherent thermal conductivity. Since CuO has a higher thermal conductivity than $Al_2O_3$, therefore RT–28HC/CuO has a higher thermal conductivity than RT–28HC/$Al_2O_3$+CuO having constant mass fraction of 1.0 wt.%. Furthermore,

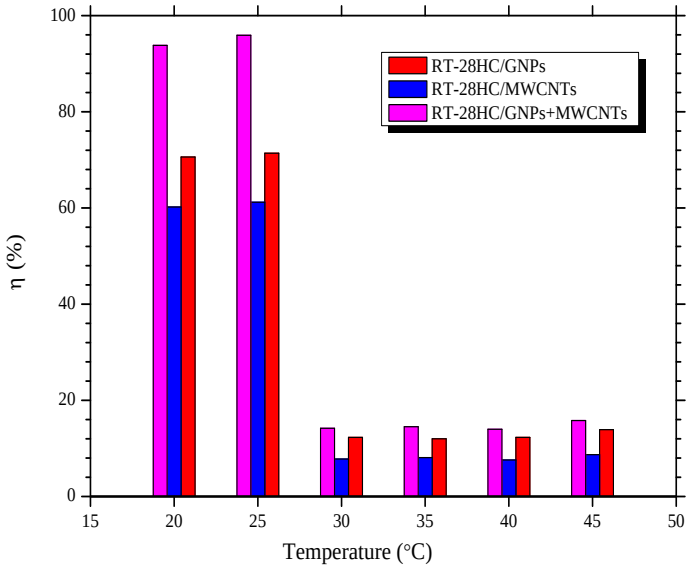


**Figure 6.22:** *Effective thermal conductivity enhancement factor of carbon–based mono and hybrid NCPCMs as a function of temperature.*

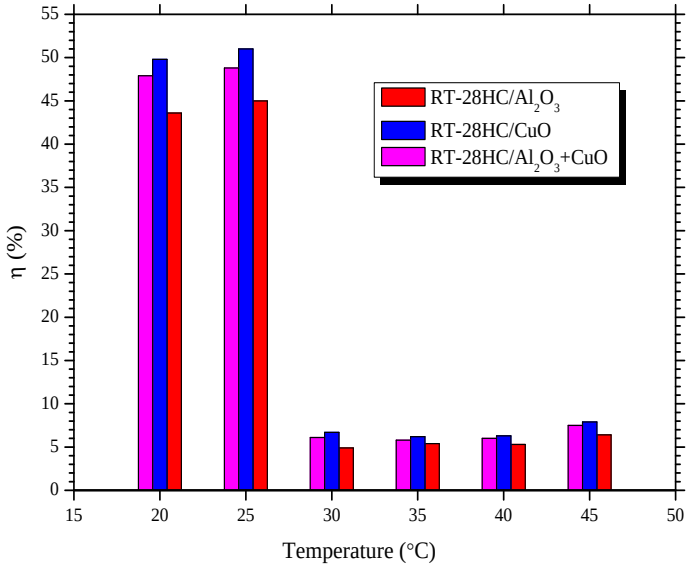


**Figure 6.23:** *Effective thermal conductivity enhancement factor of metallic oxide–based mono and hybrid NCPCMs as a function of temperature.*

the $Al_2O_3$ nanoparticles have the smaller size (13 nm) and density compared to CuO nanoparticles (< 50 nm), which have the better degree of homogenization and rate of dispersion in pure PCM. This reveals the better dispersion stability of hybrid nanoparticles of $Al_2O_3$+CuO having mass percentage ratio of 75%/25% dispersed in RT–28HC. In addition, the thermal boundary resistance between the nanoparticles and matrix molecules play a dominant factor for the discrepancy (Mahian et al., 2019). Furthermore, the results re-

veal that carbon-based hybrid NCPCMs have the much better tendency to store and release the heat rate compared to the metallic–oxide based hybrid NCPCMs, due to the higher enhancement in thermal conductivity. There are two main factors that enhance the thermal conductance rate of NCPCMs. Firstly, the higher thermal conductivity of the nanoparticles and secondly, the motion of the nanoparticles in NCPCMs in liquid–phase, which causes a quasi–convection phenomenon (Babapoor and Karimi, 2015). Furthermore, the interfacial thermal resistance is reduced with $3D$ nano–structure as compared to the $2D$ nano–structure for the case of metallic–oxide based NCPCMs between the pure PCM and nanoparticles, which improves the rate of thermal conductance.

### 6.3.7 Infrared thermography (IRT) analysis

Fig. 6.24 illustrates the IR thermographic images of the melting process of RT–28HC, RT–28HC/$Al_2O_3$+CuO and RT–28HC/GNPs+MWCNTs at different time steps from 5 min to 55 min with time step of 5 min. The heating stages of each specimen can be reflected clearing at time step. There is noticeable temperature difference between the background and specimens because of the latent–heat absorption of the specimens during phase–change. The blue colour of the specimens indicates the low temperature, which changes into the red colour during heating indicating the high temperature. The uniform melting of each specimen can be observed while heating, however, the quick flow away and shrinkage is found in pure RT–28HC, shown in Fig. 6.24d. This phase transition from solid–to–liquid causes the pure PCM to lose its shape–stability completely. In the case of hybrid NCPCMs specimens, uniform phase transition is observed with slight shrinkage and flow away due to the heating-impact effect. Since the hybrid NCPCMs contain only 1 wt.% of $Al_2O_3$+CuO and GNPs+MWCNTs, there was therefore only slight shrinkage. However, the shrinkage level and flow away decrease with the increase of the loading

of nanoparticles. The melting process of RT–28HC/GNPs+MWCNTs shows

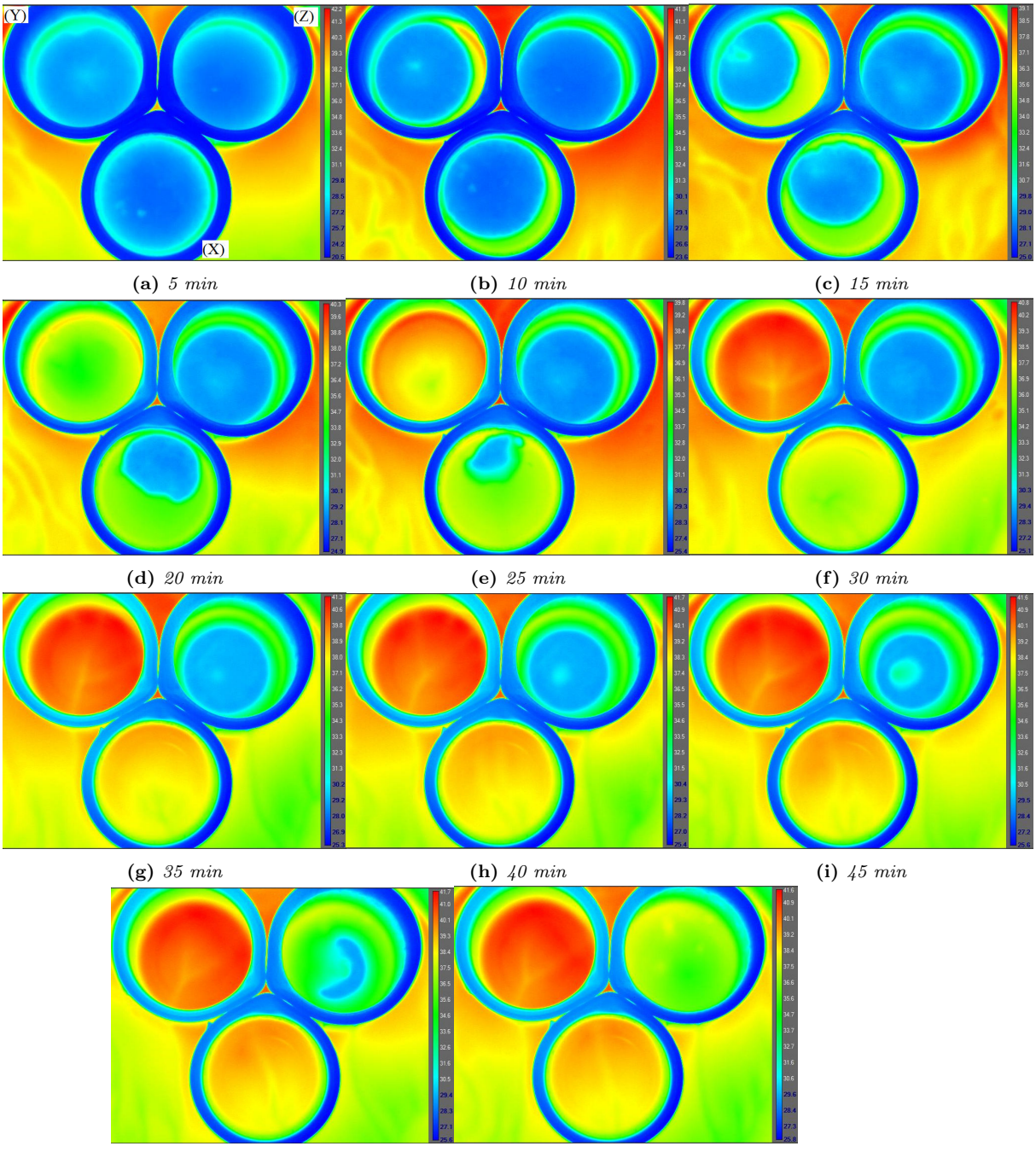


**(a)** *5 min* **(b)** *10 min* **(c)** *15 min*

**(d)** *20 min* **(e)** *25 min* **(f)** *30 min*

**(g)** *35 min* **(h)** *40 min* **(i)** *45 min*

**(j)** *50 min* **(k)** *55 min*

**Figure 6.24:** *Infrared thermography images of the melting process of RT–28HC-(X), RT–28HC/$Al_2O_3$+CuO-(Y) and RT–28HC/GNPs+MWCNTs-(Z) at different time steps with temperature variation in °C.*

there is no complete melting until 50 min and surface temperature is lower than the pure RT–28HC and RT–28HC/$Al_2O_3$+CuO, which reveals the best heat transfer enhancement due the higher thermal conductivity of GNPs and MWCNTs. The enhancement in melting process with GNPs and MWCNTs

is due to the uniform and homogenous dispersion of organic based nanoparticles in organic PCMs, which increase the viscosity and shape–stability and lowers the convection heat transfer. The phase transition duration of RT–28HC/GNPs+MWCNTs, compared to pure RT–28HC and RT–28HC/$Al_2O_3$+CuO, improves the heat dissipation rate while thermal management of microelectronics due to constant lower temperature of NCPCMs. Furthermore, the results reveal that this enhanced latent heating phase duration and uniform natural convection heat transfer of RT–28HC/GNPs+MWCNTs avoids the overheating and has a greater potential for better thermal management of microelectronics.

## 6.4 Concluding remarks

An experimental study was conducted to investigate the thermal properties of carbon-based (GNPs and MWCNTs) and metallic oxide-based ($Al_2O_3$ and CuO) mono and hybrid NCPCMs. The mass fraction of all the nanoparticles was kept constant of 1.0 wt.%, to explore the best NCPCM with optimum thermal properties for efficient thermal management of microelectronics. Various material characteristic techniques such as ESEM, FT–IR, TGA, DCS, IRT and thermal conductivity apparatus were used to explore the chemical and thermal properties. The results of the current study are summarized as follows:

- The surface morphological and structural investigation disclosed the presence of GNPs, MWCNTs, $\gamma-Al_2O_3$ and CuO in pure RT–28HC. Furthermore, ESEM and XRD results confirmed the uniform dispersion of all the nanoparticles into RT–28HC.

- The FT–IR spectrum revealed the chemical compatibility of GNPs, MWCNTs, $\gamma-Al_2O_3$ and CuO with RT–28HC and only physical interaction of nanoparticles with RT–28HC was found.

- The TGA and DTG results revealed that all the mono and hybrid NCPCMs maintained their thermal and chemical stability. The addition of nanoparticles improved the thermal and chemical stability of pure RT–28HC. Furthermore, the GNPs and MWCNTs dispersed NCPCMs showed better dispersion stability than $Al_2O_3$ and CuO dispersed NCPCM. In addition, hybrid NCPCM of GNPs+MWCNTs nanoparticles had the better stability than $Al_2O_3$+CuO nanoparticles dispersed hybrid NCPCM.

- Small variations were observed in the DSC results regarding melting temperature and latent heat of fusion. The maximum deviation in peak melting temperatures observed were $-0.17\%$ and $-0.14\%$ for RT–28HC/GNPs+MWCNTs and RT–28HC/$Al_2O_3$+CuO, respectively. Similarly, a maximum deviation of $-0.78\%$ and $-0.60\%$ were obtained in peak solidification temperatures for RT–28HC/GNPs+MWCNTs and RT–28HC/$Al_2O_3$+CuO, respectively. In addition, the maximum reduction in latent–heat of fusions were 3.75% and 2.44%, respectively, for RT–28HC/GNPs+MWCNTs and RT–28HC/$Al_2O_3$+CuO. Finally, the maximum reduction in latent–heat of solidification for RT–28HC/GNPs+MWCNTs and RT–28HC/$Al_2O_3$+CuO were 3.54% and 2.61%, respectively.

- The hybrid NCPCM containing mass percentage ratio of 25%/75% GNPs+MWCNTs showed the higher thermal conductivity enhancement of 96% than GNPs and MWCNTs based NCPCM having 71.4% and 61.2% thermal conductivity enhancement, respectively, compared to pure PCM. By comparison, a 49% enhancement in thermal conductivity of RT–28HC/$Al_2O_3$+CuO hybrid NCPCM was achieved relative to pure PCM.

- The IRT results illustrated that RT–28HC/GNPs+MWCNTs hybrid NCPCM showed uniform heating for a longer melting duration compared to RT–28HC/$Al_2O_3$+CuO and pure RT–28HC. This enhancement in phase transition of RT–28HC/GNPs+MWCNTs hybrid NCPCM during heating was due to the uniform and homogenous dispersion of carbon-

based nanoparticles (GNPs+MWCNTs) in organic PCMs, which increases the viscosity and shape–stability while lowering the convection heat transfer.

The results have proved that the prepared hybrid NCPCMs exhibit significant enhancement in thermal properties without significantly affecting TES capability. Therefore, hybrid NCPCMs may be used for passive thermal management of microelectronics after thermal cyclic tests.

# Chapter 7

# Experimental analysis of metal–foam/PCM based heat sink[1]

## Abstract

In this paper, the heat transfer enhancement is experimentally investigated of a thermal management system (TMS) integrated with metal foam embedded in phase change material (PCM). The copper metal-foam is coated with a thin hard layer of high-temperature copper oxide (CuO) which is acting as a thermal conductivity enhancer (TCE). The metal-foam/PCM composite is attached to a heat sink and effect of various variables such as filling thickness ratio, volumetric fraction of PCM and number of input power levels are experimentally studied. The filling thickness ratios of metal-foam are varied from 0.0-1.0, RT-28HC as PCM of 0.0 and 1.0 volumetric fractions and heating powers are applied from 2 to 5 W. The melting and solidifying phenomenon

[1]This Chapter is published as:
**Arshad, A.**, Jabbal, M., & Yan, Y. (2020, July). Thermal performance of PCM-based heat sink with partially filled copper oxide coated metal–foam for thermal management of microelectronics. In 2020 *19th IEEE Intersociety Conference on Thermal and Thermomechanical Phenomena in Electronic Systems (ITherm)* pp. 697-702. IEEE. doi:10.1109/ITherm45881.2020.9190574

of TMS is investigated with and without metal-foam and PCM at each input heating power. The results showed that metal-foam/PCM based heat sink can extract the base temperature during the heating period and heat transfer enhancement is improved monotonously with the increase of filling height ratio. The filling thickness ratio of 0.5 revealed the best thermal performance of PCM filled CuO coated metal-foam heat sink for passive cooling of portable electronic devices.

**Keywords:** Thermal management, Copper oxide, Metal–foam, Heat sink, Phase change material

## 7.1 Introduction

In current era, the microelectronics technology has turned into revolutionary advancement with advanced features, and smart and faster applications. At the cost of compactness of electronic devices such as mobiles, laptops, iPad, computers, robotics and personal digital assistant, the rate of internal heat generation has been increasing gradually. The mean-time-to-failure in increasing exponentially which reduces the life of electronic devices with a small change in operating temperature. The major reason of electronics failures is due to rise of temperature, which accounts for 55% of all failures (Yeh, 1995). Moreover, the increasing rate of electronics failures is 100% for the temperature rise from 10 to 20 °C. However, a 1 °C temperature reduction can reduced failure rate of 4% in electronic devises (Mithal, 1996). Therefore, it is an emerging challenge to dissipate this internal generated heat of microelectronics by an efficient thermal management (TM) technology to maintain the safe operating temperature. In the field of microelectronics and semiconductors, an efficient and effective TM of denser electronics IC chips is a significant challenge to maintain their performance and reliability (Ohring, 1998a). Thus, there is a need to develop a highly efficient and reliable TMS to absorb and dissipate the heat from heat source towards atmosphere. In such manner various active and passive TMS

have be introduced (Venkatadri et al., 2011; Ebadian and Lin, 2011). Using latent heat thermal energy storage (LHTES) based on phase change material (PCMs), that store excessive heat while phase–transition, have great potential of TMS as a passive cooling technology. Besides of the PCM, three methods i.e. metallic–fins (Ali et al., 2018b), metallic–foam matrix and nanoparticles (Leong et al., 2019; Arshad et al., 2020b) have been used in LHTES as thermal conductivity enhancers (TCEs). Based on the detailed review on these methods by Sahoo et al (Sahoo et al., 2016b), it has been concluded that metallic foams are the best TCE which enhance the heat transfer rate due to higher surface area to volume ratio. So far, many researchers have reported the thermal performance of metallic foam/PCM based heat sink as passive cooling TMS for electronic devices. Chen et al. (Chen et al., 2014) conducted the experimental and numerical study using paraffin wax and aluminum metal foam of 91.37% porosity and 9 PPI to enhance the heat transfer rate. The authors reported that metal foam enhanced the solid-liquid phase change heat transfer due to thermal conduction in metal matrix. Mancin et al. (Mancin et al., 2015) investigated the phase-change phenomenon of three different paraffin waxes of different melting temperatures of 53 °C, 57 °C and 59 °C using copper metal foam of constant porosity of 95% and PPI of 5, 10 and, 40. The results showed that inclusion of metal foam in PCM improved the heat transfer rate of a passive TMS by keeping the lower surface temperature. Nada and Alshaer (Nada and Alshaer, 2015) performed the detailed parametric study based on carbon foam of different porosities (60–85%) and pores (200–800 $\mu$m) with different PCMs for TM of electronic devices. The results proposed that increasing the porosity decreased the module temperature rise and delayed the time to approach steady–state temperature. Wang et al. (Wang et al., 2016) explored the heat transfer enhancement of a metal foam/PCM composite TMS. The copper foam of pore size 2–3 mm and 97.3% porosity and paraffin wax as a PCM were used. The results revealed that copper foam improved uniformity of internal heat transfer and reduced the heat storage time of paraffin wax

by 40%. Yang et al. (Yang et al., 2016c) investigated the solidification of distilled water in open-cell copper, aluminum and nickel metallic foam of different PPI sizes. The results showed that stacked metal foams of constant morphology reduced the solidification time more effectively than single metal foam because of the enhanced heat transfer rate. Zhu et al. Zhu et al. (2016) conducted the numerical study using aluminum metal foam with 90% porosity and 5, 10 and 20 PPI and paraffin wax composite TMS and investigated the thermal performance enhancement. The authors found the efficiency of LHTES up to 83.32% compared to the pure paraffin wax. Recently, Zhu et al. (Zhu et al., 2018) experimentally investigated the filling heights of ratio of the copper foam/PCM based heat sink TMS for thermal management. The authors used the two different PPI of 15 and 30 with constant porosity of 96%. The thermal performance was assessed by the filling effectiveness and it was proposed that 2/3 partial filling heat sink was more economical at the cost of TMS weight, material and performance. The composite of metal foam and fin, made of copper, with PCM was recently investigated experimentally by Yang et al. (Yang et al., 2019) to enhance the solidification heat transfer rate. The results revealed that inserting fin into metal foam enhanced the solidification rate by 28.35%. The literature clearly reveals that aluminum and copper metallic foams have been used for passive TM of electronic devices. In current study, the thermal performance of a TMS integrated with CuO coated copper metal–foam of various thicknesses and PCM is investigated experimentally. The metal–foam/PCM composite embedded in a heat sink and effect of various variables such as filling thickness ratios, volumetric fractions of PCM and number of input power levels are experimentally studied.

## 7.2 Experimental Setup and Measurement

In current experimental study, a passive cooling TMS was designed and built, as shown in Fig. 7.1. The schematic diagram shows that TMS consists mainly

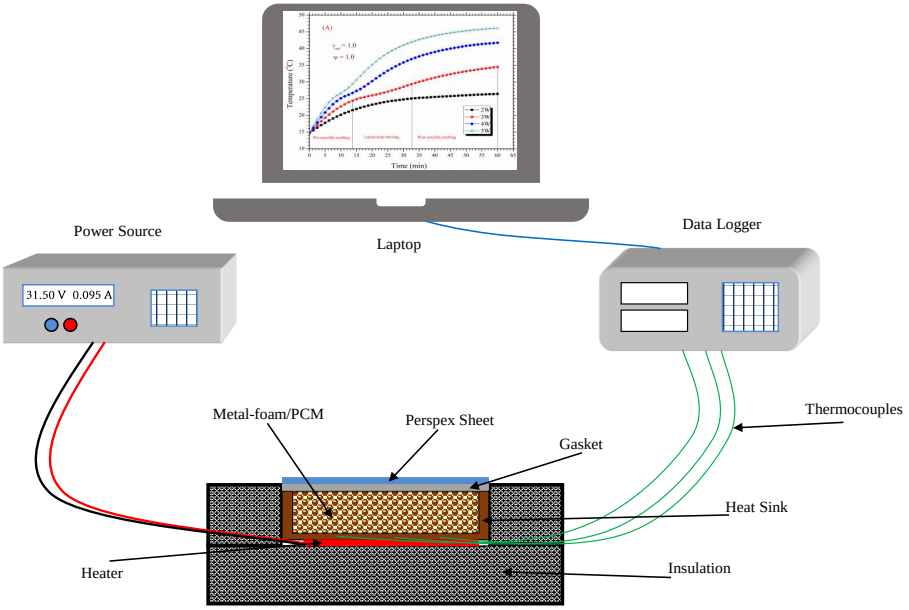


**Figure 7.1:** *Schematic diagram of experimental setup.*

the heat sink, data acquisition system, DC power supply and the desktop PC. The heat sink, having no fins and dimensions of 55×55×5 mm$^3$, was made from copper using computer numerical control (CNC) machine. A DC power supply made of Keysight Technologies (N6700C, 0.5 A/100 V) was used to provide different power levels of 2–5 W at ambient temperature, to mimic heat generation. A PC based digital data acquisition system (Agilent 34972A, USA) was used to record the temperature variation through thermocouples inserted at different points on the heat sink. The data acquisition system was connected to the desktop PC and Agilent Technologies, Inc. (Taft Ave. Loveland, USA) software is used to record the temperature at interval of 5 s during the experimentation. A heat sink assembly consists of insulating material, silicon gasket, perspex sheet, screws, heater, K–type thermocouples, PCM and metal foam filled in heat sink. The heat sink was filled with copper metal–foam having dimensions of 50×50 mm$^2$ and two different thickness/heights of 2.5 and 5 mm which is acting as a TCE, purchased from Versarien Technologies Limited, UK. The micro–porous copper metal foam has the $\varepsilon$, pore sizes and PPI of 63%, 425–850 $\mu$m and 50, respectively. The metal foam is coated with a thin

hard layer of high–temperature copper oxide (CuO) to improve the thermal conductivity. The copper foams were placed inside the heat sink and their thickness ($t$) was varied from 0 mm (no metal–foam) to 5 mm (fully filled with metal–foam). The filling thickness ratio is defined as $\gamma_{mf} = t/H$. To record the temperature variations with time, highly precision K–type (Omega, 0.5 mm wire diameter) thermocouples were inserted at different points. Two thermocouples were inserted in heat sink base at equally distanced in a 1.5 mm deep grove to measure the heat sink base temperature which in directly in contact with the heater. To fix the thermocouples on the heat sink, Araldite(TM) epoxy resin is used. All thermocouples were connected the module of data acquisition system. The OMEGALUX silicon rubber plate heater (SRFG–202/10–P–220V) of 50×50 mm$^2$ and thickness of 1.14 mm was attached at the bottom of heat sink in a 55×55×5 mm$^3$ milled cavity to mimic the heat generation in electronic devices. The heater is made of coil–type nichrome which can generate the maximum heat flux of 1.55 W/cm$^2$. The direct contact of heater with heat sink was made possible through the adhesiveness of sticker type heater. To prevent excess heat escaping to the atmosphere the heat sink is insulated in rubber insulation and placed on a rubber mat under heating and discharging. To observe the physical state of PCM, top surface of heat sink is covered with perspex sheet. To avoid leakage and overflow of PCM, silicon gasket is placed between the perspex sheet and heat sink. The heat sink with and without metal foam and PCM was tested for 0.0 and 1.0 volumetric fractions ($\psi$) of PCM. A commercial organic PCM, namely RT–28HC, was used as a PCM with melting temperature of 27–29 °C, purchased from Rubitherm GmbH, Germany. The selection of PCM is substantially a key factor for designing a LHTES for passive TM. The melting temperature of PCM should be lower than the maximum temperature raised inside the electronic devices at critical operating conditions. The latent heat of fusion of RT-28HC is 250 kJ/kg which is highly suitable for passive TM of electronic devices. The thermophysical properties of RT–28HC and copper metal foam are listed in

Table 7.1 and Table 7.2, respectively.

The uncertainty of the measured quantities is associated with the least count of the corresponding measurement devices. The uncertainty in temperature measurement according to according to ASTM standard (Burns et al., 1993) in a temperature range of 0–100 °C with maximum variation of ±0.1 °C. The uncertainty in data logger is ±0.1 °C. The uncertainties in voltage and current are measured of ±0.01 V and ±0.001 A, respectively. The uncertainty in heat input are calculated using Kline and McClintock (Kline, 1953) technique, and minimum and maximum uncertainties are obtained of 1.68% and 1.91%, respectively.

Table 7.1: Thermophysical properties of PCM and heat sink.

| **Property** | **RT–28HC** | **Cu** |
|---|---|---|
| $T_m$(K) | 301 | – |
| $T_s$(K) | 302 | – |
| $T_l$(K) | 300 | – |
| $L$ (J/kg) | 250,000 | – |
| $c_p$ (J/kg.K) | 2000 | 380 |
| $\rho$ (kg/m$^3$) | 825 | 8920 |
| $k$ (W/m.K) | 0.2 | 400 |
| $\mu$ (Pa.s) | 0.0235 | – |
| $\beta$ (1/K) | 0.0006 | – |

Table 7.2: Properties of copper metal–foam .

| **Properties** | **Copper metal-foam** |
|---|---|
| $\varepsilon$ (%) | 63 |
| PPI | 50 |
| Pore size | 425–850 $\mu$m |
| $k$ (W/m.K) | 119 |
| Coating | CuO (Black) |

## 7.3 Results and discussion

### 7.3.1 Heat transfer performance of filling thickness ratio without PCM

The heat transfer performance of heat sink is evaluated at 0.0 volumetric fraction of PCM for different filling thickness ratio copper metal-foam. Figs. 7.2a and 7.2b illustrate the temperature distribution of heat sink temperature for heating and cooling cycles, respectively, as function of time at input power of 3 W. The temperature rises rapidly for all filling thickness ratios while constant heating, as expectedly. The base temperature of heat sink is recorded of 39.64 °C, 37.67 °C and 35.76 °C for $\gamma_{mf}$ = 0.0, 0.5 and 1.0, respectively after 60 min while heating process. The reduction in the base temperature is obtained as 4.96% and 9.79% for $\gamma_{mf}$ = 0.5 and 1.0 of metal-foam based heat sink. The reduction in base temperature is because of the higher thickness of the metal-foam. Since the porosity and PPI of both samples of metal–foam is constant. In addition to this, temperature gradient is higher for $\gamma_{mf}$ = 1.0 metal-foam which improves the heat transfer rate. While cooling process, the heat sink base temperature decreases rapidly in reverse manner, except for $\gamma_{mf}$= 0.0. The rapid decrease in temperature with same order for $\gamma_{mf}$

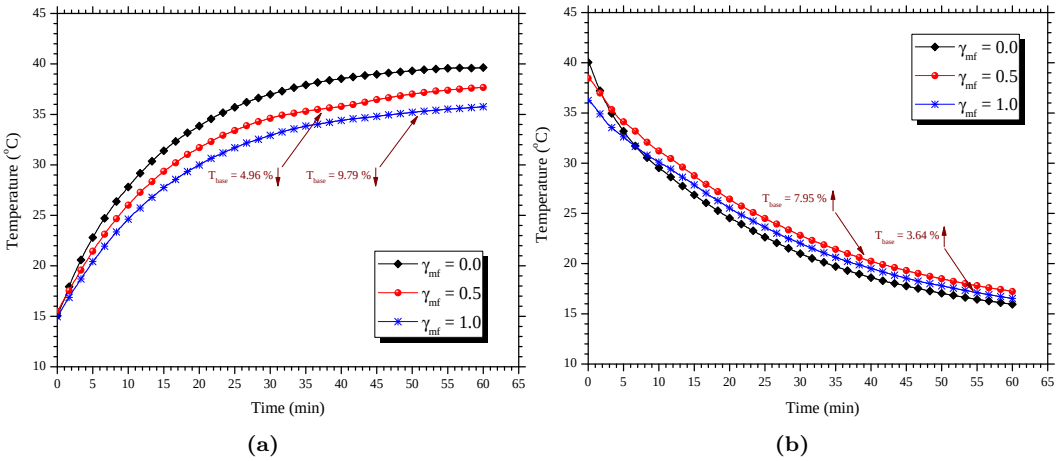


**Figure 7.2:** *Transient distribution of base temperature for different filling thickness ratios without PCM: (a) Charging, (b) Discharging.*

= 0.5 and 1.0 metal–foam based heat sinks have the same reasoning which are mentioned for heating process. The temperature is recorded at the end of 60 min cooling process of 15.95 °C, 17.22 °C and 16.53 °C for $\gamma_{mf}$ of 0.0, 1.0 and 0.5, respectively. For both case of heating and cooling, the heat sink base temperature increases and decreases monotonously, respectively. For the cases of without PCM, the heat transfer occurs for $\gamma_{mf} = 0.0$ heat sink merely by convection mode. Whereas, for $\gamma_{mf} = 0.5$ and 1.0 metal-foam based heat sinks, the transfer of heat is supported by both conduction and convection mechanisms. It can be observed that for first 10∼15 min of heating and cooling, the temperature rise and fall is more significantly, respectively. After that, the temperature raises gradually with lower rate because of heating driving force reaches to its saturation value. In similar way while cooling process, the temperature drops at a lower rate due to the less temperature gradient across the ambient conditions.

### 7.3.2 Heat transfer performance of filling thickness of metal foam ratio with PCM

The heat transfer performance of heat sinks of different $\gamma_{mf} = 0.0$, 0.5 and 1.0 filling at 1.0 volumetric fraction of PCM is evaluated for charging and discharging cycles as shown in Figs. 7.3a and 7.3b, respectively. The base temperature of heat sinks is increased sharping initially up to the first ∼12 min for each $\gamma_{mf}$ which is due the pre-sensible heating. However, a gradual decrease in base temperature is observed from 10-35 min approximately which shows the latent heating phase because of the latent heat of fusion of the PCM. Afterward the post-sensible heating phase is observed till 60 min of heating specially for $\gamma_{mf} = 1.0$. It is revealed from Fig. 7.3a that heat sink base temperature is decreased for the case of $\gamma_{mf} = 0.5$ and 1.0 due the presence of metal–foam in the presence of PCM which transfer the heat uniformly from the heat sink base towards the ambient. After 20 min of heating, the base

temperatures are recorded of 28.42 °C, 26.14 °C and 27.59 °C, respectively, for $\gamma_{mf}$ = 0.0, 0.5 and 1.0 which shows that 0.5 filling thickness ratio heat sink has the best heat transfer performance. The decreasing trend of $\gamma_{mf}$ = 0.5 can

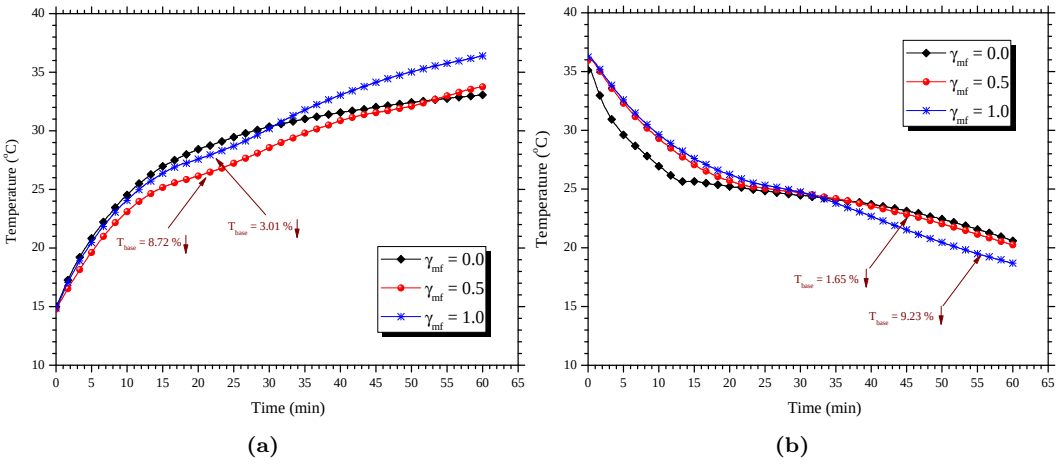


**Figure 7.3:** *Transient distribution of base temperature for different filling thickness ratios with PCM: (a) Charging, (b) Discharging.*

be observed till 40 min of heating compared to $\gamma_{mf}$ = 0.0 and 1.0. However, after 60 min of heating the base temperatures are recorded of 33.06 °C, 33.75 °C and 36.40 °C for $\gamma_{mf}$ = 0.0, 0.5 and 1.0, respectively. It can be revealed the increase in base temperature for 0.5 and 1.0 are 2.08% and 10.07% compared to $\gamma_{mf}$ = 0.0. The increasing and decreasing trend in base temperatures of copper metal-foam based heat sinks are due the inclusion of PCM and different thicknesses of metal–foams. The more amount of PCM is contained in $\gamma_{mf}$ = 0.0 because of the no metal–foam which reduced the heat transfer rate through the PCM. While for the case of $\gamma_{mf}$ = 0.5 and 1.0, the less amount of PCM is contained in the heat sink because of the different metal-foam thicknesses especially for $\gamma_{mf}$ = 1.0. As a result of this, faster heat transfer process occurs due to the higher thermal conductivity and high heat transferring area of porous structure of metal-foam. During the cooling process, as shown in Fig. 7.3b, a sharp decrease in base temperature is observed for fist 13 min which shows the pre-sensible cooling phase. However, up to the ∼35–40 min latent cooling phase can be observed for the case of $\gamma_{mf}$ = 0.5 and 1.0. Further up to the 60 min, post-cooling phase is observed of each filling thickness ratio. While

cooling, the temperatures of heat sink base are recorded of 20.59 °C, 20.25 °C, 18.69 °C for $\gamma_{mf}$ = 0.0, 0.5 and 1.0, respectively after 60 min. It can also be revealed that $\gamma_{mf}$ = 1.0 shows the faster cooling rate compare to the 0.0 and 0.5 $\gamma_{mf}$ due the less amount of PCM and higher thickness of metal-foam. Additionally, the slow cooling is occurred due the natural dissipation of heat which increases the cooling duration of compared to heating duration.

### 7.3.3 Heat transfer performance at different power levels for charging and discharging cycles

The temperature time history of filling thickness ratio of $\gamma_{mf} = 1.0$ is illustrated in Figs. 7.4a and 7.4b for charging and discharging cycles, respectively at input power levels from 2–5 W. The base temperature of heat sink is increased constantly with the increase of power level, as expected. The minimum and maximum base temperatures of 27.51 °C and 49.3 °C are achieved at 2 and 5 W, respectively, after 60 min of charging. In addition to this, it can be seen the latent heat phase reduces with the increase of power level. At 2 W power level, there is no latent heat phase change happened even after 60 min. At 3 W, latent heat phase ends after 30 min, but this phase ends just after ∼30 min at 5 W. Fig. 7.4b reveals that base temperature of heat sink is reduced gradually while discharging, and lower base temperature is achieved at lower power level, as expected. The minimum and maximum base temperatures are recorded of 13.12 °C and 15.49 °C, respectively, after 110 min of cooling. During the discharging process, the base temperature decreased sharply for each power level and PCM releases its sensible heat to cool down up to its congealing temperature. Further, the PCM starts solidifying process due to its latent heat of solidification at ambient temperature through natural convection phenomenon. It can be observed that discharging process is longer than the charging process. Also, phase change process of PCM is more prolonged during cooling process than the heating process. The reason behind of such irregular

charging and discharging phenomenon depends on the heating/cooling rate. During charging process, the heating rate is higher than the discharging process which takes the less time to change the solid–liquid phase than the discharging process during changing the liquid-solid phase.

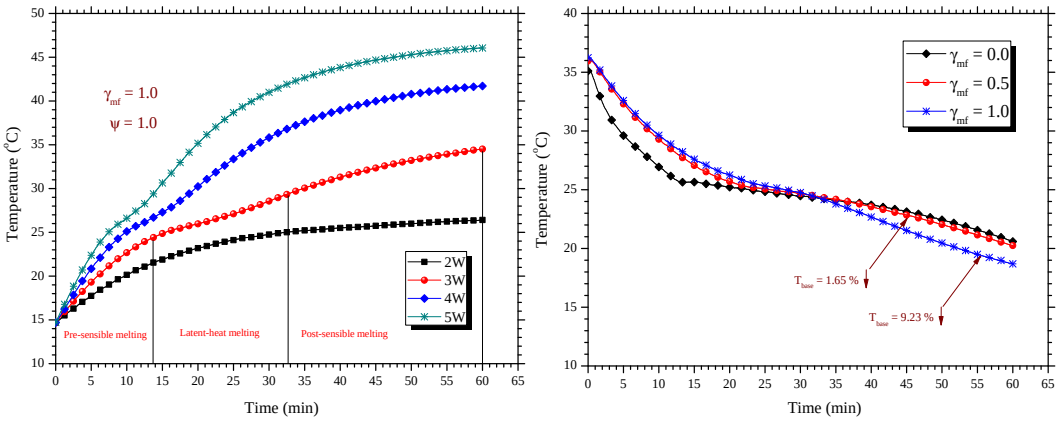


**Figure 7.4:** *Temperature distribution of $\gamma_{mf} = 1.0$ at different power levels: (a) Charging, (b) Discharging.*

## 7.4 Conclusions

In current experimental study, the transient heat transfer performance was investigated of a CuO coated metal–foam/PCM based heat sink of various metal–foam thickness of 0, 2.5 and 5 mm, volumetric fraction of 0.0 and 1.0 of RT-28HC as PCM for different input power levels from 2 to 5 W. The experiments were carried for charging and discharging cycles for both with and without metal–foam and PCM. The results revealed that lower heat sink base temperature was achieved for 1.0 filling thickness ratio of metal–foam without PCM. Whereas with PCM 0.5 filling thickness ratio of metal–foam/PCM based heat sink showed the best thermal performance in term of the reduction of base temperature. It was observed that the base temperature of heat sink increased, and latent-heat phase was shortened with the increase of power level. In addition, PCM filled metal–foam heat sink of 0.5 filling thickness ratio takes the longer time while charging and discharging cycles by keeping the

lower base temperature which proposed that a heat sink embed with partially filled metal–foam with fully filled PCM is the most preferable to attain the best thermal performance for passive cooling of electronic devices.

# Chapter 8

# Conclusions and Future Recommendations

## 8.1 Conclusions

This research has addressed the main aims as mentioned in Section 1.6: *to develop novel mono and hybrid NCPCMs based on different nanomaterials with better thermophysical properties. Moreover, to design a novel compact coated metal–foam embedded heat sink assembly filled with and without PCMs for better thermal cooling performance.*

In order to achieve these aims, a series of objectives were set and detailed experimental investigation of NCPCMs were pertained for both metallic–oxide and carbon–additives. Different experimental characterization techniques were conducted at the Wolfson Building and Nanoscale and Microscale Research Centre, parts of the University of Nottingham to characterize the NCPCMs. These techniques include ESEM, EDX, FT–IR, XRD, TGA, DTG, DSC, IRT and TCA. Additionally, heat sink assembly was designed to study thermal performance of PCMs and NCPCMs based heat sink. Most significantly, this research has identified thermophysical properties, enhancement mechanism, heat transfer enhancement and thermal cooling performance of mono and hybrid NCPCMs.

The key outcomes of this detailed experimental study are summarized as follows:

**Objective I** *To review the latest research on nanomaterials, PCMs, NCPCMs, stability and issues and challenges of NCPCMs.*

- Objective I is fulfilled in Chapter 2. A comprehensive and substantial literature review from the previous research literature revealed that TES, particularly the latent–heat TES, is the primary and significant mode for passive thermal management by employing PCMs to absorb the undesired excessive heat energy. Detailed classifications of nanomaterials, PCMs, and NCPCMs are categorized. More particularly, three different categories of NCPCMs are mentioned according to the metallic, metallic–oxides and carbon–additives nanomaterials. The detailed characteristics evaluation techniques of chemical, thermal and physical properties have been discussed. Stability and reliability of NCPCMs based on physical, chemical and thermal properties are also discussed. Moreover, the most importantly, this literature review identifies the gaps between the nanomaterials and phase change materials research. Moreover, the key issue and challenges of NCPCMs are mentioned which lead towards new paths of future research.

**Objective II** *To synthesise and study the thermophysical properties and achieve the uniform dispersion, physical, chemical and thermal stability of metallic–oxides nanomaterials based mono NCPCMs.*

- Objective II is fulfilled in Chapter 3. Chapter 3 examined the mono NCPCMs based on RT–35HC and $TiO_2$ under different loading contents from 0.0 wt.% to 2.0 wt.%. The dispersion of $TiO_2$ effectively improved the thermophysical properties and heat transfer performance compared to the pure RT–35HC. In addition to $TiO_2$, SDBS is added with the ratio of 4 : 1 for each loading of the $TiO_2$ and improved the dispersion

rate of $TiO_2$ resulting in improved the stability of the $TiO_2$ into the RT–35HC. The results of physical images, ESEM, XRD, FT–IR present the uniform dispersion and presence of $TiO_2$ into RT–35HC without occurring any chemical reaction. The optimum Value of latent–heat of 235.84 J/g at 1.0 wt.% of corresponding thermal conductivity of 0.284 W/m.K were obtained. In addition, maximum deviation in latent–heat and The latent–heat of fusion was decreased with increasing the loading of $TiO_2$. Optimum peak melting temperature were observed of 11.0% and 0.11%, respectively, at 2.0 wt.% of $TiO_2$. A higher thermal conductivity of 0.341 W/m.K was obtained in solid–phase of corresponding thermal conductivity enhancement of 59.5% at 2.0 wt.% of $TiO_2$ compared to the pure RT–35HC. The addition of the $TiO_2$ nanoparticles increases the specific heat capacity of the pure PCM for both solid and liquid phases. The uniform melting and temperature distribution were observed from IR thermographic images, which revealed that with the increase of $TiO_2$ mass concentrations heat transfer rate increases.

**Objective III** *To synthesise and study the thermophysical properties and achieve the uniform dispersion, physical, chemical and thermal stability of metallic–oxides nanomaterials based mono and hybrid NCPCMs.*

- Objective III is fulfilled in Chapter 4. Chapter 4 reported the study on metallic–oxide ($TiO_2$, $Al_2O_3$ and CuO) nanomaterials based mono and hybrid NCPCMs. Good physical stability is achieved by adding all nanomaterials with the help of SDBS which showed better dispersion of $TiO_2$, $Al_2O_3$ and CuO nanomaterials through physical images because of varying densities and particle sizes. The surface morphology, crystal structures and chemical interaction results revealed the uniform dispersion and presence of $TiO_2$, $Al_2O_3$ and CuO in RT–35HC without chemical interaction. The good chemical and thermal stability is obtained with all mono and hybrid NCPCMs. The thermal conductivity results

predicted that hybrid $Al_2O_3$+CuO based hybrid NCPCMs with mass percentage ratio of 75%/25% showed the maximum thermal conductivity of 0.328 W/m K with a thermal conductivity enhancement of 53.7% compared to RT–35HC. The optimum values of latent–heat of melting/solidification were measured of 228.46/229.34 J/g for $Al_2O_3$+CuO based hybrid NCPCMs. The uniform melting and temperature distribution were observed from IR thermographic images. An 8.23% reduction in heat sink base temperature was achieved with $Al_2O_3$+CuO based hybrid NCPCMs.

**Objective IV** *To synthesise and study the thermophysical properties and achieve the uniform dispersion, physical, chemical and thermal stability of carbon–additives nanomaterials based mono and hybrid NCPCMs.*

- Objective IV is fulfilled in Chapter 5. Chapter 5 examined the thermophysical properties of mono and hybrid NCPCMs of MWCNTs, GNPs GO and rGO based carbon–additives with RT–35HC. The comparison of mono and hybrid NCPCMs for all cases prove good physical, chemical and thermal stability for all combination of mono and hybrid nanomaterials with RT–35HC. The ESEM and XRD results of microstructure and crystalline phase reveal the presence of MWCNTs, GO, rGO and GNPs in RT–35HC and show no chemical interaction and peak shifting. The best chemical and thermal stability were observed with hybrid NCPCMs because of 3D morphological nature of GO+MWCNTs, rGO+MWCNTs and GNPs+MWCNTs hybrid nanomaterials. The maximum thermal conductivity of 0.443 W/m.K and thermal conductivity enhancement of 107.6% was obtained for GNPs+MWCNTs dispersed hybrid nanomaterials compared to the RT-35HC. Both latent–heats of melting and solidification were decreased with the addition of carbon–additives. The optimum values of latent–heats of melting and solidifications were 230.82 J/g and 234.19 J/g, respectively, for GNPs+MWCNTs dispersed hybrid

NCPCMs. The lower value of 3.47 °C of degree of subcooling and the deviation in peak melting temperature were observed of 0.22% for hybrid GNPs+MWCNTs nanomaterials. The specific heat capacity results of mono and hybrid NCPCMs revealed increasing trends of compared with RT–35HC. The enhancement in specific heat capacity of 13.75% was achieved with hybrid GNPs+MWCNTs dispersed hybrid NCPCMs compared to RT–35HC in solid–phase.

**Objective V** *To synthesise and study the thermophysical properties and achieve the uniform dispersion, physical, chemical and thermal stability of metallic–oxide and carbon–additives nanomaterials based mono and hybrid NCPCMs.*

- Objective V is fulfilled in Chapter 6. Chapter 6 presents the comparison of carbon–additives (GNPs and MWCNTs) and metallic–oxide ($Al_2O_3$ and CuO) based nano and hybrid NCPCMs. The optimum mass concentration ratio of 75%/25% of 1.0 wt% mass loading is considered for hybrid cases. The surface morphological, structural investigation and transmission spectrum disclosed the presence of GNPs, MWCNTs, $\gamma-Al_2O_3$ and CuO nanomaterials in RT–28HC. The improved physical, chemical and thermal stabilities are observed of GNPs and MWCNTs based hybrid NCPCMs compared to GNPs, MWCNTs, $Al_2O_3$ and CuO based mono NCPCMs. The maximum deviation in peak melting/solidification temperatures of 0.17%/0.78%, the maximum reduction in latent–heat of melting/solidification of 3.75%/3.54% and the maximum thermal conductivity enhancement of 96% have been measured by GNPs+MWCNTs hybrid NCPCMs. The uniform and longer melting duration is obtained with GNPs+MWCNTs hybrid NCPCMs which is because of the uniform and homogeneous dispersion of GNPs+MWCNTs carbon–additives in RT–28HC, which increases the viscosity and shape–stability results in improve the conjugate heat transfer while using in passive thermal management system.

**Objective VI** *To study the enhancement mechanism of thermal conductivity and specific heat capacity of mono and hybrid NCPCMs.*

- Objective VI is fulfilled in Chapter 3 and 5 according to the type of nanomaterials. In Chapter 3, the thermal conductivity enhancement mechanism is presented of spherical shaped $TiO_2$ nanomaterials at loading content from 0.5 wt.% to 2.0 wt.%. The lower concentration of 0.5 wt.% is well dispersed in RT–35HC, which reduces the thermal interfacial resistance and enhance the heat flow, resulting in a slightly improvement of the thermal conductivity. When the loading increases about $0.5 \sim 1.0$ wt.%, a small part of $TiO_2$ nanomaterials is formed as clusters due to the intermolecular interaction between the small particles. These clusters are in favour of forming segmental thermal conductive networks which improve the heat transferring path, and thus improve the thermal conductivity of NCPCMs. Further increasing the concentration of $TiO_2$ from $1.0 \sim 2.0$ wt.%, the nanomaterials can easily be connected to build up the complete thermal conductive networks, which lead to significant improvement in thermal conductivity. In Chapter 5, the thermal conductivity enhancement mechanism is presented through the structural arrangement of 1D MWCNTs and 2D GO/rGO/GNPs nanomaterials. The highest thermal conductivity enhancement was because of the 3D structural matrix consisting of 1D and 2D nanomaterials. This 3D matrix of hybrid NCPCMs forms the 3D path for which the phonon transmission and lattice vibration transport the heat effectively in all directions of the RT–35HC. The enhancement in specific heat capacity is based on three modes: (i) higher specific heat of nanomaterials, (ii) interfacial interactional layers between solid–liquid and (iii) semi–solid liquid layers of molecules adhering to the surface of nanomaterials.

**Objective VII** *To investigate the thermal performance of a mini heat sink filled with and without PCM and coated metal–foam at varying input heat*

*power levels to explore the optimum thickness ratio and higher latent–heating phase.*

- Objective VII is fulfilled in Chapter 7. Chapter 7 reported application of CuO coated metal–foam and PCM–based heat sink. The different thickness ratios of metal–foams and volumetric fractions of PCM have been investigated and the best transient thermal performance is obtained for 1.0 filling thickness ratio of metal–foam without PCM and 0.5 filling thickness ratio of metal–foam with PCM based heat sink. A reduction of 9.7% and 8.7% in the base temperature of heat sink was obtained for 1.0 and 0.5 filling thickness ratio of metal–foam without and with PCM, respectively. Moreover, it is suggested that a heat sink filled half thickness with CuO coated metal–foam and fully filled with PCM takes the longer time during charging and discharging cycles. Thus, it keeps the lower base temperature which proposes the most preferable, efficient and reliable the best thermal performance for passive cooling of electronics devices.

## 8.2 Recommendations for the future research

Thermal management technologies based on PCM and NCPCMs are still debatable and in the phase of evolution for the commercial usage or implementation in smart and high performance electronics devices or in latent–heat thermal energy storage systems. The new era of *green technology* with the development of electrical vehicles, new generation electronics devices, super charging Li–ion and Na–ion batteries have been driven the interest of the use of PCMs. In consideration to this, several areas or research directions for continued research have been pointed out below for the further development of NCPCMs for thermal management and thermal energy storage systems. The following is needed before practical applications can be realised.

- There is need to investigate the an in–depth study of nanomaterials agglomeration and sedimentation in the PCMs during melting and solidification processes.

- Paraffin based PCMs were chosen the to develop and characterise the NCPCMs with different types of nanomaterials. Thus, there is a foremost need to investigate inorganic PCMs and metallic, metallic–oxide and carbon–additives NCPCMs.

- The shape of the nanomaterial has a significant influence along with the other morphological parameters. Thus, there must be some research on usage of different shapes nanomaterials and detailed studies should be carried out to explore the physical and thermal stabilities along with thermophysical properties.

- There should be defined relation for the optimum mass concentration and mass concentration ratio of nanomaterials to disperse in the phase change materials especially in the development of hybrid NCPCMs.

- There is a need to develop new correlations of thermal conductivity, latent–heat of capacity, viscosity and specific heat capacity of hybrid NCPCMs as function of loading content and temperature.

- There is an important challenge to ensure a leak–proof thermal system. Thus, a shape–stable NCPCMs can be impregnated in biomimetic foam structures to prevent the leakage because of the surface tension effects.

- Most of the studies are available on passive thermal management systems based on the pure PCMs with metallic fins and foams; and a very few are on NCPCMs. Thus, there is a need of extensive and urgency need of the combination of NCPCMs with metallic–fin and metallic–foams by varying the different materials, geometrical parameters of metallic–fin and metallic–foams and types of nanomaterials at different operating conditions for steady–state and transition thermal solutions.

With further work in the aforementioned areas, practical implementation of NCPCMs may be realised for a number of applications including either for passive and/or active cooling technologies such as heat pipe, heat spreader, thermal interface materials and thermal energy storage systems for domestic and industrial usage. Additionally, modern power electronics vehicles with high–energy pulsed offensive and defensive systems based on thermal energy system are the primarily focus of the defence sector. For compact or larger, faster and higher–power thermal management systems, the researcher expect to drive the energy storage and research on NCPCMs in the coming years.

# Bibliography


Abdelrahman, H., Wahba, M., Refaey, H., Moawad, M., and Berbish, N. (2019). Performance enhancement of photovoltaic cells by changing configuration and using PCM (RT35hc) with nanoparticles al2o3. *Solar Energy*, 177:665–671.

Abhat, A. (1983). Low temperature latent heat thermal energy storage: Heat storage materials. *Solar Energy*, 30(4):313–332.

Advincula, P. A., de Leon, A. C., Rodier, B. J., Kwon, J., Advincula, R. C., and Pentzer, E. B. (2018). Accommodating volume change and imparting thermal conductivity by encapsulation of phase change materials in carbon nanoparticles. *Journal of Materials Chemistry A*, 6(6):2461–2467.

Aftab, W., Huang, X., Wu, W., Liang, Z., Mahmood, A., and Zou, R. (2018). Nanoconfined phase change materials for thermal energy applications. *Energy & Environmental Science*, 11(6):1392–1424.

Agostini, B., Fabbri, M., Park, J. E., Wojtan, L., Thome, J. R., and Michel, B. (2007). State of the art of high heat flux cooling technologies. *Heat Transfer Engineering*, 28(4):258–281.

Ahmed, S. F., Khalid, M., Rashmi, W., Chan, A., and Shahbaz, K. (2017). Recent progress in solar thermal energy storage using nanomaterials. *Renewable and Sustainable Energy Reviews*, 67:450–460.

Akashi, O., Hanaoka, T., Masui, T., and Kainuma, M. (2013). Halving global GHG emissions by 2050 without depending on nuclear and CCS. *Climatic Change*, 123(3-4):611–622.

Akhiani, A. R., Mehrali, M., Latibari, S. T., Mehrali, M., Mahlia, T. M. I., Sadeghinezhad, E., and Metselaar, H. S. C. (2015). One-step preparation of form-stable phase change material through self-assembly of fatty acid and graphene. *The Journal of Physical Chemistry C*, 119(40):22787–22796.

Akhmetov, B., Navarro, M., Seitov, A., Kaltayev, A., Bakenov, Z., and Ding, Y. (2019). Numerical study of integrated latent heat thermal energy storage devices using nanoparticle-enhanced phase change materials. *Solar Energy*, 194:724–741.

Akin, S. and Sonmezoglu, S. (2018). Metal oxide nanoparticles as electron transport layer for highly efficient dye-sensitized solar cells. In *Emerging Materials for Energy Conversion and Storage*, pages 39–79. Elsevier.

Al-Jethelah, M., Ebadi, S., Venkateshwar, K., Tasnim, S., Mahmud, S., and Dutta, A. (2019). Charging nanoparticle enhanced bio-based PCM in open cell metallic foams: An experimental investigation. *Applied Thermal Engineering*, 148:1029–1042.

Al-Waeli, A. H., Chaichan, M. T., Kazem, H. A., and Sopian, K. (2017a). Comparative study to use nano-(al 2 o 3 , CuO, and SiC) with water to enhance photovoltaic thermal PV/t collectors. *Energy Conversion and Management*, 148:963–973.

Al-Waeli, A. H., Sopian, K., Chaichan, M. T., Kazem, H. A., Ibrahim, A., Mat, S., and Ruslan, M. H. (2017b). Evaluation of the nanofluid and nano-PCM based photovoltaic thermal (PVT) system: An experimental study. *Energy Conversion and Management*, 151:693–708.

Ali, A. H., Ibrahim, S. I., Jawad, Q. A., Jawad, R. S., and Chaichan, M. T. (2019). Effect of nanomaterial addition on the thermophysical properties of iraqi paraffin wax. *Case Studies in Thermal Engineering*, 15:100537.

Ali, H. M. and Arshad, A. (2017). Experimental investigation of n-eicosane based circular pin-fin heat sinks for passive cooling of electronic devices. *International Journal of Heat and Mass Transfer*, 112:649–661.

Ali, H. M., Arshad, A., Jabbal, M., and Verdin, P. (2018a). Thermal management of electronics devices with PCMs filled pin-fin heat sinks: A comparison. *International Journal of Heat and Mass Transfer*, 117:1199–1204.

Ali, H. M., Arshad, A., Janjua, M. M., Baig, W., and Sajjad, U. (2018b). Thermal performance of LHSU for electronics under steady and transient operations modes. *International Journal of Heat and Mass Transfer*, 127:1223–1232.

Ali, H. M., Ashraf, M. J., Giovannelli, A., Irfan, M., Irshad, T. B., Hamid, H. M., Hassan, F., and Arshad, A. (2018c). Thermal management of electronics: An experimental analysis of triangular, rectangular and circular pin-fin heat sinks for various PCMs. *International Journal of Heat and Mass Transfer*, 123:272–284.

Alimohammadi, M., Aghli, Y., Alavi, E. S., Sardarabadi, M., and Passandideh-Fard, M. (2017). Experimental investigation of the effects of using nano/phase change materials (NPCM) as coolant of electronic chipsets, under free and forced convection. *Applied Thermal Engineering*, 111:271–279.

An, K., Lee, N., Park, J., Kim, S. C., Hwang, Y., Park, J.-G., Kim, J.-Y., Park, J.-H., Han, M. J., Yu, J., and Hyeon, T. (2006). Synthesis, characterization, and self-assembly of pencil-shaped CoO nanorods. *Journal of the American Chemical Society*, 128(30):9753–9760.

Anandan, S. S. and Ramalingam, V. (2008). Thermal management of electronics: A review of literature. *Thermal science*, 12(2):5–26.

Anwar, M., Turci, F., and Schilling, T. (2013). Crystallization mechanism in melts of short n-alkane chains. *The Journal of Chemical Physics*, 139(21):214904.

Aqel, A., El-Nour, K. M. A., Ammar, R. A., and Al-Warthan, A. (2012). Carbon nanotubes, science and technology part (i) structure, synthesis and characterisation. *Arabian Journal of Chemistry*, 5(1):1–23.

Arjmandi, R., Hassan, A., Othman, N., and Mohamad, Z. (2018). Characterizations of carbon-based polypropylene nanocomposites. In *Carbon-Based Polymer Nanocomposites for Environmental and Energy Applications*, pages 57–78. Elsevier.

Arshad, A., Ali, H. M., Ali, M., and Manzoor, S. (2017). Thermal performance of phase change material (PCM) based pin-finned heat sinks for electronics devices: Effect of pin thickness and PCM volume fraction. *Applied Thermal Engineering*, 112:143–155.

Arshad, A., Ali, H. M., Khushnood, S., and Jabbal, M. (2018a). Experimental investigation of PCM based round pin-fin heat sinks for thermal management of electronics: Effect of pin-fin diameter. *International Journal of Heat and Mass Transfer*, 117:861–872.

Arshad, A., Ali, H. M., Yan, W.-M., Hussein, A. K., and Ahmadlouydarab, M. (2018b). An experimental study of enhanced heat sinks for thermal management using n-eicosane as phase change material. *Applied Thermal Engineering*, 132:52–66.

Arshad, A., Jabbal, M., Shi, L., Darkwa, J., Weston, N. J., and Yan, Y. (2020a). Development of tio2/rt–35hc based nanocomposite phase change materials (ncpcms) for thermal management applications. *Sustainable Energy Technologies and Assessments*, page 100865.

Arshad, A., Jabbal, M., and Yan, Y. (2020b). Preparation and characteristics evaluation of mono and hybrid nano-enhanced phase change materials (NePCMs) for thermal management of microelectronics. *Energy Conversion and Management*, 205:112444.

Arshad, A., Jabbal, M., and Yan, Y. (2020c). Thermal performance of PCM-based heat sink with partially filled copper oxide coated metal-foam for thermal management of microelectronics. In *2020 19th IEEE Intersociety Conference on Thermal and Thermomechanical Phenomena in Electronic Systems (ITherm)*. IEEE.

Arshad, A., Jabbal, M., and Yan, Y. (2020d). Thermophysical characteristics and application of metallic-oxide based mono and hybrid nanocomposite phase change materials for thermal management systems. *Applied Thermal Engineering*, 181:115999.

Arshad, A., Jabbal, M., Yan, Y., and Darkwa, J. (2019a). The micro-/nano-pcms for thermal energy storage systems: A state of art review. *International Journal of Energy Research*, 43(11):5572–5620.

Arshad, A., Jabbal, M., Yan, Y., and Reay, D. (2019b). A review on graphene based nanofluids: Preparation, characterization and applications. *Journal of Molecular Liquids*, 279:444–484.

Asadi, A., Alarifi, I. M., Ali, V., and Nguyen, H. M. (2019). An experimental investigation on the effects of ultrasonication time on stability and thermal conductivity of MWCNT-water nanofluid: Finding the optimum ultrasonication time. *Ultrasonics Sonochemistry*, 58:104639.

Åsbrink, S. and Norrby, L.-J. (1970). A refinement of the crystal structure of copper (ii) oxide with a discussion of some exceptional esd's. *Acta Crystallographica Section B: Structural Crystallography and Crystal Chemistry*, 26(1):8–15.

Ashraf, M. J., Ali, H. M., Usman, H., and Arshad, A. (2017). Experimental passive electronics cooling: Parametric investigation of pin-fin geometries and efficient phase change materials. *International Journal of Heat and Mass Transfer*, 115:251–263.

Assael, M., Antoniadis, K., and Tzetzis, D. (2008). The use of the transient hot-wire technique for measurement of the thermal conductivity of an epoxy-resin reinforced with glass fibres and/or carbon multi-walled nanotubes. *Composites Science and Technology*, 68(15-16):3178–3183.

Atinafu, D. G., Dong, W., Huang, X., Gao, H., and Wang, G. (2018). Introduction of organic-organic eutectic PCM in mesoporous n-doped carbons for enhanced thermal conductivity and energy storage capacity. *Applied Energy*, 211:1203–1215.

Atkinson, C., Larkin, J., and Richardson, M. (1969). Enthalpy changes in molten n-alkanes and polyethylene. *The Journal of Chemical Thermodynamics*, 1(5):435–440.

Atta, N. F., Galal, A., and El-Ads, E. H. (2015). Graphene a platform for sensor and biosensor applications. In Rinken, T., editor, *Biosensors*, chapter 2. IntechOpen, Rijeka.

Aydın, A. A. (2013). Fatty acid ester-based commercial products as potential new phase change materials (PCMs) for thermal energy storage. *Solar Energy Materials and Solar Cells*, 108:98–104.

Aydın, A. A. and Aydın, A. (2012). High-chain fatty acid esters of 1-hexadecanol for low temperature thermal energy storage with phase change materials. *Solar Energy Materials and Solar Cells*, 96:93–100.

B, P. and A, V. (2020). Stability analysis of TiO2–ag nanocomposite particles dispersed paraffin wax as energy storage material for solar thermal systems. *Renewable Energy*, 152:358–367.

Babapoor, A. and Karimi, G. (2015). Thermal properties measurement and heat storage analysis of paraffinnanoparticles composites phase change material: Comparison and optimization. *Applied Thermal Engineering*, 90:945–951.

Babapoor, A., Karimi, G., and Sabbaghi, S. (2016). Thermal characteristic of nanocomposite phase change materials during solidification process. *Journal of Energy Storage*, 7:74–81.

Babar, H. and Ali, H. M. (2019). Towards hybrid nanofluids: Preparation, thermophysical properties, applications, and challenges. *Journal of Molecular Liquids*, 281:598–633.

Baby, R. and Balaji, C. (2012). Experimental investigations on phase change material based finned heat sinks for electronic equipment cooling. *International Journal of Heat and Mass Transfer*, 55(5-6):1642–1649.

Bae, H., Lee, M., Kim, W., and Rhee, C. (2003). Dispersion properties of TiO2 nano-powder synthesized by homogeneous precipitation process at low temperatures. *Colloids and Surfaces A: Physicochemical and Engineering Aspects*, 220(1-3):169–177.

Bahiraei, F., Fartaj, A., and Nazri, G.-A. (2017). Experimental and numerical investigation on the performance of carbon-based nanoenhanced phase change materials for thermal management applications. *Energy Conversion and Management*, 153:115–128.

Bailey, A. E. (1945). *Industrial oil and fat products*. Interscience Publishers, Inc.; New York.

Bakhtiari, F. and Darezereshki, E. (2011). One-step synthesis of tenorite (CuO) nano-particles from cu4 (SO4) (OH) 6 by direct thermal-decomposition method. *Materials Letters*, 65(2):171–174.

Balandin, A. A. (2011). Thermal properties of graphene and nanostructured carbon materials. *Nature Materials*, 10(8):569–581.

Baran, G. and Sari, A. (2003). Phase change and heat transfer characteristics of a eutectic mixture of palmitic and stearic acids as PCM in a latent heat storage system. *Energy Conversion and Management*, 44(20):3227–3246.

Bardeen, J. and Brattain, W. H. (1948). The transistor, a semi-conductor triode. *Physical Review*, 74(2):230.

Barrio, E. P. D., Cadoret, R., Daranlot, J., and Achchaq, F. (2016). New sugar alcohols mixtures for long-term thermal energy storage applications at temperatures between 70 c and 100 c. *Solar Energy Materials and Solar Cells*, 155:454–468.

Bashar, M. and Siddiqui, K. (2018). Experimental investigation of transient melting and heat transfer behavior of nanoparticle-enriched PCM in a rectangular enclosure. *Journal of Energy Storage*, 18:485–497.

Bashir, M. A., Giovannelli, A., Amber, K. P., Khan, M. S., Arshad, A., and Daabo, A. M. (2020). High-temperature phase change materials for short-term thermal energy storage in the solar receiver: Selection and analysis. *Journal of Energy Storage*, 30:101496.

Bashir, S. and Liu, J. (2015). Nanomaterials and their application. In *Advanced Nanomaterials and their Applications in Renewable Energy*, pages 1–50. Elsevier.

Bergman, T. L., Incropera, F. P., DeWitt, D. P., and Lavine, A. S. (2011). *Fundamentals of heat and mass transfer*. John Wiley & Sons.

Bintoro, J. S., Akbarzadeh, A., and Mochizuki, M. (2005). A closed-loop electronics cooling by implementing single phase impinging jet and mini channels heat exchanger. *Applied Thermal Engineering*, 25(17-18):2740–2753.

Biswas, D. R. (1977). Thermal energy storage using sodium sulfate decahydrate and water. *Solar Energy*, 19(1):99–100.

Black, J. (1969). Electromigration—a brief survey and some recent results. *IEEE Transactions on Electron Devices*, 16(4):338–347.

Borm, P. J., Robbins, D., Haubold, S., Kuhlbusch, T., Fissan, H., Donaldson, K., Schins, R., Stone, V., Kreyling, W., Lademann, J., Krutmann, J., Warheit, D., and Oberdorster, E. (2006). *Particle and Fibre Toxicology*, 3(1):11.

Bosselman, F., Eisen, J. B., Rossi, J., Spence, D. B., and Weaver, J. L. (2006). Energy, economics and the environment: cases and materials. *ENERGY, ECONOMICS AND THE ENVIRONMENT: CASES AND MATERIALS, Foundation Press*.

Bozzi, A., Yuranova, T., and Kiwi, J. (2005). Self-cleaning of wool-polyamide and polyester textiles by TiO2-rutile modification under daylight irradiation at ambient temperature. *Journal of Photochemistry and Photobiology A: Chemistry*, 172(1):27–34.

Bridgman, P. W. (1923). The thermal conductivity of liquids under pressure. *Proceedings of the American Academy of Arts and Sciences*, 59(7):141.

Broadhurst, M. G. (1962). An analysis of the solid phase behavior of the normal paraffins. *J. Res. Natl. Bur. Stand., Sect. A*, 66(3):241–249.

Burns, G. W., Scroger, M., Strouse, G., Croarkin, M., and Guthrie, W. (1993). Temperature-electromotive force reference functions and tables for the letter-designated thermocouple types based on the its-90. *NASA STI/Recon Technical Report N*, 93:31214.

Buzea, C. and Pacheco, I. (2016). Nanomaterials and their classification. In *Advanced Structured Materials*, pages 3–45. Springer India.

Buzea, C., Pacheco, I. I., and Robbie, K. (2007). Nanomaterials and nanoparticles: Sources and toxicity. *Biointerphases*, 2(4):MR17–MR71.

Cabeza, L. F., Castell, A., Barreneche, C., De Gracia, A., and Fernández, A. (2011). Materials used as pcm in thermal energy storage in buildings: a review. *Renewable and Sustainable Energy Reviews*, 15(3):1675–1695.

Cabeza, L. F., Svensson, G., Hiebler, S., and Mehling, H. (2003). Thermal performance of sodium acetate trihydrate thickened with different materials as phase change energy storage material. *Applied Thermal Engineering*, 23(13):1697–1704.

Cahill, D. G. (1990). Thermal conductivity measurement from 30 to 750 k: the 3 method. *Review of Scientific Instruments*, 61(2):802–808.

Cahill, D. G. and Pohl, R. (1989). Heat flow and lattice vibrations in glasses. *Solid State Communications*, 70(10):927–930.

Capinski, W. S., Maris, H. J., Ruf, T., Cardona, M., Ploog, K., and Katzer, D. S. (1999). Thermal-conductivity measurements of GaAs/AlAs superlattices using a picosecond optical pump-and-probe technique. *Physical Review B*, 59(12):8105–8113.

Capsal, J.-F., Dantras, E., Dandurand, J., and Lacabanne, C. (2011). Molecular mobility in piezoelectric hybrid nanocomposites with 0–3 connectivity: Volume fraction influence. *Journal of Non-Crystalline Solids*, 357(19-20):3410–3415.

Carrillo, A. J., Gonzalez-Aguilar, J., Romero, M., and Coronado, J. M. (2019). Solar energy on demand: A review on high temperature thermochemical heat storage systems and materials. *Chemical reviews*, 119(7):4777–4816.

Carvalho, M. R., Reis, R. L., and Oliveira, J. M. (2020). Dendrimer nanoparticles for colorectal cancer applications. *Journal of Materials Chemistry B*, 8(6):1128–1138.

Casini, M. (2016). Phase-change materials. In *Smart Buildings*, pages 179–218. Elsevier.

Cataldi, P., Athanassiou, A., and Bayer, I. (2018). Graphene nanoplatelets-based advanced materials and recent progress in sustainable applications. *Applied Sciences*, 8(9):1438.

Chaichan, M. T., Kamel, S. H., and Al-Ajeely, A. (2015). Thermal conductivity enhancement by using nano-material in phase change material for latent heat thermal energy storage systems. *Saussurea*, 5(6):48–55.

Chakraborty, S. and Panigrahi, P. K. (2020). Stability of nanofluid: A review. *Applied Thermal Engineering*, 174:115259.

Chen, G., Neagu, M., and Borca-Tasciuc, T. (1997). Thermal conductivity and heat transfer in superlattices. *MRS Proceedings*, 478.

Chen, L., Zou, R., Xia, W., Liu, Z., Shang, Y., Zhu, J., Wang, Y., Lin, J., Xia, D., and Cao, A. (2012). Electro- and photodriven phase change composites based on wax-infiltrated carbon nanotube sponges. *ACS Nano*, 6(12):10884–10892.

Chen, Y., Luo, W., Wang, J., and Huang, J. (2017). Enhanced thermal conductivity and durability of a paraffin wax nanocomposite based on carbon-coated aluminum nanoparticles. *The Journal of Physical Chemistry C*, 121(23):12603–12609.

Chen, Z., Gao, D., and Shi, J. (2014). Experimental and numerical study on melting of phase change materials in metal foams at pore scale. *International Journal of Heat and Mass Transfer*, 72:646–655.

Chieruzzi, M., Miliozzi, A., Crescenzi, T., Torre, L., and Kenny, J. M. (2015). A new phase change material based on potassium nitrate with silica and alumina nanoparticles for thermal energy storage. *Nanoscale research letters*, 10(1):273.

Chirayil, C. J., Abraham, J., Mishra, R. K., George, S. C., and Thomas, S. (2017). Instrumental techniques for the characterization of nanoparticles. In *Thermal and Rheological Measurement Techniques for Nanomaterials Characterization*, pages 1–36. Elsevier.

Choi, D. H., Lee, J., Hong, H., and Kang, Y. T. (2014). Thermal conductivity and heat transfer performance enhancement of phase change materials (PCM) containing carbon additives for heat storage application. *International Journal of Refrigeration*, 42:112–120.

Cluley, J. C. (1974). Electronic equipment reliability. *New York, Halsted Press, 1974. 170 p.*

Colla, L., Ercole, D., Fedele, L., Mancin, S., Manca, O., and Bobbo, S. (2017a). Nano-phase change materials for electronics cooling applications. *Journal of Heat Transfer*, 139(5).

Colla, L., Fedele, L., Mancin, S., Buonomo, B., Ercole, D., and Manca, O. (2015). Nano-PCMs for passive electronic cooling applications. *Journal of Physics: Conference Series*, 655:012030.

Colla, L., Fedele, L., Mancin, S., Danza, L., and Manca, O. (2017b). Nano-PCMs for enhanced energy storage and passive cooling applications. *Applied Thermal Engineering*, 110:584–589.

Comes, R., Currat, R., Denoyer, F., Lambert, M., and Quitte, A. M. (1976). Structural aspects of phase transitions. *Ferroelectrics*, 12(1):3–8.

Cui, Y., Liu, C., Hu, S., and Yu, X. (2011). The experimental exploration of carbon nanofiber and carbon nanotube additives on thermal behavior of phase change materials. *Solar Energy Materials and Solar Cells*, 95(4):1208–1212.

da Cunha, J. P. and Eames, P. (2016). Thermal energy storage for low and medium temperature applications using phase change materials – a review. *Applied Energy*, 177:227–238.

Das, S. K., Choi, S. U. S., and Patel, H. E. (2006). Heat transfer in nanofluids—a review. *Heat Transfer Engineering*, 27(10):3–19.

Deng, Y., Li, J., Qian, T., Guan, W., Li, Y., and Yin, X. (2016). Thermal conductivity enhancement of polyethylene glycol/expanded vermiculite shape-stabilized composite phase change materials with silver nanowire for thermal energy storage. *Chemical Engineering Journal*, 295:427–435.

Dğşc, D. K., Kızıl, Ç., Biçer, A., Sarı, A., and Alkan, C. (2018). Microencapsulated n -alkane eutectics in polystyrene for solar thermal applications. *Solar Energy*, 160:32–42.

Diarce, G., Gandarias, I., Campos-Celador, Á., García-Romero, A., and Griesser, U. (2015). Eutectic mixtures of sugar alcohols for thermal energy storage in the 50–90c temperature range. *Solar Energy Materials and Solar Cells*, 134:215–226.

Dimaano, M. N. R. and Watanabe, T. (2002). The capric–lauric acid and pentadecane combination as phase change material for cooling applications. *Applied Thermal Engineering*, 22(4):365–377.

Donkers, P., Sgtoglu, L., Huinink, H., Fischer, H., and Adan, O. (2017). A review of salt hydrates for seasonal heat storage in domestic applications. *Applied Energy*, 199:45–68.

Du, K., Calautit, J., Wang, Z., Wu, Y., and Liu, H. (2018). A review of the applications of phase change materials in cooling, heating and power generation in different temperature ranges. *Applied Energy*, 220:242–273.

Dubey, K. K. and Mishra, R. (2014). A review on properties of phase change material for solar thermal storage system. *International Journal*, 2(2):342–349.

Duplock, E. J., Scheffler, M., and Lindan, P. J. D. (2004). Hallmark of perfect graphene. *Physical Review Letters*, 92(22).

Ebadian, M. A. and Lin, C. X. (2011). A review of high-heat-flux heat removal technologies. *Journal of Heat Transfer*, 133(11).

Elgafy, A. and Lafdi, K. (2005). Effect of carbon nanofiber additives on thermal behavior of phase change materials. *Carbon*, 43(15):3067–3074.

Evans, W., Prasher, R., Fish, J., Meakin, P., Phelan, P., and Keblinski, P. (2008). Effect of aggregation and interfacial thermal resistance on thermal conductivity of nanocomposites and colloidal nanofluids. *International Journal of Heat and Mass Transfer*, 51(5-6):1431–1438.

Faisal, M., Khan, S. B., Rahman, M. M., Jamal, A., and Umar, A. (2011). Ethanol chemi-sensor: Evaluation of structural, optical and sensing properties of CuO nanosheets. *Materials Letters*, 65(9):1400–1403.

Fan, L. and Khodadadi, J. (2012). An experimental investigation of enhanced thermal conductivity and expedited unidirectional freezing of cyclohexane-based nanoparticle suspensions utilized as nano-enhanced phase change materials (NePCM). *International Journal of Thermal Sciences*, 62:120–126.

Fan, L.-W., Zhu, Z.-Q., Zeng, Y., Xiao, Y.-Q., Liu, X.-L., Wu, Y.-Y., Ding, Q., Yu, Z.-T., and Cen, K.-F. (2015). Transient performance of a PCM-based heat sink with high aspect-ratio carbon nanofillers. *Applied Thermal Engineering*, 75:532–540.

Faraji, H., Faraji, M., Alami, M. E., Hariti, Y., Arshad, A., Hader, A., and Benkaddour, A. (2020). Cooling of recent microprocessors by the fusion of nano-enhanced phase change materials. *Materials Today: Proceedings*.

Feldman, D. and Banu, D. (1996). DSC analysis for the evaluation of an energy storing wallboard. *Thermochimica Acta*, 272:243–251.

Feldman, D., Banu, D., and Hawes, D. (1995). Low chain esters of stearic acid as phase change materials for thermal energy storage in buildings. *Solar Energy Materials and Solar Cells*, 36(3):311–322.

Feldman, D., Banu, D., Hawes, D., and Ghanbari, E. (1991). Obtaining an energy storing building material by direct incorporation of an organic phase change material in gypsum wallboard. *Solar Energy Materials*, 22(2-3):231–242.

Feldman, D., Shapiro, M., Banu, D., and Fuks, C. (1989). Fatty acids and their mixtures as phase-change materials for thermal energy storage. *Solar Energy Materials*, 18(3-4):201–216.

Feng, D., Feng, Y., Qiu, L., Li, P., Zang, Y., Zou, H., Yu, Z., and Zhang, X. (2019). Review on nanoporous composite phase change materials: Fabrication, characterization, enhancement and molecular simulation. *Renewable and Sustainable Energy Reviews*, 109:578–605.

Finke, H. L., Gross, M. E., Waddington, G., and Huffman, H. M. (1954). Low-temperature thermal data for the nine normal paraffin hydrocarbons from octane to hexadecane. *Journal of the American Chemical Society*, 76(2):333–341.

Foerter-Barth, U. and Teipel, U. (2000). Characterization of particles by means of laser light diffraction and dynamic light scattering. In *Developments in Mineral Processing*, pages C1–1–C1–8. Elsevier.

Gargini, P. The international technology roadmap for semiconductors (ITRS): "past, present and future". In *GaAs IC Symposium. IEEE Gallium Arsenide Integrated Circuits Symposium. 22nd Annual Technical Digest 2000. (Cat. No.00CH37084)*. IEEE.

Garimella, S. V., Persoons, T., Weibel, J., and Yeh, L.-T. (2013). Technological drivers in data centers and telecom systems: Multiscale thermal, electrical, and energy management. *Applied energy*, 107:66–80.

Garimella, S. V., Yeh, L.-T., and Persoons, T. (2012). Thermal management challenges in telecommunication systems and data centers. *IEEE Transactions on Components, Packaging and Manufacturing Technology*, 2(8):1307–1316.

Ge, H., Li, H., Mei, S., and Liu, J. (2013). Low melting point liquid metal as a new class of phase change material: An emerging frontier in energy area. *Renewable and Sustainable Energy Reviews*, 21:331–346.

Ge, H. and Liu, J. (2012). Phase change effect of low melting point metal for an automatic cooling of USB flash memory. *Frontiers in Energy*, 6(3):207–209.

Ge, H. and Liu, J. (2013). Keeping smartphones cool with gallium phase change material. *Journal of Heat Transfer*, 135(5):054503.

Geng, X., Li, W., Yin, Q., Wang, Y., Han, N., Wang, N., Bian, J., Wang, J., and Zhang, X. (2018). Design and fabrication of reversible thermochromic microencapsulated phase change materials for thermal energy storage and its antibacterial activity. *Energy*, 159:857–869.

Ghossein, R. M. A., Hossain, M. S., and Khodadadi, J. (2017). Experimental determination of temperature-dependent thermal conductivity of solid eicosane-based silver nanostructure-enhanced phase change materials for thermal energy storage. *International Journal of Heat and Mass Transfer*, 107:697–711.

Graham, M., Coca-Clemente, J. A., Shchukina, E., and Shchukin, D. (2017). Nanoencapsulated crystallohydrate mixtures for advanced thermal energy storage. *Journal of Materials Chemistry A*, 5(26):13683–13691.

Gulfam, R., Zhang, P., and Meng, Z. (2019). Advanced thermal systems driven by paraffin-based phase change materials – a review. *Applied Energy*, 238:582–611.

Gunasekara, S. N., Pan, R., Chiu, J. N., and Martin, V. (2016). Polyols as phase change materials for surplus thermal energy storage. *Applied Energy*, 162:1439–1452.

Han, J., Zhao, D., Li, D., Wang, X., Jin, Z., and Zhao, K. (2018). Polymer-based nanomaterials and applications for vaccines and drugs. *Polymers*, 10(1):31.

Harikrishnan, S., Deenadhayalan, M., and Kalaiselvam, S. (2014). Experimental investigation of solidification and melting characteristics of composite PCMs for building heating application. *Energy Conversion and Management*, 86:864–872.

Harikrishnan, S. and Kalaiselvam, S. (2012). Preparation and thermal characteristics of CuO–oleic acid nanofluids as a phase change material. *Thermochimica Acta*, 533:46–55.

Harish, S., Ishikawa, K., Chiashi, S., Shiomi, J., and Maruyama, S. (2013). Anomalous thermal conduction characteristics of phase change composites with single-walled carbon nanotube inclusions. *The Journal of Physical Chemistry C*, 117(29):15409–15413.

Harish, S., Orejon, D., Takata, Y., and Kohno, M. (2015). Thermal conductivity enhancement of lauric acid phase change nanocomposite in solid and liquid state with single-walled carbon nanohorn inclusions. *Thermochimica Acta*, 600:1–6.

Hawes, D., Feldman, D., and Banu, D. (1993). Latent heat storage in building materials. *Energy and Buildings*, 20(1):77–86.

He, J., Yang, X., and Zhang, G. (2019a). A phase change material with enhanced thermal conductivity and secondary heat dissipation capability by introducing a binary thermal conductive skeleton for battery thermal management. *Applied Thermal Engineering*, 148:984–991.

He, M., Yang, L., Lin, W., Chen, J., Mao, X., and Ma, Z. (2019b). Preparation, thermal characterization and examination of phase change materials (PCMs) enhanced by carbon-based nanoparticles for solar thermal energy storage. *Journal of Energy Storage*, 25:100874.

He, M., Yang, L., Lin, W., Chen, J., Mao, X., and Ma, Z. (2019c). Preparation, thermal characterization and examination of phase change materials (PCMs) enhanced by carbon-based nanoparticles for solar thermal energy storage. *Journal of Energy Storage*, 25:100874.

He, Q., Wang, S., Tong, M., and Liu, Y. (2012). Experimental study on thermophysical properties of nanofluids as phase-change material (PCM) in low temperature cool storage. *Energy Conversion and Management*, 64:199–205.

Hellstern, E., Fecht, H. J., Fu, Z., and Johnson, W. L. (1989). Structural and thermodynamic properties of heavily mechanically deformed ru and AlRu. *Journal of Applied Physics*, 65(1):305–310.

Ho, C. and Gao, J. (2009). Preparation and thermophysical properties of nanoparticle-in-paraffin emulsion as phase change material. *International Communications in Heat and Mass Transfer*, 36(5):467–470.

Ho, C. Y., Powell, R. W., and Liley, P. E. (1972). Thermal conductivity of the elements. *Journal of Physical and Chemical Reference Data*, 1(2):279–421.

Hopkins, P. E. and Norris, P. M. (2007). Effects of joint vibrational states on thermal boundary conductance. *Nanoscale and Microscale Thermophysical Engineering*, 11(3-4):247–257.

Hornyak, G. L., Tibbals, H. F., Dutta, J., and Moore, J. J. (2008). *Introduction to nanoscience and nanotechnology*. CRC press.

Hu, P., Lu, D.-J., Fan, X.-Y., Zhou, X., and Chen, Z.-S. (2011). Phase change performance of sodium acetate trihydrate with AlN nanoparticles and CMC. *Solar Energy Materials and Solar Cells*, 95(9):2645–2649.

Hu, P., Zhao, P.-P., Jin, Y., and Chen, Z.-S. (2014). Experimental study on solid–solid phase change properties of pentaerythritol (PE)/nano-AlN composite for thermal storage. *Solar Energy*, 102:91–97.

Huang, B., Ni, Z., Millward, A., McGaughey, A., Uher, C., Kaviany, M., and Yaghi, O. (2007). Thermal conductivity of a metal-organic framework (MOF-5): Part II. measurement. *International Journal of Heat and Mass Transfer*, 50(3-4):405–411.

Huang, X., Chen, X., Li, A., Atinafu, D., Gao, H., Dong, W., and Wang, G. (2019). Shape-stabilized phase change materials based on porous supports for thermal energy storage applications. *Chemical Engineering Journal*, 356:641–661.

Huang, X., Xia, W., and Zou, R. (2014a). Nanoconfinement of phase change materials within carbon aerogels: phase transition behaviours and photo-to-thermal energy storage. *J. Mater. Chem. A*, 2(47):19963–19968.

Huang, Z., Gao, X., Xu, T., Fang, Y., and Zhang, Z. (2014b). Thermal property measurement and heat storage analysis of LiNO3/KCl – expanded graphite composite phase change material. *Applied Energy*, 115:265–271.

Hussain, A., Abidi, I. H., Tso, C., Chan, K., Luo, Z., and Chao, C. Y. (2018). Thermal management of lithium ion batteries using graphene coated nickel foam saturated with phase change materials. *International Journal of Thermal Sciences*, 124:23–35.

Hussain, S. I., Dinesh, R., Roseline, A. A., Dhivya, S., and Kalaiselvam, S. (2017). Enhanced thermal performance and study the influence of sub cooling on activated carbon dispersed eutectic PCM for cold storage applications. *Energy and Buildings*, 143:17–24.

Hyun, D. C., Levinson, N. S., Jeong, U., and Xia, Y. (2014). Emerging applications of phase-change materials (pcms): teaching an old dog new tricks. *Angewandte Chemie International Edition*, 53(15):3780–3795.

Imamura, K., Tanaka, Y., Nishiguchi, N., Tamura, S., and Maris, H. J. (2003). Lattice thermal conductivity in superlattices: molecular dynamics calculations with a heat reservoir method. *Journal of Physics: Condensed Matter*, 15(50):8679–8690.

Jebasingh, B. E. and Arasu, A. V. (2020a). A comprehensive review on latent heat and thermal conductivity of nanoparticle dispersed phase change material for low-temperature applications. *Energy Storage Materials*, 24:52–74.

Jebasingh, B. E. and Arasu, A. V. (2020b). A detailed review on heat transfer rate, supercooling, thermal stability and reliability of nanoparticle dispersed organic phase change material for low-temperature applications. *Materials Today Energy*, 16:100408.

Jegadheeswaran, S. and Pohekar, S. D. (2009). Performance enhancement in latent heat thermal storage system: A review. *Renewable and Sustainable Energy Reviews*, 13(9):2225–2244.

Jeon, J., Jeong, S.-G., Lee, J.-H., Seo, J., and Kim, S. (2012). High thermal performance composite PCMs loading xGnP for application to building using radiant floor heating system. *Solar Energy Materials and Solar Cells*, 101:51–56.

Jesumathy, S., Udayakumar, M., and Suresh, S. (2011). Experimental study of enhanced heat transfer by addition of CuO nanoparticle. *Heat and Mass Transfer*, 48(6):965–978.

Ji, P., Sun, H., Zhong, Y., and Feng, W. (2012). Improvement of the thermal conductivity of a phase change material by the functionalized carbon nanotubes. *Chemical Engineering Science*, 81:140–145.

Jiang, Y., Sun, Y., Jacob, R. D., Bruno, F., and Li, S. (2018). Novel na 2 SO 4 -NaCl-ceramic composites as high temperature phase change materials for solar thermal power plants (part i). *Solar Energy Materials and Solar Cells*, 178:74–83.

Jotzo, F., Burke, P. J., Wood, P. J., Macintosh, A., and Stern, D. I. (2012). Decomposing the 2010 global carbon dioxide emissions rebound. *Nature Climate Change*, 2(4):213–214.

Jovanović, D. B., Stojisavljević, P. N., Cvetanović, S. G., Rajić, D. S., Karkalić, R. M., Ivanković, N. D., and Senić, Ž. B. (2016). Testing of the functional garments with microencapsulated phase-change material in simulated high temperature conditions. *Hemijska Industrija*, 70(5):573.

Karaipekli, A. and Sarı, A. (2010). Preparation, thermal properties and thermal reliability of eutectic mixtures of fatty acids/expanded vermiculite as novel form-stable composites for energy storage. *Journal of Industrial and Engineering Chemistry*, 16(5):767–773.

Karunamurthy, K., Murugumohankumar, K., and Suresh, S. (2012). Use of cuo nano-material for the improvement of thermal conductivity and performance of low temperature energy storage system of solar pond. *Digest Journal of Nanomaterials and Biostructures*, 7(4):1833–1841.

Kashi, S., Gupta, R. K., Kao, N., Hadigheh, S. A., and Bhattacharya, S. N. (2018). Influence of graphene nanoplatelet incorporation and dispersion state on thermal, mechanical and electrical properties of biodegradable matrices. *Journal of Materials Science & Technology*, 34(6):1026–1034.

Kaygusuz, K. and Sari, A. (2006). Thermal energy storage performance of fatty acids as a phase change material. *Energy Sources, Part A: Recovery, Utilization, and Environmental Effects*, 28(2):105–116.

Ke, H., Li, D., Zhang, H., Wang, X., Cai, Y., Huang, F., and Wei, Q. (2013). Electrospun form-stable phase change composite nanofibers consisting of capric acid-based binary fatty acid eutectics and polyethylene terephthalate. *Fibers and Polymers*, 14(1):89–99.

Keleş, S., Kaygusuz, K., and Sarı, A. (2005). Lauric and myristic acids eutectic mixture as phase change material for low-temperature heating applications. *International Journal of Energy Research*, 29(9):857–870.

Keller, T. M., Qadri, S. B., and Little, C. A. (2004). Carbon nanotube formation in situ during carbonization in shaped bulk solid cobalt nanoparticle compositions. *Journal of Materials Chemistry*, 14(20):3063.

Keshteli, A. N. and Sheikholeslami, M. (2019). Nanoparticle enhanced PCM applications for intensification of thermal performance in building: A review. *Journal of Molecular Liquids*, 274:516–533.

Khan, M. M. A., Ibrahim, N. I., Mahbubul, I., Ali, H. M., Saidur, R., and Al-Sulaiman, F. A. (2018). Evaluation of solar collector designs with integrated latent heat thermal energy storage: A review. *Solar Energy*, 166:334–350.

Khan, Z., Khan, Z. A., and Sewell, P. (2019). Heat transfer evaluation of metal oxides based nano-PCMs for latent heat storage system application. *International Journal of Heat and Mass Transfer*, 144:118619.

Kim, D., Jung, J., Kim, Y., Lee, M., Seo, J., and Khan, S. B. (2016). Structure and thermal properties of octadecane/expanded graphite composites as shape-stabilized phase change materials. *International Journal of Heat and Mass Transfer*, 95:735–741.

Kim, J. (2007). Spray cooling heat transfer: the state of the art. *International Journal of Heat and Fluid Flow*, 28(4):753–767.

Kim, P., Shi, L., Majumdar, A., and McEuen, P. L. (2001). Thermal transport measurements of individual multiwalled nanotubes. *Physical Review Letters*, 87(21).

Kim, S. and Drzal, L. T. (2009). High latent heat storage and high thermal conductive phase change materials using exfoliated graphite nanoplatelets. *Solar Energy Materials and Solar Cells*, 93(1):136–142.

Kim, S., Paek, S., Jeong, S.-G., Lee, J.-H., and Kim, S. (2014). Thermal performance enhancement of mortar mixed with octadecane/xGnP SSPCM to save building energy consumption. *Solar Energy Materials and Solar Cells*, 122:257–263.

Kline, S. J. (1953). Describing uncertainty in single sample experiments. *Mech. Engineering*, 75:3–8.

Koca, H. D., Doganay, S., Turgut, A., Tavman, I. H., Saidur, R., and Mahbubul, I. M. (2018). Effect of particle size on the viscosity of nanofluids: A review. *Renewable and Sustainable Energy Reviews*, 82:1664–1674.

Kolesnikov, S. and Syunyaev, Z. (1985). Phase transitions in the melting and crystallization of n-c//1//8h//3//8 and n-c//2//0h//4//2. *Journal of applied chemistry of the USSR*, 58(10 pt 2):2097–2101. cited By 6.

Kong, X., Lu, S., Huang, J., Cai, Z., and Wei, S. (2013). Experimental research on the use of phase change materials in perforated brick rooms for cooling storage. *Energy and Buildings*, 62:597–604.

Kothari, R., Sahu, S. K., and Kundalwal, S. I. (2021). Investigation on thermal characteristics of nano enhanced phase change material based finned and unfinned heat sinks for thermal management system. *Chemical Engineering and Processing - Process Intensification*, 162:108328.

Kraack, H., Sirota, E. B., and Deutsch, M. (2000). Measurements of homogeneous nucleation in normal-alkanes. *The Journal of Chemical Physics*, 112(15):6873–6885.

Krishna, J., Kishore, P., and Solomon, A. B. (2017). Heat pipe with nano enhanced-PCM for electronic cooling application. *Experimental Thermal and Fluid Science*, 81:84–92.

Kumar, A., Kothari, R., Sahu, S. K., and Kundalwal, S. I. (2021). Thermal performance of heat sink using nano-enhanced phase change material (NePCM) for cooling of electronic components. *Microelectronics Reliability*, 121:114144.

Kumar, K. S., Dinesh, R., Roseline, A. A., and Kalaiselvam, S. (2017). Performance analysis of heat pipe aided NEPCM heat sink for transient electronic cooling. *Microelectronics Reliability*, 73:1–13.

Kumar, R., Misra, M. K., Kumar, R., Gupta, D., Khatri, P., Tak, B., and Meena, S. (2011). Phase change materials: Technology status and potential defence applications (review papers). *Defence Science Journal*, 61(6):576.

Kumaresan, V., Velraj, R., and Das, S. K. (2012). The effect of carbon nanotubes in enhancing the thermal transport properties of PCM during solidification. *Heat and Mass Transfer*, 48(8):1345–1355.

Lasance, C. and Simons, R. (2005). Advances in high-performance cooling for electronics. *Electronics Cooling*, 11(4):22–39. cited By 58.

Latibari, S. T., Mehrali, M., Mehrali, M., Mahlia, T. M. I., and Metselaar, H. S. C. (2013). Synthesis, characterization and thermal properties of nanoencapsulated phase change materials via sol–gel method. *Energy*, 61:664–672.

Le-Ping, Z., Bu-Xuan, W., Xiao-Feng, P., Du, X.-Z., and Yong-Ping, Y. (2010). On the specific heat capacity of cuo nanofluid. *Advances in Mechanical Engineering*, 02:1–4.

Leong, K. Y., Rahman, M. R. A., and Gurunathan, B. A. (2019). Nano-enhanced phase change materials: A review of thermo-physical properties, applications and challenges. *Journal of Energy Storage*, 21:18–31.

Lestari, E., Saptiama, I., Setiawan, H., et al. (2018). Synthesis of nano-$\alpha$-al 2 o 3 for 99 mo adsorbent. *Atom Indonesia*, 44(1):17–21.

Li, B. and Zhai, X. (2017). Experimental investigation and theoretical analysis on a mid-temperature solar collector/storage system with composite PCM. *Applied Thermal Engineering*, 124:34–43.

Li, C., Li, Q., Cong, L., jiang, F., Zhao, Y., Liu, C., Xiong, Y., Chang, C., and Ding, Y. (2019a). MgO based composite phase change materials for thermal energy storage: The effects of MgO particle density and size on microstructural characteristics as well as thermophysical and mechanical properties. *Applied Energy*, 250:81–91.

Li, C., Wang, M., Xie, B., Ma, H., and Chen, J. (2020a). Enhanced properties of diatomite-based composite phase change materials for thermal energy storage. *Renewable Energy*, 147:265–274.

Li, C., Zhang, B., Xie, B., Zhao, X., and Chen, J. (2020b). Tailored phase change behavior of na2so4·10h2o/expanded graphite composite for thermal energy storage. *Energy Conversion and Management*, 208:112586.

Li, G., Hwang, Y., Radermacher, R., and Chun, H.-H. (2013a). Review of cold storage materials for subzero applications. *Energy*, 51:1–17.

Li, M. (2013). A nano-graphite/paraffin phase change material with high thermal conductivity. *Applied Energy*, 106:25–30.

Li, M., Chen, M., Wu, Z., and Liu, J. (2014a). Carbon nanotube grafted with polyalcohol and its influence on the thermal conductivity of phase change material. *Energy Conversion and Management*, 83:325–329.

Li, M.-Y., Chen, C.-H., Shi, Y., and Li, L.-J. (2016a). Heterostructures based on two-dimensional layered materials and their potential applications. *Materials Today*, 19(6):322–335.

Li, R., Gerstler, W. D., Arik, M., and Vanderploeg, B. (2015). Heat transfer impact of synthetic jets for air-cooled array of fins. *Journal of Heat Transfer*, 138(2):021702.

Li, T., Lee, J.-H., Wang, R., and Kang, Y. T. (2014b). Heat transfer characteristics of phase change nanocomposite materials for thermal energy storage application. *International Journal of Heat and Mass Transfer*, 75:1–11.

Li, W., Dong, Y., Zhang, X., and Liu, X. (2019b). Preparation and performance analysis of graphite additive/paraffin composite phase change materials. *Processes*, 7(7):447.

Li, X., Zhou, Y., Nian, H., Zhang, X., Dong, O., Ren, X., Zeng, J., Hai, C., and Shen, Y. (2017). Advanced nanocomposite phase change material based on calcium chloride hexahydrate with aluminum oxide nanoparticles for thermal energy storage. *Energy & Fuels*, 31(6):6560–6567.

Li, Y., Li, J., Deng, Y., Guan, W., Wang, X., and Qian, T. (2016b). Preparation of paraffin/porous TiO 2 foams with enhanced thermal conductivity as PCM, by covering the TiO 2 surface with a carbon layer. *Applied Energy*, 171:37–45.

Li, Y., Shi, C., Liu, J., Liu, E., Shao, J., Chen, Z., Dorantes-Gonzalez, D. J., and Hu, X. (2013b). Improving the accuracy of the transient plane source method by correcting probe heat capacity and resistance influences. *Measurement Science and Technology*, 25(1):015006.

Li, Z., Shahsavar, A., Al-Rashed, A. A., and Talebizadehsardari, P. (2020c). Effect of porous medium and nanoparticles presences in a counter-current triple-tube composite porous/nano-PCM system. *Applied Thermal Engineering*, 167:114777.

Lian, Q., Li, Y., Sayyed, A. A. S., Cheng, J., and Zhang, J. (2018). Facile strategy in designing epoxy/paraffin multiple phase change materials for thermal energy storage applications. *ACS Sustainable Chemistry & Engineering*, 6(3):3375–3384.

Liang, G. and Mudawar, I. (2019). Review of single-phase and two-phase nanofluid heat transfer in macro-channels and micro-channels. *International Journal of Heat and Mass Transfer*, 136:324–354.

Ling, Z., Chen, J., Xu, T., Fang, X., Gao, X., and Zhang, Z. (2015). Thermal conductivity of an organic phase change material/expanded graphite composite across the phase change temperature range and a novel thermal conductivity model. *Energy Conversion and Management*, 102:202–208.

Liu, C., Li, F., Ma, L.-P., and Cheng, H.-M. (2010). Advanced materials for energy storage. *Advanced Materials*, 22(8):E28–E62.

Liu, C., Rao, Z., Zhao, J., Huo, Y., and Li, Y. (2015a). Review on nanoencapsulated phase change materials: Preparation, characterization and heat transfer enhancement. *Nano Energy*, 13:814–826.

Liu, C., Yuan, Y., Zhang, N., Cao, X., and Yang, X. (2014). A novel PCM of lauric–myristic–stearic acid/expanded graphite composite for thermal energy storage. *Materials Letters*, 120:43–46.

Liu, H., Wang, X., and Wu, D. (2017). Fabrication of graphene/TiO2/paraffin composite phase change materials for enhancement of solar energy efficiency in photocatalysis and latent heat storage. *ACS Sustainable Chemistry & Engineering*, 5(6):4906–4915.

Liu, P., Hao, J.-W., Mo, L.-P., and Zhang, Z.-H. (2015b). Recent advances in the application of deep eutectic solvents as sustainable media as well as catalysts in organic reactions. *RSC Advances*, 5(60):48675–48704.

Liu, Y.-D., Zhou, Y.-G., Tong, M.-W., and Zhou, X.-S. (2009). Experimental study of thermal conductivity and phase change performance of nanofluids PCMs. *Microfluidics and Nanofluidics*, 7(4):579–584.

Losego, M. D. and Cahill, D. G. (2013). Breaking through barriers. *Nature Materials*, 12(5):382–384.

Lu, Y., Xiao, X., Mo, J., Huan, C., Qi, S., Zhan, Y., Zhu, Y., and Xu, G. (2018). Green nano-encapsulation technique for preparation of phase change nanofibers mats with core-sheath structure. *Colloids and Surfaces A: Physicochemical and Engineering Aspects*, 555:501–506.

Lv, Y., Liu, G., Zhang, G., and Yang, X. (2020a). A novel thermal management structure using serpentine phase change material coupled with forced air convection for cylindrical battery modules. *Journal of Power Sources*, 468:228398.

Lv, Y., Yang, X., and Zhang, G. (2020b). Durability of phase-change-material module and its relieving effect on battery deterioration during long-term cycles. *Applied Thermal Engineering*, 179:115747.

Machrafi, H. (2020). On the chemical potential of nanoparticle dispersion. *Physics Letters A*, 384(19):126485.

Mahdi, J. M., Lohrasbi, S., and Nsofor, E. C. (2019). Hybrid heat transfer enhancement for latent-heat thermal energy storage systems: A review. *International Journal of Heat and Mass Transfer*, 137:630–649.

Mahian, O., Kolsi, L., Amani, M., Estellé, P., Ahmadi, G., Kleinstreuer, C., Marshall, J. S., Siavashi, M., Taylor, R. A., Niazmand, H., Wongwises, S., Hayat, T., Kolanjiyil, A., Kasaeian, A., and Pop, I. (2019). Recent advances in modeling and simulation of nanofluid flows-part i: Fundamentals and theory. *Physics Reports*, 790:1–48.

Mancin, S., Diani, A., Doretti, L., Hooman, K., and Rossetto, L. (2015). Experimental analysis of phase change phenomenon of paraffin waxes embedded in copper foams. *International Journal of Thermal Sciences*, 90:79–89.

Marcus, S. and Blaine, R. (1994). Thermal conductivity of polymers, glasses and ceramics by modulated DSC. *Thermochimica Acta*, 243(2):231–239.

Maydanik, Y., Vershinin, S., Korukov, M., and Ochterbeck, J. (2005). Miniature loop heat pipes-a promising means for cooling electronics. *IEEE Transactions on Components and Packaging Technologies*, 28(2):290–296.

Mehling, H. and Cabeza, L. F. (2007). Phase change materials and their basic properties. In *Thermal energy storage for sustainable energy consumption*, pages 257–277. Springer.

Mehra, N., Mu, L., Ji, T., Yang, X., Kong, J., Gu, J., and Zhu, J. (2018). Thermal transport in polymeric materials and across composite interfaces. *Applied Materials Today*, 12:92–130.

Mehrali, M., Latibari, S. T., Mehrali, M., Mahlia, T. M. I., Metselaar, H. S. C., Naghavi, M. S., Sadeghinezhad, E., and Akhiani, A. R. (2013a). Preparation and characterization of palmitic acid/graphene nanoplatelets composite with remarkable thermal conductivity as a novel shape-stabilized phase change material. *Applied Thermal Engineering*, 61(2):633–640.

Mehrali, M., Latibari, S. T., Mehrali, M., Mahlia, T. M. I., Sadeghinezhad, E., and Metselaar, H. S. C. (2014a). Preparation of nitrogen-doped graphene/palmitic acid shape stabilized composite phase change material with remarkable thermal properties for thermal energy storage. *Applied Energy*, 135:339–349.

Mehrali, M., Latibari, S. T., Mehrali, M., Mahlia, T. M. I., Sadeghinezhad, E., and Metselaar, H. S. C. (2014b). Preparation of nitrogen-doped graphene/palmitic acid shape stabilized composite phase change material with remarkable thermal properties for thermal energy storage. *Applied Energy*, 135:339–349.

Mehrali, M., Latibari, S. T., Mehrali, M., Metselaar, H. S. C., and Silakhori, M. (2013b). Shape-stabilized phase change materials with high thermal

conductivity based on paraffin/graphene oxide composite. *Energy conversion and management*, 67:275–282.

Mei, D., Zhang, B., Liu, R., Zhang, Y., and Liu, J. (2011). Preparation of capric acid/halloysite nanotube composite as form-stable phase change material for thermal energy storage. *Solar Energy Materials and Solar Cells*, 95(10):2772–2777.

Meng, X., Zhang, H., Sun, L., Xu, F., Jiao, Q., Zhao, Z., Zhang, J., Zhou, H., Sawada, Y., and Liu, Y. (2012). Preparation and thermal properties of fatty acids/CNTs composite as shape-stabilized phase change materials. *Journal of Thermal Analysis and Calorimetry*, 111(1):377–384.

Messerly, J. F., Guthrie, G. B., Todd, S. S., and Finke, H. L. (1967). Low-temperature thermal data for pentane, n-heptadecane, and n-octadecane. revised thermodynamic functions for the n-alkanes, c5-c18. *Journal of Chemical & Engineering Data*, 12(3):338–346.

Milián, Y. E., Gutiérrez, A., Grágeda, M., and Ushak, S. (2017). A review on encapsulation techniques for inorganic phase change materials and the influence on their thermophysical properties. *Renewable and Sustainable Energy Reviews*, 73:983–999.

Minnich, A. J. (2015). Advances in the measurement and computation of thermal phonon transport properties. *Journal of Physics: Condensed Matter*, 27(5):053202.

Missana, T. and Adell, A. (2000). On the applicability of DLVO theory to the prediction of clay colloids stability. *Journal of Colloid and Interface Science*, 230(1):150–156.

Mithal, P. (1996). Design of experimental based evaluation of thermal performance of a flichip electronic assembly. In *ASME EEP Proceedings*, volume 18, pages 109–115. ASME New York, NY.

Mller, A. and Lonsdale, K. (1948). The low-temperature form of c18h38. *Acta Crystallographica*, 1(3):129–131.

Mohamed, N. H., Soliman, F. S., Maghraby, H. E., and Moustfa, Y. (2017). Thermal conductivity enhancement of treated petroleum waxes, as phase change material, by nano alumina: Energy storage. *Renewable and Sustainable Energy Reviews*, 70:1052–1058.

Molefi, J. A., Luyt, A. S., and Krupa, I. (2010). Investigation of thermally conducting phase-change materials based on polyethylene/wax blends filled with copper particles. *Journal of Applied Polymer Science*, pages NA–NA.

Motahar, S., Nikkam, N., Alemrajabi, A. A., Khodabandeh, R., Toprak, M. S., and Muhammed, M. (2014). Experimental investigation on thermal and rheological properties of n-octadecane with dispersed tio2 nanoparticles. *International Communications in Heat and Mass Transfer*, 59:68–74.

Mudawar, I. (2001). Assessment of high-heat-flux thermal management schemes. *IEEE Transactions on Components and Packaging Technologies*, 24(2):122–141.

Mulligan, J. C., Colvin, D. P., and Bryant, Y. G. (1996). Microencapsulated phase-change material suspensions for heat transfer in spacecraft thermal systems. *Journal of Spacecraft and Rockets*, 33(2):278–284.

Murshed, S. S. and de Castro, C. N. (2017). A critical review of traditional and emerging techniques and fluids for electronics cooling. *Renewable and Sustainable Energy Reviews*, 78:821–833.

Nabil, M. and Khodadadi, J. (2013). Experimental determination of temperature-dependent thermal conductivity of solid eicosane-based nanostructure-enhanced phase change materials. *International Journal of Heat and Mass Transfer*, 67:301–310.

Nada, S. and Alshaer, W. (2015). Comprehensive parametric study of using carbon foam structures saturated with PCMs in thermal management of electronic systems. *Energy Conversion and Management*, 105:93–102.

Nagano, K., Mochida, T., Takeda, S., Domański, R., and Rebow, M. (2003). Thermal characteristics of manganese (II) nitrate hexahydrate as a phase change material for cooling systems. *Applied Thermal Engineering*, 23(2):229–241.

Nakayama, W. (1986). Thermal management of electronic equipment: A review of technology and research topics. *Applied Mechanics Reviews*, 39(12):1847.

Narayanan, S. S., Kardam, A., Kumar, V., Bhardwaj, N., Madhwal, D., Shukla, P., Kumar, A., Verma, A., and Jain, V. (2017). Development of sunlight-driven eutectic phase change material nanocomposite for applications in solar water heating. *Resource-Efficient Technologies*, 3(3):272–279.

Nejman, A., Cieślak, M., Gajdzicki, B., Goetzendorf-Grabowska, B., and Karaszewska, A. (2014). Methods of PCM microcapsules application and the thermal properties of modified knitted fabric. *Thermochimica Acta*, 589:158–163.

Nikolić, R., Marinović-Cincović, M., Gadžurić, S., and Zsigrai, I. (2003). New materials for solar thermal storage—solid/liquid transitions in fatty acid esters. *Solar Energy Materials and Solar Cells*, 79(3):285–292.

Niyas, H. and Muthukumar, P. (2018). A novel heat transfer enhancement technique for performance improvements in encapsulated latent heat storage system. *Solar Energy*, 164:276–286.

Nomura, T., Tabuchi, K., Zhu, C., Sheng, N., Wang, S., and Akiyama, T. (2015). High thermal conductivity phase change composite with percolating carbon fiber network. *Applied Energy*, 154:678–685.

Nomura, T., Zhu, C., Nan, S., Tabuchi, K., Wang, S., and Akiyama, T. (2016). High thermal conductivity phase change composite with a metal-stabilized carbon-fiber network. *Applied Energy*, 179:1–6.

Nourani, M., Hamdami, N., Keramat, J., Moheb, A., and Shahedi, M. (2016a). Preparation of a stable nanocomposite phase change material (NCPCM) using sodium stearoyl lactylate (SSL) as the surfactant and evaluation of its stability using image analysis. *Renewable Energy*, 93:404–411.

Nourani, M., Hamdami, N., Keramat, J., Moheb, A., and Shahedi, M. (2016b). Thermal behavior of paraffin-nano-al2o3 stabilized by sodium stearoyl lactylate as a stable phase change material with high thermal conductivity. *Renewable Energy*, 88:474–482.

Nyburg, S. C. and Potworowski, J. A. (1973). Prediction of unit cells and atomic coordinates for the n-alkanes. *Acta Crystallographica Section B Structural Crystallography and Crystal Chemistry*, 29(2):347–352.

Oh, D.-W., Jain, A., Eaton, J. K., Goodson, K. E., and Lee, J. S. (2008). Thermal conductivity measurement and sedimentation detection of aluminum oxide nanofluids by using the 3 method. *International Journal of Heat and Fluid Flow*, 29(5):1456–1461.

Oh, S. H. (2005). Ordered liquid aluminum at the interface with sapphire. *Science*, 310(5748):661–663.

Ohring, M. (1998a). An overview of electronic devices and their reliability. In *Reliability and failure of electronic materials and devices*, pages 1–36. Academic Press.

Ohring, M. (1998b). *Reliability and failure of electronic materials and devices*. Elsevier.

Oliver, M. and Calvert, P. (1975). Homogeneous nucleation of n-alkanes measured by differential scanning calorimetry. *Journal of Crystal Growth*, 30(3):343–351.

Ong, W.-L., Rupich, S. M., Talapin, D. V., McGaughey, A. J. H., and Malen, J. A. (2013). Surface chemistry mediates thermal transport in three-dimensional nanocrystal arrays. *Nature Materials*, 12(5):410–415.

Oya, T., Nomura, T., Tsubota, M., Okinaka, N., and Akiyama, T. (2013). Thermal conductivity enhancement of erythritol as PCM by using graphite and nickel particles. *Applied Thermal Engineering*, 61(2):825–828.

P, V. K., S, S., B, P., Venugopal, A., and Nair, S. C. (2017). Pentaerythritol with alumina nano additives for thermal energy storage applications. *Journal of Energy Storage*, 13:359–377.

Pahamli, Y., Hosseini, M., Ranjbar, A., and Bahrampoury, R. (2017). Effect of nanoparticle dispersion and inclination angle on melting of PCM in a shell and tube heat exchanger. *Journal of the Taiwan Institute of Chemical Engineers*, 81:316–334.

Pal, A., Joshi, Y., Beitelmal, M., Patel, C., and Wenger, T. (2002). Design and performance evaluation of a compact thermosyphon. *IEEE Transactions on Components and Packaging Technologies*, 25(4):601–607.

Palacios, A., Cong, L., Navarro, M., Ding, Y., and Barreneche, C. (2019). Thermal conductivity measurement techniques for characterizing thermal energy storage materials – a review. *Renewable and Sustainable Energy Reviews*, 108:32–52.

Parameshwaran, R., Deepak, K., Saravanan, R., and Kalaiselvam, S. (2014). Preparation, thermal and rheological properties of hybrid nanocomposite phase change material for thermal energy storage. *Applied Energy*, 115:320–330.

Parameshwaran, R., Jayavel, R., and Kalaiselvam, S. (2013). Study on thermal properties of organic ester phase-change material embedded with silver nanoparticles. *Journal of Thermal Analysis and Calorimetry*, 114(2):845–858.

Parameshwaran, R. and Kalaiselvam, S. (2016). Nanomaterial-based PCM composites for thermal energy storage in buildings. In *Nano and Biotech Based Materials for Energy Building Efficiency*, pages 215–243. Springer International Publishing.

Pardo, P., Deydier, A., Anxionnaz-Minvielle, Z., Rougé, S., Cabassud, M., and Cognet, P. (2014). A review on high temperature thermochemical heat energy storage. *Renewable and Sustainable Energy Reviews*, 32:591–610.

Paris, J., Falardeau, M., and Villeneuve, C. (1993). Thermal storage by latent heat: A viable option for energy conservation in buildings. *Energy Sources*, 15(1):85–93.

Parker, W. J., Jenkins, R. J., Butler, C. P., and Abbott, G. L. (1961). Flash method of determining thermal diffusivity, heat capacity, and thermal conductivity. *Journal of Applied Physics*, 32(9):1679–1684.

Parks, G. S., Moore, G. E., Renquist, M. L., Naylor, B. F., McClaine, L. A., Fujii, P. S., and Hatton, J. A. (1949). Thermal data on organic compounds. XXV. some heat capacity, entropy and free energy data for nine hydrocarbons of high molecular weight. *Journal of the American Chemical Society*, 71(10):3386–3389.

Parks, G. S., West, T. J., Naylor, B. F., Fujii, P. S., and McClaine, L. A. (1946). Thermal data on organic compounds. XXIII. modern combustion data for fourteen hydrocarbons and five polyhydroxy alcohols. *Journal of the American Chemical Society*, 68(12):2524–2527.

Pavlova, A. and Amitay, M. (2006). Electronic cooling using synthetic jet impingement. *Journal of Heat Transfer*, 128(9):897.

Pedersen, U. R. (2013). Direct calculation of the solid-liquid gibbs free energy difference in a single equilibrium simulation. *The Journal of Chemical Physics*, 139(10):104102.

Pedram, M. and Nazarian, S. (2006). Thermal modeling, analysis, and management in VLSI circuits: Principles and methods. *Proceedings of the IEEE*, 94(8):1487–1501.

Pfahl, R. and McElroy, J. (2005). The 2004 international electronics manufacturing initiative (iNEMI) technology roadmaps. In *2005 Conference on High Density Microsystem Design and Packaging and Component Failure Analysis*. IEEE.

Pielichowska, K. and Pielichowski, K. (2014). Phase change materials for thermal energy storage. *Progress in Materials Science*, 65:67–123.

Pielichowski, K. and Flejtuch, K. (2002). Differential scanning calorimetry studies on poly(ethylene glycol) with different molecular weights for thermal energy storage materials. *Polymers for Advanced Technologies*, 13(10-12):690–696.

Pielichowski, K. and Flejtuch, K. (2003a). Binary blends of polyethers with fatty acids: A thermal characterization of the phase transitions. *Journal of Applied Polymer Science*, 90(3):861–870.

Pielichowski, K. and Flejtuch, K. (2003b). Differential scanning calorimetry study of blends of poly(ethylene glycol) with selected fatty acids. *Macromolecular Materials and Engineering*, 288(3):259–264.

Pielichowski, K. and Flejtuch, K. (2005). Recent developments in polymeric phase change materials for energy storage: poly(ethylene oxide)/stearic acid blends. *Polymers for Advanced Technologies*, 16(2-3):127–132.

Pielichowski, K., Flejtuch, K., and Pielichowski, J. (2004). Step-scan alternating DSC study of melting and crystallisation in poly(ethylene oxide). *Polymer*, 45(4):1235–1242.

Piper, S. H. and Malkin, T. (1930). Crystal structure of normal paraffins. *Nature*, 126(3173):278–278.

P.M., V. and Morlanes, M. J. M., editors (2016). *Nanomaterials and Nanocomposites*. Wiley-VCH Verlag GmbH & Co. KGaA.

Pokropivny, V. and Skorokhod, V. (2007). Classification of nanostructures by dimensionality and concept of surface forms engineering in nanomaterial science. *Materials Science and Engineering: C*, 27(5-8):990–993.

Pop, E., Mann, D., Wang, Q., Goodson, K., and Dai, H. (2006). Thermal conductance of an individual single-wall carbon nanotube above room temperature. *Nano Letters*, 6(1):96–100.

Popa, I., Gillies, G., Papastavrou, G., and Borkovec, M. (2010). Attractive and repulsive electrostatic forces between positively charged latex particles in the presence of anionic linear polyelectrolytes. *The Journal of Physical Chemistry B*, 114(9):3170–3177.

Poplavko, Y. M. (2019a). Phase transitions in solids. In *Electronic Materials*, pages 601–662. Elsevier.

Poplavko, Y. M. (2019b). Thermal properties of solids. In *Electronic Materials*, pages 95–120. Elsevier.

Prasad, S., Kumar, V., Kirubanandam, S., and Barhoum, A. (2018). Engineered nanomaterials: nanofabrication and surface functionalization. In *Emerging Applications of Nanoparticles and Architecture Nanostructures*, pages 305–340. Elsevier.

Prasher, R., Bhattacharya, P., and Phelan, P. E. (2005). Brownian-motion-based convective-conductive model for the effective thermal conductivity of nanofluids. *Journal of Heat Transfer*, 128(6):588–595.

Praveen, B. and Suresh, S. (2018). Experimental study on heat transfer performance of neopentyl glycol/CuO composite solid-solid PCM in TES based heat sink. *Engineering Science and Technology, an International Journal*, 21(5):1086–1094.

Putra, N., Amin, M., Kosasih, E. A., Luanto, R. A., and Abdullah, N. A. (2017). Characterization of the thermal stability of RT 22 HC/graphene using a thermal cycle method based on thermoelectric methods. *Applied Thermal Engineering*, 124:62–70.

Putra, N., Rawi, S., Amin, M., Kusrini, E., Kosasih, E. A., and Mahlia, T. M. I. (2019). Preparation of beeswax/multi-walled carbon nanotubes as novel shape-stable nanocomposite phase-change material for thermal energy storage. *Journal of Energy Storage*, 21:32–39.

Putra, N., Sandi, A. F., Ariantara, B., Abdullah, N., and Mahlia, T. M. I. (2020). Performance of beeswax phase change material (PCM) and heat pipe as passive battery cooling system for electric vehicles. *Case Studies in Thermal Engineering*, 21:100655.

Qiu, L., Zhu, N., Feng, Y., Michaelides, E. E., Żyła, G., Jing, D., Zhang, X., Norris, P. M., Markides, C. N., and Mahian, O. (2019). A review of recent advances in thermophysical properties at the nanoscale: From solid state to colloids. *Physics Reports*.

Qiu, X., Song, G., Chu, X., Li, X., and Tang, G. (2013). Preparation, thermal properties and thermal reliabilities of microencapsulated n-octadecane with acrylic-based polymer shells for thermal energy storage. *Thermochimica Acta*, 551:136–144.

Quadrelli, R. and Peterson, S. (2007). The energy–climate challenge: Recent trends in CO2 emissions from fuel combustion. *Energy Policy*, 35(11):5938–5952.

Qureshi, Z. A., Ali, H. M., and Khushnood, S. (2018). Recent advances on thermal conductivity enhancement of phase change materials for energy storage system: A review. *International Journal of Heat and Mass Transfer*, 127:838–856.

Ramakrishnan, S., Wang, X., Sanjayan, J., and Wilson, J. (2017). Heat transfer performance enhancement of paraffin/expanded perlite phase change composites with graphene nano-platelets. *Energy Procedia*, 105:4866–4871.

Regin, A. F., Solanki, S., and Saini, J. (2008). Heat transfer characteristics of thermal energy storage system using PCM capsules: A review. *Renewable and Sustainable Energy Reviews*, 12(9):2438–2458.

Rehman, T., Ali, H. M., Janjua, M. M., Sajjad, U., and Yan, W.-M. (2019). A critical review on heat transfer augmentation of phase change materials embedded with porous materials/foams. *International Journal of Heat and Mass Transfer*, 135:649–673.

Riffat, S., Omer, S., and Ma, X. (2001). A novel thermoelectric refrigeration system employing heat pipes and a phase change material: an experimental investigation. *Renewable Energy*, 23(2):313–323.

Ross, R. G., Andersson, P., Sundqvist, B., and Backstrom, G. (1984). Thermal conductivity of solids and liquids under pressure. *Reports on Progress in Physics*, 47(10):1347–1402.

Rozanna, D., Chuah, T. G., Salmiah, A., Choong, T. S. Y., and Saari, M. (2005). Fatty acids as phase change materials (PCMs) for thermal energy storage: A review. *International Journal of Green Energy*, 1(4):495–513.

Şahan, N., Fois, M., and Paksoy, H. (2015). Improving thermal conductivity phase change materials—a study of paraffin nanomagnetite composites. *Solar Energy Materials and Solar Cells*, 137:61–67.

Sahan, N. and Paksoy, H. O. (2014). Thermal enhancement of paraffin as a phase change material with nanomagnetite. *Solar Energy Materials and Solar Cells*, 126:56–61.

Sahoo, S. K., Das, M. K., and Rath, P. (2016a). Application of TCE-PCM based heat sinks for cooling of electronic components: A review. *Renewable and Sustainable Energy Reviews*, 59:550–582.

Sahoo, S. K., Das, M. K., and Rath, P. (2016b). Application of TCE-PCM based heat sinks for cooling of electronic components: A review. *Renewable and Sustainable Energy Reviews*, 59:550–582.

Salunkhe, P. B. and Shembekar, P. S. (2012). A review on effect of phase change material encapsulation on the thermal performance of a system. *Renewable and Sustainable Energy Reviews*, 16(8):5603–5616.

Sami, S. and Etesami, N. (2017). Improving thermal characteristics and stability of phase change material containing tio2 nanoparticles after thermal cycles for energy storage. *Applied Thermal Engineering*, 124:346–352.

Sarı, A. (2003). Thermal characteristics of a eutectic mixture of myristic and palmitic acids as phase change material for heating applications. *Applied Thermal Engineering*, 23(8):1005–1017.

Sarı, A. (2005). Eutectic mixtures of some fatty acids for low temperature solar heating applications: Thermal properties and thermal reliability. *Applied Thermal Engineering*, 25(14-15):2100–2107.

Sarı, A. and Karaipekli, A. (2008). Preparation and thermal properties of capric acid/palmitic acid eutectic mixture as a phase change energy storage material. *Materials Letters*, 62(6-7):903–906.

Sarı, A., Karaipekli, A., and Alkan, C. (2009). Preparation, characterization and thermal properties of lauric acid/expanded perlite as novel form-stable composite phase change material. *Chemical Engineering Journal*, 155(3):899–904.

Sari, A., Karaipekli, A., and Kaygusuz, K. (2008). Fatty acid/expanded graphite composites as phase change material for latent heat thermal energy storage. *Energy Sources, Part A: Recovery, Utilization, and Environmental Effects*, 30(5):464–474.

Sari, A. and Kaygusuz, K. (2002). Thermal performance of a eutectic mixture of lauric and stearic acids as PCM encapsulated in the annulus of two concentric pipes. *Solar Energy*, 72(6):493–504.

Sari, A. and Kaygusuz, K. (2006). Thermal energy storage characteristics of myristic and stearic acids eutectic mixture for low temperature heating applications. *Chinese Journal of Chemical Engineering*, 14(2):270–275.

Sarı, A., Sarı, H., and nal, A. (2004). Thermal properties and thermal reliability of eutectic mixtures of some fatty acids as latent heat storage materials. *Energy Conversion and Management*, 45(3):365–376.

Sarwar, J. and Mansoor, B. (2016). Characterization of thermophysical properties of phase change materials for non-membrane based indirect solar desalination application. *Energy Conversion and Management*, 120:247–256.

Saterlie, M., Sahin, H., Kavlicoglu, B., Liu, Y., and Graeve, O. (2011). Particle size effects in the thermal conductivity enhancement of copper-based nanofluids. *Nanoscale Research Letters*, 6(1):217.

Sayyar, M., Weerasiri, R. R., Soroushian, P., and Lu, J. (2014). Experimental and numerical study of shape-stable phase-change nanocomposite toward energy-efficient building constructions. *Energy and Buildings*, 75:249–255.

Scalat, S., Banu, D., Hawes, D., Parish, J., Haghighata, F., and Feldman, D. (1996). Full scale thermal testing of latent heat storage in wallboard. *Solar Energy Materials and Solar Cells*, 44(1):49–61.

Schaller, R. R. (1997). Moore's law: past, present and future. *IEEE spectrum*, 34(6):52–59.

Schaube, F., Koch, L., Wrner, A., and Mller-Steinhagen, H. (2012). A thermodynamic and kinetic study of the de- and rehydration of ca(OH)2 at high h2o partial pressures for thermo-chemical heat storage. *Thermochimica Acta*, 538:9–20.

Schlenk, H. (1961). Crystallization of fatty acids. *Journal of the American Oil Chemists Society*, 38(12):728–736.

Shah, K. W. (2018). A review on enhancement of phase change materials - a nanomaterials perspective. *Energy and Buildings*, 175:57–68.

Shaikh, S., Lafdi, K., and Hallinan, K. (2008). Carbon nanoadditives to enhance latent energy storage of phase change materials. *Journal of Applied Physics*, 103(9):094302.

Sharaf, O. Z., Taylor, R. A., and Abu-Nada, E. (2020). On the colloidal and chemical stability of solar nanofluids: From nanoscale interactions to recent advances. *Physics Reports*, 867:1–84.

Sharma, A., Shukla, A., Chen, C., and Dwivedi, S. (2013). Development of phase change materials for building applications. *Energy and Buildings*, 64:403–407.

Sharma, A., Tyagi, V., Chen, C., and Buddhi, D. (2009). Review on thermal energy storage with phase change materials and applications. *Renewable and Sustainable Energy Reviews*, 13(2):318–345.

Sharma, R., Ganesan, P., Sahu, J., Metselaar, H., and Mahlia, T. (2014). Numerical study for enhancement of solidification of phase change materials using trapezoidal cavity. *Powder Technology*, 268:38–47.

Sharma, R., Ganesan, P., Tyagi, V., Metselaar, H., and Sandaran, S. (2015). Developments in organic solid–liquid phase change materials and their applications in thermal energy storage. *Energy Conversion and Management*, 95:193–228.

Sharma, R., Ganesan, P., Tyagi, V., Metselaar, H., and Sandaran, S. (2016). Thermal properties and heat storage analysis of palmitic acid-TiO 2 composite as nano-enhanced organic phase change material (NEOPCM). *Applied Thermal Engineering*, 99:1254–1262.

Sharma, S., Micheli, L., Chang, W., Tahir, A., Reddy, K., and Mallick, T. (2017). Nano-enhanced phase change material for thermal management of BICPV. *Applied Energy*, 208:719–733.

Sharma, S. D., Kitano, H., and Sagara, K. (2004). Phase change materials for low temperature solar thermal applications. *Res. Rep. Fac. Eng. Mie Univ*, 29(1).

Shchukina, E. M., Graham, M., Zheng, Z., and Shchukin, D. G. (2018). Nanoencapsulation of phase change materials for advanced thermal energy storage systems. *Chemical Society Reviews*, 47(11):4156–4175.

SHE, G., ZHANG, X., SHI, W., FAN, X., and CHANG, J. (2007). Electrochemical/chemical synthesis of highly-oriented single-crystal ZnO nanotube arrays on transparent conductive substrates. *Electrochemistry Communications*, 9(12):2784–2788.

Shen, S., Tan, S., Wu, S., Guo, C., Liang, J., Yang, Q., Xu, G., and Deng, J. (2018). The effects of modified carbon nanotubes on the thermal properties of erythritol as phase change materials. *Energy Conversion and Management*, 157:41–48.

Shi, J.-N., Ger, M.-D., Liu, Y.-M., Fan, Y.-C., Wen, N.-T., Lin, C.-K., and Pu, N.-W. (2013). Improving the thermal conductivity and shape-stabilization of phase change materials using nanographite additives. *Carbon*, 51:365–372.

Shi, L., Hu, Y., and He, Y. (2020a). Magneto-responsive thermal switch for remote-controlled locomotion and heat transfer based on magnetic nanofluid. *Nano Energy*, 71:104582.

Shi, L., Wang, X., Hu, Y., and He, Y. (2020b). Investigation of photocatalytic activity through photo-thermal heating enabled by fe3o4/TiO2 composite under magnetic field. *Solar Energy*, 196:505–512.

Shilei, L., Neng, Z., and Guohui, F. (2006). Eutectic mixtures of capric acid and lauric acid applied in building wallboards for heat energy storage. *Energy and Buildings*, 38(6):708–711.

Shin, D. and Banerjee, D. (2011). Enhancement of specific heat capacity of high-temperature silica-nanofluids synthesized in alkali chloride salt eutectics for solar thermal-energy storage applications. *International Journal of Heat and Mass Transfer*, 54(5-6):1064–1070.

Shon, J., Kim, H., and Lee, K. (2014). Improved heat storage rate for an automobile coolant waste heat recovery system using phase-change material in a fin–tube heat exchanger. *Applied Energy*, 113:680–689.

Siddique, A. R. M., Mahmud, S., and Heyst, B. V. (2018). A comprehensive review on a passive (phase change materials) and an active (thermoelectric cooler) battery thermal management system and their limitations. *Journal of Power Sources*, 401:224–237.

Simons, R. and Chu, R. Application of thermoelectric cooling to electronic equipment: a review and analysis. In *Sixteenth Annual IEEE Semiconductor Thermal Measurement and Management Symposium (Cat. No.00CH37068)*. IEEE.

Smith, E. L., Abbott, A. P., and Ryder, K. S. (2014). Deep eutectic solvents (dess) and their applications. *Chemical reviews*, 114(21):11060–11082.

Solé, A., Neumann, H., Niedermaier, S., Martorell, I., Schossig, P., and Cabeza, L. F. (2014). Stability of sugar alcohols as PCM for thermal energy storage. *Solar Energy Materials and Solar Cells*, 126:125–134.

Speyer, R. (1993). *Thermal analysis of materials*. CRC press.

Sreethawong, T., Shah, K. W., Zhang, S.-Y., Ye, E., Lim, S. H., Maheswaran, U., Mao, W. Y., and Han, M.-Y. (2014). Optimized production of copper nanostructures with high yields for efficient use as thermal conductivity-enhancing PCM dopant. *Journal of Materials Chemistry A*, 2(10):3417.

Steinfeld, A., Sanders, S., and Palumbo, R. (1999). DESIGN ASPECTS OF SOLAR THERMOCHEMICAL ENGINEERING—a CASE STUDY: TWO-STEP WATER-SPLITTING CYCLE USING THE fe3o4/FeO REDOX SYSTEM. *Solar Energy*, 65(1):43–53.

Su, W., Darkwa, J., and Kokogiannakis, G. (2015). Review of solid–liquid phase change materials and their encapsulation technologies. *Renewable and Sustainable Energy Reviews*, 48:373–391.

Sudha, P. N., Sangeetha, K., Vijayalakshmi, K., and Barhoum, A. (2018). Nanomaterials history, classification, unique properties, production and market. In *Emerging Applications of Nanoparticles and Architecture Nanostructures*, pages 341–384. Elsevier.

Suvarnaphaet, P. and Pechprasarn, S. (2017). Graphene-based materials for biosensors: a review. *Sensors*, 17(10):2161.

Taggart, A. M., Voogt, F., Clydesdale, G., and Roberts, K. J. (1996). An examination of the nucleation kinetics ofn-alkanes in the homologous series c13h28to c32h66, and their relationship to structural type, associated with crystallization from stagnant melts. *Langmuir*, 12(23):5722–5728.

Tang, B., Qiu, M., and Zhang, S. (2012). Thermal conductivity enhancement of PEG/SiO2 composite PCM by in situ cu doping. *Solar Energy Materials and Solar Cells*, 105:242–248.

Tarelho, J. P., dos Santos, M. P. S., Ferreira, J. A., Ramos, A., Kopyl, S., Kim, S. O., Hong, S., and Kholkin, A. (2018). Graphene-based materials and structures for energy harvesting with fluids – a review. *Materials Today*, 21(10):1019–1041.

Tariq, S. L., Ali, H. M., Akram, M. A., and Janjua, M. M. (2020a). Experimental investigation on graphene based nanoparticles enhanced phase change materials (GbNePCMs) for thermal management of electronic equipment. *Journal of Energy Storage*, 30:101497.

Tariq, S. L., Ali, H. M., Akram, M. A., Janjua, M. M., and Ahmadlouydarab, M. (2020b). Nanoparticles enhanced phase change materials (NePCMs)-a recent review. *Applied Thermal Engineering*, 176:115305.

Telkes, M. (1952). Nucleation of supersaturated inorganic salt solutions. *Industrial & Engineering Chemistry*, 44(6):1308–1310.

Teng, T.-P. and Yu, C.-C. (2012a). Characteristics of phase-change materials containing oxide nano-additives for thermal storage. *Nanoscale Research Letters*, 7(1).

Teng, T.-P. and Yu, C.-C. (2012b). The effect on heating rate for phase change materials containing mwcnts. *International Journal of Chemical Engineering and Applications*, 3(5):340.

Tian, H., Wang, W., Ding, J., Wei, X., Song, M., and Yang, J. (2015). Thermal conductivities and characteristics of ternary eutectic chloride/expanded graphite thermal energy storage composites. *Applied Energy*, 148:87–92.

Timofeeva, E. V., Routbort, J. L., and Singh, D. (2009). Particle shape effects on thermophysical properties of alumina nanofluids. *Journal of Applied Physics*, 106(1):014304.

Umair, M. M., Zhang, Y., Iqbal, K., Zhang, S., and Tang, B. (2019). Novel strategies and supporting materials applied to shape-stabilize organic phase change materials for thermal energy storage–a review. *Applied Energy*, 235:846–873.

Venkatadri, V., Sammakia, B., Srihari, K., and Santos, D. (2011). A review of recent advances in thermal management in three dimensional chip stacks in electronic systems. *Journal of Electronic Packaging*, 133(4).

Venkitaraj, K., Suresh, S., Praveen, B., and Nair, S. C. (2018). Experimental heat transfer analysis of macro packed neopentylglycol with CuO nano additives for building cooling applications. *Journal of Energy Storage*, 17:1–10.

Visakh, P. M. (2016). Introduction for nanomaterials and nanocomposites: State of art, new challenges, and opportunities. In *Nanomaterials and Nanocomposites*, pages 1–20. Wiley-VCH Verlag GmbH & Co. KGaA.

Wang, B.-X., Zhou, L.-P., and Peng, X.-F. (2006). Surface and size effects on the specific heat capacity of nanoparticles. *International Journal of Thermophysics*, 27(1):139–151.

Wang, C., Lin, T., Li, N., and Zheng, H. (2016). Heat transfer enhancement of phase change composite material: Copper foam/paraffin. *Renewable Energy*, 96:960–965.

Wang, J., Li, Y., Wang, Y., Yang, L., Kong, X., and Sundén, B. (2020). Experimental investigation of heat transfer performance of a heat pipe combined with thermal energy storage materials of CuO-paraffin nanocomposites. *Solar Energy*, 211:928–937.

Wang, J., Xie, H., Guo, Z., Guan, L., and Li, Y. (2014). Improved thermal properties of paraffin wax by the addition of TiO2 nanoparticles. *Applied Thermal Engineering*, 73(2):1541–1547.

Wang, J., Xie, H., Li, Y., and Xin, Z. (2010a). PW based phase change nanocomposites containing -al2o3. *Journal of Thermal Analysis and Calorimetry*, 102(2):709–713.

Wang, J., Xie, H., and Xin, Z. (2009a). Thermal properties of paraffin based composites containing multi-walled carbon nanotubes. *Thermochimica Acta*, 488(1-2):39–42.

Wang, J., Xie, H., Xin, Z., and Li, Y. (2010b). Increasing the thermal conductivity of palmitic acid by the addition of carbon nanotubes. *Carbon*, 48(14):3979–3986.

Wang, J., Xie, H., Xin, Z., Li, Y., and Chen, L. (2010c). Enhancing thermal conductivity of palmitic acid based phase change materials with carbon nanotubes as fillers. *Solar Energy*, 84(2):339–344.

Wang, J., Xie, H., Xin, Z., Li, Y., and Yin, C. (2011). Investigation on thermal properties of heat storage composites containing carbon fibers. *Journal of Applied Physics*, 110(9):094302.

Wang, L. and Meng, D. (2010). Fatty acid eutectic/polymethyl methacrylate composite as form-stable phase change material for thermal energy storage. *Applied Energy*, 87(8):2660–2665.

Wang, L., Tan, Z., Meng, S., Liang, D., and Li, G. (2001). Enhancement of molar heat capacity of nanostructured al2o3. *Journal of Nanoparticle Research*, 3(5/6):483–487.

Wang, N., Yang, S., Zhu, D., and Ju, X. (2010d). Preparation and heat transfer behavior of paraffin based composites containing nano-copper particles micro and nanoscale multiphase flows. In *7th International Conference on Multiphase Flow (ICMF). International Conference on Multiphase Flow (ICMF), Tampa FL USA*.

Wang, W., Yang, X., Fang, Y., and Ding, J. (2009b). Preparation and performance of form-stable polyethylene glycol/silicon dioxide composites as solid–liquid phase change materials. *Applied Energy*, 86(2):170–174.

Wang, X., Guo, Q., Zhong, Y., Wei, X., and Liu, L. (2013). Heat transfer enhancement of neopentyl glycol using compressed expanded natural graphite for thermal energy storage. *Renewable Energy*, 51:241–246.

Wang, X.-Q. and Mujumdar, A. S. (2007). Heat transfer characteristics of nanofluids: a review. *International Journal of Thermal Sciences*, 46(1):1–19.

Wang, X.-Q. and Mujumdar, A. S. (2008). A review on nanofluids - part II: experiments and applications. *Brazilian Journal of Chemical Engineering*, 25(4):631–648.

Wang, Z. L. (2006). Piezoelectric nanogenerators based on zinc oxide nanowire arrays. *Science*, 312(5771):242–246.

Waqas, A. and Din, Z. U. (2013). Phase change material (PCM) storage for free cooling of buildings—a review. *Renewable and Sustainable Energy Reviews*, 18:607–625.

Warzoha, R. J. and Fleischer, A. S. (2014). Effect of graphene layer thickness and mechanical compliance on interfacial heat flow and thermal conduction in solid–liquid phase change materials. *ACS Applied Materials & Interfaces*, 6(15):12868–12876.

Warzoha, R. J., Weigand, R. M., and Fleischer, A. S. (2015). Temperature-dependent thermal properties of a paraffin phase change material embedded with herringbone style graphite nanofibers. *Applied Energy*, 137:716–725.

Wei, G., Wang, G., Xu, C., Ju, X., Xing, L., Du, X., and Yang, Y. (2018). Selection principles and thermophysical properties of high temperature phase change materials for thermal energy storage: A review. *Renewable and Sustainable Energy Reviews*, 81:1771–1786.

Whitney, J. and Delforge, P. (2014). Data center efficiency assessment. *Issue paper on NRDC (The Natural Resource Defense Council)*.

Wi, S., Jeong, S.-G., Chang, S. J., Lee, J., and Kim, S. (2017). Evaluation of energy efficient hybrid hollow plaster panel using phase change material/xGnP composites. *Applied Energy*, 205:1548–1559.

Wick, P., Louw-Gaume, A. E., Kucki, M., Krug, H. F., Kostarelos, K., Fadeel, B., Dawson, K. A., Salvati, A., Vázquez, E., Ballerini, L., Tretiach, M., Benfenati, F., Flahaut, E., Gauthier, L., Prato, M., and Bianco, A. (2014). Classification framework for graphene-based materials. *Angewandte Chemie International Edition*, 53(30):7714–7718.

Wu, S., Yan, T., Kuai, Z., and Pan, W. (2019). Thermal conductivity enhancement on phase change materials for thermal energy storage: A review. *Energy Storage Materials*.

Wu, S., Yan, T., Kuai, Z., and Pan, W. (2020). Thermal conductivity enhancement on phase change materials for thermal energy storage: A review. *Energy Storage Materials*, 25:251–295.

Wu, S., Zhu, D., Li, X., Li, H., and Lei, J. (2009). Thermal energy storage behavior of al2o3–h2o nanofluids. *Thermochimica Acta*, 483(1-2):73–77.

Wu, S., Zhu, D., Zhang, X., and Huang, J. (2010). Preparation and melting/freezing characteristics of cu/paraffin nanofluid as phase-change material (PCM). *Energy & Fuels*, 24(3):1894–1898.

Wu, S. Y., Wang, H., Xiao, S., and Zhu, D. S. (2012). An investigation of melting/freezing characteristics of nanoparticle-enhanced phase change materials. *Journal of Thermal Analysis and Calorimetry*, 110(3):1127–1131.

Wu, W., Bostanci, H., Chow, L., Hong, Y., Wang, C., Su, M., and Kizito, J. (2013). Heat transfer enhancement of PAO in microchannel heat exchanger using nano-encapsulated phase change indium particles. *International Journal of Heat and Mass Transfer*, 58(1-2):348–355.

Wypych, G. (2019). PRODUCTION OF GRAPHENE AND ITS DERIVATIVES. In *Graphene*, pages 9–84. Elsevier.

Xamán, J., Lira, L., and Arce, J. (2009). Analysis of the temperature distribution in a guarded hot plate apparatus for measuring thermal conductivity. *Applied Thermal Engineering*, 29(4):617–623.

Xiao, C., Zhang, G., Li, Z., and Yang, X. (2020). Custom design of solid–solid phase change material with ultra-high thermal stability for battery thermal management. *Journal of Materials Chemistry A*, 8(29):14624–14633.

Xie, H., Wang, J., Xi, T., Liu, Y., Ai, F., and Wu, Q. (2002). Thermal conductivity enhancement of suspensions containing nanosized alumina particles. *Journal of Applied Physics*, 91(7):4568–4572.

Xu, Y., Chung, D., and Mroz, C. (2001). Thermally conducting aluminum nitride polymer-matrix composites. *Composites Part A: Applied Science and Manufacturing*, 32(12):1749–1757.

Xu, Y., Ren, Q., Zheng, Z.-J., and He, Y.-L. (2017). Evaluation and optimization of melting performance for a latent heat thermal energy storage unit partially filled with porous media. *Applied Energy*, 193:84–95.

Xue, L., Keblinski, P., Phillpot, S., Choi, S.-S., and Eastman, J. (2004). Effect of liquid layering at the liquid–solid interface on thermal transport. *International Journal of Heat and Mass Transfer*, 47(19-20):4277–4284.

Yan, T., Wang, R., Li, T., Wang, L., and Fred, I. T. (2015). A review of promising candidate reactions for chemical heat storage. *Renewable and Sustainable Energy Reviews*, 43:13–31.

Yang, D., Shi, S., Xiong, L., Guo, H., Zhang, H., Chen, X., Wang, C., and Chen, X. (2016a). Paraffin/palygorskite composite phase change materials for thermal energy storage. *Solar Energy Materials and Solar Cells*, 144:228–234.

Yang, J., Li, X., Han, S., Zhang, Y., Min, P., Koratkar, N., and Yu, Z.-Z. (2016b). Air-dried, high-density graphene hybrid aerogels for phase change composites with exceptional thermal conductivity and shape stability. *Journal of Materials Chemistry A*, 4(46):18067–18074.

Yang, W., Zhang, L., Guo, Y., Jiang, Z., He, F., Xie, C., Fan, J., Wu, J., and Zhang, K. (2017). Novel segregated-structure phase change materials composed of paraffin@graphene microencapsules with high latent heat and thermal conductivity. *Journal of Materials Science*, 53(4):2566–2575.

Yang, X., Niu, Z., Bai, Q., Li, H., Cui, X., and He, Y.-L. (2019). Experimental study on the solidification process of fluid saturated in fin-foam composites for cold storage. *Applied Thermal Engineering*, 161:114163.

Yang, X., Wang, W., Yang, C., Jin, L., and Lu, T. J. (2016c). Solidification of fluid saturated in open-cell metallic foams with graded morphologies. *International Journal of Heat and Mass Transfer*, 98:60–69.

Yang, Y., Luo, J., Song, G., Liu, Y., and Tang, G. (2014). The experimental exploration of nano-si3n4/paraffin on thermal behavior of phase change materials. *Thermochimica Acta*, 597:101–106.

Yasin, G., Arif, M., Shakeel, M., Dun, Y., Zuo, Y., Khan, W. Q., Tang, Y., Khan, A., and Nadeem, M. (2018). Exploring the nickel-graphene nanocomposite coatings for superior corrosion resistance: Manipulating the effect of deposition current density on its morphology, mechanical properties, and erosion-corrosion performance. *Advanced Engineering Materials*, 20(7):1701166.

Yavari, F., Fard, H. R., Pashayi, K., Rafiee, M. A., Zamiri, A., Yu, Z., Ozisik, R., Borca-Tasciuc, T., and Koratkar, N. (2011). Enhanced thermal conductivity in a nanostructured phase change composite due to low concentration

graphene additives. *The Journal of Physical Chemistry C*, 115(17):8753–8758.

Yeh, L. T. (1995). Review of heat transfer technologies in electronic equipment. *Journal of Electronic Packaging*, 117(4):333–339.

Yu, S., Wang, X., and Wu, D. (2014). Self-assembly synthesis of microencapsulated n-eicosane phase-change materials with crystalline-phase-controllable calcium carbonate shell. *Energy & Fuels*, 28(5):3519–3529.

Yu, W. and Xie, H. (2012). A review on nanofluids: Preparation, stability mechanisms, and applications. *Journal of Nanomaterials*, 2012:1–17.

Yu, Z.-T., Fang, X., Fan, L.-W., Wang, X., Xiao, Y.-Q., Zeng, Y., Xu, X., Hu, Y.-C., and Cen, K.-F. (2013). Increased thermal conductivity of liquid paraffin-based suspensions in the presence of carbon nano-additives of various sizes and shapes. *Carbon*, 53:277–285.

Zabalegui, A., Lokapur, D., and Lee, H. (2014). Nanofluid PCMs for thermal energy storage: Latent heat reduction mechanisms and a numerical study of effective thermal storage performance. *International Journal of Heat and Mass Transfer*, 78:1145–1154.

Zeng, J. L., Cao, Z., Yang, D. W., Sun, L. X., and Zhang, L. (2010). Thermal conductivity enhancement of ag nanowires on an organic phase change material. *Journal of Thermal Analysis and Calorimetry*, 101(1):385–389.

Zeng, J. L., Cao, Z., Yang, D. W., Xu, F., Sun, L. X., Zhang, X. F., and Zhang, L. (2009). Effects of MWNTs on phase change enthalpy and thermal conductivity of a solid-liquid organic PCM. *Journal of Thermal Analysis and Calorimetry*, 95(2):507–512.

Zeng, J.-L., Gan, J., Zhu, F.-R., Yu, S.-B., Xiao, Z.-L., Yan, W.-P., Zhu, L., Liu, Z.-Q., Sun, L.-X., and Cao, Z. (2014). Tetradecanol/expanded graphite composite form-stable phase change material for thermal energy storage. *Solar Energy Materials and Solar Cells*, 127:122–128.

Zeng, J. L., Liu, Y. Y., Cao, Z. X., Zhang, J., Zhang, Z. H., Sun, L. X., and Xu, F. (2007). Thermal conductivity enhancement of MWNTs on the PANI/tetradecanol form-stable PCM. *Journal of Thermal Analysis and Calorimetry*, 91(2):443–446.

Zeng, J. L., Sun, L. X., Xu, F., Tan, Z. C., Zhang, Z. H., Zhang, J., and Zhang, T. (2006). Study of a PCM based energy storage system containing ag nanoparticles. *Journal of Thermal Analysis and Calorimetry*, 87(2):371–375.

Zeng, J.-L., Zhu, F.-R., Yu, S.-B., Zhu, L., Cao, Z., Sun, L.-X., Deng, G.-R., Yan, W.-P., and Zhang, L. (2012). Effects of copper nanowires on the properties of an organic phase change material. *Solar Energy Materials and Solar Cells*, 105:174–178.

Zhang, C., Yu, M., Fan, Y., Zhang, X., Zhao, Y., and Qiu, L. (2020). Numerical study on heat transfer enhancement of PCM using three combined methods based on heat pipe. *Energy*, 195:116809.

Zhang, H., Shao, S., Xu, H., Zou, H., and Tian, C. (2014a). Free cooling of data centers: A review. *Renewable and Sustainable Energy Reviews*, 35:171–182.

Zhang, J.-J., Zhang, J.-L., He, S.-M., Wu, K.-Z., and Liu, X.-D. (2001). Thermal studies on the solid–liquid phase transition in binary systems of fatty acids. *Thermochimica Acta*, 369(1-2):157–160.

Zhang, L., Zhu, J., Zhou, W., Wang, J., and Wang, Y. (2012a). Thermal and electrical conductivity enhancement of graphite nanoplatelets on form-stable polyethylene glycol/polymethyl methacrylate composite phase change materials. *Energy*, 39(1):294–302.

Zhang, N., Yuan, Y., Cao, X., Du, Y., Zhang, Z., and Gui, Y. (2018). Latent heat thermal energy storage systems with solid-liquid phase change materials: A review. *Advanced Engineering Materials*, 20(6):1700753.

Zhang, N., Yuan, Y., Wang, X., Cao, X., Yang, X., and Hu, S. (2013). Preparation and characterization of lauric–myristic–palmitic acid ternary eutectic mixtures/expanded graphite composite phase change material for thermal energy storage. *Chemical Engineering Journal*, 231:214–219.

Zhang, Q., Deng, Y., Hu, Z., Liu, Y., Yao, M., and Liu, P. (2014b). Seaurchin-like hierarchical NiCo2o4@NiMoO4 core–shell nanomaterials for high performance supercapacitors. *Phys. Chem. Chem. Phys.*, 16(42):23451–23460.

Zhang, S., Wu, J.-Y., Tse, C.-T., and Niu, J. (2012b). Effective dispersion of multi-wall carbon nano-tubes in hexadecane through physiochemical modification and decrease of supercooling. *Solar Energy Materials and Solar Cells*, 96:124–130.

Zhang, X. X., Tao, X. M., Yick, K. L., and Fan, Y. F. (2005). Expansion space and thermal stability of microencapsulatedn-octadecane. *Journal of Applied Polymer Science*, 97(1):390–396.

Zhao, D., Qian, X., Gu, X., Jajja, S. A., and Yang, R. (2016). Measurement techniques for thermal conductivity and interfacial thermal conductance of bulk and thin film materials. *Journal of Electronic Packaging*, 138(4).

Zhichao, L., Qiang, Z., and Gaohui, W. (2015). Preparation and enhanced heat capacity of nano-titania doped erythritol as phase change material. *International Journal of Heat and Mass Transfer*, 80:653–659.

Zhong, Y., Zhou, M., Huang, F., Lin, T., and Wan, D. (2013). Effect of graphene aerogel on thermal behavior of phase change materials for thermal management. *Solar Energy Materials and Solar Cells*, 113:195–200.

Zhou, D., Zhao, C., and Tian, Y. (2012). Review on thermal energy storage with phase change materials (PCMs) in building applications. *Applied Energy*, 92:593–605.

Zhu, F., Zhang, C., and Gong, X. (2016). Numerical analysis and comparison of the thermal performance enhancement methods for metal foam/phase change material composite. *Applied Thermal Engineering*, 109:373–383.

Zhu, Z.-Q., Huang, Y.-K., Hu, N., Zeng, Y., and Fan, L.-W. (2018). Transient performance of a PCM-based heat sink with a partially filled metal foam: Effects of the filling height ratio. *Applied Thermal Engineering*, 128:966–972.

Zielińska, A., Carreiró, F., Oliveira, A. M., Neves, A., Pires, B., Venkatesh, D. N., Durazzo, A., Lucarini, M., Eder, P., Silva, A. M., Santini, A., and Souto, E. B. (2020). Polymeric nanoparticles: Production, characterization, toxicology and ecotoxicology. *Molecules*, 25(16):3731.

Zou, D., Ma, X., Liu, X., Zheng, P., and Hu, Y. (2018). Thermal performance enhancement of composite phase change materials (PCM) using graphene and carbon nanotubes as additives for the potential application in lithium-ion power battery. *International Journal of Heat and Mass Transfer*, 120:33–41.

# Appendix A

# List of Abbreviations

| | |
|---|---|
| AlN | Aluminium Nitride |
| Al | Aluminium |
| Au | Gold |
| Ag | Silver |
| $Al_2O_3$ | Aluminium Oxide |
| C | Carbon |
| Cu | Copper |
| CNTs | Carbon Nanotubes |
| CTAB | Cetyl Trimethyl Ammonium Bromide |
| CF | Carbon Foam |
| CDs | Carbon Dots |
| CuO | Copper(II) oxide |
| CES | Chemical Energy Storage |
| CRHS | Chemical Reaction Heat Storage |
| CSHS | Chemical Sorption Heat Storage |
| CA | Caprylic Acid |
| DTG | Derivative thermogravimetry |
| DSC | Differential Scanning Calorimeter |
| DTAB | Dodecyl Trimethyl Ammonium Bromide |
| DVLO | Derjaguin, Verway, Landau, and Overbeek |
| ESEM | Environmental Scanning electron microscopy |
| EDX | Energy-dispersive X-ray spectroscopy |
| EDX | Energy-dispersive X-ray spectroscopy |
| EG | Expanded Graphite |
| FT-IR | Fourier-transform infrared spectroscopy |
| GE | Graphene |
| GT | Graphite |
| GO | Graphene Oxide |
| GNPs | Graphene nanoplatelets |
| GA | Gum Arabic |
| GQDs | Graphene Quantum Dots |
| HOPG | Highly Oriented Pyrolytic Graphite |
| HCTAB | Hexadecyl Trimethyl Ammonium Bromide |
| IPCMs | Inorganic Phase Change Materials |
| ICs | Integrated Circuits |
| IRT | Infrared Thermography |

| | |
|---|---|
| $k$ | Thermal conductivity ($W/m.K$) |
| LHTES | Latent–Heat Thermal Energy Storage |
| LHSMs | latent Heat Storage Materials |
| LHS | Latent Heat Storage |
| MA | Myristic Acid |
| NCPCMs | Nanocomposite Phase Change Materials |
| NPs | Nanoparticles |
| NMs | Nanomaterials |
| OPCMs | Organic Phase Change Materials |
| PEGs | Polyethylene Glycols |
| PEO | Polyethylene Oxide |
| PPO | Polypropylene Oxide |
| PTHF | Polytetrahydrofuran |
| PCMs | Phase Change Materials |
| PVP | Poly Vinyl Pyrrolidine |
| PA | Palmatic Acid |
| SWCNTs | Single–Walled Carbon Nanotubes |
| SDS | Sodium Dodecyl Sulphate |
| SDBS | Sodium Dodecyl Benzene Sulfonate |
| SSL | Sodium Stearoyl Lactylate |
| SOCT | Sodium Octanoate |
| SC | Sodium Cholate |
| STC | Sodium Taurodeoxy Cholate |
| SWCNTs | Single–Walled Carbon Nanotubes |
| SiC | Silicon carbide |
| SHS | Sensible Heat Storage |
| SA | Stearic Acid |
| TM | Thermal Management |
| TMT | Thermal Management Technology |
| TCMs | Thermal Conductivity Materials |
| TGA | Thermogravimetric analysis |
| TCA | Thermal Conductivity Analyser |
| TA | Tannic Acid |
| $TiO_2$ | Titanium Dioxide |
| TES | Thermal Energy Storage |
| TD | Tetradecanol |
| XRD | X-ray diffraction |
| 0D | Zero-dimensional |
| 1D | One-dimensional |
| 2D | Two-dimensional |
| 3D | Three-dimensional |

# Appendix B

# List of Paraffins

Table B.1: *Thermophysical properties of paraffins.*

| **Name** | **Chemical Formula** | $T_m$ (°C) | $H$ $(kJ/kg)$ | $k$ $(W/mK)$ | $\rho$ $(kg/m^3)$ | $c_p$ $(kJ/kg)$ | **Ref. No.** |
|---|---|---|---|---|---|---|---|
| $n$-Dodecane | $C_{12}H_{26}$ | -12 | 216 | 0.12(s), 0.21(l) | 750 | – | (Sharma et al., 2004; Cabeza et al., 2011) |
| $n$-Tridecane | $C_{13}H_{28}$ | -6 | – | – | 756 | – | (Sharma et al., 2009, 2004; Cabeza et al., 2011) |
| $n$-Tetradecane | $C_{14}H_{30}$ | 4.5–5.6 | 231 | – | 771 | – | (Sharma et al., 2009, 2004; Cabeza et al., 2011) |
| $n$-Pentadecane | $C_{15}H_{32}$ | 10 | 207 | 0.17 | 768 | – | (Sharma et al., 2009; Cabeza et al., 2011) |
| $n$-Hexadecane | $C_{16}H_{34}$ | 18.2 | 238 | 0.21(s) | 774 | – | (Sharma et al., 2009; Cabeza et al., 2011; Nagano et al., 2003) |
| $n$-Heptadecane | $C_{17}H_{36}$ | 22 | 215 | – | 778 | – | (Sharma et al., 2009; Cabeza et al., 2011; Nagano et al., 2003) |
| $n$-Octadecane | $C_{18}H_{38}$ | 28.2 | 245 | 0.35(s), 0.15(l) | 814(s), 775(l) | 2.14(s), 2.66(l) | (Sharma et al., 2009; Cabeza et al., 2011; Nagano et al., 2003) |
| $n$-Nonadecane | $C_{19}H_{40}$ | 31.9 | 222 | 0.21(s) | 912(s), 769(l) | – | (Paris et al., 1993; Sharma et al., 2015) |
| $n$-eicosane | $C_{20}H_{42}$ | 36.5 | 247 | 0.212(s), 0.160(l) | 820(s), 780(l) | 1.9(s), 2.2(l) | (Arshad et al., 2018a; Ali and Arshad, 2017) |
| $n$-Heneicosane | $C_{21}H_{44}$ | 41 | 215 | – | – | – | (Sharma et al., 2009; Cabeza et al., 2011; Paris et al., 1993) |
| $n$-Docosane | $C_{22}H_{46}$ | 44 | 249 | – | – | – | (Sharma et al., 2009; Cabeza et al., 2011; Paris et al., 1993) |
| $n$-Tricosane | $C_{23}H_{48}$ | 47 | 234 | – | – | – | (Sharma et al., 2009; Cabeza et al., 2011; Paris et al., 1993) |
| $n$-Tetracosane | $C_{24}H_{50}$ | 51 | 255 | – | – | – | (Sharma et al., 2009; Cabeza et al., 2011; Paris et al., 1993) |
| $n$-Pentacosane | $C_{25}H_{52}$ | 54 | 238 | – | – | – | (Sharma et al., 2009; Cabeza et al., 2011) |
| $n$-Pentacosane | $C_{25}H_{52}$ | 54 | 238 | – | – | – | (Sharma et al., 2009; Cabeza et al., 2011; Paris et al., 1993) |

| | | | | | | | |
|---|---|---|---|---|---|---|---|
| $n$-Hexacosane | $C_{26}H_{54}$ | 56 | 257 | 0.21(s) | 770 | – | (Sharma et al., 2009, 2004; Cabeza et al., 2011; Paris et al., 1993) |
| $n$-Heptacosane | $C_{27}H_{56}$ | 59 | 236 | – | 773 | – | (Sharma et al., 2009; Cabeza et al., 2011; Paris et al., 1993) |
| $n$-Octacosane | $C_{28}H_{58}$ | 61 | 255 | – | 910(s), 765(l) | – | (Sharma et al., 2009; Cabeza et al., 2011; Paris et al., 1993) |
| $n$-Nonacosane | $C_{29}H_{60}$ | 64 | 240 | – | – | – | (Sharma et al., 2009; Cabeza et al., 2011; Paris et al., 1993) |
| $n$-Triacontane | $C_{30}H_{62}$ | 65 | 252 | – | – | – | (Sharma et al., 2009; Cabeza et al., 2011; Paris et al., 1993) |
| $n$-Hentriacontane | $C_{31}H_{64}$ | 68 | 242 | – | 930(s), 830(l) | – | (Sharma et al., 2009; Cabeza et al., 2011) |
| $n$-Dotricontane | $C_{32}H_{66}$ | 70 | 170 | – | – | – | (Sharma et al., 2009; Cabeza et al., 2011) |
| $n$-Tritricontane | $C_{33}H_{68}$ | 71 | 189 | – | – | – | (Sharma et al., 2009; Cabeza et al., 2011; Paris et al., 1993) |
| $n$-Tetratritricontane | $C_{34}H_{70}$ | 75.9 | 269 | – | 772.8(s) | – | (Sharma et al., 2009; Cabeza et al., 2011; Paris et al., 1993) |

# Appendix C

# List of Fatty acids

Table C.1: *Thermo-physical properties of fatty acids.*

| **Name** | **Chemical Formula** | $T_m$ (°C) | $H$ $(kJ/kg)$ | $k$ $(W/mK)$ | $\rho$ $(kg/m^3)$ | $c_p$ $(kJ/kg)$ | **Ref. No.** |
|---|---|---|---|---|---|---|---|
| Acetic acid | $C_2H_4O_2$ | 16.7 | 184 | – | – | – | (Abhat, 1983; Rozanna et al., 2005) |
| Caprylic acid | $C_8H_{16}O_2$ | 16.3 | 148.5 | 0.149(l) | 862(l) | – | (Abhat, 1983; Rozanna et al., 2005) |
| Capric acid (CA) | $C_{10}H_{20}O_2$ | 31.5 | 153 | 0.149(l) | 886(l) | – | (Abhat, 1983; Rozanna et al., 2005) |
| Undecylenic acid | $C_{11}H_{20}O_2$ | 24.6 | 141 | – | – | – | (Rozanna et al., 2005; Schlenk, 1961) |
| Undecylic acid | $C_{11}H_{22}O_2$ | 28.4 | 139 | – | – | – | (Solé et al., 2014) |
| Lauric acid (LA) | $C_{12}H_{24}O_2$ | 42–44 | 178 | 0.147(l) | 870(l) | 1.6 | (Rozanna et al., 2005; Abhat, 1983) |
| Myristic acid (MA) | $C_{14}H_{28}O_2$ | 51.5–53.6 | 190–204.5 | – | 844(l) | 1.6(s) | (Abhat, 1983; Rozanna et al., 2005) |
| Pentadecanoic acid | $C_{15}H_{30}O_2$ | 52.5 | 178 | – | – | – | (Sharma et al., 2009) |
| Palmitic acid (PA) | $C_{16}H_{32}O_2$ | 61–63 | 187–203.4 | 0.159–0.165(l) | 847–874(l) | – | (Abhat, 1983; Rozanna et al., 2005) |
| Stearic acid (SA) | $C_{18}H_{36}O_2$ | 70 | 203 | 0.172(l) | 941(l) | 2.35(l) | (Abhat, 1983; Rozanna et al., 2005) |
| Elaidic acid (EA) | $C_{18}H_{34}O_2$ | 47 | 218 | – | 851(l) | – | (Sharma et al., 2014) |
| Arachidic acid | $C_{20}H_{40}O_2$ | 74 | 227 | – | – | – | (Rozanna et al., 2005) |
| Acetamide acid | $C_2H_5NO$ | 81 | 241 | – | – | – | (Sharma et al., 2014) |
| Methyl fumarate | $C_5H_5O_4^-$ | 102 | 242 | – | 1045 | – | (Su et al., 2015; Bailey, 1945) |
| Tristearin | $C_{57}H_{110}O_6$ | 54.5 | 191 | – | – | – | (Su et al., 2015; Bailey, 1945) |

# Appendix D

# List of Poly(ethylene glycol)s

Table D.1: *Thermo-physical properties of PEGs.*

| **Polymer** | $T_m$ **(°C)** | $H$ $(kJ/kg)$ | **Ref. No.** |
|---|---|---|---|
| PEG 400 | 4.2 | 117.6 | (Pielichowska and Pielichowski, 2014) |
| PEG 600 | 12.5 | 129.1 | (Nagano et al., 2003) |
| PEG 1000 | 40 | 168.6 | (Pielichowski and Flejtuch, 2002, 2003b) |
| PEG 3400 | 63.4 | 166.8 | (Pielichowski and Flejtuch, 2002, 2003b) |
| PEG 10000 | 65.9 | 171.6 | (Pielichowski and Flejtuch, 2002, 2003b) |
| PEG 20000 | 67.7 | 160.2 | (Pielichowski and Flejtuch, 2002, 2003b) |
| PEG 35000 | 68.7 | 166.9 | (Pielichowski and Flejtuch, 2002, 2003b) |
| PEG 100000 | 67 | 175.8 | (Pielichowski and Flejtuch, 2002; Pielichowska and Pielichowski, 2014) |
| PEG 1000000 | 70 | 174 | (Pielichowski and Flejtuch, 2002; Pielichowska and Pielichowski, 2014) |

# Appendix E

# List of Salt and Salt hydrates

Table E.1: *Thermo-physical properties of salt hydrates.*

| Name | Chemical Formula | $T_m$ (°C) | $H$ $(kJ/kg)$ | $k$ $(W/mK)$ | $\rho$ $(kg/m^3)$ | $c_p$ $(kJ/kg)$ | Ref. No. |
|---|---|---|---|---|---|---|---|
| Lithium chlorate trihydrate | $LiClO_3.3H_2O$ | 8 | 253 | – | 1720(s), 1530(l) | – | (Sharma et al., 2009; da Cunha and Eames, 2016; Pielichowska and Pielichowski, 2014; Su et al., 2015) |
| Zinc chloride trihydrate | $ZnCl_2.3H_2O$ | 10 | – | – | – | – | (Sharma et al., 2009; da Cunha and Eames, 2016; Pielichowska and Pielichowski, 2014; Su et al., 2015) |
| Ammonium chloride Sodium sulphate decahydrate | $NH_4Cl.Na_2SO_4.10H_2O$ | 13 | 163 | – | – | – | (Sharma et al., 2009; da Cunha and Eames, 2016; Pielichowska and Pielichowski, 2014; Su et al., 2015) |
| Dipotassium hydrogen phosphate hexahydrate | $K_2HPO_4.6H_2O$ | 14 | 109 | – | – | – | (Sharma et al., 2009; da Cunha and Eames, 2016; Pielichowska and Pielichowski, 2014; Su et al., 2015) |
| Sodium chloride Sodium sulphate decahydrate | $NaCl.Na_2SO_4.10H_2O$ | 18 | 286 | – | – | – | (Sharma et al., 2009; da Cunha and Eames, 2016; Pielichowska and Pielichowski, 2014; Su et al., 2015) |
| Potassium uoride tetrahydrate | $KF.4H_2O$ | 18 | 330 | – | – | – | |
| Dipotassium hydrogen phosphate tetrahydrate | $K_2HPO_4.4H_2O$ | 18.5 | 231 | – | 1447(l), 1480(s) | 1.84(s), 2.39(l) | (Sharma et al., 2009; da Cunha and Eames, 2016; Pielichowska and Pielichowski, 2014; Su et al., 2015) |
| Iron bromide hexahydrate | $FeBr_3.6H_2O$ | 21 | 105 | – | – | – | (Sharma et al., 2009; da Cunha and Eames, 2016; Pielichowska and Pielichowski, 2014; Su et al., 2015) |
| Manganese nitrate hexahydrate | $Mn(NO_3)_2.6H_2O$ | 25.5 | 125.9148 | – | 1738(s), 1728(l) | – | (Sharma et al., 2009; da Cunha and Eames, 2016; Pielichowska and Pielichowski, 2014; Su et al., 2015) |
| Lithium metaborate octahydrate | $LiBO_28H_2O$ | 25.7 | 289 | – | – | – | (Sharma et al., 2009; da Cunha and Eames, 2016; Pielichowska and Pielichowski, 2014; Su et al., 2015) |

| | | | | | | | |
|---|---|---|---|---|---|---|---|
| Calcium chloride hexahydrate | $CaCl_26H_2O$ | 2930 | 170192 | 1.008(s), 0.561(l) | 1802(s), 1562(l) | – | |
| Calcium chloride dodecahydrate | $CaCl_212H_2O$ | 29.8 | 174 | 1.09(s), 0.53(l) | 1710(s), 1530(s) | 1.4(s), 2.2(l) | (Sharma et al., 2009; da Cunha and Eames, 2016; Pielichowska and Pielichowski, 2014; Su et al., 2015) |
| Lithium nitrate trihydrate | $LiNO_33H_2O$ | 30 | 189296 | – | – | – | (Sharma et al., 2009; da Cunha and Eames, 2016; Pielichowska and Pielichowski, 2014; Su et al., 2015) |
| Lithium nitrate dihydrate | $LiNO_32H_3O$ | 30 | 296 | – | – | – | |
| Sodium sulphate decahydrate | $Na_2SO_410H2O$ | 32 | 251254 | 0.544 | 485(s) | 2 | (Sharma et al., 2009; da Cunha and Eames, 2016; Pielichowska and Pielichowski, 2014; Su et al., 2015) |
| Sodium carbonate decahydrate | $Na_2CO_310H_2O$ | 32 | 267 | 0.514(s), 0.224(l) | 830 | 1.92(s), 3.26(l) | (Sharma et al., 2009; da Cunha and Eames, 2016; Pielichowska and Pielichowski, 2014; Su et al., 2015) |
| Iron potassium alum | $KFe(SO_4)_212H_2O$ | 33 | 173 | – | – | – | (Sharma et al., 2009; da Cunha and Eames, 2016; Pielichowska and Pielichowski, 2014; Su et al., 2015) |
| Calcium bromide hexahydrate | $CaBr_26H_2O$ | 34 | 115138 | – | 2194(s), 1956(l) | – | (Sharma et al., 2009; da Cunha and Eames, 2016; Pielichowska and Pielichowski, 2014; Su et al., 2015) |
| Lithium bromide dihydrate | $LiBr2H_2O$ | 34 | 124 | – | – | – | |
| Dipotassium hydrogen phosphate dodecahydrate | $Na_2HPO_412H_2O$ | 3540 | 256281 | – | 1522 | – | (Sharma et al., 2009; da Cunha and Eames, 2016; Pielichowska and Pielichowski, 2014; Su et al., 2015) |
| Zinc nitrate hexahydrate | $Zn(NO_3)26H_2O$ | 36 | 134147 | 0.464 | 1937(s), 1828(l) | – | (Sharma et al., 2009; da Cunha and Eames, 2016; Pielichowska and Pielichowski, 2014; Su et al., 2015) |
| Manganese nitrate tetrahydrate | $Mn(NO_3)_24H_2O$ | 37 | 115 | – | – | – | (Sharma et al., 2009; da Cunha and Eames, 2016; Pielichowska and Pielichowski, 2014; Su et al., 2015) |
| Iron chloride hexahydrate | $FeCl_36H_2O$ | 37 | 223 | – | – | – | (Sharma et al., 2009; da Cunha and Eames, 2016; Pielichowska and Pielichowski, 2014; Su et al., 2015) |
| Calcium chloride tetrahydrate | $CaCl_24H_2O$ | 39 | 158 | – | – | – | (Sharma et al., 2009; da Cunha and Eames, 2016; Pielichowska and Pielichowski, 2014; Su et al., 2015) |
| Copper sulphate heptahydrate | $CuSO_47H_2O$ | 40.7 | 171 | – | – | – | (Sharma et al., 2009; da Cunha and Eames, 2016; Pielichowska and Pielichowski, 2014; Su et al., 2015) |
| Potassium uoride dihydrate | $KF2H_2O$ | 42.0 | 162266 | – | – | – | (Sharma et al., 2009; da Cunha and Eames, 2016; Pielichowska and Pielichowski, 2014; Su et al., 2015) |

| | | | | | | | |
|---|---|---|---|---|---|---|---|
| Magnesium iodide octahydrate | $MgI_28H_2O$ | 42 | 133 | – | – | – | (Sharma et al., 2009; da Cunha and Eames, 2016; Pielichowska and Pielichowski, 2014; Su et al., 2015) |
| Calcium iodide hexahydrate | $CaI_26H_2O$ | 42 | 162 | – | – | – | (Sharma et al., 2009; da Cunha and Eames, 2016; Pielichowska and Pielichowski, 2014; Su et al., 2015) |
| Calcium nitrate tetrahydrate | $Ca(NO_3)_24H_2O$ | 4347 | 106140 | – | – | – | (Sharma et al., 2009; da Cunha and Eames, 2016; Pielichowska and Pielichowski, 2014; Su et al., 2015) |
| Zinc nitrate tetrahydrate | $Zn(NO_3)_24H2O$ | 45 | 110 | – | – | – | (Sharma et al., 2009; da Cunha and Eames, 2016; Pielichowska and Pielichowski, 2014; Su et al., 2015) |
| Tripotassium phosphate tribasic heptahydrate | $K_3PO_47H_2O$ | 45 | 145 | – | – | – | (Sharma et al., 2009; da Cunha and Eames, 2016; Pielichowska and Pielichowski, 2014; Su et al., 2015) |
| Dipotassium hydrogen phosphate heptahydrate | $K_2HPO_47H_2O$ | 45 | 145 | – | – | – | (Sharma et al., 2009; da Cunha and Eames, 2016; Pielichowska and Pielichowski, 2014; Su et al., 2015) |
| Iron nitrate nonahydrate | $Fe(NO_3)_39H_2O$ | 47 | 155-190 | – | – | – | (Sharma et al., 2009; da Cunha and Eames, 2016; Pielichowska and Pielichowski, 2014; Su et al., 2015) |
| Magnesium nitrate tetrahydrate | $Mg(NO_3)_24H_2O$ | 47 | 142 | – | – | – | (Sharma et al., 2009; da Cunha and Eames, 2016; Pielichowska and Pielichowski, 2014; Su et al., 2015) |
| Sodium sulphite pentahydrate | $Na_2SiO_35H_2O$ | 48 | 168 | – | – | – | (Sharma et al., 2009; da Cunha and Eames, 2016; Pielichowska and Pielichowski, 2014; Su et al., 2015) |
| Sodium sulphite tetrahydrate | $Na_2SiO_34H_2O$ | 48 | 168 | – | – | – | (Sharma et al., 2009; da Cunha and Eames, 2016; Pielichowska and Pielichowski, 2014; Su et al., 2015) |
| Dipotassium hydrogen phosphate heptahydrate | $Na_2HPO_47H_2O$ | 48 | 135-170 | – | – | – | (Sharma et al., 2009; da Cunha and Eames, 2016; Pielichowska and Pielichowski, 2014; Su et al., 2015) |
| Sodium thiosulfate pentahydrate | $Na_2S_2O_35H2O$ | 48 | 209 | – | 1600 | – | (Sharma et al., 2009; da Cunha and Eames, 2016; Pielichowska and Pielichowski, 2014; Su et al., 2015) |
| Dipotassium hydrogen phosphate trihydrate | $K_2HPO_43H_2O$ | 48.5 | 202 | – | – | – | (Sharma et al., 2009; da Cunha and Eames, 2016; Pielichowska and Pielichowski, 2014; Su et al., 2015) |
| Magnesium sulphate heptahydrate | $MgSO_47H_2O$ | 51 | 104 | – | – | – | (Sharma et al., 2009; da Cunha and Eames, 2016; Pielichowska and Pielichowski, 2014; Su et al., 2015) |

| | | | | | | | |
|---|---|---|---|---|---|---|---|
| Calcium nitrate trihydrate | $Ca(NO_3)_23H_2O$ | 53 | 158 | – | – | – | (Sharma et al., 2009; da Cunha and Eames, 2016; Pielichowska and Pielichowski, 2014; Su et al., 2015) |
| Sodium nitrate hexahydrate | $Na(NO_3)_26H_2O$ | 55 | 68 | – | – | – | (Sharma et al., 2009; da Cunha and Eames, 2016; Pielichowska and Pielichowski, 2014; Su et al., 2015) |
| Zinc nitrate dihydrate | $Zn(NO_3)_22H_2O$ | 56 | 90 | – | – | – | (Sharma et al., 2009; da Cunha and Eames, 2016; Pielichowska and Pielichowski, 2014; Su et al., 2015) |
| Iron chloride dihydrate | $FeCl_32H_2O$ | 57 | 115 | – | – | – | (Sharma et al., 2009; da Cunha and Eames, 2016; Pielichowska and Pielichowski, 2014; Su et al., 2015) |
| Cobaltous nitrate hexahydrate | $Co(NO_3)_26H_2O$ | 57 | 169 | – | – | – | (Sharma et al., 2009; da Cunha and Eames, 2016; Pielichowska and Pielichowski, 2014; Su et al., 2015) |
| Nick nitrate hexahydrate | $Ni(NO_3)_26H_2O$ | 58 | 151 | – | – | – | (Sharma et al., 2009; da Cunha and Eames, 2016; Pielichowska and Pielichowski, 2014; Su et al., 2015) |
| Manganese chloride tetrahydrate | $MnCl_24H_2O$ | 58 | 270-290 | – | – | – | (Sharma et al., 2009; da Cunha and Eames, 2016; Pielichowska and Pielichowski, 2014; Su et al., 2015) |
| Sodium acetate trihydrate | $CH_3COONa3H_2O$ | 58 | 251-377 | – | – | 1450 | (Sharma et al., 2009; da Cunha and Eames, 2016; Pielichowska and Pielichowski, 2014; Su et al., 2015) |
| Lithium acetate dihydrate | $LiC_2H_3O_22H_2O$ | 58 | 178 | – | – | – | (Sharma et al., 2009; da Cunha and Eames, 2016; Pielichowska and Pielichowski, 2014; Su et al., 2015) |
| Magnesium chloride tetrahydrate | $MgCl_24H_2O$ | 58 | 272 | – | – | – | (Sharma et al., 2009; da Cunha and Eames, 2016; Pielichowska and Pielichowski, 2014; Su et al., 2015) |
| Sodium hydroxide monohydrate | $NaOHH_2O$ | 59 | 98 | – | – | – | (Sharma et al., 2009; da Cunha and Eames, 2016; Pielichowska and Pielichowski, 2014; Su et al., 2015) |
| Cadmium nitrate tetrahydrate | $Cd(NO_3)_24H_2O$ | 59.5 | 107 | – | – | – | (Sharma et al., 2009; da Cunha and Eames, 2016; Pielichowska and Pielichowski, 2014; Su et al., 2015) |
| Cadmium nitrate monohydrate | $Cd(NO_3)_21H_2O$ | 60.5 | 126 | – | – | – | (Sharma et al., 2009; da Cunha and Eames, 2016; Pielichowska and Pielichowski, 2014; Su et al., 2015) |
| Iron nitrate hexahydrate | $Fe(NO_3)_26H_2O$ | 61 | 181 | – | – | – | (Sharma et al., 2009; da Cunha and Eames, 2016; Pielichowska and Pielichowski, 2014; Su et al., 2015) |

| | | | | | | | |
|---|---|---|---|---|---|---|---|
| Sodium aluminium sulphate dodecahydrate | $NaAl(SO_4)_212H_2O$ | 61 | 181 | – | – | – | (Sharma et al., 2009; da Cunha and Eames, 2016; Pielichowska and Pielichowski, 2014; Su et al., 2015) |
| Sodium aluminium sulphate decahydrate | $NaAl(SO_4)_210H_2O$ | 64 | 200 | – | – | – | (Sharma et al., 2009; da Cunha and Eames, 2016; Pielichowska and Pielichowski, 2014; Su et al., 2015) |
| Ferrous sulphate heptahydrate | $FeSO_47H_2O$ | 65 | 190 | – | – | – | (Sharma et al., 2009; da Cunha and Eames, 2016; Pielichowska and Pielichowski, 2014; Su et al., 2015) |
| Sodium phosphate dodecahydrate | $Na_3PO_412H_2O$ | 68 | – | – | – | – | |
| Sodium borate decahydrate | $Na_2B_4O_710H_2O$ | 70 | 150-251 | – | – | – | (Sharma et al., 2009; da Cunha and Eames, 2016; Pielichowska and Pielichowski, 2014; Su et al., 2015) |
| Lithium ethanoate dihydrate | $LiCH_3COO2H_2O$ | 70 | 186-230 | – | – | – | (Sharma et al., 2009; da Cunha and Eames, 2016; Pielichowska and Pielichowski, 2014; Su et al., 2015) |
| Sodium polyphosphate decahydrate | $Na_2P_2O_710H_2O$ | 70 | 186-230 | – | – | – | (Sharma et al., 2009; da Cunha and Eames, 2016; Pielichowska and Pielichowski, 2014; Su et al., 2015) |
| Aluminium nitrate nonahydrate | $Al(NO_3)_29H_2O$ | 72 | 155-176 | – | – | – | (Sharma et al., 2009; da Cunha and Eames, 2016; Pielichowska and Pielichowski, 2014; Su et al., 2015) |
| Barium hydroxide octahydrate | $Ba(OH)_28H_2O$ | 78 | 265-280 | – | – | – | (Sharma et al., 2009; da Cunha and Eames, 2016; Pielichowska and Pielichowski, 2014; Su et al., 2015) |
| Aluminium sulphate 18-hydrate | $Al_2(SO_4)_318H_2O$ | 88 | 218 | – | – | – | (Sharma et al., 2009; da Cunha and Eames, 2016; Pielichowska and Pielichowski, 2014; Su et al., 2015) |
| Strontium hydroxide octahydrate | $Sr(OH)_28H_2O$ | 89 | 370 | – | – | – | (Sharma et al., 2009; da Cunha and Eames, 2016; Pielichowska and Pielichowski, 2014; Su et al., 2015) |
| Magnesium nitrate hexahydrate | $Mg(NO_3)_26H_2O$ | 89.9 | 167 | 0.490(l) , 0.611(s) | 1550(l) , 1636(s) | – | (Sharma et al., 2009; da Cunha and Eames, 2016; Pielichowska and Pielichowski, 2014; Su et al., 2015) |
| Aluminium potassium sulphate dodecahydrate | $KAl(SO_4)_212H_2O$ | 91 | 184 | – | – | – | (Sharma et al., 2009; da Cunha and Eames, 2016; Pielichowska and Pielichowski, 2014; Su et al., 2015) |
| Ammonium alum | $(NH_4)Al(SO_4)6H_2O$ | 95 | 269 | – | – | – | (Sharma et al., 2009; da Cunha and Eames, 2016; Pielichowska and Pielichowski, 2014; Su et al., 2015) |

| | | | | | | | |
|---|---|---|---|---|---|---|---|
| Lithium chloride monohydrate | $LiClH_2O$ | 99 | 212 | – | – | – | (Sharma et al., 2009; da Cunha and Eames, 2016; Pielichowska and Pielichowski, 2014; Su et al., 2015) |
| Calcium bromide tetrahydrate | $CaBr_24H_2O$ | 110 | – | – | – | – | (Sharma et al., 2009; da Cunha and Eames, 2016; Pielichowska and Pielichowski, 2014; Su et al., 2015) |
| Aluminium sulphate 16-hydrate | $Al_2(SO_4)_216H_2O$ | 112 | – | – | – | – | (Sharma et al., 2009; da Cunha and Eames, 2016; Pielichowska and Pielichowski, 2014; Su et al., 2015) |
| Magnesium chloride hexahydrate | $MgCl_26H_2O$ | 117 | 167 | 0.570(l) , 0.704(s) | 1450(l) , 1570(s) | 2.61(l), 2.25(s) | (Sharma et al., 2009; da Cunha and Eames, 2016; Pielichowska and Pielichowski, 2014; Su et al., 2015) |

# Appendix F

# List of Metallics

Table F.1: *Thermo-physical properties of metallics PCMs.*

| **Name** | **Chemical Formula** | $T_m$ (°C) | $H$ $(kJ/kg)$ | $k$ $(W/mK)$ | $\rho$ $(kg/m^3)$ | $c_p$ $(kJ/kg)$ | **Ref. No.** |
|---|---|---|---|---|---|---|---|
| Mercury | $Hg$ | -38.87 | 11.4 | 8.34 | 13546 | 0.139 | (Sharma et al., 2009; Su et al., 2015; Ge et al., 2013) |
| Cesium | $Cs$ | 28.65 | 16.4 | 17.4 | 1796 | 0.236 | (Sharma et al., 2009; Su et al., 2015; Ge et al., 2013) |
| Gallium-gallium antimony | $Ga - GaSb^{+3}$ | 29.8 | – | – | – | – | (Sharma et al., 2009; Su et al., 2015; Ge et al., 2013) |
| Gallium | $Ga$ | 30 | 80.3 | 29.4 | 5907 | 0.37 | (Sharma et al., 2009; Su et al., 2015; Ge et al., 2013) |
| Rubidium | $Rb$ | 38.85 | 25.74 | 29.3 | 1470 | 0.363 | (Sharma et al., 2009; Su et al., 2015; Ge et al., 2013) |
| Bismuth-lead-indium-tin-cadmium | $Bi_{44.7}$ $Pb_{22.6}$ $In_{19.1}$ $Sn_{8.3}$ $Cd_{5.3}$ | 47 | 36.8 | 15 | 9160 | 0.197 | (Sharma et al., 2009; Su et al., 2015; Ge et al., 2013) |
| Bismuth-indium-lead-tin | $Bi_{49}$ $In_{21}$ $Pb_{18}$ $Sn_{12}$ | 58 | 28.9 | 10 | 9010 | 0.201 | (Sharma et al., 2009; Su et al., 2015; Ge et al., 2013) |
| Cerrolow | – | 58 | 90.9 | – | – | – | (Sharma et al., 2009; Su et al., 2015; Ge et al., 2013) |
| Potassium | $K$ | 63.2 | 59.59 | 54 | 664 | 0.78 | (Sharma et al., 2009; Su et al., 2015; Ge et al., 2013) |
| Cerrobend | – | 70 | 32.6 | – | – | – | (Sharma et al., 2009; Su et al., 2015; Ge et al., 2013) |
| Bismuth-lead-tin-cadmium | $Bi_{50}$ $Pb_{30}$ $Sn_{13.3}$ $Cd_{10}$ | 70 | 39.8 | 18 | 9580 | 0.184 | (Sharma et al., 2009; Su et al., 2015; Ge et al., 2013) |
| Bismuth-lead-indium | $Bi - Pb - In$ | 70 | 29 | – | – | – | (Sharma et al., 2009; Su et al., 2015; Ge et al., 2013) |
| Bismuth-indium | $Bi - In$ | 72 | 25 | – | – | – | (Sharma et al., 2009; Su et al., 2015; Ge et al., 2013) |
| Bismuth-lead-tin | $Bi_{52}$ $Pb_{30}$ $Sn_{18}$ | 96 | 34.7 | 24 | 9600 | 0.167 | (Sharma et al., 2009; Su et al., 2015; Ge et al., 2013) |
| Bismuth-lead-tin | $Bi - Pb - Sn$ | 96 | – | – | – | – | (Sharma et al., 2009; Su et al., 2015; Ge et al., 2013) |
| Sodium | $Na$ | 97.8 | – | – | – | – | (Sharma et al., 2009; Su et al., 2015; Ge et al., 2013) |

| | | | | | | | |
|---|---|---|---|---|---|---|---|
| Bismuth-lead | $Bi - Pb$ | 125 | – | – | – | – | (Sharma et al., 2009; Su et al., 2015; Ge et al., 2013) |
| Bismuth-tin | $Bi_{58}Sn_{42}$ | 138 | 44.8 | 19 | 8560 | 0.201 | (Sharma et al., 2009; Su et al., 2015; Ge et al., 2013) |
| Indium | $In$ | 156.8 | 28.59 | 36.4 | 7030 | 0.23 | (Sharma et al., 2009; Su et al., 2015; Ge et al., 2013) |
| Lithium | $Li$ | 186 | 433.78 | 41.3 | 515 | 4.389 | (Sharma et al., 2009; Su et al., 2015; Ge et al., 2013) |
| Tin-zinc | $Sn_{91}Zn_9$ | 199 | 32.5 | 61 | 7270 | 0.272 | (Sharma et al., 2009; Su et al., 2015; Ge et al., 2013) |
| Tin | $Sn$ | 232 | 60.5 | 15.08 | 730 | 0.221 | (Sharma et al., 2009; Su et al., 2015; Ge et al., 2013) |
| Bismuth | $Bi$ | 271.4 | 53.3 | 8.1 | 979 | 0.122 | (Sharma et al., 2009; Su et al., 2015; Ge et al., 2013) |

# Appendix G

# List of Eutectics

Table G.1: *Thermophysical properties of organic–organic (fatty acids compounds) eutectic PCMs.*

| Compound | Content ($wt.\%$) | $T_m$ (°C) | $H$ ($kJ/kg$) | Ref. No. |
|---|---|---|---|---|
| CA/LA | 90/10 | 13.3 | 142.2 | (Regin et al., 2008) |
| CA/LA | 64/36 | 19.62 | 149.95 | (Karaipekli and Sarı, 2010) |
| CA/LA | 65.1/34.9 | 19.67 | 126.56 | (Shilei et al., 2006) |
| CA/LA | 45/55 | 17–21 | 143 | (Sarı, 2005) |
| CA/LA | 70/30 | 21.09 | 123.62 | (Sharma et al., 2013) |
| CA/MA | 70/30 | 21.79 | 123.62 | (Sharma et al., 2013) |
| CA/LA | 66.75/33.25 | 22.76 | 127.2 | (Ke et al., 2013) |
| CA/PA | 76.5/23.5 | 23.12 | 156.44 | (Karaipekli and Sarı, 2010) |
| CA/SA | 83/17 | 24.68 | 178.69 | (Karaipekli and Sarı, 2010) |
| CA/SA | 83/17 | 25.39 | 188.15 | (Karaipekli and Sarı, 2010) |
| CA/MA | 78.39/21.61 | 26.02 | 155.2 | (Ke et al., 2013) |
| CA/PA | 70/30 | 27.07 | 142.61 | (Sharma et al., 2013) |
| CA/PA | 89/11 | 28.71 | 141.4 | (Ke et al., 2013) |
| LA/MA | 60/40 | 28.8–40.8 | 172 | (Sarı, 2005) |
| LA/MA/SA | 55.8/32.8/11.4 | 29.29 | 140.9 | (Liu et al., 2014) |
| LA/MA/PA | 55.24/29.75/15.02 | 31.14 | 142.6 | (Zhang et al., 2013) |
| CA/SA | 94.47/5.53 | 31.17 | 156.8 | (Ke et al., 2013) |
| LA/PA | 65/35 | 32.8–37.1 | 170.2 | (Sarı, 2005) |
| LA/SA | 60.3/39.7 | 33.8–47.6 | 189.8 | (Sari and Kaygusuz, 2002) |
| MA/SA | 50/50 | 35.2–51.8 | 189.2 | (Sarı, 2005) |
| MA/SA | 50/50 | 35.2–51.8 | 189.2 | (Sarı, 2005) |
| LA/SA | 75.1/24.9 | 36.9–37.6 | 183.4 | (Sarı et al., 2004) |
| MA/PA | 50/50 | 39.1–45.4 | 173.7 | (Sarı et al., 2004) |
| MA/PA | 50/50 | 47.91 | 153.12 | (Zhang et al., 2001) |
| PA/SA | 60/40 | 51.2–54.2 | 18.37 | (Sarı et al., 2004) |
| CA/LA | 65/35 | 18 | 148 | (Dimaano and Watanabe, 2002) |
| CA/LA | 45/55 | 21 | 143 | (Hawes et al., 1993) |
| CA/PA | 76.5/23.5 | 21.8 | 171.2 | (Sarı and Karaipekli, 2008) |
| LA/MA | 66/34 | 34.2 | 166.8 | (Keleş et al., 2005) |
| LA/PA | 69/31 | 35.2 | 166.3 | (Sarı, 2005) |
| MA/PA | 58/42 | 42.6 | 169.7 | (Sarı, 2003) |
| MA/SA | 64/36 | 44.1 | 182.4 | (Sari and Kaygusuz, 2006; Sarı, 2005) |
| MA/SA | 65.7/34.3 | 50–52 | 162 | (Kaygusuz and Sari, 2006) |
| PA/SA | 64.2/35.8 | 52.3 | 181.7 | (Baran and Sari, 2003) |

Table G.2: *Thermophysical properties of organic–organic (PEO/fatty acids compounds) eutectic PCMs.*

| **Compound** | **Weight ratio** ($w/w$) | $T_m$ (°C) | $H$ ($kJ/kg$) | **Ref. No.** |
|---|---|---|---|---|
| PEO 3400/CA | 1/1 | 32.2/42 | 169 | (Pielichowski and Flejtuch, 2003a) |
| PEO 3400/LA | 1/1 | 47.1 | 188 | (Pielichowski and Flejtuch, 2003a) |
| PEO 3400/MA | 1/1 | 50.7/54.9 | 207 | (Pielichowski and Flejtuch, 2003a) |
| PEO 3400/PA | 1/1 | 51.2/58 | 209 | (Pielichowski and Flejtuch, 2003a) |
| PEO 3400/SA | 1/1 | 54.2/60.3/68.9 | 205 | (Pielichowski and Flejtuch, 2003a) |
| PEO 10000/CA | 1:3 | 31.3/55.1 | 162 | (Pielichowska and Pielichowski, 2014) |
| PEO 10000/CA | 1:1 | 33.3/50.1 | 174 | (Pielichowski and Flejtuch, 2003b) |
| PEO 10000/CA | 3:1 | 33.3/43.9 | 174 | (Pielichowska and Pielichowski, 2014) |
| PEO 10000/LA | 1:3 | 46.8 | 195 | (Pielichowska and Pielichowski, 2014) |
| PEO 10000/LA | 1:1 | 46.4/52.3 | 203 | (Pielichowski and Flejtuch, 2003b) |
| PEO 10000/LA | 3:1 | 44.4/56.5 | 184 | (Pielichowska and Pielichowski, 2014) |
| PEO 10000/MA | 1:3 | 57.1 | 190 | (Pielichowska and Pielichowski, 2014) |
| PEO 10000/MA | 1:1 | 57.3 | 185 | (Pielichowski and Flejtuch, 2003b) |
| PEO 10000/MA | 3:1 | 58.7 | 191 | (Pielichowska and Pielichowski, 2014) |
| PEO 10000/PA | 1:3 | 58.1/63.3 | 206 | (Pielichowska and Pielichowski, 2014) |
| PEO 10000/PA | 1:1 | 63.2 | 205 | (Pielichowski and Flejtuch, 2003b) |
| PEO 10000/PA | 3:1 | 61.6 | 192 | (Pielichowska and Pielichowski, 2014) |
| PEO 10000/SA | 1:3 | 59.4/72.2 | 252 | (Pielichowska and Pielichowski, 2014) |
| PEO 10000/SA | 1:1 | 60.4/68.9 | 211 | (Pielichowski and Flejtuch, 2005) |
| PEO 10000/SA | 3:1 | 63.8 | 203 | (Pielichowski and Flejtuch, 2005) |

Table G.3: *Thermophysical properties of inorganic–inorganic eutectic PCMs.*

| **Material** | **Content** ($wt.\%$) | $T_m$ (°C) | $H$ ($kJ/kg$) | $\rho$ ($kg/m^3$) | **Ref. No.** |
|---|---|---|---|---|---|
| $Na_2SO_4$+$NaCl$+$KCl$+$H_2O$ | 31+13+16+40 | 4 | 234 | – | (Cabeza et al., 2011; Ge et al., 2013) |
| $Na_2SO_4 + NaCl + NH_4Cl + H_2O$ | 32+14+12+42 | 11 | – | – | (Cabeza et al., 2011; Ge et al., 2013) |
| $C_5H_5C_6H_5 + (C_6H_5)_2O$ | 26.5+73.5 | 12 | 97.9 | – | (Cabeza et al., 2011; Ge et al., 2013) |
| $C_5H_{12}O_3 + H_2O + CH_4N_2O$ | 38.5+31.5+30 | 13.4 | 160 | – | (Cabeza et al., 2011; Ge et al., 2013) |
| $CaCl_2.6H_2O + CaBr_2..6H_2O$ | 45+55 | 14.7 | 140 | – | (Sharma et al., 2009) |
| $Na_2SO_4 + NaCl + H_2O$ | 37+17+46 | 18 | – | – | (Su et al., 2015) |

| | | | | | |
|---|---|---|---|---|---|
| $Na_2SO_4.10H_2O + NaCl$ | 50+50 | 18 | – | – | (Paris et al., 1993) |
| $Na_2S_4 + MgSO_4 + H_2O$ | 25+21+54 | 24 | – | – | (Su et al., 2015) |
| $C_{14}H_{28}O_2 + C_{10}H_{20}O_2$ | 34+66 | 24 | 147.7 | – | (Sharma et al., 2009; Dubey and Mishra, 2014) |
| $CaCl_2 + MgCl_2.6H_2O$ | 50+50 | 25 | 95 | – | (Sharma et al., 2009) |
| $CaCl_2.6H_2O + MgCl_2.6H_2O$ | 66.7+33.3 | 25 | 127 | – | (Sharma et al., 2009; Su et al., 2015) |
| $CaCl_2 + NaCl + KCl + H_2O$ | 48+4.3+0.4+47.3 | 26.8 | 188 | – | (Sharma et al., 2009; Su et al., 2015) |
| $CH_3CONH_2 + NH_2CONH_2$ | 50+50 | 27 | 163 | – | (Sharma et al., 2009; Su et al., 2015) |
| $C_5H_{12}O_3 + CH_4N_2O$ | 62.5+37.5 | 29.8 | 218 | – | (Sharma et al., 2009; Su et al., 2015) |
| $Ca(NO_3).4H_2O + Mg(NO_3)_3.6H_2O$ | 47+53 | 30 | 136 | – | (Sharma et al., 2009; Su et al., 2015) |
| $CH_3COONa.3H_2O + NH_2CONH_2$ | 40+60 | 30 | 200.5 | – | (Sharma et al., 2009; Su et al., 2015) |
| $NH_2CONH_2 + NH_4NO_3$ | 53+47 | 46 | 95 | – | (Sharma et al., 2009; Su et al., 2015) |
| $Mg(NO_3)_3.6H_2O + NH_4NO_3$ | 61.5+38.5 | 52 | 125.5 | – | (Sharma et al., 2009; Su et al., 2015) |
| $Mg(NO_3)_3.6H_2O + MgCl_2.6H_2O$ | 58.7+41.3 | 59 | 132.2 | – | (Sharma et al., 2009; Su et al., 2015) |
| $Mg(NO_3)_3.6H_2O + MgCl_2.6H_2O$ | 50+50 | 59.1 | 144 | – | (Sharma et al., 2009; Su et al., 2015) |
| $Mg(NO_3)_3.6H_2O + Al(NO_3)_2.9H_2O$ | 53+47 | 61 | 148 | – | (Sharma et al., 2009; Su et al., 2015) |
| $CH_3CONH_2 + C_{17}H_{35}COOH$ | 50+50 | 65 | 218 | – | (Sharma et al., 2009; Su et al., 2015) |
| $Mg(NO_3)_2.6H_2O + MgBr_2.6H_2O$ | 59+41 | 66 | 168 | – | (Sharma et al., 2009; Su et al., 2015) |
| $C_{10}H_8 + C_7H_6O_2$ | 67.1+32.9 | 67 | 123.4 | – | (Sharma et al., 2009; Su et al., 2015) |
| $AlCl_3 + NaCl + ZrCl_2$ | 79+17+4 | 68 | 234 | – | (Sharma et al., 2009; Su et al., 2015) |
| $AlCl_3 + NaCl + KCl$ | 66+20+14 | 70 | 209 | – | (Sharma et al., 2009; Su et al., 2015) |
| $LiNO_3 + Mg(NO_3)_2.6H_2O$ | 14+86 | 72 | 180 | – | (Sharma et al., 2009; Pielichowska and Pielichowski, 2014) |
| $NH_2CONH_2 + NH_4Br$ | 66.6+33.4 | 76 | 151 | – | (Sharma et al., 2009; Su et al., 2015) |
| $LiNO_3 + NH_4NO_3 + NaNO_3$ | 25+65+10 | 80.5 | 113 | – | (Sharma et al., 2009; Su et al., 2015) |
| $LiNO_3 + NH_4NO_3 + KNO_3$ | 26.4+58.7+14.9 | 81.5 | 116 | – | (Sharma et al., 2009; Su et al., 2015) |
| $LiNO_3 + NH_4NO_3 + NH_4Cl$ | 27+68+5 | 81.6 | 108 | – | (Sharma et al., 2009; Su et al., 2015) |

| | | | | | |
|---|---|---|---|---|---|
| $AlCl_3 + NaCl + KCl$ | 60+26+14 | 93 | 213 | – | (Sharma et al., 2009; Su et al., 2015) |
| $AlCl_3 + NaCl$ | 66+34 | 93 | 201 | – | (Sharma et al., 2009; Su et al., 2015) |
| $NaNO_2 + NaNO_3 + KNO_3$ | 40+7+53 | 142 | – | – | (Sharma et al., 2009; Su et al., 2015) |
| $NaF+KF+LiF+MgF_2$ | 11.8+54.3+26.6+7.3 | 449 | – | 2160(l) | (Pielichowska and Pielichowski, 2014) |
| $LiF + NaF + CaF_2$ | 35.1+38.4+26.5 | 615 | – | 2225(l) | (Pielichowska and Pielichowski, 2014) |
| $LiF + NaF + MgF_2$ | 32.5+50.5+17 | 632 | – | 2105(l) | (Pielichowska and Pielichowski, 2014) |
| $NaF + CaF_2 + MgF_2$ | 51.8+34+14.2 | 645 | – | 2370(l) | (Pielichowska and Pielichowski, 2014) |
| $LiF + NaF$ | 48.1 + 51.9 | 652 | – | 1930(l) | (Pielichowska and Pielichowski, 2014) |
| $KF + NaF + MgF_2$ | 63.8+27.9+8.3 | 685 | – | 2090(l) | (Pielichowska and Pielichowski, 2014) |
| $LiF + MgF_2$ | 45.8+54.2 | 746 | – | 2305(l) | (Pielichowska and Pielichowski, 2014) |
| $NaF + MgF_2 + KF$ | 53.6+28.6+17.8 | 809 | – | 2110(l) | (Pielichowska and Pielichowski, 2014) |
| $NaF + MgF_2$ | 66.9+33.1 | 832 | – | 2190(l) | (Pielichowska and Pielichowski, 2014) |
| $H_2O + Polyacrylamide$ | – | 0 | 292 | – | (Pielichowska and Pielichowski, 2014) |
| $Na(CH_3COO).3H_2O + HCONH_2$ | 50+50 | 40 | 255 | – | (Pielichowska and Pielichowski, 2014) |

# Appendix H

# List of Metallic–additives NCPCMs

Table H.1: Summary of the developed metallic NMs additives NCPCM.

| PCM | Dispersed NMs | | | $k_{NCPCM}$ (W/m.k) | Enhancement in $k_{NCPCM}$ (%) | $L_{NCPCM}$ (J/g) | $L_{NCPCM}$ (Increase/Decrease) | Ref. |
|---|---|---|---|---|---|---|---|---|
| | Materials | Size | Loading content | | | | | |
| 1-Tetradecanol | Ag | D = 500 nm | 2 wt% | - | - | 216.5 | - | (Zeng et al., 2006) |
| | | | 3 wt% | - | - | 201.7 | - | |
| | | | 6 wt% | - | - | 204.7 | - | |
| | | | 11 wt% | - | - | 186.9 | - | |
| | | | 20 wt% | - | - | 172.8 | - | |
| | | | 33 wt% | - | - | 155.2 | - | |
| | | | 50 wt% | - | - | 119.4 | - | |
| | | | 77 wt% | - | - | 80.1 | - | |
| | | | 80 wt% | - | - | 55.5 | - | |
| | | | 89 wt% | - | - | 32.7 | - | |
| | | | 94 wt% | - | - | 17.0 | - | |
| Paraffin | Cu, Al, C/Cu | D = 25 nm | 0.1 wt% for all | - | - | - | 11.1% (m) and 11.7% (s) | (Wu et al., 2010) |
| | | | Paraffin/Cu | - | - | Paraffin/Cu | - | |
| | | | 0.5 wt% | - | - | ≈198 (m), ≈190 (s) | - | |
| | | | 1.0 wt% | 0.1878 (l), 0.2908 (s) | - | ≈183 (m), ≈179 (s) | - | |
| | | | 2.0 wt% | - | - | ≈185 (m), ≈185 (s) | - | |
| 1-Tetradecanol | Ag NWs | | 9.09 wt% | 0.43 | - | 175 | - | (Zeng et al., 2010) |
| | | | 23.08 wt% | 0.5 | - | 159 | - | |
| | | | 37.58 wt% | 0.61 | - | 140 | - | |
| | | | 46.08 wt% | 0.85 | - | 109 | - | |
| | | | 62.73 wt% | 1.46 | - | 76.5 | - | |
| Paraffin wax | Cu | D = 25 nm | 0.1 wt% | - | - | 214.3 at 60.2 °C | - | (Wang et al., 2010d) |
| | | | 0.5 wt% | | | 178.2 at 59.8 °C | - | |
| | | | 1.0 wt% | | | 175 at 60.2 °C | - | |
| | | | 2.0 wt% | | | 170.9 at 60.7 °C | - | |
| LDPE, LLDPE, Paraffin wax | Cu | D < 38 $\mu$m | LDPE/wax/Cu | ≈0.40-0.65 | - | LDPE/wax/Cu | - | (Molefi et al., 2010) |
| | | | 1 vol% | - | - | 104.7 | - | |
| | | | 3 vol% | - | - | 87.8 | - | |
| | | | 5 vol% | - | - | 68.2 | - | |
| | | | 10 vol% | - | - | 48.3 | - | |
| | | | LLDPE/wax/Cu | ≈0.41-0.70 | - | LLDPE/wax/Cu | - | |
| | | | 1 vol% | - | - | 113.5 | - | |
| | | | 3 vol% | - | - | 89.5 | - | |
| | | | 5 vol% | - | - | 74.3 | - | |
| | | | 10 vol% | - | - | 49.5 | - | |
| | | | HDPE/wax/Cu | ≈0.45-0.85 | - | HDPE/wax/Cu | - | |
| | | | 1 vol% | - | - | 150 | - | |
| | | | 3 vol% | - | - | 113.7 | - | |
| | | | 5 vol% | - | - | 91.7 | - | |
| | | | 10 vol% | - | - | 77.1 | - | |
| $C_2H_9NaO_5$ | AlN | 50 nm | 35 wt% | - | - | - | - | (Hu et al., 2011) |
| Paraffin | Cu | 25 nm | 0.2 wt% | 0.180 (s), 0.280 (l) | 14.2% (s) 18.1% (l) at 2 wt% | - | - | (Wu et al., 2012) |
| | | | 0.5 wt% | 0.185 (s), 0.281 (l) | - | - | - | |
| | | | 1.2 wt% | 0.190 (s), 0.297 (l) | - | - | - | |
| | | | 2.0 wt% | 0.200 (s), 0.310 (l) | - | - | - | |

Table H.1: Summary of the developed metallic NMs additives NCPCM.

| PCM | Dispersed NMs | | | $k_{NCPCM}$ (W/m.k) | Enhancement in $k_{NCPCM}$ (%) | $L_{NCPCM}$ (J/g) | $L_{NCPCM}$ (Increase/Decrease) | Ref. |
|---|---|---|---|---|---|---|---|---|
| | Materials | Size | Loading content | | | | | |
| Tetradecanol | Cu NWs | D = 90-120 nm, L = 40-50 $\mu$m | 0.662 wt% | 0.34 | - | 221.37 | - | (Zeng et al., 2012) |
| | | | 1.32 wt% | 0.344 | - | 201.24 | - | |
| | | | 7.42 wt% | 0.421 | - | 203.08 | - | |
| | | | 9.37 wt% | 0.444 | - | 176.56 | - | |
| | | | 13.4 wt% | 0.491 | - | 179.77 | - | |
| | | | 23.4 wt% | 0.818 | - | 170.74 | - | |
| | | | 34.7 wt% | 1.389 | - | 138.36 | - | |
| | | | 58.9 wt% | 2.856 | - | 86.95 | - | |
| | | | 36.5 wt% | 0.435 | - | 131.9 | - | |
| PEG | Cu | | 0.51 wt% | 0.377 | 38.05% at 2.1 wt% | 121.4 | - | (Tang et al., 2012) |
| | | | 2.1 wt% | 0.41 | - | 110.2 | - | |
| | | | 3.9 wt% | 0.426 | - | 100.4 | - | |
| | | | 6.3 wt% | 0.454 | - | - | - | |
| Organic ester | Ag | 15-18 nm | 0.5 wt% | 0.284 | 10-67% for 0.15.0 wt% | 1.787.88% (s) 1.178.91% (m) | - | (Parameshwaran et al., 2013) |
| $CaCl_26H_2O$ | CuNWs | D = ≈50 nm, L > 10 $\mu$m | 0.02 wt% | - | ≈22% | - | - | (Sreethawong et al., 2014) |
| | | | 0.08 wt% | - | ≈43% | - | - | |
| | | | 0.17 wt% | - | ≈52% | - | - | |
| Pentaerythritol | Nano-AlN | 50 nm | 3 wt% | - | - | 222.5 | - | (Hu et al., 2014) |
| Paraffin | Nano-$Si_3N_4$ | - | 1 wt% | 0.2532 | 35% | 192.98 | 3.4% increase at 1 wt.% | (Yang et al., 2014) |
| | | | 2 wt% | 0.2605 | - | 186.05 | - | |
| | | | 3 wt% | 0.2608 | - | 169.56 | - | |
| | | | 4 wt% | 0.2659 | - | 161.14 | - | |
| | | | 5 wt% | 0.2739 | - | 142.34 | - | |
| | | | 10 wt% | 0.309 | - | 113.63 | - | |
| PEG | Ag NWs | D = 20-10 nm, L= 5-20 $\mu$m | 7.1 wt% | 0.36 | 6.0 times | 110.0 | - | (Deng et al., 2016) |
| | | | 13.7 wt% | 0.51 | 8.5 times | 102.0 | - | |
| | | | 19.3 wt% | 0.68 | 11.3 times | 99.1 | - | |
| n-eicosane | Ag | D = 5.36 nm | 1 wt% | ≈0.42 | - | 229 | - | (Ghossein et al., 2017) |
| | | | 2 wt% | ≈0.45 | - | 208 | - | |
| | | | 3.5 wt% | ≈0.43 | - | 192 | - | |
| | | | 5 wt% | ≈0.422 | - | 177 | - | |
| | | | 6.5 wt% | ≈0.45 | - | 147 | - | |
| | | | 8 wt% | ≈0.47 | - | 134 | - | |
| | | | 10 wt% | ≈0.48 | - | 78.3 | - | |
| Paraffin | SiC | | 0.1 wt% | - | ≈3% | - | - | (Al-Waeli et al., 2017b) |
| | | | 0.5 wt% | - | ≈4% | - | - | |
| | | | 1.0 wt% | - | ≈4.1% | - | - | |
| | | | 2.0 wt% | - | ≈4.2% | - | - | |
| | | | 3.0 wt% | - | ≈4.3% | - | - | |
| | | | 4.0 wt% | | ≈4.5% | - | - | |
| | | | 5.0 wt% | | ≈5.0% | - | - | |
| Paraffin wax | Al | D = 50-100 nm | 0.2 wt% | ≈0.12 | ≈27% | ≈188 | - | (Chen et al., 2017) |
| | | | 0.4 wt% | ≈0.121 | ≈29% | ≈182 | - | |
| | | | 0.6 wt% | ≈0.128 | ≈40% | ≈188 | - | |
| | | | 0.8 wt% | ≈0.13 | ≈50% | ≈184 | - | |

Table H.1: Summary of the developed metallic NMs additives NCPCM.

| PCM | Dispersed NMs | | | $k_{NCPCM}$ (W/m.k) | Enhancement in $k_{NCPCM}$ (%) | $L_{NCPCM}$ (J/g) | $L_{NCPCM}$ (Increase/Decrease) | Ref. |
|---|---|---|---|---|---|---|---|---|
| | Materials | Size | Loading content | | | | | |
| | | | 1.0 wt% | ≈0.16 | ≈76% | ≈195 | - | |
| | | | 2.0 wt% | ≈0.18 | ≈100% | ≈168 | - | |
| | | | 4.0 wt% | ≈0.181 | ≈110% | ≈148 | - | |
| | | | 6.0 wt% | ≈0.18 | ≈103% | ≈150 | - | |
| | | | 8.0 wt% | ≈0.181 | ≈104% | ≈144 | - | |
| | | | 10.0 wt% | ≈0.183 | ≈106% | ≈135 | - | |

# Appendix I

# List of Metallic–oxide additives NCPCMs

Table I.1: Summary of the developed metallic-oxide NMs additives NCPCM.

| PCM | Dispersed NMs | | | $k_{NCPCM}$ (W/m.k) | Enhancement in $k_{NCPCM}$ (%) | $L_{NCPCM}$ (J/g) | $L_{NCPCM}$ (Increase/Decrease) | Ref. |
|---|---|---|---|---|---|---|---|---|
| | Materials | Size | Loading content | | | | | |
| $BaCl_2$ aqueous solution | $TiO_2$ | D = 20 nm | 0.167 vol% | 1.039 | 1.13 at vol% $TiO_2$ | | | (Liu et al., 2009) |
| Double distilled water | $Al_2O_3$ | D = 20 nm | 0.05 wt% | 0.6483 | 10.5% | - | - | (Wu et al., 2009) |
| n-octadecane | $Al_2O_3$ | 159.6-196.0 nm | 5 wt% | 0.128 at 55 °C | 6% at 10 wt% | 225.6 | 13% decrease at 10 wt% | (Ho and Gao, 2009) |
| | | | 10 wt% | 0.142 at 55 °C | | 212.3 | | |
| Paraffin wax | $Al_2O_3$ | D = 20 nm | 1 wt% | 0.27 at 288 K | 26% at 5 wt% | 136.1 | | (Wang et al., 2010a) |
| | | | 2 wt% | 0.26 at 288 K | | 136.3 | | |
| | | | 5 wt% | 0.28 at 288 K | | 134.1 | | |
| Cyclohexane | CuO | D = 515 nm | 1 wt% | 0.1231 (l), 0.2764 (s) | - | - | - | (Fan and Khodadadi, 2012) |
| | | | 2 wt% | 0.1238 (l), 0.2865 (s) | | | | |
| | | | 4 wt% | 0.1243 (l), 0.2716 (s) | | | | |
| Paraffin wax | CuO | D = 40 nm | 2 wt% | 0.31 at 58 °C | 6% (l) | | | (Jesumathy et al., 2011) |
| | | | 5 wt% | 0.33 at 58 °C | 6.7% (l) | | | |
| | | | 10 wt% | 0.34 at 58 °C | 7.8% (l) | | | |
| Oleic acid | CuO | D = 180 nm | 0.5 wt% | 0.29 | 31.69% | 136 (m), 133 (s) | 5.1% (m) 5.2% (s) decrease | (Harikrishnan and Kalaiselvam, 2012) |
| | | | 1.0 wt% | 0.36 | 66.07% | 135 (m), 132 (s) | | |
| | | | 1.5 wt% | 0.4 | 85.26% | 133 (m), 131 (s) | | |
| | | | 2.0 wt% | 0.44 | 98.66% | 132 (m), 131 (s) | | |
| N-docosane | CuO | - | 0.01 vol% | - | | | | (Karunamurthy et al., 2012) |
| | | | 0.02 vol% | - | | | | |
| | | | 0.03 vol% | - | | | | |
| | | | 0.04 vol% | - | | | | |
| | | | 0.05 vol% | - | | | | |
| | | | 0.10 vol% | 0.3222 | | | | |
| | | | 0.15 vol% | 0.3802 | | | | |
| Paraffin | $Al_2O_3$ $TiO_2$ $SiO_2$ ZnO | D = 2030 nm | Paraffin + $Al_2O_3$ | | | Paraffin + $Al_2O_3$ | | (Teng and Yu, 2012a) |
| | | | 1.0 wt% | | | 197.9 | 0.46% decrease | |
| | | | 2.0 wt% | | | 194.6 | | |
| | | | 3.0 wt% | | | 184.2 | | |
| | | | Paraffin + $TiO_2$ | | | Paraffin + $TiO_2$ | | |
| | | | 1.0 wt% | | | 200.6 | | |
| | | | 2.0 wt% | | | 200.1 | | |
| | | | 3.0 wt% | | | 198.7 | | |
| | | | Paraffin + $SiO_2$ | | | Paraffin + $SiO_2$ | | |
| | | | 1.0 wt% | | | 185.6 | | |
| | | | 2.0 wt% | | | 180.4 | | |
| | | | 3.0 wt% | | | 175.0 | | |
| | | | Paraffin + ZnO | | | Paraffin + ZnO | | |
| | | | 1.0 wt% | | | 187.g | | |
| | | | 2.0 wt% | | | 184.7 | | |
| | | | 3.0 wt% | | | 171.9 | | |
| $BaCl_2$ aqueous solution | $TiO_2$ | D = 20 nm | 0.167 vol% | 0.54 at -5 °C 5.59 at 25 °C | 16.74% at 25 °C | 280 | | (He et al., 2012) |

Table I.1: Summary of the developed metallic-oxide NMs additives NCPCM.

| PCM | Dispersed NMs | | | $k_{NCPCM}$ (W/m.k) | Enhancement in $k_{NCPCM}$ (%) | $L_{NCPCM}$ (J/g) | $L_{NCPCM}$ (Increase/Decrease) | Ref. |
|---|---|---|---|---|---|---|---|---|
| | Materials | Size | Loading content | | | | | |
| | | | 0.283 vol% | 0.56 at -5 °C<br>0.61 at 25 °C | | 258 | | |
| | | | 0.565 vol% | 0.58 at -5 °C<br>0.65 at 25 °C | | 256.1 | | |
| | | | 1.130 vol% | 0.60 at -5 °C<br>0.67 at 25 °C | | 254.2 | | |
| n-Octadecane | $TiO_2$ | D = 30 ± 5 nm | 0.5 wt% | 0.79 | | | | (Motahar et al., 2014) |
| | | | 1 wt% | 0.55 | | | | |
| | | | 2 wt% | 0.83 | | | | |
| | | | 3 wt% | 0.85 | | | | |
| | | | 4 wt% | 0.82 | | | | |
| | | | 5 wt% | 0.58 | | | | |
| Paraffin | $Fe_3O_4$ | | 1 wt% | | | 113 | | (Sahan and Paksoy, 2014) |
| | | | 5 wt% | | | 125 | | |
| | | | 10 wt% | | | 151 | | |
| | | | 15 wt% | | | 124 | | |
| Paraffin | $SiO_2$<br>$Al_2O_3$<br>$Fe_2O_3$<br>ZnO | D = 11 and 20 nm | Paraffin + $Fe_2O_3$ | ∼0.70-1.0 | | Paraffin + $Fe_2O_3$ | | (Babapoor and Karimi, 2015) |
| | | | 2.0 wt% | | | ∼130 | | |
| | | | 4.0 wt% | | | ∼110 | | |
| | | | 6.0 wt% | | | ∼105 | | |
| | | | 8.0 wt% | | | ∼80 | | |
| | | | Paraffin + $Al_2O_3$ | ∼0.60-1.0 | | Paraffin + $Al_2O_3$ | | |
| | | | 2.0 wt% | | | ∼218 | | |
| | | | 4.0 wt% | | | ∼205 | | |
| | | | 6.0 wt% | | | ∼205 | | |
| | | | 8.0 wt% | | | ∼190 | | |
| | | | Paraffin+ZnO | ∼0.55-0.9 | | Paraffin+ZnO | | |
| | | | 2.0 wt% | | | ∼190 | | |
| | | | 4.0 wt% | | | ∼185 | | |
| | | | 6.0 wt% | | | ∼185 | | |
| | | | 8.0 wt% | | | ∼157 | | |
| | | | Paraffin+$SiO_2$ (11 nm) | ∼0.58-0.87 | | Paraffin+$SiO_2$ (11 nm) | | |
| | | | 2.0 wt% | | | ∼218 | | |
| | | | 4.0 wt% | | | ∼175 | | |
| | | | 6.0 wt% | | | ∼168 | | |
| | | | 8.0 wt% | | | ∼162 | | |
| | | | Paraffin+$SiO_2$ (20 nm) | ∼0.40-0.9 | | Paraffin + $SiO_2$ (20 nm) | | |
| | | | 2.0 wt% | | | ∼218 | | |
| | | | 4.0 wt% | | | ∼205 | | |
| | | | 6.0 wt% | | | ∼184 | | |
| | | | 8.0 wt% | | | ∼145 | | |

Table I.1: Summary of the developed metallic-oxide NMs additives NCPCM.

| PCM | Dispersed NMs | | | $k_{NCPCM}$ (W/m.k) | Enhancement in $k_{NCPCM}$ (%) | $L_{NCPCM}$ (J/g) | $L_{NCPCM}$ (Increase/Decrease) | Ref. |
|---|---|---|---|---|---|---|---|---|
| | Materials | Size | Loading content | | | | | |
| | | | Paraffin+$Fe_2O_3$+ $Al_2O_3$+$Fe_2O_3$+ ZnO+$SiO_2$ (11 nm) +$SiO_2$ (20 nm) | ∼0.70-0.8 | | Paraffin + $Fe_2O_3$+ $Al_2O_3$+ $Fe_2O_3$+ ZnO+$SiO_2$ (11 nm) +$SiO_2$(20 nm) | | |
| | | | 2.0 wt% | | | ∼145 | | |
| | | | 4.0 wt% | | | ∼138 | | |
| | | | 6.0 wt% | | | ∼140 | | |
| | | | 8.0 wt% | | | ∼120 | | |
| PA | $TiO_2$ | | 0.5 wt% | ∼0.23 | 12.70% | 209.02 | | (Sharma et al., 2016) |
| | | | 1.0 wt% | ∼0.245 | 20.60% | 202.9 | | |
| | | | 3.0 wt% | ∼0.33 | 46.60% | 184.43 | | |
| | | | 5.0 wt% | ∼0.35 | 80% | 180.03 | | |
| Paraffin | $TiO_2$ | | 20 wt% | - | | 115.56 | | (Li et al., 2016b) |
| | | | 25 wt% | 0.302 | | 98.43 | | |
| | | | 30 wt% | - | | 97.76 | | |
| | | | 35 wt% | - | | 64.43 | | |
| Paraffin | $Fe_3O_4$ | | 10 wt% | 0.37 | - | 139.3 | 3.30% | (Şahan et al., 2015) |
| | | | 20 wt% | 0.40 | 60% | 146.8 | 8.80% | |
| Paraffin | $Al_2O_3$ | | 2.5 wt% | 0.227 (s), 0.152 (l) | | 200.16 | | (Nourani et al., 2016b) |
| | | | 5.0 wt% | 0.236 (s), 0.156 (l) | | 198.87 | | |
| | | | 7.5 wt% | 0.245 (s), 0.162 (l) | | 189.42 | | |
| | | | 10 wt% | 0.259 (s), 0.167 (l) | | 182.28 | | |
| RT20, RT25 | $Al_2O_3$ | | 1.0 wt% | 0.234 (RT20/$Al_2O_3$) | -8% | 130.495 (RT20/$Al_2O_3$) | 11% | (Colla et al., 2017b) |
| | | | | 0.242 (RT20/$Al_2O_3$) | -7% | 134.184 (RT20/$Al_2O_3$) | 1% | |
| PE | $Al_2O_3$ | | 0.1 wt% | 0.1252 | 18.11% | 260.06 | | (P et al., 2017) |
| | | | 0.5 wt% | 0.1412 | 33.21% | 255.0 | | |
| | | | 1.0 wt% | 0.1609 | 51.79% | 251.74 | | |
| $CaCl_2 6H_2O$ | γ-$Al_2O_3$ | | 0.5 wt% | 0.459 | 36.4% | ∼176 | | (Li et al., 2017) |
| | | | 1.0 wt% | 0.672 | 97.0% | ∼172 | | |
| | | | 1.5 wt% | 0.976 | 186.0% | ∼162 | | |
| | | | 2.0 wt% | 1.373 | 303.0% | ∼158 | | |
| Paraffin | $TiO_2$ | | 0.5 wt% | ∼0.152 | | ∼142 | | (Sami and Etesami, 2017) |
| | | | 0.7 wt% | ∼0.154 | | ∼157 | | |
| | | | 1.0 wt% | ∼0.17 | | ∼170 | | |
| | | | 2.0 wt% | ∼0.18 | | ∼169 | | |
| | | | 3.0 wt% | ∼0.22 | | ∼172 | | |
| | | | 4.0 wt% | ∼0.23 | | ∼141 | | |
| Neopentyl glycol | CuO | | 0.5 wt% | | | 124.4 | | (Praveen and Suresh, 2018) |
| | | | 1.0 wt% | | | 118.6 | | |
| | | | 3.0 wt% | | | 112.4 | | |
| PW-L, PW-H | $Al_2O_3$ | | PW-L | PW-L at 15 °C | | PW-L | | (Akhmetov et al., 2019) |
| | | | 2.0 wt% | ∼0.36 | | 152.98 | | |
| | | | 4.0 wt% | ∼0.43 | | 152.98 | | |
| | | | PW-H | PW-H at 15 °C | | PW-H | | |
| | | | 2.0 wt% | ∼0.37 | | 180.97 | | |
| | | | 4.0 wt% | ∼0.39 | | 178.69 | | |
| Iraqi paraffin wax | $Al_2O_3$ $ZrO_2$ SiC | | PW+$Al_2O_3$ | | | | | (Ali et al., 2019) |

Table I.1: Summary of the developed metallic-oxide NMs additives NCPCM.

| PCM | Dispersed NMs | | | $k_{NCPCM}$ (W/m.k) | Enhancement in $k_{NCPCM}$ (%) | $L_{NCPCM}$ (J/g) | $L_{NCPCM}$ (Increase/Decrease) | Ref. |
|---|---|---|---|---|---|---|---|---|
| | Materials | Size | Loading content | | | | | |
| | | | 0.1 wt% | | | | | |
| | | | 0.5 wt% | | | | | |
| | | | 1.0 wt% | | | | | |
| | | | 2.0 wt% | | | | | |
| | | | 3.0 wt% | | | | | |
| | | | 4.0 wt% | | | | | |
| | | | 5.0 wt% | | | | | |
| | | | PW+$ZrO_2$ | | | | | |
| | | | 0.1 wt% | | | | | |
| | | | 0.5 wt% | | | | | |
| | | | 1.0 wt% | | | | | |
| | | | 2.0 wt% | | | | | |
| | | | 3.0 wt% | | | | | |
| | | | 4.0 wt% | | | | | |
| | | | 5.0 wt% | | | | | |
| | | | PW+SiC | | | | | |
| | | | 0.1 wt% | | | | | |
| | | | 0.5 wt% | | | | | |
| | | | 1.0 wt% | | | | | |
| | | | 2.0 wt% | | | | | |
| | | | 3.0 wt% | | | | | |
| | | | 4.0 wt% | | | | | |
| | | | 5.0 wt% | | | | | |
| Paraffin wax | CuO | | 0.3 wt% | ∼0.245 | | 154.7 (m), 154.2 (s) | | (Wang et al., 2020) |
| | | | 0.6 wt% | ∼0.255 | | 153.9 (m), 153.1 (s) | | |
| | | | 0.9 wt% | ∼0.261 | | 153.1 (m), 152.8 (s) | | |
| | | | 1.2 wt% | ∼0.264 | | 152.8 (m), 152.6 (s) | | |
| Paraffin wax | $Al_2O_3$ | | 2.0 wt% | 4.565 | 20.73% | 132.0 | -8.20% | (Kothari et al., 2021) |
| | | | 4.0 wt% | 8.921 | 41.48% | 121.60 | -15.43% | |
| | | | 6.0 wt% | 13.277 | 62.22% | 112.5 | -21.76% | |
| Paraffin wax | CuO | | 0.5 wt% | 0.36 | 56.52% | 146.46 | -4.40% | (Kumar et al., 2021) |
| | | | 1.0 wt% | 0.406 | 76.52% | 131.09 | -14.43% | |
| | | | 3.0 wt% | 0.576 | 150.0% | 115.28 | -24.75% | |

# Appendix J

# List of Carbon–additives NCPCMs

Table J.1: Summary of the developed carbon-additives NMs additives NCPCM.

| PCM | Dispersed NMs | | | $k_{NCPCM}$ (W/m.K) | $k_{NCPCM}$ (%) | $L_{NCPCM}$ (J/g) | $L_{NCPCM}$ (Increase/ Decrease) | Ref. |
|---|---|---|---|---|---|---|---|---|
| | Materials | Size | Loading content | | | | | |
| Paraffin wax | CNF | D = 100 nm<br>L = 20 m | 1 wt% | 0.26 | | 10.5 | | (Elgafy and Lafdi, 2005) |
| | | | 2 wt% | 0.27 | | 9.5 | | |
| | | | 3 wt% | 0.29 | | 8.8 | | |
| | | | 4 wt% | 0.33 | | 7.5 | | |
| Paraffin wax | SWCNT<br>MWCNT<br>CNF | SWCNT<br>= 1 nm<br>MWCNT<br>= 10 nm<br>CNF<br>= 10 nm | SWCNT<br>= 1 nm | | | | | (Shaikh et al., 2008) |
| | | | 0.1 vol% | | | 168.2 | Increased 12.98%<br>at 1.0 vol% | |
| | | | 0.4 vol% | | | 170.6 | | |
| | | | 0.7 vol% | | | 174.6 | | |
| | | | 1.0 vol% | | | 176.6 | | |
| | | | MWNT<br>= 10 nm | | | | | |
| | | | 0.1 vol% | | | 165.2 | 10.08% increased<br>at 1.0 vol% | |
| | | | 0.4 vol% | | | 168.0 | | |
| | | | 0.7 vol% | | | 170.9 | | |
| | | | 1.0 vol% | | | 172.1 | | |
| | | | CNF<br>= 100 nm | | | | | |
| | | | 0.1 vol% | | | 161.7 | 6.8% increased<br>at 1.0 vol% | |
| | | | 0.4 vol% | | | 163.1 | | |
| | | | 0.7 vol% | | | 165.6 | | |
| | | | 1.0 vol% | | | 166.9 | | |
| PA | MWCNT | D = 30 nm<br>L = 50 um | 0.2 wt% | 0.23 (s), 0.16 (l) | 38% (l)<br>46% (s) | 200.4 | | (Wang et al., 2010c) |
| | | | 0.5 wt% | 0.23 (s), 0.17 (l) | | 197.7 | | |
| | | | 1.0 wt% | 0.33 (s), 0.22 (l) | | 184 | | |
| 1-Tetradecanol | MWCNT | D = 1030 nm<br>L = 515 um | 0.5 wt% | 0.356 | 30% at 5 wt%<br>of MWCNT | | | (Zeng et al., 2007) |
| | | | 1.0 wt% | 0.35 | | | | |
| | | | 2.5 wt% | 0.37 | | | | |
| | | | 5.0 wt% | 0.43 | | 114.49 | | |
| PA | MWCNT | D=1030 nm,<br>L= 515 um (long)<br>L = 12 um (short) | 0.1 wt% | 0.316 | 26% at 5 wt%<br>of MWCNT | | | (Zeng et al., 2009) |
| | | | 5.0 wt% | 0.402 | | | | |
| | | | 0.1 wt% | 0.31 | | | | |
| | | | 5.0 wt% | 0.38 | | | | |
| | | | 0.1 wt% | 0.281 | | | | |
| | | | 5 wt% | 0.352 | | | | |

Table J.1: Summary of the developed carbon-additives NMs additives NCPCM.

| PCM | Dispersed NMs | | | $k_{NCPCM}$ (W/m.K) | $k_{NCPCM}$ (%) | $L_{NCPCM}$ (J/g) | $L_{NCPCM}$ (Increase/ Decrease) | Ref. |
|---|---|---|---|---|---|---|---|---|
| | Materials | Size | Loading content | | | | | |
| Paraffin wax | MWCNT | D = 30 nm<br>L = 50 um | 0.2 wt% | 0.39 | 35% (s)<br>45% (l) at<br>2 wt% MWCNT | 165.4 | | (Wang et al., 2009a) |
| | | | 0.5 wt% | 0.35 | | 165.1 | | |
| | | | 1.0 wt% | 0.37 | | 164.9 | | |
| | | | 2.0 wt% | 0.28 | | 163.8 | | |
| PA | P-MWCNT<br>B-MWCNT<br>M-MWCNT<br>A-MWCNT<br>G-MWCNT | D = 30 nm<br>L = 50 um | P-MWCNT<br>/PA | P-MWCNT<br>/PA | | | | (Wang et al., 2010b) |
| | | | 0.2 wt% | 0.232 (s)<br>0.223 (l) | 42.2% at 1.0 wt%<br>MWCNT at 55 °C | | | |
| | | | 0.5 wt% | 0.240 (s)<br>0.158 (l) | | | | |
| | | | 1.0 wt% | 0.289 (s)<br>0.199 (l) | | | | |
| | | | B-MWCNT<br>/PA | B-MWCNT<br>/PA | | | | |
| | | | 0.2 wt% | 0.223 (s)<br>0.160 (l) | 43.3% at 1.0 wt%<br>MWCNT at 55 °C | | | |
| | | | 0.5 wt% | 0.244 (s)<br>0.164 (l) | | | | |
| | | | 1.0 wt% | 0.293 (s)<br>0.204 (l) | | | | |
| | | | M-MWCNT<br>/PA | M-MWCNT<br>/PA | | | | |
| | | | 0.2 wt% | 0.234 (s)<br>0.163 (l) | 55.1% at 1.0 wt%<br>MWCNT at 45 °C | | | |
| | | | 0.5 wt% | 0.245 (s)<br>0.174 (l) | | | | |
| | | | 1.0 wt% | 0.339 (s)<br>0.219 (l) | | | | |
| | | | A-MWCNT<br>/PA | A-MWCNT<br>/PA | | | | |
| | | | 0.2 wt% | 0.236 (s)<br>0.159 (l) | 49.3% at 1.0 wt%<br>MWCNT at 55 °C | | | |
| | | | 0.5 wt% | 0.247 (s)<br>0.166 (l) | | | | |
| | | | 1.0 wt% | 0.306 (s)<br>0.214 (l) | | | | |
| | | | G-MWCNT<br>/PA | G-MWCNT<br>/PA | | | | |
| | | | 0.2 wt% | 0.237 (s)<br>0.162 (l) | 34.5% at 1.0 wt%<br>MWCNT at 75 °C | | | |
| | | | 0.5 wt% | 0.243 (s)<br>0.180 (l) | | | | |
| | | | 1.0 wt% | 0.277 (s)<br>0.209 (l) | | | | |

Table J.1: Summary of the developed carbon-additives NMs additives NCPCM.

| PCM | Dispersed NMs | | | $k_{NCPCM}$ (W/m.K) | $k_{NCPCM}$ (%) | $L_{NCPCM}$ (J/g) | $L_{NCPCM}$ (Increase/ Decrease) | Ref. |
|---|---|---|---|---|---|---|---|---|
| | Materials | Size | Loading content | | | | | |
| Paraffin wax Soy wax | CNF CNT | CNF: D = 200 nm CNT: D = 30 nm L = 50 um | Soy wax /CNF | Soy wax /CNF | | | | (Cui et al., 2011) |
| | | | 1 wt% | 0.414 | | | | |
| | | | 2 wt% | 0.426 | | | | |
| | | | 5 wt% | 0.467 | | | | |
| | | | 10 wt% | 0.469 | | | | |
| | | | Soy wax /CNT | Soy wax /CNT | | | | |
| | | | 1 wt% | 0.343 | | | | |
| | | | 2 wt% | 0.354 | | | | |
| | | | 5 wt% | 0.395 | | | | |
| | | | 10 wt% | 0.403 | | | | |
| | | | Paraffin wax /CNF | Paraffin wax /CNF | | | | |
| | | | 1 wt% | 0.398 | | | | |
| | | | 2 wt% | 0.411 | | | | |
| | | | 5 wt% | 0.439 | | | | |
| | | | 10 wt% | 0.45 | | | | |
| n-Hexadecane | MWCNT | D = 1020 nm L = 0.52l um | 0.1 wt% | | | 196.58 | | (Zhang et al., 2012b) |
| | | | 0.5 wt% | | | 256.28 | | |
| | | | 1.0 wt% | | | 237.90 | | |
| | | | 2.0 wt% | | | 244.81 | | |
| | | | 10.0 wt% | | | 219.60 | | |
| PEG | GNP | D = 35 um T = 80 nm | 1 wt% | 0.45 | | 125 | | (Zhang et al., 2012a) |
| | | | 2 wt% | 0.6 | | 124 | | |
| | | | 3 wt% | 0.9 | | 121 | | |
| | | | 4 wt% | 1.2 | | 120 | | |
| | | | 5 wt% | 1.6 | | 119 | | |
| | | | 6 wt% | 1.8 | | 118 | | |
| | | | 7 wt% | 2.1 | | 116 | | |
| | | | 8 wt% | 2.3 | | 115 | | |
| Paraffin | MWCNT | D = 30-50 nm L = 10-20 um | 0.15 vol% | 0.28 | ∼30% (l) ∼40% (s) | 137.20 | | (Kumaresan et al., 2012) |
| | | | 0.30 vol% | 0.35 | | 127.28 | | |
| | | | 0.45 vol% | 0.37 | | 129.50 | | |
| | | | 0.60 vol% | 0.39 | | 133.60 | | |
| CA-LA-PA | MWCNT | D = 8-15 nm L = 50 um | 10 wt% | 0.41 | | 122.3 (m) 115.1 (s) | | (Meng et al., 2012) |
| | | | 20 wt% | 0.63 | | 101.6 (m) 100.4 (s) | | |
| | | | 30 wt% | 0.64 | | 87.1 (m) 83.6 (s) | | |
| | | | 40 wt% | 0.65 | | 76.4 (m) 69.4 (s) | | |

Table J.1: Summary of the developed carbon-additives NMs additives NCPCM.

| PCM | Dispersed NMs | | | $k_{NCPCM}$ (W/m.K) | $k_{NCPCM}$ (%) | $L_{NCPCM}$ (J/g) | $L_{NCPCM}$ (Increase/ Decrease) | Ref. |
|---|---|---|---|---|---|---|---|---|
| | Materials | Size | Loading content | | | | | |
| | | | 50 wt% | 0.66 | | 57.3 (m)<br>48.8 (s) | | |
| SA | MWCNT<br>Graphene<br>Graphite | | SA/ MWCNT | SA/ MWCNT | 12% at 5 vol% of Graphite | - | | (Li et al., 2014b) |
| | | | 0.5 vol% | - | | - | | |
| | | | 1.0 vol% | 0.45 | | 196.0 | | |
| | | | 5.0 vol% | 0.47 | | 185.3 | | |
| | | | SA/ Graphene | SA/ Graphene | | | | |
| | | | 0.5 vol% | - | | - | | |
| | | | 1.0 vol% | 0.32 | | 191.5 | | |
| | | | 5.0 vol% | 0.54 | | 187.5 | | |
| | | | SA/ Graphite | SA/ Graphite | | | | |
| | | | 0.5 vol% | - | | - | | |
| | | | 1.0 vol% | 0.8 | | 199.3 | | |
| | | | 5.0 vol% | 3.2 | | 188.6 | | |
| 1-Octadecanol | Graphene | | 1.0 wt% | 0.5 | ∼140% | | ∼15% decreased | (Yavari et al., 2011) |
| | | | 2.0 wt% | 0.62 | | | | |
| | | | 4.0 wt% | 0.91 | | | | |
| Paraffin | Graphite | D = 2-100 nm<br>L = 1-20 um | 2.8 vol% | 0.24 | | 252.9 | | (Warzoha et al., 2015) |
| | | | 5.8 vol% | 0.28 | | 251.3 | | |
| | | | 8.5 vol% | 0.32 | | 250.6 | | |
| | | | 11.4 vol% | 0.36 | | 242.7 | | |
| Paraffin wax | S-MWCNT<br>C-S-MWCNT<br>L-MWCNT<br>CNF<br>GNP | D = 8-15 nm<br>L = 0.5-2 um<br>D = 8-15 nm,<br>L = 0.5-2 $\mu$m<br>D<10 nm,<br>L = 5-15 $\mu$m<br>D = 150-200 nm,<br>L = 10-30 $\mu$m<br>D = 5-10 $\mu$m,<br>T = 4-20 nm | Paraffin wax/ S-MWCNT | | | | | (Yu et al., 2013) |
| | | | 1 wt% | 0.151 | | | | |
| | | | 2 wt% | 0.16 | | | | |
| | | | 3 wt% | 0.16 | | | | |
| | | | 4 wt% | 0.171 | | | | |
| | | | Paraffin wax/ C-S-MWCNT | | | | | |
| | | | 1 wt% | 0.155 | | | | |
| | | | 2 wt% | 0.161 | | | | |
| | | | 3 wt% | 0.17 | | | | |
| | | | 4 wt% | 0.181 | | | | |
| | | | Paraffin wax/ L-MWCNT | | | | | |
| | | | 1 wt% | 0.15 | | | | |

Table J.1: Summary of the developed carbon-additives NMs additives NCPCM.

| PCM | Dispersed NMs | | | $k_{NCPCM}$ (W/m.K) | $k_{NCPCM}$ (%) | $L_{NCPCM}$ (J/g) | $L_{NCPCM}$ (Increase/ Decrease) | Ref. |
|---|---|---|---|---|---|---|---|---|
| | Materials | Size | Loading content | | | | | |
| | | | 2 wt% | 0.152 | | | | |
| | | | 3 wt% | 0.157 | | | | |
| | | | 4 wt% | 0.161 | | | | |
| | | | CNF | | | | | |
| | | | 1 wt% | 0.155 | | | | |
| | | | 2 wt% | 0.161 | | | | |
| | | | 3 wt% | 0.17 | | | | |
| | | | 4 wt% | 0.181 | | | | |
| | | | Paraffin wax/ GNP | | | | | |
| | | | 1 wt% | 0.178 | | | | |
| | | | 2 wt% | 0.218 | | | | |
| | | | 3 wt% | 0.23 | | | | |
| | | | 4 wt% | 0.29 | | | | |
| Paraffin | GO | | 52.2 wt% | 1.04 (l)<br>0.952 (s) | | 63.11 (l)<br>64.45 (s) | | (Mehrali et al., 2013b) |
| | | | 52.61 wt% | 1.19 (l)<br>0.964 (s) | | 62.53 (l)<br>63.34 (s) | | |
| | | | 55.19 wt% | 1.45 (l)<br>1.32 (s) | | 59.12 (l)<br>60.73 (s) | | |
| | | | 51.70 wt% | 0.985 (l)<br>0.932 (s) | | 63.76 (l)<br>64.89 (s) | | |
| Paraffin | MWCNT | D = 20-30 nm | - | - | - | - | - | (Teng and Yu, 2012b) |
| PA | MWCNT | D = 20-40 nm,<br>L = 10-15 um | 1, 2, 3,<br>5, 7 wt% | - | 4565% | - | - | (Ji et al., 2012) |
| OA | GA | | 20% vol% | 2.635 | | | - | (Zhong et al., 2013) |
| n-Docosane | GNP | D = 15 $\mu$m<br>T < 10 nm | 1.0 wt% | 0.34 | | 131 | | (Kim and Drzal, 2009) |
| | | | 2.0 wt% | 0.45 | | - | | |
| | | | 3.0 wt% | 0.5 | | 128 | | |
| | | | 5.0 wt% | 0.68 | | - | | |
| | | | 7.0 wt% | 0.8 | | 130 | | |
| CA | HNT<br>Graphite | | 35 wt% | 0.26-1.0 | | 85.89 (m)<br>86.24 (s) | | (Mei et al., 2011) |
| | | | 40 wt% | | | 75.52 (m)<br>75.81 (s) | | |
| | | | 45 wt% | | | 66.76 (m)<br>67.43 (s) | | |
| | | | 50 wt% | | | 56.27 (m)<br>56.85 (s) | | |
| Paraffin | NG | D = 35 nm | 1.0 wt% | 0.365 | | 202.58 | | (Li, 2013) |
| | | | 4.0 wt% | 0.4971 | | 193.26 | | |
| | | | 7.0 wt% | 0.5685 | | 183.62 | | |
| | | | 10.0 wt% | 0.9362 | | 181.81 | | |
| SA | MWCNT<br>Graphene | MWCNT:<br>(D = 25 nm)<br>Graphene:<br>(T = 7 nm) | SA/ MWCNT | SA/ MWCNT | | | | (Choi et al., 2014) |
| | | | 0.01 vol% | - | | | | |

Table J.1: Summary of the developed carbon-additives NMs additives NCPCM.

| PCM | Dispersed NMs | | | $k_{NCPCM}$ (W/m.K) | $k_{NCPCM}$ (%) | $L_{NCPCM}$ (J/g) | $L_{NCPCM}$ (Increase/ Decrease) | Ref. |
|---|---|---|---|---|---|---|---|---|
| | Materials | Size | Loading content | | | | | |
| | | | 0.05 vol% | 0.187 | | | | |
| | | | 0.10 vol% | 0.188 | | | | |
| | | | SA/ Graphene | SA/ Graphene | | | | |
| | | | 0.01 vol% | - | | | | |
| | | | 0.05 vol% | 0.191 | | | | |
| | | | 0.10 vol% | 0.201 | | | | |
| PA | NDG | | 1 wt% | 0.34 | | 199.65 | | (Mehrali et al., 2014b) |
| | | | 2 wt% | 0.46 | | 198.84 | | |
| | | | 3 wt% | 0.98 | | 199.48 | | |
| | | | 4 wt% | 1.54 | | 197.53 | | |
| | | | 5 wt% | 1.73 | | 195.54 | | |
| PA | GNP | D < 2 nm T < 2nm | 22.01 wt% | 2.75 (l) 2.54 (s) | | 160.31 (m) 168.43 (s) | | (Mehrali et al., 2013a) |
| | | | 16.94 wt% | 2.43 (l) 2.17 (s) | | 170.72 (m) 175.34 (s) | | |
| | | | 8.06 wt% | 2.11 (l) 1.84 (s) | | 188.98 (m) 191.23 (s) | | |
| Paraffin wax | CNT | | 80% | 1.2 | | 122 | | (Chen et al., 2012) |
| | | | 90% | 0.8 | | 136 | | |
| n-Nonacosane | xGnP Graphene | | n-nonacosane/ xGnP | n-nonacosane/ xGnP | | | | (Shi et al., 2013) |
| | | | 1 wt% | 0.35 (s) ∼0.30 (l) | | | | |
| | | | 2 wt% | 0.65 (s) ∼0.32 (l) | | | | |
| | | | 5 wt% | ∼1.75 (s) ∼1.25 (l) | | | | |
| | | | 10 wt% | ∼2.7 (s) ∼2.10 (l) | | | | |
| | | | n-nonacosane/ Graphene | n-nonacosane/ Graphene | | | | |
| | | | 1 wt% | ∼0.25 (s) ∼0.23 (l) | | | | |
| | | | 2 wt% | ∼0.27 (s) ∼0.26 (l) | | | | |
| | | | 5 wt% | ∼0.28(s) ∼0.23 (l) | | | | |
| | | | 10 wt% | ∼0.5 (s) ∼0.15 (l) | | | | |
| Erythritol | SG EG Ni | SG: 8 $\mu$m EG: 6 $\mu$m Ni: 5 $\mu$m | 1-44 vol% | - | 290% at 17 vol% of SG | | | (Oya et al., 2013) |
| | | | - | - | 640% at 15 vol% of EG | | | |
| | | | - | - | 160% | | | |
| 1-octadecanol | Graphene | | 1 wt% | ∼0.5 | 140% at 4 wt% | | ∼15% decrease at 4 wt% | (Yavari et al., 2011) |
| | | | 2 wt% | ∼0.65 | | | | |

Table J.1: Summary of the developed carbon-additives NMs additives NCPCM.

| PCM | Dispersed NMs | | | $k_{NCPCM}$ (W/m.K) | $k_{NCPCM}$ (%) | $L_{NCPCM}$ (J/g) | $L_{NCPCM}$ (Increase/ Decrease) | Ref. |
|---|---|---|---|---|---|---|---|---|
| | Materials | Size | Loading content | | | | | |
| | | | 4 wt% | ∼0.91 | | | | |
| PA | CF | | 0.2 wt% | | 282.2% at 70 C | ∼203 | | (Wang et al., 2011) |
| | | | 0.5 wt% | | 305.60% | ∼204 | | |
| | | | 1.0 wt% | | 25.70% | ∼199 | | |
| | | | 2.0 wt% | | 33.60% | ∼197 | | |
| | | | 5.0 wt% | | 82.60% | ∼185 | | |
| Octadecane Hexadecane Paraffin | xGnP | | Hexadecane/ xGnP | Hexadecane/ xGnP | Hexadecane/ xGnP | Hexadecane/ xGnP | Hexadecane/ xGnP | (Jeon et al., 2012) |
| | | | 3.0 wt% | 0.992 | 49% | 217.33 (l) 214.34 (s) | 6.4% (l) 5.7% (s) | |
| | | | 5.0 wt% | 1.161 | 74% | - | - | |
| | | | Octadecane/ xGnP | Octadecane/ xGnP | Octadecane/ xGnP | Octadecane/ xGnP | Octadecane/ xGnP | |
| | | | 3.0 wt% | 0.873 | 76% | 240.92 (l) 237.29 (s) | 0.4% (l) 0.5% (s) | |
| | | | 5.0 wt% | 0.999 | 101% | - | - | |
| | | | Paraffin/ xGnP | Paraffin/ xGnP | Paraffin/ xGnP | Paraffin/ xGnP | Paraffin/ xGnP | |
| | | | 3.0 wt% | 0.454 | 28% | 140.99 (l) 142.70 (s) | 1.2% (l) 0.1% (s) | |
| | | | 5.0 wt% | 0.616 | 73% | - | | |
| $LiNO_3$/KCl | EG | | 10 wt% | ∼5.0 | | 178.10 | | (Huang et al., 2014b) |
| | | | 15 wt% | ∼7.1 | | 170.69 | | |
| | | | 20 wt% | ∼9.1 | | 164.50 | | |
| | | | 25 wt% | ∼11.1 | | 150.96 | | |
| | | | 30 wt% | ∼13.1 | | 142.41 | | |
| PA | rGO | | 0.6 wt% | 0.291 | 150% | 196.6 (l) 203.0 (s) | | (Akhiani et al., 2015) |
| | | | 1.0 wt% | 0.307 | | 187.5 (l) 194.3 (s) | | |
| | | | 1.5 wt% | 0.323 | | 184.9 (l) 190.0 (s) | | |
| | | | 2.0 wt% | 0.419 | | 181.9 (l) 189.3 (s) | | |
| 1-Hexadecanol | CNT GNP | D = 8-15 nm, L = 0.5-2 $\mu$m D = 5-10 $\mu$m, T = 4-20 nm | 1-Hexadecanol/ CNT | 1-Hexadecanol/ CNT | | 1-Hexadecanol/ CNT | | (Fan et al., 2015) |
| | | | 0.3 wt% | ∼0.25 (s) ∼0.16 (l) | | ∼228 | | |
| | | | 1.0 wt% | ∼0.256 (s) ∼0.17 (l) | | ∼226 | | |
| | | | 3.0 wt% | ∼0.31 (s) ∼0.20 (l) | | ∼223 | | |
| | | | 1-Hexadecanol/ GNP | 1-Hexadecanol/ GNP | | 1-Hexadecanol/ GNP | | |

Table J.1: Summary of the developed carbon-additives NMs additives NCPCM.

| PCM | Dispersed NMs | | | $k_{NCPCM}$ (W/m.K) | $k_{NCPCM}$ (%) | $L_{NCPCM}$ (J/g) | $L_{NCPCM}$ (Increase/ Decrease) | Ref. |
|---|---|---|---|---|---|---|---|---|
| | Materials | Size | Loading content | | | | | |
| | | | 0.3 wt% | ∼0.35 (s)<br>∼0.17 (l) | | ∼232 | | |
| | | | 1.0 wt% | ∼0.45 (s)<br>∼0.22 (l) | | ∼233 | | |
| | | | 3.0 wt% | ∼0.67 (s)<br>∼0.34 (l) | | ∼218 | | |
| LA | SWCNT | D = 2-5 nm,<br>L = 40-50 nm | 0.5 vol% | ∼0.24 | | 153 | | (Harish et al., 2015) |
| | | | 1.0 vol% | ∼0.26 | | 163 | | |
| | | | 1.5 vol% | ∼0.28 | | 165 | | |
| | | | 2.0 vol% | ∼0.30 | | 161 | | |
| NaCl/ $CaCl_2$/ $MgCl_2$ | EG | | 0.5 wt% | 1.583 | 134.84% | 204.1 | | (Tian et al., 2015) |
| | | | 1.0 wt% | 1.643 | 139.95% | 191.2 | | |
| | | | 3.0 wt% | 1.677 | 142.84% | 179.9 | | |
| | | | 5.0 wt% | 2.084 | 177.51% | 170.2 | | |
| Paraffin wax | CNF<br>GNP<br>Graphite | D = 400 nm,<br>L = 50 $\mu$m<br>T = 7 nm,<br>APS = 15 $\mu$m<br>APS = 50 nm | Paraffin wax/ CNF | Paraffin wax/ CNF | | Paraffin wax/ CNF | | (Bahiraei et al., 2017) |
| | | | 2.5 wt% | ∼0.32 | | ∼120 | | |
| | | | 5.0 wt% | ∼0.33 | | ∼115 | | |
| | | | 7.5 wt% | ∼0.36 | | ∼113 | | |
| | | | 10 wt% | ∼0.42 | | ∼111 | | |
| | | | Paraffin wax/ GNP | Paraffin wax/ GNP | | Paraffin wax/ GNP | | |
| | | | 2.5 wt% | ∼0.47 | | ∼121 | | |
| | | | 5.0 wt% | ∼0.56 | | ∼116 | | |
| | | | 7.5 wt% | ∼0.61 | | ∼114 | | |
| | | | 10 wt% | ∼0.70 | | ∼112 | | |
| | | | Paraffin wax/ Graphite | Paraffin wax/ Graphite | | Paraffin wax/ Graphite | | |
| | | | 2.5 wt% | ∼0.55 | | ∼122 | | |
| | | | 5.0 wt% | ∼1.1 | | ∼117 | | |
| | | | 7.5 wt% | ∼1.51 | | ∼115 | | |
| | | | 10 wt% | ∼2.7 | | ∼113 | | |
| Erythritol | EG | | 1.0 wt% | 0.8442 | | 119.3 | | (Li and Zhai, 2017) |
| | | | 2.0 wt% | 1.264 | | 119.2 | | |
| | | | 3.0 wt% | 2.4 | | 118.98 | | |
| | | | 4.0 wt% | 2.6743 | | 118.69 | | |
| RT-22HC | Graphene | $D_i$ 2um,<br>T < 2 nm | 0.05 wt% | 0.46 | | 161.43 (l)<br>168.68 (s) | | (Putra et al., 2017) |
| | | | 0.1 wt% | 0.92 | | 160.95 (l)<br>165.56 (s) | | |
| | | | 0.15 wt% | 1.1 | | 155.47 (l)<br>164.53 (s) | | |

Table J.1: Summary of the developed carbon-additives NMs additives NCPCM.

| PCM | Dispersed NMs | | | $k_{NCPCM}$ (W/m.K) | $k_{NCPCM}$ (%) | $L_{NCPCM}$ (J/g) | $L_{NCPCM}$ (Increase/ Decrease) | Ref. |
|---|---|---|---|---|---|---|---|---|
| | Materials | Size | Loading content | | | | | |
| | | | 0.20 wt% | 1.35 | | 155.37 (l)<br>163.98 (s) | | |
| | | | 0.25 wt% | 1.39 | | 155.20 (l)<br>163.98 (s) | | |
| | | | 0.30 wt% | 1.44 | | 155.98 (l)<br>162.44 (s) | | |
| n-Octadecane | xGnP | | 1.0 wt% | 0.91 | 225% | | | (Wi et al., 2017) |
| | | | 3.0 wt% | 0.98 | 250% | | | |
| | | | 5.0 wt% | 1.09 | 289% | | | |
| SA | rGO | | 0.5 wt% | 0.57 at 2.5 wt% | ∼50% at 2.5 wt% | 105 (l)<br>85.3 (s) | | (Advincula et al., 2018) |
| | | | 1.0 wt% | | | 155 (l)<br>163 (s) | | |
| | | | 1.5 wt% | | | 160 (l)<br>177 (s) | | |
| | | | 2.0 wt% | | | 146 (l)<br>156 (s) | | |
| | | | 2.5 wt% | | | 159 (l)<br>157 (s) | | |
| Erythritol | O-MWCNT<br>B-MWCNT<br>BB-MWCNT<br>A-MWCNT | | Erythritol/ O-MWCNT | Erythritol/ O-MWCNT | | Erythritol/ O-MWCNT | | (Shen et al., 2018) |
| | | | 1.0 wt% | ∼0.90 | | ∼345 | | |
| | | | 2.0 wt% | | | ∼344 | | |
| | | | 3.0 wt% | | | ∼340 | | |
| | | | 4.0 wt% | | | ∼322 | | |
| | | | 5.0 wt% | | | ∼320 | | |
| | | | Erythritol/ B-MWCNT | Erythritol/ B-MWCNT | | Erythritol/ B-MWCNT | | |
| | | | 1.0 wt% | ∼0.65 | | ∼360 | | |
| | | | 2.0 wt% | | | ∼351 | | |
| | | | 3.0 wt% | | | ∼331 | | |
| | | | 4.0 wt% | | | ∼330 | | |
| | | | 5.0 wt% | | | ∼329 | | |
| | | | Erythritol/ BB-MWCNT | Erythritol/ BB-MWCNT | | Erythritol/ BB-MWCNT | | |
| | | | 1.0 wt% | ∼0.74 | | ∼342 | | |
| | | | 2.0 wt% | | | ∼340 | | |
| | | | 3.0 wt% | | | ∼338 | | |
| | | | 4.0 wt% | | | ∼328 | | |
| | | | 5.0 wt% | | | ∼318 | | |
| | | | Erythritol/ A-MWCNT | Erythritol/ A-MWCNT | | Erythritol/ A-MWCNT | | |
| | | | 1.0 wt% | ∼0.75 | | ∼355 | | |
| | | | 2.0 wt% | | | ∼335 | | |
| | | | 3.0 wt% | | | ∼320 | | |
| | | | 4.0 wt% | | | ∼320 | | |
| | | | 5.0 wt% | | | ∼310 | | |

Table J.1: Summary of the developed carbon-additives NMs additives NCPCM.

| PCM | Dispersed NMs | | | $k_{NCPCM}$ (W/m.K) | $k_{NCPCM}$ (%) | $L_{NCPCM}$ (J/g) | $L_{NCPCM}$ (Increase/ Decrease) | Ref. |
|---|---|---|---|---|---|---|---|---|
| | Materials | Size | Loading content | | | | | |
| Paraffin | Graphene<br>MWCNT | | Paraffin/ Graphene | Paraffin/ Graphene | | | | (Zou et al., 2018) |
| | | | 0.2 wt% | ∼0.47 | | | | |
| | | | 0.5 wt% | ∼0.52 | | | | |
| | | | 0.8 wt% | ∼0.62 | | | | |
| | | | 1.0 wt% | ∼0.64 | | | | |
| | | | 1.2 wt% | ∼0.70 | | | | |
| | | | 1.5 wt% | ∼0.77 | | | | |
| | | | Paraffin/ MWCNT | Paraffin/ MWCNT | | | | |
| | | | 0.2 wt% | ∼0.43 | | | | |
| | | | 0.5 wt% | ∼0.50 | | | | |
| | | | 0.8 wt% | ∼0.53 | | | | |
| | | | 1.0 wt% | ∼0.54 | | | | |
| | | | 1.2 wt% | ∼0.55 | | | | |
| | | | 1.5 wt% | ∼0.57 | | | | |
| MA | GNP<br>MWCNT<br>NG | D = 5-10 $\mu$m,<br>T = 3-10 nm<br>D < 8 nm,<br>L = 10-30 $\mu$m<br>D = 3-6 $\mu$m,<br>T < 40 nm | MA/GNP | MA/GNP | MA/GNP | MA/GNP | | (He et al., 2019b) |
| | | | 1.0 wt% | 0.4405 (s)<br>0.2302 (l) | 101.51% (s)<br>24.70% (l) | 189.18 (m)<br>190.88 (s) | | |
| | | | 2.0 wt% | 0.4963 (s)<br>0.2302 (l) | 127.04% (s)<br>45.02% (l) | 187.39 (m)<br>190.77 (s) | | |
| | | | 3.0 wt% | 0.6039 (s)<br>0.2948 (l) | 176.26% (s)<br>59.70% (l) | 187.19 (m)<br>188.58 (s) | | |
| | | | MA/MWCNT | MA/MWCNT | MA/MWCNT | MA/MWCNT | | |
| | | | 1.0 wt% | 0.2923 (s)<br>0.1913 (l) | 33.71% (s)<br>3.63% (l) | 190.12 (m)<br>190.99 (s) | | |
| | | | 2.0 wt% | 0.2988 (s)<br>0.2026 (l) | 36.69% (s)<br>9.75% (l) | 191.99 (m)<br>192.19 (s) | | |
| | | | 3.0 wt% | 0.322 (s)<br>0.2083 (l) | 47.30% (s)<br>12.84% (l) | 188.47 (m)<br>188.21 (s) | | |
| | | | MA/NG | MA/NG | MA/NG | MA/NG | | |
| | | | 1.0 wt% | 0.2518 (s)<br>0.1899 (l) | 15.19% (s)<br>2.87% (l) | 191.27 (m)<br>191.15 (s) | | |
| | | | 2.0 wt% | 0.2746 (s)<br>0.1950 (l) | 25.62% (s)<br>5.63% (l) | 190.67 (m)<br>191.04 (s) | | |
| | | | 3.0 wt% | 0.3148 (s)<br>0.2059 (l) | 44.01% (s)<br>11.54% (l) | 188.90 (m)<br>188.85 (s) | | |
| Paraffin wax | Graphene<br>GO<br>EG | T = 0.55-3.8 nm<br>T = 0.8-1.2 nm | Paraffin/ Graphene | Paraffin/ Graphene | | Paraffin/ Graphene | | (Li et al., 2019b) |
| | | | 0.5 wt% | 0.266 | | 131.60 | | |
| | | | 1.0 wt% | 0.289 | | 118.51 | | |
| | | | 1.5 wt% | 0.312 | | 106.12 | | |
| | | | 2.0 wt% | 0.348 | | 98.33 | | |

Table J.1: Summary of the developed carbon-additives NMs additives NCPCM.

| PCM | Dispersed NMs | | | $k_{NCPCM}$ (W/m.K) | $k_{NCPCM}$ (%) | $L_{NCPCM}$ (J/g) | $L_{NCPCM}$ (Increase/ Decrease) | Ref. |
|---|---|---|---|---|---|---|---|---|
| | Materials | Size | Loading content | | | | | |
| | | | Paraffin/ GO | Paraffin/ GO | | Paraffin/ GO | | |
| | | | 0.5 wt% | 0.244 | | 129.41 | | |
| | | | 1.0 wt% | 0.266 | | 119.57 | | |
| | | | 1.5 wt% | 0.286 | | 108.69 | | |
| | | | 2.0 wt% | 0.309 | | 100.76 | | |
| | | | Paraffin/ EG | Paraffin/ EG | | Paraffin/ EG | | |
| | | | 0.5 wt% | 0.224 | | 137.56 | | |
| | | | 1.0 wt% | 0.239 | | 125.47 | | |
| | | | 1.5 wt% | 0.252 | | 113.98 | | |
| | | | 2.0 wt% | 0.272 | | 101.84 | | |